DISSERTATION

FROM FORESTS TO THE REMOTE OCEAN TO SMOKE PLUMES: AEROSOL MICROPHYSICS IN DIVERSE ENVIRONMENTS

Submitted by

Anna Lily Hodshire

Department of Atmospheric Science

In partial fulfillment of the requirements

For the Degree of Doctor of Philosophy

Colorado State University

Fort Collins, Colorado

Spring 2020

Doctoral Committee:

Advisor: Jeffrey R. Pierce
Co-Advisor: Shantanu H. Jathar

Jeffrey L. Collett
Delphine K. Farmer
Sonia M. Kreidenweis

ABSTRACT

FROM FORESTS TO THE REMOTE OCEAN TO SMOKE PLUMES:

AEROSOL MICROPHYSICS IN DIVERSE ENVIRONMENTS

Atmospheric aerosol are produced from terrestrial and marine sources, exist throughout the troposphere, and have impacts on climate and human health. Aerosol may be emitted directly or form in the atmosphere through gas-to-particle conversion. Once emitted, these particles are hardly static: they may grow or shrink through condensation or evaporation of vapors, coagulate together, and eventually settle out of the atmosphere through dry or wet deposition. This dissertation focuses upon the former processes, also known as aerosol microphysics: how do aerosol form, grow through condensation, shrink through evaporation, and coagulate within the atmosphere? How does the relative importance of each process change for different conditions, such as in an ambient forested environment or within biomass burning smoke plumes?

First, we model oxidation flow reactor (OFR) size distribution data taken from ambient data in a ponderosa pine forest and Amazonia with an aerosol microphysics box model. We find "the best model-to-measurement agreement when the accommodation coefficient of the larger particles (D_p > 60 nm) was 0.1 or lower (with an accommodation coefficient of 1 for smaller particles), which suggests a diffusion limitation in the larger particles. When using these low accommodation-coefficient values, the model agrees with measurements when using a published H_2SO_4-organics nucleation mechanism and previously published values of rate constants for gas-phase oxidation reactions. Further, gas-phase fragmentation was found to have a significant impact upon the size distribution, and including fragmentation was necessary for accurately simulating

the distributions in the OFR. The model was insensitive to the value of the reactive uptake coefficient on these aging timescales. Monoterpenes and isoprene could explain 24 %–95% of the observed change in total volume of aerosol in the OFR, with ambient semivolatile and intermediate-volatility organic compounds (S/IVOCs) appearing to explain the remainder of the change in total volume" (Chapter 2, overview).

Then we test the impact of methanesulfonic acid (MSA) upon global aerosol size distributions, using the GEOS-Chem chemical transport model coupled to an aerosol microphysics model. We test volatility assumptions of MSA, treating it as either having a constant volatility or a dynamic volatility range based upon temperature and relative humidity. When using the volatility parameterization (likely to be the most realistic treatment of MSA), "including MSA in the model changes the global annual averages at 900 hPa of submicron aerosol mass by 1.2 %, N3 (number concentration of particles greater than 3 nm in diameter) by −3.9% (non-nucleating) or 112.5% (nucleating), N80 by 0.8% (non-nucleating) or 2.1% (nucleating), the cloud-albedo aerosol indirect effect (AIE) by −8.6 mW m^{-2} (non-nucleating) or −26 mW m^{-2} (nucleating), and the direct radiative effect (DRE) by −15 mW m^{-2} (non-nucleating) or −14 mW m^{-2} (nucleating). The sulfate and sulfuric acid from DMS oxidation produces 4–6 times more submicron mass than MSA does, leading to approximately a 10 times stronger cooling effect in the DRE. But the changes in N80 are comparable between the contributions from MSA and from DMS-derived sulfate/sulfuric acid, leading to comparable changes in the cloud-albedo AIE" (Chapter 3, overview). We also perform model-measurement comparisons to ship-based size distribution observations and MSA mass observations from the ATom field campaign. We find that cases that allow MSA to nucleate best match the ship-based size distribution observations and that cases that use the volatility parameterization best match the ATom MSA mass observations.

The final sections of this dissertation focus on biomass burning smoke plume aerosol observations and modeling. First, we review all available field and laboratory data on near-field (within a few hours of emission) aging of aerosol mass and composition markers. On average, the field data show no increase in dilution-corrected aerosol mass with aging but laboratory data show a net increase in aerosol mass with aging. Conversely, both field and laboratory data show clear changes in compositional markers that are indicative of aerosol aging. Based on these data as well as current research directions, we propose the following hypotheses for why laboratory and field measurements do not agree on aerosol mass enhancements: (1) differences in emissions and chemistry, (2) differences in dilution rates and entrainment, (3) losses in chambers and lines within laboratory campaigns, and (4) differences in timing of the initial measurement. There is no clear trend in the field and laboratory data for hypothesis (1), emissions and chemistry, to allow us to determine how it impacts the field-laboratory discrepancies. Laboratory experiments are diluted to a ~fixed value and then not diluted further, potentially limiting losses to evaporation compared to field burns that dilute continuously. As well, laboratory burns do not entrain variable background air that may further impact partitioning rates. Thus hypothesis (2), dilution rates and entrainment, could help explain the relative increases in mass for laboratory campaigns. Laboratory experiments do suffer from particle wall and line losses and vapor wall and line partitioning. Previously published laboratory experiments (at the time of Chapter 4's publication date) had been corrected for particle wall loss but not vapor wall or tubing partitioning. As vapors lost to walls and tubing would have been able to participate in SOA formation, hypothesis (3) leads to increases in laboratory mass enhancement ratios, increasing the field-laboratory discrepancy. Finally, laboratory campaigns are able to capture all stages of photochemical aging, with "time=0" set to when aging begins. Conversely, field campaigns are unable to capture initial emissions and

instead typically measure ~10-60 minutes downwind of emission. If fast initial chemistry and SOA production occurs before the time of the initial field observation, then the field mass enhancement will be biased low. So hypothesis (4), differences in timing of the initial measurement, would potentially increase field mass enhancements and lead to closer field-laboratory agreement.

We finally test hypothesis (2) and (4) using first a theoretical modeling framework and then field observations. For the theoretical modeling framework, we simulate fires between 10^{-4} and 100 km^2 in initial size using an aerosol microphysics model that simulates plume dilution with Gaussian dispersion. The plumes are allowed to dilute into aerosol background concentrations between 0-50 $\mu g\ m^{-3}$. In our simulations, we find that "aging organic aerosol [OA] mass is controlled by competition between OA evaporation and secondary organic aerosol [SOA] condensation. Large, slowly diluting plumes evaporate little in our base set of simulations, which may allow for net increases in mass, extinction (E), cloud condensation nuclei (CCN) , and geometric mean diameter (D_g) from SOA condensation. Smaller, quickly diluting fire plumes lead to faster evaporation, which favors decreases in mass, E, CCN, and D_g. However, the SOA fraction of the smoke OA increases more rapidly in smaller fires due to faster primary organic aerosol evaporation leading to more SOA precursors. Net mass changes for smaller fires depend on background OA concentrations; increasing background aerosol concentrations decrease evaporation rates. Although coagulation does not change mass, it can decrease the number of particles in large/slowly diluting plumes, increasing D_g and E, and decreasing σ_g" (Chapter 5, overview).

Finally, we examine aircraft data from the Biomass Burning Observations Project (BBOP) field campaign that took place in July-August of 2013. BBOP sampled wildfire smoke in pseudo-Lagrangian transects in the Pacific Northwest. From measurements of five fires, we are able to

show that the initial mass of each region, determined from the first transect, “can help predict changes in smoke aerosol aging markers, number and diameter. The initial smoke mass can serve as a proxy for plume size/thickness. Dilution can in turn impact photochemistry and evaporation of aerosol. Plume cores generally have higher concentrations than edges, and we find that edges are more likely to undergo higher ozone production as well as new particle formation. We find that particle aging, evaporation, and coagulation has occurred before the first measurement, with less aging and evaporation and more coagulation occurring for thicker plumes and in plume cores (relative to edges) by the time of the first measurement” (Chapter 6, overview).

ACKNOWLEDGEMENTS

This work is the result of many remarkable people supporting me. I feel amazingly lucky to have entered into supportive communities throughout my time in school, from the physics department at Weber State University to the Colorado State University atmospheric science department to the atmospheric chemistry and aerosol communities. I greatly appreciate every scientist who has worked with me for their patience, kindness, and generosity with their time. In particular, I am indebted to Dr. John Armstrong for steering me towards atmospheric science and air quality research. I cannot thank my friends and family enough for their continual support throughout my years at WSU and CSU and I am forever grateful to my mother for encouraging me to move to Colorado. I especially thank the Pierce group, who has been a wonderful source of support, knowledge, and fun. I've had the extreme fortune of being able to play in several bands throughout college and grad school which not only helped me feel sane and balanced but also led to me meeting my incredible husband, Phil. Phil has inspired me to become a better scientist, person, and friend, and I eagerly await our many years ahead of us. Finally, I cannot thank my PhD advisor Jeff Pierce enough for his unwavering support, patience, teaching, mentoring, musical enthusiasm, and assistance in professional development. He provided me with amazing opportunities throughout my PhD and I greatly appreciate every moment of them.

"Clean out your desk, put your papers away cause class is almost done.
This is chemistry plus calisthenics."

— Blackalicious

DEDICATION

This work is dedicated to my mother, Jan, and my cat, Dee.

TABLE OF CONTENTS

CHAPTER 1
INTRODUCTION TO AEROSOL MICROPHYSICS

Aerosols are ubiquitous throughout the earth's atmosphere and play an important role in climate (Boucher et al., 2013; Charlson et al., 1992). Particles have both direct and indirect climate impacts. In the direct radiative effect (DRE), aerosol can absorb and/or scatter incoming solar radiation ((Boucher et al., 2013; Charlson et al., 1992)), altering the earth's radiation budget. In the aerosol indirect effect (AIE), particles modify cloud reflectivity through changes in cloud droplet number concentrations (CDNC; Twomey, 1974). The size and composition of the particles influence both the DRE and AIE: peak scattering and absorption efficiencies are reached between 100 nm-1 μm in diameter, dependent upon composition (Seinfeld and Pandis, 2006). Only particles capable of acting as cloud condensation nuclei (CCN) influence CDNC; typically particles with diameters larger than 40-100 nm may act as CCN but the activation diameter of a particle depends on its hygroscopicity, which is a direct function of composition (Petters and Kreidenweis, 2007). As well, particle size governs its deposition (loss) rates both in the environment (Seinfeld and Pandis, 2006) and within the respiratory tract (Kodros et al., 2018).

Particles can be emitted directly from land and marine surfaces (such as dust and sea spray; Song and Carmichael, 1999), emitted directly by combustions sources (such as wildfires, cookstoves, power plants, and vehicles; Jathar et al., 2014), or created directly in the atmosphere from gas-to-particle conversion, also known as nucleation or new particle formation (Kulmala et al., 2004; Spracklen et al., 2008). Particle composition may be comprised of inorganic compounds (such as sulfate, chlorine, ammonium, nitrate, and many trace metals; Cruz and Pandis, 1998) and carbonaceous compounds that include organics and black carbon (Shrivastava et al., 2017; Cooke and Wilson, 1996). Organic aerosol (OA) comprises a large fraction of submicron aerosol mass

(Murphy et al., 2006; Zhang et al., 2007; Jimenez et al., 2009)). Much of organic aerosol comes from secondary organic aerosol (SOA) production ((Shrivastava et al., 2017)). Volatile organic compounds (VOCs), compounds with saturation concentrations (C*) $>\sim 10^7$ μg m^{-3} are emitted into the atmosphere (Guenther et al., 1995). A portion of these vapors can react with atmospheric oxidants (primarily OH, O_c, and NO_3·) (Atkinson and Arey, 2003) to form lower-volatility products that may then partition to the condensed phase, forming SOA (Pankow, 1994). The absolute number of distinct VOC compounds is unknown but may range well above 10^5 compounds (Goldstein and Galbally, 2007), making constraining SOA production a complicated problem. Furthermore, OA in the particulate phase spans a wide range of volatilities from extremely low volatility organic compounds (ELVOCs) and low volatility organic compounds (LVOCs), where nearly all of the compounds mass exists in the particulate phase at equilibrium, to semi-volatile organic compounds (SVOCs), which have non-trivial fractions of the species mass exist in both the gaseous and particulate phases (Riipinen et al., 2011; Pierce et al., 2011; Ehn et al., 2012; Murphy et al., 2014). SVOCs may have net evaporation to the gas-phase if dilution occurs or temperature increases (Donahue et al., 2006). Finally, the details of SOA condensation and OA evaporation affect the size distribution of the particles, which impacts their climatic effects.

The focus of this dissertation is broadly upon aerosol microphysics: how do aerosol form, grow through condensation, shrink through evaporation, and coagulate within the atmosphere? What is the relative importance of each process? To test these questions, we examine and model evolving size distributions in a ponderosa pine forest and the Amazonian rainforest; we estimate the influence of methanesulfonic acid on global size distributions; and we examine smoke plumes from theory to field measurements.

Chapter 2 focuses on oxidation flow reactor (OFR) size distribution data taken during field campaigns within a ponderosa pine forest in Colorado, USA, and within central Amazonia. The OFR experimentally simulates atmospheric OH aging under short residence times (2-4 minutes, typically) through the use of high OH concentrations, leading to the equivalent of hours to days of atmospheric OH exposure within the residence time (Palm et al., 2016). We use the aerosol microphysics model TOMAS (TwO-Moment Aerosol Section model; (Adams and Seinfeld, 2002)) coupled to a volatility basis set (VBS) framework (Donahue et al., 2006), TOMAS-VBS, to constrain the observed nucleation and growth of both the pre-existing and newly formed particles within both campaigns for observations <1 day of equivalent aging. The model simulates condensation, coagulation, and nucleation and is coupled to a volatility basis set in order to track volatility of both the aerosol and gas phases. In order to fit the measurements, we test (1) nucleation rate constants and different nucleation schemes; (2) the rate constants of gas-phase functionalization and fragmentation of the organic vapors with OH; (3) the reactive uptake coefficient for heterogeneous fragmentation reactions with OH; and (4) an effective accommodation coefficient that accounts for possible gas-phase diffusion limitations for particles >60 nm in diameter, as we observed that the growth rates of the accumulation mode are slower than that of the newly formed nucleation/Aiken mode.

Chapter 3 asks the question "what impact does methanesulfonic acid (MSA) have upon global size distributions and associated radiative impacts?" Dimethylsulfide (DMS) is emitted from oceans and oxidizes to form primarily SO_2 and MSA (Barnes et al., 2006). SO_2 formation from DMS oxidation, and the subsequent formation of sulfuric acid from SO_2 oxidation, has been included within existing aerosol size-resolved global chemical transport models. This study is a first look at including MSA from DMS oxidation in an aerosol size-resolved global chemical

transport model, the GEOS-Chem chemical transport model (http://geos-chem.org; last accessed 21 November 2019) coupled to the 15 size-bin version of TOMAS. Uncertainties remain upon the effective volatility of MSA and whether MSA can participate in nucleation (Bork et al., 2014). To test these uncertainties, we run a suite of cases in which MSA is considered to be ideally nonvolatile everywhere (similar to an ELVOC described above, ideally semivolatile everywhere (similar to an SVOC described above), or is allowed to vary between nonvolatile, semivolatile, and volatile, dependent upon temperature and relative humidity. The variable volatility is parameterized with the Extended Aerosol Inorganics Model (E-AIM; http://www.aim.env.uea.ac.uk/aim/aim.php; last accessed 21 November 2019). For instances in which MSA is nonvolatile, we further run separate simulations in which MSA is or is not allowed to participate in nucleation, with the assumed nucleation efficacy of sulfuric acid (an upper bound on MSA's nucleating ability). We also isolate the size distribution and radiative impacts of sulfuric acid and sulfate from DMS oxidation for comparison.

Chapters 4-6 form a cohesive unit upon smoke observations and modeling of near-field (within a few hours of emission) aging. Fires emit vapors and particles to the atmosphere, (e.g. (Akagi et al., 2011; Yokelson et al., 2011), and these emissions can rapidly evolve as smoke plumes travel downwind, diluting and entraining background air (e.g. (Akagi et al., 2012a; Alvarado et al., 2015; Hecobian et al., 2010; Cubison et al., 2011a; May et al., 2015). If the vapors oxidize through photochemical aging and form lower-volatility products, they can condense upon smoke aerosol, increasing particle mass and size. Conversely, as the plume entrains background air and becomes more dilute, semivolatile particulate compounds can evaporate to the gas-phase, and this evaporation leads to decreases in smoke particle mass and size. Furthermore, smoke particles can coagulate together, leading to decreases in particle number (which may impact total

CCN numbers attributable to smoke) but increases in the mean particle size. Better understanding the interplay between dilution, photochemical aging, and aerosol microphysics within smoke is explored throughout Chapters 4-6.

Chapter 4 is a review of laboratory and field observations of near-field aging of smoke aerosol mass enhancement ratios,

$$Mass_{ER} = \frac{Final\ mass}{Initial\ Mass} \quad \text{(Eq. 1.1)}$$

where a $Mass_{ER}$>1 indicates an increase in aerosol mass over time. Similarly, we looked at the evolution smoke composition enhancement ratios for O:C and f_{44}/f_{60}, both calculated in a similar way as Eq 1.1. Enhancement ratios greater than 1 for either of these metrics shows that the organic aerosol is becoming more oxygenated with time in the plume. To date, most field campaigns show little change in dilution-corrected mass ($Mass_{ER} \cong 1$) with time after emission (Brito et al., 2014; Capes et al., 2008; Collier et al., 2016; Cubison et al., 2011b; Forrister et al., 2015; Garofalo et al., 2019; Hecobian et al., 2011; Liu et al., 2016; May et al., 2015; Morgan et al., 2019; Sakamoto et al., 2015; Zhou et al., 2017) with a few showing decreases ($Mass_{ER} < 1$) (Akagi et al., 2012b; Hobbs et al., 2003; Jolleys et al., 2012, 2015; May et al., 2015) and a few showing increases ($Mass_{ER} > 1$) (Cachier et al., 1995; Formenti et al., 2003; Liu et al., 2016; Nance et al., 1993; Reid et al., 1998; Vakkari et al., 2014, 2018; Yokelson et al., 2009). Conversely, laboratory studies typically show increases in mass (Hennigan et al., 2011; Ortega et al., 2013; Tkacik et al., 2017; Ahern et al., 2019), with relatively few cases showing losses or no change in mass. To add to the puzzle, essentially all observations in both the field and laboratory studies show evidence of increasing oxidation as the smoke ages, as seen by increases in O:C and f_{44}/f_{60} enhancement ratios. This discrepancy between field and laboratory mass enhancements is the driver of Chapter 4, which seeks to provide hypotheses as to why field and laboratory observations disagree on mass

enhancements. Although Chapter 4 is ostensibly not focused upon aerosol microphysics, microphysics is important for understanding mass and composition, as SOA condensation and OA evaporation will alter smoke size distributions, mass, and composition. We present four primary hypotheses for differences between field and laboratory smoke aging observations within this chapter: (1) differences in emissions and chemistry, (2) differences in dilution rates and entrainment, (3) losses in chambers and lines within laboratory campaigns, and (4) differences in timing of the initial measurement.

Chapter 5 examines hypothesis (2) of Chapter 4, differences in dilution rates and entrainment, in a theoretical modeling framework. We explore the relationships between fire size, dilution rate, and entrainment of background aerosol on particle coagulation, OA evaporation, and secondary organic aerosol (SOA) condensation in diluting smoke plumes. We model fictitious fires between 10^{-4}-100 km^2 in initial size that dilute into backgrounds of 0-50 $\mu g\ m^{-3}$ of nonvolatile organic aerosol such that we test each permutation of fire size and background concentration. We again use the TOMAS-VBS aerosol microphysics model. Each smoke plume simulates dilution within a Gaussian dispersion framework, following (Bian et al., 2017). We test variable background concentrations as entrainment of more polluted background air is anticipated to slow partitioning to the gas phase. We examine smoke OA mass, geometric mean diameter (D_g), peak lognormal modal width (σ_g), particle extinction (E), and CCN concentrations after four hours of aging. We also provide sensitivity studies to the rate of gas-phase oxidation, the number of volatility bins dropped per OH reaction, atmospheric stability (which will impact dilution rates), the accommodation coefficient (again assumed to be a proxy for diffusion limitations), and total aging period. We do acknowledge that the conclusions of Chapter 5 are limited as we chose to hold important variables fixed, such as temperature, mass flux, injection height, wind speed, and

OH concentrations. Furthermore, we do not compare our simulations to observational data. However, we hope that our framework here can motivate further smoke-plume research inclusive of the effects of fire size, dilution rates, and background OA concentrations.

Directly motivated by the work of Chapter 4 and 5, we perform an observational study in Chapter 6 of smoke plumes from the Biomass Burning Observation Project (BBOP) field campaign (Kleinman and Sedlacek, 2016). BBOP took aircraft observations of smoke plumes from wildfires in the Pacific Northwest in 2013. We use measurements of aerosol properties and ozone from six research flights sampling wildfires downwind in pseudo-Lagrangian transects that are provided on 1-second sampling rate. The high time resolution allows us to parse each smoke plume transect into core, edge, or intermediate regions, based on background-corrected CO values, as it is anticipated that the edge of a smoke plume may dilute and mix with background air more rapidly than the core of a plume.

In Chapter 7, we provide a brief synthesis of our work and discuss future work that is directly motivated by our smoke research.

REFERENCES

Adams, P. J. and Seinfeld, J. H.: Predicting global aerosol size distributions in general circulation models, J. Geophys. Res., 107(D19), 4370–4370, doi:10.1029/2001JD001010, 2002.

Ahern, A. T., Robinson, E. S., Tkacik, D. S., Saleh, R., Hatch, L. E., Barsanti, K. C., Stockwell, C. E., Yokelson, R. J., Presto, A. A., Robinson, A. L., Sullivan, R. C. and Donahue, N. M.: Production of Secondary Organic Aerosol During Aging of Biomass Burning Smoke From Fresh Fuels and Its Relationship to VOC Precursors, J. Geophys. Res. D: Atmos., 124(6), 3583–3606, doi:10.1029/2018JD029068, 2019.

Akagi, S. K., Yokelson, R. J., Wiedinmyer, C., Alvarado, M. J., Reid, J. S., Karl, T., Crounse, J. D. and Wennberg, P. O.: Emission factors for open and domestic biomass burning for use in atmospheric models, Atmos. Chem. Phys., 11(9), 4039–4072 [online] Available from: https://www.atmos-chem-phys.net/11/4039/2011/acp-11-4039-2011.pdf, 2011.

Akagi, S. K., Craven, J. S., Taylor, J. W., McMeeking, G. R., Yokelson, R. J., Burling, I. R., Urbanski, S. P., Wold, C. E., Seinfeld, J. H., Coe, H. and Others: Evolution of trace gases and particles emitted by a chaparral fire in California, Atmos. Chem. Phys., 12(3), 1397–1421 [online] Available from: https://www.atmos-chem-phys.net/12/1397/2012/acp-12-1397-2012.pdf, 2012a.

Akagi, S. K., Craven, J. S., Taylor, J. W., Mcmeeking, G. R., Yokelson, R. J., Burling, I. R., Urbanski, S. P., Wold, C. E., Seinfeld, J. H., Coe, H., Alvarado, M. J. and Weise, D. R.: Evolution of trace gases and particles emitted by a chaparral fire in California, Atmos. Chem. Phys., 12, 1397–1421, doi:10.5194/acp-12-1397-2012, 2012b.

Alvarado, M. J., Lonsdale, C. R., Yokelson, R. J., Akagi, S. K., Coe, H., Craven, J. S., Fischer, E. V., McMeeking, G. R., Seinfeld, J. H., Soni, T., Taylor, J. W., Weise, D. R. and Wold, C. E.: Investigating the links between ozone and organic aerosol chemistry in a biomass

burning plume from a prescribed fire in California chaparral, Atmos. Chem. Phys., 15(12), 6667–6688, doi:10.5194/acp-15-6667-2015, 2015.

Atkinson, R. and Arey, J.: Atmospheric Degradation of Volatile Organic Compounds Atmospheric Degradation of Volatile Organic Compounds, Chem. Rev., 103(3), 4605–4638, doi:10.1021/cr0206420, 2003.

Barnes, I., Hjorth, J. and Mihalapoulos, N.: Dimethyl sulfide and dimethyl sulfoxide and their oxidation in the atmosphere, Chem. Rev., 106(3), 940–975, doi:10.1021/cr020529+, 2006.

Bian, Q., Jathar, S. H., Kodros, J. K., Barsanti, K. C., Hatch, L. E., May, A. A., Kreidenweis, S. M. and Pierce, J. R.: Secondary organic aerosol formation in biomass-burning plumes: Theoretical analysis of lab studies and ambient plumes, Atmos. Chem. Phys., 17(8), 5459–5475, doi:10.5194/acp-17-5459-2017, 2017.

Bork, N., Elm, J., Olenius, T. and Vehkamäki, H.: Methane sulfonic acid-enhanced formation of molecular clusters of sulfuric acid and dimethyl amine, Atmos. Chem. Phys., 14(22), 12023–12030, doi:10.5194/acp-14-12023-2014, 2014.

Boucher, O., Randall, D., Artaxo, P. and Bretherton, C.: Clouds and aerosols, Climate change 2013 [online] Available from: https://pure.mpg.de/rest/items/item_2007900/component/file_2007948/content, 2013.

Brito, J., Rizzo, L. V., Morgan, W. T., Coe, H., Johnson, B., Haywood, J., Longo, K., Freitas, S., Andreae, M. O. and Artaxo, P.: Ground-based aerosol characterization during the South American Biomass Burning Analysis (SAMBBA) field experiment, Atmospheric Chemistry and Physics, 14(22), 12069–12083, doi:10.5194/acp-14-12069-2014, 2014.

Cachier, H., Liousse, C., Buat-Menard, P. and Gaudichet, A.: Particulate content of savanna fire emissions, J. Atmos. Chem., 22(1-2), 123–148, doi:10.1007/BF00708185, 1995.

Capes, G., Johnson, B., McFiggans, G., Williams, P. I., Haywood, J. and Coe, H.: Aging of biomass burning aerosols over West Africa: Aircraft measurements of chemical composition, microphysical properties, and emission ratios, J. Geophys. Res. D: Atmos., 113(23), 0–15, doi:10.1029/2008JD009845, 2008.

Charlson, R. J., Schwartz, S. E., Hales, J. M., Cess, R. D., Coakley, J. A., Jr, Hansen, J. E. and Hofmann, D. J.: Climate forcing by anthropogenic aerosols, Science, 255(5043), 423–430, doi:10.1126/science.255.5043.423, 1992.

Collier, S., Zhou, S., Onasch, T. B., Jaffe, D. A., Kleinman, L., Sedlacek, A. J., Briggs, N. L., Hee, J., Fortner, E., Shilling, J. E., Worsnop, D., Yokelson, R. J., Parworth, C., Ge, X., Xu, J., Butterfield, Z., Chand, D., Dubey, M. K., Pekour, M. S., Springston, S. and Zhang, Q.: Regional Influence of Aerosol Emissions from Wildfires Driven by Combustion Efficiency: Insights from the BBOP Campaign, Environmental Science and Technology, 50(16), 8613–8622, doi:10.1021/acs.est.6b01617, 2016.

Cooke, W. F. and Wilson, J. J. N.: A global black carbon aerosol model, J. Geophys. Res., 101(D14), 19395–19409, doi:10.1029/96JD00671, 1996.

Cruz, C. N. and Pandis, S. N.: The effect of organic coatings on the cloud condensation nuclei activation of inorganic atmospheric aerosol, J. Geophys. Res., 103(D11), 13111–13123, doi:10.1029/98JD00979, 1998.

Cubison, M. J., Ortega, A. M., Hayes, P. L., Farmer, D. K., Day, D., Lechner, M. J., Brune, W. H., Apel, E., Diskin, G. S., Fisher, J. A. and Others: Effects of aging on organic aerosol from open biomass burning smoke in aircraft and laboratory studies, Atmos. Chem. Phys., 11(23), 12049–12064 [online] Available from: https://www.atmos-chem-phys.net/11/12049/2011/acp-11-12049-2011.pdf, 2011a.

Cubison, M. J., Ortega, A. M., Hayes, P. L., Farmer, D. K., Day, D., Lechner, M. J., Brune, W. H., Apel, E., Diskin, G. S., Fisher, J. A., Fuelberg, H. E., Hecobian, A., Knapp, D. J., Mikoviny, T., Riemer, D., Sachse, G. W., Sessions, W., Weber, R. J., Weinheimer, A. J., Wisthaler, A. and Jimenez, J. L.: Effects of aging on organic aerosol from open biomass burning smoke in aircraft and laboratory studies, Atmos. Chem. Phys., 11(23), 12049–12064, doi:10.5194/acp-11-12049-2011, 2011b.

Donahue, N. M., Robinson, A. L., Stanier, C. O. and Pandis, S. N.: Coupled Partitioning, Dilution, and Chemical Aging of Semivolatile Organics, Environ. Sci. Technol., 40(8), 2635–2643, doi:10.1021/es052297c, 2006.

Ehn, M., Kleist, E., Junninen, H., Petäjä, T., Lönn, G., Schobesberger, S., Dal Maso, M., Trimborn, A., Kulmala, M., Worsnop, D. R., Wahner, A., Wildt, J. and Mentel, T. F.: Gas phase formation of extremely oxidized pinene reaction products in chamber and ambient air, Atmos. Chem. Phys., 12(11), 5113–5127, doi:10.5194/acp-12-5113-2012, 2012.

Formenti, P., Elbert, W., Maenhaut, W., Haywood, J., Osborne, S. and Andreae, M. O.: Inorganic and carbonaceous aerosols during the Southern African Regional Science Initiative (SAFARI 2000) experiment: Chemical characteristics, physical properties, and emission data for smoke from African biomass burning, J. Geophys. Res. D: Atmos., 108(D13), doi:10.1029/2002JD002408, 2003.

Forrister, H., Liu, J., Scheuer, E., Dibb, J., Ziemba, L., Thornhill, K. L., Anderson, B., Diskin, G., Perring, A. E., Schwarz, J. P., Campuzano-Jost, P., Day, D. A., Palm, B. B., Jimenez, J. L., Nenes, A. and Weber, R. J.: Evolution of brown carbon in wildfire plumes, Geophys. Res. Lett., 42(11), 4623–4630, doi:10.1002/2015GL063897, 2015.

Garofalo, L., Pothier, M. A., Levin, E. J. T., Campos, T., Kreidenweis, S. M. and Farmer, D. K.: Emission and Evolution of Submicron Organic Aerosol in Smoke from Wildfires in the Western United States, ACS Earth and Space Chemistry, acsearthspacechem.9b00125, doi:10.1021/acsearthspacechem.9b00125, 2019.

Goldstein, A. H. and Galbally, I. E.: Known and unexplored organic constituents in the earth's atmosphere, Environmental Science and Technology, 41(5), 1514–1521, doi:10.1021/es072476p, 2007.

Guenther, A., Hewitt, C. N., Erickson, D., Fall, R., Geron, C., Graedel, T., Harley, P., Klinger, L., Lerdau, M., Mckay, W. A., Pierce, T., Scholes, B., Steinbrecher, R., Tallamraju, R., Taylor, J. and Zimmerman, P.: A global model of natural volatile organic compound emissions, J. Geophys. Res., 100(D5), 8873, doi:10.1029/94JD02950, 1995.

Hecobian, A., Zhang, X., Zheng, M., Frank, N., Edgerton, E. S. and Weber, R. J.: Water-Soluble Organic Aerosol material and the light-absorption characteristics of aqueous extracts measured over the Southeastern United States, Atmos. Chem. Phys., 10(13), 5965–5977, doi:10.5194/acp-10-5965-2010, 2010.

Hecobian, A., Liu, Z., Hennigan, C. J., Huey, L. G., Jimenez, J. L., Cubison, M. J., Vay, S., Diskin, G. S., Sachse, G. W., Wisthaler, A., Mikoviny, T., Weinheimer, A. J., Liao, J., Knapp, D. J., Wennberg, P. O., Urten, A., Crounse, J. D., Clair, J. S., Wang, Y. and Weber, R. J.: Comparison of chemical characteristics of 495 biomass burning plumes intercepted by the NASA DC-8 aircraft during the ARCTAS/CARB-2008 field campaign, Atmos. Chem. Phys., 11, 13325–13337, doi:10.5194/acp-11-13325-2011, 2011.

Hennigan, C. J., Miracolo, M. A., Engelhart, G. J., May, A. A., Presto, A. A., Lee, T., Sullivan, A. P., McMeeking, G. R., Coe, H., Wold, C. E., Hao, W. M., Gilman, J. B., Kuster, W. C., De

Gouw, J., Schichtel, B. A., Collett, J. L., Kreidenweis, S. M. and Robinson, A. L.: Chemical and physical transformations of organic aerosol from the photo-oxidation of open biomass burning emissions in an environmental chamber, Atmos. Chem. Phys., 11(15), 7669–7686, doi:10.5194/acp-11-7669-2011, 2011.

Hobbs, P. V., Sinha, P., Yokelson, R. J., Christian, T. J., Blake, D. R., Gao, S., Kirchstetter, T. W., Novakov, T. and Pilewskie, P.: Evolution of gases and particles from a savanna fire in South Africa, J. Geophys. Res. D: Atmos., 108(D13), doi:10.1029/2002JD002352, 2003.

Jathar, S. H., Gordon, T. D., Hennigan, C. J., Pye, H. O. T., Pouliot, G., Adams, P. J., Donahue, N. M. and Robinson, A. L.: Unspeciated organic emissions from combustion sources and their influence on the secondary organic aerosol budget in the United States, Proc. Natl. Acad. Sci. U. S. A., 111(29), 10473–10478, doi:10.1073/pnas.1323740111, 2014.

Jimenez, J. L., Canagaratna, M. R., Donahue, N. M., Prevot, A. S. H., Zhang, Q., Kroll, J. H., DeCarlo, P. F., Allan, J. D., Coe, H., Ng, N. L., Aiken, A. C., Docherty, K. S., Ulbrich, I. M., Grieshop, A. P., Robinson, A. L., Duplissy, J., Smith, J. D., Wilson, K. R., Lanz, V. A., Hueglin, C., Sun, Y. L., Tian, J., Laaksonen, A., Raatikainen, T., Rautiainen, J., Vaattovaara, P., Ehn, M., Kulmala, M., Tomlinson, J. M., Collins, D. R., Cubison, M. J., Dunlea, J., Huffman, J. A., Onasch, T. B., Alfarra, M. R., Williams, P. I., Bower, K., Kondo, Y., Schneider, J., Drewnick, F., Borrmann, S., Weimer, S., Demerjian, K., Salcedo, D., Cottrell, L., Griffin, R., Takami, A., Miyoshi, T., Hatakeyama, S., Shimono, A., Sun, J. Y., Zhang, Y. M., Dzepina, K., Kimmel, J. R., Sueper, D., Jayne, J. T., Herndon, S. C., Trimborn, A. M., Williams, L. R., Wood, E. C., Middlebrook, A. M., Kolb, C. E., Baltensperger, U. and Worsnop, D. R.: Evolution of Organic Aerosols in the Atmosphere, Science, 326(5959), 1525–1529, doi:10.1126/science.1180353, 2009.

Jolleys, M. D., Coe, H., McFiggans, G., Capes, G., Allan, J. D., Crosier, J., Williams, P. I., Allen, G., Bower, K. N., Jimenez, J. L., Russell, L. M., Grutter, M. and Baumgardner, D.: Characterizing the aging of biomass burning organic aerosol by use of mixing ratios: A meta-analysis of four regions, Environmental Science and Technology, 46(24), 13093–13102, doi:10.1021/es302386v, 2012.

Jolleys, M. D., Coe, H., McFiggans, G., Taylor, J. W., O'Shea, S. J., Le Breton, M., Bauguitte, S. J. B., Moller, S., Di Carlo, P., Aruffo, E., Palmer, P. I., Lee, J. D., Percival, C. J. and Gallagher, M. W.: Properties and evolution of biomass burning organic aerosol from Canadian boreal forest fires, Atmos. Chem. Phys., 15(6), 3077–3095, doi:10.5194/acp-15-3077-2015, 2015.

Kleinman, L. and Sedlacek, A. J., III: Biomass Burning Observation Project (BBOP) Final Campaign Report, 2016.

Kodros, J. K., Volckens, J., Jathar, S. H. and Pierce, J. R.: Ambient Particulate Matter Size Distributions Drive Regional and Global Variability in Particle Deposition in the Respiratory Tract, GeoHealth, 2(10), 298–312, doi:10.1029/2018gh000145, 2018.

Kulmala, M., Vehkamäki, H., Petäjä, T., Dal Maso, M., Lauri, A., Kerminen, V.-M., Birmili, W. and McMurry, P. H.: Formation and growth rates of ultrafine atmospheric particles: a review of observations, J. Aerosol Sci., 35(2), 143–176, doi:10.1016/j.jaerosci.2003.10.003, 2004.

Liu, X., Zhang, Y., Huey, L. G., Yokelson, R. J., Wang, Y., Jimenez, J. L., Campuzano-Jost, P., Beyersdorf, A. J., Blake, D. R., Choi, Y., St. Clair, J. M., Crounse, J. D., Day, D. A., Diskin, G. S., Ried, A., Hall, S. R., Hanisco, T. F., King, L. E., Meinardi, S., Mikoviny, T., Palm, B. B., Peischl, J., Perring, A. E., Pollack, I. B., Ryerson, T. B., Sachse, G., Schwarz, J. P.,

Simpson, I. J., Tanner, D. J., Thornhil, K. L., Ullmann, K., Weber, R. J., Wennberg, P. O., Wisthaler, A., Wolfe, G. M. and Ziemba, L. D.: Agricultural fires in the southeastern U.S. during SEAC4RS: Emissions of trace gases and particles and evolution of ozone, reactive nitrogen, and organic aerosol, J. Geophys. Res., 121(12), 7383–7414, doi:10.1002/2016JD025040, 2016.

May, A. A., Lee, T., McMeeking, G. R., Akagi, S., Sullivan, A. P., Urbanski, S., Yokelson, R. J. and Kreidenweis, S. M.: Observations and analysis of organic aerosol evolution in some prescribed fire smoke plumes, Atmos. Chem. Phys., 15(11), 6323–6335, doi:10.5194/acp-15-6323-2015, 2015.

Morgan, W. T., Allan, J. D., Bauguitte, S., Darbyshire, E., Flynn, M. J., Lee, J., Liu, D., Johnson, B., Haywood, J., Longo, K. M., Artaxo, P. E. and Coe, H.: Transformation and aging of biomass burning carbonaceous aerosol over tropical South America from aircraft in-situ measurements during SAMBBA, Atmos. Chem. Phys. Discuss., doi:10.5194/acp-2019-157, 2019.

Murphy, B. N., Donahue, N. M., Robinson, A. L. and Pandis, S. N.: A naming convention for atmospheric organic aerosol, Atmos. Chem. Phys., 14(11), 5825–5839, doi:10.5194/acp-14-5825-2014, 2014.

Murphy, D. M., Cziczo, D. J., Froyd, K. D., Hudson, P. K., Matthew, B. M., Middlebrook, A. M., Peltier, R. E., Sullivan, A., Thomson, D. S. and Weber, R. J.: Single-particle mass spectrometry of tropospheric aerosol particles, Journal of Geophysical Research: Atmospheres, 111(D23), doi:10.1029/2006jd007340, 2006.

Nance, J. D., Hobbs, P. V. and Radkel, L. F.: Airborne Measurements of Gases and Particles From an Alaskan Wildfire, J. Geophys. Res. D: Atmos., 98(D8), 873–882, doi:10.1029/93JD01196, 1993.

Ortega, A. M., Day, D. A., Cubison, M. J., Brune, W. H., Bon, D., De Gouw, J. A. and Jimenez, J. L.: Secondary organic aerosol formation and primary organic aerosol oxidation from biomass-burning smoke in a flow reactor during FLAME-3, Atmos. Chem. Phys., 13(22), 11551–11571, doi:10.5194/acp-13-11551-2013, 2013.

Palm, B. B., Campuzano-Jost, P., Ortega, A. M., Day, D. A., Kaser, L., Jud, W., Karl, T., Hansel, A., Hunter, J. F., Cross, E. S., Kroll, J. H., Peng, Z., Brune, W. H. and Jimenez, J. L.: In situ secondary organic aerosol formation from ambient pine forest air using an oxidation flow reactor, Atmos. Chem. Phys., 16(5), 2943–2970, doi:10.5194/acp-16-2943-2016, 2016.

Pankow, J. F.: An absorption model of gas/particle partitioning of organic compounds in the atmosphere, Atmos. Environ., 28(2), 185–188, doi:10.1016/1352-2310(94)90093-0, 1994.

Petters, M. D. and Kreidenweis, S. M.: A single parameter representation of hygroscopic growth and cloud condensation nucleus activity, Atmos. Chem. Phys., 7(8), 1961–1971, doi:10.5194/acp-7-1961-2007, 2007.

Pierce, J. R., Riipinen, I., Kulmala, M., Ehn, M., Petäjä, T., Junninen, H., Worsnop, D. R. and Donahue, N. M.: Quantification of the volatility of secondary organic compounds in ultrafine particles during nucleation events, Atmos. Chem. Phys., 11(17), 9019–9036, doi:10.5194/acp-11-9019-2011, 2011.

Reid, J. S., Hobbs, P. V., Ferek, R. J., Blake, D. R., Martins, J. V., Dunlap, M. R. and Liousse, C.: Physical, chemical, and optical properties of regional hazes dominated by smoke in Brazil, J. Geophys. Res. D: Atmos., 103(D24), 32059–32080, doi:10.1029/98JD00458, 1998.

Riipinen, I., Pierce, J. R., Yli-Juuti, T., Nieminen, T., Häkkinen, S., Ehn, M., Junninen, H., Lehtipalo, K., Petäjä, T., Slowik, J., Chang, R., Shantz, N. C., Abbatt, J., Leaitch, W. R., Kerminen, V.-M., Worsnop, D. R., Pandis, S. N., Donahue, N. M. and Kulmala, M.: Organic condensation: a vital link connecting aerosol formation to cloud condensation nuclei (CCN) concentrations, Atmos. Chem. Phys., 11(8), 3865–3878, doi:10.5194/acp-11-3865-2011, 2011.

Sakamoto, K. M., Allan, J. D., Coe, H., Taylor, J. W., Duck, T. J. and Pierce, J. R.: Aged boreal biomass-burning aerosol size distributions from BORTAS 2011, Atmos. Chem. Phys., 15(4), 1633–1646, doi:10.5194/acp-15-1633-2015, 2015.

Seinfeld, J. H. and Pandis, S. N.: Atmospheric chemistry and physics: From air pollution to climate change, John Willey & Sons, Inc. , New York, 2006.

Shrivastava, M., Cappa, C. D., Fan, J., Goldstein, A. H., Guenther, A. B., Jimenez, J. L., Kuang, C., Laskin, A., Martin, S. T., Ng, N. L. and Others: Recent advances in understanding secondary organic aerosol: Implications for global climate forcing, Rev. Geophys., 55(2), 509–559 [online] Available from: https://agupubs.onlinelibrary.wiley.com/doi/abs/10.1002/2016RG000540, 2017.

Song, C. H. and Carmichael, G. R.: The aging process of naturally emitted aerosol (sea-salt and mineral aerosol) during long range transport, Atmos. Environ., 33(14), 2203–2218, doi:10.1016/S1352-2310(98)00301-X, 1999.

Spracklen, D. V., Carslaw, K. S., Kulmala, M., Kerminen, V.-M., Sihto, S.-L., Riipinen, I., Merikanto, J., Mann, G. W., Chipperfield, M. P., Wiedensohler, A., Birmili, W. and Lihavainen, H.: Contribution of particle formation to global cloud condensation nuclei concentrations, Geophys. Res. Lett., 35(6), L06808–L06808, doi:10.1029/2007GL033038, 2008.

Tkacik, D. S., Robinson, E. S., Ahern, A., Saleh, R., Stockwell, C., Veres, P., Simpson, I. J., Meinardi, S., Blake, D. R., Yokelson, R. J., Presto, A. A., Sullivan, R. C., Donahue, N. M. and Robinson, A. L.: A dual-chamber method for quantifying the effects of atmospheric perturbations on secondary organic aerosol formation from biomass burning emissions, J. Geophys. Res., 122(11), 6043–6058, doi:10.1002/2016JD025784, 2017.

Twomey, S.: Pollution and the planetary albedo, Atmos. Environ., 8(12), 1251–1256, doi:10.1016/0004-6981(74)90004-3, 1974.

Vakkari, V., Kerminen, V.-M., Beukes, J. P., Titta, P., van Zyl, P. G., Josipovic, M., Wnter, A. D., Jaars, K., Worsnop, D. R., Kulmala, M. and Laakso, L.: Rapid changes in biomass burning aerosols by atmospheric oxidation, Geophys. Res. Lett., 2644–2651, doi:10.1002/2014GL059396.Received, 2014.

Vakkari, V., Beukes, J. P., Dal Maso, M., Aurela, M., Josipovic, M. and van Zyl, P. G.: Major secondary aerosol formation in southern African open biomass burning plumes, Nat. Geosci., 11(8), 580–583, doi:10.1038/s41561-018-0170-0, 2018.

Yokelson, R. J., Crounse, J. D., DeCarlo, P. F., Karl, T., Urbanski, S., Atlas, E., Campos, T., Shinozuka, Y., Kapustin, V., Clarke, A. D., Weinheimer, A., Knapp, D. J., Montzka, D. D., Holloway, J., Weibring, P., Flocke, F., Zheng, W., Toohey, D., Wennberg, P. O., Wiedinmyer, C., Mauldin, L., Fried, A., Richter, D., Walega, J., Jimenez, J. L., Adachi, K.,

Buseck, P. R., Hall, S. R. and Shetter, R.: Emissions from biomass burning in the Yucatan, Atmos. Chem. Phys., 9(15), 5785–5812, doi:10.5194/acp-9-5785-2009, 2009.

Yokelson, R. J., Burling, I. R., Urbanski, S. P., Atlas, E. L, Adachi, K., Buseck, P. R., Wiedinmyer, C., Akagi, S. K., Toohey, D. W. and Wold, C. E.: Trace gas and particle emissions from open biomass burning in Mexico, Atmos. Chem. Phys., 11(14), 6787–6808, doi:10.5194/acp-11-6787-2011, 2011.

Zhang, Q., Jimenez, J. L., Canagaratna, M. R., Allan, J. D., Coe, H., Ulbrich, I., Alfarra, M. R., Takami, A., Middlebrook, A. M., Sun, Y. L. and Others: Ubiquity and dominance of oxygenated species in organic aerosols in anthropogenically-influenced Northern Hemisphere midlatitudes, Geophys. Res. Lett., 34(13) [online] Available from: https://agupubs.onlinelibrary.wiley.com/doi/abs/10.1029/2007GL029979%4010.1002/%28ISSN%291944-8007.GRL40, 2007.

Zhou, S., Collier, S., Jaffe, D. A., Briggs, N. L., Hee, J., Sedlacek, A. J., III, Kleinman, L., Onasch, T. B. and Zhang, Q.: Regional influence of wildfires on aerosol chemistry in the western US and insights into atmospheric aging of biomass burning organic aerosol, Atmos. Chem. Phys., 17(3), 2477–2493, doi:10.5194/acp-17-2477-2017, 2017.

CHAPTER 2

CONSTRAINING NUCLEATION, CONDENSATION, AND CHEMISTRY IN OXIDATION FLOW REACTORS USING SIZE-DISTRIBUTION MEASUREMENTS AND AEROSOL MICROPHYSICAL MODELLING[1]

Overview

Oxidation flow reactors (OFRs) allow the concentration of a given atmospheric oxidant to be increased beyond ambient levels in order to study secondary organic aerosol (SOA) formation and aging over varying periods of equivalent aging by that oxidant. Previous studies have used these reactors to determine the bulk OA mass and chemical evolution. To our knowledge, no OFR study has focused on the interpretation of the evolving aerosol size distributions. In this study, we use size distribution measurements of the OFR and an aerosol microphysics model to learn about size-dependent processes in the OFR. Specifically, we use OFR exposures between 0.09-0.9 equivalent days of OH aging from the 2011 BEACHON-RoMBAS and the GoAmazon2014/5 field campaigns. We use simulations in the TOMAS (TwO-Moment Aerosol Sectional) microphysics box model to constrain the following parameters in the OFR: (1) the rate constant of gas-phase functionalization reactions of organic compounds with OH, (2) the rate constant of gas-phase fragmentation reactions of organic compounds with OH, (3) the reactive uptake coefficient for heterogeneous fragmentation reactions with OH, (4) the nucleation rate constants for three

[1]This Chapter published as: Hodshire, A. L., Palm, B. B., Alexander, M. L., Bian, Q., Campuzano-Jost, P., Cross, E. S., Day, D. A., de Sá, S. S., Guenther, A. B., Hansel, A., Hunter, J. F., Jud, W., Karl, T., Kim, S., Kroll, J. H., Park, J.-H., Peng, Z., Seco, R., Smith, J. N., Jimenez, J. L. and Pierce, J. R.: Constraining nucleation, condensation, and chemistry in oxidation flow reactors using size-distribution measurements and aerosol microphysical modelling, Atmos. Chem. Phys., 18, 12433–12460, doi:10.5194/acp-2018-223, 2018.

different nucleation schemes, and (5) an effective accommodation coefficient that accounts for possible particle diffusion limitations of particles larger than 60 nm in diameter.

We find the best model-to-measurement agreement when the accommodation coefficient of the larger particles (D_p>60 nm) was 0.1 or lower (with an accommodation coefficient of 1 for smaller particles), which suggests a diffusion limitation in the larger particles. When using these low accommodation-coefficient values, the model agrees with measurements when using a published H_2SO_4-organics nucleation mechanism and previously published values of rate constants for gas-phase oxidation reactions. Further, gas-phase fragmentation was found to have a significant impact upon the size distribution, and including fragmentation was necessary for accurately simulating the distributions in the OFR. The model was insensitive to the value of the reactive uptake coefficient on these aging timescales. Monoterpenes and isoprene could explain 24-95% of the observed change in total volume of aerosol in the OFR, with ambient semivolatile and intermediate-volatility organic compounds (S/IVOCs) appearing to explain the remainder of the change in total volume. These results provide support to the mass-based findings of previous OFR studies, give insight to important size-distribution dynamics in the OFR, and enable the design of future OFR studies focused on new particle formation and/or microphysical processes.

2.1 Introduction

Aerosols impact the climate directly, through absorbing and scattering incoming solar radiation (Charlson et al., 1992), and indirectly, through modifying cloud properties (Rosenfeld et al., 2008; Clement et al., 2009). Both of these effects are size-dependent, with larger particles dominating both effects. Particles with diameters (D_p) greater than 50-100 nm can act as cloud condensation nuclei (CCN) and particles with D_p greater than 200-300 nm can absorb and scatter

radiation more efficiently than smaller particles (Seinfeld and Pandis, 2006). The radiative forcing predictions of these effects remain amongst the largest uncertainties in climate modelling (Boucher et al., 2013), and thus climate predictions rely greatly upon accurate simulations or assumptions of the particle-size distributions. The majority of aerosol number globally is derived from photochemically driven new particle formation (NPF) of ~1 nm particles (e.g., Spracklen et al., 2008; Pierce and Adams, 2009a). These new particles are too small to impact climate, and they must grow through uptake of vapors and similarly sized particles while avoiding being lost by coagulation to larger particles in order to reach climatically relevant sizes (Westervelt et al., 2014). Thus, accurately simulating new particle formation and growth processes is a key step towards representing particle size distributions and predicting aerosol-climate effects in regional and global models that assess aerosol impacts. In the following paragraphs, we discuss the processes that shape new-particle formation and growth processes relevant to the analyses in this paper.

A large fraction of submicron aerosol mass is composed of organic aerosols (OA) (Murphy et al., 2006; Zhang et al., 2007; Jimenez et al., 2009; Shrivistava et al., 2017). OA is composed of thousands of often-unidentified compounds (Goldstein and Galbally, 2007) and can be emitted directly in the particle phase as primary OA (POA) or formed as secondary OA (SOA) through gas-to-particle conversion. In SOA formation through the gas-phase, atmospheric oxidants (mainly OH, O_3, and NO_3) react with organic gases to form either less-volatile functionalized compounds or often more-volatile fragmentation products. If the oxidation products have a low-enough volatility, they may then partition to the particle phase, forming SOA (Pankow et al., 1994; Donahue et al., 2006). The vapors may either partition to pre-existing particles or form new particles through NPF. Alternatively, the oxidation products could react in the particle phase to form lower volatility products that then remain in the particle phase (e.g., Paulot et al., 2009).

Controlled studies of SOA formation have traditionally used large reaction chambers with residence times of hours (often referred to as "smog chambers"). Chambers are susceptible to loss of both gases and particles to the walls of the chambers (e.g., Krechmer et al., 2016; Bian et al., 2017). In order to enable the study of SOA formation from ambient air and limit wall losses, oxidation flow reactors (OFRs, i.e., the Potential Aerosol Mass [PAM] reactor; Kang et al., 2007, Lambe et al., 2011a) were developed to produce high and controllable oxidant concentrations and have short residence times (usually ~2 – 4 minutes), with the purpose of simulating hours to days or weeks of equivalent atmospheric aging (eq. days) in either laboratory or field experiments. Wall losses in OFRs can often be smaller than in large chambers due to shorter residence times (e.g. Palm et al., 2016), although a direct comparison requires specification of the operating conditions, and losses in both types of reactors are still a subject of research. Studies with OFRs have shown SOA yields from precursor gases are similar to yields from smog chambers (Kang et al., 2007; Lambe et al., 2011b, 2015; Palm et al., 2018). Previous field studies with OFRs have focused on bulk aerosol mass formation and aging, and bulk chemical evolution (e.g., Ortega et al., 2013, 2016; Tkacik et al. 2014; Palm et al. 2016, 2017a, 2018). Ortega et al. (2016) and Palm et al. (2016) showed that size distributions in OFR output were dynamic as a function of time and aging. However, to the best of our knowledge, no ambient OFR study has focused on the aerosol size distributions that form and evolve within the OFR. Processes that could help shape the size distribution within the OFR are the same as those that take place in the real atmosphere, and include nucleation, condensation of vapors, coagulation, the rate of gas-phase oxidation with OH, gas-phase fragmentation with OH, vapor-uptake and/or particle diffusion limitations, reactive uptake growth mechanisms including accretion reactions and acid-base reactions, heterogeneous reactions, and wall losses of both vapors and particles. Many of these processes have uncertainties

associated with them, necessitating model-to-measurement comparisons and sensitivity studies. Using an OFR extends the parameter space over which comparisons can be made, compared to using only ambient data where parameter variations are narrower.

Nucleation, i.e., the formation of new ~1 nm particles, can involve a number of species, including water, sulfuric acid, ammonia, amines, ions, and certain low-volatility organic compounds (e.g., Kulmala et al., 1998; Vehkamaki et al., 2002; Kulmala et al., 2002; Napari et al., 2002; Laakso et al., 2002; Yu et al., 2006a; Yu et al., 2006b; Metzger et al., 2010; Almeida et al., 2013; Jen et al., 2014; Riccobono et al., 2014). Along with multiple species, observations indicate that numerous physical and chemical reactions can be involved (e.g., Zhang et al., 2004; Chen et al., 2012; Almeida et al., 2013; Riccobono et al., 2014). Recent studies have pointed to the importance of nucleation involving sulfuric acid and oxygenated organic compounds over the forested continental boundary layer (BL) (e.g., Metzger et al., 2010; Riccobono et al., 2014). However, controlled nucleation and growth studies in smog chambers or oxidation flow reactors involving organics have traditionally focused on organics formed from the oxidation of a single precursor vapor, such as α-pinene. Previous chamber studies have examined NPF from plant emissions (e.g., Joutsensaari et al., 2005; Vanreken et al., 2006), but to our knowledge no studies have systematically investigated nucleation and growth mechanisms in OFR or other types of reactors using ambient air as the precursor source.

Condensation of vapors to newly formed aerosol particles as well as pre-existing particles increases the total aerosol particle mass, but the net condensation rate to differently sized particles is dependent upon the volatility of the vapors. The lowest-volatility vapors condense essentially irreversibly onto particles of all sizes (i.e. “kinetically limited” or irreversible condensation; Riipinen et al., 2011, Zhang et al., 2012). Semi-volatile vapors (with non-trivial partitioning

fractions in both the particle and gas phases at equilibrium) have a net condensation to particles that is determined by reversible partitioning (i.e. quasi-equilibrium condensation; Riipinen et al., 2011, Zhang et al., 2012). Kinetically limited condensation is gas-phase-diffusion limited and only possible for compounds with effective saturation concentrations (C*; Donahue et al., 2006) < ~10^{-3} μg m^{-3} (e.g., low and extremely low volatility organic compounds; LVOCs and ELVOCs); the net SOA uptake to a particle is proportional to the Fuchs-corrected surface area of the particle (Pierce et al., 2011). Conversely, thermodynamic condensation primarily involves semi-volatile organic compounds (SVOCs) with C*~10^{-1} –10^{2} μg m^{-3} that quickly reach equilibrium between the gas and particle phases for all particle sizes; as a result, the net SOA uptake to a particle is proportional to the organic mass (or volume) of the particle (Pierce et al., 2011).

The gas-phase oxidation rates of organic vapors as well as the competition between gas-phase functionalization (the addition of polar, oxygen-containing functional groups, generally lowering the volatility of the species) and gas-phase fragmentation (the cleavage of C-C bonds, with each reaction typically creating two higher-volatility products) influences the changes in volatilities of organic species from atmospheric oxidation (e.g.,, Kroll et al., 2009). Gas-phase oxidation rates have been well-quantified for many individual species in the lab (e.g., Atkinson and Arey, 2003a), but less is known about gas-phase oxidation rates that may be appropriate for lumped organic vapors in ambient air. Generally, a representative reaction rate constant (k_{OH}) for a given oxidant is chosen to describe oxidation of organic species present in ambient air in modelling studies that may be a function of organic-vapor volatility (e.g., Jathar et al., 2014; Bian et al., 2017). Beyond k_{OH} values, the volatility of the reaction products is also important. Recent modelling studies have shown significant impacts to the SOA budget when fragmentation reactions were included relative to the assumption that all products were purely functionalized

(e.g., Shrivistava et al., 2013; 2014; 2016). Several recent laboratory studies point to the likely increasing importance of fragmentation reactions as organic vapors age and become more functionalized (Jimenez et al., 2009; Kroll et al., 2009, 2011; Chacon-Madrid et al., 2010; Chacon-Madrid and Donahue, 2011; Lambe et al., 2012; Wilson et al., 2012). Reduced organic vapors generally functionalize without fragmentation upon oxidation, decreasing their volatility. However, the probability of fragmentation (and an increase in overall volatility) increases after repeated oxidation reactions (if the molecule does not leave the vapor phase first). Hence, in addition to decreasing the overall mass yield of SOA, gas-phase fragmentation reactions reduce the production of the lowest volatility species that condense through the gas-phase-diffusion limited pathway and thus the balance between fragmentation reactions and purely functionalization reactions may impact the size-dependent condensation of SOA in addition to the overall SOA yield. However, the balance between gas-phase functionalization reactions and fragmentation reactions are not well constrained for ambient organic mixtures.

Particle-phase reactions also shape OA mass and the size distribution. Heterogeneous reactions between OH and organics at the surface of the particle can yield fragmentation products with high-enough volatilities to evaporate from the particle (e.g., Kroll et al., 2009), resulting in particle mass loss. Heterogeneous reactions contribute to aerosol aging and influence aerosol lifetime (George and Abbatt, 2010; George et al., 2015; Kroll et al., 2015). Many laboratory studies have reported uptake coefficients of OH, γ_{OH}, defined as the fraction of OH collisions with a particle-phase compound that result in a reaction, with values of effective γ_{OH} ranging from ≤ 0.01 to > 1, depending upon the reaction conditions (e.g., McNeill et al., 2008; Park et al., 2008; George and Abbatt, 2010; Liu et al., 2012; Slade and Knopf, 2013; Arangio et al., 2015; Hu et al., 2016). This heterogeneous OA loss pathway is important in OFRs at very high OH concentrations

(corresponding to exposures of >>1 day) (e.g., Ortega et al., 2016; Hu et al., 2016; Palm et al., 2016), and γ_{OH} ~0.6 has been measured for ambient OA (Hu et al., 2016). Conversely, particle-phase reactions including acid-base and accretion reactions can contribute to particle mass through the formation of lower-volatility products than the parent molecules (e.g., Pankow 2003; Barsanti and Pankow 2004; Pinder et al., 2007; Pun and Seigneur et al., 2007).

SOA uptake rates may be limited by the phase state of SOA through particle diffusion limitations. Traditionally, SOA was viewed as a liquid mixture; however, SOA have been observed in solid and amorphous phases in both laboratory and field studies (Virtanen et al., 2010; 2011). Measurements taken in 2013 and during the GoAmazon2014/5 campaign (Martin et al., 2016; 2017) found that SOA produced from oxidation products from the Amazonian rainforest tended to be primarily liquid whereas SOA influenced by anthropogenic emissions (both from the Manaus pollution plume and biomass burning) tended to have higher fractions of semisolid and solid aerosol (Bateman et al., 2015; 2017). Mixing in these solid or amorphous phases could decrease (Cappa et al., 2011; Vaden et al., 2011), leading to decreases in gas-particle partitioning rates (Shiraiwa and Seinfeld, 2012). The impacts of the changes in phase state from liquid to solid/amorphous matters less for SOA uptake at smaller particle sizes (D_p < ~100 nm), but increases more with increasing particle sizes (Shiraiwa et al., 2011). Hence, one may hypothesize that vapor-uptake limitations may favor the uptake of organics to smaller particles relative to when particles are liquid and do not have vapor-uptake limitations. This boost of growth to the smallest particles due to vapor-uptake limitations may be strong if coupled with particle-phase oligomerization reactions (Zaveri et al. 2014). Zaveri et al. (2017) found that in order to model the growth of bimodal aerosol populations formed from either isoprene or α-pinene and isoprene oxidation products, the intraparticle bulk diffusivity of the accumulation mode had to be slower

(an order of magnitude less) than that of the diffusivity of the Aitken mode. Yatavelli et al. (2014) showed that gases and particles appeared to be in equilibrium over a timescale of 1 hr at the BEACHON-RoMBAS site; however, OFR timescales are significantly shorter. Recent parameterizations for α-pinene SOA, an important compound at the BEACHON-RoMBAS site, are inconclusive about the diffusion timescale of these particles due to limitations in the input data (Maclean et al., 2017).

Each of the processes discussed above (nucleation, condensation of vapors, gas-phase functionalization and fragmentation reactions, heterogeneous reactions, accretion reactions, acid-base reactions, and particle diffusion limitations) could have very different timescales in the OFR as compared to the ambient atmosphere; for example, the chemistry timescale will typically be much shorter than the condensation and coagulation timescales in the OFR since the OFR OH concentrations can greatly exceed that of the ambient OH concentrations. Thus, models must be used to help interpret the OFR processes to determine how the observations relate to the ambient atmosphere. In this study, we use OFR measurements taken from two field locations. In the first, an OFR was deployed during the BEACHON-RoMBAS field campaign (Ortega et al., 2014) that took place in a montane ponderosa pine forest in Colorado, USA during July-August 2011. The second is the GoAmazon2014/5 field campaign (Martin et al., 2016; 2017) that occurred from January 2014-December 2015 in the State of Amazonia, Brazil, in the central Amazon basin. OFR data from each of these two campaigns have been analyzed in previous work (Palm et al. 2016; 2017a; 2018; Hunter et al., 2017) to understand the bulk OA mass and chemical evolution in the OFR. These analyses showed that the presence of unspeciated S/IVOCs contribute substantial OA mass production in the OFR at both locations. However, previous work has not analyzed the evolving aerosol size distribution in the OFR to gain insight into nucleation and growth processes.

In this paper, we extend the analysis of these ambient datasets using the measured aerosol size distributions and a model of aerosol microphysics in the OFR.

2.2 Methods

2.2.1 OFR method

The aerosol measurements investigated in this work were of ambient air before and after oxidation in a Potential Aerosol Mass (PAM) reactor, which is a type of OFR (Kang 2007, Lambe 2011a). This OFR is a cylindrical aluminum tube with a volume of 13 L and a typical residence time of 2–4 min. OH radicals were produced inside the OFR by photolysis of ambient H_2O and concurrently produced O_3 using 185 and 254 nm emissions from low pressure mercury UV lamps. The OH concentrations in the OFR were stepped over a range from ~$8x10^7$ to $9x10^9$ molec cm^{-3} by adjusting the UV lamp photon flux, with only data near the lower end of the range investigated in this work (see Table 2.1). The OFR was operated outside of the measurement trailer under ambient temperature and humidity (but protected from direct sun). This allowed avoiding the use of an inlet, which minimized any possible losses of semivolatile or sticky SOA precursor gases to inlet walls. Further OFR sampling and measurement details for the data used in this work can be found in Palm et al. (2016, 2017, 2018). The chemical regime was relevant to ambient OH oxidation, as discussed in detail in Peng et al. (2015, 2016). We note that about ~½ of the RO_2 radicals reacted with NO in ambient air during BEACHON-RoMBAS (Fry et al., 2013), but this was not the case in the OFR due to very rapid oxidation of NO (Li et al., 2015; Peng et al., 2017). Thus some differences in the product distributions for ambient vs. OFR oxidation would be expected. Recently, new OFR methods have been developed that allow RO_2+NO to dominate (Lambe et al., 2017; Peng et al., 2018), but those methods were not available at the time of the field studies discussed here.

2.2.2 Field campaigns

2.2.2.1 BEACHON-RoMBAS campaign

The BEACHON-RoMBAS field campaign (referred to as BEACHON hereafter) took place in July–August 2011 at the Manitou Experimental Forest Observatory near Woodland Park, Colorado (Ortega et al., 2014). The sampling site, located in a ponderosa pine forest in a mountain valley, was influenced mainly by 2-methyl-3-buten-2-ol (MBO) during the day and monoterpenes (MT) at night. During BEACHON, an OFR was used to measure the amount and properties of SOA formed from the oxidation of real ambient SOA precursor gases and ambient aerosol. Ambient particles and SOA formation after OH oxidation in the OFR (and also O_3 or NO_3-only oxidations (Palm et al., 2017), which are not investigated in this work) were sampled using an Aerodyne high-resolution aerosol mass spectrometer (HR-ToF-AMS, hereafter referred to as AMS) and a TSI Scanning Mobility Particle Sizer (SMPS). Details of OFR sampling can be found in Palm et al. (2016; 2017; 2018). Ambient SO_2 concentrations were measured using a Thermo Environmental Model 43C-TLE analyzer. VOC concentrations were quantified using a high-resolution proton-transfer reaction time of flight mass spectrometer (PTR-TOF-MS; Graus et al. 2010; Kaser et al. 2013). Ensemble mass concentration of ambient S/IVOCs in the range of C* from 10^1 to 10^7 μg m^{-3} were measured using a novel thermal-desorption electron impact mass spectrometer (TD-EIMS; Cross et al. 2013; Hunter et al. 2017). More details pertaining to the use of these instruments in measuring SOA formation in the OFR can be found in Palm et al. (2016).

2.2.2.2 GoAmazon2014/5 campaign

The GoAmazon2014/5 field campaign (referred to as GoAmazon hereafter) took place in the area surrounding Manaus, Brazil, in central Amazonia (Martin et al., 2016; 2017), investigating the complex interactions between urban, biomass burning, and biogenic emissions. OFR

measurements of SOA formation from OH oxidation of ambient air (and also O_3-only oxidation, not investigated here) were taken at the "T3" site downwind of Manaus during two intensive operating periods (IOP1 during the wet season and IOP2 in the dry season) to study the contributions of the various emission sources to potential SOA formation. The dry season results were chosen for investigation in this study due to the generally larger concentrations of gases, particles, and potential SOA formation than during the wet season. Whereas SOA formation at the BEACHON site was dominated by a single source type (biogenic gases, related to MT), the "T3" site was influenced by a complex mixture of biogenic and anthropogenic emissions (Martin et al. 2016, Palm et al. 2018). Again, ambient particles and SOA formation after OH oxidation in the OFR were sampled by an AMS and an SMPS. Ambient SO_2 concentrations were sampled using a Thermo Fisher Model 43i-TLE SO_2 Analyzer. Ambient VOCs were sampled using a PTR-TOF-MS. More details pertaining to the use of these instruments in measuring SOA formation in the OFR can be found in Palm et al. (2018).

2.2.3 TOMAS-VBS box model

2.2.3.1 Model description

In this study, we use the TwO-Moment Aerosol Sectional (TOMAS) microphysics zero-dimensional (box) model (Adams and Seinfeld, 2002; Pierce and Adams, 2009b; Pierce et al., 2011) combined with the Volatility Basis Set (VBS; Donahue et al., 2006) as described in Bian et al. (2017). This version of TOMAS-VBS simulates condensation, coagulation, and nucleation, and it has a simple organic vapor aging scheme that moves an organic species down in volatility upon reaction with an OH molecule (Bian et al., 2017). The simulated aerosol species are sulfate, organics, and water within 40 logarithmically spaced size sections from 1.5 nm to 10 μm. We simulate 6 organic "species" within the VBS, representing lumped organics with logarithmically

spaced effective saturation concentrations (C*) spanning 10^{-4} to 10^{6} μg m^{-3} (spaced apart by factors of 100). The C*=10^{-4} μg m^{-3} bin represents extremely-low-volatility organic compounds (ELVOCs), the C*=10^{-2} μg m^{-3} bin represents low-volatility organic compounds (LVOCs), the C*=10^{0} μg m^{-3} and C*=10^{2} μg m^{-3} bins represents semivolatile organic compounds (SVOCs), and the C*=10^{4} μg m^{-3} and C*=10^{6} μg m^{-3} bins represents intermediate-volatility organic compounds (IVOCs), following the conventions proposed by Murphy et al. (2014). In the rest of this section, we discuss the base model setup and assumptions. In Sect. 2.3.3, we discuss the uncertainty space that we test in this study.

In this study, gas-phase functionalization is modelled by assuming that the organic compounds within the VBS bins react with OH and products from this reaction drop by one volatility bin (a factor of 100 drop in volatility). As a base assumption of the rate constants of our vapors in the VBS bins reacting with OH (k_{OH}), we use the relationship developed for aromatics by Jathar et al. (2014), based on data from Atkinson and Arey (2003a):

$$k_{OH} = -5.7\times10^{-12} \log10(C*) + 1.14\times10^{-10} \quad (2.1)$$

As the assumption that the ambient mixture of S/IVOCs is similar to those of aromatics may not be suitable, we treat the rate constants for this volatility-reactivity relationship as an uncertain parameter that we vary in this study (Sect. 2.3.3). Further, it has been realized after the initial completion of this study that the first term in Eq. 2.1 is instead $-5.7\times10^{-12}\ln(C^*)$ (S. Jathar, personal communication). We discuss the differences and implications in using log10(C*) versus ln(C*) in Sect. 2.3.1.1.

We account for gas-phase fragmentation reactions separately by allowing one OH reaction with a molecule in the lowest volatility bin (C*=10^{-4} μg m^{-3}; assumed to be an ELVOC molecule) to lead to an irreversible fragmentation into non-condensable volatile products that are no longer

tracked in the model. Realistically, fragmentation reactions occur for vapors across the whole range of volatilities; however, the likelihood of fragmentation increases with increasing levels of oxidation (Kroll et al., 2011) and an increase in oxidation is often correlated with a decrease in volatility (Donahue et al., 2006; Kroll et al., 2011). We only allow for fragmentation of species in our lowest volatility bin in order to limit the number of parameters in our study, but we acknowledge that this is a limitation of this study and should be considered as a sensitivity study for fragmentation. We discuss the potential implications of only allowing fragmentation in the lowest volatility bin in the conclusion section. Our base assumption for this rate constant is 10^{-10} cm^3 s^{-1}.

We further account for monoterpenes (MT) oxidation by OH for both campaigns and isoprene oxidation by OH for GoAmazon in the model. Palm et al. (2016) determined that on average during the BEACHON campaign, MT contributed 20% of the measured SOA formation, with sesquiterpenes (SQT), isoprene, and toluene contributing an additional 3% of the measured SOA formation. Since these other VOCs contributed a minor amount to the measured SOA formation, they were not included in this analysis. S/IVOCs at BEACHON contributed the remaining 77% towards the measured SOA formation, and were likely the main source for new particles in the OFR. It was observed that for the GoAmazon campaign during the dry season, the approximate average contribution to the measured SOA was 4% from isoprene and 4% from MT, with an 8% remaining contribution towards the measured SOA coming from SQT, benzene, toluene, xylenes, and trimethylbenzene (TMB), combined. Thus, less of the total SOA can be described by the VOCs included in the model (isoprene and MT) for the GoAmazon simulations than can be described for the BEACHON campaign. The remaining 83% of measured SOA formation was found to have come from unmeasured S/IVOCs, so again S/IVOCs were likely the

main source for new particles in the OFR. Including the other VOCs would only increase the model-predicted SOA yield from the initial VOCs by a few tenths of a μg m^3, and decrease the model-predicted SOA yield from the initial S/IVOCs by a similar amount, and so they were excluded for simplicity.

Table 2.1 All BEACHON-RoMBAS inputs (values where measurements are missing and we estimated values are in bold) and GoAmazon2014/5 inputs (assumed values in bold). Each value represents the ambient condition present at the beginning of each modelled exposure.

Exposure (eq. age, days)	MT [μg m^{-3}]	Isoprene [μg m^{-3}]	SO_2 [ppb]	S/IVOC [μg m^{-3}]	Total Mass [μg m^{-3}]	OA/total mass ratio	Temperature [K]	RH [%]
BEACHON-RoMBAS								
0.090	**9.09**	n/a	0.02	8.09	3.22	0.85	284	92
0.098	8.97	n/a	0.029	2.89	2.47	0.8	282	82
0.16	8.94	n/a	**0.029**	**10**	1.52	0.79	290	73
0.23	**9.09**	n/a	**0.029**	9.3	3.4	0.84	288	91
0.27	9.09	n/a	0.029	**10**	1.6	0.79	289	84
0.77	**3.6**	n/a	**0.029**	6.9	2.24	0.9	286	94
0.82	**9.09**	n/a	**0.079**	14.02	3.17	0.85	286	91
0.91	**9.09**	n/a	0.029	10.85	3.66	0.86	287	92
GoAmazon2014/5								
0.39	0.56	0.86	0.14	0.40[a]	4.85	0.88	296	102
0.40	0.42	0.90	0.06	0.30[a]	4.94	0.88	296	101
0.51	0.68	1.34	**0.11**	0.49[a]	8.7	0.81	297	99
0.53	0.87	1.17	**0.11**	0.62[a]	8.17	0.8	297	99

[a]S/IVOCs were not measured during GoAmazon2014/5. The average BEACHON-RoMBAS campaign MT:S/IVOC ratio was 1.4; this ratio was used to create an initial S/IVOC amount. See text for more details.

Table 2.2 Product fractional mass yields for lumped monoterpenes and isoprene (GoAmazon only) in each VBS bin in TOMAS. The monoterpene yields are based on Henry et al. (2012), with the yield for the C*=10^{-4} bin representing the average yield from oxidation of OH of the monoterpene species examined in Jokinen et al. (2015). The isoprene yields are from Tsimpidi et al. (2010), remapped to fit the TOMAS model's bin scheme, with the yield to the C*=10^{-4} bin from isoprene OH oxidation from Jokinen et al. (2015).

Species	Aerosol yield per bin [log(C*)]					
	-4	-2	0	2	4	6
Monoterpene	0.0075	0.00005	0.083	1.095	0.125	0.0
Isoprene	0.0003	0.0	0.023	0.03	0.0	0.0

The products of both MTs and isoprene oxidation enter the model's volatility bins in the vapor phase. For MT SOA production, we use the product yields for α-pinene OH oxidation chamber experiments of Henry et al. (2012) for the C*=10^{-2} to C*=10^{4} μg m^{-3} bins and the average OH oxidation yield for ELVOCs from four different terpene species of Jokinen et al. (2014) for the C*=10^{-4} μg m^{-3} bin (Table 2.2). However, the wall loss correction applied in Henry et al. (2012) may not be appropriate (Zhang et al., 2014) and hence these yields may contribute an additional source of uncertainty that we do not explore in this paper. The isoprene SOA yields (Table 2.2) are for low NO_x conditions (Tsimpidi et al. 2010), with the OH oxidation yield of isoprene from Jokinen et al. (2014) for the C*=10^{-4} μg m^{-3} bin. In the OFR under OH oxidation, NO_x is rapidly oxidized to HNO_3 (Li et al., 2015; Peng and Jimenez, 2017), and thus the assumption of using SOA yields developed under low NO_x conditions are valid for the OFR exposures taken during BEACHON and GoAmazon. We use the rate constants of OH oxidation for MT and isoprene of 5×10^{-11} cm^3 molec^{-1} s^{-1} and 1×10^{-10} cm^3 molec^{-1} s^{-1}, respectively (Atkinson and Arey, 2003a). In this study, TOMAS-VBS does not track the MT and isoprene oxidation products once they enter the VBS scheme separately from the products of other precursors, and further oxidation of these

products follows the k_{OH} assumptions above. Although this assumption may be reasonable for MTs, studies in isoprene-dominated forests have shown that NPF appears to be suppressed in the regions studied even when monoterpene emissions are sufficiently high (Bae et al., 2010; Kanawade et al., 2011; Pillai et al., 2013; Haller et al., 2015; Yu et al., 2015; Lee et al., 2016). Hence, the products of isoprene oxidation likely do not age similar to monoterpenes (e.g., Krechmer et al., 2015), but we do not account for this possible effect in our model.

We simulate heterogeneous fragmentation reactions of particle-phase organics in all VBS bins by OH. The resulting particle mass loss is modeled in TOMAS through:

$$\frac{dM_k[K,J]}{dt} = \gamma_{OH} J_{OH} \frac{M_K[K,J]}{\Sigma M_K[K,J]} \frac{MW_{loss}}{N_a} \quad (2.2)$$

where M_K indicates the mass in a size section, K and J indicate the size bin and particle-phase species, J_{OH} is the rate of molecules of OH hitting a particle, MW_{loss} is the mass lost per reaction (taken here to be 250 amu; Hu et al., 2016), respectively, N_a is Avogadro's number, and γ_{OH} is the reactive uptake coefficient for heterogeneous reactions with OH. Our base value of γ_{OH} is 0.6, following the measurements of Hu et al. (2016) in a very similar OFR field experiment, but we treat γ_{OH} as an uncertain parameter that we vary in this study (Sect. 2.3.3).

In this work, we explore three different possible nucleation schemes. The first two use a H_2SO_4-organics nucleation mechanism, using the nucleation parameterization of Riccobono et al. (2014),

$$J_{ORG} = k_{NUC}[H_2SO_4]^p[\text{BioOxOrg}]^q \quad (2.3)$$

where k_{NUC} is the nucleation rate constant, BioOxOrg represents later-generation oxidation products of biogenic monoterpenes, and the exponents p and q represent the power law dependence of J upon the concentrations of sulfuric acid and BioOxOrg. In Riccobono et al. (2014), J_{ORG} was parameterized for the mobility diameter of 1.7 nm; in TOMAS, the median dry diameter of the

smallest bin is 1.2 nm. In this study, we use the ELVOC ($C^*=10^{-4}$ μg m^{-3}) bin of the TOMAS VBS scheme to represent the BioOxOrg concentration:

$$J_{ORG} = k_{NUC}[H_2SO_4]^p[\text{ELVOC}]^q \quad (2.4)$$

Our primary nucleation scheme, referred to here as NUC1, uses the values of p = 2, q = 1, and a base value of $k_{NUC} = 1\times10^{-21}$ cm^6 $molec^{-1}$ s^{-1}. We will refer to this k_{NUC} as k_{NUC1} for the remainder of the manuscript. For comparison, for p = 2 and q = 1, Riccobono et al. (2014) found a k_{NUC1} value of 3.27×10^{-21} cm^6 $molec^{-1}$ s^{-1} at 278 K. We acknowledge that the values of p and q are also uncertain (Riccobono et al., 2014) and we do a further sensitivity study for the nucleation parameterization, referred to here as NUC2, using p = 1, q = 1, and a base value of $k_{NUC2} = 5\times10^{-13}$ cm^3 $molec^{-1}$ s^{-1}. NUC2 can be thought to account for possible saturation effects that could occur in the OFR that would result in shallower slopes (p and q) (Almeida et al. 2013; Riccobono et al., 2014). For comparison, Metzger et al. (2010) found a value of $k_{NUC2} = 7.5 \pm 0.3 \times10^{-14}$ cm^3 $molec^{-1}$ s^{-1} (temperature not reported) when they constrained p and q to be both one. However, their study used the lowest-volatility oxidation products of 1,3,5-trimethylbenzene as the BioOxOrg proxy (Eq. 2.4), which is an anthropogenic SOA precursor. Although a temperature-dependent form of Eq. 2.4 has been developed (Yu et al., 2017), we instead here are fitting the nucleation rate constant to the temperature of the measurements (Table 2.1). For each of these nucleation schemes, we treat k_{NUC} as an uncertain parameter that we vary in this study (Sect. 2.3.3.).

We further explore the possibility of a sulfuric-acid only nucleation scheme, as some nucleation schemes used in models only rely upon the concentration of sulfuric acid (e.g., Spracklen et al., 2008, 2010; Westervelt et al., 2014; Merikanto et al., 2016) by using an activation nucleation scheme (Kulmala et al., 2006) for our third nucleation scheme, referred to here as ACT, in which existing clusters are activated:

$$J_{ACT} = A[H_2SO_4] \quad (2.5)$$

where A is referred to as the activation coefficient. Previous studies of activation nucleation have found fits for A of between 3.3×10^{-8} and 6×10^{-6} s^{-1} for a boreal forest (Sihto et al., 2006; Riipinen et al., 2007) and between 2.6×10^{-6} and 3.5×10^{-4} s^{-1} for a polluted environment (Riipinen et al., 2007). We use as a base A value 2×10^{-6} but treat this as an uncertain parameter (Sect. 2.3.3.).

We include a simple approximation of potential vapor-uptake and/or particle diffusion limitations by setting an adjustable accommodation coefficient (α_{EFF}) that is fixed to 1 for particles below 60 nm in diameter but can vary between 0.01 and 1 for particles above 60 nm in diameter (see Sect. 2.3.3. for further discussion). This simple scheme allows the uptake of OA vapors to larger particles to be slowed relative to the uptake to smaller particles, due to the longer diffusion timescales in the larger particles (Shiraiwa et al., 2011). The cutoff of 60 nm was chosen because upon initial inspection of simulations with the accommodation coefficient set to 1 for all particle sizes, it was seen that the growing new aerosol in the Aitken mode (particles largely below 60 nm) did not require any slowing of growth but the aerosol in the accumulation mode (particles largely above 60 nm) did require slowing of growth. We acknowledge that our method here is a crude approximation of particle diffusion limitations. However, with only very limited knowledge of particle-phase diffusivities and how they may vary with size (Zaveri et al. 2017), composition, and/or ambient conditions, such as temperature and relative humidity, we use this simple scheme as a way of determining if vapor-uptake limitations, potentially due to particle-phase-diffusion limitations, may be important in limiting the growth of larger particles relative to the smallest particles.

In this study, we do not simulate acid-base reactions and accretion reactions. No gas-phase bases (ammonia or amines) were measured during either campaign, making modelling acid-base reactions in TOMAS too unconstrained. Further, the model simulations point towards high

concentrations of ELVOCs in the gas-phase needed to facilitate nucleation (Sect. 2.3.1), indicating that gas-phase ELVOC production may be the dominant ELVOC-formation pathway over particle-phase ELVOC production (through accretion reactions and/or acid-base reactions). However, we cannot rule out ELVOC production in the particle phase through particle-phase reactions, as ELVOCs are in the particle phase at equilibrium.

We simulate loss of low-volatility vapors to the OFR walls using a first-order rate constant, k_{wall}=0.0025 s^{-1}, estimated in Palm et al. (2016) following McMurry and Grosjean (1985). Palm et al. (2016) estimated this loss for condensable (low-volatility) species; we extend this loss to the C*=10^{-2} μg m^{-3} (LVOC) and the C*=10^{-4} μg m^{-3} (ELVOC) bins in our VBS system. We use this value of k_{wall} for both the BEACHON and the GoAmazon OFR simulations. We assume that the wall losses for higher volatility species and particles are slow and ignore them (this was verified for particles by Palm et al., 2016).

For the BEACHON simulations, we use the residence time distribution (RTD) in the OFR of Palm et al. (2017) assuming non-Brownian motion (their Figure S1). The RTD is less-well characterized for GoAmazon; we use the RTD for particles from Lambe et al. (2011a), but as discussed in Palm et al. (2018), the RTD from Lambe et al. (2011a) is likely more skewed than for the OFR used at GoAmazon, due to the larger inlet at GoAmazon. The SMPS data for both campaigns were corrected for diffusion losses to the walls of the sampling lines (Palm et al., 2016; Palm et al., 2018).

We simulate coagulation using the Brownian kernel in Seinfeld and Pandis (2006). However, we do not expect coagulation to be a dominant process in our OFR simulations. The condensation sink timescale for the measured size distributions were on the order of 0.5-5 minutes, which corresponds to coagulation sink timescales on the order of 1-10 minutes for 1 nm particles,

2.5-25 minutes for 2 nm particles, and 5-50 minutes for 3 nm particles (Dal Maso et al., 2002). Thus, in some cases the coagulation sink timescales for the freshly nucleated particles were similar to the residence time. However, in most cases, freshly nucleated particles grew to at least 20 nm within the OFR, so the nucleated particles spend only a small fraction (<10%) of the residence time at sizes smaller than 3 nm. Hence, the coagulation timescale of the growing particles is overall much longer than the residence time, and we expect on the order of 10% or fewer of the nucleated particles to be lost by coagulation in these OFR experiments.

2.2.3.2 Model inputs

Inputs to TOMAS to initialize each OFR exposure simulated from the BEACHON and GoAmazon field campaigns are given in Table 2.1; each input represents the initial condition present at the start of the exposure. The initial ambient size distribution from each campaign's SMPS is also used (Figs. 2.1 and A.1, black lines). The initial S/IVOC concentration (as measured by the TD-EIMS) is evenly divided between the $C^*=10^2$ to $C^*=10^6$ $\mu g\ m^{-3}$ bins in TOMAS. Although The TD-EIMS reported ambient concentrations decadally between $C^*=10^1$ to $C^*=10^7$ $\mu g\ m^{-3}$, differences in mass concentrations per bin were small (Palm et al, 2016; Hunter et al, 2017) and thus our assumed division should be within experimental uncertainty. The initial total aerosol mass (as measured by the AMS) is evenly divided between the $C^*=10^{-4}$ to $C^*=10^{-2}$ $\mu g\ m^{-3}$ bins, consistent with the overall low-volatility of the ambient OA (Stark et al., 2017); the $C^*=10^0$ $\mu g\ m^{-3}$ bin is assumed to have an initial concentration of 0 $\mu g\ m^{-3}$; Figure 2.2a shows an example of the initial ambient partitioning between the volatility bins for a case from the BEACHON campaign. Monoterpene (MT) and isoprene concentrations are simulated explicitly outside of the VBS (though their reaction products enter the VBS as discussed earlier). Note that we do not include isoprene for the model runs from the BEACHON campaign due to the low contribution to

measured SOA (1%) as compared to MT (20%, Palm et al., 2016). The isoprene concentrations (Karl et al., 2012; Kaser et al., 2013) were also consistently lower than the MT concentrations during BEACHON. Conversely, isoprene was observed to be the dominant measured VOC during IOP2 of GoAmazon, with the average mass ratio of isoprene to MT during the dry season at 4.5 $\mu g\ m^{-3}$ per $\mu g\ m^{-3}$ (Palm et al., 2018), and thus isoprene is included in our model, even though isoprene's average contribution towards the predicted SOA during the dry season of GoAmazon was only 4% (Palm et al., 2018).

Data availability during BEACHON and GoAmazon caused data gaps that overlap some of the exposures modelled. For these cases with missing measurement data, we assume concentrations; assumed values are listed in bold in Table 2.1. Each assumed value is derived from either determining the trend from the nearest-available timepoints (for short data gaps) or by determining the concentration from different days with similar ambient conditions (for large data gaps).

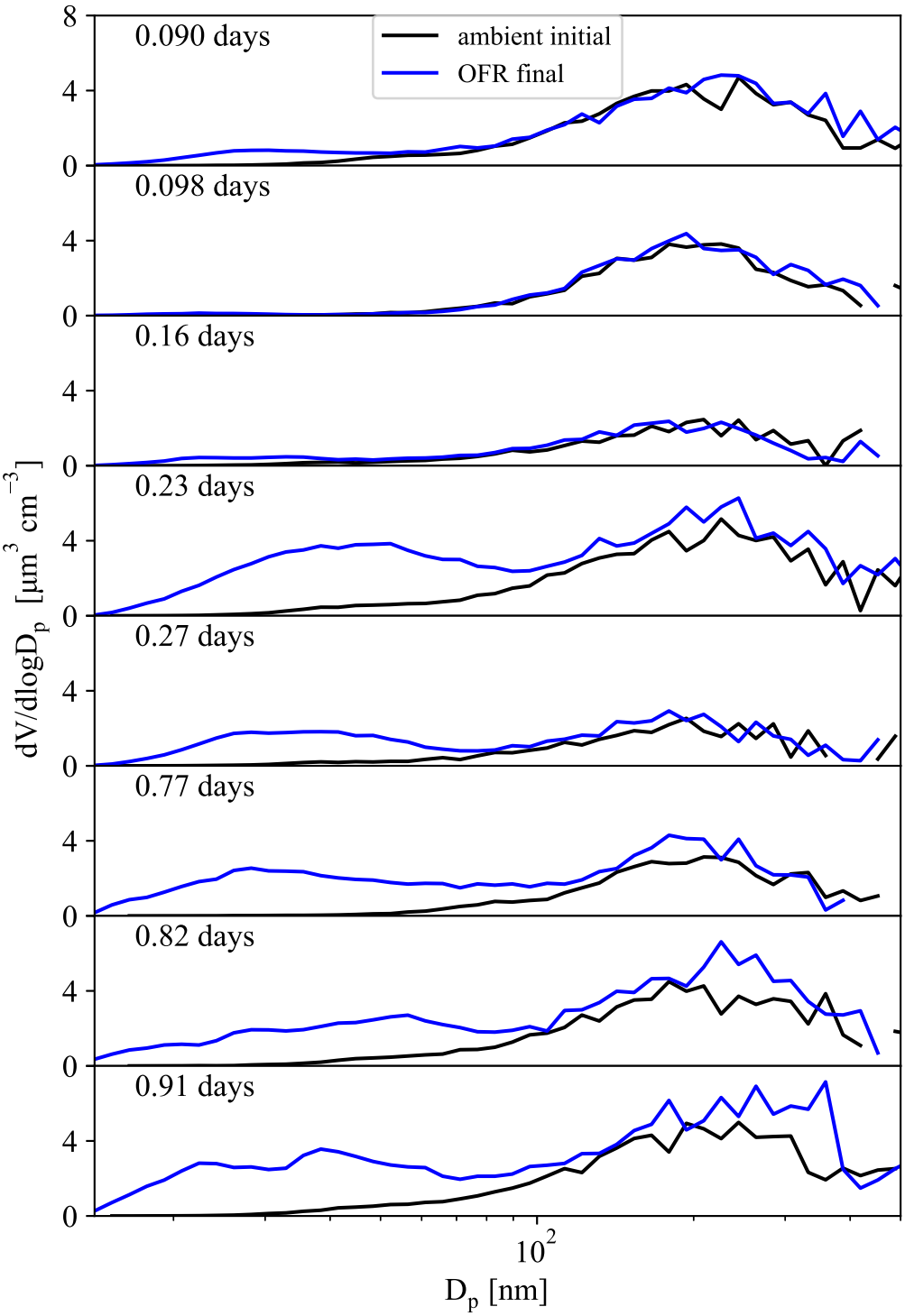

Figure 2.1 BEACHON-RoMBAS initial (i.e. ambient air, black line) and final (i.e. after OFR processing, blue line) SMPS-derived volume distributions for each individual exposure modelled in this study. The differences in SOA production between exposures of similar ages are due to the

fact that the exposures were taken from different times during the campaign and thus different precursor concentrations were present (Table 2.2).

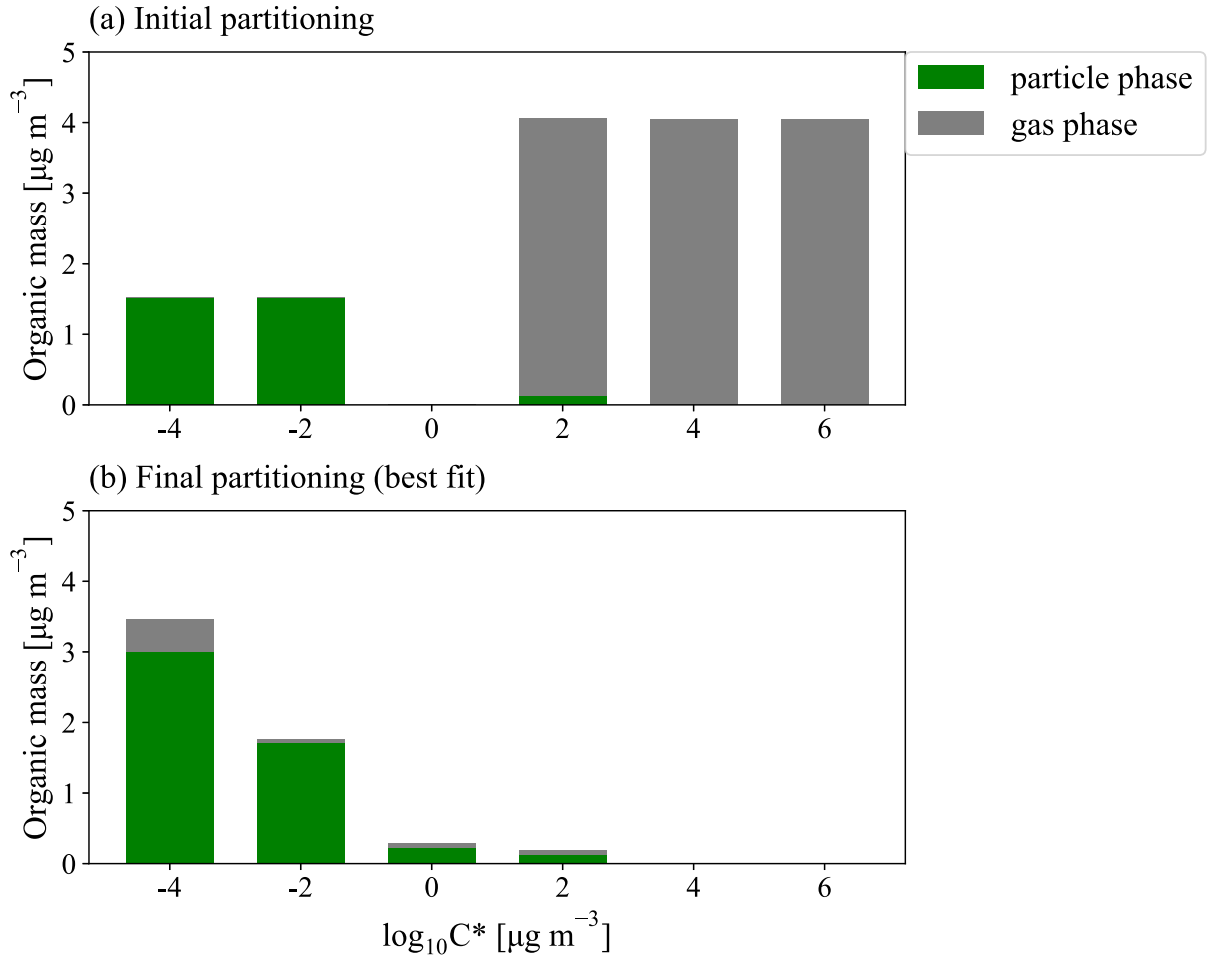

Figure 2.2 Example model (a) initial ambient and (b) final modelled partitioning for a 0.23 eq. day aging exposure from the BEACHON-RoMBAS campaign, with the particle phase loadings in green and gas phase loadings in grey (all in μg m^{-3}). The initial S/IVOC concentration is evenly divided between the C*=10^{2} to C*=10^{6} μg m^{-3} bins; the initial total aerosol mass is evenly divided between the C*=10^{-4} to C*=10^{-2} μg m^{-3} bins. The C*=10^{0} μg m^{-3} bin is assumed to have an initial concentration of 0 μg m^{-3}. The input VOCs (MT for BEACHON-RoMBAS and MT and isoprene for GoAmazon2014/5) are assumed to be in a volatility bin greater than the C*=10^{6} μg m^{-3} bin (not shown). Panel (b) is the best fit modelled final partitioning for this exposure, corresponding to 2×k_{NUC1}, 5×k_{OH}, 0.5× γ_{OH}, k_{ELVOC}, and α_{EFF} = 0.01. The C*=10^{-4} μg m^{-3} bin (assumed to represent ELVOCs) shows a significant amount of material remaining in the gas phase at the end of the modelled exposure, indicating that the production of gas-phase ELVOCs exceeded the timescale of condensation and gas-phase fragmentation within in the OFR.

2.3.3 Uncertain parameters

In order to understand the evolution of the size distributions of the OFR exposures from the BEACHON and GoAmazon field campaigns, we use TOMAS to explore the parameter spaces of five uncertain parameters. These parameters are: (1) the rate constant of gas-phase functionalization reactions with OH, (2) the rate constant of gas-phase ELVOC fragmentation reactions with OH, (3) the reactive uptake coefficient for heterogeneous fragmentation reactions with OH, (4) the nucleation rate constant for three different nucleation schemes, and (5) an effective accommodation coefficient that accounts for possible particle diffusion limitations of aerosol particles larger than 60 nm in diameter. Table 2.3 lists each uncertain parameter, the assumed base value, and the parameter space that we search through for each parameter (the 'Multipliers' column).

As discussed in Sect. 2.2.3.1, we use as the base rate of k_{OH} the relationship determined for aromatics by Jathar et al. (2014), Eq. 2.1. (Again, we note that although we use log10(C*) in the first term of Eq. 2.1, ln(C*) is the correct expression for the fit found in Jather et al., 2014; S. Jathar, personal communication). As we are assuming that the products from the reactions of organic compounds in the VBS bins with OH drop by exactly one volatility bin per reaction (a 100-fold decrease in C*) and there is uncertainty associated with the actual organic compounds (i.e. it is likely that the rates of reaction for some of the organic compounds are different than those of aromatics), we treat Eq. 2.1 as an uncertain parameter and we explore up to 10 times above and below this base equation. Jathar et al. (2014) determined the volatility-reactivity relationship of k_{OH} for both aromatics and alkanes; our choice in using the relationship for aromatics as a base case is arbitrary, as our parameter space encompasses both of the base values of k_{OH} for aromatics and alkanes from their study.

In the model, we treat fragmentation reactions separately from the functionalization reactions. As discussed above, we select 1×10^{-10} cm^3 $molec^{-1}$ s^{-1} as the base value of the gas-phase fragmentation rate constant, k_{ELVOC}, and explore up to 9 times above and below the base k_{ELVOC}. We note that this base fragmentation rate constant is one order of magnitude higher than the constant used in Palm et al. (2016) for BEACHON exposures. In their work, they used the rate constant for reactions with OH of an oxygenated molecule with no C=C bonds from Ziemann and Atkinson (2012) equal to 1×10^{-11} cm^3 $molec^{-1}$ s^{-1}. They used this for their modelled LVOC concentration and assumed that 5 reactions of an LVOC with an OH molecule led to irreversible fragmentation into oxidized molecules that could no longer condense. Further, reaching 9×10^{-10} cm^3 $molec^{-1}$ s^{-1} for k_{ELVOC} could exceed the kinetic limit for gas-phase fragmentation reactions. However, since we do not account for fragmentation reactions of higher-volatility species, a high k_{ELVOC} value can be considered to effectively account for fragmentation reactions of higher-volatility species.

As previously discussed, for the reactive uptake coefficient γ_{OH} , we use a base value of 0.6, following the findings in Hu et al. (2016), and we explore up to 4 times above and below the base γ_{OH} value, as previous studies have reported effective γ_{OH} values ranging from ≤ 0.01 to > 1 (Hu et al., 2016).

For our primary nucleation scheme, NUC1, (Eq. 2.4), we use a base nucleation rate constant value of k_{NUC1} of 1×10^{-21} cm^6 $molec^{-1}$ s^{-1} and explore up to 20 times above and below the base k_{NUC1} value. For our nucleation scheme sensitivity studies of NUC2 and ACT, (Table 2.3), we select base nucleation rate constant values of 1.25×10^{-14} cm^3 $molec^{-1}$ s^{-1} and 2×10^{-6} s^{-1}, respectively, and similarly explore up to 20 times above and below each base nucleation rate constant.

To account for possible particle-phase diffusion limitations, the effective accommodation coefficient is set to vary between 0.01 and 1 for particles larger than 60 nm in diameter (Table 2.3).

We simulate every combination of the uncertain parameters described above. In total, we run 10,125 sensitivity simulations for each BEACHON and GoAmazon OFR exposure for the first nucleation scheme (NUC1), going through each permutation for each of the five different uncertain parameters explored in this work. We further run 10,125 sensitivity simulations for both NUC2 and ACT for each experimental exposure. We acknowledge that there are further uncertainties in the measurements and modelling assumptions, including (1) potential but not modelled reactive uptake growth mechanisms, (2) uncertainties in the reported OFR OH concentration, (3) isoprene chemistry that may affect NPF, (4) whether some products from gas-phase functionalization reactions decrease more or less in volatility per reaction than the assumed factor of 100 drop in volatility, and likely other factors. However, exploring these uncertainties is outside of the scope of this paper (and some of these are not entirely orthogonal to the uncertain factors explored here) and will be left to a future study.

2.2.4 Description of cases

2.2.4.1 BEACHON-RoMBAS cases

Figure 2.1 shows the measured initial and final SMPS volume size distributions for each exposure examined in this study from the BEACHON field campaign. We simulate these eight exposures between eq. ages 0.090 to 0.91 days in the TOMAS model for each combination of parameters (Table 2.3), initializing each run with the ambient conditions recorded at the time of each exposure (Table 2.1). Each modelled exposure was taken during the nighttime, when MTs were the dominant VOC. We limit this study to exposures less than 1 eq. day of aging in order

avoid the complications of modelling the different parameters in Sect. 2.2.3.3 across several orders of magnitude of OH, and since this is the range of exposures where NPF is most obvious experimentally.

Table 2.3 All parameter value ranges for the suite of sensitivity simulations ran in TOMAS.

Parameter (abbreviation)	Base value [unit]	Multipliers
OH oxidation rate constant (k_{OH})	k_{OH} = -5.7 x 10^{-12} ln(C*) + 1.14 x 10^{-10} [cm^3 $molec^{-1}$ s^{-1}]	0.1, 0.2, 0.4, 0.7, 1, 1.5, 2.5, 5, 10
Gas-phase fragmentation rate constant (k_{ELVOC})	1 x 10^{-10} [cm^3 s^{-1}]	0.11, 0.33, 1, 3, 9
Reactive uptake coefficient (γ_{OH})	0.6 [unitless]	0.25, 0.5, 1, 2, 4
Nucleation rate constant: NUC1 (k_{nuc1})	1 x 10^{-21} [cm^{-6} s^{-1}]	0.05, 0.1, 0.25, 0.5, 1, 2, 4, 10, 20
Nucleation rate constant: NUC2 (k_{nuc2})	1.25 x 10^{-14} [cm^{-3} s^{-1}]	0.05, 0.1, 0.25, 0.5, 1, 2, 4, 10, 20
Nucleation rate constant: ACT (A)	2 x 10^{-6} [s^{-1}]	0.05, 0.1, 0.25, 0.5, 1, 2, 4, 10, 20
Effective accommodation coefficient for particles > 60 nm D_p (α_{EFF})	1 [unitless]	0.01, 0.05, 0.1, 0.5, 1

2.2.4.2 GoAmazon2014/5 cases

In order to further test the validity of our results, we apply the TOMAS model version developed to simulate OFR exposures from the BEACHON field campaign to OFR exposures taken between August 31, 2014 and September 4, 2014 during the dry season of the GoAmazon field campaign. Figure A.1 shows the initial and final SMPS volume size distributions for each exposure examined in this study from the GoAmazon field campaign. We simulate each of these exposures for the same combination of parameters as used for the BEACHON simulations, initializing each run with the ambient conditions at the corresponding times (Table 2.1). However, unlike the BEACHON simulations, we include isoprene as a source of SOA in the model, with VBS yields given in Table 2.2. Again, like BEACHON, each modelled exposure was taken during

the nighttime and are limited to exposures less than 1 eq. day of aging. During IOP2, it was observed that isoprene would peak during the day around 3-4 pm local time and MT would peak later, around 6 pm local time (Liu et al., 2016; Martin et al., 2016). Isoprene was primarily depleted through oxidation reactions by nighttime but MT had a background level that remained approximately constant between midnight to noon (local times) when the concentrations would begin to rise again (Fig. A.2). We model fewer exposures for GoAmazon than BEACHON (four vs. eight) as few of the GoAmazon OFR exposures during this time period showed significant SOA growth on top of the already-high ambient SOA concentrations as compared to BEACHON. Also, many of the OFR exposures were either between 0.4-0.5 eq. days or >> 1 eq. day, so we were not able to cover as wide a range of <1 eq. day exposures as we did for BEACHON.

Bulk S/IVOCs were not measured during the GoAmazon campaign and instead we use the model to estimate the S/IVOC concentrations required to explain the aerosol particle growth. We use as base values of S/IVOC concentrations the average MT:S/IVOC ratio from the BEACHON campaign, 1.4, as MT data is available during GoAmazon, and use the model to determine what S/IVOC concentrations are needed to help explain observed growth. This analysis is described in Sect. 2.3.2.

2.2.5 Description of simulation analyses

In order to determine the goodness-of-fit of each model simulation to the observed size distribution from the SMPS, we compute the normalized mean error (NME) statistic of the first four moments of the size distribution for each model simulation:

$$NME = \frac{\sum_{i=0}^{4} \frac{|S_i - O_i|}{O_i}}{4} \quad (2.6)$$

where S_i and O_i are simulated and observed ith moments. The ith moment is defined as

$$M_i = \int_0^\infty n_N D_p^i \, dD_p \quad (2.7)$$

where n_N is the number distribution and D_p is the diameter range of the SMPS measurements, ~14-615 nm for the BEACHON campaign and ~14-710 nm for the GoAmazon campaign. The zeroth moment (i = 0) corresponds to the total number of particles, the first moment (i = 1) corresponds to the total diameter of particles (also referred to as the total aerosol length), the second moment (i = 2) is proportional to the total surface area of particles, and the third moment (i=3) is proportional to the total volume of particles. Figure 2.3 gives an example of each measured final (OFR) moment (black solid line) as well as two different model runs' moments (colored lines) for a 0.23 eq. day aging exposure. The use of these four moments, including the less-common 1st "diameter" moment, allows us to include a broader range of the size distribution in the weighting rather than using just number or volume alone. An NME of 0 indicates a perfect fit between the simulation and observations, an NME of 0.1 indicates that the average error of the four moments between the simulation and observations is 10%, and an NME of 1.0 indicates the average error of the four moments between the simulation and observations is 100%. Since the NME is taken as an absolute value, it does not give information on whether the model is on average overpredicting or underpredicting the moments; however, there could be model cases in which e.g., number and diameter are underestimated and surface area and volume are overestimated such that the NME statistic computed without the absolute value (normalized mean bias, NMB) would be close to zero, falsely indicating a good fit despite the potentially large under- and overpredictions amongst the different moments. We determine each individual exposure's mean error of moments for both campaigns and further consider the average across all exposures for BEACHON and GoAmazon.

To determine the contribution to aerosol formation and growth for the OFR exposures studied here from the input VOCs vs the input S/IVOCs, we compare the predicted change in the

OFR in total aerosol particle number and volume between simulations with S/IVOCs to simulations with no S/IVOCs. We do this comparison for the six best-fitting simulations with S/IVOCs for each exposure and calculate the mean volume changes for these six simulations with and without S/IVOCs. With these number and volume changes, we calculate the fractional contribution of S/IVOCs to aerosol particle volume production in the OFR. We use the same technique to determine the contribution of isoprene to aerosol formation and growth for the GoAmazon OFR exposures studied here using the same methods.

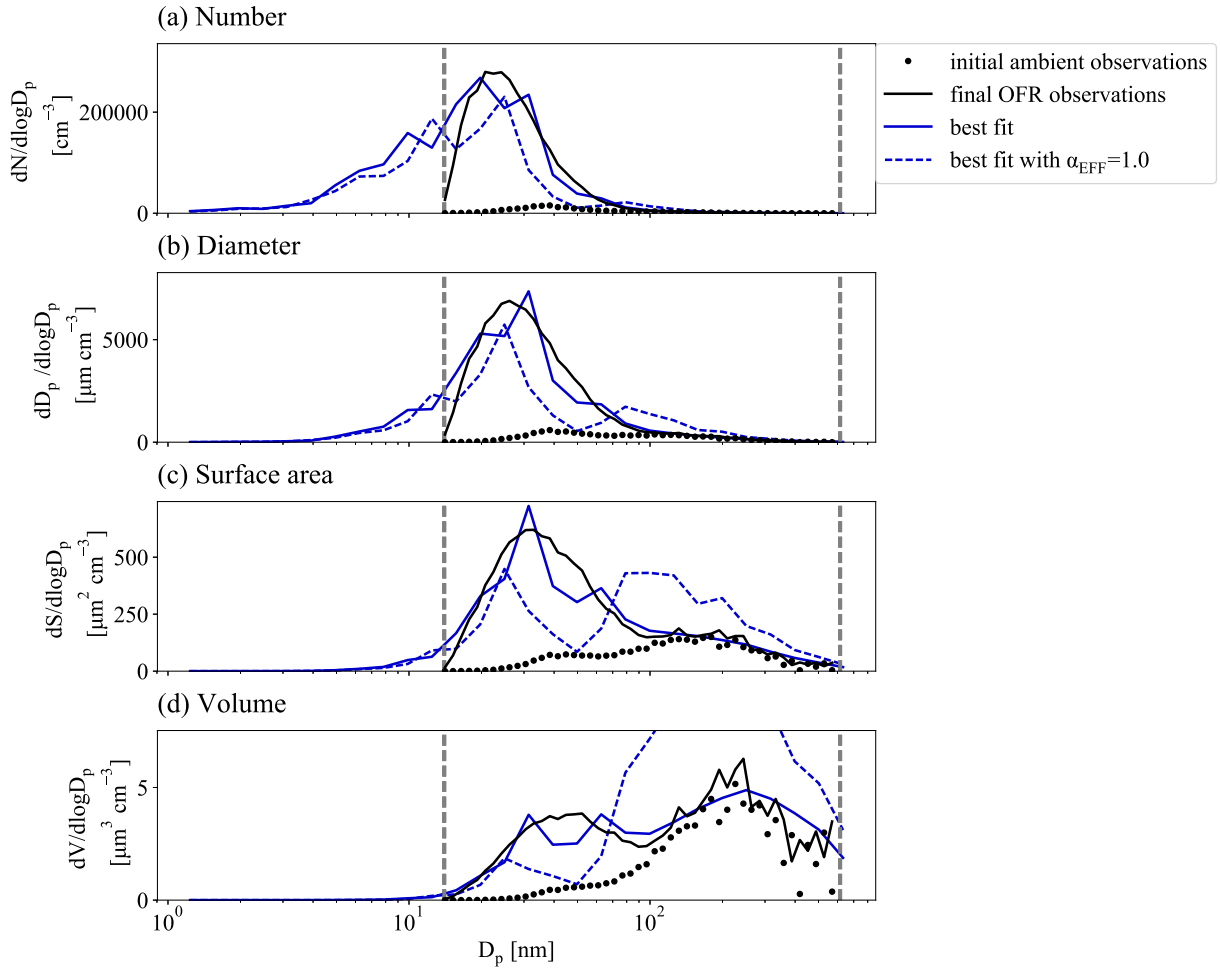

Figure 2.3 Example case of a 0.23 eq. day aging exposure from the BEACHON-RoMBAS campaign. The panels represent the moments used to calculate the normalized mean error (NME), with (a) as particle number, (b) as particle diameter (also referred to as aerosol length), (c) as particle surface area, and (d) as particle volume. The NME is calculated for each model run, using

the final (OFR output) observed size distribution (black lines) compared to each model run's final size distribution (colored lines). The solid blue lines are for the best-fit model case for this exposure, corresponding to $2\times k_{NUC1}$, $5\times k_{OH}$, $0.5\times \gamma_{OH}$, k_{ELVOC}, and $\alpha_{EFF} = 0.01$ (NME = 0.03). The dashed orange lines are for the same parameter values of the best-fit case except that $\alpha_{EFF} = 1.0$ (NME = 0.3). The vertical grey dashed lines indicate the particle size range across which the integration for calculating each mean moment was computed. The initial observed ambient size distribution (dotted black lines) is also plotted for comparison.

2.3. Results and Discussion

2.3.1 BEACHON-RoMBAS modelling results

2.3.1.1 Average behavior of exposures of eq. age 0.09 to 0.91 days for BEACHON-RoMBAS

Figure 2.4 represents the averaged NME summed across the eight 0.09-0.9 eq. day aging exposures modelled from the BEACHON field campaign, for the NUC1 H_2SO_4-organics nucleation scheme and the base value of the reactive uptake coefficient, γ_{OH}, of 0.6. (A discussion of the model sensitivity to other values of the reactive uptake coefficient is below.) Figure 2.4 shows this average NME as a function of α_{EFF} (effective accommodation coefficient of particles with diameters larger than 60 nm), k_{ELVOC} (gas-phase ELVOC fragmentation rate constant), k_{OH} (gas-phase functionalization rate constant), and k_{NUC1} (rate constant for the first H_2SO_4-organics nucleation scheme). Lower α_{EFF} values are necessary for the best fits; however, there are only slight differences between $\alpha_{EFF} = 0.01$ and $\alpha_{EFF} = 0.05$, and $\alpha_{EFF} = 0.1$ (the left three columns, respectively). Faster k_{ELVOC} values are necessary for the best fits; however, similar to α_{EFF}, the base k_{ELVOC} value (middle row), $3\times k_{ELVOC}$, and $9\times k_{ELVOC}$ values show similar results, with the regions of best fits shifting slightly with k_{OH} and k_{NUC1} values. It should be noted that more gas-phase ELVOCs are being formed than could condense during the timescales of the simulated exposures (Fig. 2.2b). As ELVOCs would be formed more slowly in the ambient atmosphere but

with a similar condensational loss timescale, nucleation is expected to proceed faster in the OFR than the ambient atmosphere. This is a reason for the potential usefulness of this OFR technique, that nucleation from chemistry of species present in ambient air can be studied, even if nucleation would not be occurrent under ambient-only conditions.

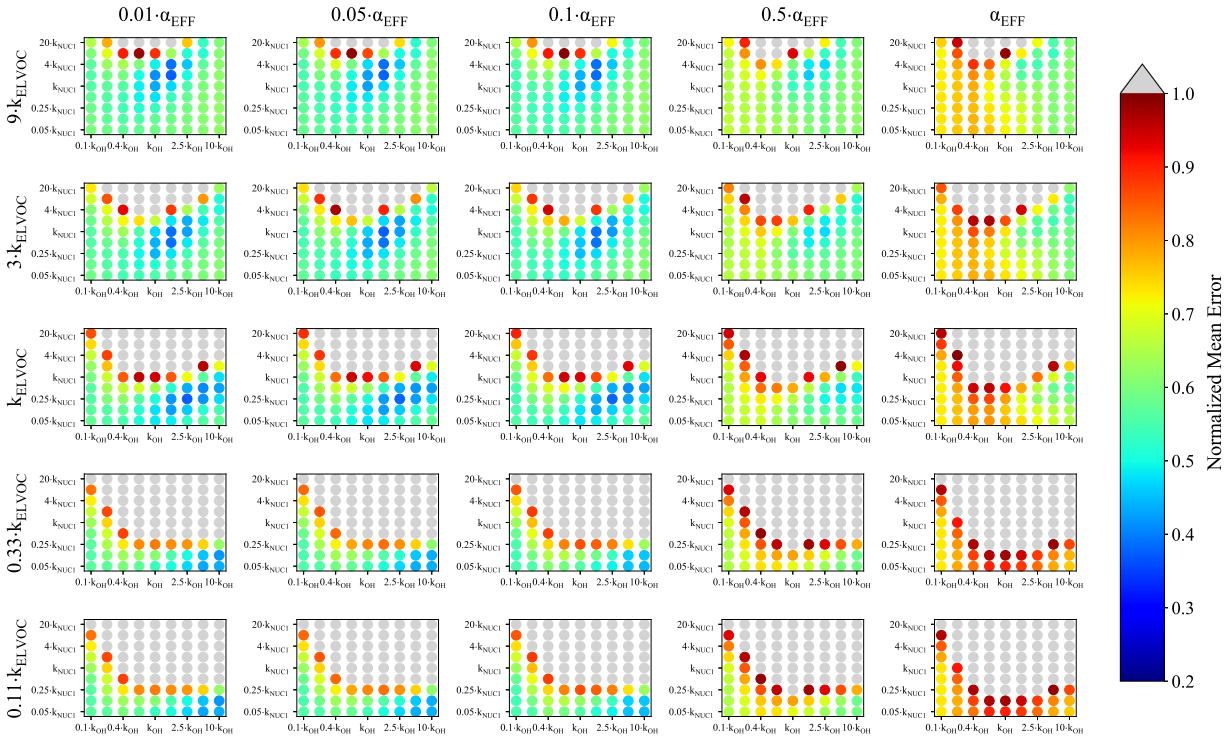

Figure 2.4 Representation of the parameter space for the average across the 0.09-0.9 day eq. aging exposures from BEACHON-RoMBAS examined in this study for the NUC1 nucleation scheme and base value of the reactive uptake coefficient of 0.6. The effective accommodation coefficient increases across each row of panels; the rate constant of gas-phase fragmentation increases up each column of panels. Within each panel, the rate constant of gas-phase reactions with OH increases along the x-axis and the rate constant for nucleation increases along the y-axis. The color bar indicates the normalized mean error (NME) value for each simulation, with the lowest values indicating the least error between model and measurement. Grey regions indicate regions within the parameter space whose NME value is greater than 1. No averaged case had an NME value less than 0.2 for the cases shown here.

For the parameter combinations of $\alpha_{EFF} = 0.01$ through $\alpha_{EFF} = 0.05$ and $9\times k_{ELVOC}$ (the top row of Figure 2.4), the $2\times k_{NUC1}$ and $4\times k_{NUC1}$ values have the best fits. These $2\times k_{NUC1}$ and $4\times k_{NUC1}$

values are similar to those found by Riccobono et al. (2014) for experimental conditions at 278 K (a k_{NUC1} value of 3.27×10^{-21} cm^6 $molec^{-1}$ s^{-1}). However, the other wells of good fits for the base k_{ELVOC} value and $3\times k_{ELVOC}$ have lower nucleation rate constants than that of Riccobono et al. (2014). As mentioned earlier, these k_{NUC1} values determined here correspond to the temperatures of the measurements (between 282-290 K; Table 2.1) which is 4-12 K warmer than the experimental conditions of Riccobono et al. (2014), hence we may expect lower k_{NUC1} values due to the temperature dependence of nucleation (Yu et al., 2017). Figure 2.4 shows that the wells of best fits for all parameter combinations require slightly higher k_{OH} values than the base k_{OH} (based on the k_{OH} values from Eq.2.1) usually on the order of 1.5-2.5 times higher.

Figures 2.2b and 2.3 show an example of the final volatility distribution and size distributions for the best-fit case for an exposure of 0.23 eq. days, corresponding to the model parameters of $2\times k_{NUC1}$, $5\times k_{OH}$, $0.5\times \gamma_{OH}$, k_{ELVOC}, and $\alpha_{EFF} = 0.01$. Figure 2.2a and b gives the initial and final partitioning for this case, respectively, showing that virtually all of the initial gas-phase S/IVOCs have reacted with OH to either enter the lower volatility bins or to fragment into VOC products no longer tracked in the model. Figure 2.3 shows each modelled moment compared to each observed moment of the size distribution used in calculating the NME for the best-fit case.

Figures A.3, A.5, A.7, A.9, A.11, A.13, A.15, and A.17 show the same analysis as presented in Figure 2.4 for each individual exposure modelled for the base value of γ_{OH}, 0.6. Figures A.4, A.6, A.8, A.10, A.12, A.14, A.16, and A.18 plot each observed final (OFR output) moment used in computing the NME statistic (number, diameter, surface area, and volume) compared to the six TOMAS cases with the lowest (best) NME statistic and six TOMAS cases with the highest (worst) NME statistic. For comparison, the observed initial (ambient air) moments are also plotted for each moment.

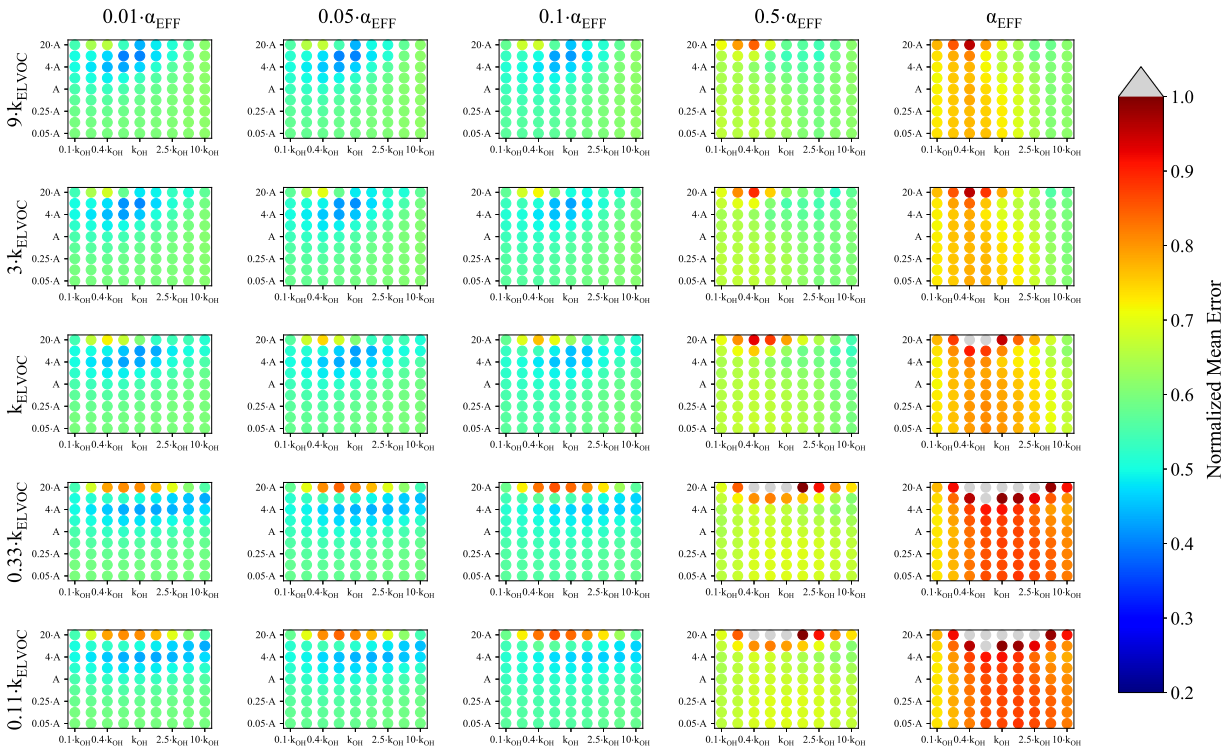

Figure 2.5 Representation of the parameter space for the average across the 0.09-0.9 day eq. aging exposures from BEACHON-RoMBAS examined in this study for the ACT nucleation scheme and base value of the reactive uptake coefficient of 0.6. The effective accommodation coefficient increases across each row of panels; the rate constant of gas-phase fragmentation increases up each column of panels. Within each panel, the rate constant of gas-phase reactions with OH increases along the x-axis and the rate constant for nucleation increases along the y-axis. The color bar indicates the normalized mean error (NME) value for each simulation, with the lowest values indicating the least error between model and measurement. Grey regions indicate regions within the parameter space whose NME value is greater than 1. No averaged case had a NME value less than 0.2 for the cases shown here.

Figure A.19 shows the same analysis as Fig. 2.4, but for the NUC2 nucleation scheme. It is qualitatively quite similar to NUC1 but with the wells of averaged best-fit regions shifted and expanded slightly for some cases. Since we do not have measurements to further constrain the system, we acknowledge that we cannot definitively select NUC1 or NUC2 as being the better nucleation parameterization and instead note that both nucleation schemes appear to provide physically-meaningful results and require further study. In contrast, Fig. 2.5 shows the same

analyses of Fig. 2.4 but for the ACT nucleation scheme (Eq. 2.5). Figure 2.5 shows that there are regions of moderate NME values between 0.45-0.5 for α_{EFF} = 0.01 through α_{EFF} = 0.05. These regions of moderate fits occur for higher values of A (between 4 and 20×A) for a wide range of k_{OH} values. The best fits are seen for higher values of k_{ELVOC} (between the base value of k_{ELVOC} and 9×k_{ELVOC}), the highest nucleation rates (for values of A between 10-20×A) and lower to mid rates of k_{OH} (in general between 0.4×k_{OH} and the base value of k_{OH}). In general, we do not see as good of fits as we do for the NUC1 and NUC2 schemes; however, it does appear that for some combinations of parameters, a reasonable model-to-measurement fit can be achieved with an activation nucleation scheme. Thus, we conclude that for this study, the H_2SO_4-organics mediated nucleation schemes fit the measurements better than the activation nucleation scheme in our model for the OFR measurements taken during the BEACHON campaign.

Further, as the best fits in the model come from the H_2SO_4-organics mediated nucleation schemes, and the best-fit k_{NUC} values are similar to those of Riccobono et al. (2014) where particle-phase chemistry was likely unimportant (low aerosol volume), this is indicative evidence that the creation of gas-phase ELVOCs through oxidation reactions could be dominant over the creation of particle-phase ELVOCs (either through accretion reactions and/or acid-base reactions) for the OFR present at BEACHON campaign, as high concentrations of gas-phase ELVOCs are necessary to facilitate nucleation. It is however important to note that we are limited in our confidence of the actual values of the best fits of the different nucleation rate constants (k_{NUC1}, k_{NUC2}, and A), since each nucleation scheme is sensitive to the concentration of sulfuric acid, and in the majority of the exposures modelled we did not have a direct measurement of SO_2 available for all cases and instead had to estimate SO_2 concentrations for nearly half of the cases.

It is of note that in general, the simulations using $\alpha_{EFF} = 0.5$ and $\alpha_{EFF} = 1.0$ do not yield good fits for any of the nucleation schemes tested here, indicating the importance of some sort of process that limits uptake to the larger aerosol. Figure 2.3 illustrates the impact of the effective accommodation coefficient for a 0.23 eq. day aging exposure: it shows each of the first four moments of the size distribution for the initial and final observations (dotted and black lines) and for the best-fit case for this exposure (solid blue lines) and the model simulation with the same best-fit parameter values but for $\alpha_{EFF} = 1.0$ (dashed blue lines). Compared to the final observations, the best-fit case closely matches the changes in each moment for the Aitken and accumulation modes. However, the best-fit case with α_{EFF} set to 1.0 clearly overestimates growth for the accumulation mode and underestimates growth for the Aitken mode. In general, when $\alpha_{EFF} = 1.0$ there was no combination of the other parameters tested that could simultaneously capture (1) the number and growth of the growing nucleation mode and (2) the change in volume of the large mode. When $\alpha_{EFF} = 1.0$, either the new particles did not grow enough or the large particles grew too much throughout our parameter space. Hence, we were unable to explain the observations without limiting the uptake of material to particles with diameters larger than 60 nm. Additionally, when we tried to lower the accommodation coefficient of smaller particles (not shown), we could not simulate the growth of these particles. While our scheme for limiting the uptake of vapors to the large particles is very simple in this study, we feel that some limitations of vapor uptake to accumulation-mode particles must be at play, possibly from particle-phase diffusion limitations or other reasons. Zaveri et al. (2017) modelled the controlled bimodal growth of aerosol from isoprene and α-pinene oxidation products and found that in order to replicate the observed growth, both the Aitken and accumulation modes required particle-phase diffusivity limitations. However,

their experimental conditions were at much lower humidity than the BEACHON exposures, and did not include any other atmospheric species that could be relevant at BEACHON.

The BEACHON simulations show very little sensitivity towards the reactive uptake coefficient (γ_{OH}) parameter, regardless of which nucleation scheme was used. Figure A.20 shows the model sensitivity towards γ_{OH}: the figure is for the NUC1 nucleation scheme and base value of k_{ELVOC}. Across each row, the effective accommodation increases and down each column, γ_{OH} increases. Within each subplot, the rate constant of gas-phase reactions with OH increases along the x-axis and the rate constant for nucleation increases along the y-axis. Isolating γ_{OH} (each column) shows that for a given set of the other four parameters, the varying values of γ_{OH} do not significantly change the NME. Thus, it would appear that gas-phase fragmentation reactions dominate over particle-phase fragmentation reactions in the OFR for exposures less than one day of equivalent aging. This is in agreement with previous studies of heterogeneous mass loss in OFRs; Hu et al. (2016) did not see significant loss of aerosol mass until exposures greater than 1 day eq. aging for OFR data collected during both the Southern Oxidant and Aerosol Study (SOAS) and the GoAmazon campaign. Because of this, we will focus the remaining discussion upon runs using only the base value of γ_{OH}, 0.6.

As discussed in Sect. 2.2.3.1, the first term of Eq. 2.1 relies on log10(C*) for the rate constant of k_{OH}; however, the fit of Jathar et al. (2014) should instead use ln(C*):

$$k_{OH} = 5.7 \times 10^{-12} \ln(C*) + 1.14 \times 10^{-10} \quad (2.8)$$

(S. Jathar, personal communication). Table A.1 gives the numerical results for k_{OH} for both Eq 2.1 and Eq. 2.7; when Eq. 2.7 is used, the highest volatility bin reacts ~2 times more quickly but the rate constants converge for $C^*=10^0$ μg m^{-3} and remain similar to each other for the lowest volatility bins. Figures A.21 and A.22 provide results of the parameter space for the average across the 0.09-0.9 day eq. aging exposures from BEACHON-RoMBAS examined in this study, using the NUC1

nucleation scheme and base value of the reactive uptake coefficient of 0.6, using Eq. 2.7 for k_{OH} (using the same multipliers for k_{OH} as listed in Table 2.3). Figure A.21 uses all parameter values listed in Table 2.3 (excepting the updated k_{OH} values) and can be directly compared to Fig. 2.4. Figure A.22 further decreases each nucleation rate constant (k_{NUC1}) value by a factor of 10 in order to match the shapes of each panel of Fig. 2.4. Although Fig. A.22 well-matches the general shapes seen in Fig. 2.4 for each k_{ELVOC} and α_{EFF}, the normalized mean errors are larger in both Figs. A.21 and A.22 than in Fig. 2.4. Thus we conclude that for this study, using the k_{OH} values from Eq. 2.1 provide better fits and that parameterizations for rate constants for k_{OH} of air containing a mixture of ambient species require further investigation.

2.3.1.2 Importance of S/IVOCs for SOA formation at BEACHON-RoMBAS

Palm et al. (2016) compared the total SOA formed in the OFR during the BEACHON campaign to the predicted yield from the measured VOCs for OH oxidation in the OFR. For the analysis, they included the measured MT, sesquiterpene (SQT), isoprene, and toluene concentrations and used low-NO_x (to match the OFR chemical regime, Li et al., 2015; Peng et al., 2015), OA-concentration-dependent chamber-derived particle yields for each species. They determined that MTs contributed on average 87% of the SOA predicted to form from these VOC precursors, but on average, the maximum measured SOA formation was 4.4 times higher than the predicted SOA formation. Palm et al. (2016) attributed the yield from measured S/IVOC concentration to the mass difference between measured and predicted SOA yields and concluded that OH oxidation of organic gases could potentially produce approximately 3.4 times more SOA from S/IVOC gases than from the measured VOCs, by using SOA yields for S/IVOC that were consistent with the literature. The correlation between measured SOA formation and ambient MT

concentrations was R^2=0.56, indicating that the S/IVOCs controlling SOA formation in the OFR were primarily related to MT and other biogenic gases with similar diurnal behavior.

To determine the contribution towards the change in total number and volume, we compare the changes in total volume between the averaged change in total volume for the six cases with the lowest (best) NME values of the original model runs for the NUC1 nucleation scheme to the same six cases (matching parameters) but with the initial S/IVOC concentration set to zero (See Sec. 2.5 for calculation details). Table 2.4 summarizes the fractional contribution of the measured initial S/IVOCs (Table 2.1) towards the total change in number and volume. The model predicts that the S/IVOCs contribute on average 85% towards the total new number formed in the OFR, indicating a strong dependence on S/IVOCs for new particle formation in the OFR at BEACHON. The contribution of S/IVOCs towards the total change in volume is lowest for the lowest exposures, and increases with increasing eq. age of each exposure. This is primarily due to the increasing equivalent timescales of the increasing OH exposures: within our model it takes more reactions with OH for S/IVOC species to reach the lowest volatility bins than the MT and isoprene species. Thus with increasing timescales (or eq. ages), the contribution of S/IVOCs towards SOA formation and growth will increase as a higher fraction of these species reach the lowest volatility bins; the results in Table 2.4 corroborate this. However, given that the chemical evolution of S/IVOC is probably more complex than is represented here, we do not know if this result of S/IVOCs contributing a lower fraction of volume for low exposures is a robust conclusion. Overall, we predict that the average fractional contribution of the initial ambient S/IVOCs towards the change in total volume is 39% for the BEACHON exposures, and that the initial ambient MT contributes the remaining 61% towards the change in total volume. Palm et al. (2016) and Hunter et al. (2017) estimated from two independent analyses that S/IVOCs contributed on average 77-78% towards

the total mass SOA formation during BEACHON. It is likely that part of the difference between our model findings and Palm et al. (2016)'s findings is due to the difference in number of samples examined between the two studies as well as differences in the length of exposures analyzed, since Palm et al. (2016) included multi-day exposures in their analysis. It is important to note that running the model with the initial S/IVOCs set to zero ("S/IVOCs off") does not perfectly inform us of the theoretical SOA yield of the MT concentration because the overall particle-phase yield of MTs products decreases with S/IVOCs off due to less mass to partition to.

2.3.2 GoAmazon2014/5 modelling results

In order to model GoAmazon size distributions with TOMAS, we assumed an initial S/IVOC concentration, as no instrumentation was present during the campaign to measure total S/IVOC mass. For a starting total S/IVOC concentration, we used the same measured ratio of S/IVOCs to MTs from BEACHON of 1.4 (Table 2.1). This initial S/IVOC concentration was not sufficient to explain the observed change in aerosol volume, nucleation, and new-particle growth in the OFR for GoAmazon (see Figs. A.21-A.22 for an example). We found that the initial S/IVOC concentration needed to be increased by between 20-40 times in order to fit the observed distributions. As BEACHON was dominated by biogenic emissions (primarily MTs), but GoAmazon had major contributions from anthropogenic and biomass burning sources as well as various biogenic emissions (Palm et al., 2018), the larger S/IVOC is thought to be dominated by emissions and partially oxidized products from the two latter sources. We present results for 30 times the base S/IVOC concentrations (Table 2.1) in Figs. 2.6 and A.23-A.32 as this amount of increase showed consistently good results across the four exposures modelled. For comparison, the total initial S/IVOC mass for the BEACHON OFR exposures modelled ranges between 2.89 and 14.02 μg m^{-3} whereas the total initial S/IVOC mass for the GoAmazon OFR exposures

modelled ranges between 9.0 and 18.6 μg m^{-3} when the assumption of 30 times higher S/IVOC:MT ratios is used. Hence, even though the S/IVOC:MT ratios were higher for GoAmazon relative to BEACHON, our assumed S/IVOC concentrations were in the same general range for the two campaigns. We note that by not including the measured concentrations of SQT, benzene, toluene, xylenes, and trimethylbenzenes in our model likely slightly biases our S/IVOC estimation high, but not by a significant amount as Palm et al. (2018) found that these species contributed on average a sum total of 8% towards the measured SOA yield from the measured VOC precursor species.

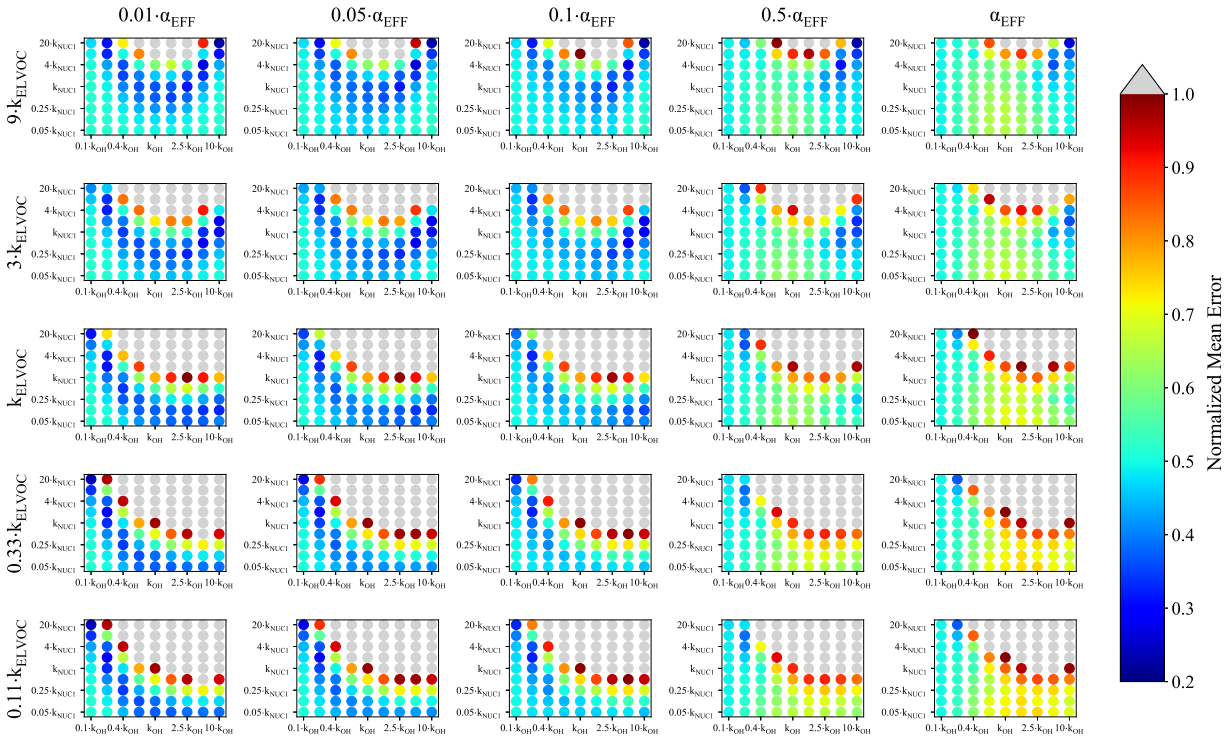

Figure 2.6 Representation of the parameter space for the average across the 0.3-0.6 day eq. aging exposures from GoAmazon examined in this study for the NUC1 nucleation scheme, base value of the reactive uptake coefficient of 0.6, and assumed S/IVOC:MT ratio of 30 times that of the BEACHON-RoMBAS S/IVOC:MT ratio. The effective accommodation coefficient increases across each row of panels; the rate constant of gas-phase fragmentation increases up each column of panels. Within each panel, the rate constant of gas-phase reactions with OH increases along the

x-axis and the rate constant for nucleation increases along the y-axis. The color bar indicates the normalized mean error (NME) value for each simulation, with the lowest values indicating the least error between model and measurement. Grey regions indicate regions within the parameter space whose NME value is greater than 1. No averaged case had a NME value less than 0.2 for the cases shown here.

Figure 2.6 represents the averaged NME across the four 0.3-0.6 eq. day aging exposures modelled from the GoAmazon field campaign for the NUC1 H_2SO_4-organics nucleation scheme and the base value of γ_{OH}, 0.6. In general, there are wider ranges of k_{OH}, k_{ELVOC}, and k_{NUC1} values that give small NMEs for the averaged GoAmazon modelled exposures than for the averaged BEACHON modelled exposures. The model simulations generally perform best with lower accommodation coefficients of the larger particles (between $\alpha_{EFF} = 0.01$ and $\alpha_{EFF} = 0.1$), similar to the BEACHON results; however, there are some similarly low-NME results between $\alpha_{EFF} = 0.05$ and $\alpha_{EFF} = 1$ for the two highest k_{ELVOC} values. Bateman et al. (2015) showed that sub-micrometer PM aerosol in the Amazon rainforest measured at the same T3 site as the GoAmazon campaign during the dry season tend to be liquid, so it is possible that the uptake/diffusion limitations to the accumulation mode inferred for BEACHON may not occur during GoAmazon. However, we do not have enough information to learn more about the causes of uptake/diffusion limitations to the accumulation mode or differences between the campaigns.

Previous ambient observations of the Amazon rainforests have not observed nucleation at the surface (e.g., Spracklen et al., 2006; Martin et al, 2010; Kanawade et al., 2011). Reasons could include low sulfuric acid (Kanawade et al., 2011), high condensation sinks resulting from a strong source of primary biogenic aerosols during the dry season (Lee et al., 2016), and possible yet currently unexplained suppression mechanisms from isoprene and its oxidation products (Lee et al., 2016), the dominant biogenic VOC of the region (Guenther et al., 2012). Wang et al. (2016) found high concentrations of small particles in the lower free troposphere during the wet season

of GoAmazon; however, they found that these particles appeared to be from NPF and subsequent condensational and coagulational growth from the outflow regions of deep convective systems, such as those common to the Amazonian rainforest during the wet season. These particles could then be transported to the boundary layer through vertical transport. By contrast, in some of the OFR-oxidized air during the GoAmazon campaign the size distributions show clear evidence of NPF and growth (e.g., Fig. A.1) and the TOMAS model simulations corroborate the observed NPF (Figs. A.28, A.30, A.32, A.34), even at the initial S/IVOC inputs (Fig. A.24). The OFR shifts the relative timescales of chemistry versus condensation, which may create higher concentrations of low-volatility vapors capable of participating in nucleation and early growth relative to the ambient atmosphere during GoAmazon. The lowest NME values (best fits) from the averaged BEACHON modelled exposures (Fig. 2.4) for the highest two k_{ELVOC} values overlap regions of wells of best fits for the averaged GoAmazon modelled exposures. For GoAmazon there is a wider range of k_{OH}, k_{ELVOC}, and k_{NUC1} values that give low NME values compared to BEACHON modelled exposures. We note that the lower number of exposures modelled for GoAmazon than modelled for BEACHON limit our confidence in comparing the two campaigns' results to each other, as does the narrower range of equivalent aging (between 0.39 and 0.52 eq. days aging for GoAmazon compared to 0.09 to 0.91 eq. days aging for BEACHON). Figures A.27, A.29, A.31, and A.33 show the same analysis as presented in Fig. 2.6 for each individual exposure modelled for the base value of γ_{OH}, 0.6. Figures A.28, A.30, A.32, and A.34 plot each observed final size distributions for the first four moments (solid black lines) used in computing the NME statistic compared to the six TOMAS cases with the lowest (best) NME statistic and six TOMAS cases with the highest (worst) NME statistic. For comparison, the observed initial (ambient) moments are also plotted for each moment.

Tests of NUC2 and ACT show similar changes from NUC1 for GoAmazon as BEACHON (Figs. A.25 and A.26). NUC2 results were qualitatively similar to NUC1, and we cannot determine which scheme performed better. The regions of lowest NME values (best fits) shifted for the ACT scheme relative to the NUC1 and NUC2 schemes, and generally the NMEs are not quite as low as for NUC1 and NUC2, although better fits are found for the ACT nucleation scheme for GoAmazon than BEACHON. Thus it would seem that either a H_2SO_4-organics mediated nucleation scheme or a H_2SO_4-only nucleation scheme can be used in our model to describe the OFR measurements taken during the GoAmazon campaign. Like BEACHON, we are still limited in our confidence of the actual values of the best fits of the different nucleation rate constants (k_{NUC1}, k_{NUC2}, and A) as each nucleation scheme is sensitive to the concentration of sulfuric acid, and some exposures had an estimated SO_2 concentration.

Similar to BEACHON, more good fits for each nucleation scheme occur at lower values of α_{EFF}, again pointing to the potential importance of vapor-uptake/diffusion limitations at least within the OFR timescales. Again, varying the reactive uptake coefficient was not seen to significantly change the NME values of each set of parameter values, regardless of nucleation scheme, and thus we only show results for the base value of the reactive uptake coefficient (Figs. 2.6, A.25-A.26, A.27, A.29, A.31, and A.33).

2.3.2.1 Importance of S/IVOCs for SOA formation at GoAmazon2014/5

Unlike the BEACHON campaign, bulk S/IVOCs were not measured directly during the GoAmazon campaign. However, Palm et al. (2018) applied a similar analysis to that of Palm et al. (2016) to determine the measured vs. predicted SOA yield. They found that on average, OH oxidation of ambient air during the GoAmazon campaign (dry season) produced 6.5 times more SOA than could be accounted for from the measured ambient VOCs. They used the low-NO_x SOA

yields (verified by standard addition during the campaign) corresponding to the expected conditions in the OFR (Li et al., 2015) for the measured MT, SQT, toluene, and isoprene concentrations. Unlike BEACHON, it was observed for GoAmazon that the slope of the measured versus predicted SOA formation from OH oxidation varied as a function of time of day, with predicted SOA lower during the nighttime than daytime but measured SOA formation higher during the nighttime than daytime. Palm et al. (2018) were uncertain of the reasons for the observed SOA trends, but hypothesize that several processes likely play a role, including diurnal changes in emissions, boundary layer dynamics, and variable ambient oxidant concentrations. Palm et al. (2018) hypothesized that, like the BEACHON campaign, S/IVOCs could make up the mass difference between measured and predicted SOA yields from OH oxidation in the OFR. In this study, it was found that between 20-40 times more initial S/IVOCs than the base concentrations of S/IVOCs (Table 2.1) derived from using the ratio of S/IVOCs:MT, 1.4, from BEACHON was required to explain the aerosol formation and growth and change in total volume observed in the OFR during GoAmazon for OH oxidation. This corroborates the findings of Palm et al. (2018) that no strong correlation was found between any one VOC precursor gas, indicating that SOA formation was impacted by multiple sources.

To determine the contribution of MT and isoprene towards the change in total number and volume for the GoAmazon exposures, we repeat the analysis done for the BEACHON exposures (Sect. 2.3.1.2.) and the results are summarized in Table 2.4, using the S/IVOC concentrations of 30 times the base S/IVOC concentrations. The model predicts that the optimized S/IVOC concentrations contribute 100% towards the new aerosol number formation observed for each exposure modelled, again pointing towards the importance of S/IVOCs for NPF in the OFR. However, since SQT, benzene, toluene, xylenes, and trimethylbenzenes (all measured ambient

VOC species predicted to contribute towards SOA formation) were not included in the model, we cannot conclude that S/IVOCs are actually responsible for 100% of the new aerosol formed in the OFR. Similar to BEACHON, the fractional contribution of S/IVOCs towards the change in total volume increases with increasing eq. age; overall, the average fractional contribution of the best-fit S/IVOC concentration towards the change in total volume is 0.66. By comparison, Palm et al. (2018) found that the fractional contribution of S/IVOCs towards the measured SOA formation during the dry season of GoAmazon was on average 0.85. We again expect that the VOCs will have artificially low SOA yields in the "S/IVOCs off" simulations, indicating that MT and/or isoprene could contribute more towards the change in total volume than indicated here. However, Palm et al. (2018) found that the yield dependence of ambient SOA precursors on ambient OA was weaker for the OFR GoAmazon exposures than it was for the chamber-derived parameterizations used to predict the OFR yield.

Table 2.4 Modelled fractional contribution of initial S/IVOCs towards the total change in number and volume between the initial and final number volume size distributions of each exposure modelled in this study. We use the measured S/IVOCs for the BEACHON-RoMBAS calculations and the best-fit initial S/IVOC concentration found for the GoAmazon calculations. The remaining fractional contribution towards the total change in number and volume is attributable to the measured initial monoterpenes (both campaigns) and measured initial isoprene (GoAmazon). Each exposure's fractional contribution is calculated using the averaged contributions of the 6 model cases with the lowest (best) NME values from the full model parameter space.

Exposure (eq. age)	Fractional contribution from S/IVOCs (number)	Fractional contribution from S/IVOCs (volume)
BEACHON-RoMBAS		
0.090	0.89	0.20
0.098	0.86	0.05
0.16	1.0	0.29
0.23	0.79	0.66
0.27	0.93	0.68
0.77	0.55	0.55
0.82	0.94	0.66
0.91	0.89	0.64
Average	0.85	0.39
GoAmazon		
0.39	1.0	0.35
0.40	1.0	0.42
0.51	1.0	0.71
0.53	1.0	0.76
Average	1.0	0.66

2.3.2.2 Importance of isoprene for SOA formation at GoAmazon2014/5

The TOMAS box model does not include isoprene-specific oxidation pathways and instead allows it to oxidize in the VBS scheme along with the other lumped oxidized species. We determine the fractional contribution of the initial isoprene concentration towards the change in total number volume for each exposure modelled (Table 2.5); the remaining fraction is the total volume change attributable from initial MT and the optimized initial S/IVOC concentrations (30 times that of the base S/IVOC concentrations). At maximum, it is predicted that within the OFR isoprene will contribute 0% and 3% towards the change in total number and volume, respectively; on average, it is predicted that isoprene will contribute 0% and 1% towards the change in total number and volume. However, this does not preclude the potential importance of isoprene towards ambient SOA formation. The OFR can only form SOA from the gases that enter it; although isoprene emissions are high, isoprene reacts quickly (Atkinson and Arey, 2003b) so that much of the potential SOA from isoprene and its oxidation products enters the chamber already in the

particle phase. Further, the OFR does not capture the most important isoprene SOA formation pathway, such as IEPOX-SOA produced from reactive uptake on time scales longer than the OFR residence time (Hu et al., 2016). Palm et al. (2018) estimated that on average during the dry season, isoprene contributes 5% towards the predicted SOA mass yield from the measured ambient VOC precursor species in the OFR. Not including isoprene-specific oxidation pathways in our model may be a source of error in calculating the contribution of isoprene towards the total change in number and mass.

Table 2.5 Modelled fractional contribution of the measured initial isoprene concentrations towards the total change in number and volume between the initial and final number and volume size distributions modelled from the GoAmazon2014/5 campaign, using the best-fit S/IVOC estimate. (Isoprene was not included in the model for the BEACHON-RoMBAS distributions.) The remaining fractional contribution is attributable to the MT and S/IVOC concentrations in the model. Each exposure's fractional contribution is calculated using the averaged contributions of the six model cases with the lowest (best) NME values from the full model parameter space.

Exposure (eq. age)	Fractional contribution from isoprene (number)	Fractional contribution from isoprene (volume)
	GoAmazon	
0.39	0.0	0.0
0.40	0.02	0.0
0.51	0.0	0.0
0.53	0.0	0.03
Average	0.0	0.01

2.4 Conclusions

In this study, aerosol size distributions between 0.09-0.9 days of eq. aging formed under OH oxidation in an OFR during the BEACHON-RoMBAS (BEACHON) and GoAmazon2014/5 (GoAmazon) field campaigns were modelled in the TOMAS box model in order to better-understand the microphysical processes that shape the size distribution under oxidative aging. We

explored the following parameter spaces to find regions of best-fit model-to-measurement agreements: (1) nucleation rate constants for two H_2SO_4-organics nucleation mechanisms versus a H_2SO_4 activation nucleation mechanism, gas-phase (2) functionalization and (3) fragmentation rate constants, (4) heterogeneous reactions with OH resulting in fragmentation and aerosol mass loss, and (5) potential particle diffusion limitations to the accumulation mode.

In order to limit the scope of this study, several uncertain processes and values were not included in this analysis. We did not include the formation of low-volatility organics through particle-phase acid-base reactions or accretion reactions, as (1) no measurements of gas-phase bases were made at either campaign and (2) the model results indicate the importance of the gas-phase ELVOC creation pathway must be fast in order to drive nucleation, which may limit the importance of particle-phase pathways. We did not consider the model sensitivity towards the input OH concentration, although there is uncertainty associated with the estimated OH exposure (Palm et al., 2016; 2018). We further did not explore the model sensitivity towards the assumed decrease of a factor of 100 in volatility for each product from OH functionalization reactions, nor did we explore the sensitivity of including fragmentation reactions for volatility bins higher than the ELVOC bin. These two uncertainties are not entirely orthogonal to the uncertainties in k_{OH} and k_{ELVOC} that we did explore, and including them would have increased the number of free parameters in the model, making it more challenging to determine what combinations of parameters most-closely match the actual processes occurring in the OFR. Finally, there is evidence for possible NPF suppression in some isoprene-dominated regions but as those mechanisms are as yet unknown (Lee et al., 2016), no isoprene chemistry was explicitly simulated for the modelled GoAmazon exposures. However, as shown in Table 2.5, isoprene was only a minor contributor to our predicted aerosol volume for the GoAmazon simulations.

We found that we could not explain the observed size-distribution shift without slowing the uptake of SOA to the accumulation-mode particles. With an accommodation coefficient of 1 assumed for the full size distribution, these larger particles underwent too much condensational growth relative to the nucleation mode for all test cases. We speculate that this slowed uptake of larger particles may be indicative of particle-phase diffusion limitations. We approximate vapor-uptake limitations by allowing the accommodation coefficient of particles larger than 60 nm diameter to vary between 0 and 1. We found that we can achieve the best fits of the size distribution when the accommodation coefficient of these larger particles was 0.1 or lower (if we similarly lowered the accommodation coefficient of smaller particles, we would not have gotten good fits as the new particles did not grow enough). Whether this is representative of ambient aerosol processes or just representative of conditions within the OFR is the subject of a future study.

We found that gas-phase fragmentation reactions also had a significant impact upon the modelled size distributions. Our best-fit gas-phase fragmentation rate constants were higher than that of a previous mass-based study of OFR exposures from BEACHON (Palm et al., 2016) required to model the distributions. However, these higher rates may be because our model only simulated fragmentation reactions of the lowest volatility compounds, that of $C^* \leq 10^{-4}$ μg m^{-3}, whereas in reality fragmentation reactions can occur to higher-volatility compounds (although the likelihood of fragmentation likely increases with decreasing volatility). Thus, the higher fragmentation rate constant can be seen as compensating for fragmentations of higher-volatility compounds. Including fragmentation of higher volatility species would lower the fraction of the organic vapors that then make it to lower volatility. This would then potentially decrease nucleation rates and slow the growth rates of the smallest particles. However, the fragmentation scheme used in this study should be viewed as a sensitivity study; the inclusion of a more-complex

fragmentation scheme would have added more free parameters to our study and will be left to a future study.

In general, the H_2SO_4-organics nucleation mechanisms performed better than the activation nucleation mechanism for both campaigns. We found that the nucleation rate constants for the H_2SO_4-organics nucleation mechanism suggested by Riccobono et al. (2014) allowed for good models fits, with the caveats that the temperatures of both campaigns were higher than the experimental conditions of Riccobono et al. (2014) (4-12 K higher for BEACHON and 18-19 K higher for GoAmazon), and that the timescales upon which ELVOCs were formed and capable of participating in nucleation could be shorter than that of the ambient atmosphere. Similarly, we found that gas-phase oxidation rate constants similar to that of Jathar et al. (2014), fit from aromatics, allowed for good fits (we assumed that these reactions were 100% functionalization and treated the fragmentation reactions separately). The gas-phase oxidation rate constants provided better fits when using a slightly different formulation than the parameterization from Jathar et al. (2014), indicating that further studies are required for fitting parameterizations for air containing a mixture of ambient species. Finally, we found that heterogeneous reactions of the OA with OH resulting in fragmentation and aerosol mass loss did not appear to significantly impact the distributions modelled in this study. As all of our equivalent exposure times tested were less than one day, these results are consistent with previous OFR studies on heterogeneous aging that found that heterogeneous losses of OA from OH were not important for these exposure timescales (Hu et al., 2016). Like Palm et al. (2016; 2018), our results indicate the importance of S/IVOCs towards aerosol growth in the OFR at both the BEACHON and GoAmazon campaigns. We find that S/IVOCs contribute on average 85% and 39% (BEACHON) and 100% and 66% (GoAmazon) towards the change in total number and volume, respectively, for the exposures modelled in this

study. There remains uncertainty in the sources of these S/IVOCs: they could be directly emitted or formed as oxidation products from both biogenic and anthropogenic sources for BEACHON (Palm et al., 2016) and from biogenic, anthropogenic, and biomass burning sources for GoAmazon (Palm et al., 2018). Further studies are required to better understand, speciate, and quantify S/IVOC sources.

This study has shown the potential for using OFRs to study factors that control NPF and size-distribution evolution using ambient-air mixtures. The fact that coagulation plays a small role in the measured number concentration indicates that this type of reactor is useful to evaluate model parameterizations of the number of nucleated particles and their growth, as a function of ambient and OFR conditions. Using an OFR greatly expands the parameter space over which comparisons can be made as well as the number of cases that can be studied, compared to using only ambient data where parameter variations are more narrow, and where NPF is not observed under many conditions. Future studies could use OFRs in nucleation studies to both better-understand the dependencies of nucleation on input species (e.g., H_2SO_4, gas-phase bases, and specific VOCs) by injecting controlled amounts of each species or precursors on top of ambient air at variable oxidant concentrations, as well as determine dominant nucleation mechanisms for different ambient environments. In order to assist in ambient nucleation studies, more-precise measurements of ambient SO_2 should be made during ambient campaigns in order to more accurately test current nucleation theories (all of which depend upon the concentration of H_2SO_4) against different ambient environments. Measurements of H_2SO_4 and ELVOCs, as well as bases such as ammonia and amine species, inside the reactor would help constrain the nucleation and growth mechanisms significantly. Additionally, studies focused on size-distribution evolution processes could include size-dependent particle-phase composition and property measurements in order to assess

parameters such as particle phase state and presence of acid-base or accretion products as a function of equivalent aging in order to better constrain the model assumptions against observations. Focusing on lower OH exposures (<<1 day, to limit fragmentation reactions prior to condensation/nucleation) as well as varying OFR residence times may allow extracting more information on new-particle formation and growth from these experiments. Another vein of research could use the best-fit parameters found in this study and similar studies to initialize ambient models in order to predict under what conditions (emissions, initial particle concentrations, OH concentrations, and so forth) one would anticipate NPF and growth. Such predictions, if well-validated by corresponding ambient measurements, could help construct simple parameterizations for use in regional and global models to better-simulate NPF and growth events in order to improve predictions of size-resolved aerosol concentrations and their corresponding impacts upon climate and health.

REFERENCES

Adams, P. J. and Seinfeld, J. H.: Predicting global aerosol size distributions in general circulation models, J. Geophys. Res., 107(D19), 4370, doi:10.1029/2001JD001010, 2002.

Almeida, J., Schobesberger, S., Kurten, A., Ortega, I. K., Kupiainen-Maatta, O., Praplan, A. P., Adamov, A., Amorim, A., Bianchi, F., Breitenlechner, M., David, A., Dommen, J., Donahue, N. M., Downard, A., Dunne, E., Duplissy, J., Ehrhart, S., Flagan, R. C., Franchin, A., Guida, R., Hakala, J., Hansel, A., Heinritzi, M., Henschel, H., Jokinen, T., Junninen, H., Kajos, M., Kangasluoma, J., Keskinen, H., Kupc, A., Kurten, T., Kvashin, A. N., Laaksonen, A., Lehtipalo, K., Leiminger, M., Leppa, J., Loukonen, V., Makhmutov, V., Mathot, S., McGrath, M. J., Nieminen, T., Olenius, T., Onnela, A., Petaja, T., Riccobono, F., Riipinen, I., Rissanen, M., Rondo, L., Ruuskanen, T., Santos, F. D., Sarnela, N., Schallhart, S., Schnitzhofer, R., Seinfeld, J. H., Simon, M., Sipila, M., Stozhkov, Y., Stratmann, F., Tome, A., Trostl, J., Tsagkogeorgas, G., Vaattovaara, P., Viisanen, Y., Virtanen, A., Vrtala, A., Wagner, P. E., Weingartner, E., Wex, H., Williamson, C., Wimmer, D., Ye, P., Yli-Juuti, T., Carslaw, K. S., Kulmala, M., Curtius, J., Baltensperger, U., Worsnop, D. R., Vehkamaki, H. and Kirkby, J.: Molecular understanding of sulphuric acid-amine particle nucleation in the atmosphere, Nature, 502(7471), 359–363 [online] Available from: http://dx.doi.org/10.1038/nature12663, 2013.

Arangio, A. M., Slade, J. H., Berkemeier, T., Pöschl, U., Knopf, D. A., and Shiraiwa, M.: Multiphase Chemical Kinetics of OH Radical Uptake by Molecular Organic Markers of Biomass Burning Aerosols: Humidity and Temperature Dependence, Surface Reaction, and Bulk Diffusion, J. Phys. Chem. A, 119, 4533–4544, doi:10.1021/jp510489z, 2015.

Atkinson, R. and Arey, J.: Atmospheric Degradation of Volatile Organic Compounds, Chem. Rev., 103, 4605–4638, doi:10.1021/cr0206420, 2003a.

Atkinson, R. and Arey, J.: Gas-phase tropospheric chemistry of biogenic volatile organic compounds: a review, Atmos. Environ., 37(Supplement 2), 197–219, doi:https://doi.org/10.1016/S1352-2310(03)00391-1, 2003b.

Bae, M.-S., Schwab, J. J., Hogrefe, O., Frank, B. P., Lala, G. G., and Demerjian, K. L.: Characteristics of size distributions at urban and rural locations in New York, Atmos. Chem. Phys., 10, 4521-4535, https://doi.org/10.5194/acp-10-4521-2010, 2010.

Barsanti, K. C. and Pankow, J. F.: Thermodynamics of the formation of atmospheric organic particulate matter by accretion reactions – Part 1: aldehydes and ketones, Atmos. Environ., 38, 4371–4382, doi:10.1016/j.atmosenv.2004.03.035, 2004.

Bateman, A. P., Gong, Z., Liu, P., Sato, B., Cirino, G., Zhang, Y., Artaxo, P., Bertram, A. K., Manzi, A. O., Rizzo, L. V., Souza, R. A. F., Zaveri, R. A. and Martin, S. T.: Sub-micrometre particulate matter is primarily in liquid form over Amazon rainforest, Nat. Geosci., 9(1), 34–37, doi:10.1038/ngeo2599, 2015.

Bateman, A. P., Gong, Z., Harder, T. H., De Sá, S. S., Wang, B., Castillo, P., China, S., Liu, Y., O'Brien, R. E., Palm, B. B., Shiu, H. W., Cirino, G. G., Thalman, R., Adachi, K., Lizabeth Alexander, M., Artaxo, P., Bertram, A. K., Buseck, P. R., Gilles, M. K., Jimenez, J. L., Laskin, A., Manzi, A. O., Sedlacek, A., Souza, R. A. F., Wang, J., Zaveri, R. and Martin, S. T.: Anthropogenic influences on the physical state of submicron particulate matter over a tropical forest, Atmos. Chem. Phys., 17(3), 1759–1773, doi:10.5194/acp-17-1759-2017, 2017.

Bian, Q., Jathar, S. H., Kodros, J. K., Barsanti, K. C., Hatch, L. E., May, A. A., Kreidenweis, S. M. and Pierce, J. R.: Secondary organic aerosol formation in biomass-burning plumes: theoretical analysis of lab studies and ambient plumes, Atmos. Chem. Phys., 17(8), 5459–5475, doi:10.5194/acp-17-5459-2017, 2017.

Boucher, O., Randall, D., Artaxo, P., Bretherton, C., Feingold, G., Forster, P., Kerminen, V.M., Kondo, Y., Liao, H., Lohmann, U., Rasch, P., Satheesh, S. K., Sherwood, S., Stevens, B., and Zhang, X. Y.: Clouds and Aerosols, in: Climate Change 2013: The Physical Science Basis. Contribution of Working Group I to the Fifth Assessment Report of the Intergovernmental Panel on Climate Change, edited by: Stocker, T. F., Qin, D., Plattner, G. K., Tignor, M., Allen, S. K., Boschung, J., Nauels, A., Xia, Y., Bex, V., and Midgley, P. M., Cambridge University Press, Cambridge, UK, and New York, NY, USA, 2013.

Bruns, E. A., Haddad, I. El, Keller, A., Klein, F., Kumar, N. K., Pieber, S. M., Corbin, J. C., Slowik, J. G., Brune, W. H., Baltensperger, U. and Prévôt, A. S. H.: Inter-comparison of laboratory smog chamber and flow reactor systems on organic aerosol yield and composition, Atmos. Meas. Tech, 8, 2315–2332, doi:10.5194/amt-8-2315-2015, 2015.

Cappa, C. D. and Wilson, K. R.: Evolution of organic aerosol mass spectra upon heating: implications for OA phase and partitioning behavior, Atmos. Chem. Phys., 11, 1895-1911, https://doi.org/10.5194/acp-11-1895-2011, 2011.

Chacon-Madrid, H. J., Presto, A. A. and Donahue, N. M.: Functionalization vs. fragmentation: n-aldehyde oxidation mechanisms and secondary organic aerosol formation, Phys. Chem. Chem. Phys., 12(42), 13975–13982, doi:10.1039/C0CP00200C, 2010.

Chacon-Madrid, H. J. and Donahue, N. M.: Fragmentation vs. functionalization: chemical aging and organic aerosol formation, Atmos. Chem. Phys., 11(20), 10553–10563, doi:10.5194/acp-11-10553-2011, 2011.

Charlson, R. J., Schwartz, S. E., Hales, J. M., Cess, R. D., Coakley, J. A., Hansen, J. E., and Hofmann, D. J.: Climate forcing by anthropogenic aerosols, Science, 255, 423–430, 1992.

Chen, M., Titcombe, M., Jiang, J., Jen, C., Kuang, C., Fischer, M. L., Eisele, F. L., Siepmann, J. I., Hanson, D. R., Zhao, J. and McMurry, P. H.: Acid-base chemical reaction model for nucleation rates in the polluted atmospheric boundary layer., Proc. Natl. Acad. Sci. U. S. A., 109(46), 18713–8, doi:10.1073/pnas.1210285109, 2012.

Clement, A. C., Burgman, R., and Norris, J. R.: Observational and Model Evidence for Positive Low-Level Cloud Feedback, Science, 325, 460–464, 2009.

Cross, E. S., Hunter, J. F., Carrasquillo, A. J., Franklin, J. P., Herndon, S. C., Jayne, J. T., Worsnop, D. R., Miake-Lye, R. C., and Kroll, J. H.: Online measurements of the emissions of intermediate-volatility and semi-volatile organic compounds from aircraft, Atmos. Chem. Phys., 13, 7845–7858, doi:10.5194/acp-13-7845-2013, 2013.

Dal Maso, M., Kulmala, M., Lehtinen, K. E. J., M̈kelä, J. M., Aalto, P. and O'Dowd, C. D.: Condensation and coagulation sinks and formation of nucleation mode particles in coastal and boreal forest boundary layers, J. Geophys. Res. Atmos., 107(19), doi:10.1029/2001JD001053, 2002.

Donahue, N. M., Robinson, A. L., Stanier, C. O., and Pandis, S. N.: Coupled Partitioning, Dilution, and Chemical Aging of Semivolatile Organics, Environ. Sci. Technol., 40, 2635–2643, doi:10.1021/es052297c, 2006.

Fry, J. L., Draper, D. C., Zarzana, K. J., Campuzano-Jost, P., Day, D. A., Jimenez, J. L., Brown, S. S., Cohen, R. C., Kaser, L., Hansel, A., Cappellin, L., Karl, T., Hodzic Roux, A., Turnipseed, A., Cantrell, C., Lefer, B. L., and Grossberg, N.: Observations of gas- and aerosol-phase organic nitrates at BEACHON-RoMBAS 2011, Atmos. Chem. Phys., 13, 8585-8605, https://doi.org/10.5194/acp-13-8585-2013, 2013.

George, I. J. and Abbatt, J. P. D.: Heterogeneous oxidation of atmospheric aerosol particles by gas-phase radicals, Nature Chemistry, 2, 713–722, 2010.

George, C., Ammann, M., D'Anna, B., Donaldson, D. J., and Nizkorodov, S. A.: Heterogeneous Photochemistry in the Atmosphere, Chem. Rev., 115 4218–4258, doi:10.1021/cr500648z, 2015.

Goldstein, A. H. and Galbally, I. E.: Known and Unexplored Organic Constituents in the Earth's Atmosphere, Environ. Sci. Technol., 41, 1514–1521, doi:10.1021/es072476p, 2007.

Graus, M., Müller, M., and Hansel, A.: High Resolution PTR-TOF: Quantification and Formula Confirmation of VOC in Real Time, J. Am. Soc. Mass. Spectr., 21, 1037–1044, doi:10.1016/j.jasms.2010.02.006, 2010.

Guenther, A. B., Jiang, X., Heald, C. L., Sakulyanontvittaya, T., Duhl, T., Emmons, L. K. and Wang, X.: The Model of Emissions of Gases and Aerosols from Nature version 2.1 (MEGAN2.1): an extended and updated framework for modeling biogenic emissions, Geosci. Model Dev., 5(6), 1471–1492, doi:10.5194/gmd-5-1471-2012, 2012.

Hallar, A. G., Petersen, R., Mccubbin, I. B., Lowenthal, D., Lee, S., Andrews, E. and Yu, F.: Climatology of New Particle Formation and Corresponding Precursors at Storm Peak Laboratory, Aerosol Air Qual. Res., 16, 816–826, doi:10.4209/aaqr.2015.05.0341, 2016.

Henry, K. M., Lohaus, T. and Donahue, N. M.: Organic Aerosol Yields from α-Pinene Oxidation: Bridging the Gap between First-Generation Yields and Aging Chemistry, Environ. Sci. Technol., 46(22), 12347–12354, doi:10.1021/es302060y, 2012.

Hu, W., Palm, B. B., Day, D. A., Campuzano-Jost, P., Krechmer, J. E., Peng, Z., De Sá, S. S., Martin, S. T., Alexander, M. L., Baumann, K., Hacker, L., Kiendler-Scharr, A., Koss, A. R., De Gouw, J. A., Goldstein, A. H., Seco, R., Sjostedt, S. J., Park, J.-H., Guenther, A. B., Kim, S., Canonaco, F., Prévôt, A. S. H., Brune, W. H., Jimenez, J. L. and Jimenez, J. L.: Volatility and lifetime against OH heterogeneous reaction of ambient isoprene-epoxydiols-derived secondary organic aerosol (IEPOX-SOA), Atmos. Chem. Phys, 16, 11563–11580, doi:10.5194/acp-16-11563-2016, 2016.

Hunter, J. F., Day, D. A., Palm, B. B., Yatavelli, R. L. N., Chan, A. W. H., Kaser, L., Cappellin, L., Hayes, P. L., Cross, E. S., Carrasquillo, A. J., Campuzano-Jost, P., Stark, H., Zhao, Y., Hohaus, T., Smith, J. N., Hansel, A., Karl, T., Goldstein, A. H., Guenther, A., Worsnop, D. R., Thornton, J. A., Heald, C. L., Jimenez, J. L. and Kroll, J. H.: Comprehensive characterization of atmospheric organic carbon at a forested site, Nat. Geosci., doi:10.1038/ngeo3018, 2017.

Jathar, S. H., Donahue, N. M., Adams, P. J. and Robinson, A. L.: Testing secondary organic aerosol models using smog chamber data for complex precursor mixtures: influence of precursor volatility and molecular structure, Atmos. Chem. Phys., 14(11), 5771–5780, doi:10.5194/acp-14-5771-2014, 2014.

Jen, C. N., McMurry, P. H., Hanson, D. R.: Stabilization of sulfuric acid dimers by ammonia, methylamine, dimethylamine, and trimethylamine, J. Geophys. Res. Atmos., 119, 7502–7514, doi:10.1002/2014JD021592, 2014.

Jimenez, J. L., Canagaratna, M. R., Donahue, N. M., Prevot, a S. H., Zhang, Q., Kroll, J. H., DeCarlo, P. F., Allan, J. D., Coe, H., Ng, N. L., Aiken, a C., Docherty, K. S., Ulbrich, I. M., Grieshop, a P., Robinson, a L., Duplissy, J., Smith, J. D., Wilson, K. R., Lanz, V. a, Hueglin, C., Sun, Y. L., Tian, J., Laaksonen, a, Raatikainen, T., Rautiainen, J., Vaattovaara, P., Ehn, M., Kulmala, M., Tomlinson, J. M., Collins, D. R., Cubison, M. J., Dunlea, E. J., Huffman, J. a, Onasch, T. B., Alfarra, M. R., Williams, P. I., Bower, K., Kondo, Y., Schneider, J., Drewnick, F., Borrmann, S., Weimer, S., Demerjian, K., Salcedo, D., Cottrell, L., Griffin, R., Takami, a, Miyoshi, T., Hatakeyama, S., Shimono, a, Sun, J. Y., Zhang, Y. M., Dzepina, K., Kimmel, J. R., Sueper, D., Jayne, J. T., Herndon, S. C., Trimborn, a M., Williams, L. R., Wood, E. C., Middlebrook, a M., Kolb, C. E., Baltensperger, U. and Worsnop, D. R.: Evolution of organic aerosols in the atmosphere., Science, 326(5959), 1525–1529, doi:10.1126/science.1180353, 2009.

Joutsensaari, J., Loivamäki, M., Vuorinen, T., Miettinen, P., Nerg, A.-M., Holopainen, J. K., and Laaksonen, A.: Nanoparticle formation by ozonolysis of inducible plant volatiles, Atmos. Chem. Phys., 5, 1489-1495, https://doi.org/10.5194/acp-5-1489-2005, 2005.

Kanawade, V. P., Jobson, B. T., Guenther, A. B., Erupe, M. E., Pressley, S. N., Tripathi, S. N., and Lee, S.-H.: Isoprene suppression of new particle formation in a mixed deciduous forest, Atmos. Chem. Phys., 11, 6013-6027, https://doi.org/10.5194/acp-11-6013-2011, 2011.

Kang, E., Root, M. J., Toohey, D. W. and Brune, W. H.: Introducing the concept of Potential Aerosol Mass (PAM), Atmos. Chem. Phys., 7(22), 5727–5744, doi:10.5194/acp-7-5727-2007, 2007.

Karl, T., Hansel, A., Cappellin, L., Kaser, L., Herdlinger-Blatt, I., and Jud, W.: Selective measurements of isoprene and 2- methyl-3-buten-2-ol based on NO^{-1}+ ionization mass

spectrometry, Atmos. Chem. Phys., 12, 11877–11884, doi:10.5194/acp- 12-11877-2012, 2012.

Kaser, L., Karl, T., Schnitzhofer, R., Graus, M., Herdlinger-Blatt, I. S., DiGangi, J. P., Sive, B., Turnipseed, A., Hornbrook, R. S., Zheng,W., Flocke, F. M., Guenther, A., Keutsch, F. N., Apel, E., and Hansel, A.: Comparison of different real time VOC measurement techniques in a ponderosa pine forest, Atmos. Chem. Phys., 13, 2893–2906, doi:10.5194/acp-13-2893-2013, 2013.

Krechmer, J. E., Coggon, M. M., Massoli, P., Nguyen, T. B., Crounse, J. D., Hu, W., Day, D. A., Tyndall, G. S., Henze, D. K., Rivera-Rios, J. C., Nowak, J. B., Kimmel, J. R., Mauldin, R. L., Stark, H., Jayne, J. T., Sipila, M., Junninen, H., St Clair, J. M., Zhang, X., Feiner, P. A., Zhang, L., Miller, D. O., Brune, W. H., Keutsch, F. N., Wennberg, P. O., Seinfeld, J. H., Worsnop, D. R., Jimenez, J. L. and Canagaratna, M. R.: Formation of Low Volatility Organic Compounds and Secondary Organic Aerosol from Isoprene Hydroxyhydroperoxide Low-NO Oxidation Atmospheric aerosols can have detrimental effects on human health 1 and are known to affect global climate both directly and indirectly. 2 Secondary Organic Aerosol (SOA) forms in the, Environ. Sci. Technol, 49, 10330–10339, doi:10.1021/acs.est.5b02031, 2015.

Krechmer, J. E. Pagonis, D. P., Ziemann, P. J., and Jimenez, J. L. L.: Quantification of gas-wall partitioning in Teflon environmental chambers using rapid bursts of low-volatility oxidized species generated in-situ, Environ. Sci. Technol., 50, 5757–5765, doi:10.1021/acs.est.6b00606, 2016.

Kroll, J. H. et al: Measurement of fragmentation and functionalization pathways in the heterogeneous oxidation of oxidized organic aerosol, Phys. Chem. Chem. Phys., 11(36), 7759, doi:10.1039/b916865f, 2009.

Kroll, J. H., Donahue, N. M., Jimenez, J. L., Kessler, S. H., Canagaratna, M. R., Wilson, K. R., Altieri, K. E., Mazzoleni, L. R., Wozniak, A. S., Bluhm, H., Mysak, E. R., Smith, J. D., Kolb, C. E. and Worsnop, D. R.: Carbon oxidation state as a metric for describing the chemistry of atmospheric organic aerosol, Nat. Chem., 3(2), 133–139, doi:10.1038/nchem.948, 2011.

Kroll, J. H., Lim, C. Y., Kessler, S. H., and Wilson, K. R.: Heterogeneous Oxidation of Atmospheric Organic Aerosol: Kinetics of Changes to the Amount and Oxidation State of Particle- Phase Organic Carbon, J. Phys. Chem. A, 119, 10767–10783, doi:10.1021/acs.jpca.5b06946, 2015.

Kulmala, M., Laaksonen, A., and Pirjola, L.: Parameterizations for sulfuric acid/water nucleation rates, J. Geophys. Res., 103, 8301– 8307, 1998.

Kulmala, M., Korhonen, P., Napari, I., Karlsson, A., Berresheim, H., and O'Dowd, C. D.: Aerosol formation during PARFORCE: Ternary nucleation of H2SO4, NH3, and H2O, J. Geophys. Res., 107, 8111, doi:10.1029/2001JD000900, 2002.

Kulmala, M., Lehtinen, K. E. J. and Laaksonen, A.: Cluster activation theory as an explanation of the linear dependence between formation rate of 3nm particles and sulphuric acid concentration, Atmos. Chem. Phys., 6(3), 787–793, doi:10.5194/acp-6-787-2006, 2006.

Laakso, L., Makela, J. M., Pirjola, L., and Kulmala, M.: Model studies on ion-induced nucleation in the atmosphere, J. Geophys. Res., 107, 4427, doi:10.1029/2002JD002140, 2002.

Lambe, A. T., Ahern, A. T., Williams, L. R., Slowik, J. G., Wong, J. P. S., Abbatt, J. P. D., Brune, W. H., Ng, N. L., Wright, J. P., Croasdale, D. R.,Worsnop, D. R., Davidovits, P., and Onasch, T. B.: Characterization of aerosol photooxidation flow reactors: heterogeneous oxidation, secondary organic aerosol formation and cloud condensation nuclei activity measurements, Atmos. Meas. Tech., 4, 445–461, doi:10.5194/amt-4-445-2011, 2011a.

Lambe, A. T., Onasch, T. B., Massoli, P., Croasdale, D. R., Wright, J. P., Ahern, A. T., Williams, L. R., Worsnop, D. R., Brune, W. H. and Davidovits, P.: Laboratory studies of the chemical composition and cloud condensation nuclei (CCN) activity of secondary organic aerosol (SOA) and oxidized primary organic aerosol (OPOA), Atmos. Chem. Phys. Atmos. Chem. Phys., 11, 8913–8928, doi:10.5194/acp-11-8913-2011, 2011b.

Lambe, A. T., Onasch, T. B., Croasdale, D. R., Wright, J. P., Martin, A. T., Franklin, J. P., Massoli, P., Kroll, J. H., Canagaratna, M. R., Brune, W. H., Worsnop, D. R. and Davidovits, P.: Transitions from Functionalization to Fragmentation Reactions of Laboratory Secondary Organic Aerosol (SOA) Generated from the OH Oxidation of Alkane Precursors, Environ. Sci. Technol., 46(10), 5430–5437, doi:10.1021/es300274t, 2012.

Lambe, A. T., Chhabra, P. S., Onasch, T. B., Brune,W. H., Hunter, J. F., Kroll, J. H., Cummings, M. J., Brogan, J. F., Parmar, Y., Worsnop, D. R.,Kolb, C. E., and Davidovits, P.: Effect of oxidant concentration, exposure time, and seed particles on secondary organic aerosol chemical composition and yield, Atmos. Chem. Phys., 15, 3063–3075, doi:10.5194/acp-15-3063-2015, 2015.

Lambe, A., Massoli, P., Zhang, X., Canagaratna, M., Nowak, J., Daube, C., Yan, C., Nie, W., Onasch, T., Jayne, J., Kolb, C., Davidovits, P., Worsnop, D., and Brune, W.: Controlled

nitric oxide production via $O(^1D)$ + N_2O reactions for use in oxidation flow reactor studies, Atmos. Meas. Tech., 10, 2283-2298, https://doi.org/10.5194/amt-10-2283-2017, 2017.

Lee, S.-H., Uin, J., Guenther, A. B., de Gouw, J. A., Yu, F., Nadykto, A. B., Herb, J., Ng, N. L., Koss, A., Brune, W. H., Baumann, K., Kanawade, V. P., Keutsch, F. N., Nenes, A., Olsen, K., Goldstein, A. and Ouyang, Q.: Isoprene suppression of new particle formation: Potential mechanisms and implications, J. Geophys. Res. Atmos., 121(24), 14,621-14,635, doi:10.1002/2016JD024844, 2016.

Li, R., Palm, B. B., Ortega, A. M., Hlywiak, J., Hu, W., Peng, Z., Day, D. A., Knote, C., Brune, W. H., de Gouw, J. A. and Jimenez, J. L.: Modeling the Radical Chemistry in an Oxidation Flow Reactor: Radical Formation and 5 Recycling, Sensitivities, and the OH Exposure Estimation Equation, J. Phys. Chem. A, 119, 4418–4432, doi:10.1021/jp509534k, 2015.

Liu, Y., Ivanov, A. V., Zelenov, V. V., and Molina, M. J.: Temperature dependence of OH uptake by carbonaceous surfaces of atmospheric importance, Russ. J. Phys. Chem. B, 6, 327–332, doi:10.1134/s199079311202008x, 2012.

Liu, Y., Brito, J., Dorris, M. R., Rivera-Rios, J. C., Seco, R., Bates, K. H., Artaxo, P., Duvoisin, S., Keutsch, F. N., Kim, S., Goldstein, A. H., Guenther, A. B., Manzi, A. O., Souza, R. A. F., Springston, S. R., Watson, T. B., McKinney, K. A., and Martin, S. T.: Isoprene photochemistry over the Amazon rainforest, P. Natl. Acad. Sci., 113, 6125–6130, https://doi.org/10.1073/pnas.1524136113, 2016.

Maclean, A. M., Butenhoff, C. L., Grayson, J. W., Barsanti, K., Jimenez, J. L., and Bertram, A. K.: Mixing times of organic molecules within secondary organic aerosol particles: a global planetary boundary layer perspective, Atmos. Chem. Phys., 17, 13037-13048, https://doi.org/10.5194/acp-17-13037-2017, 2017.

Martin, S. T., Andreae, M. O., Artaxo, P., Baumgardner, D., Chen, Q., Goldstein, A. H., Guenther, A., Heald, C. L., Mayol-Bracero, O. L., McMurry, P. H., Pauliquevis, T., Pöschl, U., Prather, K. A., Roberts, G. C., Saleska, S. R., Silva Dias, M. A., Spracklen, D. V, Swietlicki, E. and Trebs, I.: Sources and properties of Amazonian aerosol particles, Rev. Geophys., 48(2), n/a-n/a, doi:10.1029/2008RG000280, 2010.

Martin, S. T., Artaxo, P., MacHado, L. A. T., Manzi, A. O., Souza, R. A. F., Schumacher, C., Wang, J., Andreae, M. O., Barbosa, H. M. J., Fan, J., Fisch, G., Goldstein, A. H., Guenther, A., Jimenez, J. L., Pöschl, U., Silva Dias, M. A., Smith, J. N. and Wendisch, M.: Introduction: Observations and Modeling of the Green Ocean Amazon (GoAmazon2014/5), Atmos. Chem. Phys., 16(8), 4785–4797, doi:10.5194/acp-16-4785-2016, 2016.

Martin, S. T., Artaxo, P., Machado, L., Manzi, A. O., Souza, R. A. F., Schumacher, C., Wang, J., Biscaro, T., Brito, J., Calheiros, A., Jardine, K., Medeiros, A., Portela, B., de Sá, S. S., Adachi, K., Aiken, A. C., Albrecht, R., Alexander, L., Andreae, M. O., Barbosa, H. M. J., Buseck, P., Chand, D., Comstock, J. M., Day, D. A., Dubey, M., Fan, J., Fast, J., Fisch, G., Fortner, E., Giangrande, S., Gilles, M., Goldstein, A. H., Guenther, A., Hubbe, J., Jensen, M., Jimenez, J. L., Keutsch, F. N., Kim, S., Kuang, C., Laskin, A., McKinney, K., Mei, F., Miller, M., Nascimento, R., Pauliquevis, T., Pekour, M., Peres, J., Petäjä, T., Pöhlker, C., Pöschl, U., Rizzo, L., Schmid, B., Shilling, J. E., Dias, M. A. S., Smith, J. N., Tomlinson, J. M., Tóta, J. and Wendisch, M.: The Green Ocean Amazon Experiment (GoAmazon2014/5) Observes Pollution Affecting Gases, Aerosols, Clouds, and Rainfall over the Rain Forest, Bull. Am. Meteorol. Soc., 98(5), 981–997, doi:10.1175/BAMS-D-15-00221.1, 2017.

McMurry, P. H. and Grosjean, D.: Gas and aerosol wall losses in Teflon film smog chambers, Environ. Sci. Technol., 19, 1176– 1182, doi:10.1021/es00142a006, 1985.

McNeill, V. F., Yatavelli, R. L. N., Thornton, J. A., Stipe, C. B., and Landgrebe, O.: Heterogeneous OH oxidation of palmitic acid in single component and internally mixed aerosol particles: vaporization and the role of particle phase, Atmos. Chem. Phys., 8, 5465–5476, doi:10.5194/acp-8-5465-2008, 2008.

Metzger, A., Verheggen, B., Dommen, J., Duplissy, J., Prevot, A. S. H., Weingartner, E., Riipinen, I., Kulmala, M., Spracklen, D. V, Carslaw, K. S. and Baltensperger, U.: Evidence for the role of organics in aerosol particle formation under atmospheric conditions., Proc. Natl. Acad. Sci. U. S. A., 107(15), 6646–51, doi:10.1073/pnas.0911330107, 2010.

Merikanto, J., Duplissy, J., Määttänen, A., Henschel, H., Donahue, N. M., Brus, D., Schobesberger, S., Kulmala, M. and Vehkamäki, H.: Effect of ions on sulfuric acid-water binary particle formation: 1. Theory for kinetic- and nucleation-type particle formation and atmospheric implications, J. Geophys. Res. Atmos., 121(4), 1736–1751, doi:10.1002/2015JD023538, 2016.

Murphy, D. M., Cziczo, D. J., Froyd, K. D., Hudson, P. K., Matthew, B. M., Middlebrook, A. M., Peltier, R. E., Sullivan, A., Thomson, D. S., and Weber, R. J.: Single-particle mass spectrometry of tropospheric aerosol particles, J. Geophys. Res., 111, D23S32, doi:10.1029/2006jd007340, 2006.

Murphy, B. N., Donahue, N. M., Robinson, A. L. and Pandis, S. N.: A naming convention for atmospheric organic aerosol, Atmos. Chem. Phys., 14(11), 5825–5839, doi:10.5194/acp-14-5825-2014, 2014.

Napari, I., Noppel, M., Vehkamaki, H., and Kulmala, M.: Parametrization of ternary nucleation rates for H2SO4-NH3-H2O vapors, J. Geophys. Res., 107, 4381, doi:10.1029/2002JD002132, 2002.

Ortega, A. M., Day, D. A., Cubison, M. J., Brune, W. H., Bon, D., de Gouw, J. A. and Jimenez, J. L.: Secondary organic aerosol formation and primary organic aerosol oxidation from biomass-burning smoke in a flow reactor during FLAME-3, Atmos. Chem. Phys., 13(22), 11551–11571, doi:10.5194/acp-13-11551-2013, 2013.

Ortega, J., Turnipseed, A., Guenther, A. B., Karl, T. G., Day, D. A., Gochis, D., Huffman, J. A., Prenni, A. J., Levin, E. J. T., Kreidenweis, S. M., Demott, P. J., Tobo, Y., Patton, E. G., Hodzic, A., Cui, Y. Y., Harley, P. C., Hornbrook, R. S., Apel, E. C., Monson, R. K., Eller, A. S. D., Greenberg, J. P., Barth, M. C., Campuzano-Jost, P., Palm, B. B., Jimenez, J. L., Aiken, A. C., Dubey, M. K., Geron, C., Offenberg, J., Ryan, M. G., Fornwalt, P. J., Pryor, S. C., Keutsch, F. N., Digangi, J. P., Chan, A. W. H., Goldstein, A. H., Wolfe, G. M., Kim, S., Kaser, L., Schnitzhofer, R., Hansel, A., Cantrell, C. A., Mauldin, R. L. and Smith, J. N.: Overview of the Manitou experimental forest observatory: Site description and selected science results from 2008 to 2013, Atmos. Chem. Phys., 14(12), 6345–6367, doi:10.5194/acp-14-6345-2014, 2014.

Ortega, A. M., Hayes, P. L., Peng, Z., Palm, B. B., Hu, W., Day, D. A., Li, R., Cubison, M. J., Brune, W. H., Graus, M., Warneke, C., Gilman, J. B., Kuster, W. C., de Gouw, J., Gutiérrez-Montes, C. and Jimenez, J. L.: Real-time measurements of secondary organic aerosol formation and aging from ambient air in an oxidation flow reactor in the Los Angeles area, Atmos. Chem. Phys., 16(11), 7411–7433, doi:10.5194/acp-16-7411-2016, 2016.

Palm, B. B., Campuzano-Jost, P., Ortega, A. M., Day, D. A., Kaser, L., Jud, W., Karl, T., Hansel, A., Hunter, J. F., Cross, E. S., Kroll, J. H., Peng, Z., Brune, W. H. and Jimenez, J. L.: In situ secondary organic aerosol formation from ambient pine forest air using an oxidation flow reactor, Atmos. Chem. Phys., 16(5), 2943–2970, doi:10.5194/acp-16-2943-2016, 2016.

Palm, B. B., Campuzano-Jost, P., Day, D. A., Ortega, A. M., Fry, J. L., Brown, S. S., Zarzana, K. J., Dube, W., Wagner, N. L., Draper, D. C., Kaser, L., Jud, W., Karl, T., Hansel, A., Gutiérrez-Montes, C. and Jimenez, J. L.: Secondary organic aerosol formation from in situ OH, O3, and NO3 oxidation of ambient forest air in an oxidation flow reactor, Atmos. Chem. Phys., 17(8), 5331–5354, doi:10.5194/acp-17-5331-2017, 2017.

Palm, B. B., de Sá, S. S., Day, D. A., Campuzano-Jost, P., Hu, W., Seco, R., Sjostedt, S. J., Park, J.-H., Guenther, A. B., Kim, S., Brito, J., Wurm, F., Artaxo, P., Thalman, R., Wang, J., Yee, L. D., Wernis, R., Isaacman-VanWertz, G., Goldstein, A. H., Liu, Y., Springston, S. R., Souza, R., Newburn, M. K., Alexander, M. L., Martin, S. T., and Jimenez, J. L.: Secondary organic aerosol formation from ambient air in an oxidation flow reactor in central Amazonia, Atmos. Chem. Phys., 18, 467-493, https://doi.org/10.5194/acp-18-467-2018, 2018.

Pankow, J. F.: An absorption model of gas/particle partitioning of organic compounds in the atmosphere, Atmos. Environ., 28, 185–188, 1994.

Pankow, J. F.: Gas/particle partitioning of neutral and ionizing compounds to single and multi-phase aerosol particles. 1. Unified modeling framework, Atmos. Environ., 37, 3323–3333, 2003.

Park, J. H., Ivanov, A. V., and Molina, M. J.: Effect of Relative Humidity on OH Uptake by Surfaces of Atmospheric Importance, J. Phys. Chem. A, 112, 6968–6977, doi:10.1021/jp8012317, 2008.

Paulot, F., Crounse, J. D., Kjaergaard, H. G., Kürten, A., St. Clair, J. M., Seinfeld, J. H. and Wennberg, P. O.: Unexpected Epoxide Formation in the Gas-Phase Photooxidation of Isoprene, Science (80-.)., 325(5941), 730 LP-733 [online] Available from: http://science.sciencemag.org/content/325/5941/730.abstract, 2009.

Peng, Z., Day, D. A., Stark, H., Li, R., Lee-Taylor, J., Palm, B. B., Brune, W. H., and Jimenez, J. L.: HOx radical chemistry in oxidation flow reactors with low-pressure mercury lamps systematically examined by modeling, Atmos. Meas. Tech., 8, 4863-4890, https://doi.org/10.5194/amt-8-4863-2015, 2015.

Peng, Z., Day, D. A., Ortega, A. M., Palm, B. B., Hu, W., Stark, H., Li, R., Tsigaridis, K., Brune, W. H., and Jimenez, J. L.: Non-OH chemistry in oxidation flow reactors for the study of atmospheric chemistry systematically examined by modeling, Atmos. Chem. Phys., 16, 4283-4305, https://doi.org/10.5194/acp-16-4283-2016, 2016.

Peng, Z. and Jimenez, J. L.: Modeling of the chemistry in oxidation flow reactors with high initial NO, Atmos. Chem. Phys., 17, 11991-12010, https://doi.org/10.5194/acp-17-11991-2017, 2017.

Peng, Z., Palm, B. B., Day, D. A., Talukdar, R. K., Hu, W., Lambe, A. T., Brune, W. H. and Jimenez, J. L.: Model Evaluation of New Techniques for Maintaining High-NO Conditions in Oxidation Flow Reactors for the Study of OH-Initiated Atmospheric Chemistry, ACS Earth Sp. Chem., 2(2), 72–86, doi:10.1021/acsearthspacechem.7b00070, 2018.

Pierce, J. R. and Adams, P. J.: Uncertainty in global CCN concentrations from uncertain aerosol nucleation and primary emission rates, Atmos. Chem. Phys., 9(4), 1339–1356, doi:10.5194/acp-9-1339-2009, 2009a.

Pierce, J. R., Riipinen, I., Kulmala, M., Ehn, M., Petäjä, T., Junninen, H., Worsnop, D. R. and Donahue, N. M.: Quantification of the volatility of secondary organic compounds in ultrafine particles during nucleation events, Atmos. Chem. Phys., 11(17), 9019–9036, doi:10.5194/acp-11-9019-2011, 2011.

Pierce, J. R. and Adams, P. J.: A Computationally Efficient Aerosol Nucleation/ Condensation Method: Pseudo-Steady-State Sulfuric Acid, Aerosol Sci. Technol., 43(3), 216–226, doi:10.1080/02786820802587896, 2009b.

Pillai, P., Khlystov, A., Walker, J. and Aneja, V.: Observation and Analysis of Particle Nucleation at a Forest Site in Southeastern US, Atmos. , 4(2), doi:10.3390/atmos4020072, 2013.

Pinder, R. W., Adams, P. J., and Pandis, S. N.: Ammonia emission controls as a cost-effective strategy for reducing atmospheric particulate matter in the eastern United States, Environ. Sci. Technol., 41, 380–386, 2007.

Pun, B. K. and Seigneur, C.: Investigative modeling of new pathways for secondary organic aerosol formation, Atmos. Chem. Phys., 7, 2199–2216, doi:10.5194/acp-7-2199-2007, 2007.

Riccobono, F., Schobesberger, S., Scott, C. E., Dommen, J., Ortega, I. K., Rondo, L., Almeida, J., Amorim, A., Bianchi, F., Breitenlechner, M., David, A., Downard, A., Dunne, E. M., Duplissy, J., Ehrhart, S., Flagan, R. C., Franchin, A., Hansel, A., Junninen, H., Kajos, M., Keskinen, H., Kupc, A., Kurten, A., Kvashin, A. N., Laaksonen, A., Lehtipalo, K., Makhmutov, V., Mathot, S., Nieminen, T., Onnela, A., Petaja, T., Praplan, A. P., Santos,

F. D., Schallhart, S., Seinfeld, J. H., Sipila, M., Spracklen, D. V., Stozhkov, Y., Stratmann, F., Tome, A., Tsagkogeorgas, G., Vaattovaara, P., Viisanen, Y., Vrtala, A., Wagner, P. E., Weingartner, E., Wex, H., Wimmer, D., Carslaw, K. S., Curtius, J., Donahue, N. M., Kirkby, J., Kulmala, M., Worsnop, D. R. and Baltensperger, U.: Oxidation Products of Biogenic Emissions Contribute to Nucleation of Atmospheric Particles, Science (80-.)., 344(6185), 717–721, doi:10.1126/science.1243527, 2014.

Riipinen, I., Sihto, S.-L., Kulmala, M., Arnold, F., Dal Maso, M., Birmili, W., Saarnio, K., Teinilä, K., Kerminen, V.-M., Laaksonen, A. and Lehtinen, K. E. J.: Connections between atmospheric sulphuric acid and new particle formation during QUEST III–IV campaigns in Heidelberg and Hyytiälä, Atmos. Chem. Phys. Atmos. Chem. Phys., 7(8), 1899–1914, doi:10.5194/acp-7-1899-2007, 2007.

Riipinen, I., Pierce, J. R., Yli-Juuti, T., Nieminen, T., Häkkinen, S., Ehn, M., Junninen, H., Lehtipalo, K., Petäjä, T., Slowik, J., Chang, R., Shantz, N. C., Abbatt, J., Leaitch, W. R., Kerminen, V. M., Worsnop, D. R., Pandis, S. N., Donahue, N. M. and Kulmala, M.: Organic condensation: a vital link connecting aerosol formation to cloud condensation nuclei (CCN) concentrations, Atmos. Chem. Phys., 11(8), 3865–3878, doi:10.5194/acp-11-3865-2011, 2011.

Rosenfeld, D., Lohmann, U., Raga, G. B., O'Dowd, C. D., Kulmala, M., Fuzzi, S., Reissell, A., and Andreae, M. O.: Flood or Drought: How Do Aerosols Affect Precipitation?, Science, 312, 1309–1313, 2008.

Seinfeld, J. H. and Pandis, S. N.: Atmospheric Chemistry and Physics, 2nd ed., John Wiley and Sons, New York, 2006.

Shiraiwa, M., Ammann, M., Koop, T. and Poschl, U.: Gas uptake and chemical aging of semisolid organic aerosol particles, Proc. Natl. Acad. Sci., 108(27), 11003–11008, doi:10.1073/pnas.1103045108, 2011.

Shrivastava, M., Zelenyuk, A., Imre, D., Easter, R., Beranek, J., Zaveri, R. A. and Fast, J.: Implications of low volatility SOA and gas-phase fragmentation reactions on SOA loadings and their spatial and temporal evolution in the atmosphere, J. Geophys. Res. Atmos., 118(8), 3328–3342, doi:10.1002/jgrd.50160, 2013.

Shiraiwa, M. and Seinfeld, J. H.: Equilibration timescale of atmospheric secondary organic aerosol partitioning, Geophys. Res. Lett., 39(24), 1–6, doi:10.1029/2012GL054008, 2012.

Shrivastava, Manish K, Easter, R. C., Liu, X., Zelenyuk, A., Singh, B., Zhang, Kai, Ma, P.-L., Chand, D., Ghan, S. J., Jimenez, J.-L., Zhang, Q., Fast, J. D., Rasch, P. and Tiitta, P.: Global transformation and fate of SOA: Implications of low-volatility SOA and gas-phase fragmentation reactions, , 9301–9323, doi:10.1002/2014JD021636.Received, 2014.

Shrivastava, M. K., Zhao, C., Easter, R. C., Qian, Y. and Al, E.: Sensitivity analysis of simulated SOA loadings using a variance-based statistical approach, J. Adv. Model. Earth Syst., 6, 513–526, doi:10.1002/2013MS000282.Received, 2016.

Shrivastava, M., Cappa, C. D., Fan, J., Goldstein, A. H., Guenther, A. B., Jimenez, J. L., Kuang, C., Laskin, A., Martin, S. T., Ng, N. L., Petaja, T., Pierce, J. R., Rasch, P. J., Roldin, P., Seinfeld, J. H., Shilling, J., Smith, J. N., Thornton, J. A., Volkamer, R., Wang, J., Worsnop, D. R., Zaveri, R. A., Zelenyuk, A. and Zhang, Q.: Recent advances in understanding secondary organic aerosol: Implications for global climate forcing, Rev. Geophys., 55(2), 509–559, doi:10.1002/2016RG000540, 2017.

Sihto, S.-L., Kulmala, M., Kerminen, V.-M., Dal Maso, M., Petäjä, T., Riipinen, I., Korhonen, H., Arnold, F., Janson, R., Boy, M., Laaksonen, A. and Lehtinen, K. E. J.: Atmospheric sulphuric acid and aerosol formation: implications from atmospheric measurements for nucleation and early growth mechanisms, Atmos. Chem. Phys., 6(12), 4079–4091, doi:10.5194/acp-6-4079-2006, 2006.

Slade, J. H. and Knopf, D. A.: Heterogeneous OH oxidation of biomass burning organic aerosol surrogate compounds: assessment of volatilisation products and the role of OH concentration on the reactive uptake kinetics, Phys. Chem. Chem. Phys., 15, 5898–5915, doi:10.1039/c3cp44695f, 2013.

Spracklen, D. V., Carslaw, K. S., Kulmala, M., Kerminen, V.-M., Mann, G. W., and Sihto, S.-L.: The contribution of boundary layer nucleation events to total particle concentrations on regional and global scales, Atmos. Chem. Phys., 6, 5631-5648, https://doi.org/10.5194/acp-6-5631-2006, 2006.

Spracklen, D. V., Carslaw, K. S., Kulmala, M., Kerminen, V.-M., Sihto, S.-L., Riipinen, I., Merikanto, J., Mann, G. W., Chipperfield, M. P., Wiedensohler, A., Birmili, W., and Lihavainen, H.: Contribution of particle formation to global cloud condensation nuclei concentrations, Geophys. Res. Lett., 35, L06808, doi:10.1029/2007GL033038, 2008.

Spracklen, D. V., Carslaw, K. S., Merikanto, J., Mann, G. W., Reddington, C. L., Pickering, S., Ogren, J. A., Andrews, E., Baltensperger, U., Weingartner, E., Boy, M., Kulmala, M., Laakso, L., Lihavainen, H., Kivekäs, N., Komppula, M., Mihalopoulos, N., Kouvarakis, G., Jennings, S. G., O'Dowd, C., Birmili, W., Wiedensohler, A., Weller, R., Gras, J., Laj, P., Sellegri, K., Bonn, B., Krejci, R., Laaksonen, A., Hamed, A., Minikin, A., Harrison, R. M., Talbot, R. and Sun, J.: Explaining global surface aerosol number concentrations in

terms of primary emissions and particle formation, Atmos. Chem. Phys., 10(10), 4775–4793, doi:10.5194/acp-10-4775-2010, 2010.

Stark, H., Yatavelli, R. L. N., Thompson, S. L., Kang, H., Krechmer, J. E., Kimmel, J. R., Palm, B. B., Hu, W., Hayes, P. L., Day, D. A., Campuzano-Jost, P., Canagaratna, M. R., Jayne, J. T., Worsnop, D. R. and Jimenez, J. L.: Impact of Thermal Decomposition on Thermal Desorption Instruments: Advantage of Thermogram Analysis for Quantifying Volatility Distributions of Organic Species, Environ. Sci. Technol., 51(15), 8491–8500, doi:10.1021/acs.est.7b00160, 2017.

Tkacik, D. S., Lambe, A. T., Jathar, S., Li, X., Presto, A. A., Zhao, Y., Blake, D., Meinardi, S., Jayne, J. T., Croteau, P. L., and Robinson, A. L.: Secondary Organic Aerosol Formation from in-Use Motor Vehicle Emissions Using a Potential Aerosol Mass Reactor, Environ. Sci. Technol., 48, 11235–11242, doi:10.1021/es502239v, 2014.

Tsimpidi, A. P., Karydis, V. A., Zavala, M., Lei, W., Molina, L., Ulbrich, I. M., Jimenez, J. L. and Pandis, S. N.: Evaluation of the volatility basis-set approach for the simulation of organic aerosol formation in the Mexico City metropolitan area, Atmos. Chem. Phys., 10(2), 525–546, doi:10.5194/acp-10-525-2010, 2010.

Vaden, T. D., Imre, D., Beranek, J., Shrivastava, M. and Zelenyuk, A.: Evaporation kinetics and phase of laboratory and ambient secondary organic aerosol, Proc. Natl. Acad. Sci., 108(6), 2190–2195, doi:10.1073/pnas.1013391108, 2011.

VanReken, T. M., Greenberg, J. P., Harley, P. C., Guenther, A. B., and Smith, J. N.: Direct measurement of particle formation and growth from the oxidation of biogenic emissions, Atmos. Chem. Phys., 6, 4403-4413, https://doi.org/10.5194/acp-6-4403-2006, 2006.

Vehkamaki, H., Kulmala, M., Napari, I., Lehtinen, K. E. J., Timmreck, C., Noppel, M., and Laaksonen, A.: An improved parameterization for sulfuric acid-water nucleation rates for tropospheric and stratospheric conditions, J. Geophys. Res., 107, 4622, doi:10.1029/2002JD002184, 2002.

Virtanen, A., Joutsensaari, J., Koop, T., Kannosto, J., Yli-Pirilä, P., Leskinen, J., Mäkelä, J. M., Holopainen, J. K., Pöschl, U., Kulmala, M., Worsnop, D. R. and Laaksonen, A.: An amorphous solid state of biogenic secondary organic aerosol particles, Nature, 467(7317), 824–827, doi:10.1038/nature09455, 2010.

Virtanen, A., Kannosto, J., Kuuluvainen, H., Arffman, A., Joutsensaari, J., Saukko, E., Hao, L., Yli-Pirilä, P., Tiitta, P., Holopainen, J. K., Keskinen, J., Worsnop, D. R., Smith, J. N. and Laaksonen, A.: Bounce behavior of freshly nucleated biogenic secondary organic aerosol particles, Atmos. Chem. Phys., 11(16), 8759–8766, doi:10.5194/acp-11-8759-2011, 2011.

Wang, J., Artaxo, P. and Brito, J.: Amazon boundary layer aerosol concentration sustained by vertical transport during rainfall, Nature, 539(7629), 416–419, doi:10.1038/nature19819, 2016.

Westervelt, D. M., Pierce, J. R., and Adams, P. J.: Analysis of feedbacks between nucleation rate, survival probability and cloud condensation nuclei formation, Atmos. Chem. Phys., 14, 5577– 5597, doi:10.5194/acp-14-5577-2014, 2014.

Wilson, K. R., Smith, J. D., Kessler, S. H. and Kroll, J. H.: The statistical evolution of multiple generations of oxidation products in the photochemical aging of chemically reduced organic aerosol, Phys. Chem. Chem. Phys., 14(4), 1468–1479, doi:10.1039/C1CP22716E, 2012.

Yatavelli, R. L. N., Stark, H., Thompson, S. L., Kimmel, J. R., Cubison, M. J., Day, D. A., Campuzano-Jost, P., Palm, B. B., Hodzic, A., Thornton, J. A., Jayne, J. T., Worsnop, D. R. and Jimenez, J. L.: Semicontinuous measurements of gas–particle partitioning of organic acids in a ponderosa pine forest using a MOVI-HRToF-CIMS, Atmos. Chem. Phys., 14(3), 1527–1546, doi:10.5194/acp-14-1527-2014, 2014.

Yu, F.: From molecular clusters to nanoparticles: second-generation ion-mediated nucleation model, Atmos. Chem. Phys., 6, 5193– 5211, 2006a.

Yu, F. Q.: Effect of ammonia on new particle formation: A

kinetic H2SO4-H2O-NH3 nucleation model constrained by laboratory measurements, J. Geophys. Res., 111, D01204, doi:10.1029/2005JD005968, 2006b.

Yu, F., Luo, G., Pryor, S. C., Pillai, P. R., Lee, S. H., Ortega, J., Schwab, J. J., Hallar, A. G., Leaitch, W. R., Aneja, V. P., Smith, J. N., Walker, J. T., Hogrefe, O. and Demerjian, K. L.: Spring and summer contrast in new particle formation over nine forest areas in North America, Atmos. Chem. Phys., 15(24), 13993–14003, doi:10.5194/acp-15-13993-2015, 2015.

Yu, F., Luo, G., Nadykto, A. B. and Herb, J.: Impact of temperature dependence on the possible contribution of organics to new particle formation in the atmosphere, Atmos. Chem. Phys., 17(8), 4997–5005, doi:10.5194/acp-17-4997-2017, 2017.

Zaveri, R. A., Easter, R. C., Shilling, J. E. and Seinfeld, J. H.: Modeling kinetic partitioning of secondary organic aerosol and size distribution dynamics: representing effects of volatility, phase state, and particle-phase reaction, Atmos. Chem. Phys., 14(10), 5153–5181, doi:10.5194/acp-14-5153-2014, 2014.

Zaveri, R. A., Shilling, J. E., Zelenyuk, A., Liu, J., Bell, D. M., D'Ambro, E. L., Gaston, C. J., Thornton, J. A., Laskin, A., Lin, P., Wilson, J., Easter, R. C., Wang, J., Bertram, A. K., Martin, S. T., Seinfeld, J. H. and Worsnop, D. R.: Growth Kinetics and Size Distribution Dynamics of Viscous Secondary Organic Aerosol, Environ. Sci. Technol., doi:10.1021/acs.est.7b04623, 2017.

Zhang, R., Suh, I., Zhao, J., Zhang, D., Fortner, E. C., Tie, X., Molina, L. T. and Molina, M. J.: Atmospheric New Particle Formation Enhanced by Organic Acids, Science (80-.)., 304(5676), 1487 LP-1490 [online] Available from: http://science.sciencemag.org/content/304/5676/1487.abstract, 2004.

Zhang, Q., Jimenez, J. L., Canagaratna, M. R., Allan, J. D., Coe, H., Ulbrich, I., Alfarra, M. R., Takami, A., Middlebrook, A. M., Sun, Y. L., Dzepina, K., Dunlea, E., Docherty, K., DeCarlo, P. F., Salcedo, D., Onasch, T., Jayne, J. T., Miyoshi, T., Shimono, A., Hatakeyama, S., Takegawa, N., Kondo, Y., Schneider, J., Drewnick, F., Borrmann, S., Weimer, S., Demerjian, K., Williams, P., Bower, K., Bahreini, R., Cottrell, L., Griffin, R. J., Rautiainen, J., Sun, J. Y., Zhang, Y. M., and Worsnop, D. R.: Ubiquity and dominance of oxygenated species in organic aerosols in anthropogenically-influenced Northern Hemisphere midlatitudes, Geophys. Res. Lett., 34, L13801, doi:10.1029/2007GL029979, 2007.

Zhang, X., Pandis, S. N. and Seinfeld, J. H.: Diffusion-Limited Versus Quasi-Equilibrium Aerosol Growth, Aerosol Sci. Technol., 46(8), 874–885, doi:10.1080/02786826.2012.679344, 2012.

Zhang, X., Cappa, C. D., Jathar, S. H., McVay, R. C., Ensberg, J. J., Kleeman, M. J. and Seinfeld, J. H.: Influence of vapor wall loss in laboratory chambers on yields of secondary organic aerosol, Proc. Natl. Acad. Sci., 111(16), 5802–5807, doi:10.1073/pnas.1404727111, 2014.

Ziemann, P. J. and Atkinson, R.: Kinetics, products, and mechanisms of secondary organic aerosol formation, Chem. Soc. Rev., 41, 6582, doi:10.1039/c2cs35122f, 2012.

CHAPTER 3

THE POTENTIAL ROLE OF METHANESULFONIC ACID (MSA) IN AEROSOL FORMATION AND GROWTH AND THE ASSOCIATED RADIATIVE FORCINGS[2]

Overview

Atmospheric marine aerosol particles impact Earth's albedo and climate. These particles can be primary or secondary and come from a variety of sources, including sea salt, dissolved organic matter, volatile organic compounds, and sulfur-containing compounds. Dimethylsulfide (DMS) marine emissions contribute greatly to the global biogenic sulfur budget, and its oxidation products can contribute to aerosol mass, specifically as sulfuric acid and methanesulfonic acid (MSA). Further, sulfuric acid is a known nucleating compound, and MSA may be able to participate in nucleation when bases are available. As DMS emissions, and thus MSA and sulfuric acid from DMS oxidation, may have changed since pre-industrial times and may change in a warming climate, it is important to characterize and constrain the climate impacts of both species. Currently, global models that simulate aerosol size distributions include contributions of sulfate and sulfuric acid from DMS oxidation, but to our knowledge, global models typically neglect the impact of MSA on size distributions.

In this study, we use the GEOS-Chem-TOMAS (GC-TOMAS) global aerosol microphysics model to determine the impact on aerosol size distributions and subsequent aerosol radiative effects from including MSA in the size-resolved portion of the model. The effective

[2] This Chapter published as: Hodshire, A. L., Campuzano-Jost, P., Kodros, J. K., Croft, B., Nault, B. A., Schroder, J. C., Jimenez, J. L. and Pierce, J. R.: The potential role of methanesulfonic acid (MSA) in aerosol formation and growth and the associated radiative forcings, Atmos. Chem. Phys., 19(5), 3137–3160, doi:10.5194/acp-19-3137-2019, 2019.

equilibrium vapor pressure of MSA is currently uncertain, and we use the Extended Aerosol Inorganics Model (E-AIM) to build a parameterization for GC-TOMAS of MSA's effective volatility as a function of temperature, relative humidity, and available gas-phase bases, allowing MSA to condense as an ideally nonvolatile or semivolatile species or too volatile to condense. We also present two limiting cases for MSA's volatility, assuming that MSA is always ideally nonvolatile (irreversible condensation) or that MSA is always ideally semivolatile (quasi-equilibrium condensation but still irreversible condensation). We further present simulations in which MSA participates in binary and ternary nucleation with the same efficacy as sulfuric acid whenever MSA is treated as ideally nonvolatile. When using the volatility parameterization described above (both with and without nucleation), including MSA in the model changes the global annual averages at 900 hPa of submicron aerosol mass by 1.2%, N3 (number concentration of particles greater than 3 nm in diameter) by -3.9% (non-nucleating) or 112.5% (nucleating), N80 by 0.8% (non-nucleating) or 2.1% (nucleating), the cloud-albedo aerosol indirect effect (AIE) by -8.6 mW m^{-2} (non-nucleating) or -26 mW m^{-2} (nucleating), and the direct radiative effect (DRE) by -15 mW m^{-2} (non-nucleating) or -14 mW m^{-2} (nucleating). The sulfate and sulfuric acid from DMS oxidation produces 4-6 times more submicron mass than MSA does, leading to ~10 times a stronger cooling effect in the DRE. But the changes in N80 are comparable between the contributions from MSA and from DMS-derived sulfate/sulfuric acid, leading to comparable changes in the cloud-albedo AIE.

Model-measurement comparisons with the Heintzenberg et al. (2000) dataset over the Southern Ocean indicate that the default model has a missing source or sources of ultrafine particles: the cases in which MSA participates in nucleation (thus increasing ultrafine number) most closely match the Heintzenberg distributions, but we cannot conclude nucleation from MSA

is the correct reason for improvement. Model-measurement comparisons with particle-phase MSA observed with a customized Aerodyne high-resolution time-of-flight aerosol mass spectrometer (AMS) from the ATom campaign show that cases with the MSA volatility parameterizations (both with and without nucleation) tend to fit the measurements the best (as this is the first use of MSA measurements from ATom, we provide a detailed description of these measurements and their calibration). However, no one model sensitivity case shows the best model-measurement agreement for both Heintzenberg and the ATom campaigns. As there are uncertainties in both MSA's behavior (nucleation and condensation) and the DMS emissions inventory, further studies on both fronts are needed to better constrain MSA's past, current and future impacts upon the global aerosol size distribution and radiative forcing.

3.1 Introduction

Atmospheric marine particles contribute significantly to the global aerosol budget and impact the planetary albedo and climate (Quinn et al., 2015; Reddington et al., 2017). The number concentration, size, and chemical composition of these marine particles determine their ability to affect climate, through either absorbing and scattering incoming solar radiation (the direct radiative effect [DRE]; Charlson et al., 1992; Erlick et al., 2001) or indirectly, by modifying cloud properties (the cloud-albedo aerosol indirect effect [AIE]; de Leeuw et al., 2011). For the DRE, the magnitude and relative division between absorbing and scattering will depend on both the particle size and composition (Bond et al., 2006; 2013); peak efficiencies for scattering and absorbing solar radiation are typically reached with particles between 100 nm to 1 μm in diameter (Seinfeld and Pandis, 2006). The cloud-albedo AIE refers to aerosols' ability to alter the reflectivity (albedo) of clouds by changing properties such as the cloud droplet number concentration (CDNC) (Twomey,

1974). Typically, particles act as cloud condensation nuclei (CCN) if they are larger than 40-100 nm; the ability of a particle to act as a CCN is also dependent upon particle hygroscopicity (Petters and Kreidenweis, 2007). The number of particles in these size ranges depend on primary emissions, as well as nucleation, condensation, and coagulation (Pierce and Adams, 2009a). To improve model estimates of the DRE and cloud-albedo AIE, models must account for nucleation and condensational growth of marine particles.

Biologically productive oceans emit volatile organic compounds (VOCs), primary biological particles, primary organic particles, and halocarbons (Quinn et al., 2015). Sources of marine particles often indicate organic species present (e.g. Heintzenberg et al., 2001; O'Dowd et al., 2007; Frossard et al., 2014, Wang et al., 2017) that could dominate submicron aerosol mass (O'Dowd et al., 2004; Facchini et al., 2008). Sulfur-containing organic compounds in the form of dimethylsulfide (DMS; CH_3SCH_3) and organosulfates (Bates et al., 1992, Quinn et al., 2015) are important precursors and contributors to marine aerosol. DMS accounts for approximately one-fifth of the global sulfur budget (Fiddes et al., 2017), with DMS flux estimates ranging from 9 to 35 Tg yr^{-1} of sulfur (Belviso et al., 2004; Elliott, 2009; Woodhouse et al., 2010; Tesdal et al., 2016), although global DMS fluxes remain uncertain (Tesdal et al., 2016; Royer et al., 2015). DMS and its oxidation products have been the focus of many studies determining the gas-phase chemistry (e.g. Barnes et al. 2006 and references therein), gas-phase kinetics (e.g. Wilson and Hirst, 1996 and references therein), and possible impact to the aerosol size distribution and radiative budget (e.g. Korhonen et al., 2008; Woodhouse et al., 2013). Much of this research has stemmed from efforts to test the hypothesis that DMS emissions may regulate climate through a temperature-emissions feedback (the CLAW hypothesis, Charlson et al. (1987)).

The main products of DMS from oxidation by the hydroxyl radical are sulfur dioxide (SO_2) and methanesulfonic acid ($CH_3S(O)_2OH$, MSA) (Andreae et al., 1985). SO_2 can further oxidize to create sulfuric acid (H_2SO_4). The relative yields of SO_2 and MSA from DMS oxidation are still uncertain, with reported branching ratios from oxidation of DMS by OH addition of SO_2:MSA varying across 75:25, 65:4, 27:6, and 38:11 (Yin et al., 1990; Chin et al., 1996; Sørensen et al., 1996; Arsene et al., 2001). The effective equilibrium vapor pressure of sulfuric acid in the presence of water in the troposphere is negligible compared to sulfuric acid concentrations under all atmospherically relevant conditions (Marti et al., 1997), allowing sulfuric acid to readily condense onto particles of all sizes and participate in particle nucleation (e.g. Kulmala et al., 2000). Gas-phase concentrations of MSA have been observed to be 10-100% of sulfuric acid concentrations in coastal marine boundary layers (Eisele and Tanner, 1993; Berresheim et al., 2002; Mauldin et al., 2003), and MSA can contribute to the growth of pre-existing marine particles, at times contributing over half as much bulk aerosol mass as non-sea salt sulfate to the total aerosol burden (e.g. Preunkert et al., 2008; Legrand et al., 2017). To our knowledge, the effective equilibrium vapor pressure of MSA, which should depend on temperature, relative humidity, and availability of bases, has not previously been well-quantified for the range of potential atmospheric conditions. Also to our knowledge, MSA has not yet been observed in the field to directly contribute to aerosol nucleation, although Dall'Osto et al. (2018) observed new particle formation events over Greenland that suggest that MSA could be involved in a portion of the events. Bork et al. (2014) determined through the Atmospheric Cluster Dynamics Code kinetic model (McGrath et al., 2012; Olenius et al., 2013) that the presence of MSA could increase the molecular cluster formation rates by as much as one order of magnitude for a MSA-H_2SO_4-DMA (DMA = dimethylamine) system under atmospherically relevant MSA concentrations. This enhancement is predicted to be

typically less than 300% at 258 K and less than 15% at 298 K for the case of [DMA] = 10^9 molecules cm^{-3} (Bork et al., 2014). Chen et al. (2015) observed an MSA-H_2O-TMA (TMA = trimethylamine) system to nucleate in the laboratory, but at an efficiency lower than that of the H_2SO_4-H_2O system. Chen and Finlayson-Pitts (2017) further observed nucleation of MSA/H_2O systems with TMA, DMA, MA (MA = methylamine) and ammonia. To our knowledge, global models that simulate aerosol number concentrations (e.g. D'Andrea et al. 2013; Kodros et al., 2018; Ma and Yu, 2015; Regayre et al., 2018; Xausa et al., 2018) only track the effect of sulfuric acid and aqueous sulfate from DMS/SO_2 oxidation on the aerosol size distribution and not MSA. Thus, the potential contribution towards nucleation and/or size-resolved particle growth by MSA and the resulting radiative impacts has not yet been quantified.

The effective volatility (equilibrium vapor pressure above the particle-phase mixture) of MSA will modulate its impact on the aerosol size distribution. Condensational growth of vapors to the particle phase is controlled by both the volatility of the condensing species and the concentration of the species in the gas phase. Riipinen et al. (2011) presented two limiting cases of growth for gas-phase condensable material:

(1) Compounds with low enough saturation vapor concentrations (C*; Donahue et al., 2006) may be considered essentially nonvolatile to condense irreversibly through kinetic, gas-phase-diffusion-limited condensation (Riipinen et al. 2011; Zhang et al., 2012). This type of growth is referred to as "kinetic condensation" by Riipinen et al. (2011) and can be thought of as effectively nonvolatile condensation. The effective volatility required to achieve effectively nonvolatile condensation typically must be less than $C^* <\approx 10^{-3}$ $\mu g\ m^{-3}$ (e.g. low and extremely low volatility organic compounds; LVOCs and ELVOCs) (Pierce et al., 2011; Donahue et al., 2011). The contribution to growth from effectively nonvolatile condensation is proportional to the Fuchs-

corrected particle surface area (Pandis et al., 1991). We will refer to this type of condensation as "ELVOC-like" condensation in this work.

(2) In contrast, semi-volatile species (e.g. semi-volatile organic compounds; SVOCs) with average C* between 10^0-10^2 μg m^{-3} (Murphy et al., 2014) quickly reach equilibrium between gas and particle phases for all particle sizes. As a result, the contribution to growth is proportional to the aerosol mass distribution (Pierce et al., 2011; Riipinen et al., 2011; Donahue et al., 2011; Zhang et al., 2012), limiting the growth of ultrafine particles. This type of growth is referred to as "thermodynamic condensation" by Riipinen et al. (2011) and "quasi-equilibrium" growth by Zhang et al. (2012); we will refer to this type of condensation as "SVOC-like" condensation in this work.

Important characteristics for growth in these regimes is that under ELVOC-like condensation, particles in the kinetic regime (D_p < ~50 nm) all grow in diameter at the same rate (e.g. nm h^{-1}) regardless of diameter, whereas in the continuum regime (Dp > ~1 μm), particle growth rates are proportional to $1/D_p$. Conversely, SVOC-like condensation growth rates scale with D_p for all particle sizes, favoring the largest particles. Thus, if MSA participates in ELVOC-like condensation, ultrafine particles are able to grow more quickly to climatically relevant sizes (e.g. CCN) as compared to SVOC-like condensation. In reality, MSA's contribution towards growth likely lies between these two limiting cases: as MSA is an acid, its volatility will depend on not only temperature but also relative humidity and gas-phase bases (e.g. Barsanti et al., 2009; Yli-Juuti et al., 2013; Hodshire et al., 2016).

In this study, we use the GEOS-Chem-TOMAS global chemical transport model to estimate the contribution of MSA to the aerosol size distribution and resulting radiative effects. We examine (1) MSA condensation assumptions, testing the limiting cases of growth (ELVOC-

like vs SVOC-like) as well as a parameterization of volatility dependent on temperature, water vapor, and gas-phase bases built from a phase-equilibrium model and (2) how the contribution of MSA changes depending on whether or not it is allowed participate in nucleation. We further use global measurements of aerosol size distributions as compiled by Heintzenberg et al. (2000) and MSA mass as observed on the ATom mission to compare the various model assumptions. Our goals are to determine the sensitivity of the aerosol size distribution and radiative impacts implied by the various assumptions, and to see if the assumptions can be constrained by observations. This study is a first look at how MSA might impact the global aerosol size distribution and associated climate effects by considering the sensitivity of its assumed volatility and ability to impact nucleation. Along with our model analyses of MSA, we provide a detailed overview of the calibration applied to an Aerodyne high-resolution time-of-flight aerosol mass spectrometer (AMS) for detecting MSA during the ATom mission in Appendix B as a general reference for the AMS community.

3.2 Methods

3.2.1 Model description

In this work, we use the GEOS-Chem chemical transport model version 10.01 (http://geos-chem.org) coupled to the online TwO-Moment Aerosol Sectional (TOMAS) microphysical module (Adams and Seinfeld, 2002; GEOS-Chem-TOMAS as described in Kodros et al., 2016; 2017) to test the sensitivity of the aerosol size distribution to the addition of a marine secondary organic aerosol (SOA) species, represented in this work by methanesulfonic acid (MSA), of varying effective volatility and nucleation capability. The version of GEOS-Chem-TOMAS (GC-TOMAS) used here has 47 vertical levels, a horizontal resolution of 4°x5° (~400 km at mid

latitudes), and GEOS-FP reanalysis (http://gmao.gsfc.nasa.gov) for meteorological inputs. GC-TOMAS uses 15 size sections spanning dry diameters from approximately 3 nm - 10 μm and explicitly tracks total particle number as well as sulfate, sea salt, dust, hydrophilic OA, hydrophobic OA, internally mixed BC, externally mixed BC, and water mass (Lee and Adams, 2012). Biomass burning emissions are simulated using the Fire INventory from NCAR version 1.0 (FINNv1) (Wiedinmyer et al., 2011). Dust emissions follow the parameterization of the DEAD scheme (Zender et al., 2003); sea-salt aerosol emissions follow the parameterization of Jaegle et al. (2011). Anthropogenic emissions except for ammonia, black carbon, and organic aerosol are from the Emissions Database for Global Atmospheric Research (EDGAR; Janssens-Maenhout et al., 2010). In Europe, Canada, the U.S., and Asia, anthropogenic emissions are overwritten by the European Monitoring and Evaluation Programme (Centre on Emissions Inventories and Projections, 2013), the Criteria Air Contaminant Inventory (http://www.ec.gc.ca/air/default.asp?lang=En&n=7C43740B-1), the National Emission Inventory from the U.S. EPA (http://www.epa.gov/ttnchie1/net/2011inventory.html), and the MIX (Li et al., 2017) inventories, respectively. Black and organic carbon emissions from fossil-fuel and biofuel combustion processes are from Bond et al. (2007). Grid-box gas-phase concentrations of NH_3 are used in determining the volatility regime of MSA in the MSA parameterization (Sect. 3. 2.2): global anthropogenic, biofuel, and natural ammonia sources are from the Global Emissions InitiAtive (GEIA) (Bouwman et al., 1997). Anthropogenic ammonia emissions are overwritten over Europe, Canada, the U.S., and Asia using the same regional inventories discussed above for these regions. Ammonia emission from biomass burning are from FINNv1 (above). All simulations are run for 2014, with one month of model spinup that is not included in the analysis. All results are presented as annual or monthly averages.

We use the default (at the time of this model version) GEOS-Chem DMS emissions inventory (Kettle et al., 1999; Kettle and Andreae 2000) for this study. We acknowledge that the updated DMS inventory of Lana et al. (2011) includes more up-to-date measurements than the default DMS inventory for GEOS-Chem v10.01. Their work found that the default climatology overpredicted DMS emissions in some latitudes/seasons but underpredicted DMS emissions in other latitudes/seasons. We found, however, that using the Lana emission inventory led to minor differences in MSA impacts spatially but overall, similar magnitudes of changes were observed. Appendix B Sect. B2 provides more analysis of the two different emissions inventories.

In the standard GEOS-Chem DMS mechanism, DMS reacts with OH through the OH addition pathway to form molar yields of 0.75 SO_2 and 0.25 MSA (Chatfield and Crutzen, 1990; Chin et al., 1996). As discussed in the introduction, laboratory studies have reported variable yields of SO_2 and MSA from DMS oxidation by OH addition. We do not test the sensitivity of our simulations to other pathways, and this is a source of uncertainty. DMS also reacts with the nitrate radical (NO_3) to form a molar yield of 1 SO_2. SO_2 can then (1) react further in the model with OH to form gas-phase sulfuric acid, (2) undergo aqueous oxidation with H_2O_2 or O_3 to form condensed sulfate, or (3) be lost through dry and wet deposition processes (Pierce et al., 2013). Pierce et al. (2013) found that in GC-TOMAS (v8.02.02), 26% of global SO2 formed sulfate through aqueous chemistry and 13% formed sulfuric acid through gas-phase reaction with OH (the rest was lost through dry and wet deposition). The sulfate formed through aqueous chemistry is added to CCN-sized particles when activated in clouds, whereas the sulfuric acid formed from OH reactions participates in nucleation and irreversible condensation to particles of all sizes. Prior to this work, the DMS/SO_2-oxidized sulfuric acid and sulfate was included in the size-resolved portion of the GC-TOMAS model but MSA was not. In this study, we include MSA in the size-resolved

microphysics of the model. The contribution of MSA from DMS towards the sulfate budget and the size distribution as a function of particle size will then depend on both MSA's volatility and ability to participate in nucleation, as discussed below. A discussion of alternative oxidation pathways of DMS and the potential importance of aqueous-phase DMS chemistry (currently not included in GEOS-Chem) is provided in Sect 2.6.

Nucleation is simulated via a ternary nucleation scheme involving water, sulfuric acid, and ammonia (Napari et al., 2002), scaled with a global tuning factor of 10^{-5} (Jung et al., 2010; Westervelt et al., 2013). In ammonia-limited regions (less than 1 pptv), a binary nucleation scheme involving water and sulfuric acid (Vehkamaki et al., 2002) is instead used. When MSA is assumed to participate in nucleation, it is treated as an extra source of sulfuric acid for the ternary and binary nucleation schemes within the model. Growth and loss of nucleated particles between 1 and 3 nm is simulated using the parameterization of Kerminen et al. (2004) (Lee et al. 2013) with growth in this size range controlled by the pseudo-steady-state sulfuric acid (Pierce and Adams, 2009b) and MSA when it participates in nucleation.

SOA in GC-TOMAS is traditionally formed from terrestrial biogenic sources, with the biogenic source represented by 10% of the monoterpene emissions, totalling to 19 Tg(SOA) yr^{-1}; we further include 100 Tg(SOA) yr^{-1} spatially correlated with CO to represent anthropogenic SOA and anthropogenically-controlled biogenic SOA (Spracklen et al., 2011; D'Andrea et al., 2013). The default GC-TOMAS setting is for SOA to form through effective nonvolatile condensation (ELVOC-like condensation) onto pre-existing particles at the time of emission of the parent compound. However, it is possible to instead have SOA form in GC-TOMAS through quasi-equilibrium condensation (SVOC-like condensation, but still irreversible, e.g. not allowing for re-evaporation, in the model) by distributing the SOA across aerosol sizes proportional to the aerosol

mass distribution. In this work, we assuming ELVOC-like SOA condensation as it performed best relative to size-distribution measurements in D'Andrea et al. (2013).

3.2.2 MSA volatility assumptions, calculations, and parameterization

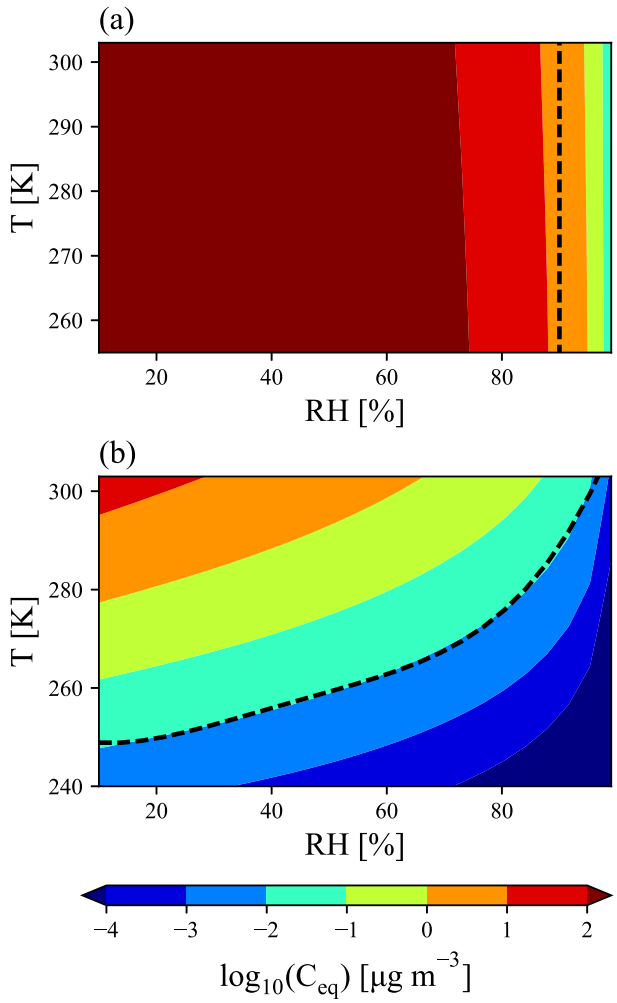

Figure 3.1 E-AIM prediction of MSA equilibrium vapor pressure above the particle mixture (C_{eq}) under conditions with (a) no free ammonia and (b) high free ammonia (3 times as many moles of ammonia as MSA). (a) The dashed line at 90% RH indicates the cut-off for representing MSA as a VOC-like (left of the line) or an SVOC-like (right of the line) species. (b) The dashed line is described by Eq. 1 in the text. Above the dashed line, MSA is treated as an SVOC-like species; below the dashed line, MSA is treated as an ELVOC-like species.

As the effective volatility of MSA is uncertain, we use the Extended Aerosol Inorganics Model (E-AIM; http://www.aim.env.uea.ac.uk/aim/aim.php, Clegg et al., 1992; Clegg and Seinfeld, 2006a, b; Wexler and Clegg, 2002) to build a parameterization for GC-TOMAS of MSA's potential volatility as a function of temperature, relative humidity, and available gas-phase bases. E-AIM calculates the MSA equilibrium vapor pressure above the particle mixture (C_{eq} in units of μg m^{-3}), and thus we get an MSA volatility parameterization in terms of C_{eq} (Fig. 3.1). We also consider two ideal assumptions of MSA volatility: (1) MSA condenses as an ELVOC-like species, condensing irreversibly to aerosol of all sizes, with net condensation of MSA proportional to the Fuchs-corrected aerosol surface area. Conversely, (2) MSA condenses as an SVOC-like species, where the net condensation of MSA is proportional to the aerosol mass distribution.

Table 3.1 Fit coefficients for the MSA volatility parameterization equation.

Variable	Value [T]
a	2.52×10^{2}
b	6.19×10^{-1}
c	3.49×10^{-2}
d	5.6×10^{-4}
e	3.32×10^{-6}

As MSA is a strong acid (pKa=-1.96; Haynes, 2017), we must consider the amount of atmospheric gas-phase base present; ammonia is used in E-AIM as the representative base. Although Chen and Finlayson-Pitts (2017) found in laboratory experiments that MSA had different rates of new particle formation with amines than ammonia, GC-TOMAS currently does not include any amine species and thus we do not attempt to account for these variations. Figure B1 and B2 provides global annual and seasonally averaged NH_3 concentrations from GEOS-Chem-TOMAS. The effective volatility of MSA also depends on the ambient temperature (Donahue et al. 2006)

and relative humidity (RH) (Chen et al., 2018). We run E-AIM for between 10-100% RH and between 240-310 K. Figure 3.1 shows the resulting volatility as a function of RH and temperature for conditions with no free ammonia and excess ammonia (3 times as many moles of free ammonia than moles of MSA). At low-base conditions (Fig. 3.1a), MSA acts essentially as a VOC (will all stay in vapor phase) below 90% RH and condenses as an ideally SVOC-like species above 90% RH for the entire input temperature range. Conversely, for excess-base conditions, we see that MSA transitions between volatilities as a function of both temperature and RH. We parameterize a transition between ELVOC-like behavior and SVOC-like behavior for excess-base conditions along the $C_{eq} = 10^{-2}$ μg m^{-3} line using the dashed line in Fig. 3.1b, given by:

$$T_{trans}\,(RH) = a - b \cdot RH + c \cdot RH^2 - d \cdot RH^3 + e \cdot RH^4 \quad (3.1)$$

where *RH* is the relative humidity, *T* is the temperature, T_{trans} is the transition temperature, and *a, b, c, d,* and *e* are fit coefficients, whose values are listed in Table 3.1. If $T > T_{trans}$, then MSA is treated as an ideally SVOC-like species that undergoes quasi-equilibrium condensation in GC-TOMAS. If $T < T_{trans}$, then MSA is low to extremely low in volatility and will be treated as an ideally ELVOC-like species that undergoes gas-phase-diffusion-limited condensation in GC-TOMAS. We do not include a volatile region under excess-base conditions: the high-temperature, low-RH regions that this would be applicable to are globally limited and likely only occur over desert regions, where MSA formation is likely negligible. Although E-AIM predicts that MSA's volatility varies smoothly across the volatility space as a function of temperature and RH, for simplicity, we only assume three condensational regimes: SVOC-like condensation, ELVOC-like condensation, and VOC-like (no condensation).

When using this parameterization in GC-TOMAS, we use a gas-phase ammonia mixing ratio of 10 pptv as a cutoff between the no-ammonia and excess-ammonia cases as this roughly

marks the transition from acidic to neutral aerosol (Croft et al., 2016, Supplementary Fig. 3.4). The gas-phase MSA production rate is explicitly tracked in the model, but not the MSA gas-phase concentrations. At the time of production, the model will then determine whether to treat MSA condensation as an effectively volatile species (no MSA condensing), an SVOC-like species (with all of the MSA produced condensing to the mass distribution), or an ELVOC-like species (with all of the MSA produced condensing to the Fuchs surface area and participating in the nucleation calculation in some simulations), based on the current *T*, *RH*, and available ammonia. For both SVOC-like and ELVOC-like condensation, the condensation is irreversible; we do not let MSA partition back to the gas phase once it is condensed as gas-phase MSA is not tracked in the model. Even this simple parameterization is a significant increase in the physical representation of MSA volatility over assuming a fixed volatility.

3.2.3 Descriptions of simulations

The different GEOS-Chem-TOMAS (GC-TOMAS) simulations in this study are summarized in Table 3.2. The default (DEFAULT_NoMSA) simulation represents a default GEOS-Chem-TOMAS simulation with only sulfate and sulfuric acid from DMS/SO_2 oxidation included in TOMAS; DEFAULT_NoMSA will be the comparison simulation for all other cases. PARAM_NoNuc uses the volatility parameterization from E-AIM (Sect 2.2), treating MSA as a non-nucleating ELVOC, an SVOC, or a VOC, depending upon the temperature, RH, and amount of ammonia in the gas-phase. ELVOC_NoNuc treats MSA condensation as ELVOC-like condensation. SVOC_NoNuc treats MSA condensation as SVOC-like condensation (but irreversible, Sect. 3.2.2). PARAM_Nuc and ELVOC_Nuc are identical to PARAM_NoNuc and ELVOC_NoNuc except that MSA is allowed to participate in nucleation with the properties of

sulfuric acid, providing an upper bound on the role of MSA in nucleation. For PARAM_Nuc, MSA only participates in nucleation when MSA is in the ELVOC-like regime; for ELVOC_Nuc, MSA is always able to participate in nucleation. Finally, to determine the contribution of sulfate and sulfuric acid from DMS/SO_2 oxidation alone to the default size distribution, we run a case with DMS emissions turned off (NoDMS_NoMSA).

In Appendix B we test the sensitivity of the model to the DMS concentration with two additional DMS inventories: the first is the DMS emissions inventory of Lana et al. (2011) and the second is the default DMS emissions inventory increased globally by a factor of two. As the sulfate and sulfuric acid from DMS/SO_2 oxidation is included in the default case simulation, we run new default simulations with the new DMS inventories (DEFAULT_NoMSA_Lana and DEFAULT_NoMSA_2xDMS). We use the PARAM_NoNuc case settings to determine the change in MSA's impact to the size distribution under the new DMS emissions inventories (PARAM_NoNuc_Lana and PARAM_NoNuc_2xDMS). However, the results for the contribution of MSA to the size distribution do not qualitatively change between the default DMS emissions inventory and the Lana DMS emission inventory. The contribution of MSA towards the submicron aerosol mass and thus the aerosol DRE in the 2xDMS case is roughly double that of the base DMS case (DEFAULT_NoMSA) but N3 and N80 do not significantly change for our tested metrics. Hence, we will not include these model results in the main portion of the paper. See Appendix B, Sect. B2, Tables B1-B2, and Figs. B3-B5 for a brief analysis of the different inventories.

Table 3.2 Description of simulations.

Simulation	Description
DEFAULT_NoMSA	Default model simulation: MSA does not contribute to the particle size distribution in GEOS-Chem-TOMAS (GC-TOMAS). The default GC-TOMAS v10.01 DMS emissions are used, and SO_2, sulfate, and sulfuric acid from DMS does influence the particle size distribution.
PARAM_NoNuc (NoNuc = does not nucleate particles)	Parameterization for MSA from E-AIM simulations: volatility is based on NH_3, T and RH. MSA can act as non-volatile and non-nucleating, semivolatile, or volatile (no condensation).
ELVOC_NoNuc	MSA is assumed to be non-volatile and condenses proportionally to the surface area distribution.
SVOC_NoNuc	MSA is assumed to be semivolatile and condenses proportional to the mass distribution.
ELVOC_Nuc	Like ELVOC_NoNuc, but MSA acts like sulfuric acid in nucleation.
NoDMS_NoMSA	All DMS emissions are turned off in the model; all other parameters are the same as the DEFAULT_NoMSA case.
DEFAULT_NoMSA_Lana	Default case using the Lana et al. (2010) DMS emissions inventory.
DEFAULT_NoMSA_2xDMS	Default case with global DMS emissions increased by a factor of two.
PARAM_NoNuc_Lana	Use the settings of PARAM_NoNuc with the Lana et al. (2010) DMS emissions inventory.
PARAM_NoNuc_2xDMS	Increase DMS emissions by a factor of two, using the settings of PARAM_NoNuc

3.2.4 Analysis of simulated radiative effects

We calculate aerosol DRE and cloud-albedo AIE following Kodros et al., (2016). The all-sky DRE is calculated offline using the monthly mean aerosol mass and number distributions from

the GC-TOMAS output. The refractive indices are from GADS (Global Aerosol Dataset; Koepke et al., 1997). Aerosol optical depth (AOD), single-scattering albedo, and the asymmetry parameter are calculated from Mie code (Bohren and Huffman, 1983). Optical properties and the monthly mean albedo and cloud fractions from GEOS5 are used as inputs to the offline version of the Rapid Radiative Transfer Model for Global Climate Models (RRTMG: Iacono et al., 2008) that has been implemented for the standard (non-TOMAS) version of GEOS-Chem (Heald et al., 2014). We assume an internal mixture, spherical particles, non-absorptive OA (brown carbon is not considered in this work) and a core-shell morphology. We note that the mixing state may vary both regionally and temporally, and that using only one mixing state globally for the full year is a limitation of our analysis of the DRE.

The cloud-albedo AIE is calculated as follows: first, the CDNC is found using the activation parameterization of Abdul-Razzak and Ghan (2002) for the monthly mean aerosol mass and number distribution from the GC-TOMAS output. A constant updraft velocity of 0.5 m s^{-1} is assumed. We again assume the aerosol species are internally mixed within each TOMAS size bin to determine κ, the hygroscopicity parameter, as a volume-weighted average of the individual aerosol species (Petters and Kreidenweis, 2007). For the cloud-albedo AIE, we use an effective cloud drop radii of 10 μm as a control and then perturb this value with the ratio of the CDNC of each sensitivity case to the default case to the one-third power, following the methods of Rap et al., (2013), Scott et al., (2014), and Kodros et al., (2016):

$$r_{perturbed} = \left(\frac{CDNC_{base\ case}}{CDNC_{sensitivity\ case}}\right)^{1/3} \cdot 10\mu m \qquad \text{(Eq. 3.2)}$$

RRTMG is again used to determine the changes in the top-of-the-atmosphere radiative flux from the changes in effective cloud drop radii, with monthly mean meteorological data needed as inputs

again informed by GEOS5. For more details on the methods used for the DRE and cloud-albedo AIE calculations, refer to Kodros et al. (2016) and references therein.

3.2.5 Measurement comparisons

Heintzenberg et al. (2000) compiled 30 years (between ~1970-1999) of physical marine aerosol data from both sampling sites and field campaigns to create annual global size distribution parameters, fitting the size distributions to bimodal lognormal distributions for latitudinal bands spaced 15° apart. We compare their fitted size distributions for 30°-45°S, 45°-60°S and 60°-75°S to the annual zonal-mean size distributions for the DEFAULT_NoMSA case and each sensitivity case from the model. (There is no data available from Heintzenberg et al. (2000) for 75°S-90°S.) We note that changes in the aerosol size distributions between the measurement years and our simulated year (2014) are possible, even for these remote latitudes, and may result in apparent simulation errors and/or apparent model to measurement agreement biases.

The first and second Atmospheric Tomography Missions (ATom-1 and ATom-2) (https://espo.nasa.gov/missions/atom/content/ATom) took place from July 28 to August 22 of 2016 and January 26-February 22 of 2017, respectively. Carrying a comprehensive gas and particle chemistry payload, the NASA DC-8 aircraft systematically sampled the remote atmosphere, profiling continuously between 0.2 and 12 km. The data for both missions is publicly available (Wofsy et al, 2018). As a part of the instrumentation on board, a highly customized Aerodyne high-resolution time-of-flight aerosol mass spectrometer (AMS in the following; DeCarlo et al, 2006; Canagaratna et al, 2007) continuously measured the composition of submicron (PM_1), non-refractory aerosol at 1 Hz time resolution. The principle of operation and instrument/aircraft-operation specifics have been described in detail elsewhere (Dunlea et al., 2009; Kimmel et al.,

2011; Schroder et al., 2018; Nault et al., 2018) and only the aspects specific to MSA quantification are discussed here.

The instrument flew in the same configuration for all four ATom missions. MSA data from the third and fourth ATom missions, ATom-3 and ATom-4, were not used in this study, but the calibration details discussed in Sect. B5 apply to these missions, as well. Overall sensitivity (as determined daily from the ionization efficiency of nitrate, IE_{NO3}), relative ionization efficiencies and particle transmission (all determined periodically in the field) were stable over all four deployments. Particle phase MSA concentrations for all ATom flights are reported based on the intensity of the highly specific marker ion $CH_3SO_2^+$ (Phinney et al, 2006, Zorn et al, 2008). The quantification of MSA PM_1 concentrations from the signal intensity of the $CH_3SO_2^+$ fragment is described in detail in the SI, Sect. B5. Positive Matrix Factorization (Paatero 1994; Ulbrich et al., 2009) of the ATom-1 organic aerosol (OA) and sulfate data confirmed the specificity of the marker ion for MSA and the consistency of the field mass spectra with those acquired in the MSA calibrations. Importantly, it also confirmed that the AMS response to MSA is independent of the aerosol acidity, which varied significantly over the range of conditions found in ATom. Further details are provided in Sect S5.

For the data presented here, the AMS raw data was processed at 1 minute resolution. Under those conditions, the detection limit of MSA was in the range 1.5-3 ng sm^{-3} (0.3-0.6 pptv), and will decrease with the square root of the number of averaged 1-minute data points. The uncertainty in the MSA quantification as detailed in the SI, Sect. B5, is comparable to that of sulfate, hence the overall uncertainty in the quantification is estimated to be +/-35% (2 standard deviations; Bahreini et al., 2009).

We compare our sensitivity simulations to the ATom-1 and ATom-2 data as follows: we subtract the DEFAULT_NoMSA sulfate mass (that accounts for sulfate and sulfuric acid from DMS/SO_2 oxidation but not MSA) for the months of August (ATom-1) and February (ATom-2) from the sulfate mass for the months of August and February for each sensitivity case that includes MSA for each grid box. The resultant differences in sulfate mass represents the model-predicted contributions of MSA to the total sulfur budget for each case. This is an imperfect approach, as the additional aerosol mass from the contribution of MSA will change the size distribution, therefore changing rates of wet and dry deposition, and is a limitation of this study. We then compare the measured and predicted MSA mass by first averaging every ATom data point that falls within a given GC-TOMAS grid box. We then compare each averaged data point to that model grid box. The ATom data used in our analysis lies within 150-180° W (the Pacific ocean basin) and 10-40° W (the Atlantic ocean basin), and thus we use zonal averages of these longitude bands for both the ATom data and the GC-TOMAS output. We note that comparing monthly mean simulated values from 2014 to airborne measurements from a single point in time in 2016 and 2017 contributes to the apparent simulation errors. We also note that we use the full size range (3 nm -10 μm) of sulfate from the model output whereas the ATom data is submicron. However, the model-predicted percent difference in MSA mass between the full range and the submicron mass is well under 1% (not shown).

To evaluate model performance, we calculate the log-mean bias (LMB), the slope of the log-log regression (m), and the coefficient of determination (R^2) between each cosampled GC-TOMAS grid box and averaged measurement point that falls within that GC-TOMAS grid box. The LMB is calculated through:

$$LMB = \frac{\sum_i^N (log_{10}(S_i) - log_{10}(O_i)}{N} \quad \text{(Eq. 3.3)}$$

where S_i and O_i are the simulated and observed MSA masses, respectively, for each data point i, and N is the number of data points. An LMB of 1 means that on average, the model overestimates the measurements by a factor of 10^1 (10); an LMB of -1 means that on average, the model underestimates the measurements by a factor of 10^{-1} (0.1); a LMB of 0 indicates no bias between the model and measurements ($10^0 = 1.00$). LMB, m, and R^2 are summarized in Fig. 3.8 (discussed in Sect. 3. 3.4). Since MSA is observed only in the particle-phase in the ATom measurements, we do not include the NoDMS_NoMSA (no DMS emissions in the model) sensitivity case in our analysis of the ATom data. We present the aggregated results of the two campaigns, as well as results for each campaign and ocean basin. The ATom-1 mission provided more data points than the ATom-2 missions (1258 vs. 1000) and thus the aggregate results are slightly skewed towards the ATom-1 results.

3.2.6 Study caveats

This study is intended to examine the sensitivity of the aerosol size distribution and radiative impacts implied by the various sensitivity treatments of MSA (Table 3.2). However, our treatments of DMS and MSA still fall short of what is currently known about organic condensational behavior. Assuming idealized semivolatile condensation with no re-evaporation due to conditional changes (e.g. change in temperatures, RH) may overestimate the amount of MSA able to condense on particles; but it may also underestimate particle-phase MSA if conditions for condensation switch from unfavorable to favorable after MSA chemical production. Further, relying on E-AIM simulations to construct our volatility parameterization could have hidden biases due to an incomplete understanding of the system. We are also neglecting known as well as gas-phase and aqueous-phase oxidation pathways of DMS that are currently not included in GEOS-Chem. The standard GEOS-Chem model does not include DMS oxidation through the OH or

halogen addition pathways to dimethylsulfoxide (DMSO). DMSO chemistry reduces the yield of sulfate formation from DMS/SO_2 oxidation (Breider et al., 2014) by increasing the yields of both gas-phase and aqueous phase MSA as well as aqueous-phase dimethyl sulfone ($DMSO_2$), another stable oxidation product (Hoffmann et al. 2016). To reduce the number of parameters for this study, we do not include the DMSO pathway. We acknowledge that neglecting this pathway will slightly bias our estimates of the contributions to the aerosol size distribution of sulfate and MSA mass high and low, respectively. Further, aqueous-phase production of MSA would condense on CCN-sized particles, similar to aqueous phase sulfate (Sect 2.1), shifting the size distribution to larger sizes. Heterogeneous oxidation may limit the lifetime of MSA in the particle phase (Mungall et al., 2017; Kwong et al., 2018), although the reactive uptake coefficients from these studies are somewhat dissimilar, indicating a need for further study of the system. Regardless, neglecting heterogeneous chemistry could overestimate the estimate of the contribution of MSA to aerosol mass. Finally, if MSA does participate in nucleation, it is unlikely that it will behave exactly like sulfuric acid, as it is treated here. All of the limitations described above are important and require further testing in detailed chemical models and chemical-transport models in order to determine their effects.

Another limitation of this study is our reliance upon the current ammonia inventory in GEOS-Chem as well as our cutoff value of 10 ppt of ammonia between the no ammonia and excess ammonia regimes (Sect. 3. 2.2). Uncertainties in the ammonia inventories over the oceans could change our results, as could a different cutoff value. As this study is focused on MSA sensitivities, we will leave sensitivities of MSA to ammonia for a future study. It is important to note that other bases such as amines could also have an important effect on MSA's effective volatility (e.g. Chen

and Finlayson-Pitts, 2017). However, the standard GEOS-Chem currently does not account for gas-phase bases beyond ammonia, and this sensitivity will also be left for a future study.

We do not test the sensitivity of our simulations to the binary and ternary nucleation schemes used in this study, including potential sensitivity to the global tuning factor of 10^{-5} that was developed for continental regions (Jung et al., 2010; Westervelt et al., 2013). This source of uncertainty should be tested in future studies, as well.

3.3 Results and Discussion

Figure 3.2 shows the global annual mean percent change (at 900 hPa and zonally) for submicron mass by adding MSA for the PARAM_NoNuc, ELVOC_NoNuc, SVOC_NoNuc, PARAM_Nuc, and ELVOC_Nuc simulations. Figure 3.3 shows the global annual mean percent change in N3 and N80 due to addition of MSA at 900 hPa and zonally for all model levels for each of these cases, and Fig. 3.4 shows the corresponding global annual cloud-albedo AIE and DRE of MSA. Figure 3.5 shows the global annual mean percent contribution from DMS/SO_2 oxidation (at 900 hPa and zonally) alone (not including MSA) to submicron mass, N3, N80, AID, and DRE. Figure 3.6 and Table B3 summarises the results of Figs. 3.2, 3.3, 3.4, and 3.5. All of the numerical statistics presented in Sects. 3.1-3.4 are for the annual mean, either globally or between 30°-90°S. Each case with MSA is analyzed for the change relative to DEFAULT_NoMSA to determine the impact that MSA has on the size distribution and resulting radiative effects (positive values indicate that the inclusion of MSA increases a given metric). For reference, Figure B6 provides the absolute number concentration for N3 and N80 at 900 hPa and zonally for all model levels for the DEFAULT_NoMSA simulation. We will refer back to these figures in the following sections.

3.3.1 Volatility-dependent impact of MSA if MSA does not participate in nucleation

The top rows of Figs. 3.2 and 3.3 show the global annual mean percent change at 900 hPa and zonally from adding MSA using the volatility parameterization without nucleation (PARAM_NoNuc - DEFAULT_NoMSA) for submicron aerosol mass (Fig. 3.2) and N3 and N80 (Fig. 3.3). By adding MSA with these assumptions, we predict at 900 hPa an increase in submicron mass of 0.7% globally and 1.3% between 30°S-90°S; a decrease in N3 of -3.9% globally and -8.5% between 30°S-90°S; and an increase in N80 of 0.8% globally and 1.7% between 30°S-90°S (Fig. 3.6 and Table B3). These MSA impacts are limited by ammonia availability. Figures B1 and B2 show that many oceanic regions are predicted to have annual and seasonal ammonia mixing ratios of less than 10 ppt. Below 10 pptv of ammonia, MSA condensation as SVOC-like or VOC-like (no condensation) (Fig. 3.1a) and MSA condensation will only be SVOC-like if the RH > 90%; under these conditions for the majority of the year, MSA will be a VOC-like species over Antarctica (low RH conditions) and often an SVOC-like species over the southern-ocean boundary layer (high RH conditions). Only in the Southern Hemisphere (SH) winter months does ammonia exceed 10 ppt over appreciable regions in the southern oceans (Fig. B2); during this time, MSA condensation is ELVOC-like due to cold temperatures (Fig. 3.1b). As shown in D'Andrea et al. (2013), ideal-SVOC material largely condenses primarily to accumulation-mode particles, which in turn suppresses N3 through increased coagulation and reduced nucleation and has little impact on N80. In the midlatitudes, the annual and seasonal ammonia concentrations often exceed 10 ppt, and thus MSA condensation will be either ELVOC-like under low-temperature and/or high-RH conditions or SVOC-like under high-temperature and/or low-RH conditions. D'Andrea et al. (2013) showed that adding ELVOC material can increase N80 by increasing growth of ultrafine

particles but also can suppress N3 through the same coagulation/nucleation feedbacks. This combination of ammonia-rich and ammonia-poor regions lead to MSA giving an overall weak increase in N80 with a large suppression of N3 in some regions. We note that these results are somewhat sensitive to the simulated ammonia concentrations and may be sensitivity to the ammonia cutoff of 10 ppt in the MSA-volatility parameterization. As there are already uncertainties in many other dimensions, we do not attempt to quantify the sensitivity of MSA towards ammonia in this work.

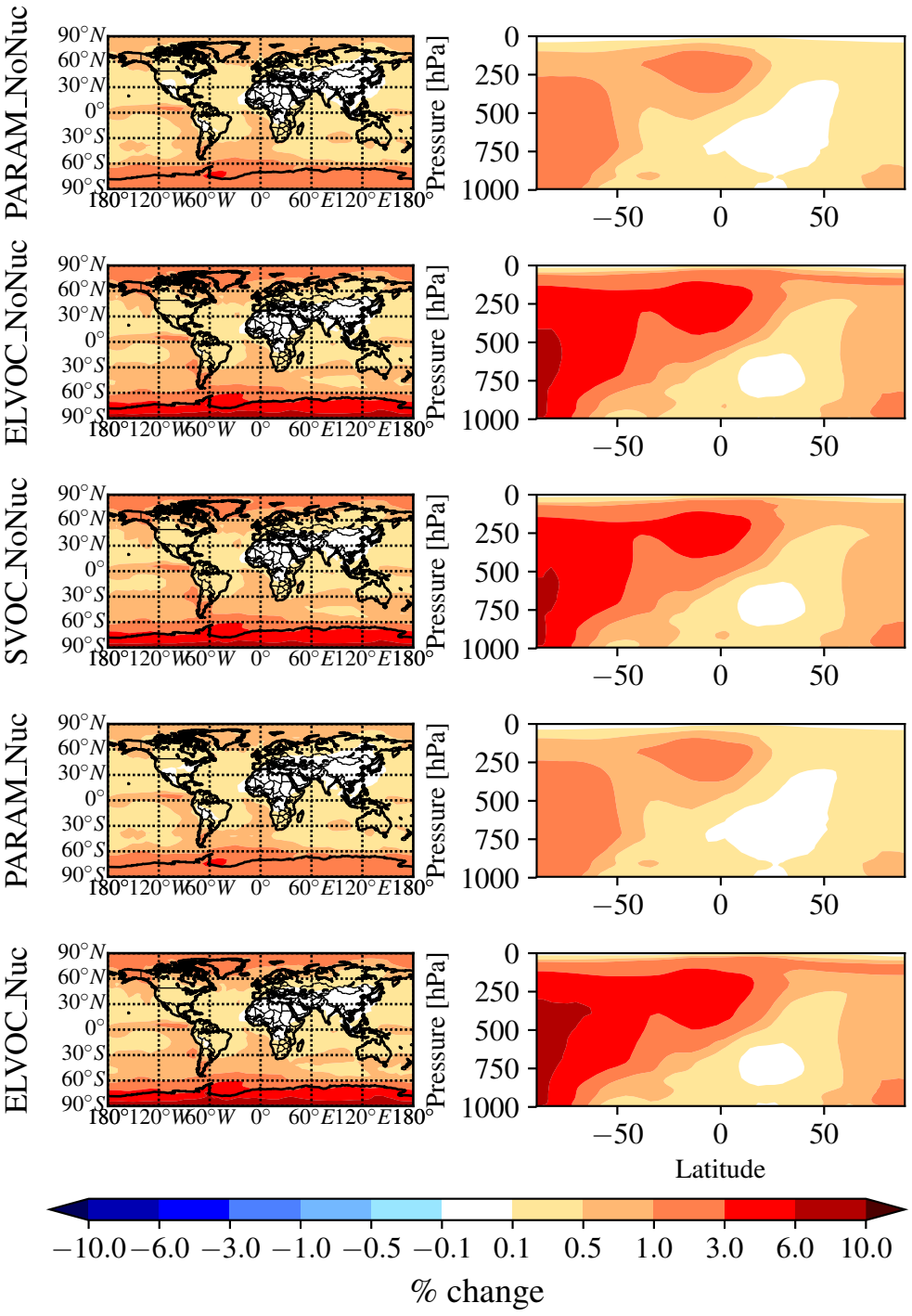

Figure 3.2 Global annual mean percent change in submicron aerosol mass due to the addition of MSA at 900 hPa (first column) and global zonal annual mean percent change (second column) between DEFAULT_NoMSA and PARAM_NoNuc (first row), ELVOC_NoNuc (second row), SVOC_Nuc (third row), PARAM_Nuc (fourth row), and ELVOC_Nuc (fifth row) (warm colors indicate an increase in submicron mass as compared to DEFAULT_NoMSA).

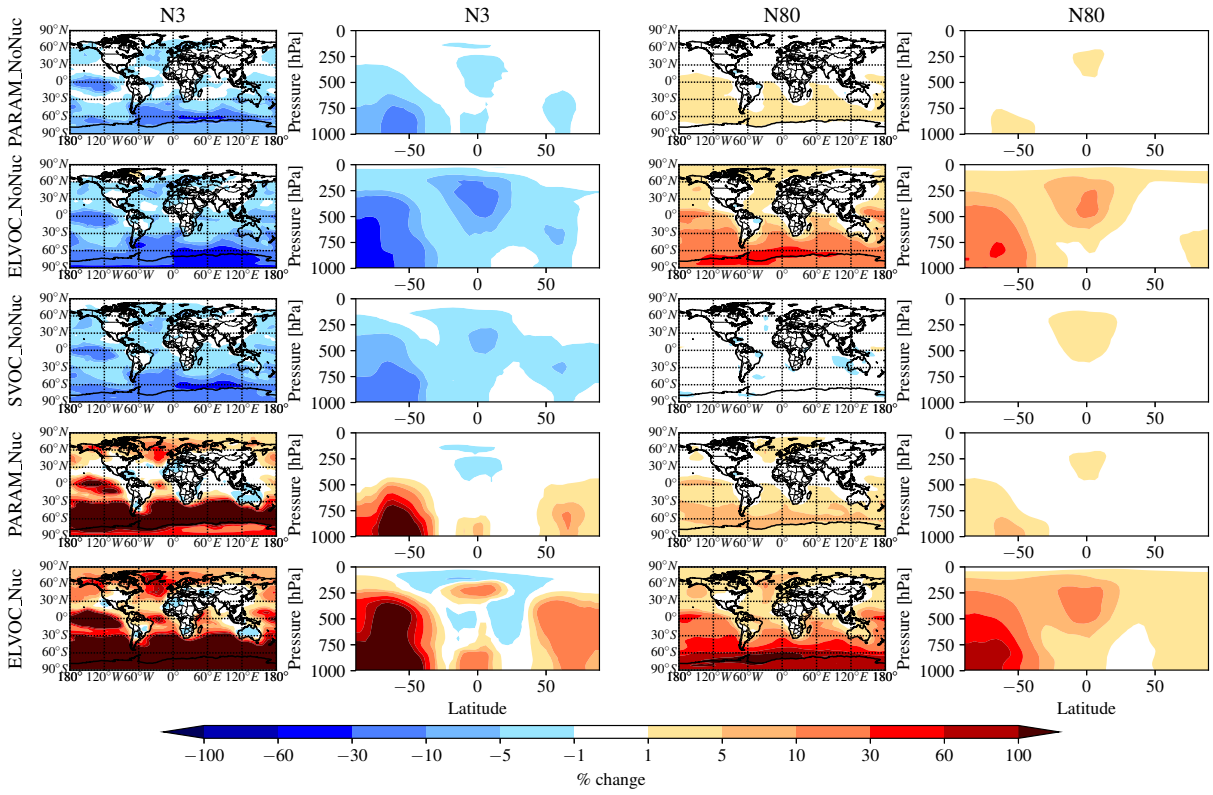

Figure 3.3 Global annual mean percent change in N3 and N80 at 900 hPa (first and third columns) and global zonal annual mean percent change (second and fourth columns) between DEFAULT_NoMSA and PARAM_NoNuc (first row), ELVOC_NoNuc (second row), SVOC_Nuc (third row), PARAM_Nuc (fourth row), and ELVOC_Nuc (fifth row) (warm colors indicate an increase in N3/N80 as compared to DEFAULT_NoMSA). First and second column: N3 (the number concentration of particles with diameters larger than 3 nm). Third and fourth column: N80.

The idealized volatility cases, ELVOC_NoNuc (Figs. 3.2 and 3.3, second row) and SVOC_NoNuc (Figs. 3.2 and 3.3, third row) help to highlight and further explain MSA's volatility-dependent contribution towards growth. In both of these cases, 100% of the formed MSA goes to the particle phase, unlike with the MSA volatility parameterization, where MSA may not condense in the absence of base at lower RHs. Hence, the global annual MSA mass is nearly double in these cases compared to when using the parameterization (Table 2; Fig. 3.2). The addition of MSA in the ELVOC_NoNuc case allows for an increase in condensable material that condenses to the Fuchs-corrected surface area through ELVOC-like condensation, which increases the

growth rate of all particle sizes. Conversely, MSA in SVOC_NoNuc allows for an increase of SVOC-like material that will condense preferentially to larger particles through SVOC-like condensation (but still irreversible condensation). In both the ELVOC_NoNuc and SVOC_NoNuc cases, N3 concentrations are reduced due to increased coagulational losses and decreased nucleation rates because of the added MSA mass (D'Andrea et al., 2013). When MSA condensation is treated as ELVOC-like, the smaller particles grow more quickly into the larger sizes, so N80 increases by 9.1% globally and by 22.2% between 30°S-90°S at 900 hPa (Fig. 3.6 and Table B3). When MSA condensation is instead treated as SVOC-like, the largest particles uptake MSA preferentially to smaller particles, and the N80 are not greatly impacted by the addition of MSA. The slight boost in N80 for SVOC_NoNuc in the tropical upper troposphere (UT) is due to the very low accumulation-mode concentration in this region: the SVOC material condenses to ultrafine particles in this region.

The changes in DRE and cloud-albedo AIE resulting from the addition of MSA for these three no-MSA-nucleation cases (Fig. 3.4, top three rows) depend roughly on the changes in N80 (the activation diameter for determining CDNC will depend on local particle hygroscopicity and concentrations). The DRE generally scales linearly with aerosol mass (Fig. 3.2, top three rows). As MSA is assumed to have the same properties as sulfate, which is is assumed to be purely scattering, any increases in MSA mass results in a negative radiative effect. However, the DRE also depends on aerosol size; the scattering efficiency peaks between ~300-900 nm, depending upon the aerosol composition and shape (Seinfeld and Pandis, 2016, their Fig. 15.8). The change in DRE when MSA is included using the volatility parameterization (PARAM_NoNuc) is less negative than that of ELVOC_NoNuc and SVOC_NoNuc at -15 mW m^{-2} globally (-26 mW m^{-2} between 30°S-90°S), because the parameterization yielded a smaller mass increase than the ideal

volatility simulations. ELVOC_NoNuc and SVOC_NoNuc have almost identical changes in submicron aerosol mass (Fig. 3.6; Table B3) but the DRE is -25 mW m^{-2} globally (-44 mW m^{-2} between 30°S-90°S) for SVOC_NoNuc and -0.02 W m^{-2} globally (-34 mW m^{-2} between 30°S-90°S) for ELVOC_NoNuc (Fig.3. 6; Table B3). MSA will preferentially condense to larger aerosol when its condensation is SVOC-like, and so even though ELVOC_NoNuc shows a larger increase in N80, SVOC_NoNuc increases the fraction of particulate mass in the peak scattering efficiency regime.

The cloud-albedo AIE instead scales the with aerosol number concentration of particles large enough to act as CCN: PARAM_NoNuc's cloud-albedo AIE (-8.6 mW m^{-2} globally, -17 mW m^{-2} between 30°S-90°S) reflects the small increase in N80 (0.8% globally and 1.7% between 30°S-90°S at 900 hPa) (Fig. 3.6; Table B3). The larger increase in N80 for ELVOC_NoNuc results in the larger cooling tendency in the cloud-albedo AIE, at -0.075 W m^{-2} globally (-150 mW m^{-2} between 30°S-90°S), and the slight decrease in N80 for SVOC_NoNuc results in the slight warming tendency in cloud-albedo AIE at 7.5 mW m^{-2} globally (11 mW m^{-2} between 30°S-90°S) (Fig. 3.6; Table B3).

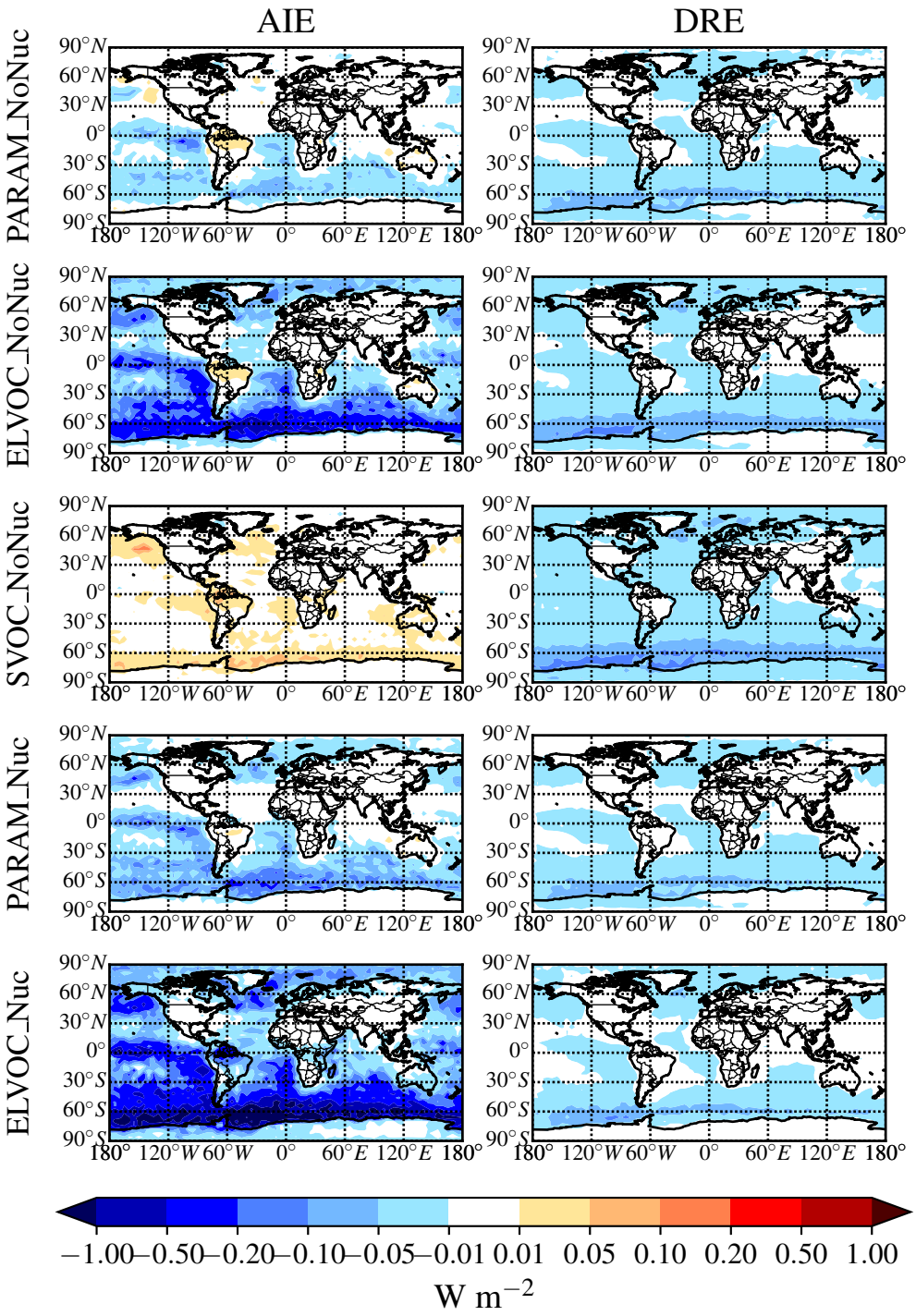

Figure 3.4 Global annual mean percent change for the aerosol indirect effect (AIE; first column) and the direct radiative effect (DRE; second column) between DEFAULT_NoMSA and PARAM_NoNuc (first row), ELVOC_NoNuc (second row), SVOC_Nuc (third row), PARAM_Nuc (fourth row), and ELVOC_Nuc (fifth row) (warm colors indicate an increase in the AIE/DRE as compared to DEFAULT_NoMSA).

These annual results show in Fig. 3.6 and Table B3 that if MSA does not take part in nucleation, the submicron aerosol mass will increase, causing a cooling tendency in the DRE, and N3 will decrease regardless of the volatility assumed. However, the changes in N80 are sensitive to the volatility assumption and will only increase if MSA condensation is ELVOC-like at least over some spatial and temporal scales, thereby causing a further cooling tendency in the cloud-albedo AIE.

3.3.2 Volatility-dependent impact of MSA if MSA does participate in nucleation

To test the potential influence on aerosol size distributions if MSA contributes to nucleation, we allow MSA to participate in binary and ternary nucleation with the same efficacy as sulfuric acid. This provides an upper bound in the potential contribution of MSA towards nucleation (at least for the nucleation schemes tested here). Figures 3.2, 3.3, and 3.4 (fourth rows) show the global annual mean percent changes between DEFAULT_NoMSA and PARAM_Nuc. MSA will have the same effective volatility as discussed for PARAM_NoNuc (Sect. 3. 3.1) but will now participate in nucleation under ELVOC-like regimes. For PARAM_Nuc, we can clearly see that when the ammonia concentrations reach above 10 ppt in the SH winter months over the Southern Ocean (Fig. B4), MSA acts as an ELVOC-like species and contributes strongly to nucleation in these sulfuric-acid poor regions. The addition of MSA in ELVOC_Nuc has the largest impact on N3, N80, and the cloud-albedo AIE of any of our cases with an increase in N3 of 153.4% globally (397.7% between 30°S-90°S), an increase in N80 of 23.8% globally (56.3% between 30°S-90°S), and a decrease for the cloud-albedo AIE of -0.18 W m^{-2} globally (-0.39 W m^{-2} between 30°S-90°S). MSA in PARAM_Nuc also has a large increase in N3 (112.5% globally and 309.9% between 30°-90° Sat 900 hPa) but only increase N80 by 2.1% globally (4.4% between

30°-90° S), again indicating that MSA often undergoes SVOC-like or ELVOC-like condensation within the volatility parameterization.

The increase in N80 from MSA in PARAM_Nuc is about double that of the increase from MSA in PARAM_NoNuc, and the change in cloud-albedo AIE is similarly slightly double for PARAM_Nuc. The global annual changes in submicron mass and the DRE is quite similar between the two PARAM cases. However, N80 increases more over the northern hemisphere (NH) high latitude ocean regions for PARAM_Nuc than for PARAM_NoNuc, and as a result, the northern oceans experience a stronger regional negative cloud-albedo AIE when MSA is allowed to participate in nucleation. As noted in Sect. 3. 3.1, there are uncertainties from the ammonia concentrations and cutoff point of 10 ppt for PARAM_Nuc, but we will not attempt to quantify them here.

These results indicate that if MSA does participate in nucleation, the largest climate-relevant change is anticipated to be an increased cooling tendency for the cloud-albedo AIE as compared to if MSA does not participate in nucleation. The change in DRE will be similar though, as MSA mass is not predicted to significantly change between non-nucleating and nucleating cases. This study provides an upper bound on the contribution of MSA to nucleation: if MSA is less efficient at nucleating than sulfuric acid, it is present in relatively sulfuric-acid poor regions and would still be able to increase N3 concentrations (although possible by less than predicted here). Microphysical feedbacks (increased condensation and coagulation sinks from increased N80) will then limit the effect that small changes in N3 can have on N80 and radiative effects.

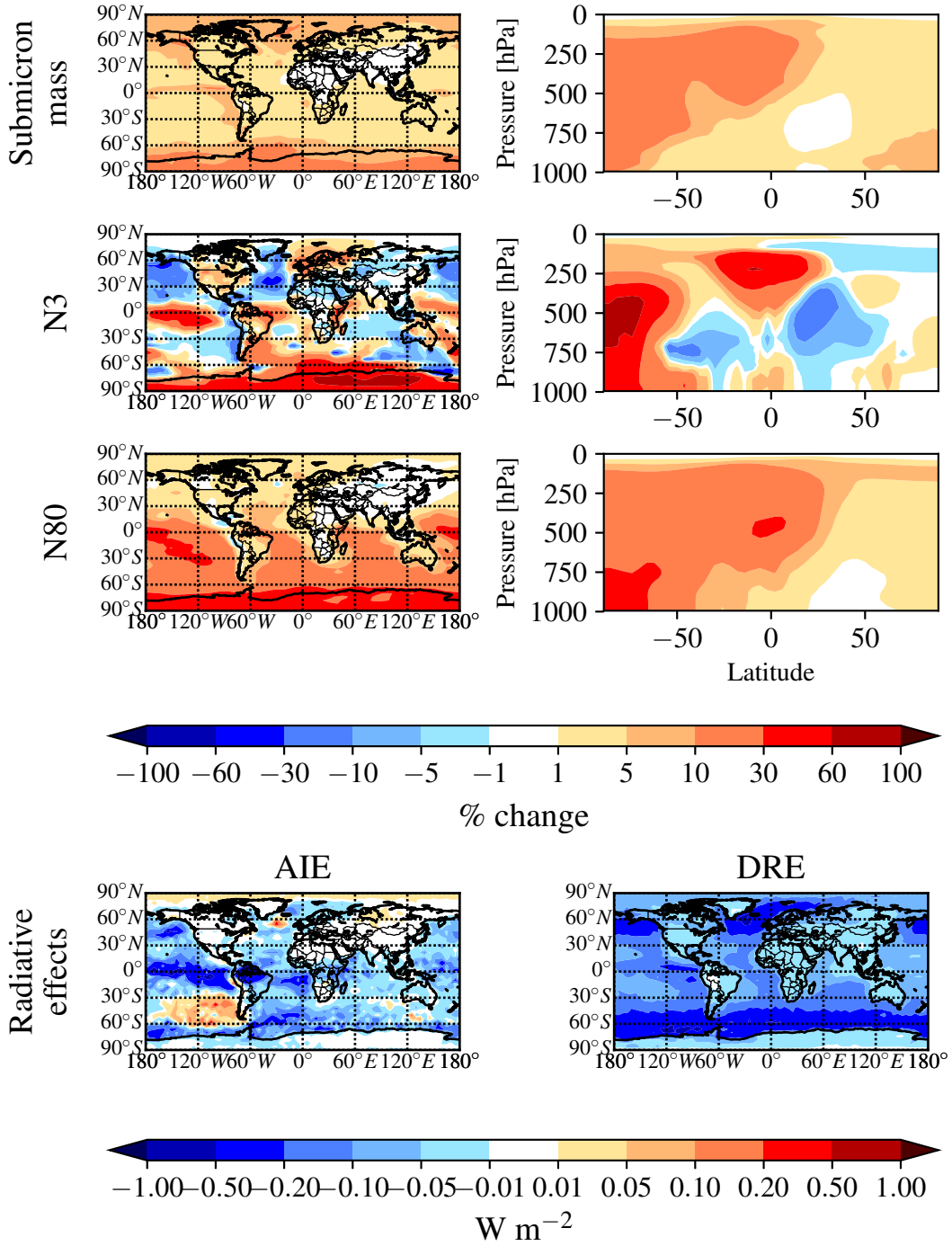

Figure 3.5 Global annual mean percent changes between the NoDMS_NoMSA and DEFAULT_NoMSA simulation. First row: change in submicron aerosol mass at 900 hPa (left) and zonally (right). Second row: change in N3 at 900 hPa (left) and zonally (right). Third row: change in N80 at 900 hPa (left) and zonally (right). Fourth row: radiative effects. This figures gives the contribution from sulfate and sulfuric acid produced from DMS/SO_2 oxidation to the

aerosol mass, number, and radiative effects. Warm colors indicate that sulfate and sulfuric acid produced from DMS/SO_2 oxidation increase the metric.

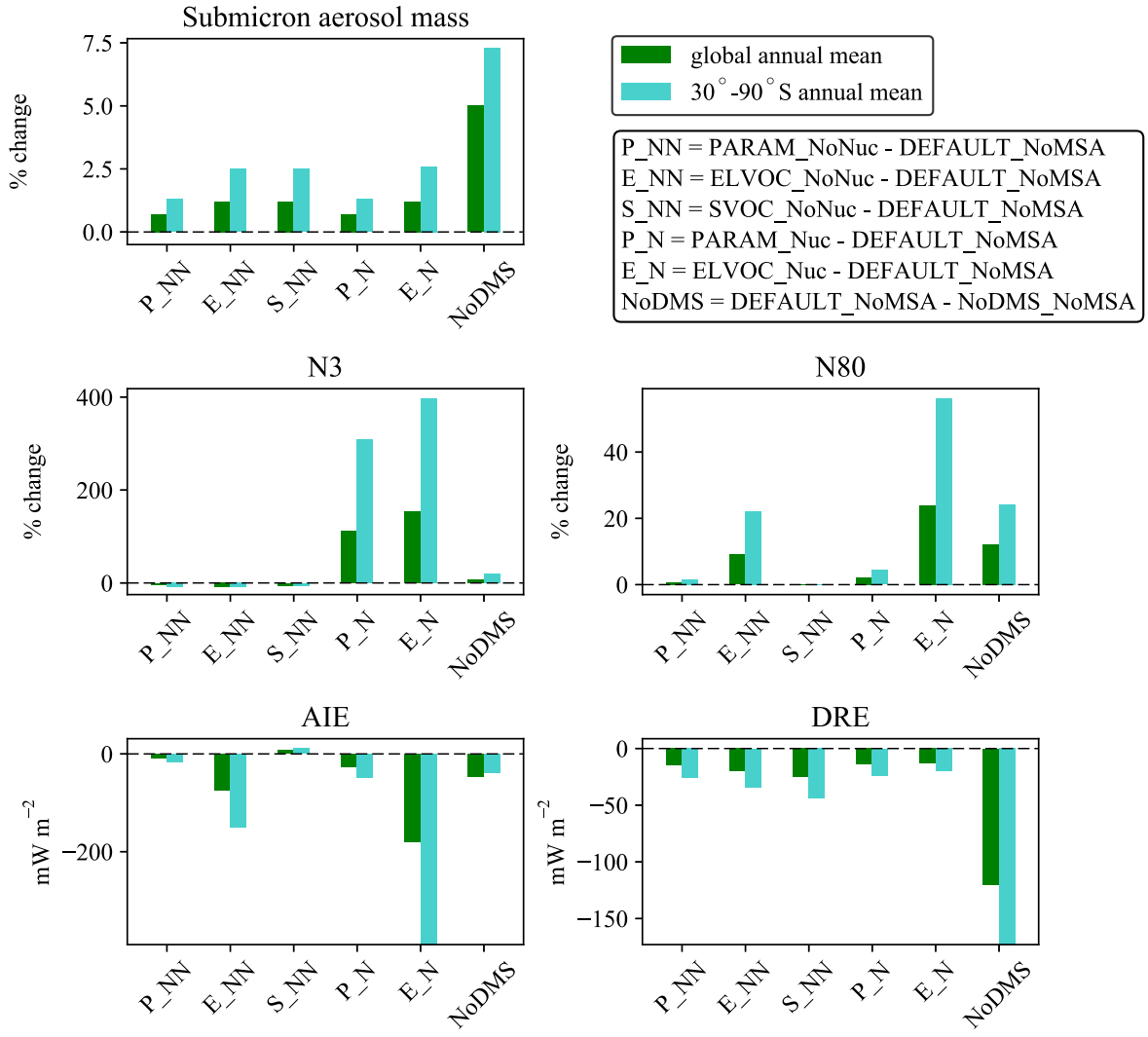

Figure 3.6 Annual mean % changes due to MSA at 900 hPa for each MSA simulation relative to the DEFAULT_NoMSA simulation for submicron aerosol mass, N3, N80, and radiative forcing changes in AIE and DRE. Positive values for any metric for PARAM_NoNuc (P_NN), ELVOC_NoNuc (E_NN), SVOC_NoNuc (S_NN), PARAM_Nuc (P_N), and ELVOC_Nuc (E_N) all indicate that the addition of MSA increases that metric relative to the DEFAULT_NoMSA simulation. The DEFAULT_NoMSA-NoDMS_NoMSA (NoDMS) columns shows the contribution of the sulfate and sulfuric acid from DMS/SO_2 oxidation present in the DEFAULT_NoMSA simulation; positive values of a metric indicate that the sulfate and sulfuric acid increases that metric compared to a simulation with no DMS emissions. Numerical values for each bar are provided in Table B3.

3.3.3 Comparison of MSA impacts to the contribution from SO_2 formed in DMS oxidation

By removing DMS from the simulation entirely (NoDMS_NoMSA case; Figs. 3.5 and 3.6 and Table B3), we determine the baseline contribution of the simulated sulfuric acid and sulfate from DMS/SO_2 oxidation to the aerosol size distribution in GEOS-Chem-TOMAS at 900 hPa. The sulfate and sulfuric acid from DMS/SO_2 oxidation provides larger changes in submicron mass and N80 than MSA does in any of our sensitivity cases. The contribution of SO_2 from DMS to submicron mass is 4-6 times that of the MSA contribution. However, about ⅔ of this mass increase from DMS/SO_2 comes through aqueous oxidation of SO_2 to sulfate, which adds mass (but not number) to already-CCN-sized particles (Pierce et al., 2013) suppressing nucleation and growth. The remaining ~⅓ of the mass comes from gas-phase formation of sulfuric acid, which nucleates particles and condenses irreversibly to the Fuchs-corrected surface area, potentially increasing the number of CCN-sized particles. Overall, N3 and N80 increase due to the inclusion of the DMS/SO_2 pathway (N3 by 7.3% and N80 by 12.2% globally and N3 by 19.5% and N80 by 24.3% between 30°S-90°S at 900 hPa). The increases in both N3 and N80 are strongly damped by the formation of aqueous sulfate. The changes in N3 at 900 hPa indicate the relative importance of the sulfuric acid produced by DMS/SO_2 oxidation for nucleation compared to other sources of sulfuric acid. N3 generally increases in remote regions where sulfuric acid from DMS/SO_2 oxidation would be the main source of sulfuric acid. There are also regions of decrease in N3 in remote regions: the condensation and coagulation sinks increase from aqueous sulfate formation, and in some regions this competition effectively scavenges N3 faster than sulfuric acid from DMS/SO_2 oxidation forms new particles. Because of the large increase in submicron mass from the sulfuric acid and sulfate

from DMS/SO_2 oxidation, the DRE from DMS/SO2 is -120 mW m^{-2} globally (-173 mW m^{-2} between 30°S-90°S), about 5 times larger than MSA for any of our assumptions. On the other hand, the cloud-albedo AIE cooling tendency of -46 mW m^{-2} globally and -38 mW m^{-2} between 30°S-90°S, was within the range of cloud-albedo AIEs from MSA that we predicted, which is due to the N80 damping of DMS/SO_2 due to aqueous sulfate formation. Thus, overall we predict the DRE from MSA to be at least 5 times weaker than from DMS/SO_2, but the cloud-albedo AIE may be of similar magnitude depending on the properties of MSA.

3.3.4 Analysis of model-measurement comparisons

Figure 3.7 shows the comparison between the annual zonal-mean particle number size distributions compiled in Heintzenberg et al. (2000; hereon referred to as Heintzenberg) and the GC-TOMAS simulated annual-mean particle number size distributions within the boundary layer for the latitude bands of 30°S-45°S, 45°S-60°S, and 60°S-75°S (no data was provided in Heintzenberg between 75°S-90°S). We focus this comparison to the southern oceans region as this region has the strongest influence from DMS and its oxidation products. It is also less likely to be influenced by changing anthropogenic emissions that may have occurred between the time of the measurements compiled in Heintzenberg (between ~1970-1999) and 2014 (the year of the model run) than higher latitudes (e.g. Pierce and Adams, et al., 2009a; Gordon et al., 2017). We see that all model simulations underpredict both the Aitken and accumulation modes of Heintzenberg, but that the simulations that allow MSA to participate in nucleation (ELVOC_Nuc and PARAM_Nuc) give the best model-to-measurement agreements for the Aitken mode for each latitude band, with ELVOC_Nuc performing the best across the model cases. Further, ELVOC_Nuc shows the highest number of particles in the accumulation mode, particularly between 60°-75° S. These results point

to the necessity of another source of ultrafine particles over the southern oceans than is being currently accounted for in the model. These particles may be produced locally from ultrafine sea spray (Pierce and Adams, 2006), local nucleation (not necessarily through MSA), or entrainment of ultrafine particles from the free troposphere (Clarke et al., 2002).

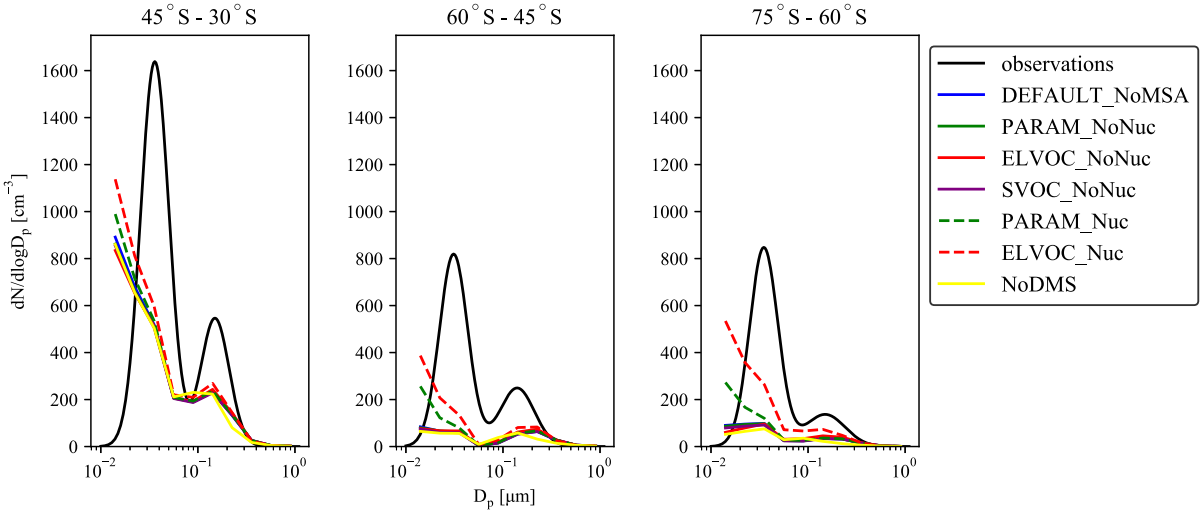

Figure 3.7 Comparison of simulated annual mean particle number size distributions to the annual zonal particle number size distributions compiled in Heintzenberg et al. (2000) (black lines) for the southern oceans. No data was available in Heintzenberg et al. (2000) for 75-90° S. We match the grid boxes sampled in their study to the GEOS-Chem-TOMAS grid boxes; due to sparseness of data, we do not attempt to discuss seasonal variabilities in this comparison.

For the ATom mission, Figure 3.8 provides 1:1 plots for each sensitivity case's predicted MSA mass versus the observed MSA mass from the aggregated ATom-1 and ATom-2 campaigns. Each subplot provides the LMB, *m*, and R^2 statistics for the given sensitivity case. LMB, *m*, and R^2 statistics are also provided for each campaign and ocean basin in Figs. B7-B10; Figures B11-B14 show the zonally averaged simulated MSA concentrations for each basin and campaign with the corresponding particle-phase MSA measurements overlaid. Figure 3.8 indicates that for the aggregated campaigns, the model cases in which MSA always condenses to the particle phase (the

SVOC_NoNuc, ELVOC_NoNuc, and ELVOC_Nuc cases) overpredict MSA mass, with positive LMBs between 0.27 and 0.3 (overpredictions of a factor of 1.9-2). The PARAM_NoNuc and PARAM_Nuc cases do not allow MSA to condense to the particle phase under low-base/high-temperature/low-RH conditions (Fig. 3.1). As a result, the PARAM cases instead slightly underpredict MSA mass, with LMBs of -0.1 and -0.08 (underpredictions by a factor of 0.79 and 0.83). Overall, when the parameterization is not used, too much MSA mass is allowed to condense relative to the observations. Given the large improvement in LMB through the use of the parameterization (with roughly similar R^2 and m values), we feel that these results support the use of the volatility parameterization of MSA.

The R^2 values are quite low across cases, with the parameterization cases giving the highest R^2 values, at 0.09. The m values are similarly low, with the SVOC_NoNuc, ELVOC_NoNuc, and ELVOC_Nuc cases giving the highest m values, at 0.33-0.34. However, we are comparing monthly grid-box mean model predictions to individually grid-box averaged measurements taken during a different year than the simulation year. Further, using monthly mean model predictions on the y-axis (Fig. 3.8) decreases variability, which reduces the slope. These considerations contribute to lower values of R^2 and m.

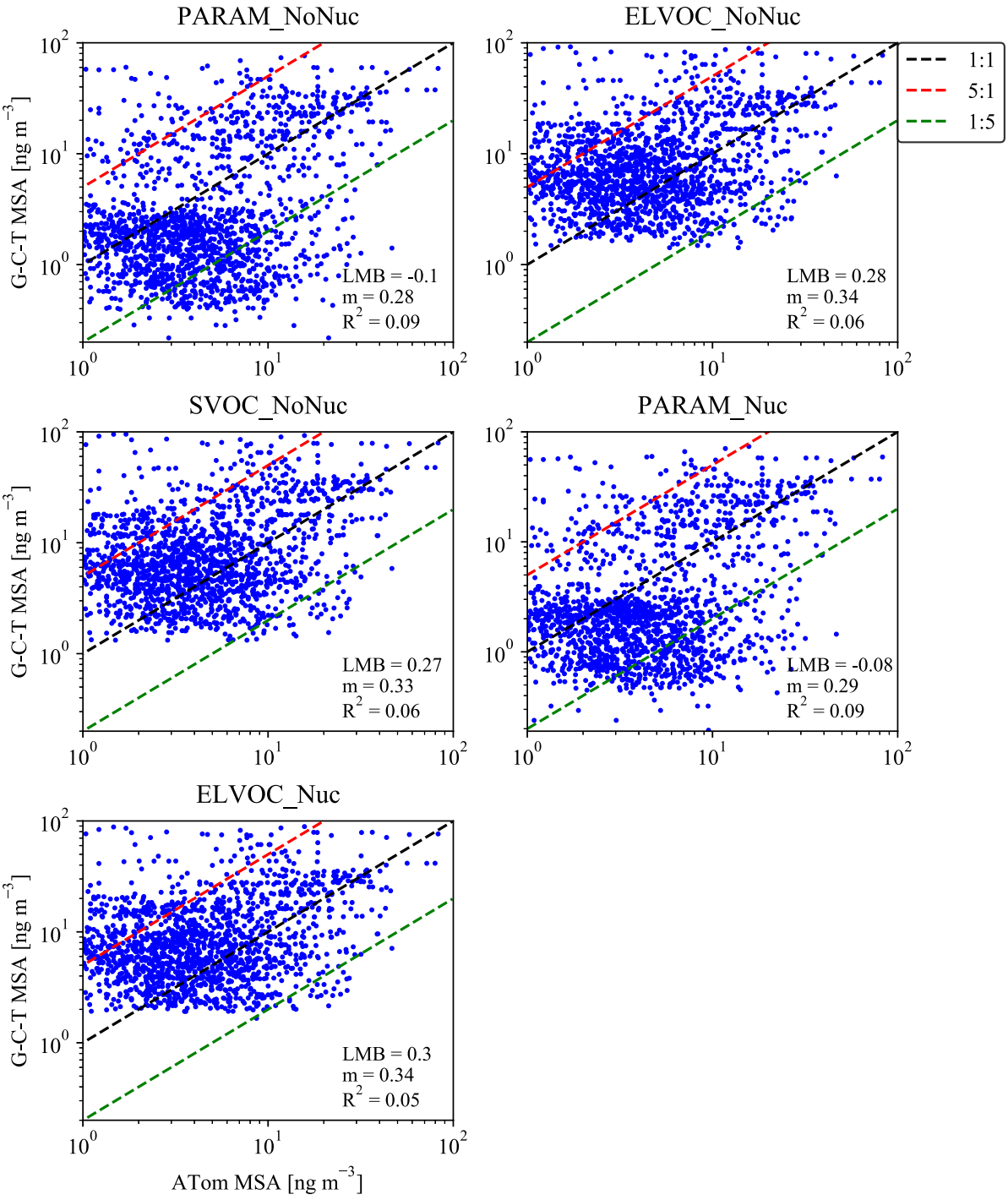

Figure 3.8 1:1 (black dashed line) plots for the simulated mean MSA mass for the months of August/February and measured MSA mass during the ATom-1/Atom-2 campaigns (July 28-August 22 2016 / January 26-February 22 2017). Each subpanel gives the calculated log-mean bias (LMB), slope (*m*), and coefficient of determination (R^2) between the ATom data and the sensitivity simulation. The red and green dashed lines indicate 5:1 and 1:5 lines. Simulated MSA mass is calculated by subtracting the total sulfate mass for the base case from each sensitivity case.

The Heintzenberg and ATom model-measurement comparisons disagree on which MSA assumptions lead to the best performance in GC-TOMAS. However, the Heintzenberg analysis considers number size distribution whereas the ATom analysis considers total particle-phase MSA mass. The model-measurement improvement for the Heintzenberg study is most strongly seen within the Aitken mode (the smallest reported particle sizes). Aitken-mode-sized particles contribute little to total mass compared to larger particles. Further, it is not possible to determine from this study whether the source of ultrafine particles that could explain the size of the Aitken modes in Heintzenberg comes from MSA another primary or secondary source. On the other hand, the ATom comparison suggests that using the MSA volatility parameterization helps predict the MSA mass concentrations more accurately.

3.4 Conclusions

We used the GEOS-Chem chemical transport model coupled to the TOMAS aerosol microphysics module to test the sensitivity of the aerosol size distribution and resulting changes in the direct and indirect effects to the condensational and nucleating behavior of methanesulfonic acid (MSA), an oxidation product of dimethylsulfide (DMS). GEOS-Chem-TOMAS (GC-TOMAS) normally simulates sulfuric acid and sulfate from DMS/SO_2 oxidation but does not include MSA within the size-resolved portion of the model; we used this setup as our default model case (DEFAULT_NoMSA). We considered both the global annual mean size distributions and the annual mean in the southern ocean regions (30S°-90°S) at 900 hPa for each sensitivity case compared to DEFAULT_NoMSA. We further evaluated the model output against two different measurement sets: zonal-mean number size distributions compiled from ship-based measurements

taken in the southern oceans and particle-phase MSA mass concentrations obtained from aircraft data over the Atlantic and Pacific ocean basins for the months of August and February.

As the effective volatility of MSA is uncertain, we used the Extended Aerosol Inorganics Model (E-AIM) to build a parameterization for GC-TOMAS of MSA's potential volatility as a function of temperature, relative humidity, and available gas-phase base. For simplicity, we only allowed MSA to condense as ideally nonvolatile or semivolatile, or to be volatile and not condense at all under the parameterization. If MSA was ideally nonvolatile, it contributed to the size distribution through condensation proportional to the Fuchs-corrected aerosol surface area distribution (effectively nonvolatile or ELVOC-like condensation). If MSA was instead ideally semivolatile, it contributed to the size distribution through condensation proportional to the aerosol mass distribution (quasi-equilibrium or SVOC-like condensation). Regardless of the volatility treatment, condensed MSA was not allowed to evaporate back to the gas-phase, as gas-phase MSA was not explicitly tracked in the model. Along with the parameterization, we tested limiting volatility cases, allowing MSA to only be ELVOC-like or SVOC-like. We also performed separate simulations in which MSA could participate in nucleation, using both the MSA volatility parameterization and the ELVOC-like and SVOC-like MSA assumptions. (MSA participated in nucleation only when it was under ELVOC-like conditions in the parameterization; it always participated in nucleation in the ELVOC simulation). When using the volatility parameterization, including MSA in the model changed the global annual averages of submicron aerosol mass by 1.2%, N3 by -3.9% (non-nucleating) or 112.5% (nucleating), N80 by 0.8% (non-nucleating) or 2.1% (nucleating), the aerosol indirect effect by -8.6 mW m^{-2} (non-nucleating) or -26 mW m^{-2} (nucleating), and the direct radiative effect by -15 mW m^{-2} (non-nucleating) or -14 mW m^{-2} (nucleating). Across all simulations, including MSA in the model changed the global annual

averages of submicron aerosol mass by 0.7% to 1.2%, N3 by -3.9% to 153.4%, N80 by -0.2% to 23.8%, the aerosol indirect effect by -0.18 W m^{-2} to 0.0075 W m-2, and the direct radiative effect by -25 mW m^{-2} to -13 mW m^{-2}, depending on the assumed volatility and nucleating ability of MSA.

The contribution from the sulfuric acid and sulfate from DMS/SO_2 oxidation to the submicron aerosol mass is 4-6 times that of the contribution from DMS/MSA, leading to a global cooling from the DRE 5-10 times that of MSA, at -120 mW m^{-2}. However, because much of the aerosol mass from DMS/SO2 is added through aqueous sulfate formation, which suppresses nucleation and growth, the changes in N3, N80, and the cloud-albedo AIE from DMS/SO_2 oxidation products are smaller and on the order of changes in these metrics from including MSA in the model.

The model-measurement annual zonal number size distribution comparisons to the ship-based measurements compiled in Heintzenberg et al. (2000) of the southern-ocean region (Fig. 3.11) show an underprediction of the Aitken mode across cases, with the best agreement in the Aitken mode coming from the cases that allow MSA to act as a nucleating nonvolatile compound (ELVOC_Nuc and PARAM_Nuc). These results indicate the necessity of another source of ultrafine particles over the southern oceans that is currently not being accounted for in the model. However, it is not possible to conclude based on this study where the source of extra ultrafines is coming from. More studies over the oceans detailing the chemical compositions of the smallest particle sizes are needed in order to help determine the origins of nucleating material in these remote regions.

The model-measurement comparisons of total particle-phase MSA mass from the aircraft data taken during the ATom-1 and ATom-2 campaigns compared to the predicted mean MSA mass indicate that PARAM_Nuc and PARAM_NoNuc cases perform the best, and that the cases in

which MSA is always allowed to condense to the particle phase overpredict MSA mass. As the Heintzenberg and the ATom model-measurement comparisons are based on dissimilar metrics (number size distribution versus particle-phase MSA mass) over dissimilar spatial extents (surface-based ground and ship measurements versus aircraft measurements continuously profiling between 0.2 and ~13 km), we cannot definitively state that any one sensitivity case appears to best-fit both the Heintzenberg and ATom measurements. Along with these model-measurement comparisons, we provided a detailed description of the calibration for detecting MSA applied to the Aerodyne high-resolution time-of-flight aerosol mass spectrometer (AMS) present during the ATom campaigns in the supplement as a reference for the AMS community.

As there are uncertainties in both MSA's behavior (nucleation and condensation) and the DMS emissions inventory, further modelling and measurement studies on both fronts are needed to better constrain MSA's current and future impact upon the global aerosol size distribution and radiative effect. Under the simulation tested in this work, MSA tends to have small (< -0.1 W m^{-2}) global annual radiative effects (DRE and cloud-albedo AIE); in general, the forcings are predicted to be cooling effects. The contributions to the size distribution and radiative effects increase in magnitude in the southern oceans, where MSA concentrations are highest and more-pristine conditions exist. Although small, the radiative effects from MSA and the associated size distribution dependencies should be well-characterized to more-fully understand the role of changing DMS emissions in a changing climate. This study provides a first look at some of these potential dependencies and indicates possible directions for future modelling and measurement studies.

REFERENCES

Abdul-Razzak, H. and Ghan, S. J.:A parameterization of aerosol activation 3. Sectional representation, J. Geophys. Res., 107, 4026, doi:10.1029/2001JD000483, 2002.

Adams, P. J. and Seinfeld, J. H.: Predicting global aerosol size distributions in general circulation models, J. Geophys. Res., 107(D19), 4370, doi:10.1029/2001JD001010, 2002.

Andreae, M. O., Ferek, R. J., Bermond, F., Byrd, K. P., Engstrom, R. T., Hardin, S., Houmere, P. D., LeMarrec, F., Raemdonck, H. and Chatfield, R. B.: Dimethyl sulfide in the marine atmosphere, J. Geophys. Res., 90(D7), 12891, doi:10.1029/JD090iD07p12891, 1985.

Andreae, M. O., R. J. Ferek, F. Bermond, K. P. Byrd, R. T. Engstrom, S. Hardin, P. D. Houmere, F. LeMarrec, H. Raemdonck, and R. B. Chatfield: Dimethyl sulfide in the marine atmosphere, *J. Geophys. Res.*, 90(D7), 12891–12900, doi:10.1029/JD090iD07p12891, 1985.

Andreae, M. O.: Ocean-atmosphere interactions in the global biogeochemical sulfur cycle, Mar. Chem., 30, 1–29, doi:https://doi.org/10.1016/0304-4203(90)90059-L, 1990.

Arsene, C., Barnes, I., Becker, K. H. and Mocanu, R.: FT-IR product study on the photo-oxidation of dimethyl sulphide in the presence of NOx—Temperature dependence, Atmos. Environ., 35(22), 3769–3780, doi:10.1016/S1352-2310(01)00168-6, 2001.

Bahreini, R., Ervens, B., Middlebrook, A. M., Warneke, C., De Gouw, J. A., DeCarlo, P. F., Jimenez, J. L., Brock, C. A., Neuman, J. A., Ryerson, T. B., Stark, H., Atlas, E., Brioude, J., Fried, A., Holloway, J. S., Peischl, J., Richter, D., Walega, J., Weibring, P., Wollny, a. G., and Fehsenfeld, F. C.: Organic aerosol formation in urban and industrial plumes near Houston and Dallas, Texas, J. Geophys. Res., 114(16), D00F16, doi:10.1029/2008JD011493, 2009.

Barnes, I., Hjorth, J. and Mihalapoulos, N.: Dimethyl sulfide and dimethyl sulfoxide and their oxidation in the atmosphere, Chem. Rev., 106(3), 940–975, doi:10.1021/cr020529+, 2006.

Barsanti, K. C., McMurry, P. H., and Smith, J. N.: The potential contribution of organic salts to new particle growth, Atmos. Chem. Phys., 9, 2949–2957, doi:10.5194/acp-9-2949-2009, 2009.

Bates, T., Lamb, B., Guenther, A., Dignon, J. and E. Stoiber, R.: Sulfur Emissions to the Atmosphere from Natural Sources., 1992.

Belviso, S., Bopp, L., Moulin, C., Orr, J. C., Anderson, T. R., Aumont, O., Chu, S., Elliott, S., Maltrud, M. E., and Simó, R.: Comparison of global climatological maps of sea surface dimethyl sulfide, Global Biogeochem. Cy., 18, GB3013, https://doi.org/10.1029/2003GB002193, 2004.

Berresheim, H., Elste, T., Tremmel, H. G., Allen, A. G., Hansson, H.-C., Rosman, K., Dal Maso, M., Mäkelä, J. M., Kulmala, M., and O'Dowd, C. D.,: Gas-aerosol relationships of H2SO4, MSA, and OH: Observations in the coastal marine boundary layer at Mace Head, Ireland, *J. Geophys. Res.*, 107 (D19), 8100, doi:10.1029/2000JD000229, 2002.

Bohren, C. F. and Huffman, D. R.: Absorption and scattering of light by small particles,Wiley Interscience, New York, USA, 1983.

Bond, T. C., Habib, G., and Bergstrom, R. W.: Limitations in the enhancement of visible light absorption due to mixing state, J. Geophys. Res., 111, D20211, doi:10.1029/2006JD007315, 2006.

Bond, T. C., Bhardwaj, E., Dong, R., Jogani, R., Jung, S., Ro- den, C., Streets, D. G., and Trautmann, N. M.: Historical emissions of black and organic carbon aerosol from energy-

related combustion, 1850–2000, Global Biogeochem. Cy., 21, GB2018, doi:10.1029/2006GB002840, 2007.

Bond, T. C., Doherty, S. J., Fahey, D. W., Forster, P. M., Berntsen, T., DeAngelo, B. J., Flanner, M. G., Ghan, S., Kärcher, B., Koch, D., Kinne, S., Kondo, Y., Quinn, P. K., Sarofim, M. C., Schultz, M. G., Schulz, M., Venkataraman, C., Zhang, H., Zhang, S., Bellouin, N., Guttikunda, S. K., Hopke, P. K., Jacobson, M. Z., Kaiser, J. W., Klimont, Z., Lohmann, U., Schwarz, J. P., Shindell, D., Storelvmo, T., Warren, S. G., and Zender, C. S.: Bounding the role of black carbon in the climate system: A scientific assessment, J. Geophys. Res. Atmos., 118, 5380–5552, doi:10.1002/jgrd.50171, 2013.

Bork, N., Elm, J., Olenius, T. and Vehkamäki, H.: Methane sulfonic acid-enhanced formation of molecular clusters of sulfuric acid and dimethylamine, Atmos. Chem. Phys., 14(22), 12023–12030, doi:10.5194/acp-14-12023-2014, 2014.

Bouwman, A. F., Lee, D. S., Asman, W. A. H., Dentener, F. J., Van Der Hoek, K. W., and Olivier, J. G. J.: A global high-resolution emission inventory for ammonia, Global Biogeochem. Cycles, 11(4), 561–587, 1997.

Breider, T. J., Mickley, L. J., Jacob, D. J., Wang, Q., Fisher, J. A., Chang, R. Y.-W., and Alexander, B.: Annual distributions and sources of Arctic aerosol components, aerosol optical depth, and aerosol absorption, J. Geophys. Res. Atmos., 119, 4107–4124, doi:10.1002/2013JD020996, 2014

Canagaratna, M. R., Jayne, J. T. J. T., Jimenez, J. L., Allan, J. D., Alfarra, M. R., Zhang, Q. Q., Onasch, T. B., Drewnick, F., Coe, H., Middlebrook, A. M., Delia, A., Williams, L. R., Trimborn, A. M., Northway, M. J., DeCarlo, P. F., Kolb, C. E., Davidovits, P. and Worsnop, D. R.: Chemical and microphysical characterization of ambient aerosols with the

Aerodyne Aerosol Mass Spectrometer, Mass Spectrom. Rev., 26(2), 185–222, doi:10.1002/mas, 2007.

Dall´Osto, M., Simo, R., Harrison, R. M., Beddows, D. C. S., Saiz-Lopez, A., Lange, R., Skov, H., Nøjgaard, J. K., Nielsen, I. E. and Massling, A.: Abiotic and biotic sources influencing spring new particle formation in North East Greenland, Atmos. Environ., 190(July), 126–134, doi:10.1016/j.atmosenv.2018.07.019, 2018.

DeCarlo, P. F., Kimmel, J. R., Trimborn, A., Northway, M. J., Jayne, J. T., Aiken, A. C., Gonin, M., Fuhrer, K., Horvath, T., Docherty, K. S., Worsnop, D. R. and Jimenez, J. L.: Field-Deployable, High-Resolution, Time-of-Flight Aerosol Mass Spectrometer, Anal. Chem., 78(24), 8281–8289, doi:10.1021/ac061249n, 2006.

Centre on Emission Inventories and Projections (2013), EMEP emissions, Austrian Environment Agency. [Available at http://www.ceip.at/.]

Charlson, R. J., Lovelock, J. E., Andreae, M. O. and Warren, S. G.: Oceanic phytoplankton, atmospheric sulphur, cloud albedo and climate, Nature, 326, 655 [online] Available from: http://dx.doi.org/10.1038/326655a0, 1987.

Charlson, R. J., Schwartz, S. E., Hales, J. M., Cess, R. D., Coakley, J. A., Hansen, J. E., and Hofmann, D. J.: Climate forcing by anthropogenic aerosols, Science, 255, 423–430, 1992.

Chatfield, R. B. and Crutzen, P. J.: Are There Interactions of Iodine and Sulfur Species in Marine Air Photochemistry, J. Geophys. Res., 95(D13), 22319–22341, doi:10.1029/JD095iD13p22319, 1990.

Chen, H., Ezell, M. J., Arquero, K. D., Varner, M. E., Dawson, M. L., Gerber, R. B. and Finlayson-Pitts, B. J.: New particle formation and growth from methanesulfonic acid, trimethylamine

and water, Phys. Chem. Chem. Phys. Phys. Chem. Chem. Phys, 17(17), 13699–13709, doi:10.1039/c5cp00838g, 2015.

Chen, H. and Finlayson-Pitts, B. J.: New Particle Formation from Methanesulfonic Acid and Amines/ Ammonia as a Function of Temperature, Environmental Science & Technology 2017 51 (1), 243-252, doi: 10.1021/acs.est.6b04173, 2017.

Chen, H., Hodshire, A. L., Ortega, J., Greenberg, J., Mcmurry, P. H., Carlton, A. G., Pierce, J. R., Hanson, D. R. and Smith, J. N.: Vertically resolved concentration and liquid water content of atmospheric nanoparticles at the US DOE Southern Great Plains site, Atmos. Chem. Phys, 185194, 311–326, doi:10.5194/acp-18-311-2018, 2018.

Chin, M., Jacob, D. J., Gardner, G. M., Foreman-fowler, M. S., Spiro, P. A. and Savoie, D. L.: A global three-dimensional model of tropospheric sulfate acid, , 101, doi:10.1029/ 96JD01221, 1996.

Clarke, A. D. and Kapustin, V. N.: A Pacific Aerosol Survey. Part I: A Decade of Data on Particle Production, Transport, Evolution, and Mixing in the Troposphere, J. Atmos. Sci., 59(3), 363–382, doi:10.1175/1520-0469(2002)059<0363:APASPI>2.0.CO;2, 2002.

Clegg, S. L., Brimblecombe, P., and Wexler, A. S.: Extended AIM Aerosol Thermodynamics model, available at: http://www.aim. env.uea.ac.uk/aim/aim.php, last access: March 2018.

Clegg, S. L., Pitzer, K. S., and Brimblecombe, P.: Thermodynamics of Multicomponent, Miscible, Ionic Solutions. 2. Mixtures Including Unsymmetrical Electrolytes, J. Phys. Chem., 96, 9470– 9479, doi:10.1021/j100202a074, 1992.

Clegg, S. L. and Seinfeld, J. H.: Thermodynamic models of aqueous solutions containing inorganic electrolytes and dicarboxylic acids at 298.15 K. 1. The acids as non-dissociating components, J. Phys. Chem. A, 110, 5692–5717, 2006a.

Clegg, S. L. and Seinfeld, J. H.: Thermodynamic models of aqueous solutions containing inorganic electrolytes and dicarboxylic acids at 298.15 K. 2. Systems including dissociation equilibria, J. Phys. Chem. A, 110, 5718–5734, 2006b.

Croft, B., Wentworth, G. R., Martin, R. V, Leaitch, W. R., Murphy, J. G., Murphy, B. N., Kodros, J. K., Abbatt, J. P. D. and Pierce, J. R.: Contribution of Arctic seabird-colony ammonia to atmospheric particles and cloud-albedo radiative effect, Nat. Commun., 7, 13444 [online] Available from: http://dx.doi.org/10.1038/ncomms13444, 2016.

D'Andrea, S. D., Häkkinen, S. A. K.,Westervelt, D. M., Kuang, C., Levin, E. J. T., Kanawade, V. P., Leaitch,W. R., Spracklen, D. V., Riipinen, I., and Pierce, J. R.: Understanding global secondary organic aerosol amount and size-resolved condensational behavior, Atmos. Chem. Phys., 13, 11519–11534, doi:10.5194/acp-13- 11519-2013, 2013.

D'Andrea, S. D., Acosta Navarro, J. C., Farina, S. C., Scott, C. E., Rap, A., Farmer, D. K., Spracklen, D. V., Riipinen, I., and Pierce, J. R.: Aerosol size distribution and radiative forcing response to anthropogenically driven historical changes in biogenic secondary organic aerosol formation, Atmos. Chem. Phys., 15, 2247–2268, doi:10.5194/acp-15-2247-2015, 2015.

de Leeuw, G., Andreas, E. L., Anguelova, M. D., Fairall, C. W., Lewis, E. R., O'Dowd, C., Schulz, M. and Schwartz, S. E.: Production flux of sea spray aerosol, Rev. Geophys., 49(2), n/a-n/a, doi:10.1029/2010RG000349, 2011.

Donahue, N. M., Robinson, A. L., Stanier, C. O. and Pandis, S. N.: Coupled Partitioning, Dilution, and Chemical Aging of Semivolatile Organics, Environ. Sci. Technol., 40(8), 2635–2643, doi:10.1021/es052297c, 2006.

Donahue, N. M., Trump, E. R., Pierce, J. R. and Riipinen, I.: Theoretical constraints on pure vapor-pressure driven condensation of organics to ultrafine particles, Geophys. Res. Lett., 38(16), n/a-n/a, doi:10.1029/2011GL048115, 2011.

Dunlea, E. J., DeCarlo, P. F., Aiken, A. C., Kimmel, J. R., Peltier, R. E., Weber, R. J., Tomlinson, J., Collins, D. R., Shinozuka, Y., McNaughton, C. S., Howell, S. G., Clarke, A. D., Emmons, L. K., Apel, E. C., Pfister, G. G., van Donkelaar, A., Martin, R. V., Millet, D. B., Heald, C. L., and Jimenez, J. L.: Evolution of Asian aerosols during transpacific transport in INTEX-B, Atmos. Chem. Phys., 9, 7257-7287, https://doi.org/10.5194/acp-9-7257-2009, 2009.

Eisele, F. L., and D. J. Tanner: Measurement of the gas phase concentration of H2SO4 and methane sulfonic acid and estimates of H2SO4 production and loss in the atmosphere, *J. Geophys. Res.*, 98(D5), 9001–9010, doi:10.1029/93JD00031, 1993.

Elliott, S.: Dependence of DMS global sea-air flux distribution on transfer velocity and concentration field type, J. Geophys. Res.- Biogeo., 114, 1–18, https://doi.org/10.1029/2008JG000710, 2009.

Erlick, C., Russell, L. M. and Ramaswamy, V.: A microphysics-based investigation of the radiative effects of aerosol-cloud interactions for two MAST Experiment case studies, J. Geophys. Res., 106(D1), 1249–1269, doi:10.1029/2000JD900567, 2001.

Facchini, M. C., Rinaldi, M., Decesari, S., Carbone, C., Finessi, E., Mircea, M., Fuzzi, S., Ceburnis, D., Flanagan, R., Nilsson, E. D., de Leeuw, G., Martino, M., Woeltjen, J., and O'Dowd, C. D.: Primary submicron marine aerosol dominated by insoluble organic colloids and aggregates, Geophys. Res. Lett., 35, L17814, https://doi.org/10.1029/2008GL034210, 2008.

Frossard, A. A., Russell, L. M., Burrows, S. M., Elliott, S. M., Bates, T. S. and Quinn, P. K.: Journal of Geophysical Research : Atmospheres mass in marine aerosol particles, , (Table 2), doi:10.1002/2014JD021913.Received, 2014.

Gordon, H., Kirkby, J., Baltensperger, U., Bianchi, F., Breitenlechner, M., Curtius, J., Dias, A., Dommen, J., Donahue, N. M., Dunne, E. M., Duplissy, J., Ehrhart, S., Flagan, R. C., Frege, C., Fuchs, C., Hansel, A., Hoyle, C. R., Kulmala, M., Kürten, A., Lehtipalo, K., Makhmutov, V., Molteni, U., Rissanen, M. P., Stozkhov, Y., Tröstl, J., Tsagkogeorgas, G., Wagner, R., Williamson, C., Wimmer, D., Winkler, P. M., Yan, C. and Carslaw, K. S.: Causes and importance of new particle formation in the present-day and preindustrial atmospheres, J. Geophys. Res. Atmos., 122(16), 8739–8760, doi:10.1002/2017JD026844, 2017.

Haynes, W.: CRC Handbook of Chemistry and Physics, 98th Edition., CRC Press, Boca Raton, 2017.

Seinfeld, J. H. and Pandis, S. N.: Atmospheric Chemistry and Physics, 2nd ed., John Wiley and Sons, New York, 2006.

Heald, C. L., Ridley, D. A., Kroll, J. H., Barrett, S. R. H., Cady- Pereira, K. E., Alvarado, M. J., and Holmes, C. D.: Contrasting the direct radiative effect and direct radiative forcing of aerosols, Atmos. Chem. Phys., 14, 5513–5527, doi:10.5194/acp-14-5513- 2014, 2014.

Heintzenberg, J., Covert, D. C. and Van Dingenen, R.: Size distribution and chemical composition of marine aerosols: a compilation and review, Tellus, 52, 1104–1122, doi:10.1034/j.1600-0889.2000.00136.x, 2000.

Hodshire, A. L., Lawler, M. J., Zhao, J., Ortega, J., Jen, C., Yli-Juuti, T., Brewer, J. F., Kodros, J. K., Barsanti, K. C., Hanson, D. R., McMurry, P. H., Smith, J. N. and Pierce, J. R.: Analysis

of multiple new-particle growth pathways observed at the US DOE Southern Great Plains field site, Atmos. Chem. Phys. Discuss., (March), 1–49, doi:10.5194/acp-2016-157, 2016.

Hoffmann, E. H., Tilgner, A., Schrödner, R., Bräuer, P., Wolke, R. and Herrmann, H.: An advanced modeling study on the impacts and atmospheric implications of multiphase dimethyl sulfide chemistry, Proc. Natl. Acad. Sci., 113(42), 11776–11781, doi:10.1073/pnas.1606320113, 2016.

Huang, L., Jiang, J. H., Tackett, J. L., Su, H. and Fu, R. .: Seasonal and diurnal variations of aerosol extinction profile and type distribution from CALIPSO 5-year observations, J. Geophys. Res. Atmos., 118(10), 4572–4596, doi:10.1002/jgrd.50407, 2013.

Iacono, M. J., Delamere, J. S., Mlawer, E. J., Shephard, M. W., Clough, S. A., and Collins, W. D.: Radiative forcing by long-lived greenhouse gases: Calculations with the AER radiative transfer models, J. Geophys. Res., 113, D13103, doi:10.1029/2008JD009944, 2008.

Jaeglé, L., Quinn, P. K., Bates, T. S., Alexander, B., and Lin, J.-T.: Global distribution of sea salt aerosols: new constraints from in situ and remote sensing observations, Atmos. Chem. Phys., 11, 3137–3157, doi:10.5194/acp-11-3137-2011, 2011.

Janssens-Maenhout, A., Petrescu, A., Muntean, M., and Blujdea,V.: Verifying Greenhouse Gas Emissions: Methods to Support International Climate Agreements, The National Academies Press, Washington, DC, available at: http://www.nap.edu/openbook. php?record_id=12883 (last access: 17 March 2014), 2010.

Jung, J., Fountoukis, C., Adams, P. J., and Pandis, S. N.: Simulation of in situ ultrafine particle formation in the eastern United States using PMCAMx-UF, J. Geophys. Res., 115, D03203, doi:10.1029/2009JD012313, 2010.

Kerminen, V. M., Anttila, T., Lehtinen, K. E. J., and Kulmala, M.: Parameterization for atmospheric new-particle formation: Application to a system involving sulfuric acid and condensable water soluble organic vapors, Aerosol Sci. Technol., 38, 1001–1008, 2004.

Kettle, A. J., Amouroux, D., Andreae, T. W., Bates, T. S., Berresheim, H., Bingemer, H., Boniforti, R., Helas, G., Leck, C., Maspero, M., Matrai, P., McTaggart, A. R., Mihalopoulos, N., Nguyen, B. C., Novo, A., Putaud, J. P., Rapsomanikis, S., Roberts, G., Schebeske, G., Sharma, S., Simó, R., Staubes, R., Turner, S. and Uher, G.: A global database of sea surface dimethyl sulfide (DMS) measurements and a simple model to predict sea surface DMS as a function of latitude, longitude, and month, Glob. Biogeochem. Cycles, 13(2), 399–444, 1999.

Kettle, A. J., and Andreae, M. O.: Flux of dimethylsulfide from the oceans: A comparison of updated data sets and flux models, *J. Geophys. Res.*, 105(D22), 26793–26808, doi:10.1029/2000JD900252, 2000.

Kimmel, J. R., Farmer, D. K., Cubison, M. J., Sueper, D., Tanner, C., Nemitz, E., Worsnop, D. R., Gonin, M. and Jimenez, J. L.: Real-time aerosol mass spectrometry with millisecond resolution, Int. J. Mass Spectrom., 303(1), 15–26, doi:10.1016/j.ijms.2010.12.004, 2011.

Kodros, J. K., Cucinotta, R., Ridley, D. A., Wiedinmyer, C. and Pierce, J. R.: The aerosol radiative effects of uncontrolled combustion of domestic waste, Atmos. Chem. Phys, 16, 6771–6784, doi:10.5194/acp-16-6771-2016, 2016.

Kodros, J. K. and Pierce, J. R.: Important global and regional differences in aerosol cloud-albedo effect estimates between simulations with and without prognostic aerosol microphysics, J. Geophys. Res. Atmos., 122(7), 4003–4018, doi:10.1002/2016JD025886, 2017.

Kodros, J. K., Hanna, S., Bertram, A., Leaitch, W. R., Schulz, H., Herber, A., Zanatta, M., Burkart, J., Willis, M., Abbatt, J. P. D., and Pierce, J. R.: Size-resolved mixing state of black carbon in the Canadian high Arctic and implications for simulated direct radiative effect, Atmos. Chem. Phys., https://doi.org/10.5194/acp-18-11345-2018, 2018.

Koepke, P., Hess, M., Schult, I., and Shettle, E.: Global aerosol data set, MPI Meteorol. Hamburg Rep. 243, 44 pp., Max-Planck-Institut für Meteorologie, Hamburg, Germany, 1997.

Korhonen, H., Carslaw, K. S., Spracklen, D. V, Mann, G. W. and Woodhouse, M. T.: Influence of oceanic dimethyl sulfide emissions on cloud condensation nuclei concentrations and seasonality over the remote Southern Hemisphere oceans: A global model study, J. Geophys. Res. Atmos., 113(D15), n/a-n/a, doi:10.1029/2007JD009718, 2008.

Kulmala, M., Pirjola, L. and Makela, J. M.: Stable sulphate clusters as a source of new atmospheric particles, Nature, 404(6773), 66–69, doi:10.1038/35003550, 2000.

Kwong, K. C., Chim, M. M., Hoffmann, E. H., Tilgner, A., Herrmann, H., Davies, J., Wilson, K. R. and Chan, M.: Chemical Transformation of Methanesulfonic Acid and Sodium Methanesulfonate through Heterogeneous OH Oxidation, ACS Earth Sp. Chem., doi:10.1021/acsearthspacechem.8b00072, 2018.

Lana, A., Bell, T. G., Simó, R., Vallina, S. M., Ballabrera-Poy, J., Kettle, A. J., Dachs, J., Bopp, L., Saltzman, E. S., Stefels, J., Johnson, J. E. and Liss, P. S.: An updated climatology of surface dimethlysulfide concentrations and emission fluxes in the global ocean, Global Biogeochem. Cycles, 25(1), 1–17, doi:10.1029/2010GB003850, 2011.

Lee, Y. H. and Adams, P. J.: A Fast and Efficient Version of the TwO-Moment Aerosol Sectional (TOMAS) Global Aerosol Microphysics Model, Aerosol Sci. Technol., 46(6), 678–689, doi:10.1080/02786826.2011.643259, 2012.

Lee, Y.H., Pierce, J.R., Adams, P.J.: Representation of nucleation mode microphysics in global aerosol microphysics models, Geosci. Model Dev., 6, 1221-1232, doi:10.5194/gmd-6-1221-2013, 2013.

Legrand, M., Preunkert, S., Weller, R., Zipf, L., Elsässer, C., Merchel, S., Rugel, G., and Wagenbach, D.: Year-round record of bulk and size-segregated aerosol composition in central Antarctica (Concordia site) – Part 2: Biogenic sulfur (sulfate and methanesulfonate) aerosol, Atmos. Chem. Phys., 17, 14055-14073, https://doi.org/10.5194/acp-17-14055-2017, 2017.

Li, M., Zhang, Q., Kurokawa, J.-I., Woo, J.-H., He, K., Lu, Z., Ohara, T., Song, Y., Streets, D. G., Carmichael, G. R., Cheng, Y., Hong, C., Huo, H., Jiang, X., Kang, S., Liu, F., Su, H., and Zheng, B.: MIX: a mosaic Asian anthropogenic emission inventory under the international collaboration framework of the MICS-Asia and HTAP, Atmos. Chem. Phys., 17, 935-963, https://doi.org/10.5194/acp-17-935-2017, 2017.

Ma, X. and Yu, F.: Seasonal and spatial variations of global aerosol optical depth: multi-year modelling with GEOS-Chem-APM and comparisons with multiple platform observations, Tellus B: Chem. Phys. Met., 67:1, 25115, DOI: 10.3402/tellusb.v67.2511, 2015.

Maudlin, R. L. III, Cantrell, C. A., Zondlo, M., Kosciuch, E., Eisele, F. L., Chen, G., Davis, D., Weber, R., Crawford, J., Blake, D., Bandy, A., and Thornton, D. : Highlights of OH, H2SO4, and methane sulfonic acid measurements made aboard the NASA P-3B during Transport and Chemical Evolution over the Pacific, J. Geophys. Res. Atmos., 108(D20), doi:10.1029/2003JD003410, 2003.

Marti, J. J., Jefferson, A., Cai, X. P., Richert, C., McMurry, P. H.,

and Eisele, F.: H2SO4 vapor pressure of sulfuric acid and ammonium sulfate solutions, J. Geophys. Res.-Atmos., 102, 3725– 3735, doi:10.1029/96JD03064, 1997.

McGrath, M. J., Olenius, T., Ortega, I. K., Loukonen, V., Paasonen, P., Kurtén, T., Kulmala, M., and Vehkamäki, H.: Atmospheric Cluster Dynamics Code: a flexible method for solution of the birth-death equations, Atmos. Chem. Phys., 12, 2345–2355, doi:10.5194/acp-12-2345-2012, 2012.

Mungall, E. L., Wong, J. P. S. and Abbatt, J. P. D.: Heterogeneous Oxidation of Particulate Methanesulfonic Acid by the Hydroxyl Radical: Kinetics and Atmospheric Implications, ACS Earth Sp. Chem., 2, 1, 48-55, doi:10.1021/acsearthspacechem.7b00114, 2017.

Murphy, B. N., Donahue, N. M., Robinson, A. L. and Pandis, S. N.: A naming convention for atmospheric organic aerosol, Atmos. Chem. Phys., 14(11), 5825–5839, doi:10.5194/acp-14-5825-2014, 2014.

Napari, I., Noppel, M., Vehkamäki, H., and Kulmala, M.:

Parametrization of ternary nucleation rates for H2SO4-NH3-H2O vapors, J. Geophys. Res.-Atmos., 107,AAC 6–1–AAC 6–6, doi:10.1029/2002JD002132, 2002.l

Nault, B. A., Campuzano-Jost, P., Day, D. A., Schroder, J. C., Anderson, B., Beyersdorf, A. J., Blake, D. R., Brune, W. H., Choi, Y., Corr, C. A., de Gouw, J. A., Dibb, J., DiGangi, J. P., Diskin, G. S., Fried, A., Huey, L. G., Kim, M. J., Knote, C. J., Lamb, K. D., Lee, T., Park, T., Pusede, S. E., Scheuer, E., Thornhill, K. L., Woo, J.-H., and Jimenez, J. L.: Secondary Organic Aerosol Production from Local Emissions Dominates the Organic Aerosol Budget over Seoul, South Korea, during KORUS-AQ, Atmos. Chem. Phys. Discuss., https://doi.org/10.5194/acp-2018-838, in review, 2018.

O'Dowd, C. D., Facchini, M. C., Cavalli, F., Ceburnis, D., Mircea, M., Decesari, S., Fuzzi, S., Yoon, Y. J. and Putaud, J.-P.: Biogenically driven organic contribution to marine aerosol, Nature, 431(7009), 676–680, doi:10.1038/nature02959, 2004.

O'Dowd, C. D. and de Leeuw, G.: Marine aerosol production: a review of the current knowledge., Philos. Trans. A. Math. Phys. Eng. Sci., 365(1856), 1753–74, doi:10.1098/rsta.2007.2043, 2007.

Olenius, T., Kupiainen-Määttä, O., Ortega, I., Kurtén, T., and Vehkamäki, H.: Free energy barrier in the growth of sulfuric acid–ammonia and sulfuric acid–dimethylamine clusters, J. Chem. Phys., 139, 084312, doi10.1063/1.4819024, 2013.

Paatero, P. and Tapper, U.: Positive Matrix Factorization - A Nonnegative Factor Model With Optimal Utilization of Error-Estimates of Data Values, Environmetrics, 5(2), 111–126, 1994.

Pandis, S. N., Baltensperger, U., Wolfenbarger, J. K. and Seinfeld, J. H.: Inversion of aerosol data from the epiphaniometer, J. Aerosol Sci., 22(4), 417–428, doi:https://doi.org/10.1016/0021-8502(91)90002-Y, 1991.

Petters, M. D. and Kreidenweis, S. M.: A single parameter representation of hygroscopic growth and cloud condensation nucleus activity, Atmos. Chem. Phys., 7, 1961–1971, doi:10.5194/acp-7- 1961-2007, 2007.

Pierce, J. R. and Adams, P. J.: Uncertainty in global CCN concentrations from uncertain aerosol nucleation and primary emission rates, Atmos. Chem. Phys., 9, 1339–1356, doi:10.5194/acp-9- 1339-2009, 2009a.

Pierce, J.R., Adams, P.J., A computationally efficient aerosol nucleation/condensation method: Pseudo-steady-state sulfuric acid, Aerosol Science and Technology, 43, 216-226, 2009b.

Pierce, J. R., Riipinen, I., Kulmala, M., Ehn, M., Petäjä, T., Junninen, H., Worsnop, D. R. and Donahue, N. M.: Quantification of the volatility of secondary organic compounds in ultrafine particles during nucleation events, Atmos. Chem. Phys., 11(17), 9019–9036, doi:10.5194/acp-11-9019-2011, 2011.

Pierce, J. R., Evans, M. J., Scott, C. E., D'Andrea, S. D., Farmer, D. K., Swietlicki, E., and Spracklen, D. V.: Weak global sensitivity of cloud condensation nuclei and the aerosol indirect effect to Criegee + SO2 chemistry, Atmos. Chem. Phys., 13, 3163-3176, https://doi.org/10.5194/acp-13-3163-2013, 2013.

Phinney, L., Richard Leaitch, W., Lohmann, U., Boudries, H., Worsnop, D. R., Jayne, J. T., Toom-Sauntry, D., Wadleigh, M., Sharma, S., Shantz, N., Leaitch, W. R., Lohmann, U., Boudries, H., Worsnop, D. R., Jayne, J. T., Toom-Sauntry, D., Wadleigh, M., Sharma, S., Shantz, N., Richard Leaitch, W., Lohmann, U., Boudries, H., Worsnop, D. R., Jayne, J. T., Toom-Sauntry, D., Wadleigh, M., Sharma, S., Shantz, N., Leaitch, W. R., Lohmann, U., Boudries, H., Worsnop, D. R., Jayne, J. T., Toom-Sauntry, D., Wadleigh, M., Sharma, S. and Shantz, N.: Characterization of the aerosol over the sub-arctic north east Pacific Ocean, Deep. Res. II-Topical Stud. Oceanogr., 53(20–22), 2410–2433, doi:10.1016/j.dsr2.2006.05.044|ISSN 0967-0645, 2006.

Preunkert, S., Jourdain, B., Legrand, M., Udisti, R., Becagli, S., and Cerri, O.: Seasonality of sulfur species (dimethyl sulfide, sulfate, and methanesulfonate) in Antarctica: Inland versus coastal regions, J. Geophys. Res., 113, D15302, https://doi.org/10.1029/2008JD009937, 2008.

Quinn, P. K., Collins, D. B., Grassian, V. H., Prather, K. A. and Bates, T. S.: Chemistry and Related Properties of Freshly Emitted Sea Spray Aerosol, Chem. Rev., 115(10), 4383–4399, doi:10.1021/cr500713g, 2015.

Rap, A., Scott, C. E., Spracklen, D. V., Bellouin, N., Forster, P. M., Carslaw, K. S., Schmidt, A., and Mann, G.: Natural aerosol direct and indirect radiative effects, Geophys. Res. Lett., 40, 3297– 3301, doi:10.1002/grl.50441, 2013.

Reddington, C. L., Carslaw, K. S., Stier, P., Schutgens, N., Coe, H., Liu, D., Allan, J., Browse, J., Pringle, K. J., Lee, L. A., Yoshioka, M., Johnson, J. S., Regayre, L. A., Spracklen, D. V., Mann, G. W., Clarke, A., Hermann, M., Henning, S., Wex, H., Kristensen, T. B., Leaitch, W. R., Pöschl, U., Rose, D., Andreae, M. O., Schmale, J., Kondo, Y., Oshima, N., Schwarz, J. P., Nenes, A., Anderson, B., Roberts, G. C., Snider, J. R., Leck, C., Quinn, P. K., Chi, X., Ding, A., Jimenez, J. L. and Zhang, Q.: The global aerosol synthesis and science project (GASSP): Measurements and modeling to reduce uncertainty, Bull. Am. Meteorol. Soc., 98(9), 1857–1877, doi:10.1175/BAMS-D-15-00317.1, 2017.

Regayre, L. A., Johnson, J. S., Yoshioka, M., Pringle, K. J., Sexton, D. M. H., Booth, B. B. B., Lee, L. A., Bellouin, N., and Carslaw, K. S.: Aerosol and physical atmosphere model parameters are both important sources of uncertainty in aerosol ERF, Atmos. Chem. Phys., 18, 9975-10006, https://doi.org/10.5194/acp-18-9975-2018, 2018.

Riipinen, I., Pierce, J. R., Yli-Juuti, T., Nieminen, T., Häkkinen, S., Ehn, M., Junninen, H., Lehtipalo, K., Petäjä, T., Slowik, J., Chang, R., Shantz, N. C., Abbatt, J., Leaitch, W. R., Kerminen, V.-M., Worsnop, D. R., Pandis, S. N., Donahue, N. M. and Kulmala, M.: Organic condensation: a vital link connecting aerosol formation to cloud condensation

nuclei (CCN) concentrations, Atmos. Chem. Phys., 11(8), 3865–3878, doi:10.5194/acp-11-3865-2011, 2011.

Royer, S. J., Mahajan, A. S., Galí, M., Saltzman, E., and Simõ, R.: Small-scale variability patterns of DMS and phytoplankton in surface waters of the tropical and subtropical Atlantic, Indian, and Pacific Oceans, Geophys. Res. Lett., 42, 475–483, https://doi.org/10.1002/2014GL062543, 2015.

Schroder, J. C., Campuzano-Jost, P., Day, D. A., Shah, V., Larson, K., Sommers, J. M., Sullivan, A. P. Campos, T. Reeves, J. M. Hills, A., Hornbrook, R. S., Blake, N. J., Scheuer, E., Guo, H., Fibiger, D. L. McDuffie, E. E., Hayes, P. L., Weber, R. J., Dibb, J. E. Apel, E. C., Jaeglé, L. Brown, S. S. Thornton, J. A. and Jimenez, J. L. Sources and secondary production of organic aerosols in the northeastern United States during WINTER. Journal of Geophysical Research: Atmospheres, 123, 7771–7796. doi: 10.1029/2018JD028475, 2018.

Scott, C. E., Rap, A., Spracklen, D. V., Forster, P. M., Carslaw, K. S., Mann, G. W., Pringle, K. J., Kivekäs, N., Kulmala, M., Lihavainen, H., and Tunved, P.: The direct and indirect radiative effects of biogenic secondary organic aerosol, Atmos. Chem. Phys., 14, 447–470, doi:10.5194/acp-14-447-2014, 2014.

Seinfeld, J. H. and Pandis, S. N.: Atmospheric Chemistry and Physics, 2nd ed., John Wiley and Sons, New York, 2006.

Sheng, J. X., Weisenstein, D. K., Luo, B. P., Rozanov, E., Stenke, A., Anet, J., Bingemer, H., and Peter, T.: Global atmospheric sulfur budget under volcanically quiescent conditions: Aerosol-chemistry-climate model predictions and validation, J. Geophys. Res.-Atmos., 120, 256–276, https://doi.org/10.1002/2014JD021985, 2015.

Sørensen, S., Falbe-Hansen, H., Mangoni, M., Hjorth, J., and. Jensen, N. R: Observation of DMSO and CH3S(O)OH from the gas phase reaction between DMS and OH, J. Atmos. Chem., 24(3), 299–315, doi:10.1007/BF00210288, 1996.

Spracklen, D. V., Carslaw, K. S., Pöschl, U., Rap, A., and Forster, P. M.: Global cloud condensation nuclei influenced by carbonaceous combustion aerosol, Atmos. Chem. Phys., 11, 9067–9087, doi:10.5194/acp-11-9067-2011, 2011.

Streets, D. G., Bond., T. C., Carmichael., G. R., Fernandes, S. D., Fu, Q., He, D., Klimont, Z., Nelson, S. M., Tsai, N. Y., Wang, M. Q., Woo, J.-H., Yarber, K. F.: An inventory of gaseous and primary aerosol emissions in Asia in the year 2000, J. Geophys. Res., 108(D21), 8809, doi:10.1029/2002JD003093, 2003.

Tesdal, J. E., Christian, J. R., Monahan, A. H., and Von Salzen, K.: Evaluation of diverse approaches for estimating sea-surface DMS concentration and air-sea exchange at global scale, Environ. Chem., 13, 390–412, https://doi.org/10.1071/EN14255, 2016.

Textor, C., Schulz, M., Guibert, S., Kinne, S., Balkanski, Y., Bauer, S., Berntsen, T., Berglen, T., Boucher, O., Chin, M., Dentener, F., Diehl, T., Easter, R., Feichter, H., Fillmore, D., Ghan, S., Ginoux, P., Gong, S., Grini, A., Hendricks, J., Horowitz, L., Huang, P., Isaksen, I., Iversen, I., Kloster, S., Koch, D., Kirkevåg, A., Kristjansson, J. E., Krol, M., Lauer, A., Lamarque, J. F., Liu, X., Montanaro, V., Myhre, G., Penner, J., Pitari, G., Reddy, S., Seland, Ø., Stier, P., Takemura, T., and Tie, X.: Analysis and quantification of the diversities of aerosol life cycles within AeroCom, Atmos. Chem. Phys., 6, 1777-1813, https://doi.org/10.5194/acp-6-1777-2006, 2006.

Twomey, S.: Pollution and the planetary albedo, Atmos. Environ., 8, 1251–1256, 1974.

Ulbrich, I. M., Canagaratna, M. R., Zhang, Q., Worsnop, D. R. and Jimenez, J. L.: Interpretation of organic components from Positive Matrix Factorization of aerosol mass spectrometric data, Atmos. Chem. Phys., 9(9), 2891–2918, doi:10.5194/acp-9-2891-2009, 2009.

Vehkamäki, H.: An improved parameterization for sulfuric acid– water nucleation rates for tropospheric and stratospheric conditions, J. Geophys. Res., 107, 4622, doi:10.1029/2002JD002184, 2002.

Wang, X., Deane, G. B., Moore, K. A., Ryder, O. S., Stokes, M. D., Beall, C. M., Collins, D. B., Santander, M. V, Burrows, S. M., Sultana, C. M. and Prather, K. A.: The role of jet and film drops in controlling the mixing state of submicron sea spray aerosol particles, Proc. Natl. Acad. Sci., 114(27), 6978 LP-6983 [online] Available from: http://www.pnas.org/content/114/27/6978.abstract, 2017.

Westervelt, D. M., Pierce, J. R., Riipinen, I., Trivitayanurak, W., Hamed, A., Kulmala, M., Laaksonen, A., Decesari, S., and Adams, P. J.: Formation and growth of nucleated particles into cloud condensation nuclei: model-measurement comparison, Atmos. Chem. Phys., 13, 7645–7663, doi:10.5194/acp-13-7645- 2013, 2013.

Wexler, A. S. and Clegg, S. L.: Atmospheric aerosol models for

systems including the ions H+, NH4+, Na+, SO42−, NO3−, Cl−, Br−, and H2O, J. Geophys. Res.-Atmos., 107, ACH-14-1– ACH-14-14, doi:10.1029/2001JD000451, 2002.

Wiedinmyer, C., Akagi, S. K., Yokelson, R. J., Emmons, L. K., Al-Saadi, J. A., Orlando, J. J., and Soja, A. J.: The Fire INventory from NCAR (FINN): a high resolution global model to estimate the emissions from open burning, Geosci. Model Dev., 4, 625-641, https://doi.org/10.5194/gmd-4-625-2011, 2011.

Wilson, C. and Hirst, D. M.: Kinetics of gas phase oxidation of reduced sulfur compounds, Prog. React. Kinet., 21(2–3), 69–132, 1996.

Woodhouse, M. T., Carslaw, K. S., Mann, G. W., Vallina, S. M., Vogt, M., Halloran, P. R., and Boucher, O.: Low sensitivity of cloud condensation nuclei to changes in the sea-air flux of dimethyl-sulphide, Atmos. Chem. Phys., 10, 7545–7559, https://doi.org/10.5194/acp-10-7545-2010, 2010.

Woodhouse, M. T., Mann, G. W., Carslaw, K. S., and Boucher, O.: Sensitivity of cloud condensation nuclei to regional changes in dimethyl-sulphide emissions, Atmos. Chem. Phys., 13, 2723-2733, https://doi.org/10.5194/acp-13-2723-2013, 2013.

Wofsy, S.C., S. Afshar, H.M. Allen, E. Apel, E.C. Asher, B. Barletta, J. Bent, H. Bian, B.C. Biggs, D.R. Blake, N. Blake, I. Bourgeois, C.A. Brock, W.H. Brune, J.W. Budney, T.P. Bui, A. Butler, P. Campuzano-Jost, C.S. Chang, M. Chin, R. Commane, G. Correa, J.D. Crounse, P. D. Cullis, B.C. Daube, D.A. Day, J.M. Dean-Day, J.E. Dibb, J.P. DiGangi, G.S. Diskin, M. Dollner, J.W. Elkins, F. Erdesz, A.M. Fiore, C.M. Flynn, K. Froyd, D.W. Gesler, S.R. Hall, T.F. Hanisco, R.A. Hannun, A.J. Hills, E.J. Hintsa, A. Hoffman, R.S. Hornbrook, L.G. Huey, S. Hughes, J.L. Jimenez, B.J. Johnson, J.M. Katich, R. Keeling, M.J. Kim, A. Kupc, L.R. Lait, J.-F. Lamarque, J. Liu, K. McKain, R.J. Mclaughlin, S. Meinardi, D.O. Miller, S.A. Montzka, F.L. Moore, E.J. Morgan, D.M. Murphy, L.T. Murray, B.A. Nault, J.A. Neuman, P.A. Newman, J.M. Nicely, X. Pan, W. Paplawsky, J. Peischl, M.J. Prather, D.J. Price, E. Ray, J.M. Reeves, M. Richardson, A.W. Rollins, K.H. Rosenlof, T.B. Ryerson, E. Scheuer, G.P. Schill, J.C. Schroder, J.P. Schwarz, J.M. St.Clair, S.D. Steenrod, B.B. Stephens, S.A. Strode, C. Sweeney, D. Tanner, A.P. Teng, A.B. Thames, C.R. Thompson, K. Ullmann, P.R. Veres, N. Vieznor, N.L. Wagner, A. Watt, R. Weber, B.

Weinzierl, P. Wennberg, C.J. Williamson, J.C. Wilson, G.M. Wolfe, C.T. Woods, and L.H. Zeng. 2018. ATom: Merged Atmospheric Chemistry, Trace Gases, and Aerosols. ORNL DAAC, Oak Ridge, Tennessee, USA. https://doi.org/10.3334/ORNLDAAC/1581

Xausa, F., Paasonen, P., Makkonen, R., Arshinov, M., Ding, A., Denier Van Der Gon, H., Kerminen, V.-M., and Kulmala, M.: Advancing global aerosol simulations with size-segregated anthropogenic particle number emissions, Atmos. Chem. Phys., 18, 10039-10054, https://doi.org/10.5194/acp-18-10039-2018, 2018.

Yli-Juuti, T., Barsanti, K., Hildebrandt Ruiz, L., Kieloaho, A.-J., Makkonen, U., Petäjä, T., Ruuskanen, T., Kulmala, M. and Riipinen, I.: Model for acid-base chemistry in nanoparticle growth (MABNAG), Atmos. Chem. Phys., 13(24), 12507–12524, doi:10.5194/acp-13-12507-2013, 2013.

Yin, F., Grosjean, D., Flagan, R.C., and Seinfeld, J. H.: Photooxidation of dimethyl sulfide and dimethyl disulfide. II: Mechanism evaluation, J. Atmos. Chem., 11(4), 365–399, doi:10.1007/BF00053781, 1990.

Zender, C. S.: Mineral Dust Entrainment and Deposition (DEAD) model: Description and 1990s dust climatology, J. Geophys. Res., 108, 4416, doi:10.1029/2002JD002775, 2003.

Zhang, X., Pandis, S. N. and Seinfeld, J. H.: Diffusion-Limited Versus Quasi-Equilibrium Aerosol Growth, Aerosol Sci. Technol., 46(8), 874–885, doi:10.1080/02786826.2012.679344, 2012.

Zorn, S. R., Drewnick, F., Schott, M., Hoffmann, T. and Borrmann, S.: Characterization of the South Atlantic marine boundary layer aerosol using an aerodyne aerosol mass spectrometer, Atmos. Chem. Phys., 8(16), 4711–4728, doi:10.5194/acp-8-4711-2008, 2008

CHAPTER 4

AGING EFFECTS ON BIOMASS BURNING AEROSOL MASS AND COMPOSITION: A CRITICAL REVIEW OF FIELD AND LABORATORY STUDIES[3]

Overview

Biomass burning is a major source of atmospheric particulate matter (PM) with impacts on health, climate, and air quality. The particles and vapors within biomass burning plumes undergo chemical and physical aging as they are transported downwind. Field measurements of the evolution of PM with plume age range from net decreases to net increases, with most showing little to no change. In contrast, laboratory studies tend to show significant mass increases on average. On the other hand, similar effects of aging on the average PM composition (e.g. oxygen-to-carbon ratio) are reported for lab and field studies. Currently, there is no consensus on the mechanisms that lead to these observed similarities and differences. This review summarizes available observations of aging-related biomass burning aerosol mass concentrations and composition markers, and discusses four broad hypotheses to explain variability within and between field and laboratory campaigns: (1) variability in emissions and chemistry, (2) differences in dilution/entrainment, (3) losses in chambers and lines, and (4) differences in the timing of the initial measurement, the baseline from which changes are estimated. We conclude with a concise set of research needs for advancing our understanding of the aging of biomass burning aerosol.

[3] This chapter published as: Hodshire, A. L., Akherati, A., Alvarado, M. J., Brown-Steiner, B., Jathar, S. H., Jimenez, J. L., Kreidenweis, S. M., Lonsdale, C. R., Onasch, T. B., Ortega, A. M., & Pierce, J. R. (2019). Aging Effects on Biomass Burning Aerosol Mass and Composition: A Critical Review of Field and Laboratory Studies. *Environmental Science & Technology*, *53*(17), 10007–10022. https://doi.org/10.1021/acs.est.9b02588

4.1 Introduction

Fires have been part of Earth's landscape for over 400 million years (Scott and Glasspool, 2006), with an estimated annual average of 464 Mha (~3.5% of Earth's ice-free land surface) burning each year between 2001-2010 (Randerson et al., 2012). Emissions from biomass burning (BB) provide a major source of primary particles (aerosols) and aerosol precursor vapors to the atmosphere (Akagi et al., 2011; Baker et al., 2016; Gilman et al., 2015; Hatch et al., 2015, 2017, 2018; Jen et al., 2019; Koss et al., 2018; Reid et al., 2005; Yokelson et al., 2009, 2011). Emissions include primary carbonaceous aerosols (black carbon (BC) and primary organic aerosol, POA; (Akagi et al., 2011; Bytnerowicz et al., 2016; Dreessen et al., 2016; Reid et al., 2005; Yokelson et al., 2009, 2011)); inorganic aerosol species including potassium, chloride, sulfate, and other inorganic salts and trace minerals (Lewis et al., 2009; Reid et al., 2005; Yokelson et al., 2009); and inorganic and organic vapors (Akagi et al., 2011; Gilman et al., 2015; Hatch et al., 2015, 2017, 2018; Jen et al., 2019; Koss et al., 2018), all of which undergo chemical and physical aging as the plume is transported downwind (Akagi et al., 2012; Alvarado et al., 2015; Briggs et al., 2016; Brito et al., 2014; Cachier et al., 1995; Capes et al., 2008; Collier et al., 2016; Cubison et al., 2011; Formenti et al., 2003; Forrister et al., 2015; Garofalo et al., 2019; Hecobian et al., 2011; Hobbs et al., 2003; Jolleys et al., 2012, 2015; Landis et al., 2018; Lei et al., 2013; Lindaas et al., 2017; Liu et al., 2016b; Mallia et al., 2015; Martin et al., 2006; May et al., 2015; Nance et al., 1993; Reid et al., 1998; Sakamoto et al., 2015, 2016; Vakkari et al., 2014, 2018; Voulgarakis and Field, 2015; Yokelson et al., 2009; Zhou et al., 2017). In this review, we focus on BB emissions from the open-air combustion of fuels present in wildfires, prescribed fires (planned fires used for land

management), and agricultural burns, and do not include contained combustion of residential biomass fuels and commercial biofuels. We primarily discuss daytime aging, as few studies have thus far explicitly studied nighttime aging of BB emissions (Decker et al., 2019; Vakkari et al., 2014, 2018).

Aerosol derived from BB sources contribute to the total ambient particulate matter (PM) concentration(Akagi et al., 2011; Reid et al., 2005; Yokelson et al., 2009, 2011), with significant implications for climate (Bond et al., 2013; Ramnarine et al., 2019; Voulgarakis et al., 2015; Voulgarakis and Field, 2015), air quality (Brey et al., 2018; Jaffe and Wigder, 2012; Lassman et al., 2017; Nie et al., 2015; Xie et al., 2015), and human health (Ford et al., 2018; Janssen and Joint, 2012; Johnston et al., 2012; Naeher et al., 2007; Roberts et al., 2011; Samburova et al., 2016; Zhang et al., 2009). BB smoke aerosols impact the climate directly by absorbing and scattering incoming solar radiation (Charlson et al., 1992; Heald et al., 2014) and indirectly by acting as cloud condensation and ice nuclei , thereby altering cloud properties (Boucher et al., 2013; DeMott et al., 2009; Petters et al., 2009; Twomey, 2007). Both of these effects depend on the particle size, mass, and composition (Petters and Kreidenweis, 2007; Seinfeld and Pandis, 2016). As the climate warms, North American wildfires have increased in frequency, intensity, and area (Kasischke and Turetsky, 2006; Westerling, 2016) and are predicted to continue to do so (Liu et al., 2016a; Yue et al., 2013). Air quality regulations have successfully decreased $PM_{2.5}$ concentrations (that is, total mass of particles 2.5 μm in diameter and smaller) in the U.S. (EPA, 2018), but these reductions may be offset in the future by $PM_{2.5}$ from increasing BB sources (Ford et al., 2018; McClure and Jaffe, 2018; O'Dell et al., 2019).

As smoke ages, the mass, composition, and properties of BB vapors and aerosols evolve due to complex competing chemical and physical processes (Akagi et al., 2012; Alvarado et al.,

2015; Brito et al., 2014; Cachier et al., 1995; Capes et al., 2008; Collier et al., 2016; Cubison et al., 2011; Formenti et al., 2003; Forrister et al., 2015; Garofalo et al., 2019; Hecobian et al., 2011; Hobbs et al., 2003; Jolleys et al., 2012; Liu et al., 2016b; May et al., 2015; Morgan et al., 2019; Nance et al., 1993; Reid et al., 1998; Sakamoto et al., 2015, 2016; Vakkari et al., 2014, 2018; Yokelson et al., 2009; Zhou et al., 2017) . The vapors and particles are composed of many thousands of different chemical compounds that span a wide range in volatility (vapor pressures), reactivity, and other properties (Goldstein and Galbally, 2007; Shiraiwa et al., 2014). Volatility governs the partitioning of compounds between the gas- and particle-phase (Donahue et al., 2006; Odum et al., 1996; Pankow, 1994) and is often reported as the effective saturation concentration in μg m^{-3} (C*(Donahue et al., 2006)). Organic compounds are grouped into volatility categories (Murphy et al., 2014): volatile organic compounds (VOCs; C*$\geq\sim10^{7}$), intermediate-volatility organic compounds (IVOCs, C*$\sim10^{3}$-10^{6}), semivolatile organic compounds (SVOCs, C*$\sim10^{0}$-10^{2}), low-volatility organic compounds (LVOCs, C*$\sim10^{-3}$-10^{-1}), and extremely low-volatility organic compounds (ELVOCs, C*$\leq\sim10^{-4}$). With chemical aging within plumes, the volatility of compounds may decrease – primarily through functionalization or oligomerization reactions – or increase – primarily through fragmentation (Donahue et al., 2011; Jathar et al., 2015; Kroll et al., 2009; Zhang et al., 2014). Gas-phase compounds that decrease in volatility may partition to the particle phase through condensation, creating secondary organic aerosol (SOA) and adding to aerosol mass. Conversely, semivolatile condensed compounds may evaporate upon dilution of the smoke plume, decreasing aerosol mass. These evaporated compounds may act as SOA precursors that can undergo reactions and recondense with continued aging of the plume. Recent work suggests that the timescales for evaporation may vary based on the particle phase state, and

evaporation may also be modified by particle-phase and surface reactions (Shiraiwa and Seinfeld, 2012; Zaveri et al., 2014).

BB emissions have been extensively studied through field measurements and laboratory experiments to understand the aging of PM mass and composition in BB plumes, as well as to provide bottom-up estimates of BB PM. However, there is significant variability in the observed aging within and between field and laboratory studies. Field campaigns allow for BB plumes to be characterized in natural settings, but are often truncated/limited by uncontrollable and variable field conditions. A number of studies have focused on determining OA evolution by following plumes downwind to track changes in the gas- and particle-phase as a plume ages (Akagi et al., 2012; Capes et al., 2008; Cubison et al., 2011; DeCarlo et al., 2008; Forrister et al., 2015; Garofalo et al., 2019; Hecobian et al., 2011; Hobbs et al., 2003; Jolleys et al., 2012, 2015; Liu et al., 2016b; May et al., 2015; Morgan et al., 2019; Yokelson et al., 2011). Aircraft observations tend to be the dominant measurement platform for characterizing aging plumes, as aircraft can track plumes in a pseudo-Lagrangian manner. Some ground sites have also provided information on plumes that have aged between hours and days (Brito et al., 2014; Collier et al., 2016; Vakkari et al., 2014, 2018; Zhou et al., 2017). BB laboratory studies have been generally focused on characterizing emissions and simulating atmospheric chemical aging under controlled conditions (e.g. fixed fuel/dilution ratios, controlled oxidants).

Laboratory studies provide control over the environmental and chemical conditions, and can be used to examine the effect of changing one variable at a time, but face challenges in recreating the atmospheric conditions of plumes in the field.

Top-down estimates of BB PM also exist that compare models with bottom up inventories to satellite-based and in situ measurements, and a low-bias of the model could be indicative of BB

SOA (Konovalov et al., 2015, 2017; Reddington et al., 2016; Shrivastava et al., 2015). However, these discrepancies are dominated by uncertainties in the emissions inventories (Koplitz et al., 2018), which is beyond the scope of this paper.

To date there are significant knowledge gaps that limit a full understanding of how field and laboratory observations can be reconciled. A more-complete understanding of the underlying physics and chemistry could explain the observed variability in the evolution of BB mass and composition in field and laboratory experiments. The purpose of this critical review is to provide an overview of observed changes in PM mass and composition markers in field and laboratory studies (Section 4.2), present possible hypotheses for differences between observations (Section 4.3), and present research needs for creating a unified framework on BB aerosol aging (Section 4.4).

4.2 Overview of observations

4.2.1 Field studies

Figure 4.1A shows whether OA or PM mass was observed to increase or decrease with age in field campaigns. Specifically, ratios of final to initial values of normalized BB aerosol mass are expressed as the mass enhancement ratio (ER),

$$OA_{ER} = \frac{\Delta OA/\Delta CO\ (f)}{\Delta OA/\Delta CO\ (i)} \quad (4.1)$$

(where PM replaces OA in Eq. 4.1 for PM mass enhancements) for published field campaigns on BB aerosol aging. Δ indicates the difference between the in-plume and background value of OA and CO (i.e. the enhancement of these species concentrations due to BB), f indicates the final available measurement, and i indicates the first (initial) available measurement. Values greater

than 1 indicate a net increase in dilution-corrected OA or PM concentrations with aging and values less than 1 indicate a net decrease. CO is used in BB studies as an inert tracer for these short-term (hours to a few days) aging studies to correct for dilution effects, as it has an atmospheric lifetime on the order of 2 months (Seinfeld and Pandis, 2006) with negligible impacts from chemical production (Griffin et al., 2007).

Figure 4.1A only includes studies that have both fresh (within 1 hour of emission) and aged measurements, and is sequentially arranged by the final age from youngest (leftmost) to oldest (rightmost). All studies in Figure 4.1A provide ΔOA/ΔCO from Aerosol Mass Spectrometer (AMS) instruments except the SAFARI observations detailed in Hobbs et al. (2003) and the Vakkari et al. (2014, 2018) studies (see supporting information). AMS sensitivities (collection and relative ion efficiencies) have been shown in some studies to vary with organic oxidation levels (see supporting information), but these issues are unlikely to explain differences between lab and field measurements.

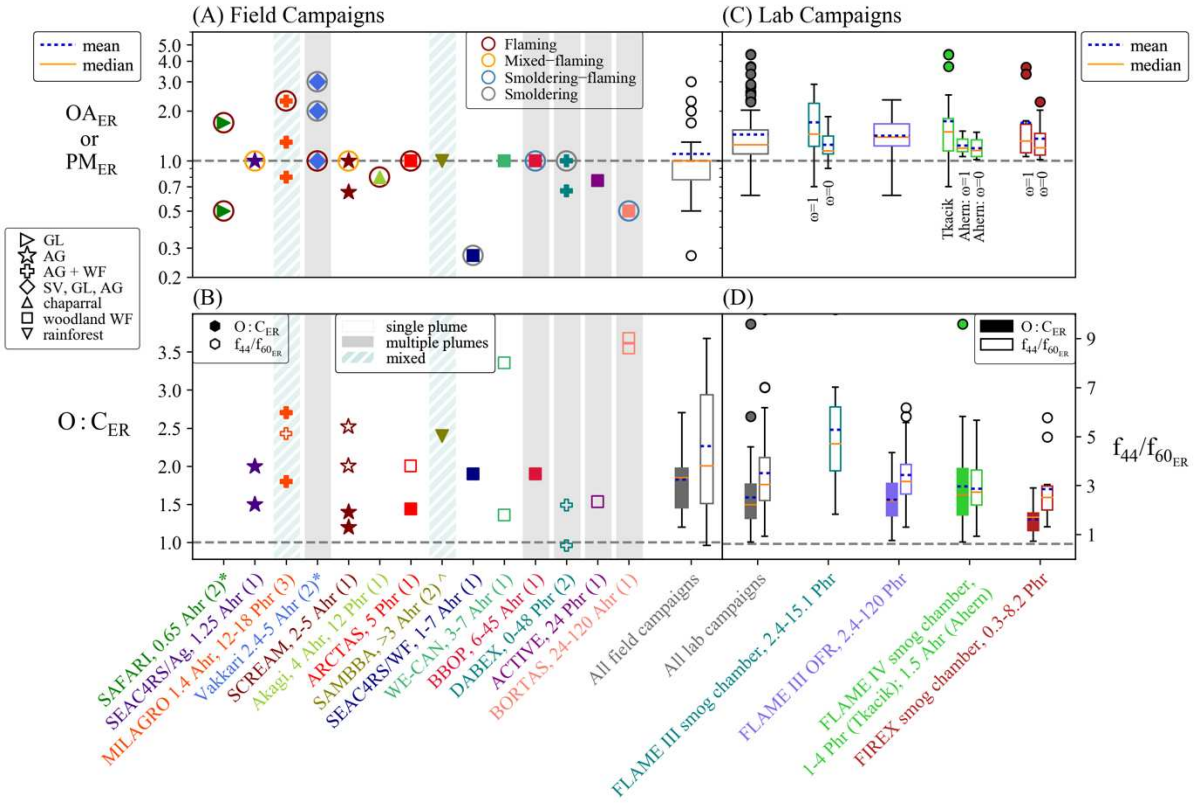

Figure 4.1 (A) The OA or PM mass enhancement ratio (OA_{ER} or $PM_{ER\ R}$) and (B) $O{:}C_{ER}$ (left y axis; closed symbols) and $f_{44}/f_{60_{ER}}$ (right y axis; open symbols) values for each published field campaign that provides both fresh (within 1 reported hour of emission) and aged measurements. The x axis labels indicate campaign or first-author name; final age as actual/physical (A) or photochemical (P); and number of studies associated with a campaign in "()". Photochemical age is the number of hours with an OH exposure of 1.5×10^6 molec cm^{-3} that equals the same total estimated OH exposure of the field data. Not all studies provide $O{:}C_{ER}$ and $f_{44}/f_{60_{ER}}$ information. Excluding the SAFARI study (which has two separate estimates from the same plume), multiple points within a study indicate the range of observations. Studies within grey bars indicate that multiple fires/plumes are included in the analyses; studies within grey hatched bars indicate that both multiple fires and a single fire was included in the campaign's analyses; and studies without bars indicate that a single plume was tracked downwind by aircraft. Each symbol indicates the fuel or biome type, as given by the publications. WF=wildfire, SV=savannah, AG=agricultural, GL=grassland. The colored circles around OA_{ER} values indicate burn conditions, where mixed--flaming and smoldering--flaming indicates that a range between mixed and flaming or smoldering to flaming was reported. Burn conditions were reported in each publication by modified combustion efficiency, $\Delta BC/\Delta CO$, or visual appearance (Table C1). (C) OA_{ER} and (D) $O{:}C_{ER}$ (left y axis; closed symbols or box-and-whisker) and $f_{44}/f_{60_{ER}}$ (right y axis; open symbols or box-and-whisker) for each laboratory campaign that has focused on aging. Each box-and-whisker represents

all experiments performed within a study. The x axis labels indicate campaign name and final photochemical or actual age. The FLAME III OFR data is for the maximum OA_{ER} reported for each burn. The horizontal dashed grey line at 1 in each panel indicates no change from the initial values with age. The whiskers here and in all other box plots extend to the last datum greater than Q1-whisker*IQR and less than Q3+whisker*IQR (IQR = interquartile range, Q3-Q1).

*SAFARI (Alvarado and Prinn, 2009; Hobbs et al., 2003) and the Vakkari studies (Vakkari et al., 2014, 2018) reported total excess particulate matter (TPM) and PM_1; all other studies reported OA.

^The two published reports from SAMMBA on BB aerosol aging (one ground-based (Brito et al., 2014) and one aircraft-based (Morgan et al., 2019)) both report no net OA_{ER}

Across field campaigns (Figure 4.1A), the OA_{ER} (or PM_{ER}) observations range from increases to no change to decreases in mass with age, with the median, mean, and interquartile ranges (IQR) OA_{ER} values at 1, 1.1, and 0.77-1.0, respectively. These values are much lower than for urban pollution, where OA_{ER} ~5-10 are often observed with aging, in part due to much smaller urban POA emissions relative to CO and SOA precursors (de Gouw and Jimenez, 2009; Nault et al., 2018). The primary observable trend in mass across the campaigns is that in the few cases where increases in mass were observed, they occured at shorter transport ages, with the oldest observation of a net increase in mass from Vakkari et al. (2018), at up to 5 hours old. However, it is unclear if this trend is real due to a relatively low number of data points along with variability in fuels, burn conditions, and initial times. No trend is observed when comparing the age of the earliest measurement (ranging from <10 - 60 minutes; Table C1) to OA_{ER}.

Figure 4.1B focuses on OA composition, providing enhancement ratios of oxygen-to-carbon, $O{:}C_{ER}$,

$$O{:}C_{ER} = \frac{O{:}C\ (f)}{O{:}C\ (i)} \tag{4.2}$$

and the enhancement ratios of f_{44}/f_{60}, $f_{44}/f_{60_{ER}}$,

$$f_{44}/f_{60_{ER}} = \frac{f_{44}/f_{60}\ (f)}{f_{44}/f_{60}\ (i)} \tag{4.3}$$

from AMS observations, when available. An elevated fraction of the AMS OA spectra at *m/z* 60, f_{60}, from the fragmentation of "levoglucosan-like" species (levoglucosan and other molecules that similarly fragment in the AMS(Aiken et al., 2009; Cubison et al., 2011; Lee et al., 2010)) has been shown to be a tracer of BB (Cubison et al., 2011). Although f_{60} decreases under photochemical aging (Huffman et al., 2009; Sullivan et al., 2014), it can still remain present at levels above background on aging timescales of at least one day (Cubison et al., 2011). Mass fraction f_{44} can be used as a surrogate for SOA (Cappa and Jimenez, 2010; Jimenez et al., 2009; Volkamer et al., 2006) with relative increases in f_{44} indicative of more-oxidized OA (Alfarra et al., 2004). In recent years, f_{44}/f_{60} has been used to qualitatively explore the amount of oxidative processing of particles in BB plumes (Cubison et al., 2011; Jolleys et al., 2015; May et al., 2015). AMS measurements also provide the total elemental oxygen and carbon content of the measured aerosol, with the atomic oxygen/carbon ratio (O:C) shown to be linearly correlated with f_{44} in OA (Aiken et al., 2008; Canagaratna et al., 2015). Thus, increases in either or both of f_{44} /f_{60} and O:C indicate BB OA aging.

Unlike OA_{ER}, all observations except one of composition increase in $O{:}C_{ER}$ and $f_{44}/f_{60_{ER}}$, (Figure 4.1B). The median and IQR $O{:}C_{ER}$ values lie at 1.85 and 1.5-2.0; the median and IQR $f_{44}/f_{60_{ER}}$ values lie at 3.8 and 2.3-6.7. This increase indicates that particles are almost always becoming more oxidized even if OA_{ER} decreases with age. These values are similar to urban environments, where the $O{:}C_{ER}$ would be 1.2-2.1 for 6-48 hours of photochemical aging (Hayes et al., 2015). However, the balance of chemical and physical processes affecting OA aging may differ between urban and BB systems.

The field campaigns in Figure 4.1A,B fall into two general study designs: either a single smoke plume is sampled by aircraft as it travels downwind or multiple plumes are characterized

both at and near the fires' sources. In the latter design, characterization of smoke transported downwind from these fire becomes more complex. In many of these aggregate (multiple plume) cases, the smoke characterized downwind was unlikely to be the same smoke that was sampled near the source, which introduces irreducible uncertainty into plume intercomparisons (Brito et al., 2014; Capes et al., 2008; DeCarlo et al., 2010; Jolleys et al., 2015; Vakkari et al., 2014, 2018). No clear trend for mass or composition appears between the single plume and aggregate studies.

We have attempted to categorize fires by fuel type and burn conditions (e.g. flaming, smoldering, or both) in Figure 4.1A,B based on information in existing publications. Burn conditions are often estimated using (1) the modified combustion efficiency (MCE = $\Delta CO_2/(\Delta CO+CO_2)$(Yokelson et al., 1996)), (2) the ratio of excess BC to CO, $\Delta BC/\Delta CO$ (Yokelson et al., 2009), or (3) the visual appearance of the fire. We use an MCE cutoff of 0.9, with MCE>0.9 indicating more flaming, MCE<0.9 indicating more smoldering, and MCE around 0.9 indicating a mixture of flaming and smoldering conditions (Akagi et al., 2011). Three studies use $\Delta BC/\Delta CO$ to classify the burn conditions and we follow their classifications (Vakkari et al., 2014, 2018; Yokelson et al., 2009). The implications of the burn conditions and fuel types are discussed in Section 4.3.1.

The findings from the field campaigns evident in Figure 4.1A, B are:

OA_{ER} and PM_{ER} observations show variability, with median and mean changes of 1.0 and 1.1, respectively. All cases with increases in mass occurred at shorter transport ages (<5 hours). These ratios are much lower than that for urban pollution.

All studies investigating OA composition markers showed increased oxidation with aging (increasing $O{:}C_{ER}$ and $f_{44}/f_{60_{ER}}$).

4.2.2 Laboratory studies

Figure 4.1C,D detail the aggregate OA_{ER}, $O{:}C_{ER}$, and $f_{44}/f_{60_{ER}}$ for each campaign as box-and-whisker plots (Figure C1 provides the same information for all individual burns). Figure 4.1C,D include results from three studies at the U.S. Forest Service Fire Science Laboratory (FSL) in Missoula, MT, with specific focus on BB aging: FLAME III, FLAME IV, and FIREX. These campaigns provided data from 22 fuel types and 8 different oxidation methods across 84 experiments (Ahern et al., 2019; Hennigan et al., 2011; Ortega et al., 2013; Tkacik et al., 2017). FLAME III, FLAME IV, and FIREX analysed aging of smoke in Teflon environmental ("smog") chambers (Ahern et al., 2019; Hennigan et al., 2011; Tkacik et al., 2017). FLAME III also performed aging experiments in an oxidation flow reactor (OFR) (Ortega et al., 2013). The residence times within the smog chambers range between 1-6 hours, with photochemical ages between 0.3-25 equivalent hours (assuming OH = 1.5 x 10^6 molec. cm^{-3} for all studies except Tkacik et al.(2017) which assumed OH = 2 x 10^6 molec. cm^{-3} and 60 ppb of O_3; Figures 4.1 and C2). The OFR had a residence time of 180 seconds, with maximum OA_{ER} values observed at 40-105.6 hours (Figures 4.1 and C2). Further details can be found in the supporting information.

The laboratory OA_{ER} values in Figure 4.1C are mostly >1. The range of values in the smog-chamber experiments depend on the assumptions used to correct for particle wall losses (PWL; details on each study's PWL methods are included in the supporting information). Vapors can either partition with aerosol that have deposited on the chamber walls ("ω=1" case (Weitkamp et al., 2007)) or only partition to suspended particles ("ω=0" case(Weitkamp et al., 2007)). Figure 4.1C shows both box-and-whiskers for both the ω=1 and ω=0 cases from the Hennigan et al.(2011) Ahern et al.(2019) and FIREX analyses (Tkacik et al.(2017) only provided the ω=1 case). As

expected, the ω=0 case yields a slightly lower mass enhancement. For FLAME IV, Ahern et al. (2019) included six fewer experiments than Tkacik et al.(2017) and used different final times (Eq. 4.1), so caution should be taken when directly comparing OA_{ER} between the two studies. None of the data presented were corrected for vapor wall losses, which is important for determining OA_{ER} in smog chamber studies (Bian et al., 2017; Krechmer et al., 2016), and is discussed in Section 4.3.3. As the residence time is short in the OFR and particle losses are measured to be small, Ortega et al. (2013) instead reports OA_{ER} without correcting for potential wall losses.

Despite the variation in both physical and photochemical ages (Figure 4.1 and Figure C2) and PWL correction methods between the campaigns, the median, mean, and IQR OA_{ER} values are generally similar. The median and mean mass enhancements range between 1.15-1.45 and 1.2-1.74, respectively, and the IQRs range between 1.07 and 2.23 (Figures 4.1C). The median and mean OA_{ER} for all reported laboratory data are 1.25 and 1.44, 25% and 30% higher than the median and mean mass enhancements observed for all reported field data. Further, the IQR for the field data is 0.76-1.3 and 1.1-1.54 for the laboratory data, indicating that the laboratory data are consistently higher in mass enhancement than the field data. A two-sided Mann-Whitney U test on the means between the field and laboratory OA_{ER} data shows the means were significantly different with a p-value of 5×10^{-5}.

In contrast to the mass enhancement observations, the range in the reported $O{:}C_{ER}$ and $f_{44}/f_{60_{ER}}$ laboratory data are consistent with the field data in the direction and magnitude of change with aging. The median and IQR $O{:}C_{ER}$ across all laboratory data are 1.5 and 1.3-1.8 and the median and IQR for $f_{44}/f_{60_{ER}}$ across all laboratory data are 3.0 and 1.8-3.6. Sampled plumes in the field undergo, on average, slightly more compositional aging than the emissions in the laboratory aging studies, although the number of data points for the field data is small (N≤10). The

FLAME III data show a higher $f_{44}/f_{60_{ER}}$ mean and median than the field data, potentially due to this study's AMS detecting fragments other than those from CO_2^+ (Ortega et al., 2013).

The findings from the laboratory campaigns evident in Figure 4.1C, D are:

OA_{ER} in laboratory observations tends to increase under aging, with a median and mean OA_{ER} of 1.4 and 1.7.

OA_{ER} values in smog-chamber experiments are sensitive to PWL correction methods.

All studies show chemical signs of aging (increasing $O{:}C_{ER}$ and $f_{44}/f_{60_{ER}}$), overlapping the range of the field data.

4.2.3 Variability between field and laboratory campaigns limits the community from creating a unified framework for BB aging

When comparing OA_{ER}, $O{:}C_{ER}$, and $f_{44}/f_{60_{ER}}$ between field and laboratory data (Figure 4.1), the broad points are:

On average, laboratory observations show increases in mass with age (OA_{ER} that are mostly >1), whereas on average the field data undergo no net change in mass with age ($OA_{ER} \sim 1$).

Across all studies, $O{:}C_{ER}$ and $f_{44}/f_{60_{ER}}$increase with age, with field observations showing on average a slightly greater increase in $O{:}C_{ER}$ and $f_{44}/f_{60_{ER}}$.

The variability within and between field and laboratory studies currently prevents the community from creating a unified framework for predicting the aging of BB aerosol. Given the magnitude of the global BB POA source (Cubison et al., 2011), this results in a significant uncertainty in the global OA budgets.

4.3. Hypotheses for variability within and between lab and field observations

In this section, we present four broad categories of hypotheses for the observed variability in OA aging within and between lab and field observations: (1) variability in emissions and chemistry; (2) differences in dilution rates, partitioning, and absolute OA loading; (3) line and chamber wall losses; and (4) differences in the timing of the initial measurement.

4.3.1 Variability in emissions and chemistry

Much of the focus in BB aging studies has been on how emissions and chemistry vary between fuels/biomes and burn conditions (Ahern et al., 2019; Hennigan et al., 2011; Hobbs et al., 2003; Ortega et al., 2013; Tkacik et al., 2017; Vakkari et al., 2018; Yokelson et al., 2013). Hence, we present this as our starting hypothesis for variability in OA aging: variations in emissions and chemistry could explain much of the variability between field and laboratory measurements.

Differences in fuel mixtures lead to differences in emissions: Differences in fuel mixtures and conditions (e.g., fuel-moisture content) can lead to differing emissions of gas- and particle-phase species between different burns, leading to potential differences in initial distributions of mass across volatility bins and composition markers. Emission factors (EFs) from BB for a given gas or aerosol species can vary by more than an order of magnitude across different biomasses (Akagi et al., 2011; Jiang et al., 2018; Stefenelli et al., 2019). Selimovic et al. (2018) found that laboratory burns of both individual and grouped fuels were in reasonable agreement with field data for select trace gases, although this study has limited PM and VOC measurements and more field-

to-lab emissions comparisons are required. Emissions vary with time (May et al., 2015), but the impact of this variability on mass and composition has not yet been well-characterized.

Modelling studies suggest that known SOA precursors like aromatics and terpenes are not sufficient to explain SOA formation in BB plumes (Alvarado et al., 2015; Alvarado and Prinn, 2009; Jathar et al., 2014; Ortega et al., 2013). Intensive efforts have been made during the FIREX and FLAME IV campaigns to carefully characterize previously unspeciated and often unmeasured SOA-precursor emissions (Hatch et al., 2015, 2017, 2018; Jen et al., 2019; Koss et al., 2018; Sekimoto et al., 2018; Stockwell et al., 2014, 2015), and studies are now beginning to connect these species to BB SOA formation (Ahern et al., 2019).

The studies in Figure 4.1A are classified by biome and/or fire type based on the published descriptions. It is difficult to determine any trend across the fuel types given the small number of samples. Although all woodland wildfire samples show either no change or a decrease in mass enhancement with age, these aged samples are all over 5 photochemical hours old, the cutoff at which no mass gains are observed within the available data. In addition, there are many important fire-prone biomes not represented within the current studies such as peatlands and moorlands (Davies et al., 2016; Van der Werf et al., 2010). Figure C3 arranges Figure 4.1A and B by geographic region. The U.S. and boreal North American studies all show no change or decreases in OAER with aging; no other apparent trends are evident. The published BB aging field studies thus far are primarily in North America, with few studies in Africa, Australia, and South America, and no studies in Europe or Asia.

Across the 84 experiments and 161 estimated OA_{ER} values only 10 OA_{ER} values decrease and all but two of the available $O{:}C_{ER}$ and $f_{44}/f_{60_{ER}}$ values show net increases (Figure C1). However, inter-study differences make it difficult to draw conclusions for fuel types. Different

fuel and oxidant combinations were used within each experiment and almost all experiments show variable OA_{ER}, $O{:}C_{ER}$, and $f_{44}/f_{60_{ER}}$within a given fuel type, even within the same study and oxidation method. This variability could come from variable burn conditions (discussed below).

A limited number of fuel-specific comparisons can be made between the laboratory and field studies. The dominant fuel in the Akagi et al.(2012) field study, chaparral, was examined in the OFR and CSU smog chamber experiments. The chaparral laboratory burns observe positive mass enhancements while Akagi et al.(2012) observes a negative mass enhancement. Similarly, the woodland forest fire studies likely contained mixtures of different pine species and may be compared to the laboratory burns of black spruce, ponderosa pine, lodgepole pine, white spruce, douglas fir, subalpine fir, and engelmann spruce. Two of the field studies show no change (Collier et al., 2016; Cubison et al., 2011), three show decreases in mass ratios (Forrister et al., 2015; Jolleys et al., 2012, 2015), and the majority of laboratory experiments of the listed pine fuels show net increases in OA. It is more than likely that other laboratory-studied fuels were present in many of the field burns, however, due to lack of specific information we cannot analyze this topic further. As well, POA EFs and/or initial OA/CO are highly variable even for a given fuel type within lab and field burns (as previous reviews have synthesized; Andreae and Merlet, 2001; Akagi et al., 2011), which adds to the challenge of comparing OA aging across field and lab studies.

Burn conditions influence emissions and there may be key differences between field and laboratory conditions: Burn conditions (e.g. flaming, smoldering) also influence emissions and aerosol mass, as VOC emissions can decrease with increased flaming combustion (Liu et al., 2017; Yokelson et al., 2013). SOA precursor emissions may similarly decrease with increased flaming combustion; however, some SOA precursors vary with high- and low-temperature pyrolysis factors instead of directly with MCE (Sekimoto et al., 2018). In the field, burn conditions will

change both temporally and spatially over time (Sekimoto et al., 2018), potentially resulting in changing emissions, and aircraft studies that track a single plume in a semi-Lagrangian sense are unlikely to sufficiently sample a plume with changing burning conditions. Of the fifteen field studies that reported burn conditions (Figure 4.1A, Table C1), the majority report flaming to mixed average conditions. For the BORTAS campaign, Jolleys et al. (2015) caution that the fresh smoke appeared to be coming from more smoldering conditions but that the aged smoke appeared to be coming from more flaming conditions. Vakkari et al. (2018) found that over a 5-year period, observations from the most flaming conditions did not undergo any mass enhancement, whereas the remaining observations increased PM_{ER} in normalized mass with age. Except for Vakkari et al. (2018), there appears to be no pattern between flaming, smoldering, and mixed for net mass changes. Similarly, the relative differences in $O{:}C_{ER}$ and $f_{44}/f_{60_{ER}}$between studies do not appear to systematically depend on burn conditions.

All but three of the laboratory aging studies that have reported MCE have been for more flaming fires (MCE>0.9; Figure C4). Laboratory studies of the aging of open-air BB aerosol emissions is currently a small subset of the work done to quantify the primary emission factors (EF) of BB aerosol emissions and within the context of the primary EF work, it is still an open question as to how well laboratory burns represent field variability. Some species, such as BC, appear to correlate well between laboratory and field for primary EF measurements (May et al., 2015). POA emissions from laboratory work exhibit wide and not fully explained variability for a given fuel type and combustion condition. These laboratory measurements of POA can also differ when compared with field observations. One of the drivers underlying the observed discrepancies in POA emissions between laboratory and field measurements may be variable combustion conditions driven by flame propagation through the fuel and the availability of oxygen due to the

level of turbulent mixing (Jolleys et al., 2014). Combustion conditions are typically defined by an average MCE but are governed in part by wind, fuel density, and flame dynamics (Finney et al., 2015), which may be important factors when comparing laboratory and field measurements (Yokelson et al., 2013). Other important factors between laboratory and field measurements that influence burn conditions include differences in fuel moisture content (May et al., 2015; Yokelson et al., 2013), mixtures of fuel types (Selimovic et al., 2018) and fractions of these fuels that burn in the laboratory relative to the field (Campbell et al., 2007; Santín et al., 2015).

Sekimoto et al. (2018) identified two distinct high- and low-temperature pyrolysis emission profiles of VOCs that explained on average 85% of the VOC emissions for 15 fuel types. The high- and low- temperature profiles do not correspond exactly to the more commonly used flaming and smoldering categories, and require further study to determine how these temperature-based profiles may aid in predicting both POA and SOA formation, as well as how the different temperature regimes may be identified in field burns. These differences in VOC profiles for the two pyrolysis regimes may help explain why some given fuels show variability in OA_{ER} between experiments even for the same oxidant and campaign.

Oxidant concentrations influence chemistry: In-plume reactions and oxidant concentrations can influence the aerosol mass and composition markers. Higher oxidant concentrations lead to increased rates of reactions that could both functionalize and fragment gas-phase molecules, and enhance heterogeneous chemistry. Functionalization tends to lead to vapors with lower volatilities that can partition to the particle phase, but fragmentation and heterogeneous reactions tend to lead to higher-volatility products that will remain in or enter the gas phase (Kroll et al., 2009, 2011; Smith et al., 2009). Three studies in Figure 4.1A explicitly attempt to account for the in-plume OH concentration: Hobbs et al. (2003) and Yokelson et al. (2009) report OH

concentrations >10^7 molec cm^{-3} (typical daily-averaged ambient tropospheric OH concentrations are ~ 1.5×10^6 molec cm^{-3}) and both of these plumes see a positive mass enhancement (assuming that the analyses of Alvarado and Prinn(2009) are correct). Akagi et al. (2012) report a slightly elevated in-plume OH concentration of $5.27x10^6$ molec cm^{-3} and observe a net decrease in mass. However, each of these fires were for different environments, fuels, and burn conditions. Without corresponding knowledge of what the ratios of functionalization to fragmentation were, no conclusions can be drawn as to how the enhanced OH concentrations influenced the plumes' PM masses.

Plume oxidant levels can be influenced by NO_X emissions (and thus combustion phase), solar zenith angle, optical depth, temperature, and absolute humidity. The rates of oxidation of VOCs and the resulting production of O_3 in BB plumes is NO_X-limited (Jaffe and Wigder, 2013), and fires with higher NO_X emissions have higher oxidant levels and more active oxidation of VOCs. NO_X emissions depend on the fuel N content as well as the combustion phase, leading to more rapid oxidation in grassland and savannah fires (mainly flaming combustion) than in boreal fires (low fuel N content and more smoldering combustion(Andreae and Merlet, 2001; Mebust and Cohen, 2013)). The solar zenith angle influences the sun's intensity, and the optical depth controls how far sunlight may penetrate the plume, impacting photolysis rates and oxidant concentrations. Temperature controls rates of chemical reactions, with plumes in colder environments (e.g. plumes that reach the free troposphere) likely undergoing slower reactions. Humidity determines the fraction of OH production from O_3 photolysis. However, these factors have not been explicitly accounted for in field or laboratory campaigns.

The roles of multiphase and nighttime chemistry are under-characterized: The importance of multiphase/condensed-phase reactions and nighttime chemistry (when the nitrate radical can be the most important oxidant(Brown et al., 2004)) is currently unclear. Multiphase reactions have not yet been explicitly characterized in aging BB studies, although observations of tarball formation may be indicative of heterogeneous chemistry (Pósfai et al., 2004; Sedlacek et al., 2018). Vakkari et al. (2018) observed no net increase in total PM_1 mass concentrations at nighttime but did see net increases in aged mass during daytime conditions (excluding the most flaming fires, as discussed below). Wildfire plumes in the northwest U.S. transported primarily at night versus day showed little difference in mass enhancement (Zhou et al., 2017). Zhou et al. (2017) also find that the OA from plumes transported at night appeared to be less oxidized than the daytime plumes, with daytime $O{:}C_{ER}$ values higher than nighttime $O{:}C_{ER}$ values. None of the laboratory data in our review include experiments where the nitrate radical is the primary oxidant, although we do include experiments with dark O3 chemistry (O3 is added but UV lights are off) (Figure C1). These "Dark O3" experiments generally do not give higher OA_{ER} values than experiments with UV lights, and hence they are likely not a cause of the relatively high bias in OA_{ER} relative to field experiments.

4.3.2 Differences in dilution rates, partitioning, and absolute OA loading

SVOCs can make up between ~20-90% of fresh BB particles (Eatough et al., 2003; Grieshop et al., 2009; Huffman et al., 2009; May et al., 2013, 2015) and upon dilution, they may evaporate. Evaporated POA can act as precursor vapors for SOA if they react and form lower-volatility products (Bian et al., 2017; Hodshire et al., 2019), and the resultant SOA is likely to have

a more-aged signal (higher $O{:}C_{ER}$ and $f_{44}/f_{60_{ER}}$) than the original POA compounds, even if OA_{ER} does not change (POA evaporation could be balanced by recondensation of oxidation products). However, the rate and yield at which evaporated POA forms SOA is uncertain (Akherati et al., 2019) and has not been yet studied for smoke plumes.

As partitioning and evaporation rates depend on absolute aerosol mass loading (Donahue et al., 2006, 2009), the initial OA concentration, dilution rate, and concentration of OA in the entrained background air will impact OA aging (Hodshire et al., 2019). In addition, the partitioning of semi-volatile OA is temperature dependent, with an order of magnitude shift in C* for every 20 K change in temperature (Donahue et al., 2006). As dilution proceeds differently within and between laboratory and field studies, dilution differences could help explain variability in OA_{ER}, $O{:}C_{ER}$, and $f_{44}/f_{60_{ER}}$. Evaporation is also influenced by oligomerization reactions and the bulk diffusion coefficient. Oligomerization reactions create lower-volatility products (Barsanti and Pankow, 2004), decreasing evaporation rates. Similarly, a decreased particle-phase diffusion coefficient leads to decreased evaporation rates (Shiraiwa and Seinfeld, 2012). Oligomerization reactions and the diffusion coefficient for BB aerosol are currently not well-studied, although tar ball formation in BB plumes may indicate both oligomerization processes and a low particle-phase diffusion coefficient (Sedlacek et al., 2018).

Field burns undergo variable dilution rates: In the field, dilution is influenced by the size of the fire, atmospheric conditions (e.g., stability of the layer of smoke injection), and regional topography. Figure 4.2 provides the range and distribution of fire sizes for the U.S. for 2014, indicating the importance of small (<0.1 km^2 of burned area) fires. Well over half of the globe's landmass experiences average fire sizes ≤ 1 km^2 (Andela et al., 2019). Plumes that dilute quickly, either due to being formed by small fires and/or being dispersed quickly due to atmospheric

conditions, will lose more mass to evaporation, all other conditions being equal. Conversely, plumes that dilute slowly, either due to being formed by large fires and/or being dispersed slowly due to atmospheric conditions or regional topography, may lose less mass to evaporation (Bian et al., 2017; Hodshire et al., 2019). Slowly diluting plumes may also undergo fewer chemical reactions if the plume is dense enough to limit sunlight to the interior of the plume, slowing photochemistry (Colarco et al., 2004; Hobbs et al., 2003; Liousse et al., 1995). Thus, mass and composition markers may change slowly in large plumes if little mass is lost by evaporation or gained from chemistry. However, scattered light from smoke aerosols may compensate for light lost by aerosol absorption (Baylon et al., 2018).

Five of the field studies in Figure 4.1 explicitly characterized the fire size (Figure 4.2; Table C1, between 0.01-10 km^2), and all showed no change or decreases in mass with age. The five woodland wildfires (Collier et al., 2016; Cubison et al., 2011; Forrister et al., 2015; Jolleys et al., 2012, 2015) were likely larger than 10 km^2 but also show no change or decreases in mass with age. As mentioned above, there are differences in study design for field campaigns between aircraft studies and ground-based studies, as well as if the aircraft study is explicitly tracking one plume downwind or instead measuring smoke within a region. These differences in measurement design may impact the apparent influence of dilution and is a source of uncertainty.

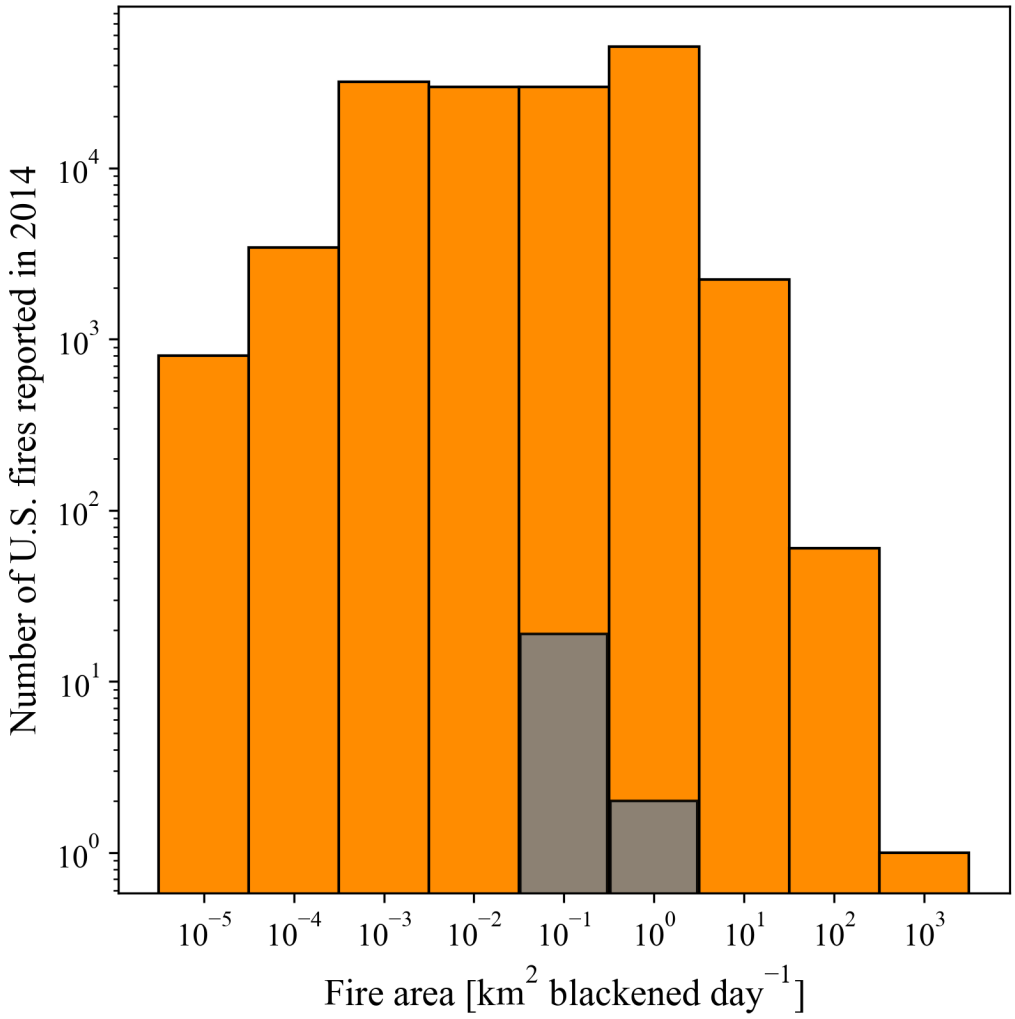

Figure 4.2 Annual data for the United States in 2014 for the number of recorded fires by fire size in km^2 blackened per day (that is, the total area in km^{2}burned per day) from the National Emissions Inventory (U.S. EPA NEI, 2014). Overlain in grey are the number of fires by size from the field campaigns in Figure 4.1A for each fire with sizes either explicitly reported or estimated within the publication. Note that some campaigns in Fig. 4.1 are not included as this information was not provided, and they typically tended to be larger fires.

Laboratory studies do not undergo variable dilution rates: Unlike field campaigns, laboratory campaigns keep chambers at an effectively fixed dilution ratio. Most laboratory smog-chamber experiments initially dilute OA concentrations to 10-100 μg m^{-3}, and the concentrations generally stay in this range throughout the aging experiment. Hence, smog-chamber and OFR

experiments do not sample continuous dilution with time, which may control evaporation and the availability of SOA precursors.

Initial POA concentrations influence SOA production: The FLAME III OFR introduced significantly higher initial OA concentrations into its chamber compared to the three smog chamber experiments, impacting mass. Figure 4.3 shows OA_{ER} versus the initial OA concentration for all experiments, with Figure C5 showing the same for $O{:}C_{ER}$ and $f_{44}/f_{60_{ER}}$. The three smog chambers introduce between ~5-400 μg m^{-3} of OA and the OFR introduces between ~110-18,000 μg m^{-3} of POA. For the OFR, there is a decreasing trend of OA_{ER} with increasing initial OA (R^2 = 0.62). Ortega et al. (2013) hypothesized that increasing initial OA concentrations drives more SVOCs (and potentially even IVOCs) to the particle phase, leading to fewer gas-phase SOA precursors available to react and condense onto the particles. A significant amount of mass exists in the C*=10^3-10^4 μg m^{-3} range (Bian et al., 2017; Hatch et al., 2018). These species are POA at high organic mass concentrations but gas-phase SOA precursors at low organic mass concentrations (Donahue et al., 2006; Hatch et al., 2018). The smog chambers in Figure 4.3 are dilute enough that species with C*=10^3-10^4 μg m^{-3} range are mostly in the gas phase for all experiments, so additional dilution (lower POA concentrations) does not result in a strong trend in OA_{ER}: Tkacik et al. (2017) has an R^2 value of 0.47 and the remaining campaigns have R^2<0.25. The OFR $O{:}C_{ER}$ and $f_{44}/f_{60_{ER}}$ data have an inverse correlation to POA with R^2 values of 0.42 and 0.3, respectively. This inverse correlation indicates less condensation of oxidized organics at higher POA loadings, supporting the hypothesis that higher POA loadings reduce OA aging and enhancement.

Figure 4.3 also includes the field campaigns that provided initial in-plume absolute OA. Many of these field studies provided mass time series, and here we qualify the initial OA as the highest observed OA concentration. In general, the field OA_{ER} are close to 1 for low initial OA loadings (~<100 μg m^{-3}). However, the field observations with higher initial OA loadings generally have lower OA_{ER} values compared to the trend for the FLAME III OFR. This low field bias is potentially because the observed ambient plumes diluted between the initial and final observations while the OA concentrations in the OFR are held approximately fixed during aging.

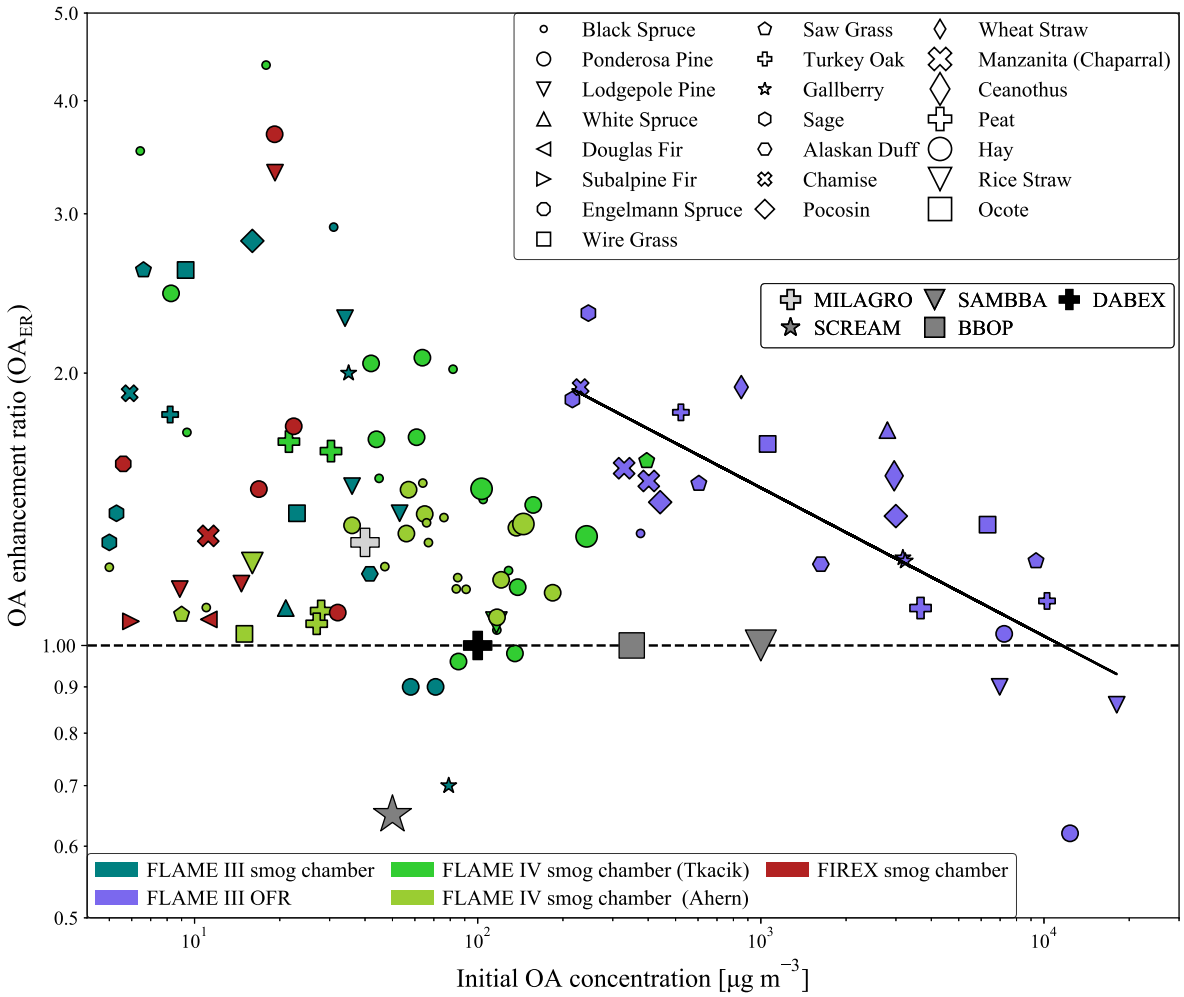

Figure 4.3 The OA enhancement ratio (OA_{ER}) to the initial OA concentration in $\mu g\ m^{-3}$ within each chamber for all experiments within the laboratory campaigns of Figure 4.1C and D. Symbols indicate fuel type and colors indicate study type. The horizontal dashed black line at $OA_{ER}=1$ indicates no net change in OA mass from the initial mass. The black solid line indicates the trend line for the OFR data, with a slope of -0.16 and an R^2 value of 0.62. Also included on this figure are the studies that report initial OA concentrations. Where field campaigns published time series of OA, we used the highest concentrations as this is likely the closest overpass over a plume.

Background OA differs between field studies: Hodshire et al. (2019) indicated that elevated (>20 $\mu g\ m^{-3}$) background aerosol concentrations can impact SOA formation in plumes from smaller fires (<10 km^2), as entrainment of the elevated background aerosol mass can slow evaporation of semivolatile compounds, effectively slowing evaporation caused by dilution. None of the studies in Figure 4.1A explicitly report the background aerosol concentration (although this information likely is available within the campaign data repositories). This background OA effect could be particularly important in regions that experience large numbers of small fires, such as the Amazon basin during the dry season (Martin et al., 2016; Reid et al., 1998). Figure C6 shows that for the U.S. in 2014, 3% of total reported fires occured in background $PM_{2.5}$ concentrations of ≥20 $\mu g\ m^{-3}$, accounting for 7% of total $PM_{2.5}$ fire emissions. No study to date has explicitly considered the effects on OA_{ER}, $O{:}C_{ER}$, or $f_{44}/f_{60_{ER}}$ from plume size, dilution rates, mixing, and background aerosol and vapor concentrations with ambient data.

Temperature differs between field and laboratory studies: Temperatures at the height of plume injection may be significantly colder than those at the surface, and these temperature differences could lead to different OA partitioning and aging for plumes at different heights/temperatures. In laboratory experiments, temperature is generally held fixed and there is

currently no published controlled analysis of the net effect of temperature on biomass-burning OA aging.

4.3.3 Line and chamber wall losses

Partitioning of vapors to walls in laboratory experiments may alter apparent SOA production: Laboratory results are dependent on losses of both vapors and particles to the chamber walls and instrument/chamber tubing, which influences mass. Each smog chamber analysis in this review has corrected for PWL assuming either that the particles lost to the walls remain in equilibrium with semi-volatile vapors (ω=1) or that vapors only interact with suspended particles (ω=0): assuming ω=0 decreases the mean mass enhancement by 3-26% (Figure 4.1C). In reality, vapor uptake by deposited particles likely lies between the ω=1 and ω=0 cases (Weitkamp et al., 2007) and this remains an uncertainty moving forward. None of the published laboratory studies here correct for partitioning of vapors to walls directly into the Teflon surfaces, which may be more than an order-of-magnitude larger than losses to particles on the walls (Krechmer et al., 2016). The published OFR study does not correct for either particle or vapor wall losses, although these losses are predicted to be relatively low in OFRs (Eluri et al., 2018; Lambe et al., 2011; Palm et al., 2016). We do not correct for vapor wall losses in this review as it requires simulating all prior experiments in an aerosol microphysics model and knowledge of chamber turbulence within each experiment. Rather, we rely on the work of Bian et al. (2017) in Figure C7 to demonstrate the potential importance of correcting for these vapor wall losses (see below).

To date, two published modeling studies have characterized partitioning of vapors to Teflon walls for chamber BB aging experiments (Bian et al., 2017; Pratap et al., 2019). Bian et al. (2017) modeled both PWL and vapor wall partitioning for the smog chamber in the FLAME III campaign, using size-dependent PWL rates and volatility-dependent vapor partitioning rates

(Krechmer et al., 2016). Although uncertainties remained for PWL and vapor partitioning rates, Bian et al. (2017) found that simulations without vapor partitioning led to roughly a doubling of OA_{ER} values. Figure C7 shows the results from Bian et al. (2017) next to the Hennigan et al. (2011) results with the vapor-wall-loss corrections lifting the mean and median OA_{ER} values to over 3. In a similar modelling study for the dark period within the chamber before lights are turned on (~75 minutes), Bian et al. (2015) found that over one-third of the initial particle-phase mass was lost during this time to PWL and vapor partitioning, with 35% of this loss coming from evaporation of particles driven by vapor wall losses to the Teflon chamber walls. As vapor partitioning is a function of volatility, these losses could also impact composition markers.

The tubing that transports the smoke between the burn chamber and the smog chambers is also susceptible to losses/delays of gas-phase SOA-precursor material (Deming et al., 2019; Liu et al., 2019; Pagonis et al., 2017). To illustrate this point, we provide a new analysis using the absorptive partitioning model for tubing built by Pagonis et al. (2017) ("tubing model") to estimate potential losses of gas-phase material from tubing delay for the smog chamber set-up in FLAME III (Hennigan et al., 2011). We assume the fresh-smoke VBS distribution of Bian et al. (2017) and the supporting information provides further details on our methods. At a tubing temperature of 40 °C and residence time of ~4.3 seconds (Hennigan et al., 2011), the heated aerosol may not achieve equilibrium instantaneously (Riipinen et al., 2010) and we assume two bounding cases on evaporation in which (1) the particles do not evaporate or (2) the particles reach equilibrium instantaneously. For these bounding cases and an initial mass loading of 50 μg m^{-3}, ~16-25% of the S/IVOC gas-phase material does not exit the tubing after 15 minutes of continual flow of smoke through the tubing (Figure C8). This loss increases to ~30% if the tube is not heated. Estimated OA_{ER} values (neglecting further chamber wall losses and making simple assumptions for SOA

yields; supporting information) the OA_{ER} ranges between 1.3-1.8 for the cases with transfer lines but increase to 2.5 for a case with no assumed tubing loses (Figure C8D).

Partitioning of vapors to the chamber walls and tubing decreases the concentrations of gas-phase precursors that could participate in SOA formation, biasing OA_{ER} in laboratory campaigns low (Figure C7), further increasing the discrepancies between field and laboratory studies.

4.3.4 Differences in the time of the initial measurement

Pre-measurement chemistry may impact SOA: All of the field and laboratory measurements in Figure 4.1 are expressed as ratios referenced to an observation that is treated as the initial condition ("time zero"). For field studies, the time after emission at which these initial observations are made can be highly variable between studies, and in some cases significant evaporation and/or chemistry may have occurred prior to that first observation. Generally, the earliest measurements for aircraft campaigns are on the order of ~2-3 minutes after emission with most being 10 minutes or more after emission (Table C1). In the FIREX laboratory experiments conducted, Koss et al. (2018) found a substantial fraction of higher molecular weight organic emissions, including heterocyclic (e.g., furans) and phenolic (e.g., phenol, guaiacol) compounds, that could already have contributed to SOA on these very short timescales (Stefenelli et al., 2019). Results for modeling of residential wood combustion indicate the importance of these species to SOA formation (Stefenelli et al., 2019), though these results have yet to be tested for ambient BB plumes. As these compounds have short atmospheric lifetimes with respect to OH (~15-60 minutes), it is possible that some SOA is rapidly formed in the plume after emission but before the "initial" condition of the smoke plume can be measured by aircraft. Furthermore, many plumes

undergo relatively rapid dilution during the first several minutes (e.g. vertical mixing into an unstable layer), which may lead to evaporation during this initial time period. Hence, we hypothesize that observed enhancement ratios in the field may be sensitive to the location/timing of the near-field measurement.

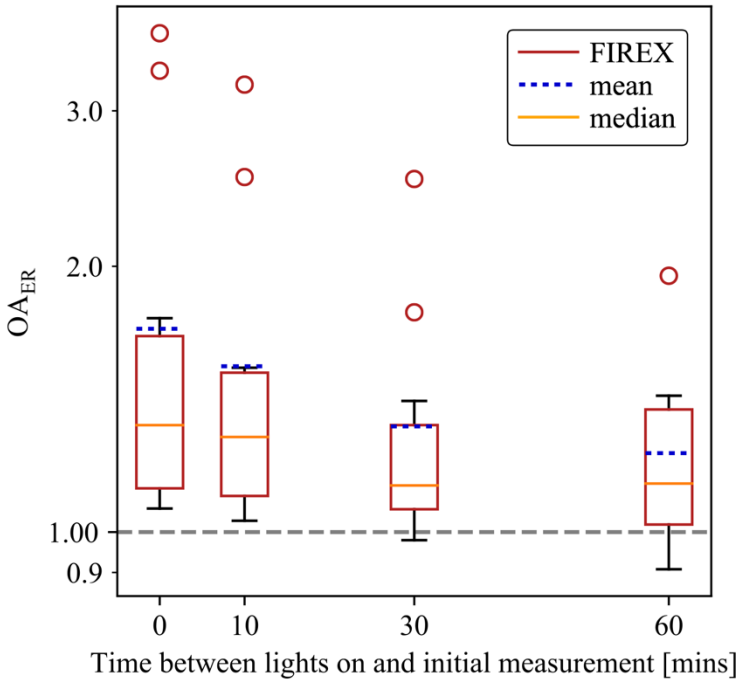

Figure 4.4 OA enhancement ratios (OA_{ER}) for the FIREX data (ω=1 case), as a function of where time zero (the initial measurement) is defined (relative to when the lights were turned on, or 0 minutes). Plotted are offsets of 0 (what is always used in laboratory analysis), 10, 30, and 60 minutes, with the non-zero offsets representative of time zero in field experiments (Table C1). The horizontal dashed grey line at OA_{ER} =1 indicates no net change in OA mass from the initial mass.

Laboratory campaigns have high temporal resolution and can capture early-stage chemistry. The time zero in most of the laboratory experiments discussed here occurs when chemistry is initiated (lights are turned on or ozone is added). If rapid reactions are important to BB SOA formation, the differences between time zero in laboratory and field campaigns could be responsible for higher OA_{ER} values in laboratory experiments.

To illustrate how OA_{ER} is sensitive to the definition of time zero, we provide a novel analysis with the FIREX smog chamber data of the impact on OA_{ER} as a function of where time zero is defined relative to when the lights were turned on (Figure 4.4). Plotted are offsets of 0 (what is always used in laboratory analysis), 10, 30, and 60 minutes, with the non-zero offsets representative of time zero in field experiments. The OA_{ER} values estimated for a time zero offset of 30 minutes are about half of these values when there is no offset. For the cases when time zero offset is 60 minutes after the lights turned on, about a quarter of the experiments have an OA_{ER} less than 1 (only 10 of all reported laboratory OA_{ER} values are less than 1 when there is no offset in time zero). Hence, the FIREX data demonstrate that the difference in definition of time zero in the laboratory experiments and field experiments might explain, at least in part, why OA_{ER} values are generally higher in laboratory experiments than field experiments. However, the trend shown in Figure 4.4 could also be due to wall losses of gases, which occur on timescales of tens of minutes (Krechmer et al., 2016), and thus may not be applicable to field studies. In addition, the BB OFR study of Ortega et al., (2013) found that most of the OA_{ER} increases did not occur on these sub-hour photochemical timescales. Oxidant concentrations decreased with time during the FIREX smog chamber experiments, which could also favor early OA_{ER} production, but OH has also been observed to decrease in ambient BB plumes with time (Yokelson et al., 2009). As well, initially thick plumes may have low oxidant concentrations due to slow photolysis rates until the plume disperses. More research is needed to understand the initial chemistry occurring in smoke plumes.

4.4 Future research needs

In this study, we have reviewed prior studies of smoke particle aging in the field and lab and discussed hypotheses for differences within and between the two types of studies. In order to

create a unified framework to explain variability in the BB aging, we present the following recommendations for key research priorities for the community. We do not rank these priorities, as we hope that ongoing research efforts will guide the relative importance of each priority. We order each subsection by scale, from the molecular level to larger spatial scales:

Under-characterized variables in field campaigns:

Better characterization of in-plume chemistry that will allow for improved estimates of, amongst others, oxidant and radical concentrations, optical thickness, vertical structure, photolysis rates, and reaction rate constants with OH, O_3, and NO_3 for different classes of smoke compounds. Consideration of how well variability in source emissions is characterized to obtain an estimate of how much variability would be expected downwind, independent of chemistry.

Better characterization of the fire size/dilution rate, absolute OA concentrations, and the background aerosol/OA concentration to improve understanding of the influence of these properties on OA aging. A wider range of fire sizes should be sampled from, as field studies thus far appear to have disproportionately sampled mid-sized fires (Figure 4.3), and aging may depend on fire size and background concentrations.

A broader set of study locations, as a majority of existing field studies have occurred in the Americas and a few occurring in Africa. Many important fire-prone biomes remain under-studied including peatlands and moorlands (Davies et al., 2016; Van der Werf et al., 2010).

Under-characterized variables in laboratory campaigns:

Better characterization of particle and vapor wall losses for all transfer line and reaction vessel surfaces, and clear documentation of those corrections. Consistent methods for correcting data for each of these losses must also be used to compare across studies.

A more systematic testing of dilution levels as well as variable temperatures (including rapid changes in temperature) for the same fire conditions in order to understand changes in evaporation and SOA production during plume dilution and temperature changes.

A wider range of MCEs, as the burn conditions within the available laboratory studies have almost all been with high MCEs, indicating a dominance of flaming fires. More smoldering fires within the laboratory setting should be studied. As well, methods to more closely match field burns should be developed, such as burning more compact fuels/larger amounts, varying fuel water-content and/or adding heat lamps to increase fuel temperature prior to combustion.

A wider sampling of fuels as laboratory studies have been focused predominantly on fuels that may exist in North American fires.

Reconciling laboratory and field campaigns:

Expanding use of emerging techniques that allow molecular-level measurements of OA in real-time(Lopez-Hilfiker et al., 2019) should be applied to both field and lab studies to allow more direct connections than can be made with using only OA and O:C to characterize the composition of emissions.

Increased reporting and analysis of emissions correlations such as the high- and low-temperature emissions profiles of VOCs identified by Sekimoto et al. (2018). These profiles provide tractable methods that can be compared in field and laboratory campaigns for understanding the thousands of compounds emitted in fires and could be applied to aging studies in order to determine which correlations may increase understanding of aged smoke.

Better characterization of the OA evolution of individual fuels for variable starting mass concentrations to explore more dilution regimes in laboratory experiments. As observed for the FLAME III OFR data, more SOA was formed with a lower initial POA concentration (increased

dilution), likely due to more available precursors (Hatch et al., 2018; Ortega et al., 2013). Careful observation of both mass and compositional changes in these experiments can test the impacts of dilution on smoke aging.

Expanded use of OFRs, given their relative ease-of-use compared to environmental chambers. In lab studies, OFRs can provide anticipated particle mass, composition markers, and size distribution changes with variable levels of aging (Hodshire et al., 2018) for the same fuel or fuels burned. In field studies, OFRs can be set up at ground-based sites to sample directly from ground-level plumes and have also successfully operated from aircraft (Nault et al., 2018). Aging information from field OFRs could be directly compared to aircraft observations of the downwind plume.

Models as tools to interpret field measurements. Models can help to understand the chemical and physical impacts of dilution in plumes. As well, combinations of modeling and laboratory efforts can constrain initial, fast chemistry anticipated in smoke plumes and should be then applied to field measurements in order to determine anticipated changes in mass and composition that can occur between the time of emission and the time of the initial field measurements

REFERENCES

Ahern, A. T., Robinson, E. S., Tkacik, D. S., Saleh, R., Hatch, L. E., Barsanti, K. C., Stockwell, C. E., Yokelson, R. J., Presto, A. A., Robinson, A. L., Sullivan, R. C. and Donahue, N. M.: Production of Secondary Organic Aerosol During Aging of Biomass Burning Smoke From Fresh Fuels and Its Relationship to VOC Precursors, J. Geophys. Res. D: Atmos., 124(6), 3583–3606, 2019.

Aiken, A. C., Decarlo, P. F., Kroll, J. H., Worsnop, D. R., Huffman, J. A., Docherty, K. S., Ulbrich, I. M., Mohr, C., Kimmel, J. R., Sueper, D., Sun, Y., Zhang, Q., Trimborn, A., Northway, M., Ziemann, P. J., Canagaratna, M. R., Onasch, T. B., Alfarra, M. R., Prevot, A. S. H., Dommen, J., Duplissy, J., Metzger, A., Baltensperger, U. and Jimenez, J. L.: O/C and OM/OC ratios of primary, secondary, and ambient organic aerosols with high-resolution time-of-flight aerosol mass spectrometry, Environ. Sci. Technol., 42(12), 4478–4485, 2008.

Aiken, A. C., Salcedo, D., Cubison, M. J., Huffman, J. A., DeCarlo, P. F., Ulbrich, I. M., Docherty, K. S., Sueper, D., Kimmel, J. R., Worsnop, D. R. and Others: Mexico City aerosol analysis during MILAGRO using high resolution aerosol mass spectrometry at the urban supersite (T0)--Part 1: Fine particle composition and organic source apportionment, Atmos. Chem. Phys., 9(17), 6633–6653, 2009.

Akagi, S. K., Yokelson, R. J., Wiedinmyer, C., Alvarado, M. J., Reid, J. S., Karl, T., Crounse, J. D. and Wennberg, P. O.: Emission factors for open and domestic biomass burning for use in atmospheric models, Atmos. Chem. Phys., 11(9), 4039–4072, 2011.

Akagi, S. K., Craven, J. S., Taylor, J. W., McMeeking, G. R., Yokelson, R. J., Burling, I. R., Urbanski, S. P., Wold, C. E., Seinfeld, J. H., Coe, H. and Others: Evolution of trace gases and particles emitted by a chaparral fire in California, Atmos. Chem. Phys., 12(3), 1397–

1421, 2012.

Akherati, A., Cappa, C. D., Kleeman, M. J., Docherty, K. S., Jimenez, J. L., Griffith, S. M., Dusanter, S., Stevens, P. S. and Jathar, S. H.: Simulating secondary organic aerosol in a regional air quality model using the statistical oxidation model--Part 3: Assessing the influence of semi-volatile and intermediate-volatility organic compounds and NO x, Atmos. Chem. Phys., 19(7), 4561–4594, 2019.

Alfarra, M. R., Coe, H., Allan, J. D., Bower, K. N., Boudries, H., Canagaratna, M. R., Jimenez, J. L., Jayne, J. T., Garforth, A. A., Li, S.-M. and Worsnop, D. R.: Characterization of urban and rural organic particulate in the Lower Fraser Valley using two Aerodyne Aerosol Mass Spectrometers, Atmos. Environ., 38(34), 5745–5758, 2004.

Alvarado, M. J. and Prinn, R. G.: Formation of ozone and growth of aerosols in young smoke plumes from biomass burning: 1. Lagrangian parcel studies, J. Geophys. Res., 114(D9), D09307, 2009.

Alvarado, M. J., Lonsdale, C. R., Yokelson, R. J., Akagi, S. K., Coe, H., Craven, J. S., Fischer, E. V., McMeeking, G. R., Seinfeld, J. H., Soni, T. and Others: Investigating the links between ozone and organic aerosol chemistry in a biomass burning plume from a prescribed fire in California chaparral, Atmos. Chem. Phys., 15(12), 6667–6688, 2015.

Andela, N., Morton, D. C., Giglio, L., Paugam, R., Chen, Y., Hantson, S., Werf, G. R. and Randerson, J. T.: The Global Fire Atlas of individual fire size, duration, speed and direction, Earth System Science Data, 11(2), 529–552, 2019.

Andreae, M. O. and Merlet, P.: Emission of trace gases and aerosols from biomass burning, Global Biogeochem. Cycles, 15(4), 955–966, 2001.

Baker, K. R., Woody, M. C., Tonnesen, G. S., Hutzell, W., Pye, H. O. T., Beaver, M. R., Pouliot,

G. and Pierce, T.: Contribution of regional-scale fire events to ozone and PM2.5 air quality estimated by photochemical modeling approaches, Atmos. Environ., 140, 539–554, 2016.

Barsanti, K. C. and Pankow, J. F.: Thermodynamics of the formation of atmospheric organic particulate matter by accretion reactions—Part 1: aldehydes and ketones, Atmos. Environ., 38(26), 4371–4382, 2004.

Baylon, P., Jaffe, D. A., Hall, S. R., Ullmann, K., Alvarado, M. J. and Lefer, B. L.: Impact of Biomass Burning Plumes on Photolysis Rates and Ozone Formation at the Mount Bachelor Observatory, J. Geophys. Res. D: Atmos., 123(4), 2272–2284, 2018.

Bian, Q., May, A. A., Kreidenweis, S. M. and Pierce, J. R.: Investigation of particle and vapor wall-loss effects on controlled wood-smoke smog-chamber experiments, Atmos. Chem. Phys., 15(19), 11027–11045, 2015.

Bian, Q., Jathar, S. H., Kodros, J. K., Barsanti, K. C., Hatch, L. E., May, A. A., Kreidenweis, S. M. and Pierce, J. R.: Secondary organic aerosol formation in biomass-burning plumes: theoretical analysis of lab studies and ambient plumes, Atmos. Chem. Phys., 17(8), 5459–5475, 2017.

Bond, T. C., Doherty, S. J., Fahey, D. W., Forster, P. M., Berntsen, T., DeAngelo, B. J., Flanner, M. G., Ghan, S., Kärcher, B., Koch, D., Kinne, S., Kondo, Y., Quinn, P. K., Sarofim, M. C., Schultz, M. G., Schulz, M., Venkataraman, C., Zhang, H., Zhang, S., Bellouin, N., Guttikunda, S. K., Hopke, P. K., Jacobson, M. Z., Kaiser, J. W., Klimont, Z., Lohmann, U., Schwarz, J. P., Shindell, D., Storelvmo, T., Warren, S. G. and Zender, C. S.: Bounding the role of black carbon in the climate system: A scientific assessment, J. Geophys. Res. D: Atmos., 118(11), 5380–5552, 2013.

Boucher, O., Randall, D., Artaxo, P., Bretherton, C., Feingold, G., Forster, P., Kerminen, V.-M.,

Kondo, Y., Liao, H., Lohmann, U. and Others: Clouds and aerosols, in Climate change 2013: the physical science basis. Contribution of Working Group I to the Fifth Assessment Report of the Intergovernmental Panel on Climate Change, pp. 571–657, Cambridge University Press., 2013.

Brey, S. J., Barnes, E. A., Pierce, J. R., Wiedinmyer, C. and Fischer, E. V.: Environmental Conditions, Ignition Type, and Air Quality Impacts of Wildfires in the Southeastern and Western United States, Earths Future, 6(10), 1442–1456, 2018.

Briggs, N. L., Jaffe, D. A., Gao, H., Hee, J. R., Baylon, P. M., Zhang, Q., Zhou, S., Collier, S. C., Sampson, P. D. and Cary, R. A.: Particulate matter, ozone, and nitrogen species in aged wildfire plumes observed at the Mount Bachelor Observatory, Aerosol and Air Quality Research, 16(12) [online] Available from: https://www.osti.gov/biblio/1425944, 2016.

Brito, J., Rizzo, L. V., Morgan, W. T., Coe, H., Johnson, B., Haywood, J., Longo, K., Freitas, S., Andreae, M. O. and Artaxo, P.: Ground-based aerosol characterization during the South American Biomass Burning Analysis (SAMBBA) field experiment, Atmos. Chem. Phys., 14(22), 12069–12083, 2014.

Brown, S. S., Dibb, J. E., Stark, H., Aldener, M., Vozella, M., Whitlow, S., Williams, E. J., Lerner, B. M., Jakoubek, R., Middlebrook, A. M. and Others: Nighttime removal of NOx in the summer marine boundary layer, Geophys. Res. Lett., 31(7) [online] Available from: https://agupubs.onlinelibrary.wiley.com/doi/abs/10.1029/2004GL019412, 2004.

Bytnerowicz, A., Hsu, Y.-M., Percy, K., Legge, A., Fenn, M. E., Schilling, S., Frączek, W. and Alexander, D.: Ground-level air pollution changes during a boreal wildland mega-fire, Sci. Total Environ., 572, 755–769, 2016.

Cachier, H., Liousse, C., Buat-Menard, P. and Gaudichet, A.: Particulate content of savanna fire

emissions, J. Atmos. Chem., 22(1-2), 123–148, 1995.

Campbell, J., Donato, D., Azuma, D. and Law, B.: Pyrogenic carbon emission from a large wildfire in Oregon, United States, Journal of Geophysical Research: Biogeosciences, 112(G4) [online] Available from: https://agupubs.onlinelibrary.wiley.com/doi/abs/10.1029/2007JG000451, 2007.

Canagaratna, M. R., Jimenez, J. L., Kroll, J. H., Chen, Q., Kessler, S. H., Massoli, P., Hildebrandt Ruiz, L., Fortner, E., Williams, L. R., Wilson, K. R., Surratt, J. D., Donahue, N. M., Jayne, J. T. and Worsnop, D. R.: Elemental ratio measurements of organic compounds using aerosol mass spectrometry: characterization, improved calibration, and implications, Atmos. Chem. Phys., 15(1), 253–272, 2015.

Capes, G., Johnson, B., McFiggans, G., Williams, P. I., Haywood, J. and Coe, H.: Aging of biomass burning aerosols over West Africa: Aircraft measurements of chemical composition, microphysical properties, and emission ratios, J. Geophys. Res. D: Atmos., 113(D23) [online] Available from: https://agupubs.onlinelibrary.wiley.com/doi/abs/10.1029/2008JD009845%4010.1002/%28ISSN%292169-8996.DABEX1, 2008.

Cappa, C. D. and Jimenez, J. L.: Quantitative estimates of the volatility of ambient organic aerosol, Atmos. Chem. Phys., 10(12), 5409–5424, 2010.

Charlson, R. J., Schwartz, S. E., Hales, J. M., Cess, R. D., Coakley, J. A., Jr, Hansen, J. E. and Hofmann, D. J.: Climate forcing by anthropogenic aerosols, Science, 255(5043), 423–430, 1992.

Colarco, P. R., Schoeberl, M. R., Doddridge, B. G., Marufu, L. T., Torres, O. and Welton, E. J.: Transport of smoke from Canadian forest fires to the surface near Washington, DC:

Injection height, entrainment, and optical properties, J. Geophys. Res. D: Atmos., 109(D6) [online] Available from: https://agupubs.onlinelibrary.wiley.com/doi/abs/10.1029/2003JD004248, 2004.

Collier, S., Zhou, S., Onasch, T. B., Jaffe, D. A., Kleinman, L., Sedlacek, A. J., 3rd, Briggs, N. L., Hee, J., Fortner, E., Shilling, J. E., Worsnop, D., Yokelson, R. J., Parworth, C., Ge, X., Xu, J., Butterfield, Z., Chand, D., Dubey, M. K., Pekour, M. S., Springston, S. and Zhang, Q.: Regional Influence of Aerosol Emissions from Wildfires Driven by Combustion Efficiency: Insights from the BBOP Campaign, Environ. Sci. Technol., 50(16), 8613–8622, 2016.

Cubison, M. J., Ortega, A. M., Hayes, P. L., Farmer, D. K., Day, D., Lechner, M. J., Brune, W. H., Apel, E., Diskin, G. S., Fisher, J. A. and Others: Effects of aging on organic aerosol from open biomass burning smoke in aircraft and laboratory studies, Atmos. Chem. Phys., 11(23), 12049–12064, 2011.

Davies, G. M., Kettridge, N., Stoof, C. R., Gray, A., Ascoli, D., Fernandes, P. M., Marrs, R., Allen, K. A., Doerr, S. H., Clay, G. D., McMorrow, J. and Vandvik, V.: The role of fire in UK peatland and moorland management: the need for informed, unbiased debate, Philos. Trans. R. Soc. Lond. B Biol. Sci., 371(1696), doi:10.1098/rstb.2015.0342, 2016.

DeCarlo, P. F., Dunlea, E. J., Kimmel, J. R., Aiken, A. C., Sueper, D., Crounse, J., Wennberg, P. O., Emmons, L., Shinozuka, Y., Clarke, A., Zhou, J., Tomlinson, J., Collins, D. R., Knapp, D., Weinheimer, A. J., Montzka, D. D., Campos, T. and Jimenez, J. L.: Fast airborne aerosol size and chemistry measurements above Mexico City and Central Mexico during the MILAGRO campaign, Atmos. Chem. Phys., 8(14), 4027–4048, 2008.

DeCarlo, P. F., Ulbrich, I. M., Crounse, J., Foy, B. de, Dunlea, E. J., Aiken, A. C., Knapp, D.,

Weinheimer, A. J., Campos, T., Wennberg, P. O. and Others: Investigation of the sources and processing of organic aerosol over the Central Mexican Plateau from aircraft measurements during MILAGRO, Atmos. Chem. Phys., 10(12), 5257–5280, 2010.

Decker, Z. C. J., Zarzana, K. J. and Coggon, M.: Nighttime Chemical Transformation in Biomass Burning Plumes: A Box Model Analysis Initialized with Aircraft Observations, Sci. Technol. China [online] Available from: https://pubs.acs.org/doi/abs/10.1021/acs.est.8b05359, 2019.

Deming, B. L., Pagonis, D., Liu, X., Day, D. A., Talukdar, R., Krechmer, J. E., Gouw, J. A. de, Jimenez, J. L. and Ziemann, P. J.: Measurements of delays of gas-phase compounds in a wide variety of tubing materials due to gas–wall interactions, Atmospheric Measurement Techniques, 12(6), 3453–3461, 2019.

DeMott, P. J., Petters, M. D., Prenni, A. J., Carrico, C. M., Kreidenweis, S. M., Collett, J. L., Jr. and Moosmüller, H.: Ice nucleation behavior of biomass combustion particles at cirrus temperatures, J. Geophys. Res., 114(D16), 1770, 2009.

Donahue, N. M., Robinson, A. L., Stanier, C. O. and Pandis, S. N.: Coupled partitioning, dilution, and chemical aging of semivolatile organics, Environ. Sci. Technol., 40(8), 2635–2643, 2006.

Donahue, N. M., Robinson, A. L. and Pandis, S. N.: Atmospheric organic particulate matter: From smoke to secondary organic aerosol, Atmos. Environ., 43(1), 94–106, 2009.

Donahue, N. M., Trump, E. R., Pierce, J. R. and Riipinen, I.: Theoretical constraints on pure vapor-pressure driven condensation of organics to ultrafine particles, Geophys. Res. Lett., 38(16) [online] Available from: https://agupubs.onlinelibrary.wiley.com/doi/abs/10.1029/2011gl048115, 2011.

Dreessen, J., Sullivan, J. and Delgado, R.: Observations and impacts of transported Canadian wildfire smoke on ozone and aerosol air quality in the Maryland region on June 9–12, 2015, J. Air Waste Manage. Assoc., 66(9), 842–862, 2016.

Eatough, D. J., Eatough, N. L., Pang, Y., Sizemore, S., Kirchstetter, T. W., Novakov, T. and Hobbs, P. V.: Semivolatile particulate organic material in southern Africa during SAFARI 2000, J. Geophys. Res. D: Atmos., 108(D13) [online] Available from: https://agupubs.onlinelibrary.wiley.com/doi/abs/10.1029/2002JD002296%4010.1002/%28ISSN%292169-8996.SAF1, 2003.

Eluri, S., Cappa, C. D., Friedman, B., Farmer, D. K. and Jathar, S. H.: Modeling the formation and composition of secondary organic aerosol from diesel exhaust using parameterized and semi-explicit chemistry and thermodynamic models, Atmos. Chem. Phys., 18(19), 13813–13838, 2018.

Finney, M. A., Cohen, J. D., Forthofer, J. M., McAllister, S. S., Gollner, M. J., Gorham, D. J., Saito, K., Akafuah, N. K., Adam, B. A. and English, J. D.: Role of buoyant flame dynamics in wildfire spread, Proc. Natl. Acad. Sci. U. S. A., 112(32), 9833–9838, 2015.

Ford, B., Val Martin, M., Zelasky, S. E., Fischer, E. V., Anenberg, S. C., Heald, C. L. and Pierce, J. R.: Future Fire Impacts on Smoke Concentrations, Visibility, and Health in the Contiguous United States, GeoHealth, 2(8), 229–247, 2018.

Formenti, P., Elbert, W., Maenhaut, W., Haywood, J., Osborne, S. and Andreae, M. O.: Inorganic and carbonaceous aerosols during the Southern African Regional Science Initiative (SAFARI 2000) experiment: Chemical characteristics, physical properties, and emission data for smoke from African biomass burning, J. Geophys. Res. D: Atmos., 108(D13) [online] Available from:

https://agupubs.onlinelibrary.wiley.com/doi/abs/10.1029/2002JD002408, 2003.

Forrister, H., Liu, J., Scheuer, E., Dibb, J., Ziemba, L., Thornhill, K. L., Anderson, B., Diskin, G., Perring, A. E., Schwarz, J. P. and Others: Evolution of brown carbon in wildfire plumes, Geophys. Res. Lett., 42(11), 4623–4630, 2015.

Garofalo, L. A., Pothier, M. A., Levin, E. J. T., Campos, T., Kreidenweis, S. M. and Farmer, D. K.: Emission and Evolution of Submicron Organic Aerosol in Smoke from Wildfires in the Western United States, ACS Earth Space Chem., doi:10.1021/acsearthspacechem.9b00125, 2019.

Gilman, J. B., Lerner, B. M., Kuster, W. C., Goldan, P. D., Warneke, C., Veres, P. R., Roberts, J. M., Gouw, J. A. de, Burling, I. R. and Yokelson, R. J.: Biomass burning emissions and potential air quality impacts of volatile organic compounds and other trace gases from fuels common in the US, Atmos. Chem. Phys., 15(24), 13915–13938, 2015.

Goldstein, A. H. and Galbally, I. E.: Known and Unexplored Organic Constituents in the Earth's Atmosphere, Environ. Sci. Technol., 41(5), 1514–1521, 2007.

de Gouw, J. and Jimenez, J. L.: Organic aerosols in the Earth's atmosphere, Environ. Sci. Technol., 43(20), 7614–7618, 2009.

Grieshop, A. P., Donahue, N. M. and Robinson, A. L.: Laboratory investigation of photochemical oxidation of organic aerosol from wood fires 2: analysis of aerosol mass spectrometer data, Atmos. Chem. Phys., 9(6), 2227–2240, 2009.

Griffin, R. J., Chen, J., Carmody, K., Vutukuru, S. and Dabdub, D.: Contribution of gas phase oxidation of volatile organic compounds to atmospheric carbon monoxide levels in two areas of the United States, J. Geophys. Res. D: Atmos., 112(D10) [online] Available from: https://agupubs.onlinelibrary.wiley.com/doi/abs/10.1029/2006JD007602, 2007.

Hatch, L. E., Luo, W., Pankow, J. F., Yokelson, R. J., Stockwell, C. E. and Barsanti, K. C.: Identification and quantification of gaseous organic compounds emitted from biomass burning using two-dimensional gas chromatography--time-of-flight mass spectrometry, Atmos. Chem. Phys., 15(4), 1865–1899, 2015.

Hatch, L. E., Yokelson, R. J., Stockwell, C. E., Veres, P. R., Simpson, I. J., Blake, D. R., Orlando, J. J. and Barsanti, K. C.: Multi-instrument comparison and compilation of non-methane organic gas emissions from biomass burning and implications for smoke-derived secondary organic aerosol precursors, Atmos. Chem. Phys., 17(2), 1471–1489, 2017.

Hatch, L. E., Rivas-Ubach, A., Jen, C. N., Lipton, M., Goldstein, A. H. and Barsanti, K. C.: Measurements of I/SVOCs in biomass-burning smoke using solid-phase extraction disks and two-dimensional gas chromatography, Atmos. Chem. Phys., 18(24), 17801–17817, 2018.

Hayes, P. L., Carlton, A. G., Baker, K. R., Ahmadov, R., Washenfelder, R. A., Alvarez, S., Rappenglück, B., Gilman, J. B., Kuster, W. C., de Gouw, J. A., Zotter, P., Prévôt, A. S. H., Szidat, S., Kleindienst, T. E., Offenberg, J. H., Ma, P. K. and Jimenez, J. L.: Modeling the formation and aging of secondary organic aerosols in Los Angeles during CalNex 2010, Atmos. Chem. Phys., 15(10), 5773–5801, 2015.

Heald, C. L., Ridley, D. A., Kroll, J. H., Barrett, S. R. H., Cady-Pereira, K. E., Alvarado, M. J. and Holmes, C. D.: Contrasting the direct radiative effect and direct radiative forcing of aerosols, Atmos. Chem. Phys., 14(11), 5513–5527, 2014.

Hecobian, A., Liu, Z., Hennigan, C. J., Huey, L. G., Jimenez, J. L., Cubison, M. J., Vay, S., Diskin, G. S., Sachse, G. W., Wisthaler, A., Mikoviny, T., Weinheimer, A. J., Liao, J., Knapp, J., Wennberg, P. O., Kürten, A., Crounse, J. D., St. Clair, J., Wang, Y. and Weber, R. J.:

Comparison of chemical characteristics of 495 biomass burning plumes intercepted by the NASA DC-8 aircraft during the ARCTAS/CARB-2008 field campaign, Atmos. Chem. Phys., 11(24), 13325–13337, 2011.

Hennigan, C. J., Miracolo, M. A., Engelhart, G. J., May, A. A., Presto, A. A., Lee, T., Sullivan, A. P., McMeeking, G. R., Coe, H., Wold, C. E., Hao, W.-M., Gilman, J. B., Kuster, W. C., Gouw, J. de, Schichtel, B. A., Collett, J. L., Jr., Kreidenweis, S. M. and Robinson, A. L.: Chemical and physical transformations of organic aerosol from the photo-oxidation of open biomass burning emissions in an environmental chamber, Atmos. Chem. Phys., 11(15), 7669–7686, 2011.

Hobbs, P. V., Sinha, P., Yokelson, R. J., Christian, T. J., Blake, D. R., Gao, S., Kirchstetter, T. W., Novakov, T. and Pilewskie, P.: Evolution of gases and particles from a savanna fire in South Africa, J. Geophys. Res. D: Atmos., 108(D13) [online] Available from: https://agupubs.onlinelibrary.wiley.com/doi/abs/10.1029/2002JD002352%4010.1002/%28ISSN%292169-8996.SAF1, 2003.

Hodshire, A. L., Palm, B. B., Alexander, M. L., Bian, Q., Campuzano-Jost, P., Cross, E. S., Day, D. A., Sá, S. S. de, Guenther, A. B., Hansel, A., Hunter, J. F., Jud, W., Karl, T., Kim, S., Kroll, J. H., Park, J.-H., Peng, Z., Seco, R., Smith, J. N., Jimenez, J. L. and Pierce, J. R.: Constraining nucleation, condensation, and chemistry in oxidation flow reactors using size-distribution measurements and aerosol microphysical modeling, Atmos. Chem. Phys., 18(16), 12433–12460, 2018.

Hodshire, A. L., Bian, Q., Ramnarine, E., Lonsdale, C. R., Alvarado, M. J., Kreidenweis, S. M., Jathar, S. H. and Pierce, J. R.: More Than Emissions and Chemistry: Fire Size, Dilution, and Background Aerosol Also Greatly Influence Near-Field Biomass Burning Aerosol

Aging, J. Geophys. Res. D: Atmos., 30, 1783, 2019.

Huffman, J. A., Docherty, K. S., Mohr, C., Cubison, M. J., Ulbrich, I. M., Ziemann, P. J., Onasch, T. B. and Jimenez, J. L.: Chemically-Resolved Volatility Measurements of Organic Aerosol from Different Sources, Environ. Sci. Technol., 43(14), 5351–5357, 2009.

Jaffe, D. A. and Wigder, N. L.: Ozone production from wildfires: A critical review, Atmos. Environ., 51, 1–10, 2012.

Janssen, N. A. H. and Joint, W. H. O.: Health effects of black carbon, WHO Regional Office for Europe Copenhagen., 2012.

Jathar, S. H., Gordon, T. D., Hennigan, C. J., Pye, H. O. T., Pouliot, G., Adams, P. J., Donahue, N. M. and Robinson, A. L.: Unspeciated organic emissions from combustion sources and their influence on the secondary organic aerosol budget in the United States, Proc. Natl. Acad. Sci. U. S. A., 111(29), 10473–10478, 2014.

Jathar, S. H., Cappa, C. D., Wexler, A. S., Seinfeld, J. H. and Kleeman, M. J.: Multi-generational oxidation model to simulate secondary organic aerosol in a 3-D air quality model, Geoscientific Model Development; Katlenburg-Lindau, 8(8), 2553–2567, 2015.

Jen, C. N., Hatch, L. E., Selimovic, V., Yokelson, R. J., Weber, R., Fernandez, A. E., Kreisberg, N. M., Barsanti, K. C. and Goldstein, A. H.: Speciated and total emission factors of particulate organics from burning western US wildland fuels and their dependence on combustion efficiency, Atmos. Chem. Phys., 19(2), 1013–1026, 2019.

Jiang, X., Tsona, N. T., Jia, L., Liu, S., Xu, Y. and Du, L.: Secondary organic aerosol formation from photooxidation of furan: effects of NOx level and humidity, Atmos. Chem. Phys. Discuss., 2018, 1–27, 2018.

Jimenez, J. L., Canagaratna, M. R., Donahue, N. M., Prevot, A. S. H., Zhang, Q., Kroll, J. H.,

DeCarlo, P. F., Allan, J. D., Coe, H., Ng, N. L., Aiken, A. C., Docherty, K. S., Ulbrich, I. M., Grieshop, A. P., Robinson, A. L., Duplissy, J., Smith, J. D., Wilson, K. R., Lanz, V. A., Hueglin, C., Sun, Y. L., Tian, J., Laaksonen, A., Raatikainen, T., Rautiainen, J., Vaattovaara, P., Ehn, M., Kulmala, M., Tomlinson, J. M., Collins, D. R., Cubison, M. J., Dunlea, E. J., Huffman, J. A., Onasch, T. B., Alfarra, M. R., Williams, P. I., Bower, K., Kondo, Y., Schneider, J., Drewnick, F., Borrmann, S., Weimer, S., Demerjian, K., Salcedo, D., Cottrell, L., Griffin, R., Takami, A., Miyoshi, T., Hatakeyama, S., Shimono, A., Sun, J. Y., Zhang, Y. M., Dzepina, K., Kimmel, J. R., Sueper, D., Jayne, J. T., Herndon, S. C., Trimborn, A. M., Williams, L. R., Wood, E. C., Middlebrook, A. M., Kolb, C. E., Baltensperger, U. and Worsnop, D. R.: Evolution of organic aerosols in the atmosphere, Science, 326(5959), 1525–1529, 2009.

Johnston, F. H., Henderson, S. B., Chen, Y., Randerson, J. T., Marlier, M., Defries, R. S., Kinney, P., Bowman, D. M. J. S. and Brauer, M.: Estimated global mortality attributable to smoke from landscape fires, Environ. Health Perspect., 120(5), 695–701, 2012.

Jolleys, M. D., Coe, H., McFiggans, G., Capes, G., Allan, J. D., Crosier, J., Williams, P. I., Allen, G., Bower, K. N., Jimenez, J. L., Russell, L. M., Grutter, M. and Baumgardner, D.: Characterizing the aging of biomass burning organic aerosol by use of mixing ratios: a meta-analysis of four regions, Environ. Sci. Technol., 46(24), 13093–13102, 2012.

Jolleys, M. D., Coe, H., McFiggans, G., McMeeking, G. R., Lee, T., Kreidenweis, S. M., Collett, J. L., Jr and Sullivan, A. P.: Organic aerosol emission ratios from the laboratory combustion of biomass fuels, J. Geophys. Res. D: Atmos., 119(22), 12–850, 2014.

Jolleys, M. D., Coe, H., McFiggans, G., Taylor, J. W., O'Shea, S. J., Le Breton, M., Bauguitte, S. J.-B., Moller, S., Di Carlo, P., Aruffo, E., Palmer, P. I., Lee, J. D., Percival, C. J. and

Gallagher, M. W.: Properties and evolution of biomass burning organic aerosol from Canadian boreal forest fires, Atmos. Chem. Phys., 15(6), 3077–3095, 2015.

Kasischke, E. S. and Turetsky, M. R.: Recent changes in the fire regime across the North American boreal region—Spatial and temporal patterns of burning across Canada and Alaska, Geophys. Res. Lett., 33(9), 1996, 2006.

Konovalov, I. B., Beekmann, M., Berezin, E. V., Petetin, H., Mielonen, T., Kuznetsova, I. N. and Andreae, M. O.: The role of semi-volatile organic compounds in the mesoscale evolution of biomass burning aerosol: a modeling case study of the 2010 mega-fire event in Russia, Atmos. Chem. Phys., 15(23), 13269–13297, 2015.

Konovalov, I. B., Beekmann, M., Berezin, E. V., Formenti, P. and Andreae, M. O.: Probing into the aging dynamics of biomass burning aerosol by using satellite measurements of aerosol optical depth and carbon monoxide, Atmos. Chem. Phys., 17(7), 4513–4537, 2017.

Koplitz, S. N., Nolte, C. G., Pouliot, G. A., Vukovich, J. M. and Beidler, J.: Influence of uncertainties in burned area estimates on modeled wildland fire PM2.5 and ozone pollution in the contiguous U.S, Atmos. Environ., 191, 328–339, 2018.

Koss, A. R., Sekimoto, K., Gilman, J. B., Selimovic, V., Coggon, M. M., Zarzana, K. J., Yuan, B., Lerner, B. M., Brown, S. S., Jimenez, J. L., Krechmer, J., Roberts, J. M., Warneke, C., Yokelson, R. J. and Gouw, J. de: Non-methane organic gas emissions from biomass burning: identification, quantification, and emission factors from PTR-ToF during the FIREX 2016 laboratory experiment, Atmos. Chem. Phys., 18(5), 3299–3319, 2018.

Krechmer, J. E., Pagonis, D., Ziemann, P. J. and Jimenez, J. L.: Quantification of Gas-Wall Partitioning in Teflon Environmental Chambers Using Rapid Bursts of Low-Volatility Oxidized Species Generated in Situ, Environ. Sci. Technol., 50(11), 5757–5765, 2016.

Kroll, J. H., Smith, J. D., Che, D. L., Kessler, S. H., Worsnop, D. R. and Wilson, K. R.: Measurement of fragmentation and functionalization pathways in the heterogeneous oxidation of oxidized organic aerosol, Phys. Chem. Chem. Phys., 11(36), 8005–8014, 2009.

Kroll, J. H., Donahue, N. M., Jimenez, J. L., Kessler, S. H., Canagaratna, M. R., Wilson, K. R., Altieri, K. E., Mazzoleni, L. R., Wozniak, A. S., Bluhm, H., Mysak, E. R., Smith, J. D., Kolb, C. E. and Worsnop, D. R.: Carbon oxidation state as a metric for describing the chemistry of atmospheric organic aerosol, Nat. Chem., 3(2), 133–139, 2011.

Lambe, A. T., Ahern, A. T., Williams, L. R., Slowik, J. G., Wong, J. P. S., Abbatt, J. P. D., Brune, W. H., Ng, N. L., Wright, J. P., Croasdale, D. R. and Others: Characterization of aerosol photooxidation flow reactors: heterogeneous oxidation, secondary organic aerosol formation and cloud condensation nuclei activity measurements, Atmospheric Measurement Techniques, 4(3), 445–461, 2011.

Landis, M. S., Edgerton, E. S., White, E. M., Wentworth, G. R., Sullivan, A. P. and Dillner, A. M.: The impact of the 2016 Fort McMurray Horse River Wildfire on ambient air pollution levels in the Athabasca Oil Sands Region, Alberta, Canada, Sci. Total Environ., 618, 1665–1676, 2018.

Lassman, W., Ford, B., Gan, R. W., Pfister, G., Magzamen, S., Fischer, E. V. and Pierce, J. R.: Spatial and temporal estimates of population exposure to wildfire smoke during the Washington state 2012 wildfire season using blended model, satellite, and in situ data: Multimethod Estimates of Smoke Exposure, GeoHealth, 1(3), 106–121, 2017.

Lee, T., Sullivan, A. P., Mack, L., Jimenez, J. L., Kreidenweis, S. M., Onasch, T. B., Worsnop, D. R., Malm, W., Wold, C. E., Hao, W. M. and Collett, J. L.: Chemical Smoke Marker

Emissions During Flaming and Smoldering Phases of Laboratory Open Burning of Wildland Fuels, Aerosol Sci. Technol., 44(9), i–v, 2010.

Lei, W., Li, G. and Molina, L. T.: Modeling the impacts of biomass burning on air quality in and around Mexico City, Atmos. Chem. Phys., 13(5), 2299–2319, 2013.

Lewis, K. A., Arnott, W. P., Moosmüller, H., Chakrabarty, R. K., Carrico, C. M., Kreidenweis, S. M., Day, D. E., Malm, W. C., Laskin, A., Jimenez, J. L. and Others: Reduction in biomass burning aerosol light absorption upon humidification: roles of inorganically-induced hygroscopicity, particle collapse, and photoacoustic heat and mass transfer, Atmos. Chem. Phys., 9(22), 8949–8966, 2009.

Lindaas, J., Farmer, D. K., Pollack, I. B., Abeleira, A., Flocke, F., Roscioli, R., Herndon, S. and Fischer, E. V.: Changes in ozone and precursors during two aged wildfire smoke events in the Colorado Front Range in summer 2015, Atmos. Chem. Phys., 17(17), 10691–10707, 2017.

Liousse, C., Devaux, C., Dulac, F. and Cachier, H.: Aging of savanna biomass burning aerosols: Consequences on their optical properties, J. Atmos. Chem., 22(1), 1–17, 1995.

Liu, J. C., Mickley, L. J., Sulprizio, M. P., Dominici, F., Yue, X., Ebisu, K., Anderson, G. B., Khan, R. F. A., Bravo, M. A. and Bell, M. L.: Particulate Air Pollution from Wildfires in the Western US under Climate Change, Clim. Change, 138(3), 655–666, 2016a.

Liu, X., Zhang, Y., Huey, L. G., Yokelson, R. J., Wang, Y., Jimenez, J. L., Campuzano-Jost, P., Beyersdorf, A. J., Blake, D. R., Choi, Y. and Others: Agricultural fires in the southeastern US during SEAC4RS: Emissions of trace gases and particles and evolution of ozone, reactive nitrogen, and organic aerosol, J. Geophys. Res. D: Atmos., 121(12), 7383–7414, 2016b.

Liu, X., Huey, L. G., Yokelson, R. J., Selimovic, V., Simpson, I. J., Müller, M., Jimenez, J. L., Campuzano-Jost, P., Beyersdorf, A. J., Blake, D. R. and Others: Airborne measurements of western US wildfire emissions: Comparison with prescribed burning and air quality implications, J. Geophys. Res. D: Atmos., 122(11), 6108–6129, 2017.

Liu, X., Deming, B., Pagonis, D., Day, D. A., Palm, B. B., Talukdar, R., Roberts, J. M., Veres, P. R., Krechmer, J. E., Thornton, J. A., Gouw, J. A. de, Ziemann, P. J. and Jimenez, J. L.: Effects of gas–wall interactions on measurements of semivolatile compounds and small polar molecules, Atmospheric Measurement Techniques, 12(6), 3137–3149, 2019.

Lopez-Hilfiker, F. D., Pospisilova, V., Huang, W., Kalberer, M., Stefenelli, G., Thornton, J. A., Baltensperger, U., Prevot, A. S. H. and Slowik, J. G.: An Extractive Electrospray Ionization Time-of-Flight Mass Spectrometer (EESI-TOF) for online measurement of atmospheric aerosol particles, Atmospheric Measurement Techniques Discussions, doi:10.5194/amt-2019-45, 2019.

Mallia, D. V., Lin, J. C., Urbanski, S., Ehleringer, J. and Nehrkorn, T.: Impacts of upwind wildfire emissions on CO, CO2, and PM2. 5 concentrations in Salt Lake City, Utah, J. Geophys. Res. D: Atmos., 120(1), 147–166, 2015.

Martin, M. V., Honrath, R. E., Owen, R. C., Pfister, G., Fialho, P. and Barata, F.: Significant enhancements of nitrogen oxides, black carbon, and ozone in the North Atlantic lower free troposphere resulting from North American boreal wildfires, J. Geophys. Res. D: Atmos., 111(D23) [online] Available from: https://agupubs.onlinelibrary.wiley.com/doi/abs/10.1029/2006JD007530%4010.1002/%28ISSN%292169-8996.INCARTTNA1, 2006.

Martin, S. T., Artaxo, P. and Machado, L. A. T.: Introduction: Observations and modeling of the

green ocean Amazon (GoAmazon2014/5), Atmospheric [online] Available from: https://scholar.colorado.edu/chem_facpapers/68/, 2016.

May, A. A., Levin, E. J. T., Hennigan, C. J., Riipinen, I., Lee, T., Collett, J. L., Jimenez, J. L., Kreidenweis, S. M. and Robinson, A. L.: Gas-particle partitioning of primary organic aerosol emissions: 3. Biomass burning, J. Geophys. Res. D: Atmos., 118(19) [online] Available from: http://onlinelibrary.wiley.com/doi/10.1002/jgrd.50828/full, 2013.

May, A. A., Lee, T., McMeeking, G. R., Akagi, S., Sullivan, A. P., Urbanski, S., Yokelson, R. J. and Kreidenweis, S. M.: Observations and analysis of organic aerosol evolution in some prescribed fire smoke plumes, Atmos. Chem. Phys., 15(11), 6323–6335, 2015.

McClure, C. D. and Jaffe, D. A.: US particulate matter air quality improves except in wildfire-prone areas, Proc. Natl. Acad. Sci. U. S. A., 115(31), 7901–7906, 2018.

Mebust, A. K. and Cohen, R. C.: Observations of a seasonal cycle in NOx emissions from fires in African woody savannas, Geophys. Res. Lett. [online] Available from: https://agupubs.onlinelibrary.wiley.com/doi/abs/10.1002/grl.50343, 2013.

Morgan, W. T., Allan, J. D., Bauguitte, S., Darbyshire, E., Flynn, M. J., Lee, J., Liu, D., Johnson, B., Haywood, J., Longo, K. M., Artaxo, P. E. and Coe, H.: Transformation and aging of biomass burning carbonaceous aerosol over tropical South America from aircraft in-situ measurements during SAMBBA, Atmospheric Chemistry and Physics Discussions, 1–32, doi:10.5194/acp-2019-157, 2019.

Murphy, B. N., Donahue, N. M., Robinson, A. L. and Pandis, S. N.: A naming convention for atmospheric organic aerosol, Atmos. Chem. Phys., 14(11), 5825–5839, 2014.

Naeher, L. P., Brauer, M., Lipsett, M. and Zelikoff, J. T.: Woodsmoke health effects: a review, Inhal. Toxicol. [online] Available from:

https://www.tandfonline.com/doi/abs/10.1080/08958370600985875, 2007.

Nance, J. D., Hobbs, P. V., Radke, L. F. and Ward, D. E.: Airborne measurements of gases and particles from an Alaskan wildfire, J. Geophys. Res., 98(D8), 14873, 1993.

Nault, B. A., Campuzano-Jost, P., Day, D. A., Schroder, J. C., Anderson, B., Beyersdorf, A. J., Blake, D. R., Brune, W. H., Choi, Y., Corr, C. A., Gouw, J. A. de, Dibb, J., DiGangi, J. P., Diskin, G. S., Fried, A., Huey, L. G., Kim, M. J., Knote, C. J., Lamb, K. D., Lee, T., Park, T., Pusede, S. E., Scheuer, E., Thornhill, K. L., Woo, J.-H. and Jimenez, J. L.: Secondary organic aerosol production from local emissions dominates the organic aerosol budget over Seoul, South Korea, during KORUS-AQ, Atmos. Chem. Phys., 18(24), 17769–17800, 2018.

Nie, W., Ding, A. J., Xie, Y. N., Xu, Z., Mao, H., Kerminen, V.-M., Zheng, L. F., Qi, X. M., Huang, X., Yang, X.-Q., Sun, J. N., Herrmann, E., Petäjä, T., Kulmala, M. and Fu, C. B.: Influence of biomass burning plumes on HONO chemistry in eastern China, Atmos. Chem. Phys., 15(3), 1147–1159, 2015.

O'Dell, K., Ford, B., Fischer, E. V. and Pierce, J. R.: Contribution of Wildland-Fire Smoke to US PM2.5 and Its Influence on Recent Trends, Environ. Sci. Technol., 53(4), 1797–1804, 2019.

Odum, J. R., Hoffmann, T., Bowman, F., Collins, D., Flagan, R. C. and Seinfeld, J. H.: Gas/Particle Partitioning and Secondary Organic Aerosol Yields, Environ. Sci. Technol., 30(8), 2580–2585, 1996.

Ortega, A. M., Day, D. A., Cubison, M. J., Brune, W. H., Bon, D., De Gouw, J. A. and Jimenez, J. L.: Secondary organic aerosol formation and primary organic aerosol oxidation from biomass-burning smoke in a flow reactor during FLAME-3, Atmos. Chem. Phys., 13(22),

11551–11571, 2013.

Pagonis, D., Krechmer, J. E., de Gouw, J., Jimenez, J. L. and Ziemann, P. J.: Effects of gas–wall partitioning in Teflon tubing and instrumentation on time-resolved measurements of gas-phase organic compounds, Atmospheric Measurement Techniques; Katlenburg-Lindau, 10(12), 4687–4696, 2017.

Palm, B. B., Campuzano-Jost, P., Ortega, A. M., Day, D. A., Kaser, L., Jud, W., Karl, T., Hansel, A., Hunter, J. F., Cross, E. S., Kroll, J. H., Peng, Z., Brune, W. H. and Jimenez, J. L.: In situ secondary organic aerosol formation from ambient pine forest air using an oxidation flow reactor, Atmos. Chem. Phys., 16(5), 2943–2970, 2016.

Pankow, J. F.: An absorption model of gas/particle partitioning of organic compounds in the atmosphere, Atmos. Environ., 28(2), 185–188, 1994.

Petters, M. D. and Kreidenweis, S. M.: A single parameter representation of hygroscopic growth and cloud condensation nucleus activity, Atmos. Chem. Phys., 7(8), 1961–1971, 2007.

Petters, M. D., Carrico, C. M., Kreidenweis, S. M., Prenni, A. J., DeMott, P. J., Collett, J. L., Jr and Moosmüller, H.: Cloud condensation nucleation activity of biomass burning aerosol, J. Geophys. Res. D: Atmos., 114(D22) [online] Available from: https://agupubs.onlinelibrary.wiley.com/doi/abs/10.1029/2009JD012353, 2009.

Pósfai, M., Gelencsér, A., Simonics, R., Arató, K., Li, J., Hobbs, P. V. and Buseck, P. R.: Atmospheric tar balls: Particles from biomass and biofuel burning, J. Geophys. Res., 109(D6), doi:10.1029/2003JD004169, 2004.

Pratap, V., Bian, Q., Kiran, S. A., Hopke, P. K., Pierce, J. R. and Nakao, S.: Investigation of levoglucosan decay in wood smoke smog-chamber experiments: The importance of aerosol loading, temperature, and vapor wall losses in interpreting results, Atmos. Environ., 199,

224–232, 2019.

Ramnarine, E., Kodros, J. K., Hodshire, A. L., Lonsdale, C. R., Alvarado, M. J. and Pierce, J. R.: Effects of near-source coagulation of biomass burning aerosols on global predictions of aerosol size distributions and implications for aerosol radiative effects, Atmos. Chem. Phys., 19(9), 6561–6577, 2019.

Randerson, J. T., Chen, Y., van der Werf, G. R., Rogers, B. M. and Morton, D. C.: Global burned area and biomass burning emissions from small fires: BURNED AREA FROM SMALL FIRES, J. Geophys. Res., 117(G4), doi:10.1029/2012JG002128, 2012.

Reddington, C. L., Spracklen, D. V., Artaxo, P., Ridley, D. A., Rizzo, L. V. and Arana, A.: Analysis of particulate emissions from tropical biomass burning using a global aerosol model and long-term surface observations, Atmos. Chem. Phys., 16(17), 11083–11106, 2016.

Reid, J. S., Hobbs, P. V., Ferek, R. J., Blake, D. R., Martins, J. V., Dunlap, M. R. and Liousse, C.: Physical, chemical, and optical properties of regional hazes dominated by smoke in Brazil, J. Geophys. Res., 103(D24), 32059–32080, 1998.

Reid, J. S., Koppmann, R., Eck, T. F. and Eleuterio, D. P.: A review of biomass burning emissions part II: intensive physical properties of biomass burning particles, Atmos. Chem. Phys., 5(3), 799–825, 2005.

Riipinen, I., Pierce, J. R., Donahue, N. M. and Pandis, S. N.: Equilibration time scales of organic aerosol inside thermodenuders: Evaporation kinetics versus thermodynamics, Atmos. Environ., 44(5), 597–607, 2010.

Roberts, J. M., Veres, P. R. and Cochran, A. K.: Isocyanic acid in the atmosphere and its possible link to smoke-related health effects, Proceedings of the [online] Available from:

https://www.pnas.org/content/108/22/8966.short, 2011.

Sakamoto, K. M., Allan, J. D., Coe, H., Taylor, J. W., Duck, T. J. and Pierce, J. R.: Aged boreal biomass-burning aerosol size distributions from BORTAS 2011, Atmos. Chem. Phys., 15(4), 1633–1646, 2015.

Sakamoto, K. M., Laing, J. R., Stevens, R. G., Jaffe, D. A. and Pierce, J. R.: The evolution of biomass-burning aerosol size distributions due to coagulation: dependence on fire and meteorological details and parameterization, Atmos. Chem. Phys., 16(12), 7709–7724, 2016.

Samburova, V., Connolly, J., Gyawali, M., Yatavelli, R. L. N., Watts, A. C., Chakrabarty, R. K., Zielinska, B., Moosmüller, H. and Khlystov, A.: Polycyclic aromatic hydrocarbons in biomass-burning emissions and their contribution to light absorption and aerosol toxicity, Sci. Total Environ., 568, 391–401, 2016.

Santín, C., Doerr, S. H., Preston, C. M. and González-Rodríguez, G.: Pyrogenic organic matter production from wildfires: a missing sink in the global carbon cycle, Glob. Chang. Biol., 21(4), 1621–1633, 2015.

Scott, A. C. and Glasspool, I. J.: The diversification of Paleozoic fire systems and fluctuations in atmospheric oxygen concentration, Proc. Natl. Acad. Sci. U. S. A., 103(29), 10861–10865, 2006.

Sedlacek, A. J., III, Buseck, P. R., Adachi, K., Onasch, T. B., Springston, S. R. and Kleinman, L.: Formation and evolution of tar balls from northwestern US wildfires, Atmos. Chem. Phys., 18(15), 11289–11301, 2018.

Seinfeld, J. H. and Pandis, S. N.: Atmospheric Chemistry and Physics: From Air Pollution to Climate Change, John Wiley & Sons., 2016.

Sekimoto, K., Koss, A. R., Gilman, J. B., Selimovic, V., Coggon, M. M., Zarzana, K. J., Yuan, B., Lerner, B. M., Brown, S. S., Warneke, C., Yokelson, R. J., Roberts, J. M. and de Gouw, J. A.: High- and low-temperature pyrolysis profiles describe volatile organic compound emissions from western US wildfire fuels, Atmos. Chem. Phys., 18(13), doi:10.5194/acp-18-9263-2018, 2018.

Selimovic, V., Yokelson, R. J., Warneke, C., Roberts, J. M., Gouw, J. de, Reardon, J. and Griffith, D. W. T.: Aerosol optical properties and trace gas emissions by PAX and OP-FTIR for laboratory-simulated western US wildfires during FIREX, Atmos. Chem. Phys., 18(4), 2929–2948, 2018.

Shiraiwa, M. and Seinfeld, J. H.: Equilibration timescale of atmospheric secondary organic aerosol partitioning, Geophys. Res. Lett., 39(24), doi:10.1029/2012GL054008, 2012.

Shiraiwa, M., Berkemeier, T., Schilling-Fahnestock, K. A., Seinfeld, J. H. and Pöschl, U.: Molecular corridors and kinetic regimes in the multiphase chemical evolution of secondary organic aerosol, Atmos. Chem. Phys., 14(16), 8323–8341, 2014.

Shrivastava, M., Easter, R. C., Liu, X., Zelenyuk, A., Singh, B., Zhang, K., Ma, P.-L., Chand, D., Ghan, S., Jimenez, J. L. and Others: Global transformation and fate of SOA: Implications of low-volatility SOA and gas-phase fragmentation reactions, J. Geophys. Res. D: Atmos., 120(9), 4169–4195, 2015.

Smith, J. D., Kroll, J. H., Cappa, C. D., Che, D. L., Liu, C. L., Ahmed, M., Leone, S. R., Worsnop, D. R. and Wilson, K. R.: The heterogeneous reaction of hydroxyl radicals with sub-micron squalane particles: a model system for understanding the oxidative aging of ambient aerosols, Atmos. Chem. Phys., 9(9), 3209–3222, 2009.

Stefenelli, G., Jiang, J., Bertrand, A., Bruns, E. A., Pieber, S. M., Baltensperger, U., Marchand,

N., Aksoyoglu, S., Prévôt, A. S. H., Slowik, J. G. and El Haddad, I.: Secondary organic aerosol formation from smoldering and flaming combustion of biomass: a box model parametrization based on volatility basis set, Atmospheric Chemistry and Physics Discussions, 1–41, doi:10.5194/acp-2018-1308, 2019.

Stockwell, C. E., Yokelson, R., Kreidenweis, S. M., Robinson, A. L., DeMott, P. J., Sullivan, R. C., Reardon, J., Ryan, K. C., Griffith, D. W. T. and Stevens, L.: Trace gas emissions from combustion of peat, crop residue, domestic biofuels, grasses, and other fuels: configuration and Fourier transform infrared (FTIR) component of the fourth Fire Lab at Missoula Experiment (FLAME-4), [online] Available from: https://ro.uow.edu.au/smhpapers/2312/, 2014.

Stockwell, C. E., Veres, P. R., Williams, J. and Yokelson, R. J.: Characterization of biomass burning emissions from cooking fires, peat, crop residue, and other fuels with high-resolution proton-transfer-reaction time-of-flight mass spectrometry, Atmos. Chem. Phys., 15(2), 845–865, 2015.

Sullivan, A. P., May, A. A., Lee, T., McMeeking, G. R., Kreidenweis, S. M., Akagi, S. K., Yokelson, R. J., Urbanski, S. P. and Collett, J. L., Jr: Airborne characterization of smoke marker ratios from prescribed burning, Atmos. Chem. Phys., 14(19), 10535–10545, 2014.

Tkacik, D. S., Robinson, E. S., Ahern, A., Saleh, R., Stockwell, C., Veres, P., Simpson, I. J., Meinardi, S., Blake, D. R., Yokelson, R. J., Presto, A. A., Sullivan, R. C., Donahue, N. M. and Robinson, A. L.: A dual-chamber method for quantifying the effects of atmospheric perturbations on secondary organic aerosol formation from biomass burning emissions: Investigation of Biomass Burning SOA, J. Geophys. Res. D: Atmos., 122(11), 6043–6058, 2017.

Twomey, S.: Pollution and the Planetary Albedo, Atmos. Environ., 41, 120–125, 2007.

Vakkari, V., Kerminen, V.-M., Beukes, J. P., Tiitta, P., van Zyl, P. G., Josipovic, M., Venter, A. D., Jaars, K., Worsnop, D. R., Kulmala, M. and Others: Rapid changes in biomass burning aerosols by atmospheric oxidation, Geophys. Res. Lett., 41(7), 2644–2651, 2014.

Vakkari, V., Beukes, J. P., Dal Maso, M., Aurela, M., Josipovic, M. and van Zyl, P. G.: Major secondary aerosol formation in southern African open biomass burning plumes, Nat. Geosci., 11(8), 580–583, 2018.

Van der Werf, G. R., Randerson, J. T., Giglio, L., Collatz, G. J., Mu, M., Kasibhatla, P. S., Morton, D. C., DeFries, R. S., van Jin, Y. and van Leeuwen, T. T.: Global fire emissions and the contribution of deforestation, savanna, forest, agricultural, and peat fires (1997--2009), Atmos. Chem. Phys., 10(23), 11707–11735, 2010.

Volkamer, R., Jimenez, J. L., San Martini, F., Dzepina, K., Zhang, Q., Salcedo, D., Molina, L. T., Worsnop, D. R. and Molina, M. J.: Secondary organic aerosol formation from anthropogenic air pollution: Rapid and higher than expected, Geophys. Res. Lett., 33(17), 4407, 2006.

Voulgarakis, A. and Field, R. D.: Fire Influences on Atmospheric Composition, Air Quality and Climate, Current Pollution Reports, 1(2), 70–81, 2015.

Voulgarakis, A., Marlier, M. E., Faluvegi, G., Shindell, D. T., Tsigaridis, K. and Mangeon, S.: Interannual variability of tropospheric trace gases and aerosols: The role of biomass burning emissions, J. Geophys. Res. D: Atmos., 120(14), 7157–7173, 2015.

Weitkamp, E. A., Sage, A. M., Pierce, J. R., Donahue, N. M. and Robinson, A. L.: Organic aerosol formation from photochemical oxidation of diesel exhaust in a smog chamber, Environ. Sci. Technol., 41(20), 6969–6975, 2007.

Westerling, A. L.: Increasing western US forest wildfire activity: sensitivity to changes in the timing of spring, Philos. Trans. R. Soc. Lond. B Biol. Sci., 371(1696), doi:10.1098/rstb.2015.0178, 2016.

Xie, Y., Ding, A., Nie, W., Mao, H., Qi, X., Huang, X., Xu, Z., Kerminen, V.-M., Petäjä, T., Chi, X., Virkkula, A., Boy, M., Xue, L., Guo, J., Sun, J., Yang, X., Kulmala, M. and Fu, C.: Enhanced sulfate formation by nitrogen dioxide: Implications from in situ observations at the SORPES station, J. Geophys. Res. D: Atmos., 120(24), 12679–12694, 2015.

Yokelson, R. J., Griffith, D. W. T. and Ward, D. E.: Open-path Fourier transform infrared studies of large-scale laboratory biomass fires, J. Geophys. Res. D: Atmos., 101(D15), 21067–21080, 1996.

Yokelson, R. J., Crounse, J. D., DeCarlo, P. F., Karl, T., Urbanski, S., Atlas, E, Campos, T., Shinozuka, Y., Kapustin, V., Clarke, A. D., Weinheimer, A., Knapp, D. J., Montzka, D. D., Holloway, J., Weibring, P., Flocke, F., Zheng, W., Toohey, D., Wennberg, P. O., Wiedinmyer, C., Mauldin, L., Fried, A., Richter, D., Walega, J., Jimenez, J. L., Adachi, K., Buseck, P. R., Hall, S. R. and Shetter, R.: Emissions from biomass burning in the Yucatan, Atmos. Chem. Phys., 9(15), 5785–5812, 2009.

Yokelson, R. J., Burling, I. R., Urbanski, S. P., Atlas, E. L, Adachi, K., Buseck, P. R., Wiedinmyer, C., Akagi, S. K., Toohey, D. W. and Wold, C. E.: Trace gas and particle emissions from open biomass burning in Mexico, Atmos. Chem. Phys., 11(14), 6787–6808, 2011.

Yokelson, R. J., Burling, I. R., Gilman, J. B., Warneke, C., Stockwell, C. E., Gouw, J. de, Akagi, S. K., Urbanski, S. P., Veres, P., Roberts, J. M. and Others: Coupling field and laboratory measurements to estimate the emission factors of identified and unidentified trace gases for prescribed fires, Atmos. Chem. Phys., 13(1), 89–116, 2013.

Yue, X., Mickley, L. J., Logan, J. A. and Kaplan, J. O.: Ensemble projections of wildfire activity and carbonaceous aerosol concentrations over the western United States in the mid-21st century, Atmos. Environ. , 77, 767–780, 2013.

Zaveri, R. A., Easter, R. C., Shilling, J. E. and Seinfeld, J. H.: Modeling kinetic partitioning of secondary organic aerosol and size distribution dynamics: representing effects of volatility, phase state, and particle-phase reaction, Atmos. Chem. Phys., 14(10), 5153–5181, 2014.

Zhang, X., Cappa, C. D., Jathar, S. H., McVay, R. C., Ensberg, J. J., Kleeman, M. J. and Seinfeld, J. H.: Influence of vapor wall loss in laboratory chambers on yields of secondary organic aerosol, Proc. Natl. Acad. Sci. U. S. A., 111(16), 5802–5807, 2014.

Zhang, Y., Tao, S., Shen, H. and Ma, J.: Inhalation exposure to ambient polycyclic aromatic hydrocarbons and lung cancer risk of Chinese population, Proc. Natl. Acad. Sci. U. S. A., 106(50), 21063–21067, 2009.

Zhou, S., Collier, S., Jaffe, D. A., Briggs, N. L., Hee, J., Sedlacek, A. J., III, Kleinman, L., Onasch, T. B. and Zhang, Q.: Regional influence of wildfires on aerosol chemistry in the western US and insights into atmospheric aging of biomass burning organic aerosol, Atmos. Chem. Phys., 17(3), 2477–2493, 2017.

CHAPTER 5

MORE THAN EMISSIONS AND CHEMISTRY: FIRE SIZE, DILUTION, AND BACKGROUND AEROSOL ALSO GREATLY INFLUENCE NEAR-FIELD BIOMASS BURNING AEROSOL AGING[4]

Overview

Biomass burning emits particles (black carbon and primary organic aerosol; POA) and precursor vapors to the atmosphere that chemically and physically age in the atmosphere. This theoretical study explores the relationships between fire size (determining the initial plume width and concentration), dilution rate, and entrainment of background aerosol on particle coagulation, OA evaporation, and secondary organic aerosol (SOA) condensation in smoke plumes. We examine the impacts of these processes on aged smoke OA mass, geometric mean diameter (D_g), peak lognormal modal width (σ_g), particle extinction (E), and cloud condensation nuclei (CCN) concentrations. In our simulations, aging OA mass is controlled by competition between OA evaporation and SOA condensation. Large, slowly diluting plumes evaporate little in our base set of simulations, which may allow for net increases in mass, E, CCN, and D_g from SOA condensation. Smaller, quickly diluting fire plumes lead to faster evaporation, which favors decreases in mass, E, CCN, and D_g. However, the SOA fraction of the smoke OA increases more rapidly in smaller fires due to faster POA evaporation leading to more SOA precursors. Net mass changes for smaller fires depend on background OA concentrations; increasing background aerosol concentrations decrease evaporation rates. Although coagulation does not change mass, it

[4] This Chapter published as: Hodshire, A. L., Bian, Q., Ramnarine, E., Lonsdale, C. R., Alvarado, M. J., Kreidenweis, S. M., Jathar, S. H. and Pierce, J. R.: More than emissions and chemistry: Fire size, dilution, and background aerosol also greatly influence near-field biomass burning aerosol aging, J. Geophys. Res. Atmos., 2018JD029674, doi:10.1029/2018JD029674, 2019.

can decrease the number of particles in large/slowly diluting plumes, increasing D_g and E, and decreasing σ_g. While our conclusions are limited by being a theoretical study, we hope they help motivate future smoke-plume analyses to consider the effects of fire size, meteorology, and background OA concentrations.

5.1 Introduction

Biomass burning smoke is a significant source of primary and secondary atmospheric particles that have impacts on climate (Bond et al., 2013), air quality (e.g. Jaffe and Widger, 2012; Nie et al., 2015; Xie et al., 2015), and health (e.g. Jassen et al., 2012; Johnston et al., 2012; Naeher et al., 2007; Zhang et al., 2009). Biomass burning emits primary carbonaceous aerosol (both as black carbon and primary organic aerosol; POA) (Akagi et al., 2011; Reid et al., 2005a and references therein), inorganic aerosol, and vapors, where some vapors may serve as aerosol precursors (e.g. Alvarado and Pimm, 2009; Bertrand et al., 2018; Hatch et al., 2017; Jen et al., 2018). Biomass burning particle emissions are dominated by an accumulation mode, with a less-concentrated coarse mode and occasionally a nucleation mode (Reid et al., 2005a). Although the coarse mode is comprised mainly of dust, ash, unburned fuel, and carbon aggregates (Formenti et al., 2003; Gaudichet et al., 1995; Hungershoefer et al., 2008), the accumulation mode is comprised mainly of organic material, with black carbon and inorganic species (such as potassium, chlorine, calcium, and sulfate) making up ~10% each of the remaining fraction, depending on the fuel (Bian et al., 2015; Reid et al., 2005a).

Both the POA and vapors evolve as the initial smoke plume dilutes, entrains background air, and undergoes oxidative aging along with aerosol microphysical processes such as evaporation, condensation, coagulation, and deposition (e.g. Akagi et al., 2012; Alvarado et al., 2015; Hecobian et al., 2011; Sakamoto et al., 2016, Vakkari et al., 2014). Each of these processes

help shape the aerosol mass and number size distributions. Understanding the bulk mass evolution of biomass burning aerosols is important from a regulatory and health standpoint and allows for an estimate of their direct radiative effect (DRE) on the Earth's energy balance (Charlson et al., 1992, Heald et al., 2014). Understanding the number size distribution evolution of biomass burning aerosols further allows for a more precise understanding of their DRE and provides an estimate of their indirect effect on the earth's radiative budget through altering cloud properties (e.g., the cloud-albedo aerosol indirect effect [AIE]; Boucher et al., 2013). Further, particle size influences the lung-deposition efficiency and hence may impact health (Hussein et al., 2013; Löndahl et al., 2007; 2009).

The DRE of particles depends, in part, on their relative amounts of scattering and absorption in the atmosphere. The sum of scattering and absorption is given as the particles' extinction (Seinfeld & Pandis, 2006). The mass extinction efficiency is the ratio of the extinction of the particle to the particle's mass; similarly, the mass scattering and absorption efficiencies are the ratios of each particle's scattering and absorption to its mass. Peak mass extinction (or scattering/absorption) efficiencies typically occur for particles between 100 nm to 1 μm in diameter (D_p). The AIE is determined by cloud condensation nuclei (CCN) properties and concentrations: particles that become cloud condensation nuclei (CCN) can alter cloud reflectivity (albedo) by changing the cloud droplet number concentration (CDNC) (Twomey, 1974). The ability of a particle to act as a CCN depends both on its size and hygroscopicity (Petters and Kreidenweis, 2007); for typical cloud conditions, particles with D_p larger than 40-100 nm can activate into droplets. As biomass burning plumes age, both particle extinction and CCN concentrations are impacted through changes in mass, number, size, and composition.

A large number of field campaigns have analyzed the aging of various normalized biomass burning aerosol properties within the plume. In this study, normalized refers to correcting a property for dilution and background concentrations by subtracting off the background value and then dividing the property by a conserved quantity, usually an effectively inert species, such as CO. Studies focusing on the aging of organic aerosol mass report a range of changes to the net (difference between total secondary organic aerosol [SOA] production and OA evaporation) normalized OA within the plume: some of these studies reported an OA gain (Alvarado and Prinn, 2009; Cachier et al., 1995; Formenti et al., 2003; Liu et al., 2016; Reid et al., 1998; Vakkari et al., 2014; Vakkari et al., 2018; Yokelson et al., 2009), some an OA loss (Akagi et al., 2012; Forrister et al., 2015; Hobbs et al., 2003; Jolleys et al., 2012; Jolleys et al., 2015; May et al., 2015), and others showed no significant change in OA (Brito et al., 2014; Capes et al., 2008; Collier et al, 2016; Cubison et al., 2011; Hecobian et al., 2011; Liu et al., 2016; May et al., 2015; Nance et al., 1993; Sakamoto et al., 2015; Zhou et al., 2017). However, sampling noise due to different sampling times, collection efficiencies, and other issues can also make it ambiguous whether net normalized OA increased in a single fire (e.g., the analysis of Alvarado and Prinn, 2009 of the Timbavati fire from Hobbs et al., 2003). Studies that measured aspects of particle extinction tend to report net normalized increases in total extinction (e.g. Abel et al., 2003; Radke et al., 1995; Reid et al., 1998; Vakkari et al., 2014; Yokelson et al., 2009), although loss in total extinction has been observed past 10 hours of aging (Radke et al., 1995). The majority of studies that have explored CCN aging within plumes have found a normalized increase in CCN with aging (e.g. Eagan et al., 1974; Vakkari et al., 2014) with Vakkari et al. (2014) further reporting no change in CCN for some observed fires. It is as yet unclear if changes in size, total number, or composition are driving observed changes.

The net change of organic aerosol (OA) mass in a smoke plume as it dilutes and ages is determined from the balances between initial emissions (which depends upon e.g. fuel type and burn conditions), SOA production, and evaporation of both POA and SOA (Bian et al, 2017). Biomass burning POA has been observed to undergo evaporation (e.g. Formenti et al., 2003; Huffman et al., 2009; Liousse et al., 1995; May et al., 2013) as semivolatile compounds that are susceptible to evaporation due to dilution can make up a significant fraction, ~20-90% of particle-phase biomass burning POA (Eatough et al., 2003; Grieshop et al., 2009; May et al., 2013; May et al., 2015). The initial plume width (characterized by the fire width) as well as the atmospheric stability (often characterized by stability class; Pasquill, 1961) will determine the dilution and therefore potential OA evaporation rates, with larger fires and more stable atmospheres diluting more slowly and losing less OA through evaporation relative to smaller fires and less stable atmospheres (e.g. Bian et al., 2017). The plume edges will mix more rapidly than the plume core in all cases. Regardless, large smoke plumes will maintain higher particle concentrations (averaged across plume transects at a given distance from the fire) than smaller smoke plumes, all else equal. The evolution of the total number of particles from biomass burning emissions is controlled by coagulation (Akagi et al., 2012; Capes et al., 2008; Formenti et al., 2003; Radke et al., 1995; Ramnarine et al., 2018; Sakamoto et al., 2016), although deposition plays a minor role early in the plume, and nucleation may contribute to number in some cases (e.g. Andreae et al., 2001; Hennigan et al., 2012; Hobbs et al., 2003; Vakkari et al., 2018). The rate of coagulation is proportional to the square of the particle number concentration for particles of fixed sizes. Hence, coagulation within plumes will occur the most rapidly within the initial (densest) time period of the plume, and observed net changes in CCN for plumes are likely highly sensitive to the range of the ages of the measurements within the plume (e.g., if the measurements begin after some

aging/dilution, coagulation may have already slowed greatly). As well, large fires that dilute more slowly will have more sustained coagulation in plumes than fires with smaller fluxes.

The particle size distribution is impacted by both coagulation and SOA condensation/OA evaporation: coagulation leads to growth of the mean diameter of particles in the plume and a narrowing of the modal width while reducing particle number (Janhall et al. 2011; Sakamoto et al., 2016). Similarly, SOA condensation/OA evaporation leads to growth/shrinkage of the mean diameter. Changes in the modal width depend on the volatility of the vapors: semivolatile vapors quickly reach equilibrium and condense or evaporate in the quasi-equilibrium limit, which yields diameter growth rates proportional to particle diameter D_p at all sizes (Pierce et al., 2011; Riipinen et al., 2011; Zhang et al., 2012), leading to no changes in lognormal modal width with condensation or evaporation. Conversely, low volatility vapors condense yielding diameter growth rates independent of particle size in the kinetic regime (D_p <~50 nm) but yield diameter growth rates proportional to 1/ D_p for the continuum regime (D_p >~ 1 μm) (Pierce et al., 2011; Riipinen et al., 2011; Zhang et al., 2012), and thus condensation of low volatility vapors decreases the lognormal modal width. Thus, understanding the balances between SOA formation, OA evaporation, and coagulation in biomass burning plumes are all essential for understanding net changes in OA mass, number, and size.

As we will argue in this study, the background aerosol concentration that plumes dilute into and entrain in also impacts plume OA mass, number, and size. If smaller fires occur in polluted atmospheres with a high background concentration of OA, evaporation will be reduced as the entraining background aerosol provides organic vapors and mass for organic vapors to partition into (Donahue et al., 2006), assuming that the OA in the background and plume effectively mix with each other, thermodynamically. These background effects can be important for the total size

and mass of particles produced, especially in regions that experience high numbers of small fires, such as the Amazon Basin during the dry season (e.g. Martin et al., 2016; Reid et al., 1998), creating high ambient OA concentrations for new smoke plumes to mix into (Baars et al., 2012; Martin et al., 2010; Reid et al., 1998). Only a few studies have reported the explicit ambient background aerosol concentrations in their publications (Cachier et al., 1995; Nance et al., 1993), and as best we can tell, no published field analyses have explicitly accounted for or discussed the potential effect that background aerosol entraining into the diluting plume may have on evaporation rates. We note that for most field studies, data for these background concentrations exist, but for most studies, it has not been explicitly considered in published work.

To our knowledge, no study has systematically investigated how fire size, dilution rates, and background aerosol concentrations are expected to influence biomass burning aerosol aging. In this study, we perform a theoretical analysis of the importance of these factors on total OA mass, number concentration, and particle size through changes to OA evaporation, SOA condensation, and coagulation. Throughout this study, we use 'fire size' to mean the area of the fire that is currently burning. The initial plume width is a function of this fire size, and hence, fire size directly impacts the dilution rate of the plume. We use an aerosol microphysics model (described in Sect. 2) to simulate a representative range of plume sizes diluting into different background aerosol concentrations. We do not attempt to simulate any specific previously observed plumes here; instead we simulate simplified plume test cases that undergo different dilution rates (as represented by different initial plume sizes) into variable background aerosol concentrations in order to carefully characterize the importance of dilution rates and background aerosol concentrations. In these simulations, we hold many known important factors (such as emissions flux; oxidant concentrations; temperature; the amount of UV radiation in the plume, which may be attenuated

in thick plumes; and chemical rate constants and yields) fixed in order to isolate the potential impacts of fire size and background OA concentrations; however, we do test the sensitivity of our results to some of these factors. As well, we do not consider black carbon, or the potential formation of tar balls within the plume, although these are likely important features in many smoke plumes (e.g. Forrister et al., 2015; Sedlacek et al., 2018). In this idealized system, we examine the effect of aging on aerosol mass (Sect. 3.1), aerosol size distribution properties (mean diameter and peak lognormal modal width; Sect. 3.2), and aerosol properties that impact radiative effects (through total extinction cross section and CCN; Sect. 3.3). We discuss limitations of this study in Sect. 3.4. Section 4 discusses real-world fire sizes and background aerosol concentrations and observational studies. Section 5 provides a synthesis of our findings, as well as recommendations for future studies.

5.2 Methods

5.2.1 Model description

We perform simulations of biomass burning aging using the TOMAS (TwO-Moment Aerosol Sectional) microphysics box model (Adams & Seinfeld, 2002; Pierce et al., 2011), coupled to the Volatility Basis Set (VBS; Donahue et al. 2006) as a single-box, expanding, Lagrangian plume model as described in Bian et al. (2017). By assuming a single, Lagrangian box, we do not resolve the effects that dilution may have at the edge (rather than the core) of plumes, which is a limitation of this study that we will discuss more in Sect. 3.4. TOMAS explicitly tracks and conserves number and mass while simulating condensation and coagulation. Condensation and evaporation is calculated through aerosol partitioning theory (Pankow, 1994) using kinetic mass transfer (Pierce et al., 2011). Coagulation is simulated using the (size-dependent) Brownian kernel in Seinfeld and Pandis (2006). We assume that the model simulations occur over timescales short

enough that dry deposition is negligible. We do not account for any wet deposition or other aqueous processes (see Sect. 3.4 for a full discussion of the limitations of this study). Our model set-up is identical to that of the study of Bian et al. (2017); here we provide a brief overview.

We use 36 logarithmically spaced size sections from 3 nm to 10 μm. The simulated aerosol species are a non-volatile inorganic species to represent a generic non-volatile inorganic species, water, and 15 organic "species" that represent lumped organics with logarithmically spaced effective saturation concentrations (C^*) spanning from 10^{-3} to 10^{11} μg m^{-3} within the VBS framework. The inorganic species is assumed to remain inert within the particle throughout each simulation, as our optical and hygroscopicity properties are held fixed (Sect. 2.3). We do not explicitly include black carbon as a separate aerosol species but rather it is implicitly included in the generic inorganic species. All species are assumed to be internally mixed within each size section. We assume a starting organic mass fraction of 0.9, a value roughly representative of many natural fuel types (Bian et al., 2015), with the remaining mass fraction assumed to be the non-volatile inorganic species. Each simulation is initialized with the initial volatility distribution from Bian et al. (2017), which adapts the findings of May et al. (2013) (for $C^* \leq 10^4$ μg m^{-3}) and Hatch et al. (2017) (for $C^* > 10^4$ μg m^{-3}). This merged volatility distribution has significant mass in the $C^* = 10^4$ μg m^{-3} bin and little mass in the $C^* = 10^5$ μg m^{-3} $C^* = 10^6$ μg m^{-3} bins, which is likely due to limitations of the two methods. In reality, we expect a more even distribution of volatility across these bins. However, as most of the initial material in the $C^* = 10^4$ μg m^{-3} bin is in the vapor phase (Figs. D4 and D5 in the supporting information) for all fire sizes, we do not expect this volatility uncertainty to qualitative impact our results across fire sizes. We assume a fixed temperature of 298 K throughout the entire simulation, both spatially and temporarily, a limitation of this study further discussed in Sect 3.4.

Table 5.1 Initial input parameters. All cases are run within the parameter space of the primary sensitivity simulations (fire size, background aerosol concentration, and chemistry/coagulation), using the constants listed in the final section of the table. The base simulations are comprised of the bolded values in the secondary sensitivity simulations. Secondary sensitivity simulations are run using the values in parentheses within the secondary sensitivity simulations.

Parameter	Description	Value
	Primary sensitivity simulations	
Fire size	Area of fire emissions, km^2	10^{-4}, 10^{-3}, 10^{-2}, 10^{-1}, 1, 10, 100
Background concentration	Background aerosol mass concentration, $\mu g\ m^{-3}$	0, 5, 20, 50
Chemistry and coagulation	Whether or not gas-phase chemistry and/or coagulation is on	Chemistry on/off; Coagulation on/off
	Secondary sensitivity simulations[a]	
k_{OH}	In-plume reaction rate constant, $cm^3\ molecule^{-1}\ s^{-1}$	**Upper- bound chemistry: $-5.7 \times 10^{-12} \ln(C^*) + 1.14 \times 10^{-10}$** (Lower- bound chemistry: $-1.84 \times 10^{-12} \ln(C^*) + 4.27 \times 10^{-10}$)
Decrease in volatility bins per reaction	Number of volatility bins decreased per reaction with OH	**Upper- bound chemistry: 4** (Lower- bound chemistry: 2)
Stability class	Pasquill stability classes for atmospheric turbulence	**D** (B, F)
α	Accommodation coefficient	**1.0** (0.1, 0.01)
Simulated aging period	How long the simulation is run for, in hours	**4** (8)
	Constants	
D_g and $D_{g,\ bg}$	Dry peak number diameter of emissions and background, nm	70, 157
σ_g and $\sigma_{g,\ bg}$	Particle size distribution standard deviation of emissions and background	2.0, 1.7
Mass flux	Fire emission mass flux, $kg\ m^{-2}\ s^{-1}$	5×10^{-6}

Wind speed	Mean boundary-layer wind speed, m s^{-1}	5
T	Ambient temperature during dilution, K	298
Maximum plume mixing depth	Maximum depth the plume can mix within, m	2500
[OH]	In-plume OH concentration, molecules cm^{-3}	1.08×10^6

[a]Values in bold are used for the base simulations discussed and shown in the main text; values in parentheses represent further sensitivity cases briefly discussed in the main text with results shown in Appendix D.

Gas-phase functionalization of the organic species within the VBS is simulated assuming that reaction with OH leads to a product vapor four volatility bins lower than the parent molecule. The OH concentration is set to 1.08×10^6 molec cm^{-3}, following Bian et al. (2017), and is held fixed throughout each model run. This OH concentration is lower than what has been reported in studies that have characterized in-plume OH (Akagi et al., 2012; Hobbs et al., 2003; Yokelson et al., 2009), but this may be balanced by our relatively fast OA aging scheme presented below. OH is likely a function of fire size/dilution rates, as these factors can control the amount of light available in-plume as well as the amount of oxidants, and we will leave the exploration of OH and fire size to a future study. We assume that the rate of reactions of OH with organics follows the relationship determined by Jathar et al. (2014) for aromatics: $k_{OH}= -5.7\times10^{-12}\ \ln(C^*)+1.14\times10^{-10}$. Jathar et al. (2014) also provides a relationship for alkanes: $k_{OH}= -1.84\times10^{-12}\ \ln(C^*)+4.27\times10^{-10}$. The fit for aromatics represents faster chemistry than that of alkanes. For this study, we will assume the reaction rate of aromatics with a four volatility bin drop as an upper bound on SOA condensation, following Bian et al., (2017), as this was the chemistry assumption that best fit smog chamber data from the third Fire Lab At Missoula Experiment (FLAME III). The initial OA concentrations in the smog chamber in FLAME III were between ~16-86 μg m^{-3}. We present our base results using this upper-bound assumption on OA oxidation ("upper-bound chemistry"), as this set of

assumptions provided the best fits with chamber data in Bian et al. (2017), but we also show in the supplementary information (SI Sect. D5 and Figs. D13-D14) a sensitivity test using the alkane reaction rate with a two-bin volatility bin drop as a lower bound on OA oxidation ("lower-bound chemistry"; Bian et al., 2017). The lower-bound chemistry simulations could not only be insightful for conditions with reduced reaction rates, but can also act as a proxy for conditions with reduced OH concentrations, as may occur for plumes with reduced amounts of light available within the plume. These reaction rates are applied uniformly to all gas-phase organics within the model's VBS (regardless of species type) so as to represent an "average" reaction rate. We further assume that fragmentation is trivial at the timescale of our study (four hours; Shrivistava et al., 2013) and do not include any fragmentation reactions in the model.

The expansion of our Lagrangian box is simulated with a Gaussian dispersion framework, assuming a uniform pollutant distribution across the expanding volume. The assumption of a uniform pollutant distribution is a limitation of this study that is discussed further in Sect. 2.4. Following Bian et al. (2017), we assume a fixed wind speed in the x direction (the plume's long axis) of 5 m s^{-1}. The crosswind width and height of the initial and expanding plume is $4\sigma_y$ and $4\sigma_z$, respectively, but with a maximum plume mixing depth of 2500 m. We do not explicitly assume that the plume remains within the boundary layer (BL) (i.e., this layer with a 2500 m maximum mixing depth is not necessarily in the BL), but we do not change the temperature and pressure to be representative of free troposphere (FT) conditions. Dispersion may be slower in the FT than the BL, as the FT is generally stable due to lack of significant heating at the bottom of any given layer (Wallace and Hobbs, 2006). We test the sensitivity of our results to moderately stable conditions that may be more representative of dispersion in the free troposphere, as discussed in Sect. 2.2. (Pasquill, 1961) represent atmospheric stability in the model, and are used to estimate the values

of σ_y and σ_z, following Klug (1969). The initial plume width of $4\sigma_y$ is set to be the same as the fire width (square root of the fire area, which is defined here as the area that is currently burning). Thus in the model, the initial plume concentration is defined by the time spent over the fire and initial values of $4\sigma_y$ and $4\sigma_z$.. The dilution rate of the plume is controlled by the initial plume size, the wind speed in the x direction, and the atmospheric stability class within the Gaussian dispersion framework. Figure 5.1d shows the dilution ratio as a function of time for fire sizes of 100, 1, 10^{-2}, and 10^{-4} km^2. The model simulates the expanding plume downwind as it ages in a Lagrangian framework. We assume that depositional processes (wet or dry) are minor within the modelled time period (4-8 hours) and do not include them in the model.

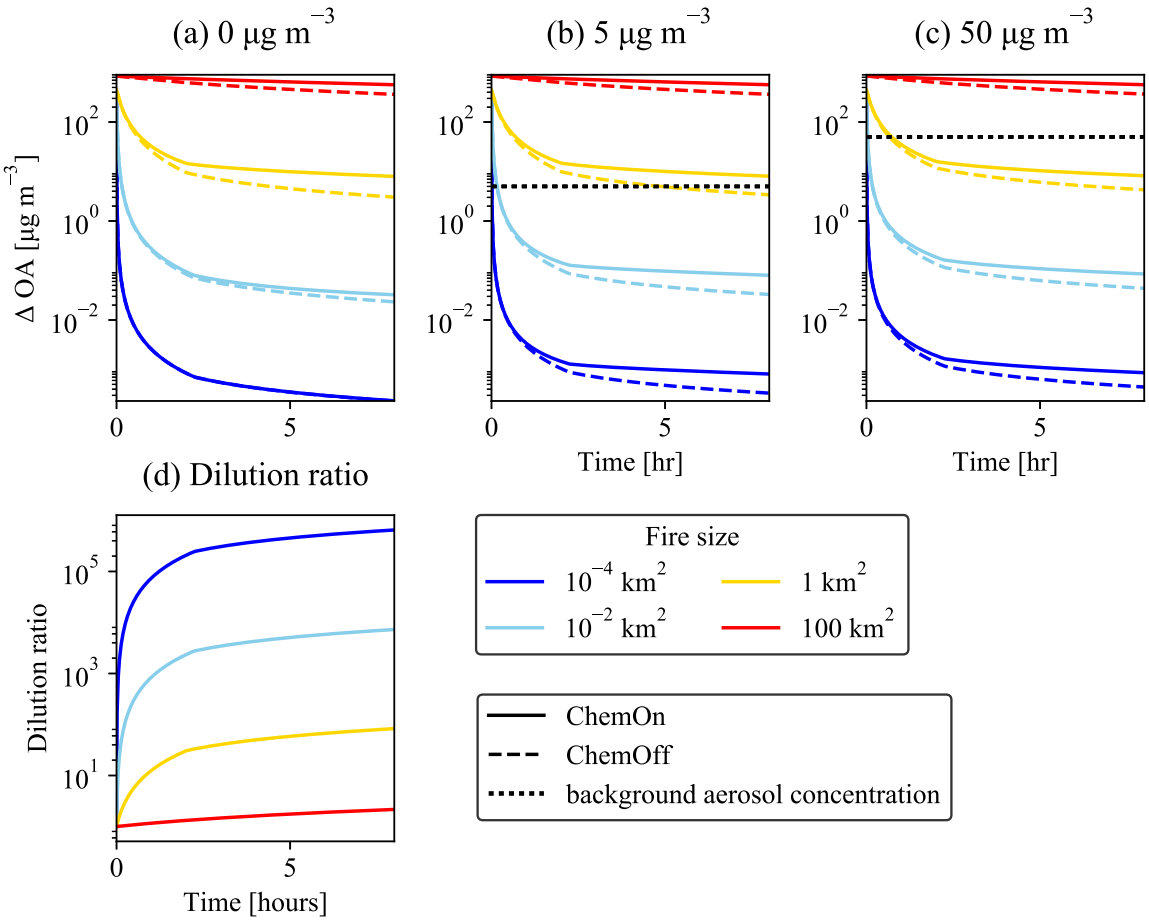

Figure 5.1 (a)-(d) Time evolution of total smoke organic aerosol mass concentration enhancement (background organic aerosol subtracted off) in the particle phase for chemistry-on (solid lines) and chemistry-off (dashed lines) simulations for the fire areas of 10^{-4}, 10^{-2}, 1, and 100 km^2 (colored lines) and background aerosol concentrations (black dotted lines) of (a) 0, (b) 5, and (c) 50 μg m^{-1}. (d) Time evolution of the dilution ratio for each fire size. Results are for the base simulations (Table 5.1) from the CoagOn version of each ChemOff/ChemOn case.

5.2.2 Description of simulations

Table 5.1 provides an overview of the simulations performed in this study. The primary sensitivity studies are for seven fires sizes between 10^{-4} and 100 km^2 (0.01 to 10^4 ha; each fire size is separated by an order of magnitude in fire area). Throughout this study, fire size is meant to indicate the area of the fire that is currently burning. Fires between 10^{-4} and 0.1 km^2 are approximately representative of small prescribed burns (e.g. Huang et al., 2018); the larger fire sizes are representative of the range of large prescribed burns and wildfire sizes (e.g. Giglio et al., 2010). Each simulated plume entrains constant background aerosol concentrations of 0, 5, 20, or 50 μg m^{-3} as the plume expands. The background size distribution is assumed to be composed of nonvolatile organics (e.g. well-aged), and once entrained into the plume, these particles undergo coagulation and may take up organic vapors. The background aerosol also provides mass for the plume aerosols and vapors to partition into (Pankow, 1994). These constant background aerosol concentrations of 5-50 μg m^{-3} can exceed the smoke mass from the fire within the diluting plume, depending upon the initial mass emissions and dilution rate, the consequences of which will be discussed in Sect. 3.1. Real-world background aerosol concentrations vary spatially, hence our simulated background is idealized. Each initial plume and background size distribution are assumed to be single lognormal modes with lognormal modal number median diameters (D_g and $D_{g,\,bg}$) of 70 nm and 157 nm (corresponding to lognormal modal mass median diameters of 296 and 365 nm) and lognormal modal widths (σ_g and $\sigma_{g,\,bg}$) of 2.0 and 1.7, respectively (Table 5.1).

These values were chosen following Carrico et al. (2016) for fresh biomass burning emissions and D'Andrea et al. (2013) for background aerosol, respectively.

In order to determine the individual and combined effects of SOA condensation and coagulation on the smoke size distribution, we run four simulations for each fire size and background combination: (1) chemistry off , coagulation off (ChemOff_CoagOff), (2) chemistry off, coagulation on (ChemOff_CoagOn), (3) chemistry on, coagulation off (ChemOn_CoagOff), and (4) chemistry on, coagulation on (ChemOn_CoagOn). We also run simulations with coagulation on and coagulation off for each background concentration that has no smoke emissions and instead simulates aging of the background as it would be without the presence of the plume over the same time period used for the full (plume plus background) simulations. These simulations are used to determine the number and mass enhancement of the plume above background. Note that since we assume a non-volatile background without available gas-phase vapors, changes in the background size distribution occur only if coagulation is on.

The base set of primary sensitivity simulations in this work are with the upper-bound chemistry scheme (Table 5.1), a constant mass flux of 5×10^{-6} kg m^{-2} s^{-1}, neutral atmospheric stability (stability class D), and the mass accommodation coefficient, α, set to 1. As the mass flux and emissions size distribution are held fixed, the particle number emissions per area are also held constant; the total initial number concentrations for each fire size are provided in Table D1. We further run "secondary sensitivity simulations" on a number of parameters (Table 5.1, Sect. 2) to provide a more complete framework of the relative importances of fire size, background concentration, SOA condensation, OA evaporation, and coagulation under different potential atmospheric and chemical conditions. Each sensitivity simulation tests one parameter while holding all others at the values of the base cases. We test the following sensitivities: the rate of

SOA condensation (using the lower-bound chemistry parameterization, discussed above, and a two bin drop in volatility per reaction); α (testing α=0.1 and α=0.01); and the stability class (testing B, moderately unstable, and F, moderately stable). Reducing the accommodation coefficient can be used to compensate for potential particle-phase diffusion limitations that would occur if the aerosol increased in viscosity (Hodshire et al., 2018). As particle-phase diffusion limitations slow or halt the rate at which condensing vapors can diffuse through the particle, the condensing vapors can more easily evaporate. Reducing α accounts for this net reduction in the condensation rate, but it does not account for potential size-dependent diffusion limitations (Zaveri et al., 2017). (We assume liquid particles in our primary cases, which will likely have accommodation coefficients at or close to unity; Julin et al., 2014). Bateman et al. (2017) found that SOA influenced by biomass burning increased in viscosity over the Amazonian rainforest as compared to purely biogenic SOA, indicating that biomass burning could potentially yield high-viscosity aerosol. As well, some field studies have observed the presence of tar balls, nearly spherical and highly viscous particles (e.g. Adachi & Buseck, 2011; Pósfai et al., 2003, 2004; Sedlacek et al., 2018). Changing the stability class effectively models differing dilution rates, and has an effect similar to changing fire sizes, which is why we treat stability as a secondary sensitivity. The results of the secondary sensitivity tests are briefly discussed in the text, and figures are provided in the supporting information. All cases are run with the constants described in the final section of Table 5.1.

For brevity, we only show results for fire sizes of 10^{-2}, 1, and 100 km^2 with background concentrations of 0, 5, and 50 $\mu g\ m^{-3}$ for each base case and sensitivity simulation as these capture the main features of these dimensions; we also include the fire size of 10^{-4} in our mass discussion. Results for all fires sizes and background are included in the supporting information: Figures D1, D3, D6, D7, D10, and D12 for the base cases. We analyze all simulations after 4 hours of aging

but also provide results for the base simulations after 8 hours of aging in the supporting information. We chose 4 hours as our analysis time as dilution is generally slow past this time, and the assumption of a constant OH concentration is less valid over longer time periods.

Two-moment sectional models can artificially distort the size distribution through size-bin emptying, and thus to remove numerical artifacts, the simulated distributions were smoothed. The supporting information (Sect. D1.1) provides further details on the smoothing technique used (Stevens et al., 1996).

5.2.3 Calculations of smoke size distribution, CCN, and extinction

We determine each simulation's contribution of smoke towards total OA mass, total extinction cross section (*E*), and CCN. We find the in-plume enhancement of each metric (OA mass, *E*, and CCN) by subtracting the matching metric from the background aerosol size distribution (that is, the background OA mass, *E*, and CCN) of an otherwise identical simulation that has no smoke emissions, as described in Sect. 2.2. (We match both the background concentration used and whether coagulation is on or off in our background correction.) Each enhancement(ΔOA mass, Δ*E*, and ΔCCN) is normalized by the enhancement of CO above its background (ΔCO) to allow us to determine if these metrics have increased or decreased relative to their values at emission. Emissions factors of CO vary from study to study but are generally on the order of 10 times greater than that of $PM_{2.5}$ emissions (e.g. Akagi et al., 2011; Burling et al., 2011), and so for this study we assume that CO emissions are 10 times that of particle mass emissions. Correcting the distributions for the background and normalizing the time-evolving simulations by ΔCO can be referred to as the normalized excess mixing ratio (NEMR; e.g.Akagi et al., 2012), a common metric in field campaigns, in which the in-plume concentrations of species

X are background-corrected (ΔX) and normalized by the inert background-corrected tracer ΔY that has been measured at the same time and location. We note that the exact values of ΔOA/ΔCO, ΔE/ΔCO, and ΔCCN/ΔCO will vary with the values of mass, number, and CO emissions under different real plumes, as well as the values used for particle hygroscopicity and refractive index (as described below). However, we are not attempting to simulate any specific observed plumes and argue that the specific values of these metrics are less important than their relative changes between different fire sizes/dilution rates and background aerosol concentrations. We hypothesize that the qualitative conclusions of this work will hold across studies. The total initial and final OA mass from smoke is found by summing the mass (explicitly tracked in TOMAS) across all bins. We calculate the peak diameter ($D_{g,}$) and lognormal modal width (σ_g) of the smoke plume using the methods of Whitby et al. (1991); further details are given in Section S2of the supporting information.

ΔE/ΔCO is calculated through:

$$\frac{\Delta E}{\Delta CO} = \frac{\sum_1^i \Delta N_i \cdot Q_{ext,i} \cdot A_i}{\Delta CO} \quad (5.1)$$

where *i* indicates the size bin, ΔN_i is the total number of background-corrected particles in the plume per bin, $Q_{ext,i}$ is the extinction efficiency in each bin, and A_i is the cross-sectional area of the particles per bin, assuming spherical particles. $Q_{ext,i}$ is calculated through the Python module bhmie_herbert_kaiser_july2012.py (https://code.google.com/archive/p/scatterlib/downloads). The module finds $Q_{ext,i}$ through Mie scattering theory, using the code published in Bohren and Huffman (1983). We assumed a wavelength of 500 nm and a refractive index of 1.5 - 0.08*i* (Mack et al., 2010) for the particles regardless of OA and inorganic aerosol content. We also ignore potential changes to the refractive index that would occur if black carbon or brown carbon was

present in the particles, since we do not include black carbon or brown carbon as a modelled aerosol species. Our rationale for using a fixed refractive index is to isolate how the changes in the aerosol size and number affect extinction. The particle extinction is also a function of potentially evolving particle morphology and refractive index in the plume during aging (Pei et al., 2018), but we do not attempt to address these changes here with justification given in the next paragraph.

ΔCCN/ΔCO at 0.2% supersaturation was calculated using the Kappa formulation of Petters and Kreidenweis (2007), assuming a hygroscopicity parameter, κ, of 0.2 for both the smoke aerosol and the background aerosol. Aging biomass burning aerosol have been observed to rapidly converge to a κ value of 0.2 ± 0.1 (Englehart et al., 2012). Similar to extinction, we do not attempt to address aging of κ within the plume and hold this value fixed for all simulations and thus changes in CCN are effectively functions of the change in number concentration and size for this study. We note that both optical and hygroscopic properties are anticipated to change through aging. However, the changes in the refractive index and κ with aging are inconsistent between aging cases, with some cases showing increases and some studies showing decreases with age in each of these parameters (e.g. Adler et al., 2011; Englehart et al., 2012; Haywood et al., 2003). As the direction of change with aging is likely fuel and burn-conditions dependent, we limit this study to determining the impacts of size distribution changes through aging.

In order to determine the relative contributions of SOA and POA to the aging size smoke OA, we make a simple estimate of the mass fraction of SOA to the total mass as follows:

$$SOA\ mass\ fraction(t) = \frac{(OA\_ChemOn_{total\ mass}(t) - OA\_ChemOff_{total\ mass}(t)}{OA\_ChemOn_{total\ mass}(t)} \quad (5.2)$$

where $OA\_ChemOn_{total\_mass}(t)$ and $OA\_ChemOff_{total\_mass}(t)$ are the total mass concentrations of the ChemOn_CoagOn and ChemOff_CoagOn cases, respectively, at time t for a given fire size and background aerosol concentration (coagulation does not impact mass and therefore we do not look

at the CoagOff cases). And then the POA mass fraction is simply (POA mass fraction)= 1 - (SOA mass fraction). A limitation of the approach is that SOA condensation in the ChemOn simulations reduces the amount of POA evaporation relative to the ChemOff simulations; however, Eq. 2 allows us to qualitatively show under which conditions we expect the SOA fraction (or the amount of oxygenation of the OA) to increase more or less rapidly.

A discussion of the limitations of our methods in this study are presented in Section 3.4.

5.3 Results

5.3.1 Smoke mass aging depends on fire size, dilution, evaporation, and condensation

In a diluting plume, the total organic aerosol (OA) mass will depend on how much OA evaporates versus how much SOA is formed through condensation, at least for our modelled system. The total mass is mostly unaffected by coagulation, as coagulation conserves mass (although not number and hence affects the size distribution and may change the condensation sink timescale). Figure 5.1 provides the time-evolving absolute smoke mass enhancement (that is, the excess OA from smoke above the background aerosol concentration), ΔOA (in μg m^{-3}), and the time-evolving dilution ratio for fire sizes of 10^{-4}, 10^{-2}, 1, and 100 km^2 and constant background aerosol concentrations of 0, 5, and 50 μg m^{-3} for the base simulations from the CoagOn version of each ChemOff/ChemOn case (Fig. D1 provides the same information for all modelled fire sizes and background concentrations. Fig. D2 provides the time-evolving ΔCO for fire sizes of 10^{-4}, 10^{-2}, 1, and 100 km^2.). When the background aerosol concentration is 0 μg m^{-3}, ChemOn cases lose less mass with a mass increase of up to ~140% between ChemOn and ChemOff than the ChemOff cases due to SOA condensation. However, SOA condensation is minor (around a 1% increase

compared to ChemOff) for the smallest fire size with no background due to very low OA concentrations inside the plume to facilitate partitioning. As the background aerosol concentration increases, evaporation of the plume aerosol is slowed due to increased aerosol mass from the background aerosol concentration being entrained in. As vapors can partition into this background aerosol, this extra mass from the background facilitates increased partitioning of the plume aerosol to the particle phase (Donahue et al., 2006, 2009), and SOA condensation increases by over 200% compared to the 0 μg m^{-3} background case for the 10^{-2} and 10^{-4} km^2 fire sizes. Conversely, the evaporation and condensation rates for the 1 and 100 km^2 fire sizes are unaffected by the background aerosol concentrations, as their mass enhancements remain above or near the background concentration throughout the dilution period shown (8 hours). OA for the smaller fires quickly decreases to at or below the variability in background aerosol concentrations (Fig. 5.1, panels b and c), making these plumes difficult to follow downwind in observational studies and also making the accuracy of the excess values measured in the plume marginal.

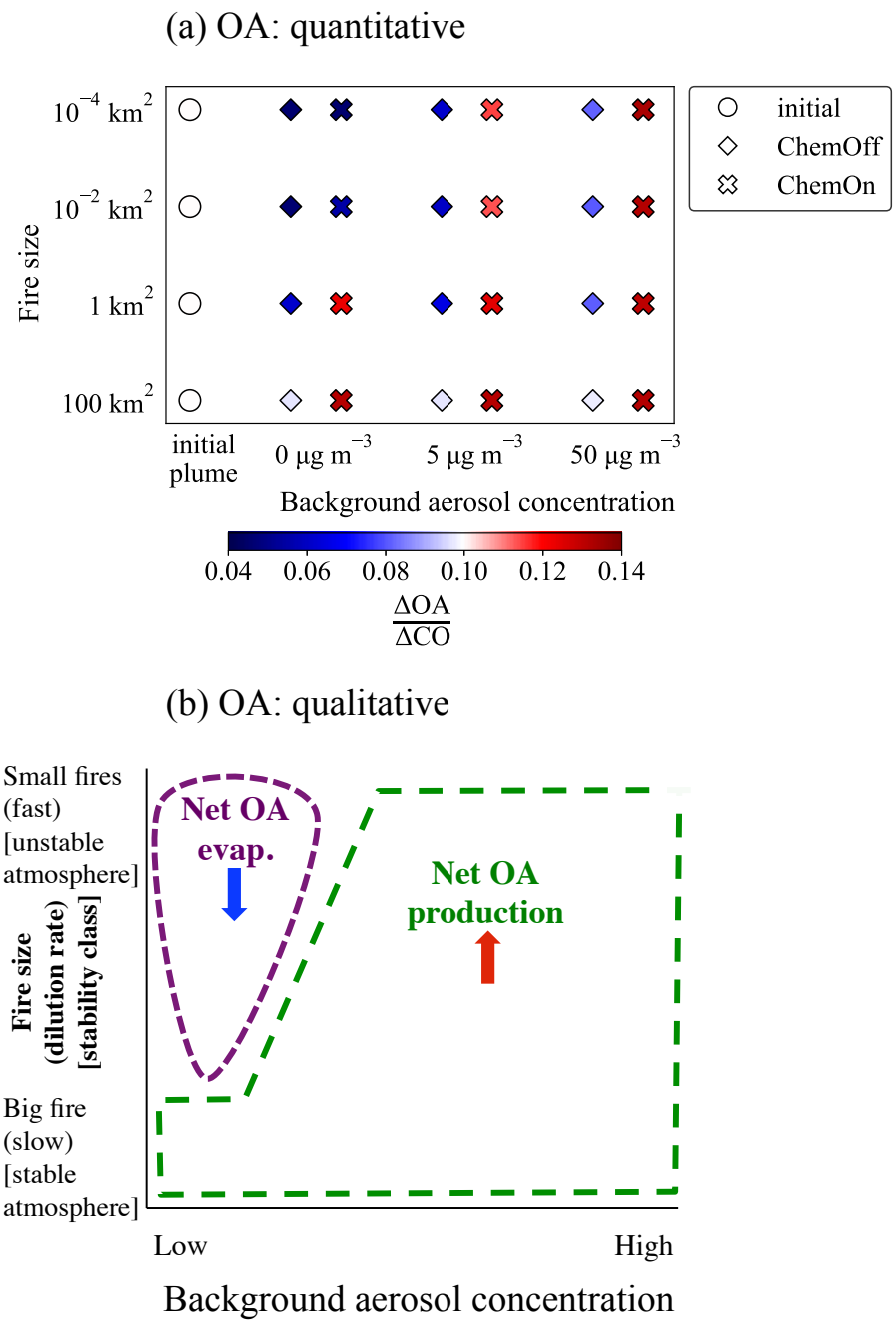

Figure 5.2 (a) The in-plume normalized organic aerosol mass enhancement (ΔOA/ΔCO) initially and after 4 hours of aging for the ChemOff and ChemOn base cases (Table 5.1). Warm colors indicate an increase in ΔOA/ΔCO after 4 hours of aging, and cool colors represent a decrease. The y axis represents fire size/dilution rate; the x axis represents the background aerosol concentration. (b) Qualitative summary of the impacts of fire size (y axis) and background aerosol concentration (x axis) on ΔOA/ΔCO.

The top panel of Fig. 5.2 provides ΔOA normalized by ΔCO (ΔOA/ΔCO) for the base simulations at the time of emission and after 4 hours of aging, again showing only the CoagOn version of each ChemOff/ChemOn case (Figure D3 provides the same information for all modelled fire sizes and background concentrations and includes the CoagOff cases). We note that the y axis for Figs. 5.2-5.5 is fire size, as fire size is a simple proxy for dilution rate in this study. However, the y axis increases from slow to fast dilution rates, represented by large to small fires. Under the assumptions of the base simulations, ΔOA/ΔCO decreases when chemistry is off (ChemOff) between 10-60% due to OA evaporation for all fire sizes and background aerosol concentrations modelled. When chemistry is on (ChemOn), organic vapors in our simulations shift to lower volatilities through gas-phase reactions with OH and may partition to the condensed phase. Figures D4 and D5 in the supporting information provide initial and final volatility distributions after 4 hours for both ChemOn and ChemOff, showing how dilution alone (ChemOff) and chemistry (ChemOn) change the aging volatility distributions.

For ChemOn cases, ΔOA/ΔCO always increases by 15-20% for the 1 and 100 km^2 fires, regardless of background aerosol concentration. For the 10^{-2} and 10^{-4} km^2 fire sizes, evaporation exceeds condensation for the 0 $\mu g\ m^{-3}$ background aerosol concentration and ΔOA/ΔCO decreases by up to 60%. Condensation instead exceeds evaporation when the background aerosol concentration reaches 5-50 $\mu g\ m^{-3}$ (Figs. 5.2 and D2), indicating that normalized ΔOA in small fires can still undergo net (overall change when accounting for all processes) increases up to 40% under non-zero background aerosol loadings, even when ΔOA is less than the background aerosol concentration (Fig. 5.1). OA concentrations in summertime forested regions are often on the order of 5 $\mu g\ m^{-3}$ (Jimenez et al., 2009), and although there are likely some instances in which smoke plumes in e.g. boreal remote regions would be diluting into truly pristine (between 0.1 and 1 μg

m^{-3}) backgrounds, we expect results from such cases to scale between the 0 and 5 μg m^{-3} cases. For the cases shown in Fig. 5.2, the maximum OA gain after 4 hours is only ~40% above the initial plume, a modest increase consistent with some studies that do report a net increase in OA at the time of measurement (e.g. Reid et al., 1998). We reiterate that the exact values of ΔOA/ΔCO here depend on our assumed emissions ration between OA and CO, and many factors vary between real fires/plumes that we are not testing here.

We note that for our simplified system of only changing fire size and background aerosol (all else fixed) that ΔOA/ΔCO is predicted to increase over the first 4 hours for the 1 through 100 km^2 fire sizes, regardless of background concentration, but that some studies have reported net losses or no net change for larger fires (e.g. Collier et al., 2016, Forrister et al., 2015). This discrepancy could be related to potential light attenuation within the plume (Hobbs et al., 2003), leading to reduced oxidant concentrations and chemistry rates, as well as differences in POA volatility and precursor vapors. As well, some studies show no net change or slight decreases in normalized OA for intermediate fire sizes (e.g. Akagi et al., 2012; Liu et al., 2016). There are regions within our parameter space of our sensitivity studies in which intermediate plumes do not increase in normalized OA mass (Figs. D15 and D17 in the supporting information). Further, some field experiments have seen factors of 2-3 in mass enhancements (Vakkari et al., 2014, 2018; Yokelson et al., 2009), higher than observed in this study, and this discrepancy could be related to differences in particle and precursor-vapor emissions, in-plume oxidant concentrations (Yokelson et al., 2009), or other factors not explored in this study. The differences in our model results here and previously observed measurements should be investigated in a future study in order to attempt to discern what other factors are strongly controlling net OA mass, especially in larger fires.

Regarding the time evolution of OA, many cases with increases in ΔOA/ΔCO do not show a net gain in ΔOA/ΔCO (above the initial value) until after 2-3 hours of aging (Fig. D6), indicating that field studies that measure plumes only within the first 1-2 hours after emission may observe and conclude that the fire undergoes a net OA loss rather than gain. Further, sets of observations in which the earliest measurement is taken 1-2 hours after emissions may be biased high in their estimate of net production from subsequent measurements. We note that Fig. D6, which shows ΔOA/ΔCO as a function of time for 8 hours of aging, could be interpreted to imply that OA mass will continually be added to the diluting plume over time. In the real atmosphere, as the plume continues to dilute and age further, many processes will likely slow, halt, or reverse further OA production, such as diurnal cycles in oxidants, OA loss to fragmentation (e.g. Kroll et al., 2009), and depositional processes (e.g. Knote et al., 2014).

The bottom panel in Fig. 5.2 qualitatively summarizes the key message for the impact of fire size and background aerosol concentration on aging of smoke OA. For our specific modeled system, ΔOA/ΔCO is anticipated to increase for large fires due to greater SOA condensation rates than evaporation rates. For smaller fires, ΔOA/ΔCO is anticipated to decrease when the background aerosol concentration is low (evaporation exceeds condensation) but will instead increase when the background aerosol concentration is high enough to slow evaporation rates enough that condensation exceeds evaporation.

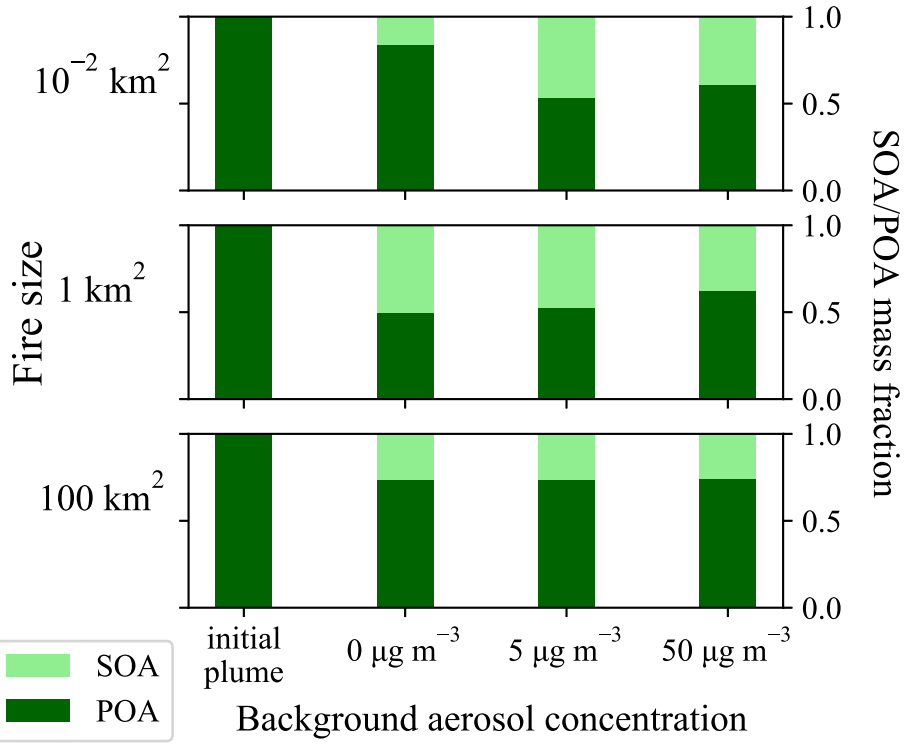

Figure 5.3 The relative fractions of SOA and POA to total ΔOA (just the OA enhancement above background) initially and after 4 hours of aging. The y axis represents fire size/dilution rate; the x axis represents the background aerosol concentration. The simulation with the smallest fire (10^{-2} km^2) and 0 μg m^{-3} background concentration is far out of equilibrium partitioning (due to a low condensation sink), which is why the SOA fraction is lower for this case than expected.

Atmospheric or chemical conditions that favor decreasing condensation or increasing evaporation all lead to slower OA formation, causing relative decreases in ΔOA/ΔCO from the base cases (Fig. 5.2). Table 5.1 and Sect 2.2 describe the sensitivity cases performed in this study: decreasing the accommodation coefficient, rate of chemical reactions and number of volatility bins dropped per reaction (lower-bound chemistry), and simulating a moderately unstable atmosphere all lead to relative decreases in ΔOA/ΔCO. As discussed in Sect. 2.1, the lower-bound chemistry simulation can provide insight to conditions with reduced OH concentrations (e.g. a thick plume from a large fire with little actinic flux). If plumes from large fires do indeed have lower UV and oxidant levels, our sensitivity simulations indicate that there may be less net OA mass produced than if oxidants

were held fixed (Fig. D17). Simulating a moderately stable atmosphere and running the base simulation for 8 hours instead favor increased net condensation and lead to increases in ΔOA/ΔCO. Section S5 and Figs. D13-D24 in the supporting information provide further discussion on the impact of the sensitivity simulations on ΔOA/ΔCO as well as normalized smoke extinction, CCN, modal width, and lognormal number median diameter.

Figures 5.2, D3, and D6 show that the mass results for fire sizes 10^{-2}, 10^{-3}, and 10^{-4} km^2 are very similar. Thus for the remainder of the main analyses, we will only discuss fires between 10^{-2} and 100 km^2, and note that our results for the 10^{-2} km^2 fire are likely applicable to fires smaller than 10^{-2} km^2.

Figure 5.3 shows an important point related to Fig. 5.2: even though the ΔOA/ΔCO is lower after 4 hours for smaller fires than larger fires, when chemistry is on, the relative contribution of SOA (vs. POA) is higher for smaller fires in all but the cleanest background. Figure 5.3 provides the mass fractions of smoke POA and smoke SOA to total ΔOA (calculations described in Sect. 2.3) for fire sizes 10^{-2}, 1, and 100 km^2 and constant background aerosol concentrations of 0, 5, and 50 $\mu g\ m^{-3}$. The SOA mass fraction for the largest fire modelled is ~25% SOA after 4 hours, and this ratio increases as fire size decreases to up to ~40-50% SOA. As shown earlier by Bian et al. (2017), the low fractional contribution of SOA for large fires is because little POA evaporates from these fires, which (1) keeps the POA contribution high and (2) limits the SOA precursors to just IVOCs and VOCs as the SVOCs remain as POA in the particle phase. For smaller fires, SVOCs evaporate from the POA and act as SOA precursors that can undergo chemical aging and recondense, which (1) reduces the POA contribution and (2) increases the SOA contribution. An exception to this SOA-fraction trend occurs in Fig. 5.3 for the smallest fire with no OA background, where the SOA fraction is lower than expected. This exception is due to the low

condensation sink in this small-fire/no-background case, so that even though low-volatility vapors are being created in the gas phase, they take hours to find a particle to condense on. If given enough time to approach equilibrium, this small-fire/no-background case would similarly show an SOA fraction around 0.4-0.5. Additionally, increasing the background OA contribution decreases the SOA fraction for similar reasons: high background OA prevents POA from evaporating, which increases the POA contribution and limits the amount of SOA precursor vapors. Hence, our results show that for our system, OA should become oxidized (e.g. as measured by Aerosol Mass Spectrometer measurements) more quickly in plumes of small fires and/or under lower background concentrations (when all else is equal). Under conditions where OA concentrations remain high, we expect OA to become oxidized more slowly.

5.3.2 Smoke aerosol size distribution aging

The plume lognormal modal number mean diameter, D_g, and lognormal modal width, σ_g, also evolve as the plume dilutes and undergoes coagulation, OA evaporation, and SOA condensation. The top panel of Fig. 5.4 shows the initial and final (after 4 hours of aging) plume D_g and σ_g values for the base simulations fire sizes of 10^{-2}, 1, and 100 km^2 and constant background aerosol concentrations of 0, 5, and 50 μg m^{-3}, colored by ΔOA/ΔCO. (The colorbars in Figs. 5.2 and 5.4 are the same). Figure D7 in the supporting information provides the same information for all modelled fire sizes down to 10^{-2} km^2 and all background concentrations. Figures D8 and D9 in the supporting information also provide the final number and volume size distributions for a subset of fire sizes and background concentrations for the base cases. OA evaporation and SOA condensation are still important processes for controlling D_g, σ_g and the smoke OA mass (Sec. 3);

however, for the size distribution, coagulation also is an important process for controlling D_g and σ_g in plumes that do not undergo rapid dilution (the larger fires in Fig. 5.3a).

OA evaporation results in smaller particles, shifting D_g to smaller values. Without coagulation and chemistry (ChemOff_CoagOff), evaporation does not change σ_g for the largest fire sizes but slightly broadens the distribution (increasing σ_g) for the smaller fire sizes. Conversely, SOA condensation grows particles, shifting D_g to larger values, and narrowing the size distribution, decreasing σ_g, as evident in the ChemOn cases. The impact of evaporation and condensation on σ_g is dependent on both the volatilities of the evaporating/condensing vapors as well as the sizes of the growing particles (e.g. Pierce et al., 2011; Riipinen et al., 2011; Zhang et al., 2012); Sect. D4 of the supporting information provides a detailed discussion of evaporation condensational growth, and the roles of volatility and size on changes to the lognormal width.

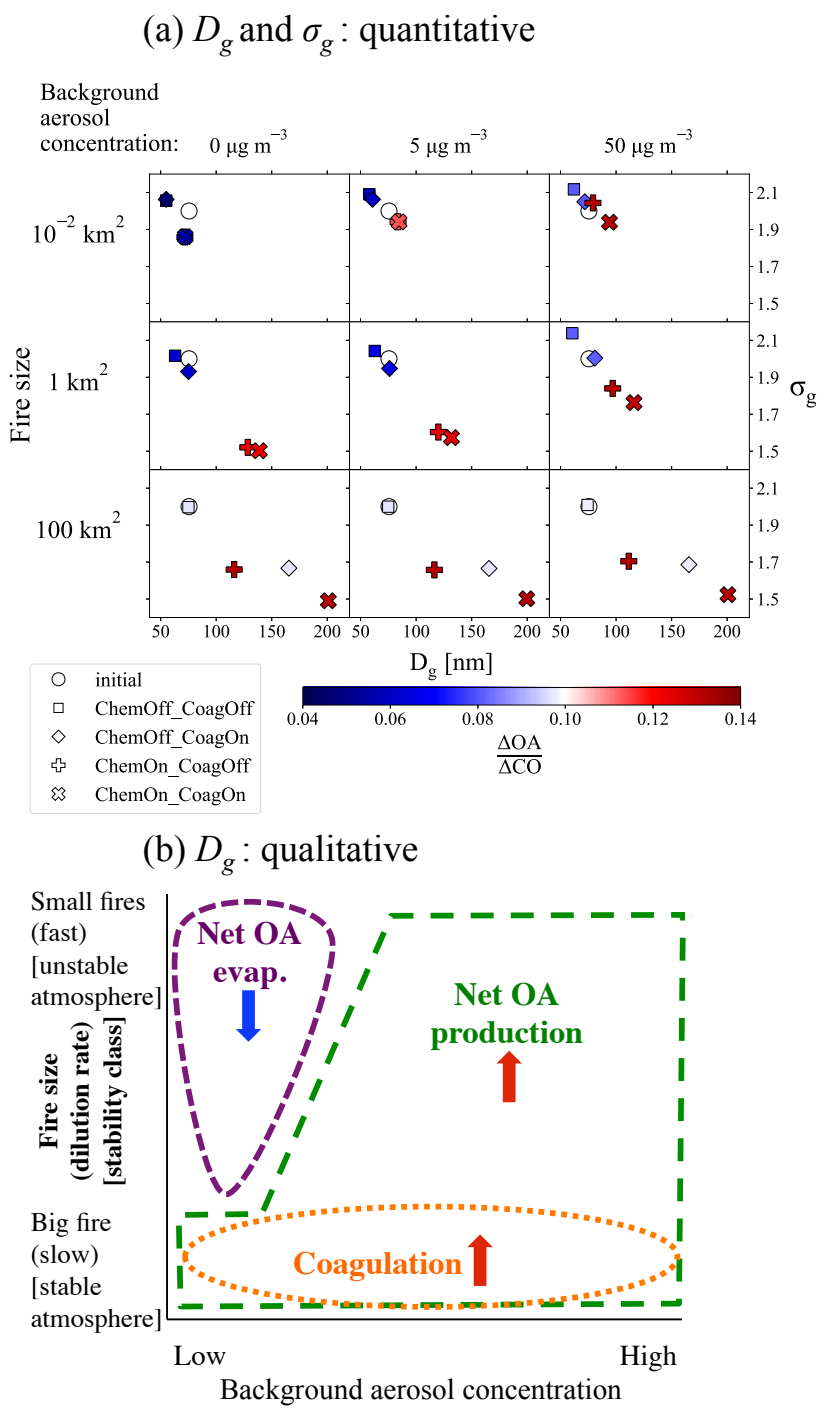

Figure 5.4 (a) Smoke (background corrected) lognormal median diameter of the lognormal mode (D_g; x axis) and lognormal modal width (σ_g; y axis) initially and after 4 hours of aging for the base cases (Table 5.1). The colorbar is ΔOA/ΔCO initially and after 4 hours of aging for the base cases (same colorbar as Fig. 5.2a). (b) Qualitative summary of the impacts of fire size (y axis) and background aerosol concentration (x axis) on aged biomass burning D_g. Although not

shown, σ_g has approximately the opposite behavior as that of D_g, although changes in σ_g depends also on the volatility of condensing/evaporating vapors.

Coagulation also shifts D_g to larger values (through coagulational growth) and narrows the size distribution, decreasing σ_g, by removing smaller particles (Sakamoto et al., 2016). Figure 5.4 shows that for CoagOn cases, this coagulational increase in D_g is most evident in larger (1 km^2 and greater) fire sizes, with increases up to a D_g of 200 nm from coagulation alone. As discussed in the introduction, coagulation rates are proportional to the square of the number concentration, and thus the coagulation-caused increase in D_g amplifies with increasing fire sizes that take longer to dilute as well as for fires with higher emission fluxes leading to higher initial concentrations (Sakamoto et al., 2016). Additionally, decreasing dilution rates through a more-stable atmosphere for a given smoke emission flux and size will also amplify the coagulational effect on D_g (Sect. D5; Figs. D20 and D22). For the largest fire size (100 km^2), coagulation alone (ChemOff_CoagOn) increases D_g more than SOA condensation alone (ChemOn_CoagOff); for the remaining fire sizes, SOA condensation increases D_g more than coagulation.

The bottom panel of Fig. 5.4 provides a qualitative summary of the anticipated impact of fire size and background aerosol concentrations on aging smoke D_g. For the system we have modelled, background aerosol concentration impacts D_g similar to OA mass; in general, an increasing background allows for a greater increase in D_g (more SOA condensation and less OA evaporation). However, the effect of background aerosol on D_g is slight for all but the smallest simulated fires, and coagulation plays an important role in increasing D_g, especially for the largest fires simulated. The qualitative summary of aging smoke σ_g (not shown) is essentially the opposite of D_g. For σ_g, coagulation and SOA condensation generally decrease σ_g for large and medium sized fires and small fires with high background concentrations. Like D_g, if OA evaporation is the dominant process over SOA condensation and coagulation (small fires with low background

concentrations), σ_g also decreases. Background aerosol has little effect on σ_g except for the smallest fire sizes in which σ_g slightly increases with increasing background concentration, due to more vapors being allowed to condense (see the discussion in Sect. D4).

5.3.3 Radiative properties: Extinction and CCN evolution

5.3.3.1 Extinction cross section as a proxy for the direct radiative effect

The extinction cross section enhancement, ΔE, normalized by ΔCO ($\Delta E/\Delta$CO) is used to quantify the changes in extinction as our simulated plumes age (ignoring potential composition/morphology changes). $\Delta E/\Delta$CO further allows for an estimate of the changes in the direct radiative effect (DRE). Figure 5.5a shows the initial and final $\Delta E/\Delta$CO for fire sizes of 10^{-2}, 1, and 100 km^2 and constant background aerosol concentrations of 0, 5, and 50 μg m^{-3} . (Figure D10 in the supporting information provides the same information for all modelled fire sizes down to 10^{-2} km^2 and all background concentrations). For the assumptions of our study of spherical particles with a refractive index of 1.5 - 0.08i at a wavelength of 500 nm, the peak extinction efficiency is at a particle diameter of ~500 nm (Fig. D11 in the supporting information).

The aged $\Delta E/\Delta$CO values corroborate the expectation that as plume OA mass increases through SOA condensation and particle size increases through SOA condensation and/or coagulation, $\Delta E/\Delta$CO will increase, as D_g increases towards the peak of mass extinction efficiency. SOA condensation (OA evaporation) is the strongest driver of increases (decreases) in $\Delta E/\Delta$CO. However, it can be seen that for fires 1 km^2 and larger, coagulation increases $\Delta E/\Delta$CO compared to cases without coagulation by up to 40%, due to the shifting of particle mass to larger diameters. Similar to mass, increasing background concentrations for fires with rapid dilution rates decreases

loss of OA to evaporation, allowing for a greater increase in total extinction cross section than similar cases with cleaner background concentrations.

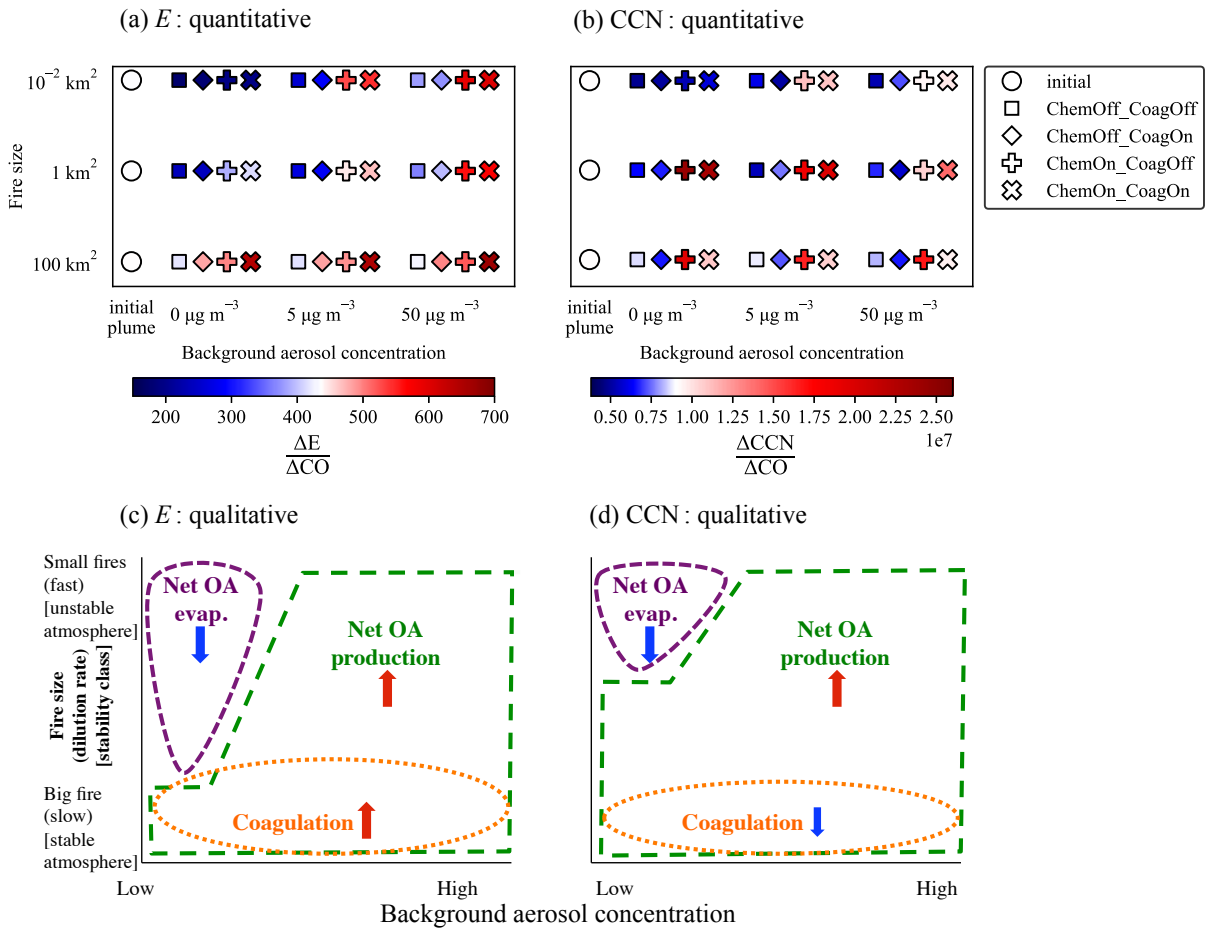

Figure 5.5 (a) The normalized extinction efficiency (Δ*E*/ΔCO) initially and after 4 hours of aging for the primary cases (Table 5.1). (b) The normalized CCN (ΔCCN/ΔCO) from smoke aerosol at 0.2% supersaturation initially and after 4 hours of aging, for the base cases (Table 5.1). Warm colors in (a) and (b) indicate an increase in the normalized values while cool colors represent a decrease. (c) and (d): Qualitative summaries of the impacts of fire size (y axis) and background aerosol concentration (x axis) on aged biomass burning (c) Δ*E*/ΔCO and (d) ΔCCN/ΔCO. Although we predicted that the net change in normalized CCN to be an increase for all fire sizes and background concentrations for the primary cases presented in Fig. 5.5, we expect normalized CCN will decrease under sufficient OA evaporation/low SOA condensation rates (Sect. D4 and D5; Figs. D13-D24).

Figure 5.5c shows the qualitative summary of the anticipated impact of fire size and background aerosol concentration on aging smoke extinction: for our specific system modeled

here, SOA condensation, coagulation, and increasing background concentrations all contribute to greater values of extinction, with an expected increase in the DRE, with the largest fire sizes producing the highest values of extinction. Similar to mass, OA evaporation decreases smoke extinction, and this process is expected to dominate for small fires in clean conditions.

5.3.3.2 CCN as a proxy for the aerosol indirect effect

The aerosol indirect effect (AIE) depends on the number concentration of particles large enough to act as CCN. Figure 5.5b shows the enhancement of CCN (ΔCCN) from smoke aerosol normalized by ΔCO (ΔCCN/ΔCO) for the base cases (Table 5.1) after 4 hours of aging for the same fire sizes and background concentrations as Fig. 5.5a. (Figure D12 in the supporting information provides the same information for all modelled fire sizes down to 10^{-2} km^2 and all background concentrations). These results are for a supersaturation of 0.2% (a supersaturation typical of stratiform clouds) and the assumption that both the plume and the background particles have a hygroscopicity parameter of $\kappa = 0.2$; these metrics correspond to a critical activation diameter of 121 nm, with 25% of the total initial particles in each plume able to act as a CCN.

When dilution and evaporation are the only processes occurring (ChemOff_CoagOff), ΔCCN/ΔCO after 4 hours of aging is reduced for all fire sizes as the particles shrink, leaving fewer particles above the activation diameter (121 nm). The impact of coagulation alone (ChemOff_CoagOn) on the 100 km^2 fire sizes is to decrease ΔCCN/ΔCO further, as coagulation acts to reduce particle number, including CCN-sized particles (this CCN reduction by coagulation exceeds CCN production from coagulation due to the increase in the mode diameter [Figure 5.4]). As previously discussed, coagulation rates are proportional to the square of the number concentration *N*, and thus coagulation rapidly decreases *N* for large fires where number

concentrations are sustained through high initial concentrations (air spends a longer time over larger fires leading to larger concentrations in our simulations) and slow dilution rates. However, as is the case for total plume mass, mean diameter, modal width, and total extinction, once the fire is small enough (~1 km^2) for coagulation rates to be trivial, coagulation has little impact on the aged ΔCCN/ΔCO concentrations, although for the smaller fire sizes, ChemOff_CoagOn cases sometimes slightly increase ΔCCN/ΔCO compared to ChemOff_CoagOff cases due to coagulational growth influencing CCN more than coagulational losses (Figs. 5.4 and 5.5). We note there are likely conditions in which coagulation is still important for smaller fires. For instance, Akagi et al. (2012) observed that coagulation was likely important within a smoke plume from a fire that was ~1 km^2 for increasing net normalized scattering. However, the wind speeds in that study were much slower than the wind speeds used in this study (0.5-2.2 m s^{-1} compared to 5 m s^{-1}), which would lead to an increased initial concentration and slower dilution rate.

SOA condensation in the ChemOn (relative to the ChemOff cases) greatly increases the ΔCCN/ΔCO through particle growth for all cases except for the smallest fire with no background aerosol, with ΔCCN/ΔCO increases of up to 70% for the ChemOn_CoagOff cases. However, when both chemistry and coagulation are on, coagulation decreases ΔCCN/ΔCO (as compared to ChemOn_CoagOff) by up to ~40% for the 100 km^2 fire size simulations due to the relatively high coagulation rates. Indeed, after 8 hours of aging, ΔCCN/ΔCO has decreased below the initial ΔCCN/ΔCO values for the 100 km^2 fire size simulations (Fig. D23 in the supporting information). Similarly, our sensitivity simulations show that conditions that lead to relatively lower SOA condensation (e.g. the lower-bound chemistry case; Figs. D17-D18) leads to a net decrease in ΔCCN/ΔCO after 4 hours of aging, due to the high coagulation rates not being sufficiently compensated by particle growth. Conversely, for the smaller fires, in the highest background cases,

ChemOn_CoagOn cases increase CCN concentrations beyond ChemOn_CoagOff cases, as coagulation is able to grow enough particles to past the activation diameter (121) nm (although coagulation will slightly decrease particle number).

Figure 5.5d gives the qualitative summary of the anticipated impact of fire size and background aerosol concentration on aging smoke CCN. For the system we have modelled in this study, coagulation decreases CCN for the largest fires. When the fire size is small enough that coagulation rates are slow and SOA condensation / OA evaporation are the dominant modelled processes, CCN follows the same patterns as smoke extinction, OA mass, and mode diameter. Although we predicted that the net change in normalized CCN to be an increase for most fire sizes and background concentrations for the primary cases presented in Fig. 5.5b, normalized CCN will decrease with aging under sufficient conditions that lead to decreases in the lognormal modal width or mean diameter, caused by significant OA evaporation and/or low SOA condensation rates (see Sect. D4 and D5 for further discussion). Again, we note that the precise values of both CCN and extinction may change under variable mass, number, and CO emissions, but we hypothesize that the qualitative conclusions will remain similar.

5.3.4 Study limitations

In this study, our objective is to isolate the impact of fire size, dilution, and background OA concentrations on coagulation and OA partitioning. There are many important processes that we are not simulating, and many important factors vary between fires/plumes that we leave fixed in this study.

We note that our simulations do not provide context for how the aerosol size distribution may change under aqueous processing for plumes that interact with clouds or elevated relative

humidities as they age, so our results here illustrate factors that may be important during clear-sky conditions. We also do not account for particle-phase or heterogeneous chemistry that could occur within the plume. Accretion reactions in the particle phase of organic molecules have been observed in laboratory studies to create lower-volatility products (e.g. Barsanti and Pankow, 2004; Kalberer et al., 2004; Wang et al., 2010), which would decrease the rate at which OA can evaporate, potentially leading to a greater than predicted increase in net (difference between total SOA condensation and OA evaporation) OA. Gelencser et al. (2000) demonstrated that phenolic acids from biomass burning readily undergo polymerization under reaction with OH. Further, it is hypothesized that tar balls may be formed through oligomerization (Adachi & Buseck et al., 2011; Pósfai et al., 2004). Conversely, heterogeneous reactions of OA with OH can result in fragmentation products that can evaporate from the particle if the volatility is sufficiently increased, contributing to aerosol aging (e.g. Hodshire et al., 2018; Hu et al., 2016; Kroll et al., 2009) and potentially leading to a greater loss in net OA than predicted in this study. Although we ran tests varying the accommodation coefficient as a proxy for phase state, we did not explicitly address potential size-dependent changes in phase state (Zaveri et al., 2017). We do not explicitly include black carbon or brown carbon as an aerosol-phase species, although black carbon and brown carbon has been observed within smoke plumes and can alter smoke aerosol optical properties (e.g. Forrister et al., 2015). We hold the organic to inorganic/black-carbon emissions flux constant throughout the study, although the actual ratio will depend both on fuel type and burn conditions (e.g. Akagi et al., 2012; Bian et al., 2015, Zhang et al., 2015).

We assume that each plume is homogeneous in their dilution across their widths (orthogonal to the direction of plume transport) as well as homogeneous concentrations of OH, whereas real plumes always display varying degrees of heterogeneity within the plume. This

heterogeneity could arise both from imperfect mixing as well as potential light attenuation within the plume (Hobbs et al., 2003), particularly within larger plumes, that could reduce oxidant concentrations and thus in-plume chemistry. We also do not explicitly explore variable injection heights in our analyses. While we do test the sensitivity of our results to different stability classes (we expect dispersion to generally follow stable conditions in the free troposphere), we do not change any of the temperature and pressure assumptions to be representative of free troposphere (FT) conditions. As well, we do not address changes to oxidation rates related to variable OH concentrations; reported in-plume OH concentrations estimates range between $5x10^6$ to $> 10^7$ molec cm^{-3}, but we are only aware of a few studies have made these estimates (Akagi et al., 2012; Hobbs et al., 2003; Yokelson et al., 2009). We test two chemistry assumptions based on the results of Bian et al. (2017), applying the reaction rates to all species uniformly within each VBS bin as a representative average reaction rate. However, real-world species of similar volatility will undergo variable reaction rates and this is not accounted for. As well, we have not accounted for the possibility that the in-plume average reaction rate may be even faster or slower than that of our chemistry two assumptions. We hold the emissions flux and size distribution constant for all the simulations, even though in reality the mass and number flux will change between different fuels and even within the same fire over time. We also hold the hygroscopicity and refractive index of the particles constant throughout the simulation time period, as the changes (including the sign of the changes) in these parameters during aging are likely burn- and fuel-dependent (e.g. Adler et al., 2011; Englehart et al., 2013; Haywood et al., 2003; Reid et al., 2005b and references therein). We assume that each plume has the same volatility distribution (regardless of size), that the temperature is held constant throughout the entire plume and entire simulation time period, and that the plumes entrain in constant nonvolatile background aerosol concentrations (representative

of e.g. aged organics) with no additional background gas-phase compounds. In reality, the plume's initial volatility distribution is likely to change based on the fuel burned (e.g. Hatch et al., 2017), which can impact SOA formation due to the variable mix of available SOA precursors. TThe background will likely contain both additional gas-phase compounds and semivolatile particles that would further alter the partitioning of smoke compounds between the particle and gas phases, and this will further increase the sensitivity of the plume evolution to background concentrations beyond what we predict here. As well, the plume can entrain in further species such as NO_x and O_3 that may impact the aging plume's chemistry. Finally, we only assume a temperature of 298 K in this study. Plumes in the free troposphere may be at much colder temperatures, which will impact the organic partitioning in the plumes and will impact the results (e.g. Donahue et al., 2006; Huffman et al., 2009). Each of these processes will be left to future studies.

5.4 Fire size, background aerosol concentrations, and observational studies

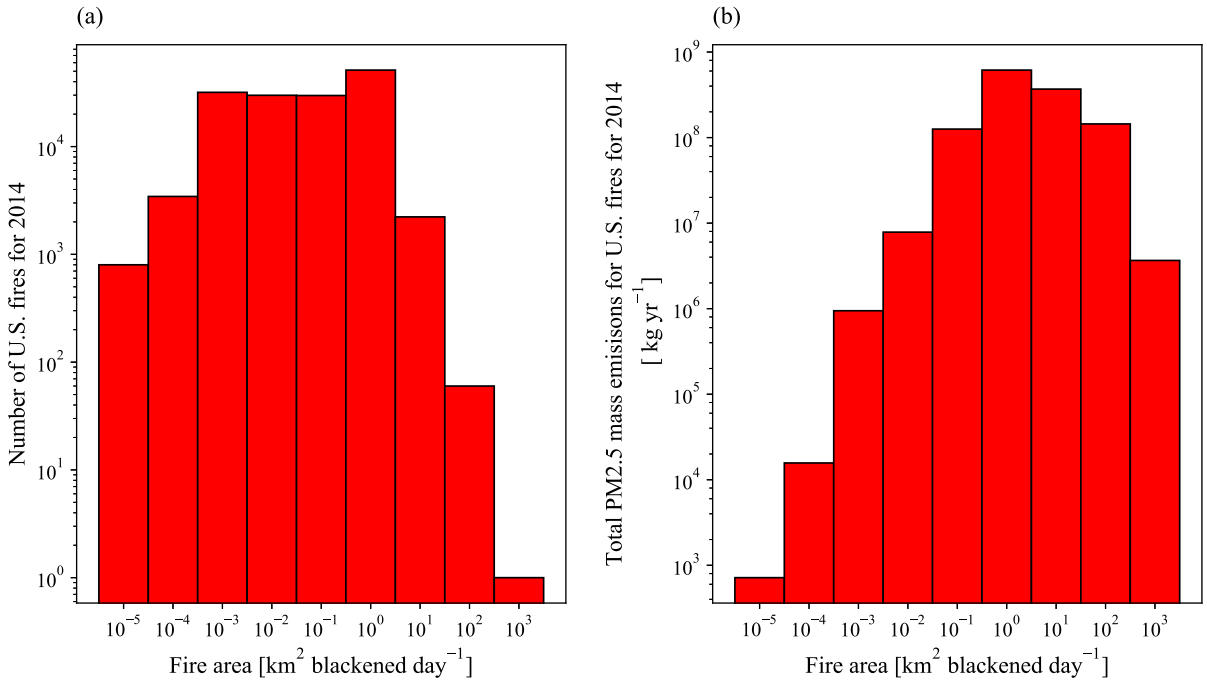

Figure 5.6 (a) Annual data for the number of recorded fires with different fire sizes in km^2 blackened per day (that is, the total area in km^2 burned per day) for the United States for 2014, from the National Emissions Inventory (U.S. EPA NEI, 2014). (b) Total annual $PM_{2.5}$ emissions in kg from each fire size for 2014 from the same dataset.

Our test cases indicate that fire size is anticipated to play an important role in determining the climate impacts from smoke plumes through its impact on plume dilution rates. Fig. 5.6 is an estimate for the distribution of fire sizes (both for wildland and prescribed fires) for the United States in 2014 from the National Emissions Inventory (U.S. EPA NEI, 2014). Panel (a) is the histogram of fire sizes, reported in km^2 blackened per day (not the area of the fire burning at any instant, but the closest proxy that we could find), showing that in the U.S., the majority of fires by number are smaller than 1 km^2 per day, the size range at which we find that the interacting background aerosol concentration begins to impact the evaporation rates of the plume aerosol size distributions. Panel (b) shows the total $PM_{2.5}$ emissions for each bin in kg. While the annual estimated emissions from fires within the 0.1, 1, 10, and 100 km^2 fire sizes have a similar

magnitude of $PM_{2.5}$ emissions, this study shows that the aging of smoke $PM_{2.5}$ could differ between these fire sizes, all other important factors (e.g. emissions flux, oxidant concentrations, chemistry rates/yields) set equal. Although it is likely that the exact fire-size distribution will vary within different geographical regions as well as from year to year, (small) agricultural and prescribed fires are among the dominant sources of biomass burning for many tropical and midlatitude regions (e.g. Giglio et al., 2010; Reid et al., 1998; van der Werf et al., 2010). We note that it is likely that the histogram in Fig. 5.6a underestimated the number of small fires: the burned area detection methods used to construct the database may not detect some of the small fires (e.g. Larkin et al., 2014), as even active fire detection misses many small fires (e.g. Nowell et al., 2018). Also, the total $PM_{2.5}$ emissions estimated in Fig. 5.6b may underestimate the importance of larger fires, as larger fires have been observed to have higher emissions factors than smaller fires (e.g. Liu et al., 2016) but the NEI estimate assumes that emission factors do not depend explicitly on fire size (Anderson et al., 2004, Raffuse et al., 2012).

Regarding background concentrations, isolated smoke plumes will generally evolve in a clean background (generally similar to the 5 μg m-3 case tested here, Jimenez et al., 2009). However, regions with many small concurrent fires can create a high background aerosol concentration (Baars et al., 2012; Martin et al., 2010; Reid et al., 1998), which can then influence the aging and evaporation rates of individual plumes. For example, within the Amazon basin during the dry season, daily average background aerosol concentrations can reach between 50-600 μg m-3 (Reid et al., 1998; Martin et al., 2010). Mid-latitude regions with many nearby wild or prescribed fires may also have elevated background OA concentrations (Brey et al., 2018).

A number of field campaigns have taken place over the last few decades with the explicit purpose of characterizing plume aging. Table D2 (Sect. D6) in the supporting information provides

an overview of our attempt at a complete set of published biomass burning field studies that focus on plume aging. Table D2 provides the available details of fire size and type, approximate age of the measurement, atmospheric conditions, background concentration, and the normalized OA, extinction, and CCN that were provided in publications. Many of the published studies do not provide fire size and/or emissions rates. Similarly, few published studies report direct background aerosol concentrations or in-plume aerosol concentrations, even though some studies are of fires small enough that the background concentration may be able to influence the OA concentrations (e.g. Akagi et al., 2012; Cachier et al., 1995; Liu et al., 2016; Yokelson et al., 2009). For field observations, dilution rates can be directly obtained from the change of CO concentrations (or another inert tracer) with time rather than relying on the fire-size/Gaussian-plume method that we used here, but we find that regardless, the absolute OA concentration and absolute background OA concentrations should be important to understand the evolution of particle properties within the diluting plume. Further, direct comparisons of ΔOA/ΔCO between campaigns can miss the key differences between the systems (fire, atmospheric, and background conditions) and may incorrectly attribute differences in observed ΔOA/ΔCO evolution solely to differences in chemistry or emissions (even if these factors are also very important). Due to each of the published field analyses having a missing piece or pieces of information (e.g. fire size, background aerosol concentration, wind speed), and each measured fire having different emission fluxes, oxidant levels etc., the interpretation of the published field analyses through the lens of the present study is a challenging endeavor for future work. Many of these data parameters currently missing from published field analyses described in Sect. 4 may be available in the campaign data repositories, and we highlight key needs for the modelling community in Sect. 5.

5.5 Synthesis, recommendations, and conclusions

In this study, we have investigated the potential importances of fire size / dilution rate and background aerosol concentrations on OA evaporation, SOA production from condensation of vapors, and coagulation, which in turn impact normalized aged smoke OA mass, median diameter and modal width, total extinction cross section, and CCN. There are a number of important limitations of our study, as detailed in Sect. 3.4; many of these limitations stem from our simplification of the smoke-plume system to isolate potential fire-size and background effects. This study did not attempt to simulate any specific plumes that have been observed. Discrepancies between our results here and observational studies (Sect. 3.1) indicate that our current modelling framework still requires further improvements in future studies. For example, some studies have seen much higher mass enhancements than any of the cases modelled here, indicated potentially a missing major OA source for those specific systems (Vakkari et al., 2014, 2018; Yokelson et al., 2009). We fix many aerosol/plume properties that are likely to vary across real plumes. These include the initial volatility distribution and plume size distribution parameters, temperature, emissions flux, oxidant concentrations, available light within the plume for photooxidation, chemical rate constants and yields, aerosol hygroscopicity, refractive indices, and the explicit impacts of varying injection heights. Further, we assume that our plume expands as a homogeneously mixed box, whereas real plumes have concentration gradients in vertical and cross-wind transects, which would impact our results.

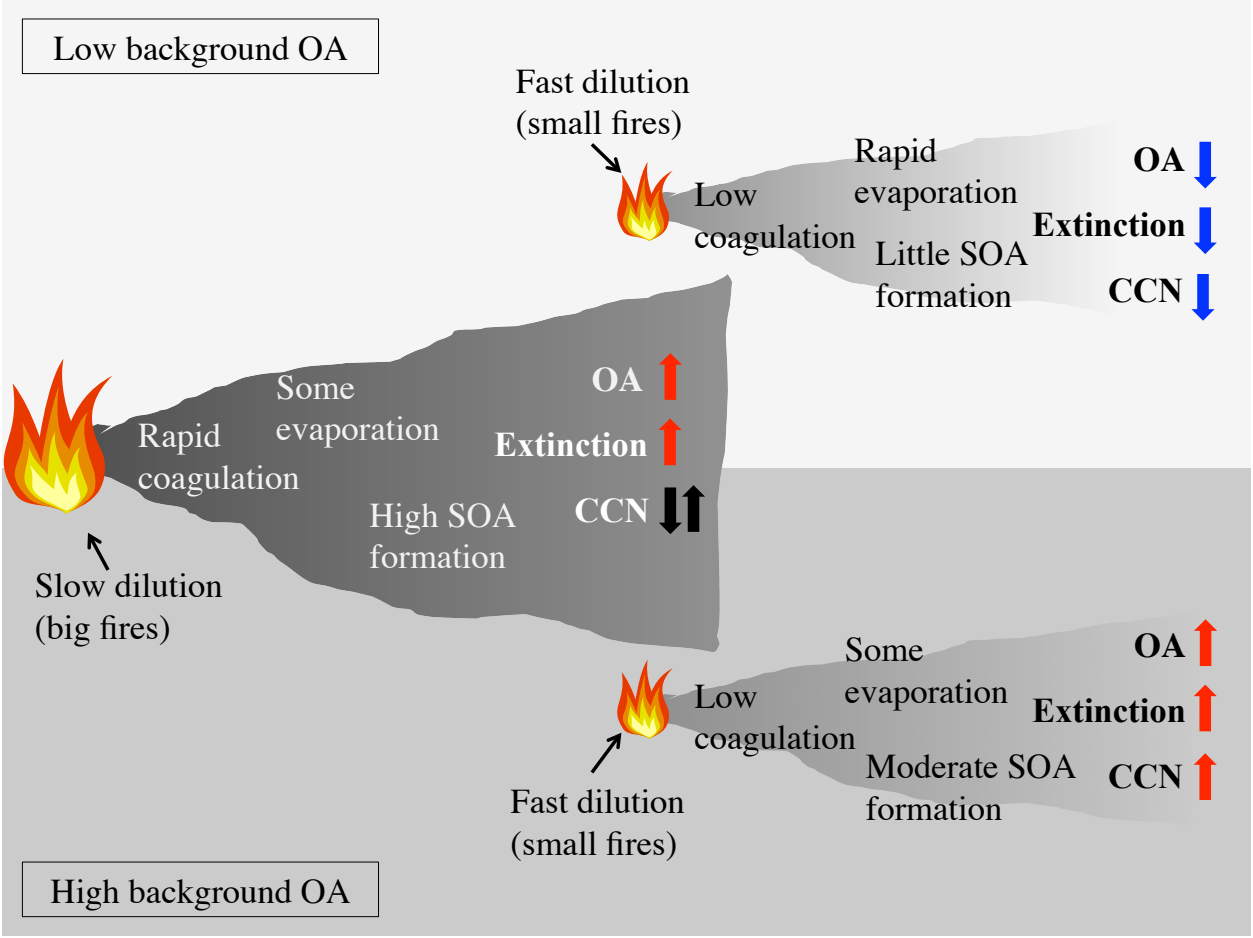

Figure 5.7 Conceptual overview of the roles of fire size and background concentration on net normalized changes to aged smoke OA and number concentrations. Shown are the anticipated net normalized changes to OA mass, extinction, and CCN for large versus small fires in high versus low background concentrations.

Within our test framework we have shown that fire size and a non-volatile background aerosol concentration can impact aged mass, extinction, and CCN, even with accounting for these other factors, indicating that fire size and background aerosol are important factors that should be included in future analyses**.** Figure 5.7 provides a qualitative summary of the importances of fire size and background concentration on OA, extinction, and the CCN for the general system modelled in this study. Total extinction cross section was used as a proxy for the DRE, as to first order, the DRE will scale with extinction, ignoring refractive index changes and changes to the phase function (Chylek and Wong, 1995). CCN was used as a proxy for the AIE, as to first order,

the AIE will scale sub-linearly with CCN (Twomey, 1977). Although both large and small fires lose mass through dilution-driven evaporation, the rate of SOA condensation versus the rate of OA evaporation will determine if the net normalized change in smoke OA mass is an increase or a decrease.

Large, slowly diluting fires with slow rates of evaporation can undergo sufficient SOA condensation relative to POA evaporation to yield a net increase in smoke OA, provided the fire produces sufficient precursor vapors. The aerosol concentration within these large plumes greatly exceeds that of most background aerosol concentrations, and evaporation rates will not be significantly impacted by background aerosol concentrations, leading to very similar net smoke OA changes under variable background aerosol concentrations. However, as evaporation rates are so low in large fires, the majority of the total aged OA will remain as POA (rather than SOA). However, if chemistry is slowed due to e.g. reduced available UV radiation within the plume, then production of SOA will also be slowed, leading to relatively less SOA formation.

Conversely, small, rapidly diluting fires will undergo much faster rates of POA evaporation that may exceed that rate of SOA condensation (at least initially). The smoke contribution to OA concentrations within these small plume can quickly dilute to concentrations near or below the background contributions to OA concentrations, and thus more-polluted background conditions reduce evaporation more than cleaner conditions, leading to greater net smoke OA mass changes during aging. Due to rapid evaporation rates that provide a relatively higher concentration of vapors that could oxidize and recondense, a higher fraction of the total aged OA mass will be SOA (rather than POA) for small fires over large fires. The inclusion of background aerosol is anticipated to be particularly important for regions that experience intense fire seasons that may provide large ambient background concentrations into which fresh plumes are mixed. To our

knowledge, however, the background aerosol concentration has not been explicitly considered in previous analyses of field data.

As extinction generally scales with mass, it will also tend to increase/decrease with increasing/decreasing OA, following a similar pattern with changing background aerosol and fire size. Extinction undergoes some additional shifts dependent upon particle size as discussed in Sect. 3.1.1. CCN instead scales with number and particle size. Within large fires that undergo significant SOA condensation and little OA evaporation, CCN will increase if a sufficient number of particles can grow past the critical activation diameter. However, particle coagulation rates can also be significant within large fires, and thus whether CCN increases or decreases with plume aging depends on the relative strengths of SOA condensation and coagulation.Small fires undergo less coagulation on these timescales and thus if OA mass increases, CCN concentrations will increase due to particle growth to larger sizes. If the modal width decreases or evaporation is large (decreasing the mode diameter), CCN concentrations will decrease, and thus the tendency of aged CCN will depend strongly upon the relative OA evaporation/SOA condensation rates.

In order for the modeling community to better verify the conclusions presented here as well as improve upon the limitations of this study, we recommend that future publications on analyses of field studies should characterize and report as many of the following conditions as possible: fire size, emissions rate/flux, background aerosol concentrations, and relevant meteorological conditions (e.g,. wind speeds, temperature, the amount of UV radiation in the plume, stability class, boundary layer height, plume injection height) that help control dilution, mixing, and chemical rates in future studies of $PM_{2.5}$ and OA biomass burning plumes. We also encourage a wider sampling of fire sizes when possible, but we acknowledge the challenge of tracking highly diluted plumes, especially for cases when the absolute excess OA concentration in the plume is less than

the variability in the background OA concentration. Finally, size-distribution measurements of aging plumes also across a wide sampling will assist in better constraining the radiative impacts from smoke, as both the direct and indirect effects have particle size and number dependencies. These data will allow for more comprehensive comparisons between measured plumes and allow the hypotheses presented in this paper to be tested.

This study has shown that fire size and the background aerosol concentration may impact aged mass, extinction, and CCN. As a next step, our conclusions and simplifications must be tested in plume models, including models that can better-resolve in-plume gradients (e.g. Liu et al., 2016), against well-characterized observed plumes of different sizes and background aerosol concentrations. The validation of this work and related studies against field data can then allow for future work on creating plume-processing parameterizations to be used in regional and global atmospheric models that do not explicitly spatially resolve plumes.

REFERENCES

Abel, S. J., Haywood, J. M., Highwood, E. J., Li, J., & Buseck, P. R. (2003). Evolution of biomass burning aerosol properties from an agricultural fire in southern Africa. *Geophysical Research Letters, 30*(15). https://doi.org/10.1029/2003GL017342

Andreae, M. O., Artaxo, P., Fischer, H., Freitas, S. R., Grégoire, J. M., Hansel, A., et al. (2001). Transport of biomass burning smoke to the upper troposphere by deep convection in the equatorial region. *Geophysical Research Letters, 28*(6), 951–954. https://doi.org/10.1029/2000GL012391

Adachi, K., & Buseck, P. R. (2011). Atmospheric tar balls from biomass burning in Mexico. *Journal of Geophysical Research*, *116*, D05204, doi:10.1029/2010JD015102 Adams, P. J., & Seinfeld, J. H. (2002). Predicting global aerosol size distributions in general circulation models. *Journal of Geophysical Research, 107*(D19), 4370. https://doi.org/10.1029/2001JD001010

Akagi, S. K., Craven, J. S., Taylor, J. W., Mcmeeking, G. R., Yokelson, R. J., Burling, I. R., et al. (2012). Evolution of trace gases and particles emitted by a chaparral fire in California. *Atmospheric Chemistry and Physics, 12*, 1397–1421. https://doi.org/10.5194/acp-12-1397-2012

Akagi, S. K., Yokelson, R. J., Wiedinmyer, C., Alvarado, M. J., Reid, J. S., Karl, T., Crounse, J. D., & Wennberg, P. O. (2011). Emission factors for open and domestic biomass burning for use in atmospheric models, *Atmospheric Chemistry and Physics, 11*, 4039–4072. doi:10.5194/acp-11-4039-2011

Alvarado, M. J., Lonsdale, C. R., Yokelson, R. J., Akagi, S. K., Coe, H., Craven, J. S., Fischer, E. V., McMeeking, G. R., Seinfeld, J. H., Soni, T., Taylor, J. W., Weise, D. R., and Wold, C.

E. (2015). Investigating the links between ozone and organic aerosol chemistry in a biomass burning plume from a prescribed fire in California chaparral, *Atmospheric Chemistry and Physics, 15,* 6667-6688. https://doi.org/10.5194/acp-15-6667-2015

Alvarado, M. J., & Prinn, R. G. (2009). Formation of ozone and growth of aerosols in young smoke plumes from biomass burning: 1. Lagrangian parcel studies. *Journal of Geophysical Research Atmospheres*, *114*(9), 9306. https://doi.org/10.1029/2008JD011144

Anderson, G. K., D. V. Sandberg, and R. A. Norheim (2004), Fire Emission

Production Simulator (FEPS) user's guide, version 1.0, For. Serv., U.S. Dep. of Agric., Portland, Oreg. [Available at http://www.fs.fed.us/pnw/fera/publications/fulltext/FEPS_User_Guide.pdf.]

Barsanti, K. C., & Pankow, J. F. (2004). Thermodynamics of the formation of atmospheric organic particulate matter by accretion reactions—Part 1: aldehydes and ketones. *Atmospheric Environment, 38*(26), 4371–4382. https://doi.org/10.1016/j.atmosenv.2004.03.035

Baars, H., Ansmann, A., Althausen, D., Engelmann, R., Heese, B., Mller, D., et al. (2012). Aerosol profiling with lidar in the Amazon Basin during the wet and dry season. *Journal of Geophysical Research Atmospheres*, *117*(21), 21201. https://doi.org/10.1029/2012JD018338

Bateman, A. P., Gong, Z., Harder, T. H., De Sá, S. S., Wang, B., Castillo, P., et al. (2017). Anthropogenic influences on the physical state of submicron particulate matter over a tropical forest. *Atmospheric Chemistry and Physics, 17*(3), 1759–1773. https://doi.org/10.5194/acp-17-1759-2017

Bertrand, A., Stefenelli, G., Jen, C. N., Pieber, S. M., Bruns, E. A., Ni, H., et al. (2018). Evolution of the chemical fingerprint of biomass burning organic aerosol during aging. *Atmospheric Chemistry and Physics*, *18*(10), 7607–7624. https://doi.org/10.5194/acp-18-7607-2018

Bian, Q., Jathar, S. H., Kodros, J. K., Barsanti, K. C., Hatch, L. E., May, A. A., et al. (2017). Secondary organic aerosol formation in biomass-burning plumes: Theoretical analysis of lab studies and ambient plumes. *Atmospheric Chemistry and Physics, 17*(8)*,* 5459–5475. https://doi.org/10.5194/acp-17-5459-2017

Bian, Q., May, A. A., Kreidenweis, S. M., & Pierce, J. R. (2015). Investigation of particle and vapor wall-loss effects on controlled wood-smoke smog-chamber experiments. *Atmospheric Chemistry and Physics, 15*(19), 11027–11045. https://doi.org/10.5194/acp-15-11027-2015

Bohren, C. F. & Huffman, D.R. (1983). *Absorption and Scattering of Light by Small Particles.* Weinham, John Wiley & Sons.

Bond, T.C, Doherty S. J., Fahey, D. W., Forster, P. M., Berntsen, T., DeAngelom B. J., et al. (2013). Bounding the role of black carbon in the climate system: A scientific assessment. *Journal of Geophysical Research: Atmospheres, 118*(11), 5380–5552. https://doi.org/10.1002/jgrd.50171

Boucher, O., Randall, D., Artaxo, P., Bretherton, C., Feingold, G., Forster, P., et al. (2013). Clouds and Aerosols. in: Climate Change 2013: The Physical Science Basis. Contribution of Working Group I to the Fifth Assessment Report of the Intergovernmental Panel on Climate Change. Cambridge, United Kingdom and New York, NY, USA Cambridge University Press.

Brey, S. J., Barnes, E. A., Pierce, J. R., Wiedinmyer, C., & Fischer, E. V. (2018). Environmental conditions, ignition type, and air quality impacts of wildfires in the southeastern and western United States. Earth's Future, 6, 1442–1456. https://doi.org/10.1029/2018EF000972

Brito, J., Rizzo, L. V, Morgan, W. T., Coe, H., Johnson, B., Haywood, J., et al. (2014). Ground-based aerosol characterization during the South American Biomass Burning Analysis (SAMBBA) field experiment. *Atmospheric Chemistry and Physic*, *14*, 12069–12083. https://doi.org/10.5194/acp-14-12069-2014

Burling, I. R., Yokelson, R. J., Akagi, S. K., Urbanski, S. P., Wold, C. E., Griffith, D. W. T., et al. (2011). Airborne and ground-based measurements of the trace gases and particles emitted by prescribed fires in the United States. *Atmospheric Chemistry and Physics, 11*(23), 12197–12216. https://doi.org/10.5194/acp-11-12197-2011

Cachier, H., Liousse, C., Buat-Menard, P., & Gaudichet, A. (1995). Particulate content of savanna fire emissions. *Journal of Atmospheric Chemistry, 22*(1–2), 123–148. https://doi.org/10.1007/BF00708185

Capes, G., Johnson, B., Mcfiggans, G., Williams, P. I., Haywood, J., & Coe, H. (2008). Aging of biomass burning aerosols over West Africa: Aircraft measurements of chemical composition, microphysical properties, and emission ratios. *Journal of Geophysical Research, 113*, 0–15. https://doi.org/10.1029/2008JD009845

Carrico, C. M., A. J. Prenni, S. M. Kreidenweis, E. J. T. Levin, C. S. McCluskey, P. J. DeMott, G. R. McMeeking, S. Nakao, C. Stockwell, and R. J. Yokelson (2016), Rapidly evolving ultrafine and fine mode biomass smoke physical properties: Comparing laboratory and field results, J. Geophys. Res. Atmos., 121, 5750–5768, doi: 10.1002/2015JD024389.

Charlson, R. J., Schwartz, S. E., Hales, J. M., Cess, R. D., Coakley, J. A., Hansen, J. E., & Hofmann, D. J. (1992). Climate forcing by anthropogenic aerosols. *Science, 255*(5043), 423 –430. https://doi.org/10.1126/science.255.5043.423

Chen, J., Li, C., Ristovski, Z., Milic, A., Gu, Y., Islam, M. S., et al. (2017). A review of biomass burning: Emissions and impacts on air quality, health and climate in China. *Science of the Total Environment, 579*(November 2016), 1000–1034. https://doi.org/10.1016/j.scitotenv.2016.11.025

Chylek, P., & Wong, J. (2018). Effect of absorbing aerosols on global radiation budget. *Geophysical Research Letters, 22*(8), 929–931. https://doi.org/10.1029/95GL00800

Collier, S., Zhou, S., Onasch, T. B., Jaffe, D. A., Kleinman, L., Sedlacek, A. J., et al. (2016). Regional Influence of Aerosol Emissions from Wildfires Driven by Combustion Efficiency: Insights from the BBOP Campaign. *Environmental Science and Technology, 50*(16), 8613–8622. https://doi.org/10.1021/acs.est.6b01617

Cubison, M. J., Ortega, A. M., Hayes, P. L., Farmer, D. K., Day, D., Lechner, M. J., et al. (2011). Effects of aging on organic aerosol from open biomass burning smoke in aircraft and laboratory studies. *Atmospheric Chemistry and Physics, 11*, 12049–12064. https://doi.org/10.5194/acp-11-12049-2011

D'Andrea, S. D., Häkkinen, S. A. K., Westervelt, D. M., Kuang, C., Levin, E. J. T., Kanawade, V. P., et al. (2013). Understanding global secondary organic aerosol amount and size-resolved condensational behavior. *Atmospheric Chemistry and Physics*, *13*(22), 11519–11534. https://doi.org/10.5194/acp-13-11519-2013

Donahue, N. M., Robinson, A. L., Stanier, C. O., & Pandis, S. N. (2006). Coupled Partitioning, Dilution, and Chemical Aging of Semivolatile Organics. *Environmental Science & Technology, 40*(8), 2635–2643. https://doi.org/10.1021/es052297c

Donahue, N. M., Robinson, A. L., & Pandis, S. N. (2009). Atmospheric organic particulate matter: From smoke to secondary organic aerosol. *Atmospheric Environment*, *43*(1), 94–106. https://doi.org/10.1016/j.atmosenv.2008.09.055

Eagan, R. C. R., Hobbs, P. V., & Radke, L. F. (1974). Measurements of cloud condensation nuclei and cloud droplet size distributions in the vicinity of forest fires. *Journal of Applied Meteorology, 1*3(5), 553–557. https://doi.org/10.1175/1520-0450(1974)013<0553:MOCCNA>2.0.CO;2

Eatough, D. J., Eatough, N. L., Pang, Y., Sizemore, S., Kirchstetter, T. W., Novakov, T., & Hobbs, P. V. (2003). Semivolatile particulate organic material in southern Africa during SAFARI 2000. *Journal of Geophysical Research, 108*(D13), 8479--+. https://doi.org/10.1029/2002JD002296

Engelhart, G. J., Hennigan, C. J., Miracolo, M. A., Robinson, A. L., & Pandis, S. N. (2012). Cloud condensation nuclei activity of fresh primary and aged biomass burning aerosol. *Atmospheric Chemistry and Physics, 12*, 7285–7293. https://doi.org/10.5194/acp-12-7285-2012

Formenti, P., Elbert, W., Maenhaut, W., Haywood, J., Osborne, S., & Andreae, M. O. (2003). Inorganic and carbonaceous aerosols during the Southern African Regional Science Initiative (SAFARI 2000) experiment: Chemical characteristics, physical properties, and emission data for smoke from African biomass burning. *Journal of Geophysical Research*, *108*, 8488. doi: 10.1029/2002JD002408, D13

Forrister, Haviland, et al. (2015). Evolution of brown carbon in wildfire plumes. *Geophysical Research Letters, 42(*2), 7623–7932. https://doi.org/10.1002/2015GL063897

Gaudichet, A., Echalar, F., Chatenet, B., Quisefit, J. P., Malingre, G., Cachier, H., Buat-Menard, P., Artaxo, P., and Maenhaut,W. (1995). Trace Elements in Tropical African Savanna, *Journal of Atmospheric Chemistry*, *22*, 19–39. https://doi.org/10.1007/BF00708179

Gelencsér, A., Hoffer, A., Molnár, A., Krivácsy, Z., Kiss, G., & Mészáros E. (2000). Thermal behaviour of carbonaceous aerosol from a continental background site. *Atmospheric Environment, 34*, 823 – 831. DOI: 10.1016/S1352-2310(99)00206-X

Giglio, L., Randerson, J. T., Van Der Werf, G. R., Kasibhatla, P. S., Collatz, G. J., Morton, D. C., & Defries, R. S. (2010). Assessing variability and long-term trends in burned area by merging multiple satellite fire products. *Biogeosciences, 7*, 1171–1186. https://doi.org/10.5194/bg-7-1171-2010

Grieshop, A. P., Logue, J. M., Donahue, N. M., & Robinson, A. L. (2009). Laboratory investigation of photochemical oxidation of organic aerosol from wood fires 1: measurement and simulation of organic aerosol evolution. *Atmospheric Chemistry and Physics, 9*, 1263–1277. https://doi.org/10.5194/acp-9-1263-2009

Hatch, L. E., Yokelson, R. J., Stockwell, C. E., Veres, P. R., Simpson, I. J., Blake, D. R., et al. (2017). Multi-instrument comparison and compilation of non-methane organic gas emissions from biomass burning and implications for smoke-derived secondary organic aerosol precursors. *Atmospheric Chemistry and Physics*, *17,* 1471–1489. https://doi.org/10.5194/acp-17-1471-2017

Heald, C. L., Ridley, D. A., Kroll, J. H., Barrett, S. R. H., Cady-Pereira, K. E., Alvarado, M. J., & Holmes, C. D. (2014). Contrasting the direct radiative effect and direct radiative forcing

of aerosols. *Atmospheric Chemistry and Physics, 14*, 5513–5527. https://doi.org/10.5194/acp-14-5513-2014(11)

Hecobian, A., Liu, Z., Hennigan, C. J., Huey, L. G., Jimenez, J. L., Cubison, M. J., et al. (2011). Comparison of chemical characteristics of 495 biomass burning plumes intercepted by the NASA DC-8 aircraft during the ARCTAS/CARB-2008 field campaign. *Atmospheric Chemistry and Physics, 11*, 13325–13337. https://doi.org/10.5194/acp-11-13325-2011

Hennigan, C. J., Miracolo, M. A., Engelhart, G. J., May, A. A., Presto, A. A., Lee, T., et al. (2011). Chemical and physical transformations of organic aerosol from the photo-oxidation of open biomass burning emissions in an environmental chamber. *Atmospheric Chemistry and Physics, 11*(15), 7669–7686. https://doi.org/10.5194/acp-11-7669-2011

Hennigan, C. J., Westervelt, D. M., Riipinen, I., Engelhart, G. J., Lee, T., Collett, J. L., et al. (2012). New particle formation and growth in biomass burning plumes: An important source of cloud condensation nuclei. *Geophysical Research Letters, 39(*9), 1–5. https://doi.org/10.1029/2012GL050930

Hobbs, P. V., Sinha, P., Yokelson, R. J., Christian, T. J., Blake, D. R., Gao, S., et al. (2003). Evolution of gases and particles from a savanna fire in South Africa. *Journal of Geophysical Research: Atmospheres, 108*(D13), n/a-n/a. https://doi.org/10.1029/2002JD002352

Hodshire, A. L., Palm, B. B., Alexander, M. L., Bian, Q., Campuzano-Jost, P., Cross, E. S., et al. (2018). Constraining nucleation, condensation, and chemistry in oxidation flow reactors using size-distribution measurements and aerosol microphysical modelling. *Atmospheric Chemistry and Physics Discussions*, (May), 1–53. https://doi.org/10.5194/acp-2018-223

Hu, W., Palm, B. B., Day, D. A., Campuzano-Jost, P., Krechmer, J. E., Peng, Z., et al. (2016). Volatility and lifetime against OH heterogeneous reaction of ambient isoprene-epoxydiols-derived secondary organic aerosol (IEPOX-SOA). *Atmospheric Chemistry and Physics*, *16,* 11563–11580. https://doi.org/10.5194/acp-16-11563-2016

Huang, R., Zhang, X., Chan, D., Kondragunta, S., Russell, A. G., & Talat Odman, M. (2018). Burned Area Comparisons between Prescribed Burning Permits in Southeastern USA and two Satellite-derived Products. *Journal of Geophysical Research: Atmospheres, 1–12*. https://doi.org/10.1029/2017JD028217

Huffman, J. A., Docherty, K. S., Mohr, C., Cubison, M. J., Ulbrich, I. M., Ziemann, P. J., Onasch, T. B., & Jimenez, J. L. (2009). Chemically-Resolved Volatility Measurements of Organic Aerosol from Different Sources. *Environmental Science and Technology, 43*, 5351–5357. doi:10.1021/es803539d

Hungershoefer, K., Zeromskiene, K., Iinuma, Y., Helas, G., Trentmann, J., Trautmann, T., Parmar, R. S., Wiedensohler, A., Andreae, M. O., & Schmid, O. (2008). Modelling the optical properties of fresh biomass burning aerosol produced in a smoke chamber: results from the EFEU campaign. *Atmospheric Chemistry and Physics*, *8*, 3427-3439. https://doi.org/10.5194/acp-8-3427-2008

Hussein, T., Löndahl, J., Paasonen, P., Koivisto, A. J., Petäjä, T., Hämeri, K. & Kulmala, M. (2013). Modeling regional deposited dose of submicron aerosol particles. *Science of the Total Environmen*t, 458–460, 140–149. doi:10.1016/J.SCITOTENV.2013.04.022

Jaffe, D. A. & Wigder, N. L. (2012), Ozone production from wildfires: A critical review*, Atmospheric Environment,*, *51*, 1–10. https://doi.org/10.1016/j.atmosenv.2011.11.063

Janhäll, S., Andreae, M. O., & Pöschl, U. (2010). Biomass burning aerosol emissions from vegetation fires: particle number and mass emission factors and size distributions. *Atmospheric Chemistry and Physics, 10*, 1427–1439. https://doi.org/10.5194/acp-10-1427-2010

Jassen, N. A. H., Gerlofs-Nijland, M. E., Lanki, T., Salonen, R. O., Cassee, F., Hoek, G., Fischer, P., Brunekreef, B., & Krzyzonowsk, M. (2010). Health Effects of Black Carbon, World Health Organization, Regional Office for Europe, available at: http://www.euro.who.int/__data/assets/pdf_ file/0004/162535/e96541.pdf (last access: June 2018)

Jathar, S. H., Donahue, N. M., Adams, P. J., & Robinson, A. L. (2014). Testing secondary organic aerosol models using smog chamber data for complex precursor mixtures: influence of precursor volatility and molecular structure. *Atmospheric Chemistry and Physics, 14*(11), 5771–5780. https://doi.org/10.5194/acp-14-5771-2014

Jen, C. N., Hatch, L. E., Selimovic, V., Yokelson, R. J., Weber, R., Fernandez, A. E., et al. (2018). Speciated and total emission factors of particulate organics from burning western U.S. wildland fuels and their dependence on combustion efficiency. Atmospheric Chemistry and Physics Discussions, 1–22. https://doi.org/10.5194/acp-2018-840

Jimenez, J. L., Canagaratna, M. R., Donahue, N. M., Prevot, a S. H., Zhang, Q., Kroll, J. H., et al. (2009). Evolution of organic aerosols in the atmosphere. *Science (New York, N.Y.)*, *326*(5959), 1525–1529. https://doi.org/10.1126/science.1180353

Johnston, F.H., Henderson, S. B., Chen, Y., Randerson, J. T., Marlier, M., DeFries, R. S., Kinney, P., Bowman, D. M., & Brauer, M. (2012). Estimated Global Mortality Attributable to

Smoke from Landscape Fires, *Environmental Health Perspectives, 120*, 695–701. http://dx.doi.org/10.1289/ehp.1104422

Jolleys, M. D., Coe, H., McFiggans, G., Capes, G., Allan, J. D., Crosier, J., et al. (2012). Characterizing the Aging of Biomass Burning Organic Aerosol by Use of Mixing Ratios: A Meta-analysis of Four Regions. *Environmental Science & Technology, 46*(24), 13093–13102. https://doi.org/10.1021/es302386v

Jolleys, M. D., Coe, H., McFiggans, G., Taylor, J. W., Le Breton, M., J-B Bauguitte, S., et al. (2015). Properties and evolution of biomass burning organic aerosol from Canadian boreal forest fires. *Atmospheric Chemistry and Physics, 15*, 3077–3095. https://doi.org/10.5194/acp-15-3077-2015

Julin, J., Winkler, P. M., Donahue, N. M., Wagner, P. E., & Riipinen, I. (2014). Surface and bulk accommodation of organic molecules of varying structure. *Environmental Science & Technology*, *48*, 12083–12089. https://doi.org/10.1021/es501816h

Kalberer, M., Paulsen, D., Sax, M., Steinbacher, M., Dommen, J., Prevot, A. S. H., et al. (2004). Identification of polymers as major components of atmospheric organic aerosols. *Science*, *303*(5664), 1659–62. https://doi.org/10.1126/science.1092185

Klug, W. (1969). A method for determining diffusion conditions from synoptic observations. *Staub - Reinhaltung der Luft, 29*, 14–20.

Knote, C., Hodzic, A., & Jimenez, J. L. (2015). The effect of dry and wet deposition of condensable vapors on secondary organic aerosols concentrations over the continental US, *Atmospheric Chemistry and Physics, 15*, 1-18. https://doi.org/10.5194/acp-15-1-2015

Kroll, J. H., Smith, J. D., Che, D. L., Kessler, S. H., Worsnop, D., R., & Wilson, K., R. (2009). Measurement of fragmentation and functionalization pathways in the heterogeneous

oxidation of oxidized organic aerosol. *Physical Chemistry Chemical Physics : PCCP, 11*(36), 7759. https://doi.org/10.1039/b916865f

Liousse, C., Devaux, C., Dulac, F., & Cachier, H. (1995). Aging of savanna biomass burning aerosols: Consequences on their optical properties. *Journal of Atmospheric Chemistry, 22*(1–2), 1–17. https://doi.org/10.1007/BF00708178

Liu, X., Zhang, Y., Huey, L. G., Yokelson, R. J., Wang, Y., Jimenez, J. L., et al. (2016). Agricultural fires in the southeastern U.S. during SEAC4RS: Emissions of trace gases and particles and evolution of ozone, reactive nitrogen, and organic aerosol. *Journal of Geophysical Research, 121*(12), 7383–7414. https://doi.org/10.1002/2016JD025040

Löndahl, J., Massling, A., Pagels, J., Swietlicki, E., Vaclavik, E. & Loft, S. (2007). Size-Resolved Respiratory-Tract Deposition of Fine and Ultrafine Hydrophobic and Hygroscopic Aerosol Particles During Rest and Exercise. *Inhalation Toxicology, 19*(2), 109–116, doi:10.1080/08958370601051677

Löndahl, J., Massling, A., Swietlicki, E., Bräuner, E. V., Ketzel, M., Pagels, J. & Loft, S. (2009). Experimentally Determined Human Respiratory Tract Deposition of Airborne Particles at a Busy Street. *Environmental Science & Technology, 43*(13), 4659–4664, doi:10.1021/es803029b

Mack, L. A., Levin, E. J. T., Kreidenweis, S. M., Obrist, D., Moosmüller, H., Lewis, K. A., et al. (2010). Optical closure experiments for biomass smoke aerosols. *Atmospheric Chemistry and Physics,10*, 9017–9026. https://doi.org/10.5194/acp-10-9017-2010

Martin, S. T., et al. (2010). Sources and properties of Amazonian aerosol particles, *Review of Geophysics, 48*, RG2002, doi: 10.1029/2008RG000280

Martin, S. T., Artaxo, P., MacHado, L. A. T., Manzi, A. O., Souza, R. A. F., Schumacher, C., et al. (2016). Introduction: Observations and Modeling of the Green Ocean Amazon (GoAmazon2014/5). *Atmospheric Chemistry and Physics, 16*(8), 4785–4797. https://doi.org/10.5194/acp-16-4785-2016

May, A. A., Lee, T., Mcmeeking, G. R., Akagi, S., Sullivan, A. P., Urbanski, S., et al. (2015). Observations and analysis of organic aerosol evolution in some prescribed fire smoke plumes. *Atmospheric Chemistry and Physics*, *15*, 6323–6335. https://doi.org/10.5194/acp-15-6323-2015

May, A. A., Levin, E. J. T., Hennigan, C. J., Riipinen, I., Lee, T., Collett, J. L., et al. (2013). Gas-particle partitioning of primary organic aerosol emissions: 3. Biomass burning. Journal of *Geophysical Research Atmospheres, 118*(19), 11327–11338. https://doi.org/10.1002/jgrd.50828

Naeher, L. P., Brauer, M., Lipsette M., Zelikoff, J. T., Simpson, C. D., Koenig, J. Q., & Smith, K. R. (2007). Woodsmoke health effects: a review. *Inhalation Toxicology, 19*, 67–106, doi:10.1080/08958370600985875

Nance, J. D., Hobbs, P. V, & Radke, L. F. (1993). Airborne Measurements of Gases and Particles From an Alaskan Wildfire. *Journal of Geophysical Research: Atmospheres, 98*(D8), 873–882. https://doi.org/10.1029/93JD01196

Nie, W., Ding, A. J., Xie, Y. N., Xu, Z., Mao, H., Kerminen, V.-M., et al. (2015). Influence of biomass burning plumes on HONO chemistry in eastern China. *Atmospheric Chemistry and Physics*, *15*(3), 1147–1159. https://doi.org/10.5194/acp-15-1147-2015

Nowell, H. K., Holmes, C. D., Robertson, K., Teske, C., & Hiers, J. K. (2018). A new picture of fire extent, variability, and drought interaction in prescribed fire landscapes: Insights from

Florida government records. Geophysical Research Letters, 45, 7874–7884. https://doi.org/10.1029/2018GL078679

Ortega, A. M., Day, D. A., Cubison, M. J., Brune, W. H., Bon, D., de Gouw, J. A., & Jimenez, J. L. (2013). Secondary organic aerosol formation and primary organic aerosol oxidation from biomass-burning smoke in a flow reactor during FLAME-3. *Atmospheric Chemistry and Physics, 13*(22), 11551–11571. https://doi.org/10.5194/acp-13-11551-2013

Pankow, J. F. (1994). An absorption model of gas/particle partitioning of organic compounds in the atmosphere. *Atmospheric Environment, 28*(2), 185–188. https://doi.org/10.1016/1352-2310(94)90093-0

Pasquill, F. (1961).The Estimation of the Dispersion of Windborne Material. *Meteorological Magazine, 90*, 33 – 49.

Pei, X., Hallquist, M., Eriksson, A. C., Pagels, J., Donahue, N. M., Mentel, T., Svenningsson, B., Brune, W., and Pathak, R. K (2018). Morphological transformation of soot: investigation of microphysical processes during the condensation of sulfuric acid and limonene ozonolysis product vapors, *Atmospheric Chemistry and Physics, 18,* 9845-9860. https://doi.org/10.5194/acp-18-9845-2018

Petters, M. D., & Kreidenweis, S. M. (2007). A single parameter representation of hygroscopic growth and cloud condensation nucleus activity. *Atmospheric Chemistry and Physics, 7*(8), 1961–1971. https://doi.org/10.5194/acp-7-1961-2007

Pierce, J. R., & Adams, P. J. (2007). Efficiency of cloud condensation nuclei formation from ultrafine particles. *Atmospheric Chemistry and Physics, 7*(5), 1367–1379. https://doi.org/10.5194/acp-7-1367-2007

Pierce, J. R., Riipinen, I., Kulmala, M., Ehn, M., Petäjä, T., Junninen, H., et al. (2011). Quantification of the volatility of secondary organic compounds in ultrafine particles during nucleation events. *Atmospheric Chemistry and Physics, 11*(17), 9019–9036. https://doi.org/10.5194/acp-11-9019-2011

Pósfai, M., R. Simonics, J. Li, P. V. Hobbs, and P. R. Buseck (2003), Individual aerosol particles from biomass burning in southern Africa: 1. Compositions and size distributions of carbonaceous particles, *Journal of Geophysical Research, 108*, 8483, doi:10.1029/2002JD002291, D13.

Pósfai, M., Gelencsér, A., Simonics, R., Arató, K., Li, J., Hobbs, P. V. & Buseck P. R. (2004). Atmospheric tar balls: Particles from biomass and biofuel burning. *Journal of Geophysical Research, 109*, D06213, doi:10.1029/2003JD004169

Radke, L. F., Hegg, A. S., Hobbs, P. V, & Penner, J. E. (1995). Effects of aging on the smoke from a large forest fire. *Atmospheric Research, 38*, 315–332. DOI: 10.1016/0169-8095(95)00003-A

Raffuse, S. M., N. K. Larkin, P. W. Lahm, and Y. Du (2012), Development of Version 2 of the Wildland Fire Portion of the National Emissions Inventory, paper presented at 20th International Emission Inventory Conference, Tampa, Florida, August 13 - 16, 2012.

Ramnarine, E., Kodros, J. K., Hodshire, A. L., Lonsdale, C. R., Alvarado, M. J. and Pierce, J. R.: Effects of near-source coagulation of biomass burning aerosols on global predictions of aerosol size distributions and implications for aerosol radiative effects, Atmos. Chem. Phys, 19, 6561–6577, doi:10.5194/acp-19-6561-2019, 2019.

Reid, J. S., Hobbs, P. V., Ferek, R. J., Blake, D. R., Martins, J. V., Dunlap, M. R., & Liousse, C. (1998). Physical, chemical, and optical properties of regional hazes dominated by smoke

in Brazil. *Journal of Geophysical Research: Atmospheres, 103*(D24), 32059–32080. https://doi.org/10.1029/98JD00458

Reid, J. S., Koppmann, R., Eck, T. F., & Eleuterio, D. P. (2005a). A review of biomass burning emissions, part II: Intensive physical properties of biomass burning particles. *Atmospheric Chemistry and Physics, 5*, 799-825. https://doi.org/10.5194/acp-5-799-2005

Reid, J. S., Eck, T. F., Christopher, S. A., Koppmann, R., Dubovik, O., Eleuterio, D. P., et al. (2005b). A review of biomass burning emissions part III: intensive optical properties of biomass burning particles. *Atmospheric Chemistry and Physics, 5*, 827-849. https://doi.org/10.5194/acp-5-827-2005,

Riipinen, I., Pierce, J. R., Yli-Juuti, T., Nieminen, T., Häkkinen, S., Ehn, M., et al. (2011). Organic condensation: a vital link connecting aerosol formation to cloud condensation nuclei (CCN) concentrations. *Atmospheric Chemistry and Physics, 11*(8), 3865–3878. https://doi.org/10.5194/acp-11-3865-2011

Sakamoto, K. M., Allan, J. D., Coe, H., Taylor, J. W., Duck, T. J., & Pierce, J. R. (2015). Aged boreal biomass-burning aerosol size distributions from BORTAS 2011. *Atmospheric Chemistry and Physics*, *15*, 1633–1646. https://doi.org/10.5194/acp-15-1633-2015

Sakamoto, K. M., Laing, J. R., Stevens, R. G., Jaffe, D. A., & Pierce, J. R. (2016). The evolution of biomass-burning aerosol size distributions due to coagulation: Dependence on fire and meteorological details and parameterization. *Atmospheric Chemistry and Physics, 16*(12), 7709–7724. https://doi.org/10.5194/acp-16-7709-2016

Sedlacek III, A. J., Buseck, P. R., Adachi, K., Onasch, T. B., Springston, S. R., & Kleinman, L. (2018). Formation and evolution of Tar Balls from Northwestern US wildfires. *Atmos. Chem. Phys.*, *18*(Figure 1), 1–28. https://doi.org/10.5194/acp-2018-41

Seinfeld, J. H. & Pandis, S. N. (2006). *Atmospheric Chemistry and Physics*. (*2nd ed*.). New York, John Wiley & Sons.

Shrivastava, M., Cappa, C. D., Fan, J., Goldstein, A. H., Guenther, A. B., Jimenez, J. L., et al. (2017). Recent advances in understanding secondary organic aerosol: Implications for global climate forcing. *Reviews of Geophysics, 55*(2), 509–559. https://doi.org/10.1002/2016RG000540

Stevens, B., G. Feingold, W.R. Cotton, and R.L. Walko, 1996: Elements of the Microphysical Structure of Numerically Simulated Nonprecipitating Stratocumulus. *Journal of the Atmospheric Sciences*, *53*, 980-1006, https://doi.org/10.1175/15200469(1996)053<0980:EOTMSO>2.0.CO;2

Ten Hoeve, J. E., Jacobson, M. Z., & Remer, L. A. (2012). Comparing results from a physical model with satellite and in situ observations to determine whether biomass burning aerosols over the Amazon brighten or burn off clouds. *Journal of Geophysical Research, 117*, D08203, doi: 10.1029/2011JD016856.

Tkacik, D. S., Robinson, E. S., Ahern, A., Saleh, R., Stockwell, C., Veres, P., et al. (2017). A dual-chamber method for quantifying the effects of atmospheric perturbations on secondary organic aerosol formation from biomass burning emissions. *Journal of Geophysical Research, 122*(11), 6043–6058. https://doi.org/10.1002/2016JD025784

Twomey, S. (1974). Pollution and the planetary albedo. *Atmospheric Environment*, *8*, 1251–1256. https://doi.org/10.1016/0004-6981(74)90004-3

Twomey, S. (1977). The influence of pollution on the shortwave albedo of clouds. *Journal of the Atmospheric Sciences, 34*, 1149-1152. *https://doi.org/10.1175/1520-0469(1977)034<1149:TIOPOT>2.0.CO;2*

Tzivion, S., Feingold, G., & Levin, Z. (1987). An efficient numerical solution to the stochastic coalescence equation. *Journal of the Atmospheric Sciences*, 3139-3149. *https://doi.org/10.1175/1520-0469(1987)044<3139:AENSTT>2.0.CO;2*

US EPA National Emissions Inventory (NEI) Documentation (2014). Retrieved from: https://www.epa.gov/air-emissions-inventories/2014-national-emissions-inventory-nei-documentation (Accessed 11 July 2018)

Vakkari, V., Kerminen, V.-M., Beukes, J. P., Titta, P., Zyl, P. G. van, Josipovic, M., et al. (2014). Rapid changes in biomass burning aerosols by atmospheric oxidation. *Geophysical Research Letters*, 2644–2651. https://doi.org/10.1002/2014GL059396

Vakkari, V., Beukes, J. P., Dal Maso, M., Aurela, M., Josipovic, M., & van Zyl, P. G. (2018). Major secondary aerosol formation in southern African open biomass burning plumes. *Nature Geoscience, 11*(8), 580–583. https://doi.org/10.1038/s41561-018-0170-0

van der Werf, G. R., Randerson, J. T., Giglio, L., Collatz, G. J., Mu, M., Kasibhatla, P. S., et al. (2010). Global fire emissions and the contribution of deforestation, savanna, forest, agricultural, and peat fires (1997–2009). *Atmospheric Chemistry and Physics, 10*, 11707–11735. https://doi.org/10.5194/acp-10-11707-2010

Wallace, J. M., & Hobbs, P. V. (2006). Atmospheric science: An introductory survey. Amsterdam: Elsevier Academic Press.

Wang, L., Khalizov, A. F., Zheng, J., Xu, W., Ma, Y., Lal, V., & Zhang, R. (2010). Atmospheric nanoparticles formed from heterogeneous reactions of organics. *Nature Geoscience, 3*(4), 238–242. https://doi.org/10.1038/ngeo778

Whitby, E., McMurry, P., Shankar, U., & Binkowski, F. S. (1991). *Modal Aerosol Dynamics Modeling* (Tech. rep., Office of research and development, US Environmental Protection Agency.)

Xie, Y., Ding, A., Nie, W., Mao, H., Qi, X., Huang, X., Xu, Z., Kerminen, V.M., Petäjä, T., Chi, X., et al. (2015). Enhanced sulfate formation by nitrogen dioxide: Implications from in situ observations at the SORPES station. *Journal of Geophysical Research: Atmospheres*, *120*, 12679–12694. doi: 10.1002/2015JD023607

Yokelson, R. J., Crounse, J. D., Decarlo, P. F., Karl, T., Urbanski, S., Atlas, E., et al. (2009). Emissions from biomass burning in the Yucatan. *Atmospheric Chemistry and Physics, 9*, 5785–5812. https://doi.org/10.5194/acp-9-5785-2009

Zaveri, R. A., Shilling, J. E., Zelenyuk, A., Liu, J., Bell, D. M., D'Ambro, E. L., et al. (2017). Growth kinetics and size distribution dynamics of viscous secondary organic aerosol. *Environmental Science & Technology*, *52*(3), 1191-1199 DOI: 10.1021/acs.est.7b04623

Zhang, T., Wooster, M. J., Green, D. C., & Main, B. (2015). New field-based agricultural biomass burning trace gas, PM2.5, and black carbon emission ratios and factors measured in situ at crop residue fires in Eastern China. *Atmospheric Environment, 121*, 22-34. https://doi.org/10.1016/j.atmosenv.2015.05.010.

Zhang, X., Pandis, S. N., & Seinfeld, J. H. (2012). Diffusion-Limited Versus Quasi-Equilibrium Aerosol Growth. *Aerosol Science and Technology, 46*(8), 874–885. https://doi.org/10.1080/02786826.2012.679344

Zhang, Y., Tao, S., Shen, H., & Ma, J. (2009). Inhalation exposure to ambient polycyclic aromatic hydrocarbons and lung cancer risk of Chinese population. *Proceedings of the National*

Academy of Sciences, 106(50), 21063 LP-21067. Retrieved from http://www.pnas.org/content/106/50/21063.abstract

Zhou, S., Collier, S., Jaffe, D. A., Briggs, N. L., Hee, J., Iii, A. J. S., et al. (2017). Regional influence of wildfires on aerosol chemistry in the western US and insights into atmospheric aging of biomass burning organic aerosol. *Atmospheric Chemistry and Physics, 17*(3), 2477–2493. https://doi.org/10.5194/acp-17-2477-2017

CHAPTER 6

DILUTION IMPACTS ON SMOKE AGING: EVIDENCE IN BBOP DATA[5]

Overview

Biomass burning emits vapors and aerosols into the atmosphere that can rapidly evolve as smoke plumes travel downwind and dilute, affecting climate- and health-relevant properties of the smoke. To date, theory has been unable to explain variability in smoke evolution. Here, we use observational data from the BBOP field campaign and show that initial smoke concentrations can help predict changes in smoke aerosol aging markers, number, and diameter. Because initial field measurements of plumes are generally >10 minutes downwind, smaller plumes will have already undergone substantial dilution relative to larger plumes. However, the extent to which dilution has occurred prior to the first observation is not a measurable quantity. Hence, initial observed concentrations can serve as an indicator of dilution, which impacts photochemistry and aerosol evaporation. Cores of plumes have higher concentrations than edges. By segregating the observed plumes into cores and edges, we infer that particle aging, evaporation, and coagulation occurred before the first measurement, and we find that edges generally undergo higher increases in oxidation tracers, more decreases in semivolatile compounds, and less coagulation than the cores.

6.1 Introduction

[5] This paper to be submitted as: 'Dilution impacts on smoke aging: Evidence in BBOP data', Anna L. Hodshire, Emily Ramnarine, Ali Akherati, Matthew J. Alvarado, Delphine K. Farmer, Shantanu H. Jathar, Sonia M. Kreidenweis, Chantelle R. Lonsdale, Timothy B. Onasch, Stephen R. Springston, Jian Wang, Yang Wang, Lawrence I. Kleinman, Arthur J. Sedlacek, Jeffrey R. Pierce

Smoke from biomass burning is a major source of atmospheric primary aerosol and vapors (Akagi et al., 2011; Gilman et al., 2015; Hatch et al., 2015, 2017; Jen et al., 2019; Koss et al., 2018; Reid et al., 2005; Yokelson et al., 2009), influencing air quality, local radiation budgets, cloud properties, and climate (Carrico et al., 2008; O'Dell et al., 2019; Petters et al., 2009; Ramnarine et al., 2019; Shrivastava et al., 2017), as well as the health of smoke-impacted communities (Ford et al., 2018; Gan et al., 2017; Reid et al., 2016). Vapors and particles emitted from fires can rapidly evolve as smoke travels downwind (Adachi et al., 2019; Akagi et al., 2012; Bian et al., 2017; Cubison et al., 2011; Hecobian et al., 2011; Hodshire et al., 2019a, 2019b; Jolleys et al., 2012, 2015; Konovalov et al., 2019; May et al., 2015; Noyes et al., 2020; Sakamoto et al., 2015), diluting and entraining regional background air. Fires span an immense range in size, from small agricultural burns, which may be only a few m^2 in total area and last a few hours, to massive wildfires, which may burn 10,000s of km^2 over the course of weeks (Andela et al., 2019). This range in size leads to variability in initial plume size and dilution, as large, thick plumes dilute more slowly than small, thin plumes for similar atmospheric conditions (Akagi et al., 2012; Bian et al., 2017; Cubison et al., 2011; Hecobian et al., 2011; Hodshire et al., 2019a, 2019b; Jolleys et al., 2012, 2015; Konovalov et al., 2019; May et al., 2015; Sakamoto et al., 2015)). Plumes can dilute unevenly, with edges of the plume mixing in with surrounding air more rapidly than the core of the plume. Variability in dilution leads to variability in the evolution of smoke emissions as instantaneous plume thickness will control shortwave fluxes (and thus photolysis rates and oxidant concentrations), gas-particle partitioning, and particle coagulation rates ((Akagi et al., 2012; Bian et al., 2017; Cubison et al., 2011; Hecobian et al., 2011; Hodshire et al., 2019a, 2019b; Jolleys et al., 2012, 2015; Konovalov et al., 2019; May et al., 2015; Sakamoto et al., 2015), (Garofalo et al., 2019), (Ramnarine et al., 2019; Sakamoto et al., 2016)). Thus, capturing variability in plume

thickness and dilution between fires and within fires can aid in understanding how species change within the first few hours of emission for a range of plume sizes.

The evolution of total particulate matter (PM) or organic aerosol (OA) mass from smoke has been the focus of many studies, as PM influences both human health and climate. Secondary organic aerosol (SOA) production may come about through oxidation of gas-phase volatile organic compounds (VOCs) that can form lower-volatility products that partition to the condensed phase (Jimenez et al., 2009; Kroll and Seinfeld, 2008). SOA formation may also arise from heterogeneous and multi-phase reactions in both the organic and aqueous phases (Jimenez et al., 2009; Volkamer et al., 2009). In turn, oxidant concentrations depend on shortwave fluxes (Tang et al., 1998; Tie, 2003; Yang et al., 2009). Smoke particles contain semivolatile organic compounds (SVOCs) (Eatough et al., 2003); (May et al., 2013), which may evaporate off of particles as the plume becomes more dilute (Formenti et al., 2003; Huffman et al., 2009; May et al., 2013), leading to losses in total aerosol mass. Field observations of smoke PM and OA mass normalized for dilution (e.g. through an inert tracer such as CO) report that for near-field (<24 hours) physical aging, net PM or OA mass can increase (Cachier et al., 1995; Formenti et al., 2003; Liu et al., 2016; Nance et al., 1993; Reid et al., 1998; Vakkari et al., 2014, 2018; Yokelson et al., 2009), decrease (Akagi et al., 2012; Hobbs et al., 2003; Jolleys et al., 2012, 2015; May et al., 2015), or remain nearly constant (Brito et al., 2014; Capes et al., 2008; Collier et al., 2016; Cubison et al., 2011; Forrister et al., 2015; Garofalo et al., 2019; Hecobian et al., 2011; Liu et al., 2016; May et al., 2015; Morgan et al., 2019; Sakamoto et al., 2015; Sedlacek et al., 2018; Zhou et al., 2017). It is theorized that both losses and gains in OA mass are likely happening concurrently in most plumes through condensation and evaporation (Bian et al., 2017; Hodshire et al., 2019a, 2019b; May et al., 2015), with the balance between the two determining whether net increases or decreases

or no change in mass occurs during near-field aging. However, there is currently no reliable predictor of how smoke aerosol mass (normalized for dilution) may change for a given fire.

Evolution of total aerosol number, size, and composition is critical in improving quantitative understanding of how biomass burn smoke plumes impact climate. These impacts include smoke aerosols' abilities to both act as cloud condensation nuclei (CCN) and to scatter/absorb solar radiation, each of which is determined by particle size and composition (Albrecht, 1989; Petters and Kreidenweis, 2007; Seinfeld and Pandis, 2006; Twomey, 1974; Wang et al., 2008). Particles can increase or decrease in size as well as undergo compositional changes through condensation or evaporation of vapors. In contrast, coagulation always decreases total number concentrations and increases average particle diameter; plumes with higher concentrations will undergo more coagulation than those with lower concentrations (Sakamoto et al., 2016).

Being able to predict smoke aerosol mass, number, size, and composition accurately is an essential component in constraining the influence of fires on climate, air quality, and health. Fires in the western United States region are predicted to increase in size, intensity, and frequency (Dennison et al., 2014; Ford et al., 2018; Spracklen et al., 2009; Yue et al., 2013). In response, several large field campaigns have taken place in the last 7 years examining wildfires in this region (Kleinman and Sedlacek, 2016)https://www.eol.ucar.edu/field_projects/we-can; https://esrl.noaa.gov/csd/projects/firex-aq/(Kleinman and Sedlacek, 2016). Here, we present smoke plume observations from the Biomass Burning Observation Project (BBOP) campaign of aerosol properties from five research flights sampling wildfires downwind in seven pseudo-Lagrangian sets of transects to investigate aging of OA mass and oxidation, and aerosol number and mean diameter. A range of initial plume OA mass concentrations were captured within these flights and sufficiently fast (1 second) measurements of aerosols and key vapors were taken. We

segregate each transect into edge, core, or intermediate regions of the plume and examine aerosol properties within the context of both the location within the plume (edge, core, or intermediate) and the initial OA mass loading of the given location, with the differences in aerosol loading serving as a proxy for differences in dilution rates, as the extent to which dilution has occurred prior to the first observation is not a measurable quantity. We create mathematical fits for predicting OA oxidation markers and mean particle diameter given initial plume mass and physical age (time) of the smoke. These fits may be used to evaluate other smoke datasets and assist in building parameterizations for regional and global climate models to better-predict smoke aerosol climate and health impacts.

6.2 Methods

The BBOP field campaign occurred in 2013 and included a deployment of the United States Department of Energy Gulfstream 1 (G-1) research aircraft in the Pacific Northwest region of the United States (Kleinman and Sedlacek, 2016; Sedlacek et al., 2018) from June 15 to September 13. We analyze five cloud-free BBOP research flights that had seven total sets of across-plume transects that followed the smoke plume downwind in a pseudo-Lagrangian manner (see Figures E1-E6 for examples; Table S1) from approximately 15 minutes after emission to 2-4 hours downwind (Kleinman and Sedlacek, 2016). The G-1 sampling setup is described in (Kleinman and Sedlacek, 2016; Sedlacek et al., 2018).

Number size distributions were obtained with a Fast-integrating Mobility Spectrometer (FIMS), providing particle size distributions nominally from ~20-350 nm (Kulkarni and Wang, 2006; Olfert and Wang, 2009); data was available between 20-262 nm for the flights used in this study. A Soot Photometer Aerosol Mass Spectrometer (SP-AMS) provided organic and inorganic

(sulfate, chlorine, nitrate, ammonium) aerosol masses, select fractional components (the fraction of the AMS OA spectra at a given mass-to-charge ratio) (Onasch et al., 2012), and elemental analysis (O/C and H/C) (Aiken et al., 2008; Canagaratna et al., 2015). We use the f_{60} and f_{44} fractional components (the mass concentrations of m/z 60 and 44 normalized by the total OA mass concentration) and O/C and H/C elemental ratios of OA as tracers of smoke and oxidative aging. Elevated f_{60} values are indicative of "levoglucosan-like" species (levoglucosan and other molecules that similarly fragment in the AMS) (Aiken et al., 2009; Cubison et al., 2011; Lee et al., 2010) and are shown to be tracers of smoke primary organic aerosol (POA) (Cubison et al., 2011). The f_{44} fractional component (arising from primarily CO_2+ as well as some acid groups;) is indicative of SOA arising from oxidative aging (Alfarra et al., 2004; Cappa and Jimenez, 2010; Jimenez et al., 2009; Volkamer et al., 2006). Fractional components f_{60} and f_{44} have been shown to decrease and increase with photochemical aging, respectively, likely due to both evaporation and/or oxidation of semivolatile f_{60}-containing species and addition of oxidized f_{44}-containing species (Alfarra et al., 2004; Huffman et al., 2009). O/C tends to increase with oxidative aging (Decarlo et al., 2008) whereas H/C ranges from increasing to decreasing with oxidative aging, depending on the types of reactions occurring (Heald et al., 2010). Thus, tracking H/C with aging may provide clues upon the types of reactions that may be occuring. A Single-Particle Soot Photometer (SP2; Droplet Measurement Technologies) was used to measure refractory black carbon (rBC) through laser-induced incandescence (Moteki and Kondo, 2010; Schwarz et al., 2006). An Off-Axis Integrated-Cavity Output Spectroscopy instrument (Los Gatos, Model 907) provided CO measurements. An SPN1 radiometer (Badosa et al., 2014; Long et al., 2010) provided total shortwave irradiance. Appendix E includes more details on the instruments used.

To determine the contribution of species X from smoke, the background concentration of X is subtracted off and normalized by background-corrected CO (ΔCO), which is inert on timescales of near-field aging (Yokelson et al., 2009), to correct for dilution. Increases or decreases of ΔX/ΔCO with time indicate whether the total amount of X in the plume has increased or decreased since time of emission. We background correct the number size distribution, OA, O, H, C, and rBC data in this manner by determining an average regional background for each species by using the lowest 10% of the CO data for a given flight with a similar altitude, latitude, and longitude as the smoke plume (excluding data from flying to and from the fire). Elemental O, H, and C are calculated using the O/C and H/C and OA data from the SP-AMS, allowing us to calculate ΔO/ΔC and ΔH/ΔC. We also background-correct f_{60} and f_{44} (using the mass concentrations of m/z 60, m/z 44, and OA inside and outside of the plume), we but do not normalize by CO due to these values already being normalized by OA. We only consider data to be in-plume if the absolute CO >= 150 ppbv, as comparisons of CO and the number concentration show that in-plume data has CO >150 ppbv and out-of-plume (background) data has CO < 150 ppbv. This threshold appears to be capturing clear plume features while excluding background air (Figures E7-E11); we perform sensitivity analyses of our results to our assumptions about background and in-plume values in Section 3.

From the FIMS, we examine the background-corrected, normalized number concentrations of particles with diameters between 40-262 nm, $\Delta N_{40\text{-}262\ nm}/\Delta CO$. $\Delta N_{40\text{-}262\ nm}/\Delta CO$ allows us to exclude potential influence of fresh nucleation upon the total number concentrations, as the bulk of observed newly formed particles observed fell below 40 nm (Figs. S7-S11). Smoke plumes contain particles with diameters larger than 262 nm (Janhäll et al., 2009), and so although we cannot provide total number concentrations, we can infer how the evolution of $\Delta N_{40\text{-}262\ nm}/\Delta CO$

will impact number concentrations overall. We also obtain an estimate of how the mean diameter between 40-262 nm, $\underline{D_p}$, changes with aging through:

$$\underline{D_p} = \frac{\Sigma N_i * D_{p,i}}{\Sigma N_i} \quad 6.1$$

Where N_i and $D_{p,\,i}$ are the number concentration and geometric mean diameter within each FIMS size bin, respectively.

All of the data are provided at 1 Hz and all but the SP-AMS fractional component data are available on the DOE ARM web archive (https://www.arm.gov /research/campaigns/aaf2013bbop). As the plane traveled at ~100 m s^{-1} on average, data were collected every 100 m across the plume. The instruments used here had a variety of time lags (all <10 seconds) relative to a TSI 3563 nephelometer used as reference. The FIMS also showed an additional lag in flushing smoky air with cleaner air when exiting the plume with maximum observed flushing timescales around 30 seconds, but generally less (Figure E12). To test if these lags impact our results, we perform an additional analysis where we only consider the first half of each in-plume transect, when concentrations are generally rising with time (Figures E12-E13), and our main conclusions are unaffected. We do not test the impacts of other timelags.

We use MODIS Terra and Aqua fire and thermal anomalies detection data to determine fire locations (Giglio et al., 2006, 2008) and estimate the fire center to be the approximate center of all clustered MODIS detection points for a given sampled fire (Figures E1-E6). Depending upon the speed of the fire front, the true fire location and center at the time of sampling is likely different than the MODIS estimates. To estimate the physical age of the plume, we use the estimated fire center as well as the FIMS number distribution to determine an approximate centerline of the

plume as the smoke travels downwind (Figures E1-E6) and use mean wind speed and this estimated centerline to get an estimated physical age for each transect. We did not propagate uncertainty in fire location, wind speed, or centerline through to the physical age, which is a limitation of this study.

6.3 Results & Discussion

As a case example, we examine the aging profiles of smoke from the Colockum fire during the first set of pseudo-Lagrangian transects on flight 730b (Table S1). Figure 6.1 provides ΔOA/ΔCO, ΔrBC/ΔCO Δf_{60}, Δf_{44}, ΔH/ΔC, ΔO/ΔC, $\Delta N_{40\text{-}262\ nm}$/ΔCO, and $\underline{D_p}$ as a function of the estimated physical age; Figures E14-E18 provide this information for the other pseudo-Lagrangian transect sets studied. We have divided each transect into four regions: between the 5-15 (edge), 15-50 (intermediate, outer), 50-90 (intermediate, inner), and 90-100 (core) percentile of ΔCO within each transect. Figure 6.1 shows the edge and core data, both averaged per transect, with Figures E14-E18 providing all four percentile bins for each flight. These percentile bins correspond with the thinnest to thickest portions of the plume, respectively, and if a fire has uniform emissions ratios across all regions and dilutes evenly downwind, these percentile bins would correspond to the edges, intermediate regions, and the core of the diluting plume. We use this terminology in this study but note that uneven emissions, mixing, and/or dilution lead to the percentile bins not corresponding physically to our defined regions in some cases. However, the lowest two ΔCO bins tend more towards the physical edges of the plume and the highest two tend more towards the physical center of the plume (Figures E2-E6). We do not use the data from the lowest 5% of ΔCO to reduce uncertainty at the plume-background boundary. We do not know

where the plane is vertically in the plume, which is a limitation as vertical location will also impact the amount of solar flux able to penetrate through the plume.

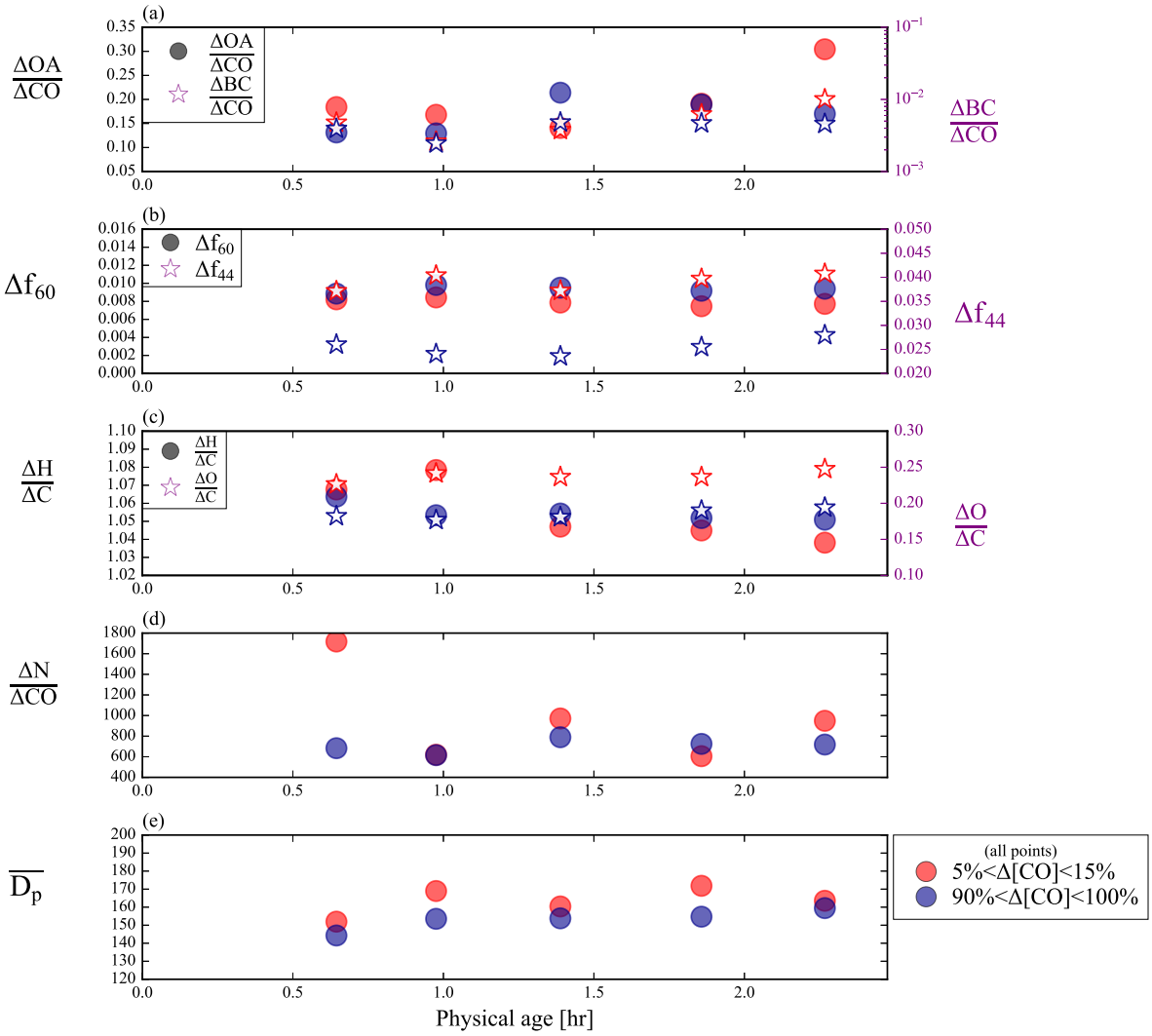

Figure 6.1 Aerosol properties from the first set of pseudo-Lagrangian transects from the Colockum fire on flight '730b' (a) ΔOA/ΔCO (right y-axis) and ΔrBC/ΔCO (left y-axis), (b) Δf_{60} (right y-axis) and Δf_{44} (left y-axis), (c) ΔH/ΔC (right y-axis) and ΔO/ΔC (left y-axis), (d) ΔN/ΔCO, and (e) Dp against physical age. For each transect, the data is divided into edge (the lowest 5-15% of ΔCO data; red points) and core (90-100% of ΔCO data; blue points). ΔrBC/ΔCO is shown in log scale to improve clarity.

Figure 6.1 shows that ΔOA/ΔCO and ΔrBC/ΔCO vary little with age. A true Lagrangian flight with the aircraft sampling the same portion of the plume and no measurement artifacts (e.g. coincidence errors at high concentrations) would have a constant ΔrBC/ΔCO for each transect. This flight and other flights studied here have slight variations in ΔrBC/ΔCO (Figure 6.1; Figures E14-E18), which may be indicative of deviations from a Lagrangian flight path with temporal variations in emission and/or measurement uncertainties. For this flight, Δf_{60} changes little (~±6% between edge and core) while Δf_{44} increases slightly (~8% for both edge and core) with age, with edges showing the highest Δf_{44}. ΔH/ΔC decreases while ΔO/ΔC increases with the edges showing higher values of ΔO/ΔC. Mean aerosol diameter increases and normalized number concentration decreases between 40-262 nm with aging. The decrease in number concentration is presumably due to coagulation, as little dry deposition would occur within these timescales (<2.5 hours). These trends are discussed for all flights in the following sections.

6.3.1 Organic aerosol aging: ΔOA/ΔCO, Δf_{60}, Δf_{44}, ΔH/ΔC, and ΔO/ΔC

Figure 6.2a-e show available ΔOA/ΔCO, Δf_{60}, Δf_{44} ΔH/ΔC, and ΔO/ΔC edge and core data versus physical age for each transect for each flight of this study, colored by the mean ΔOA within a ΔCO percentile bin from the transect closest to the fire, $\Delta OA_{initial}$. We show the 5-15 (edge) and 90-100 (core) ΔCO percentile bins here; Figure E19 shows the same information for all four ΔCO percentiles. We note that although some of the physical ages appear to be at ~0 hours, this is from a limitation of our physical age estimation method (Sect. 2), as no flights captured data before ~15 minutes after emission (Kleinman et al., 2016). Also included in Figure 6.2 are the Spearman rank-order correlation tests (hereafter Spearman tests) that show correlation coefficients (R) with initial plume OA mass, $\Delta OA_{initial}$ ($R_{\Delta OA,initial}$), and physical age (R_{age}) against each

variable (for the correlations with $\Delta OA_{initial}$, all transects in a set are given the same $\Delta OA_{initial}$ value). Figures E13, E19-E21 show the same details as Figure 6.2 but provide sensitivity tests to potential FIMS measurement artifacts (Figure E13) and our assumed background CO and ΔCO percentile spacing (Figures E19-E21). Although these figures show slight variability, the findings discussed below remain robust and we constrain the rest of our discussion to the FIMS measurements and background and ΔCO percentile spacings used in Figure 6.2.

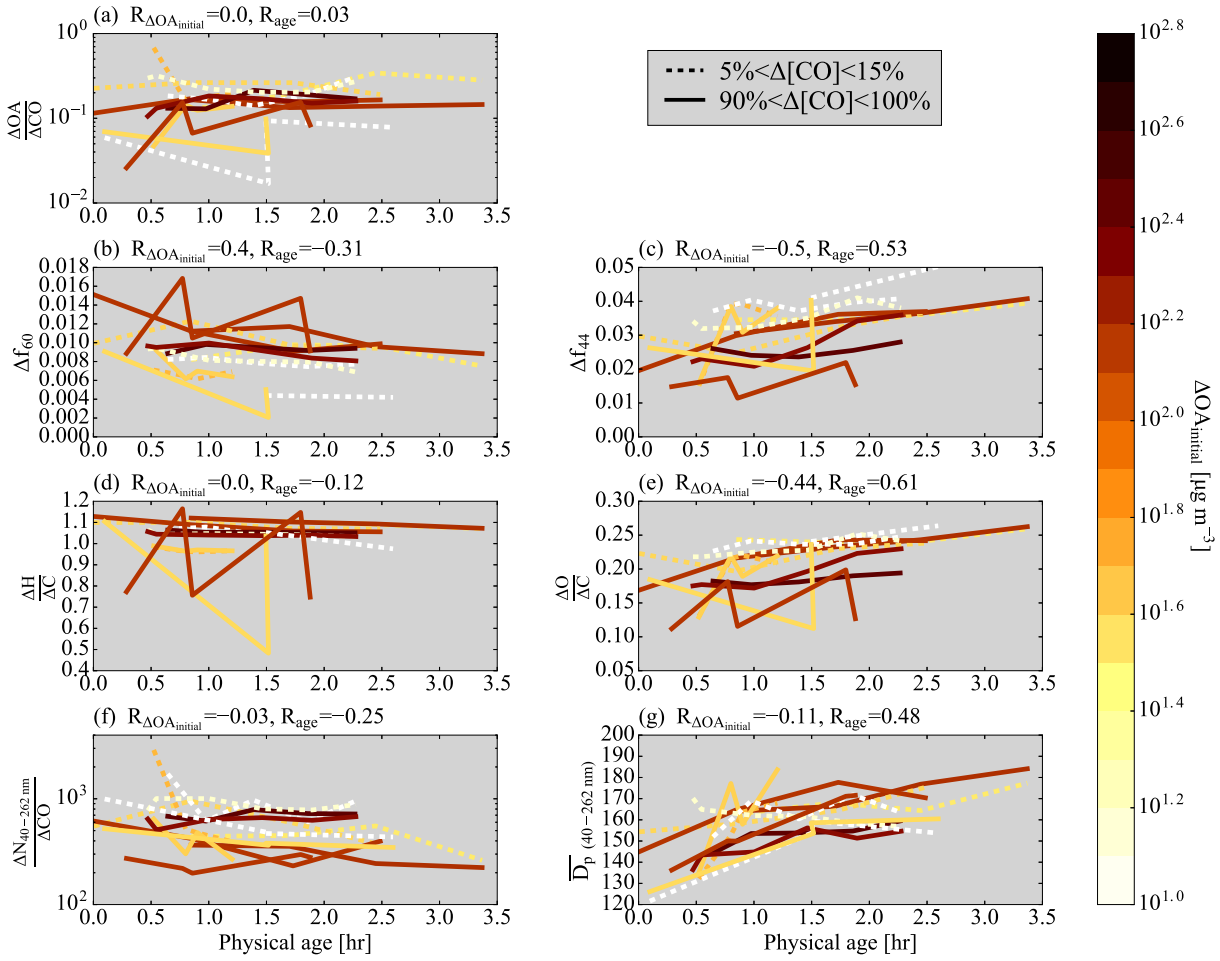

Figure 6.2 Various normalized parameters as a function of age for the 7 sets of pseudo-Lagrangian transects. Separate lines are shown for the edges (lowest 5-15% of ΔCO; dashed lines) and cores (highest 90-100% of ΔCO; solid lines). (a) ΔOA/ΔCO, (b) Δf_{60}, (c) Δf_{44}, (d) ΔH/ΔC, (e) ΔO/ΔC, (f) ΔN/ΔCO, and (g) D_p between 40-262 nm against physical age for all flights, colored by $\Delta OA_{initial}$. Some flights have missing data. Also provided is the Spearman

correlation coefficient, R, between each variable and $\Delta OA_{initial}$ and physical age for each variable. Note that panels (a), (d), and (g) have a log y-axis.

In general, both the cores and edges show little change in ΔOA/ΔCO with physical aging, with $R_{\Delta OA,initial}$ and R_{age} both at 0.03 (the absolute variability is dominated by differences between plumes). While the observed trends in ΔOA/ΔCO with aging are small, Δf_{60} and Δf_{44} show clear signs of changes with aging, consistent with previous studies(Cubison et al., 2011; Garofalo et al., 2019; May et al., 2015). Spearman tests on physical age vs. Δf_{60} and Δf_{44} give R_{age} values of -0.25 and 0.54, respectively. Δf_{60} generally decreases with plume age, consistent with the hypotheses that Δf_{60} may be evaporating off through heterogeneous oxidation and/or has a decreasing fractional contribution due to condensation of other compounds. In contrast, Δf_{44} generally increases with age for all plumes with available data, and hence it would appear that for plumes with little change in ΔOA/ΔCO, evaporation of f_{60}-containing compounds is roughly balanced by condensation of more-oxidized compounds, including those that contain f_{44}, suggesting the possibility that heterogeneous or particle-phase oxidation that would alter the balance of Δf_{60}, and Δf_{44}. However, estimates of heterogeneous mass losses indicate that after three hours of aging for a range of OH concentrations and reactive uptake coefficients over 90% of aerosol mass remains (Figure E23; see Appendix E for more details on the calculation).

Two more important features of Δf_{60} and Δf_{44} can be seen within Figure 6.2: (1) Δf_{60} and Δf_{44} depend on $\Delta OA_{initial}$ ($R_{\Delta OA,initial}$ = 0.38 and -0.5, respectively), with more concentrated plumes having consistently higher Δf_{60} and lower Δf_{44}. (2) Differences in Δf_{60} and Δf_{44} for the nearest-to-source measurements indicate that evaporation and/or chemistry likely occurred before the time of these first measurements (assuming that emitted Δf_{60} and Δf_{44} do not correlate with $\Delta OA_{initial}$). The amounts of evaporation and/or chemistry depend on $\Delta OA_{initial}$, with higher rates of evaporation

and chemistry occurring for lower values of $\Delta OA_{initial}$. This result is consistent with the hypothesis that aircraft observations are missing evaporation and chemistry prior to the first aircraft observation (Hodshire et al., 2019b). The differences in $\Delta OA_{initial}$ between plumes may be due to different emissions fluxes (e.g., due to different fuels or combustion phases), or plume widths, where larger/thicker plumes dilute more slowly than smaller/thinner plumes; these larger plumes have been predicted to have less evaporation and may undergo relatively less photooxidation (Bian et al., 2017; Hodshire et al., 2019a, 2019b).

(Garofalo et al., 2019) segregated smoke data from the WE-CAN field campaign by distance from the center of a given plume and showed that the edges of one of the fires studied have less f_{60} and more f_{44} (not background-corrected) than the core of the plume. Similarly, we find that the 730b flight shows a very similar pattern in f_{60} and f_{44} (Figures E24-E25) to that shown in (Garofalo et al., 2019) (their Figure 6). The 821b and 809a flights also hint at elevated f_{44} and decreased f_{60} at the edges but the remaining plumes do not show a clear trend from edge to core in f_{60} and f_{44}. This could be as CO concentrations (and thus presumably other species) do not evenly increase from the edge to the core for many of the plume transects studied (Figures E2-E6). We do not have UV measurements that allow us to calculate photolysis rates but the in-plume shortwave measurements in the visible show a dimming in the fresh cores that has a similar pattern to f_{44} and the inverse of f_{60} (Figure E26; the rapid oscillations in this figure could be indicative of sporadic cloud cover above the plumes).

We also plot core and edge $\Delta H/\Delta C$ and $\Delta O/\Delta C$ as a function of physical age (Figure 6.2d-e). Similar to Δf_{44}, $\Delta O/\Delta C$ increases with physical age and is well correlated to both physical age and $\Delta OA_{initial}$ ($R_{age} = 0.61$ and $R_{\Delta OA,initial} = -0.42$). Conversely, $\Delta H/\Delta C$ tends to be fairly constant or slightly decreasing with physical age and is poorly correlated to physical age and $\Delta OA_{initial}$. A

Van Krevelen diagram of ΔH/ΔC versus ΔO/ΔC (Figure E27) indicates that oxygenation reactions or a combination of oxygenation and hydration reactions are likely dominant (Heald et al., 2010); however, without further information, we cannot conclude which reactions are occurring.

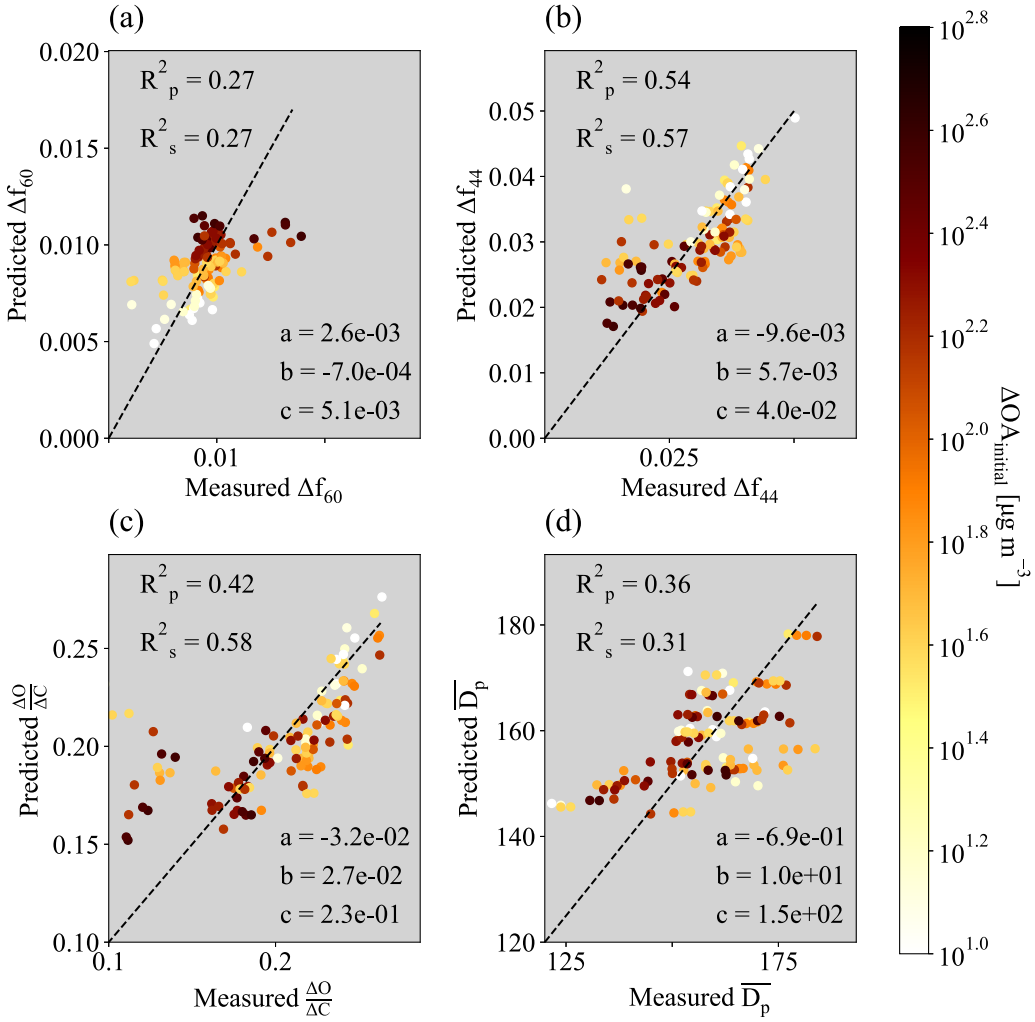

Figure 6.3 Measured versus predicted (a) Δf_{60}, (b) Δf_{44}, (c) ΔO/ΔC, and (d) Dpbetween 40-262 nm. The predicted values are from the equation $X = a\ log_{10}(OAinitial) + b\ (Physical\ age) + c$ where $X = \Delta f_{60}$, Δf_{44}, ΔO/ΔC, or D_p. The values of *a, b,* and *c* are provided within each subpanel, as are the Pearson and Spearman coefficients of determination (R^2_p and R^2_s, respectively). Note that Figure 2 provides R values rather than R^2 to provide information upon the trend of the correlation. Included in the fit and figure are points from all four ΔCO regions within the plume (the 5-15%, 15-50%, 50-90%, and 90-100% of ΔCO), all colored by the mean $\Delta OA_{initial}$ of each ΔCO percentile range.

Both physical age and $\Delta OA_{initial}$ appear to influence Δf_{60}, Δf_{44}, and $\Delta O/\Delta C$: oxidation reactions and evaporation from dilution occur with aging, and the extent of photochemistry and dilution should depend on plume thickness. Being able to predict biomass burning aerosol aging parameters can provide a framework for interstudy-comparisons and can aid in modeling efforts. We construct mathematical fits for predicting Δf_{60}, Δf_{44}, and $\Delta O/\Delta C$:

$$X = a\ log_{10}(\Delta OA_{initial}) + b\ (Physical\ age)\ + c \qquad 6.2$$

where X is Δf_{60}, Δf_{44}, or $\Delta O/\Delta C$ and *a, b,* and *c* are fit coefficients. The measured vs. fit data and values of *a, b,* and *c* are shown in Figure 6.3a-c. The Pearson and Spearman coefficients of determination (R^2_p and R^2_s, respectively) are also summarized in Figure 6.3 and indicate moderate goodness of fits (R^2 between 0.21-0.25 for Δf_{60}, between 0.53-0.58 for Δf_{44}, and between 0.41-0.58 for $\Delta O/\Delta C$). Although no models that we are aware of currently predict aerosol fractional components (e.g. f_{60} or f_{44}), O/H and H/C are predicted by some models (e.g., (Cappa and Wilson, 2012) and these fit parameters may assist in biomass burning modeling.

Other functional fits were explored (Figures E28-E29), with

$$ln(\Delta X) = a\ ln(\Delta OA_{initial}) + b\ ln(Physical\ age)\ + c \qquad 6.3$$

(Figure E28) and $\Delta N_{initial}$ in the place of $\Delta OA_{initial}$ in Eq. 6.2 (Figure E29) providing similar fits for Δf_{60} and Δf_{44}. Aged Δf_{60} and Δf_{44} show scatter, limiting the predictive skill of measurements available from BBOP. The scatter is likely to variability in emissions due to source fuel or combustion conditions, instrument noise and response under large concentration ranges

encountered in these smoke plumes, inhomogeneous mixing within the plume, variability in background concentrations not captured by our background correction method, inaccurate characterizations of physical age due to variable wind speed, and deviations from a true Lagrangian flight path. There may be another variable not available to us from the BBOP data that aids this prediction, such as photolysis rates. We encourage these fits to be tested out with further data sets and modeling.

6.3.2 Aerosol size distribution properties: $\Delta N_{40\text{-}262\ nm}/\Delta CO$ and $\overline{D_p}$

The observations of the normalized number concentration between 40-262 nm, $\Delta N_{40\text{-}262\ nm}/\Delta CO$ (Figure 6.2f), show that plume edges and cores generally show decreases in $\Delta N_{40\text{-}262\ nm}/\Delta CO$ with physical age, with $R_{age} = -0.25$. The plume edges and cores with the highest initial ΔOA generally have lower normalized number concentrations by the time of the first measurement, and the edges generally have higher initial normalized number concentrations than the cores, potentially due to differences in coagulation rates. A few dense cores have normalized number concentrations comparable or higher than the thinner edges, leading to no correlation with $\Delta OA_{initial}$. We note that variability in number emissions (due to e.g. burn conditions) adds noise not captured by the R values.

The mean particle size between 40-262 nm, $\underline{D_p}$ (Eq. 6.1), is shown to increase with aging (Figure 6.2g) for all plumes ($R_{age} = 0.48$). Coagulation and SOA condensation will increase $\underline{D_p}$ and OA evaporation will decrease $\underline{D_p}$. The plumes do not show significant changes in $\Delta OA/\Delta CO$ (Figure 6.2a), indicating that coagulation is likely responsible for the majority of increases in $\underline{D_p}$. The functional fits for Δf_{60} and Δf_{44} (Eq. 6.2; where X is $\underline{D_p}$ in this case) can also moderately predict

$\underline{D_p}$ (R^2_p and R^2_s of 0.36 and 0.31; Figure 6.3d) but do not well-predict $\Delta N_{40\text{-}300\ nm}/\Delta CO$ (not shown). Sakamoto et al. (2016) provide fit equations for modeled $\underline{D_p}$ as a function of age, but they include a known initial $\underline{D_p}$ at the time of emission in their parameterization, which is not available here. $\Delta N_{initial}$ in the place of $\Delta OA_{initial}$ in Eq. 6.2 predicts $\underline{D_p}$ similarly (Figure E29). As discussed in Section 3.1, scatter in number concentrations limits our prediction skill.

Nucleation-mode particles (inferred in this study from particles appearing between 20-40 nm in the FIMS measurements) are observed for some of the transects (Figures E7-E11). Some days also show nucleation-mode particles downwind of fires in between transects (Figures E7, E8, E9, and E11). Nucleation-mode particles appear to primarily occur in the outer portion of plumes, although one day did show nucleation-mode particles within the core of the plume (Figure E11). Nucleation at edges could be due to increased photooxidation from higher total irradiance relative to the core (Figure E26). However, given the relatively small number of data points showing nucleation mode particles and limited photooxidation and gas-phase information, we do not have confidence in the underlying source of the nucleation-mode particles. The nucleation mode tends to be ~one order of magnitude less concentrated than the larger particles, and appears to be coagulating or evaporating away as the plumes travel downwind.

6.4 Summary

The BBOP field campaign provided high time resolution (1 s) measurements of gas- and particle-phase smoke measurements downwind of western U.S. wildfires along pseudo-Lagrangian transects. These flights have allowed us to examine near-field (<4 hours) aging of smoke particles to provide analyses on how these species vary across a range of initial aerosol

mass loadings (a proxy for the relative rates at which the plume is anticipated to dilute as dilution before the first observation is not a measurable quantity) as well as how they vary between the edges and cores of each plume. We find that although ΔOA/ΔCO shows little variability, Δf_{60} (a marker for evaporation) decreases with physical aging; Δf_{44} and ΔO/ΔC (markers for photochemical aging) increases with physical aging; and each correlate with both $\Delta OA_{initial}$ and physical age. $\Delta N_{40\text{-}262\ nm}/\Delta CO$ decreases with physical aging through coagulation, with thicker plumes tending to show lower number concentrations, indicative of higher rates of coagulation. Mean aerosol diameter between 40-262 nm increases with age primarily due to coagulation, as organic aerosol mass does not change significantly. Nucleation is observed within a few of the fires and appears to occur primarily on the edges of the plumes. Differences in initial values of Δf_{60} , Δf_{44}, and ΔO/ΔC between higher- and lower-concentrated plumes indicate that evaporation and/or chemistry has likely occurred before the time of initial measurement and that plumes or plume regions (such as the outer parts of the plume) with lower initial aerosol loading can undergo these changes more rapidly than thicker plumes. We encourage future studies to attempt to quantify these chemical and physical changes before the initial measurement using combinations of modeling and laboratory measurements, where sampling is possible at the initial stages of the fire and smoke. We also encourage future near-field (<24 hours) analyses of recent and future biomass burning field campaigns to include differences in initial plume mass concentrations and location within the plume as considerations for understanding chemical and physical processes in plumes.

REFERENCES

Adachi, K., Sedlacek, A. J., Kleinman, L., Springston, S. R., Wang, J. and Chand, D.: Spherical tarball particles form through rapid chemical and physical changes of organic matter in biomass-burning smoke, Proceedings of the National Academy of Sciences, 1–6, 2019.

Aiken, A. C., Decarlo, P. F., Kroll, J. H., Worsnop, D. R., Huffman, J. A., Docherty, K. S., Ulbrich, I. M., Mohr, C., Kimmel, J. R., Sueper, D., Sun, Y., Zhang, Q., Trimborn, A., Northway, M., Ziemann, P. J., Canagaratna, M. R., Onasch, T. B., Alfarra, M. R., Prevot, A. S. H., Dommen, J., Duplissy, J., Metzger, A., Baltensperger, U. and Jimenez, J. L.: O/C and OM/OC ratios of primary, secondary, and ambient organic aerosols with high-resolution time-of-flight aerosol mass spectrometry, Environmental Science and Technology, 42(12), 4478–4485, 2008.

Aiken, A. C., Salcedo, D., Cubison, M. J., Huffman, J. A., DeCarlo, P. F., Ulbrich, I. M., Docherty, K. S., Sueper, D., Kimmel, J. R., Worsnop, D. R. and Others: Mexico City aerosol analysis during MILAGRO using high resolution aerosol mass spectrometry at the urban supersite (T0)--Part 1: Fine particle composition and organic source apportionment, Atmos. Chem. Phys., 9(17), 6633–6653, 2009.

Akagi, S. K., Yokelson, R. J., Wiedinmyer, C., Alvarado, M. J., Reid, J. S., Karl, T., Crounse, J. D. and Wennberg, P. O.: Emission factors for open and domestic biomass burning for use in atmospheric models, Atmos. Chem. Phys., 11(9), 4039–4072, 2011.

Akagi, S. K., Craven, J. S., Taylor, J. W., Mcmeeking, G. R., Yokelson, R. J., Burling, I. R., Urbanski, S. P., Wold, C. E., Seinfeld, J. H., Coe, H., Alvarado, M. J. and Weise, D. R.: Evolution of trace gases and particles emitted by a chaparral fire in California, Atmos. Chem. Phys., 12, 1397–1421, 2012.

Albrecht, B. A.: Aerosols, cloud microphysics, and fractional cloudiness, Science, 245(4923),

1227–1230, 1989.

Alfarra, M. R., Coe, H., Allan, J. D., Bower, K. N., Boudries, H., Canagaratna, M. R., Jimenez, J. L., Jayne, J. T., Garforth, A. A., Li, S.-M. and Worsnop, D. R.: Characterization of urban and rural organic particulate in the Lower Fraser Valley using two Aerodyne Aerosol Mass Spectrometers, Atmos. Environ., 38(34), 5745–5758, 2004.

Andela, N., Morton, D. C., Giglio, L., Paugam, R., Chen, Y., Hantson, S., Werf, G. R. and Randerson, J. T.: The Global Fire Atlas of individual fire size, duration, speed and direction, Earth System Science Data, 11(2), 529–552, 2019.

Badosa, J., Wood, J., Blanc, P., Long, C. N., Vuilleumier, L., Demengel, D. and Haeffelin, M.: Solar irradiances measured using SPN1 radiometers: uncertainties and clues for development, Atmospheric Measurement Techniques, 7, 4267–4283, 2014.

Bian, Q., Jathar, S. H., Kodros, J. K., Barsanti, K. C., Hatch, L. E., May, A. A., Kreidenweis, S. M. and Pierce, J. R.: Secondary organic aerosol formation in biomass-burning plumes: Theoretical analysis of lab studies and ambient plumes, Atmos. Chem. Phys., 17(8), 5459–5475, 2017.

Brito, J., Rizzo, L. V., Morgan, W. T., Coe, H., Johnson, B., Haywood, J., Longo, K., Freitas, S., Andreae, M. O. and Artaxo, P.: Ground-based aerosol characterization during the South American Biomass Burning Analysis (SAMBBA) field experiment, Atmospheric Chemistry and Physics, 14(22), 12069–12083, doi:10.5194/acp-14-12069-2014, 2014.

Cachier, H., Liousse, C., Buat-Menard, P. and Gaudichet, A.: Particulate content of savanna fire emissions, J. Atmos. Chem., 22(1-2), 123–148, 1995.

Canagaratna, M. R., Jimenez, J. L., Kroll, J. H., Chen, Q., Kessler, S. H., Massoli, P., Hildebrandt Ruiz, L., Fortner, E., Williams, L. R., Wilson, K. R. and Others: Elemental ration

measurements of organic compounds using aerosol mass spectrometry: characterization, improved calibration, and implications, Atmos. Chem. Phys., 15, 253–272, 2015.

Capes, G., Johnson, B., McFiggans, G., Williams, P. I., Haywood, J. and Coe, H.: Aging of biomass burning aerosols over West Africa: Aircraft measurements of chemical composition, microphysical properties, and emission ratios, J. Geophys. Res. D: Atmos., 113(23), 0–15, 2008.

Cappa, C. D. and Jimenez, J. L.: Quantitative estimates of the volatility of ambient organic aerosol, Atmos. Chem. Phys., 10(12), 5409–5424, 2010.

Cappa, C. D. and Wilson, K. R.: Multi-generation gas-phase oxidation, equilibrium partitioning, and the formation and evolution of secondary organic aerosol, Atmos. Chem. Phys., 12(20), 9505–9528, 2012.

Carrico, C. M., Petters, M. D., Kreidenweis, S. M., Collett, J. L., Jr., Engling, G. and Malm, W. C.: Aerosol hygroscopicity and cloud droplet activation of extracts of filters from biomass burning experiments, J. Geophys. Res., 113(D8), 4767, 2008.

Collier, S., Zhou, S., Onasch, T. B., Jaffe, D. A., Kleinman, L., Sedlacek, A. J., Briggs, N. L., Hee, J., Fortner, E., Shilling, J. E., Worsnop, D., Yokelson, R. J., Parworth, C., Ge, X., Xu, J., Butterfield, Z., Chand, D., Dubey, M. K., Pekour, M. S., Springston, S. and Zhang, Q.: Regional Influence of Aerosol Emissions from Wildfires Driven by Combustion Efficiency: Insights from the BBOP Campaign, Environmental Science and Technology, 50(16), 8613–8622, 2016.

Cubison, M. J., Ortega, A. M., Hayes, P. L., Farmer, D. K., Day, D., Lechner, M. J., Brune, W. H., Apel, E., Diskin, G. S., Fisher, J. A., Fuelberg, H. E., Hecobian, A., Knapp, D. J., Mikoviny, T., Riemer, D., Sachse, G. W., Sessions, W., Weber, R. J., Weinheimer, A. J.,

Wisthaler, A. and Jimenez, J. L.: Effects of aging on organic aerosol from open biomass burning smoke in aircraft and laboratory studies, Atmos. Chem. Phys., 11(23), 12049–12064, 2011.

Decarlo, P. F., Dunlea, E. J., Kimmel, J. R., Aiken, A. C., Sueper, D., Crounse, J., Wennberg, P. O., Emmons, L., Shinozuka, Y., Clarke, A., Zhou, J., Tomlinson, J., Collins, D. R., Knapp, D., Weinheimer, A. J., Montzka, D. D., Campos, T. and Jimenez, J. L.: Fast airborne aerosol size and chemistry measurements above Mexico City and Central Mexico during the MILAGRO campaign., 2008.

Dennison, P. E., Brewer, S. C., Arnold, J. D. and Moritz, M. A.: Large wildfire trends in the western United States, 1984-2011, Geophysical Research Letters, 41(8), 2928–2933, doi:10.1002/2014gl059576, 2014.

Eatough, D. J., Eatough, N. L., Pang, Y., Sizemore, S., Kirchstetter, T. W., Novakov, T. and Hobbs, P. V.: Semivolatile particulate organic material in southern Africa during SAFARI 2000, J. Geophys. Res. D: Atmos., 108(D13) [online] Available from: https://agupubs.onlinelibrary.wiley.com/doi/abs/10.1029/2002JD002296%4010.1002/%28ISSN%292169-8996.SAF1, 2003.

Ford, B., Val Martin, M., Zelasky, S. E., Fischer, E. V., Anenberg, S. C., Heald, C. L. and Pierce, J. R.: Future Fire Impacts on Smoke Concentrations, Visibility, and Health in the Contiguous United States, GeoHealth, doi:10.1029/2018GH000144, 2018.

Formenti, P., Elbert, W., Maenhaut, W., Haywood, J., Osborne, S. and Andreae, M. O.: Inorganic and carbonaceous aerosols during the Southern African Regional Science Initiative (SAFARI 2000) experiment: Chemical characteristics, physical properties, and emission data for smoke from African biomass burning, J. Geophys. Res. D: Atmos., 108(D13),

doi:10.1029/2002JD002408, 2003.

Forrister, H., Liu, J., Scheuer, E., Dibb, J., Ziemba, L., Thornhill, K. L., Anderson, B., Diskin, G., Perring, A. E., Schwarz, J. P., Campuzano-Jost, P., Day, D. A., Palm, B. B., Jimenez, J. L., Nenes, A. and Weber, R. J.: Evolution of brown carbon in wildfire plumes, Geophys. Res. Lett., 42(11), 4623–4630, 2015.

Gan, R. W., Ford, B., Lassman, W., Pfister, G., Vaidyanathan, A., Fischer, E., Volckens, J., Pierce, J. R. and Magzamen, S.: Comparison of wildfire smoke estimation methods and associations with cardiopulmonary-related hospital admissions, GeoHealth, 1(3), 122–136, 2017.

Garofalo, L., Pothier, M. A., Levin, E. J. T., Campos, T., Kreidenweis, S. M. and Farmer, D. K.: Emission and Evolution of Submicron Organic Aerosol in Smoke from Wildfires in the Western United States, ACS Earth and Space Chemistry, acsearthspacechem.9b00125, 2019.

Giglio, L., Csiszar, I. and Justice, C. O.: Global distribution and seasonality of active fires as observed with the Terra and Aqua Moderate Resolution Imaging Spectroradiometer (MODIS) sensors, Journal of Geophysical Research: Biogeosciences, 111(G2) [online] Available from: https://agupubs.onlinelibrary.wiley.com/doi/abs/10.1029/2005JG000142, 2006.

Giglio, L., Csiszar, I., Restás, Á., Morisette, J. T., Schroeder, W., Morton, D. and Justice, C. O.: Active fire detection and characterization with the advanced spaceborne thermal emission and reflection radiometer (ASTER), Remote Sensing of Environment, 112(6), 3055–3063, doi:10.1016/j.rse.2008.03.003, 2008.

Gilman, J. B., Lerner, B. M., Kuster, W. C., Goldan, P. D., Warneke, C., Veres, P. R., Roberts, J.

M., De Gouw, J. A., Burling, I. R. and Yokelson, R. J.: Biomass burning emissions and potential air quality impacts of volatile organic compounds and other trace gases from fuels common in the US, Atmos. Chem. Phys., 15(24), 13915–13938, 2015.

Hatch, L. E., Luo, W., Pankow, J. F., Yokelson, R. J., Stockwell, C. E. and Barsanti, K. C.: Identification and quantification of gaseous organic compounds emitted from biomass burning using two-dimensional gas chromatography-time-of-flight mass spectrometry, Atmos. Chem. Phys., 15(4), 1865–1899, 2015.

Hatch, L. E., Yokelson, R. J., Stockwell, C. E., Veres, P. R., Simpson, I. J., Blake, D. R., Orlando, J. J. and Barsanti, K. C.: Multi-instrument comparison and compilation of non-methane organic gas emissions from biomass burning and implications for smoke-derived secondary organic aerosol precursors, Atmos. Chem. Phys., 17, 1471–1489, 2017.

Heald, C. L., Kroll, J. H., Jimenez, J. L., Docherty, K. S., DeCarlo, P. F., Aiken, A. C., Chen, Q., Martin, S. T., Farmer, D. K. and Artaxo, P.: A simplified description of the evolution of organic aerosol composition in the atmosphere, Geophys. Res. Lett., 37(8), doi:10.1029/2010GL042737, 2010.

Hecobian, A., Liu, Z., Hennigan, C. J., Huey, L. G., Jimenez, J. L., Cubison, M. J., Vay, S., Diskin, G. S., Sachse, G. W., Wisthaler, A., Mikoviny, T., Weinheimer, A. J., Liao, J., Knapp, D. J., Wennberg, P. O., Urten, A., Crounse, J. D., Clair, J. S., Wang, Y. and Weber, R. J.: Comparison of chemical characteristics of 495 biomass burning plumes intercepted by the NASA DC-8 aircraft during the ARCTAS/CARB-2008 field campaign, Atmos. Chem. Phys., 11, 13325–13337, 2011.

Hobbs, P. V., Sinha, P., Yokelson, R. J., Christian, T. J., Blake, D. R., Gao, S., Kirchstetter, T. W., Novakov, T. and Pilewskie, P.: Evolution of gases and particles from a savanna fire in

South Africa, J. Geophys. Res. D: Atmos., 108(D13), doi:10.1029/2002JD002352, 2003.

Hodshire, A. L., Akherati, A., Alvarado, M. J., Brown-Steiner, B., Jathar, S. H., Jimenez, J. L., Kreidenweis, S. M., Lonsdale, C. R., Onasch, T. B., Ortega, A. M. and Pierce, J. R.: Aging Effects on Biomass Burning Aerosol Mass and Composition: A Critical Review of Field and Laboratory Studies, Environ. Sci. Technol., 53(17), 10007–10022, 2019a.

Hodshire, A. L., Bian, Q., Ramnarine, E., Lonsdale, C. R., Alvarado, M. J., Kreidenweis, S. M., Jathar, S. H. and Pierce, J. R.: More than emissions and chemistry: Fire size, dilution, and background aerosol also greatly influence near-field biomass burning aerosol aging, J. Geophys. Res. D: Atmos., 2018JD029674, 2019b.

Huffman, J. A., Docherty, K. S., Aiken, A. C., Cubison, M. J., Ulbrich, I. M., Decarlo, P. F., Sueper, D., Jayne, J. T., Worsnop, D. R., Ziemann, P. J. and Jimenez, J. L.: Chemically-resolved aerosol volatility measurements from two megacity field studies., 2009.

Janhäll, S., Andreae, M. O. and Pöschl, U.: Biomass burning aerosol emissions from vegetation fires: particle number and mass emission factors and size distributions, Atmos. Chem. Phys. Disc., 9(4), 17183–17217, 2009.

Jen, C. N., Hatch, L. E., Selimovic, V., Yokelson, R. J., Weber, R., Fernandez, A. E., Kreisberg, N. M., Barsanti, K. C. and Goldstein, A. H.: Speciated and total emission factors of particulate organics from burning western US wildland fuels and their dependence on combustion efficiency, Atmos. Chem. Phys., 19, 1013–1026, 2019.

Jimenez, J. L., Canagaratna, M. R., Donahue, N. M., Prevot, a. S. H., Zhang, Q., Kroll, J. H., DeCarlo, P. F., Allan, J. D., Coe, H., Ng, N. L., Aiken, a. C., Docherty, K. S., Ulbrich, I. M., Grieshop, a. P., Robinson, a. L., Duplissy, J., Smith, J. D., Wilson, K. R., Lanz, V. a., Hueglin, C., Sun, Y. L., Tian, J., Laaksonen, A., Raatikainen, T., Rautiainen, J.,

Vaattovaara, P., Ehn, M., Kulmala, M., Tomlinson, J. M., Collins, D. R., Cubison, M. J., Dunlea, E. J., Huffman, J. a., Onasch, T. B., Alfarra, M. R., Williams, P. I., Bower, K., Kondo, Y., Schneider, J., Drewnick, F., Borrmann, S., Weimer, S., Demerjian, K., Salcedo, D., Cottrell, L., Griffin, R., Takami, A., Miyoshi, T., Hatakeyama, S., Shimono, A., Sun, J. Y., Zhang, Y. M., Dzepina, K., Kimmel, J. R., Sueper, D., Jayne, J. T., Herndon, S. C., Trimborn, a. M., Williams, L. R., Wood, E. C., Middlebrook, a. M., Kolb, C. E., Baltensperger, U. and Worsnop, D. R.: Evolution of organic aerosols in the atmosphere, Science, 326(5959), 1525–1529, 2009.

Jolleys, M. D., Coe, H., McFiggans, G., Capes, G., Allan, J. D., Crosier, J., Williams, P. I., Allen, G., Bower, K. N., Jimenez, J. L., Russell, L. M., Grutter, M. and Baumgardner, D.: Characterizing the aging of biomass burning organic aerosol by use of mixing ratios: A meta-analysis of four regions, Environmental Science and Technology, 46(24), 13093–13102, 2012.

Jolleys, M. D., Coe, H., McFiggans, G., Taylor, J. W., O'Shea, S. J., Le Breton, M., Bauguitte, S. J. B., Moller, S., Di Carlo, P., Aruffo, E., Palmer, P. I., Lee, J. D., Percival, C. J. and Gallagher, M. W.: Properties and evolution of biomass burning organic aerosol from Canadian boreal forest fires, Atmos. Chem. Phys., 15(6), 3077–3095, 2015.

Kleinman, L. and Sedlacek, A. J., III: Biomass Burning Observation Project (BBOP) Final Campaign Report, 2016.

Konovalov, I. B., Beekmann, M., Golovushkin, N. A. and Andreae, M. O.: Nonlinear behavior of organic aerosol in biomass burning plumes: a microphysical model analysis, Atmos. Chem. Phys. Disc., 1–44, 2019.

Koss, A. R., Sekimoto, K., Gilman, J. B., Selimovic, V., Coggon, M. M., Zarzana, K. J., Yuan, B.,

Lerner, B. M., Brown, S. S., Jimenez, J. L., Krechmer, J., Roberts, J. M., Warneke, C., Yokelson, R. J. and De Gouw, J.: Non-methane organic gas emissions from biomass burning: Identification, quantification, and emission factors from PTR-ToF during the FIREX 2016 laboratory experiment, Atmos. Chem. Phys., 18(5), 3299–3319, 2018.

Kroll, J. H. and Seinfeld, J. H.: Chemistry of secondary organic aerosol: Formation and evolution of low-volatility organics in the atmosphere, Atmos. Environ., 42, 3593–3624, 2008.

Kulkarni, P. and Wang, J.: New fast integrated mobility spectrometer for real-time measurement of aerosol size distribution—I: Concept and theory, J. Aerosol Sci., 37(10), 1303–1325, 2006.

Lee, T., Sullivan, A. P., Mack, L., Jimenez, J. L., Kreidenweis, S. M., Onasch, T. B., Worsnop, D. R., Malm, W., Wold, C. E., Hao, W. M. and Collett, J. L.: Chemical Smoke Marker Emissions During Flaming and Smoldering Phases of Laboratory Open Burning of Wildland Fuels, Aerosol Sci. Technol., 44(9), i–v, 2010.

Liu, X., Zhang, Y., Huey, L. G., Yokelson, R. J., Wang, Y., Jimenez, J. L., Campuzano-Jost, P., Beyersdorf, A. J., Blake, D. R., Choi, Y., St. Clair, J. M., Crounse, J. D., Day, D. A., Diskin, G. S., Ried, A., Hall, S. R., Hanisco, T. F., King, L. E., Meinardi, S., Mikoviny, T., Palm, B. B., Peischl, J., Perring, A. E., Pollack, I. B., Ryerson, T. B., Sachse, G., Schwarz, J. P., Simpson, I. J., Tanner, D. J., Thornhil, K. L., Ullmann, K., Weber, R. J., Wennberg, P. O., Wisthaler, A., Wolfe, G. M. and Ziemba, L. D.: Agricultural fires in the southeastern U.S. during SEAC4RS: Emissions of trace gases and particles and evolution of ozone, reactive nitrogen, and organic aerosol, J. Geophys. Res., 121(12), 7383–7414, 2016.

Long, C. N., Bucholtz, A., Jonsson, H., Schmid, B., Vogelmann, A. and Wood, J.: A Method of Correcting for Tilt from Horizontal in Downwelling Shortwave Irradiance Measurements

on Moving Platforms, The Open Atmospheric Science Journal, 4(1), 78–87, doi:10.2174/1874282301004010078, 2010.

May, A. A., Levin, E. J. T., Hennigan, C. J., Riipinen, I., Lee, T., Collett, J. L., Jimenez, J. L., Kreidenweis, S. M. and Robinson, A. L.: Gas-particle partitioning of primary organic aerosol emissions: 3. Biomass burning, J. Geophys. Res. D: Atmos., 118(19), 11327–11338, 2013.

May, A. A., Lee, T., McMeeking, G. R., Akagi, S., Sullivan, A. P., Urbanski, S., Yokelson, R. J. and Kreidenweis, S. M.: Observations and analysis of organic aerosol evolution in some prescribed fire smoke plumes, Atmos. Chem. Phys., 15(11), 6323–6335, 2015.

Morgan, W. T., Allan, J. D., Bauguitte, S., Darbyshire, E., Flynn, M. J., Lee, J., Liu, D., Johnson, B., Haywood, J., Longo, K. M., Artaxo, P. E. and Coe, H.: Transformation and aging of biomass burning carbonaceous aerosol over tropical South America from aircraft in-situ measurements during SAMBBA, Atmos. Chem. Phys. Discuss., doi:10.5194/acp-2019-157, 2019.

Moteki, N. and Kondo, Y.: Dependence of Laser-Induced Incandescence on Physical Properties of Black Carbon Aerosols: Measurements and Theoretical Interpretation, Aerosol Sci. Technol., 44(8), 663–675, 2010.

Nance, J. D., Hobbs, P. V. and Radkel, L. F.: Airborne Measurements of Gases and Particles From an Alaskan Wildfire, J. Geophys. Res. D: Atmos., 98(D8), 873–882, 1993.

Noyes, K. J., Kahn, R., Sedlacek, A., Kleinman, L., Limbacher, J. and Li, Z.: Wildfire Smoke Particle Properties and Evolution, from Space-Based Multi-Angle Imaging, Remote Sensing, 12(5), 769, doi:10.3390/rs12050769, 2020.

O'Dell, K., Ford, B., Fischer, E. V. and Pierce, J. R.: Contribution of Wildland-Fire Smoke to US

PM2.5 and Its Influence on Recent Trends, Environmental Science & Technology, 53(4), 1797–1804, doi:10.1021/acs.est.8b05430, 2019.

Olfert, J. S. and Wang, J.: Dynamic Characteristics of a Fast-Response Aerosol Size Spectrometer, Aerosol Sci. Technol., 43(2), 97–111, 2009.

Onasch, T. B., Trimborn, A., Fortner, E. C., Jayne, J. T., Kok, G. L., Williams, L. R., Davidovits, P. and Worsnop, D. R.: Soot Particle Aerosol Mass Spectrometer: Development, Validation, and Initial Application, Aerosol Science and Technology, 46(7), 804–817, doi:10.1080/02786826.2012.663948, 2012.

Petters, M. D. and Kreidenweis, S. M.: A single parameter representation of hygroscopic growth and cloud condensation nucleus activity, Atmos. Chem. Phys., 7(8), 1961–1971, 2007.

Petters, M. D., Carrico, C. M., Kreidenweis, S. M., Prenni, A. J., DeMott, P. J., Collett, J. L. and Moosmüller, H.: Cloud condensation nucleation activity of biomass burning aerosol, J. Geophys. Res. D: Atmos., 114(22), 22205, 2009.

Ramnarine, E., Kodros, J. K., Hodshire, A. L., Lonsdale, C. R., Alvarado, M. J. and Pierce, J. R.: Effects of near-source coagulation of biomass burning aerosols on global predictions of aerosol size distributions and implications for aerosol radiative effects, Atmos. Chem. Phys., 19(9), 6561–6577, 2019.

Reid, C. E., Brauer, M., Johnston, F. H., Jerrett, M., Balmes, J. R. and Elliott, C. T.: Critical review of health impacts of wildfire smoke exposure, Environmental Health Perspectives, 124(9), 1334–1343, doi:10.1289/ehp.1409277, 2016.

Reid, J. S., Hobbs, P. V., Ferek, R. J., Blake, D. R., Martins, J. V., Dunlap, M. R. and Liousse, C.: Physical, chemical, and optical properties of regional hazes dominated by smoke in Brazil, J. Geophys. Res. D: Atmos., 103(D24), 32059–32080, 1998.

Reid, J. S., Eck, T. F., Christopher, S. A., Koppmann, R., Dubovik, O., Eleuterio, D. P., Holben, B. N., Reid, E. A. and Zhang, J.: A review of biomass burning emissions part III: intensive optical properties of biomass burning particles, Atmos. Chem. Phys., 5, 827–849, 2005.

Sakamoto, K. M., Allan, J. D., Coe, H., Taylor, J. W., Duck, T. J. and Pierce, J. R.: Aged boreal biomass-burning aerosol size distributions from BORTAS 2011, Atmos. Chem. Phys., 15(4), 1633–1646, 2015.

Sakamoto, K. M., Laing, J. R., Stevens, R. G., Jaffe, D. A. and Pierce, J. R.: The evolution of biomass-burning aerosol size distributions due to coagulation: Dependence on fire and meteorological details and parameterization, Atmos. Chem. Phys., 16(12), 7709–7724, 2016.

Schwarz, J. P., Gao, R. S., Fahey, D. W., Thomson, D. S., Watts, L. A., Wilson, J. C., Reeves, J. M., Darbeheshti, M., Baumgardner, D. G., Kok, G. L. and Others: Single-particle measurements of midlatitude black carbon and light-scattering aerosols from the boundary layer to the lower stratosphere, J. Geophys. Res. D: Atmos., 111(D16) [online] Available from: https://agupubs.onlinelibrary.wiley.com/doi/abs/10.1029/2006JD007076, 2006.

Sedlacek, A. J., Iii, Buseck, P. R., Adachi, K., Onasch, T. B., Springston, S. R. and Kleinman, L.: Formation and evolution of Tar Balls from Northwestern US wildfires, Atmos. Chem. Phys. Discuss., (Figure 1), 1–28, 2018.

Seinfeld, J. H. and Pandis, S. N.: Atmospheric chemistry and physics: From air pollution to climate change, John Willey & Sons, Inc. , New York, 2006.

Shrivastava, M., Cappa, C. D., Fan, J., Goldstein, A. H., Guenther, A. B., Jimenez, J. L., Kuang, C., Laskin, A., Martin, S. T., Ng, N. L. and Others: Recent advances in understanding secondary organic aerosol: Implications for global climate forcing, Rev. Geophys., 55(2),

509–559, 2017.

Spracklen, D. V., Mickley, L. J., Logan, J. A., Hudman, R. C., Yevich, R., Flannigan, M. D. and Westerling, A. L.: Impacts of climate change from 2000 to 2050 on wildfire activity and carbonaceous aerosol concentrations in the western United States, J. Geophys. Res., 114(D20), 1418, 2009.

Tang, X., Madronich, S., Wallington, T. and Calamari, D.: Changes in tropospheric composition and air quality, J. Photochem. Photobiol. B, 46(1-3), 83–95, 1998.

Tie, X.: Effect of clouds on photolysis and oxidants in the troposphere, J. Geophys. Res., 108(D20), 23,073, 2003.

Twomey, S.: Pollution and the planetary albedo, Atmos. Environ., 8(12), 1251–1256, 1974.

Vakkari, V., Kerminen, V.-M., Beukes, J. P., Titta, P., van Zyl, P. G., Josipovic, M., Wnter, A. D., Jaars, K., Worsnop, D. R., Kulmala, M. and Laakso, L.: Rapid changes in biomass burning aerosols by atmospheric oxidation, Geophys. Res. Lett., 2644–2651, 2014.

Vakkari, V., Beukes, J. P., Dal Maso, M., Aurela, M., Josipovic, M. and van Zyl, P. G.: Major secondary aerosol formation in southern African open biomass burning plumes, Nat. Geosci., 11(8), 580–583, 2018.

Volkamer, R., Jimenez, J. L., San Martini, F., Dzepina, K., Zhang, Q., Salcedo, D., Molina, L. T., Worsnop, D. R. and Molina, M. J.: Secondary organic aerosol formation from anthropogenic air pollution: Rapid and higher than expected, Geophys. Res. Lett., 33(17), 4407, 2006.

Volkamer, R., Ziemann, P. J. and Molina, M. J.: Secondary Organic Aerosol Formation from Acetylene (C_2H_2): seed effect on SOA yields due to organic photochemistry in the aerosol aqueous phase, Atmos. Chem. Phys., 9(6), 1907–1928, 2009.

Wang, J., -N. Lee, Y., Daum, P. H., Jayne, J. and Alexander, M. L.: Effects of aerosol organics on cloud condensation nucleus (CCN) concentration and first indirect aerosol effect, Atmospheric Chemistry and Physics, 8(21), 6325–6339, doi:10.5194/acp-8-6325-2008, 2008.

Yang, M., Blomquist, B. W. and Huebert, B. J.: Constraining the concentration of the hydroxyl radical in a stratocumulus-topped marine boundary layer from sea-to-air eddy covariance flux measurements of dimethylsulfide, Atmos. Chem. Phys., 9(23), 9225–9236, 2009.

Yokelson, R. J., Crounse, J. D., DeCarlo, P. F., Karl, T., Urbanski, S., Atlas, E., Campos, T., Shinozuka, Y., Kapustin, V., Clarke, A. D., Weinheimer, A., Knapp, D. J., Montzka, D. D., Holloway, J., Weibring, P., Flocke, F., Zheng, W., Toohey, D., Wennberg, P. O., Wiedinmyer, C., Mauldin, L., Fried, A., Richter, D., Walega, J., Jimenez, J. L., Adachi, K., Buseck, P. R., Hall, S. R. and Shetter, R.: Emissions from biomass burning in the Yucatan, Atmos. Chem. Phys., 9(15), 5785–5812, 2009.

Yue, X., Mickley, L. J., Logan, J. A. and Kaplan, J. O.: Ensemble projections of wildfire activity and carbonaceous aerosol concentrations over the western United States in the mid-21st century, Atmospheric Environment, 77, 767–780, doi:10.1016/j.atmosenv.2013.06.003, 2013.

Zhou, S., Collier, S., Jaffe, D. A., Briggs, N. L., Hee, J., Sedlacek, A. J., III, Kleinman, L., Onasch, T. B. and Zhang, Q.: Regional influence of wildfires on aerosol chemistry in the western US and insights into atmospheric aging of biomass burning organic aerosol, Atmos. Chem. Phys., 17(3), 2477–2493, 2017.

APPENDIX A

SUPPLEMENT TO: CONSTRAINING NUCLEATION, CONDENSATION, AND CHEMISTRY IN OXIDATION FLOW REACTORS USING SIZE-DISTRIBUTION MEASUREMENTS AND AEROSOL MICROPHYSICAL MODELLING

A1. GoAmazon2014/5 SMPS-derived volume exposures and mean diurnal cycle of monoterpenes and isoprene

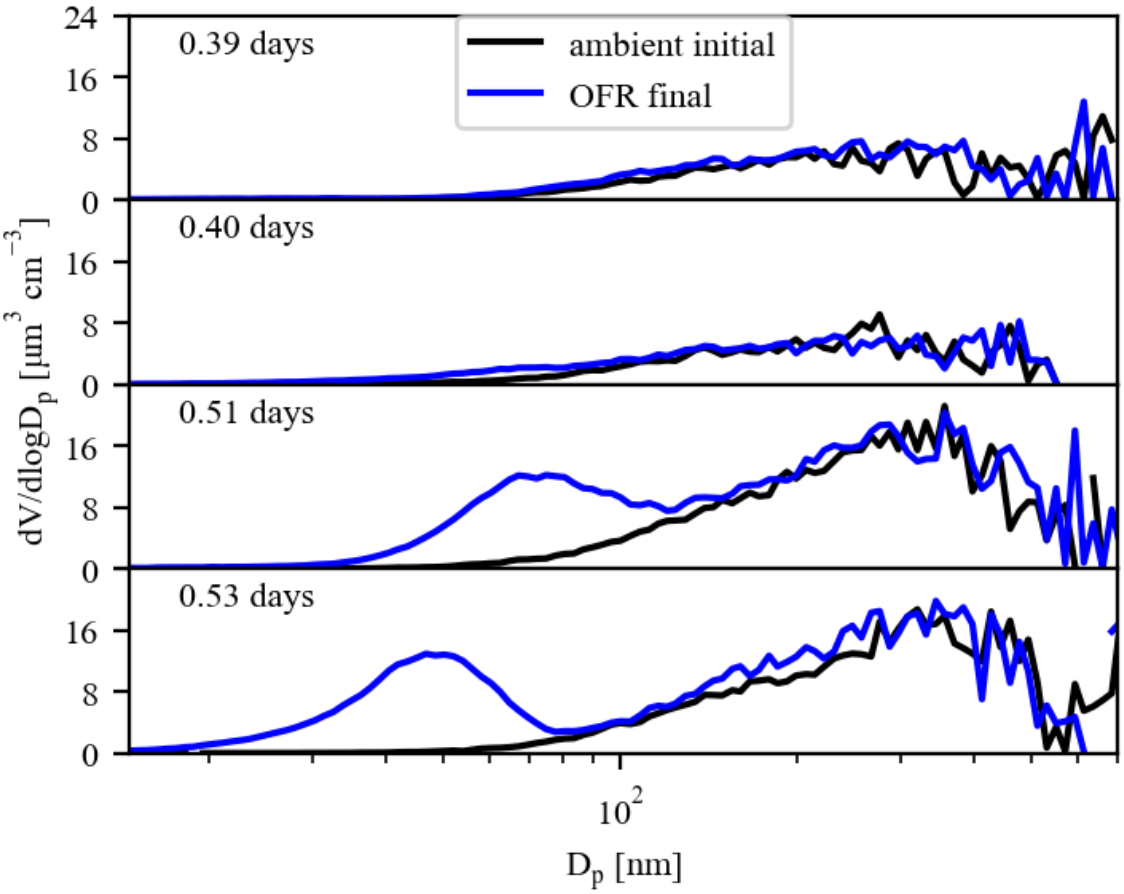

Figure A1. GoAmazon initial (i.e. ambient air, black line) and final (i.e. after OFR processing, blue line) SMPS-derived volume distributions for each individual exposure modelled in this study. The differences in SOA production between exposures of similar ages are due to the fact that the exposures were taken from different times during the campaign and thus different precursor concentrations were present (Table 2.2).

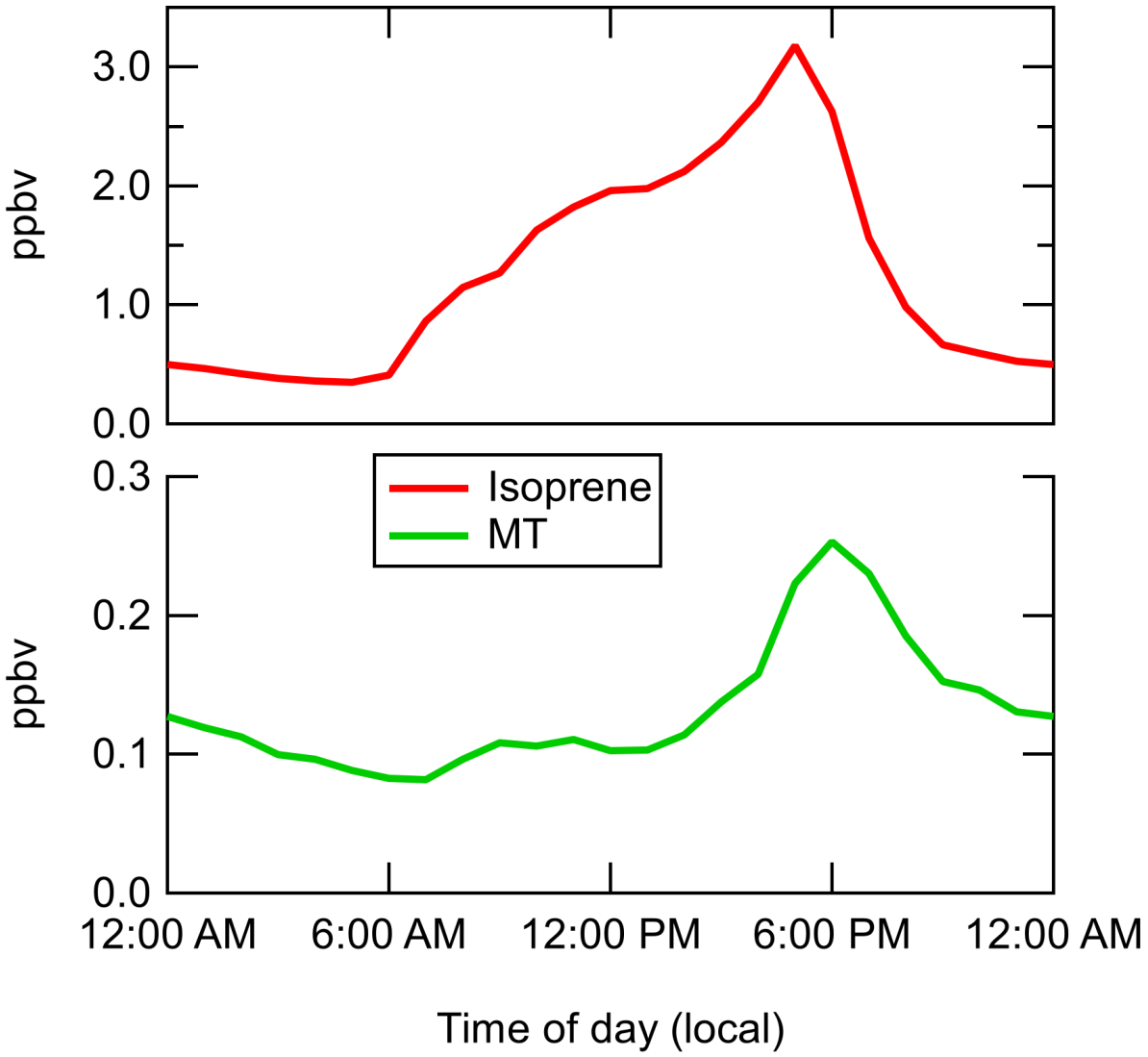

Figure A2. The mean observed diurnal cycle of isoprene (red line) and monoterpenes (MT; green line) for the dry season during the GoAmazon2014/5 campaign.

A2. BEACHON-RoMBAS individual exposures and best/worst case distributions

The following are the individual representations of the model simulations for each BEACHON-RoMBAS exposure modelled in this study. Figures A3, A5, A7, A9, A11, A13, A15, and A17 give the normalized mean error (NME) values for the parameter space that lies within (Table 2.3) the NUC1 nucleation scheme and base value of the reactive uptake coefficient. Figures A4, A6, A8, A10, A12, A14, A16, and A18 plot each observed final moment (solid black lines) used in computing the NME statistic (number, diameter, surface area, and volume) compared to the six TOMAS cases with the lowest (best) NME statistic (solid colored lines) and six TOMAS cases with the highest (worst) NME statistic (solid dotted lines). For comparison, the observed initial moments are also plotted for each moment (dotted black lines).

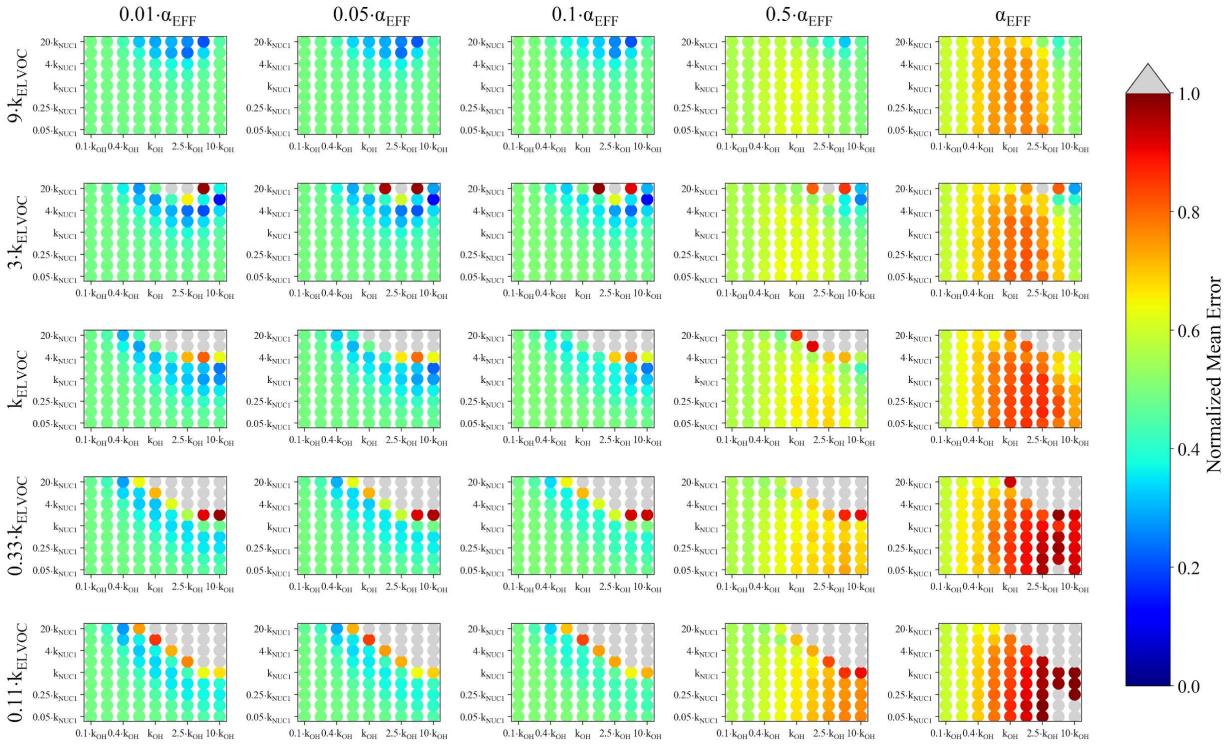

Figure A3. Representation of the parameter space for a 0.090 eq. day aging exposure from BEACHON-RoMBAS for the NUC1 nucleation scheme and base value of the reactive uptake coefficient of 0.6. The effective accommodation coefficient increases across each row of panels; the rate constant of gas-phase fragmentation increases up each column of panels. Within each panel, the rate constant of gas-phase reactions with OH increases along the x-axis and the rate constant for nucleation increases along the y-axis. The color bar indicates the normalized mean error (NME) value for each simulation, with the lowest values indicating the least error between model and measurement. Grey regions indicate regions within the parameter space whose NME value is greater than 1.

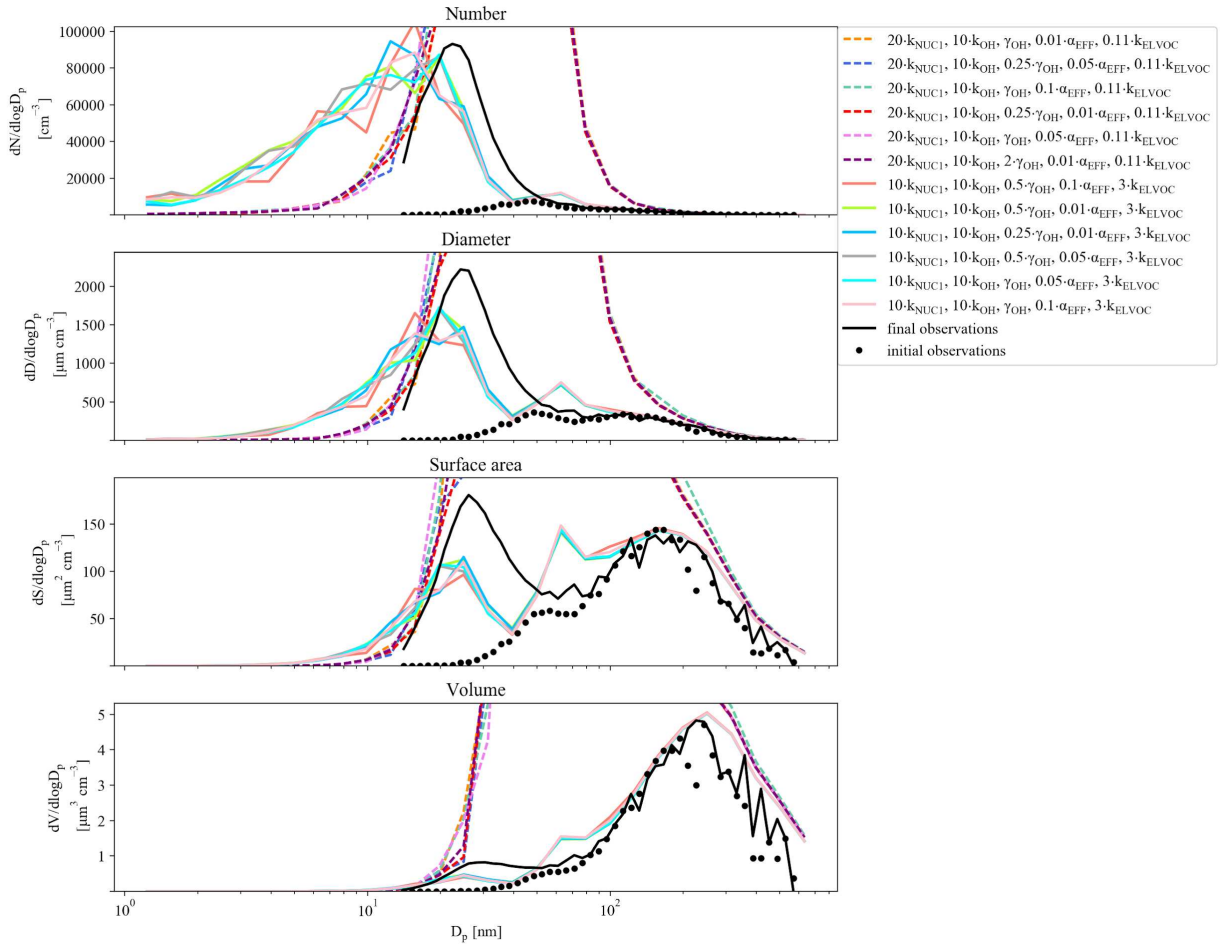

Figure A4. Example of best (solid lines) and worst (dashed lines) fit size distributions compared to the observed (black line) final OFR size distribution for a 0.090 eq days aging case from BEACHON-RoMBAS for the NUC1 nucleation scheme. The fits are determined using the mean error of moments method (see methods); each panel represents a separate moment. The top panel represents the number distribution; the second panel represents the diameter distribution; the third panel represents the surface area distribution; and the final (bottom) distribution represents the volume distribution.

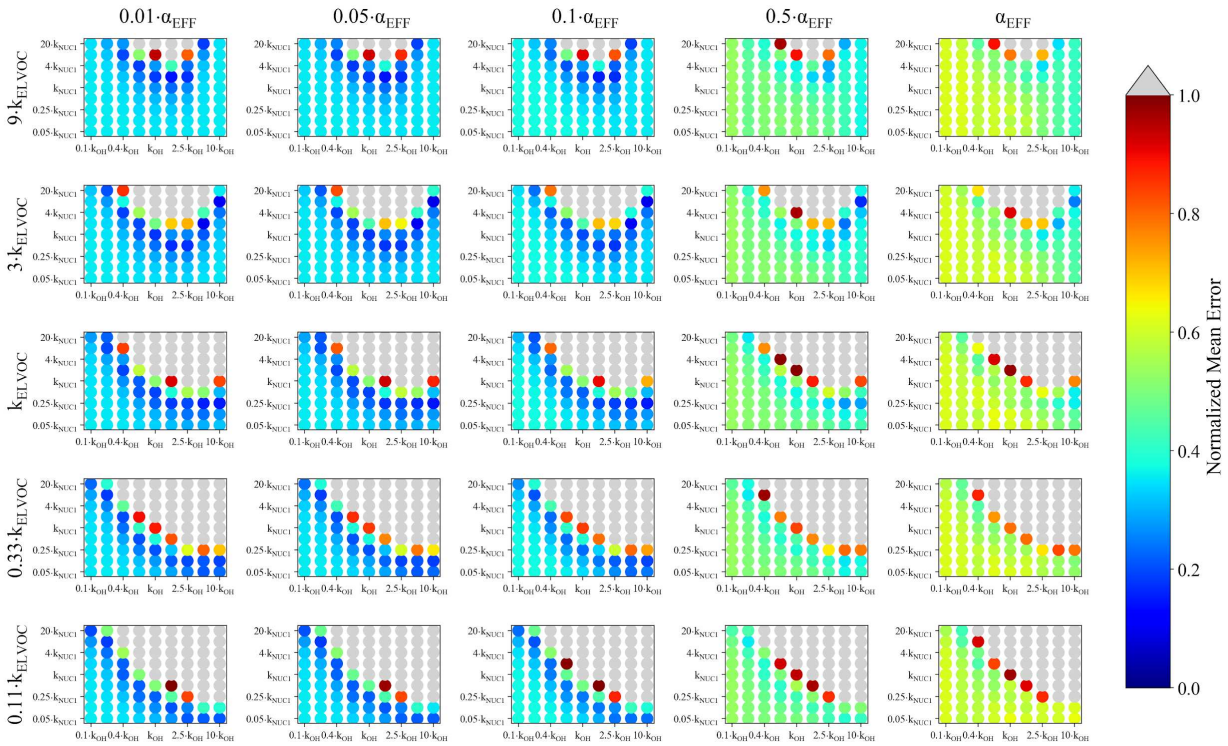

Figure A5. Representation of the parameter space for a 0.098 eq. day aging exposure from BEACHON-RoMBAS for the NUC1 nucleation scheme and base value of the reactive uptake coefficient of 0.6. The effective accommodation coefficient increases across each row of panels; the rate constant of gas-phase fragmentation increases up each column of panels. Within each panel, the rate constant of gas-phase reactions with OH increases along the x-axis and the rate constant for nucleation increases along the y-axis. The color bar indicates the normalized mean error (NME) value for each simulation, with the lowest values indicating the least error between model and measurement. Grey regions indicate regions within the parameter space whose NME value is greater than 1.

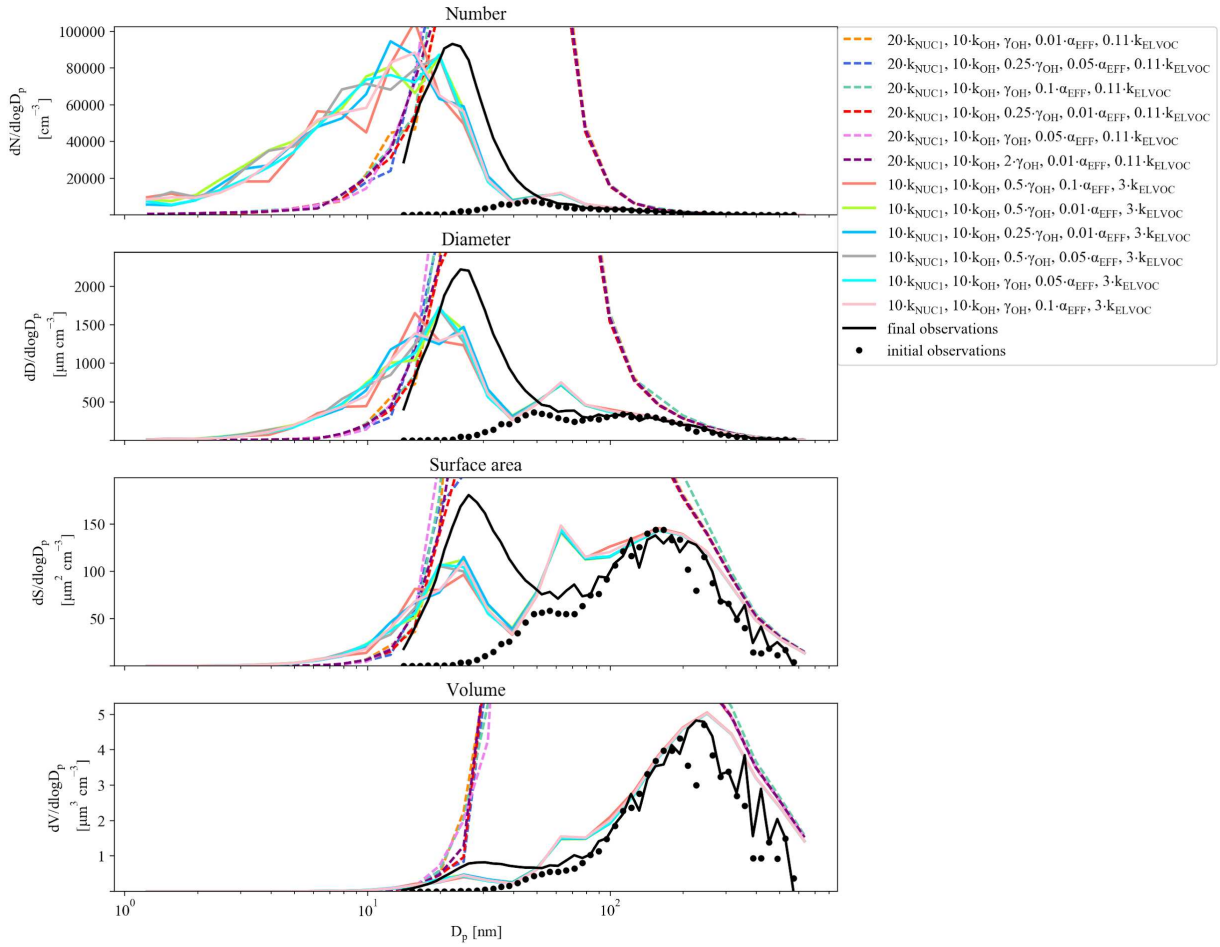

Figure A6. Example of best (solid lines) and worst (dashed lines) fit size distributions compared to the observed (black line) final OFR size distribution for a 0.098 eq days aging case from BEACHON-RoMBAS for the NUC1 nucleation scheme. The fits are determined using the mean error of moments method (see methods); each panel represents a separate moment. The top panel represents the number distribution; the second panel represents the diameter distribution; the third panel represents the surface area distribution; and the final (bottom) distribution represents the volume distribution.

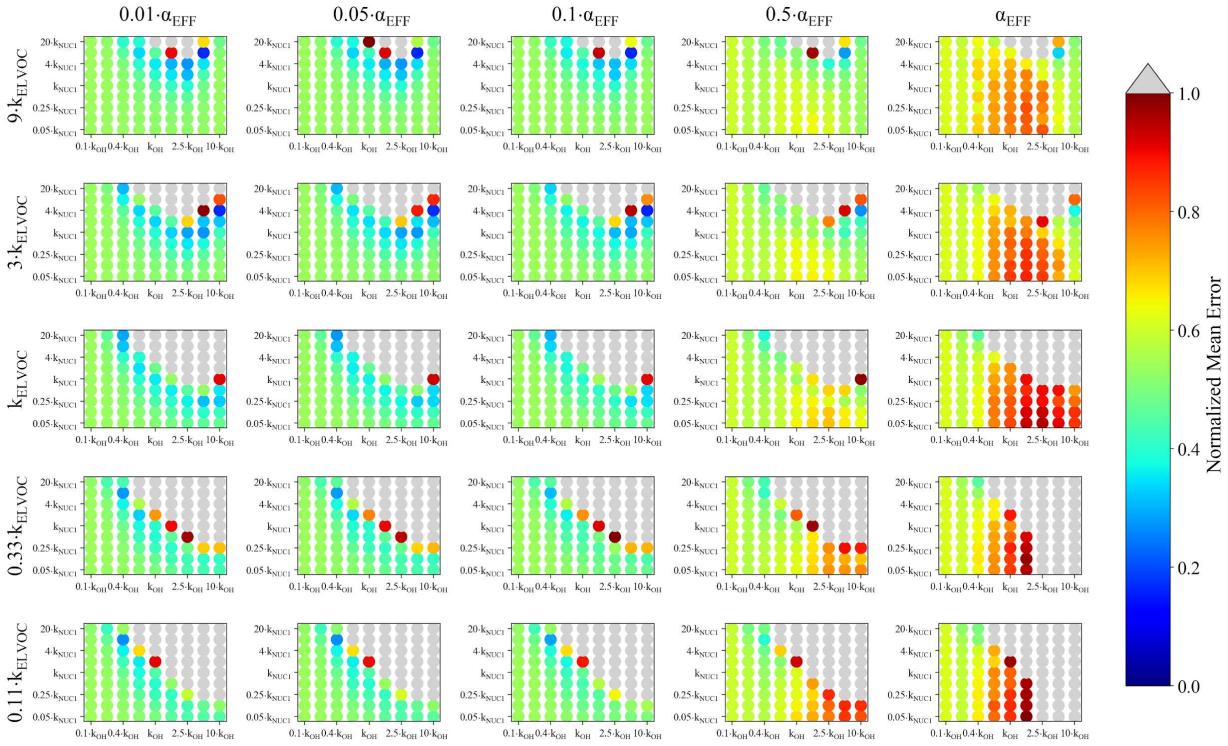

Figure A7. Representation of the parameter space for a 0.16 eq. day aging exposure from BEACHON-RoMBAS for the NUC1 nucleation scheme and base value of the reactive uptake coefficient of 0.6. The effective accommodation coefficient increases across each row of panels; the rate constant of gas-phase fragmentation increases up each column of panels. Within each panel, the rate constant of gas-phase reactions with OH increases along the x-axis and the rate constant for nucleation increases along the y-axis. The color bar indicates the normalized mean error (NME) value for each simulation, with the lowest values indicating the least error between model and measurement. Grey regions indicate regions within the parameter space whose NME value is greater than 1.

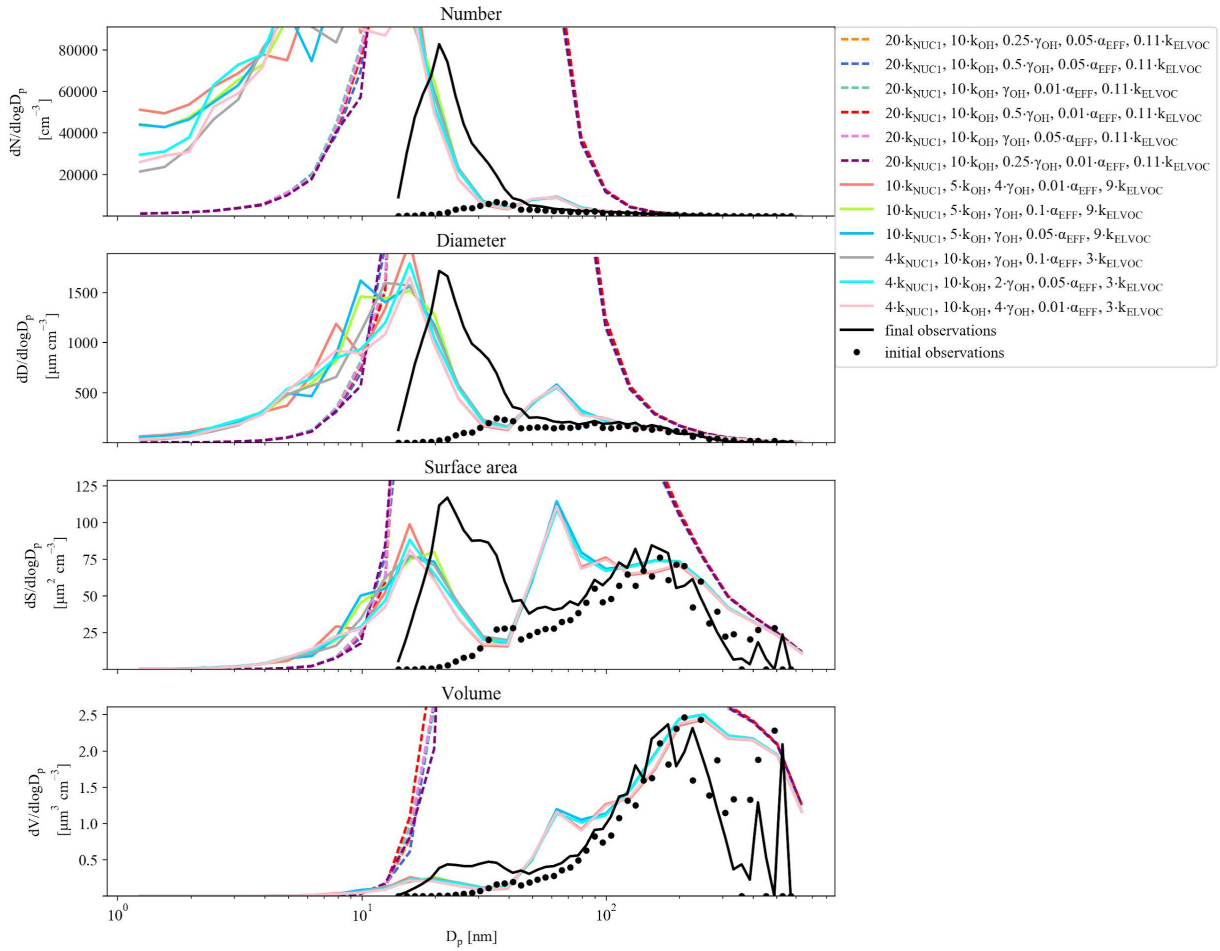

Figure A**8.** Example of best (solid lines) and worst (dashed lines) fit size distributions compared to the observed (black line) final OFR size distribution for a 0.16 eq days aging case from BEACHON-RoMBAS for the NUC1 nucleation scheme. The fits are determined using the mean error of moments method (see methods); each panel represents a separate moment. The top panel represents the number distribution; the second panel represents the diameter distribution; the third panel represents the surface area distribution; and the final (bottom) distribution represents the volume distribution.

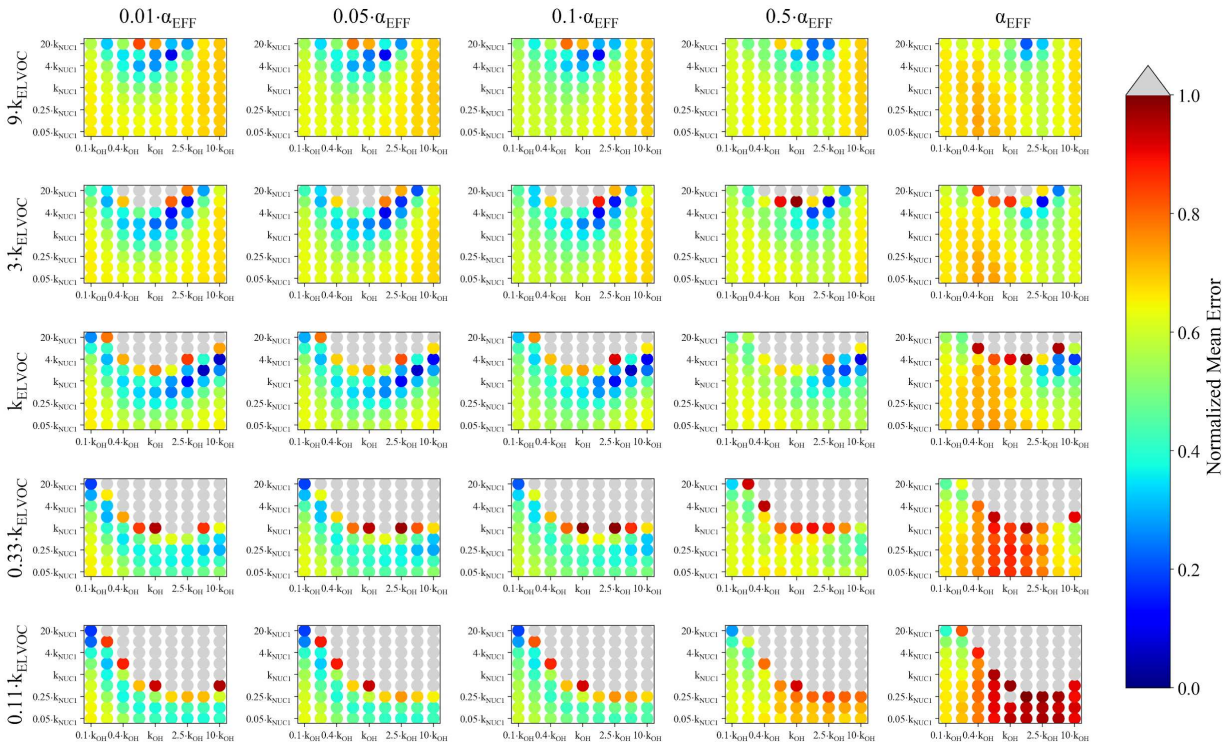

Figure A9. Representation of the parameter space for a 0.23 eq. day aging exposure from BEACHON-RoMBAS for the NUC1 nucleation scheme and base value of the reactive uptake coefficient of 0.6. The effective accommodation coefficient increases across each row of panels; the rate constant of gas-phase fragmentation increases up each column of panels. Within each panel, the rate constant of gas-phase reactions with OH increases along the x-axis and the rate constant for nucleation increases along the y-axis. The color bar indicates the normalized mean error (NME) value for each simulation, with the lowest values indicating the least error between model and measurement. Grey regions indicate regions within the parameter space whose NME value is greater than 1.

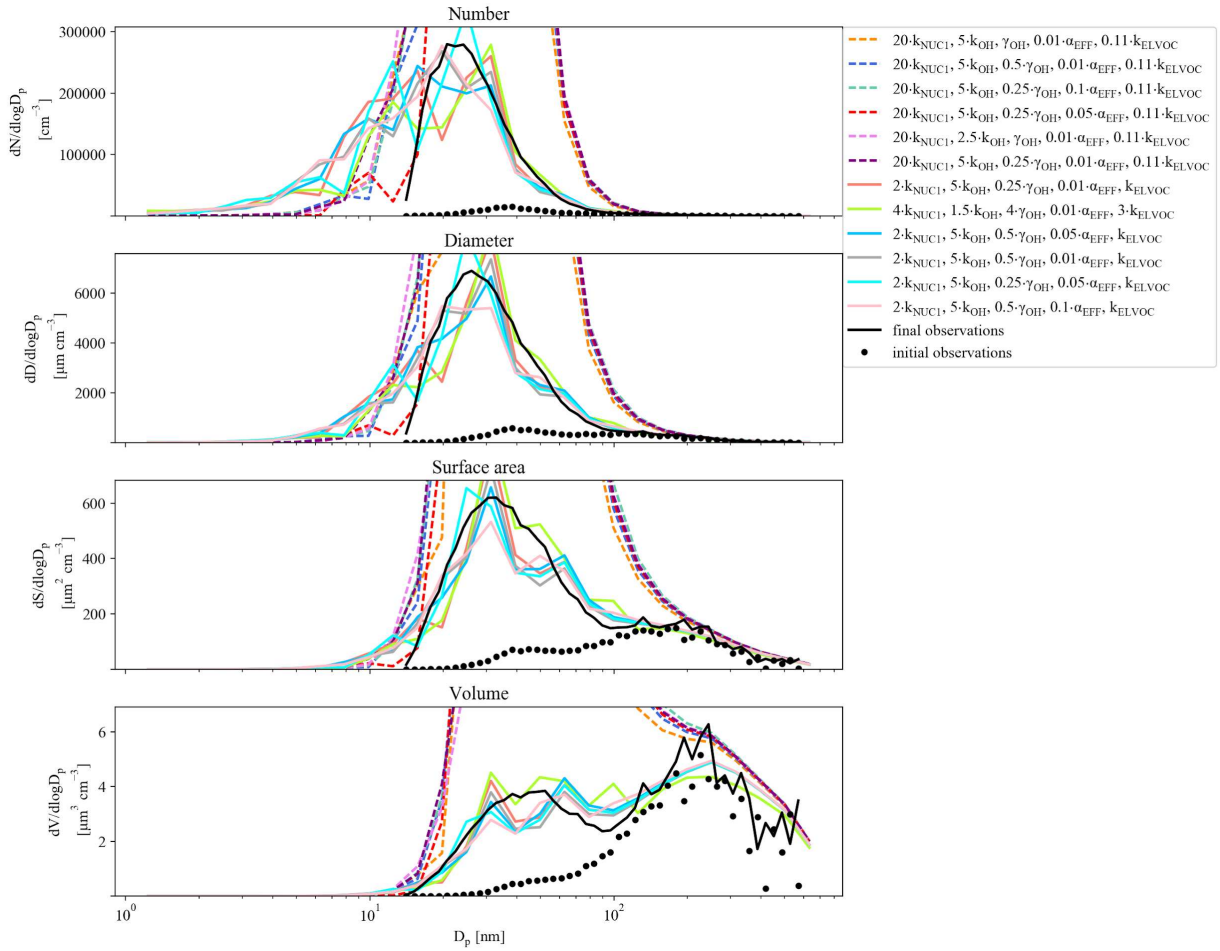

Figure A10. Example of best (solid lines) and worst (dashed lines) fit size distributions compared to the observed (black line) final OFR size distribution for a 0.23 eq days aging case from BEACHON-RoMBAS for the NUC1 nucleation scheme. The fits are determined using the mean error of moments method (see methods); each panel represents a separate moment. The top panel represents the number distribution; the second panel represents the diameter distribution; the third panel represents the surface area distribution; and the final (bottom) distribution represents the volume distribution.

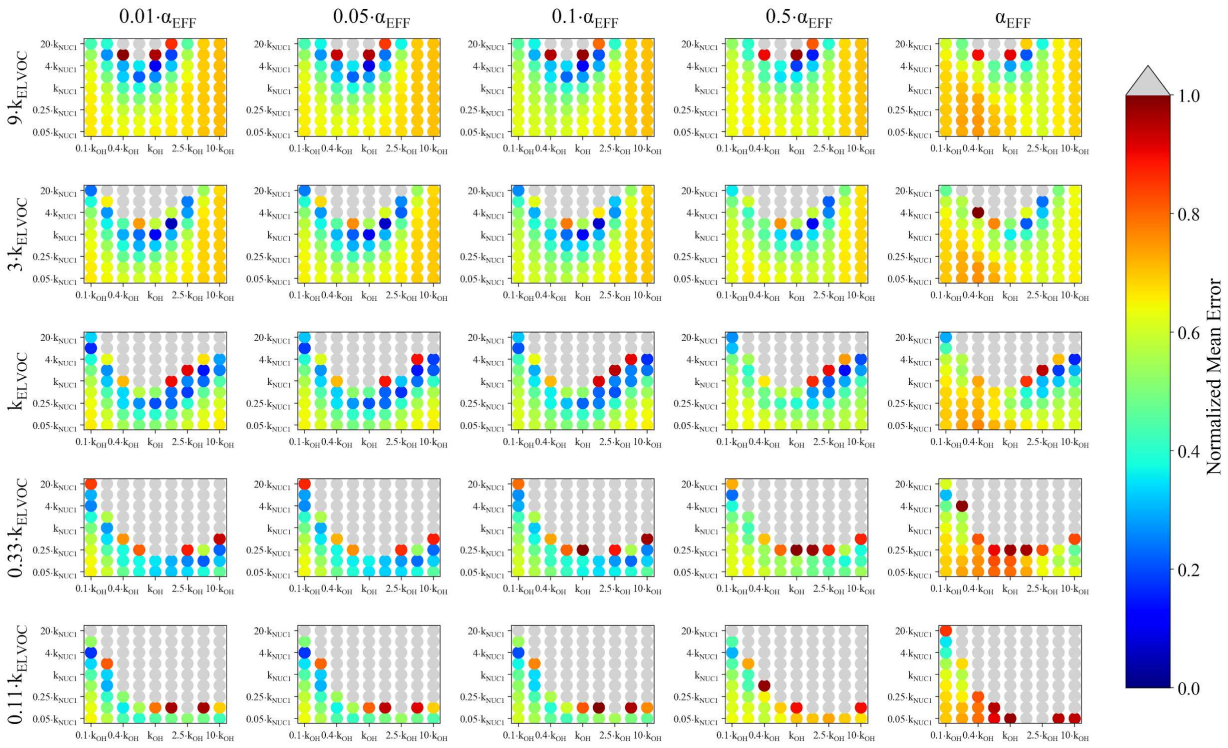

Figure A11. Representation of the parameter space for a 0.27 eq. day aging exposure from BEACHON-RoMBAS for the NUC1 nucleation scheme and base value of the reactive uptake coefficient of 0.6. The effective accommodation coefficient increases across each row of panels; the rate constant of gas-phase fragmentation increases up each column of panels. Within each panel, the rate constant of gas-phase reactions with OH increases along the x-axis and the rate constant for nucleation increases along the y-axis. The color bar indicates the normalized mean error (NME) value for each simulation, with the lowest values indicating the least error between model and measurement. Grey regions indicate regions within the parameter space whose NME value is greater than 1.

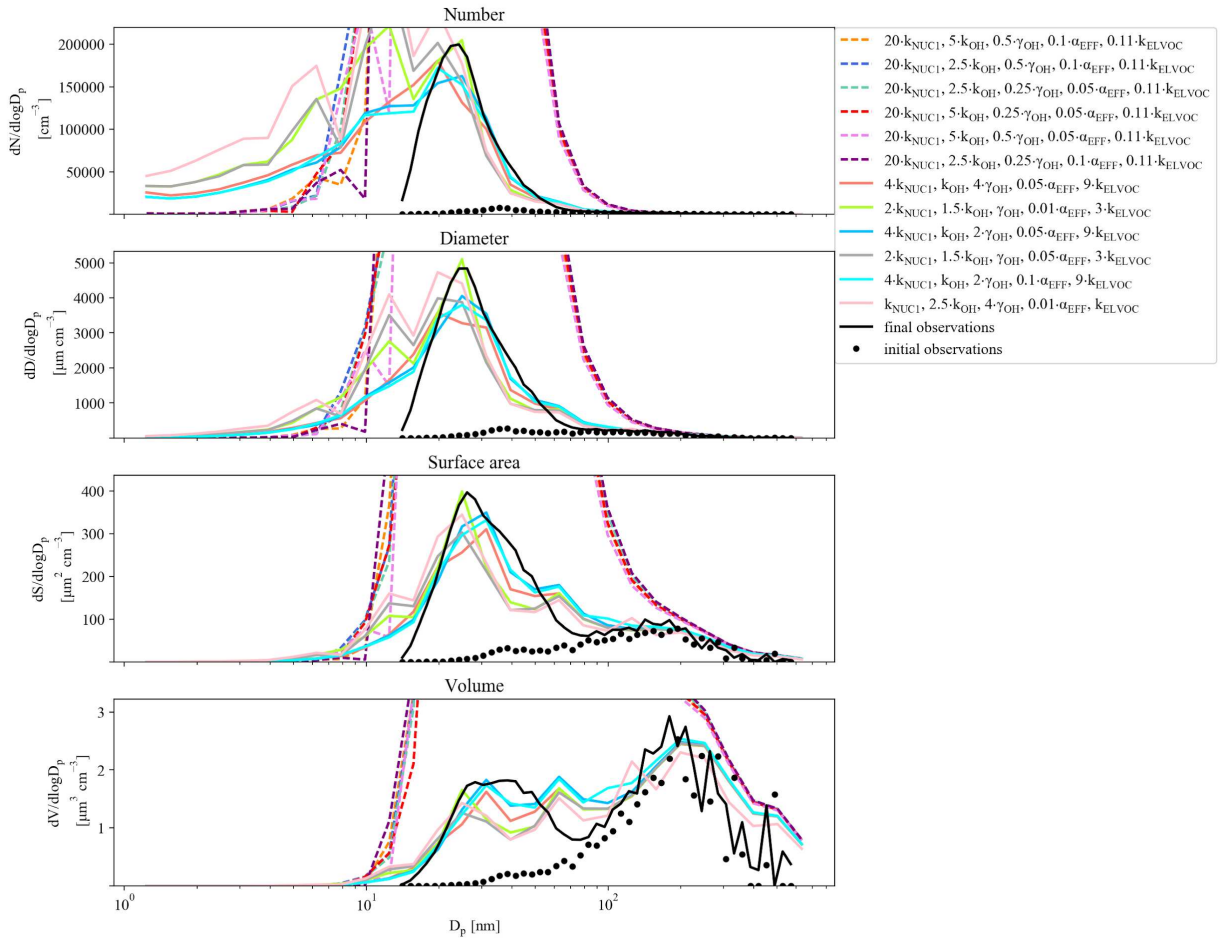

Figure A12. Example of best (solid lines) and worst (dashed lines) fit size distributions compared to the observed (black line) final OFR size distribution for a 0.27 eq days aging case from BEACHON-RoMBAS for the NUC1 nucleation scheme. The fits are determined using the mean error of moments method (see methods); each panel represents a separate moment. The top panel represents the number distribution; the second panel represents the diameter distribution; the third panel represents the surface area distribution; and the final (bottom) distribution represents the volume distribution.

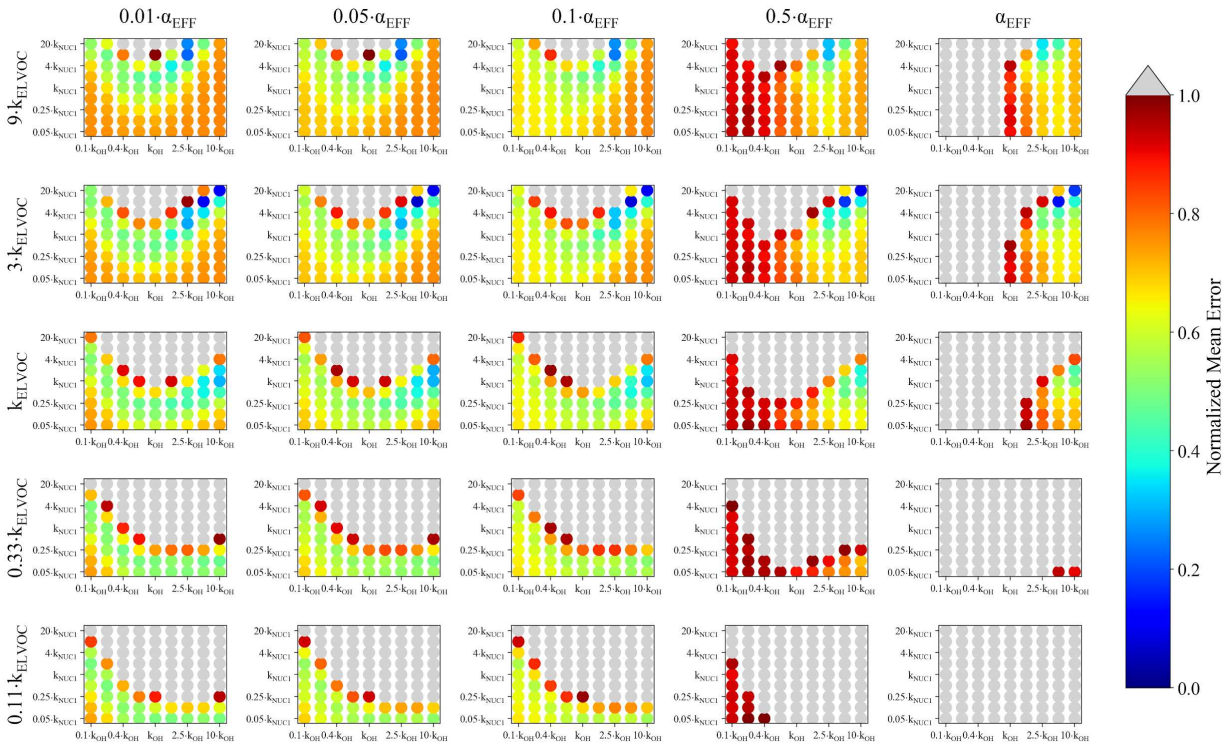

Figure A13. Representation of the parameter space for a 0.77 eq. day aging exposure from BEACHON-RoMBAS for the NUC1 nucleation scheme and base value of the reactive uptake coefficient of 0.6. The effective accommodation coefficient increases across each row of panels; the rate constant of gas-phase fragmentation increases up each column of panels. Within each panel, the rate constant of gas-phase reactions with OH increases along the x-axis and the rate constant for nucleation increases along the y-axis. The color bar indicates the normalized mean error (NME) value for each simulation, with the lowest values indicating the least error between model and measurement. Grey regions indicate regions within the parameter space whose NME value is greater than 1.

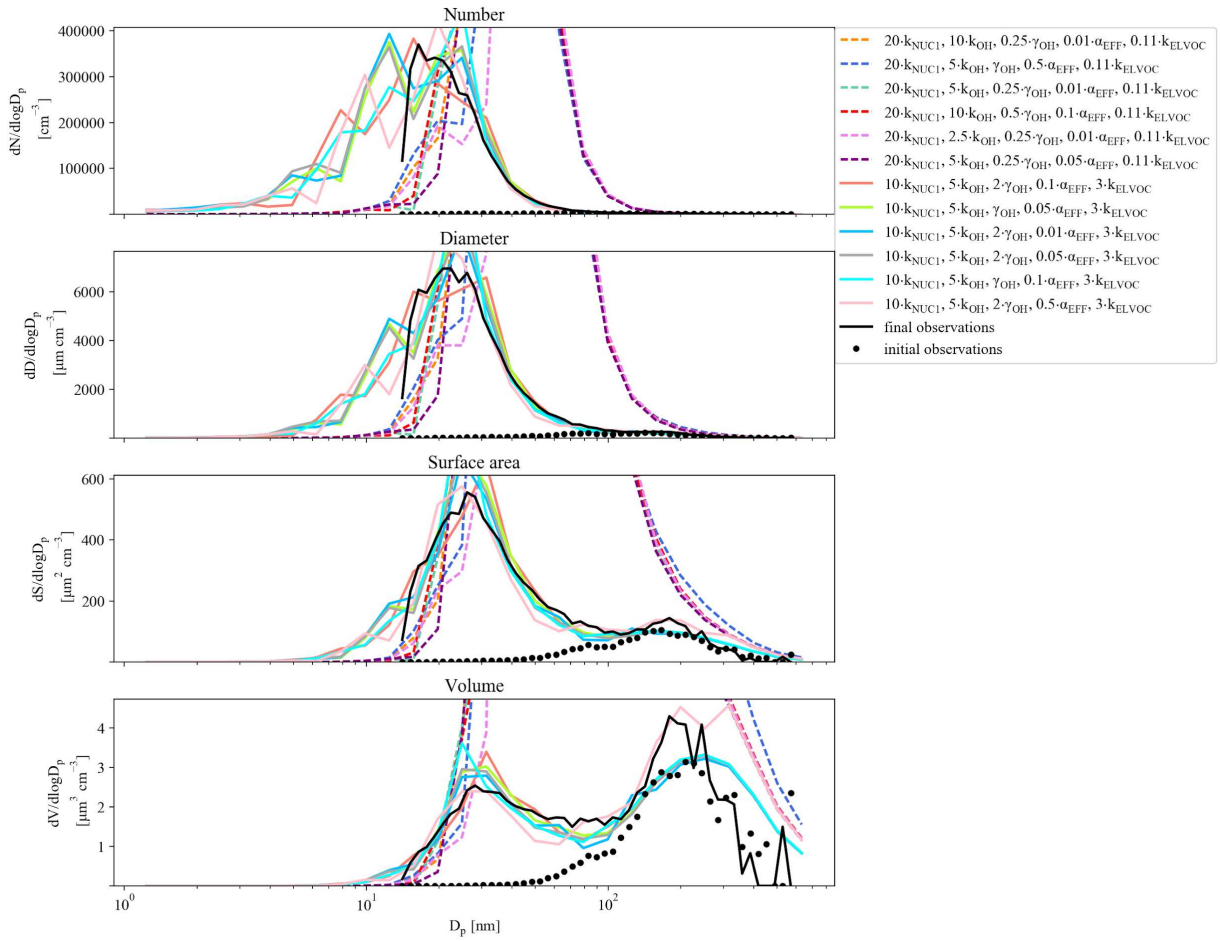

Figure A14. Example of best (solid lines) and worst (dashed lines) fit size distributions compared to the observed (black line) final OFR size distribution for a 0.77 eq days aging case from BEACHON-RoMBAS for the NUC1 nucleation scheme. The fits are determined using the mean error of moments method (see methods); each panel represents a separate moment. The top panel represents the number distribution; the second panel represents the diameter distribution; the third panel represents the surface area distribution; and the final (bottom) distribution represents the volume distribution.

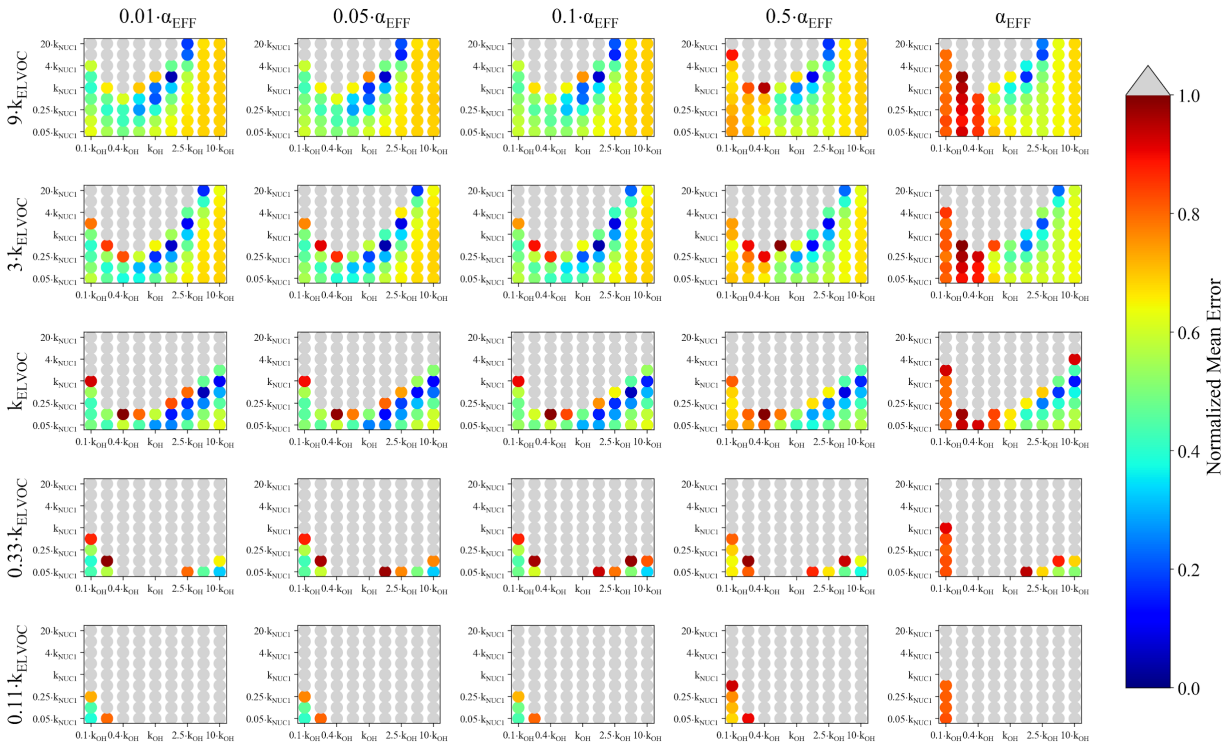

Figure A15. Representation of the parameter space for a 0.82 eq. day aging exposure from BEACHON-RoMBAS for the NUC1 nucleation scheme and base value of the reactive uptake coefficient of 0.6. The effective accommodation coefficient increases across each row of panels; the rate constant of gas-phase fragmentation increases up each column of panels. Within each panel, the rate constant of gas-phase reactions with OH increases along the x-axis and the rate constant for nucleation increases along the y-axis. The color bar indicates the normalized mean error (NME) value for each simulation, with the lowest values indicating the least error between model and measurement. Grey regions indicate regions within the parameter space whose NME value is greater than 1.

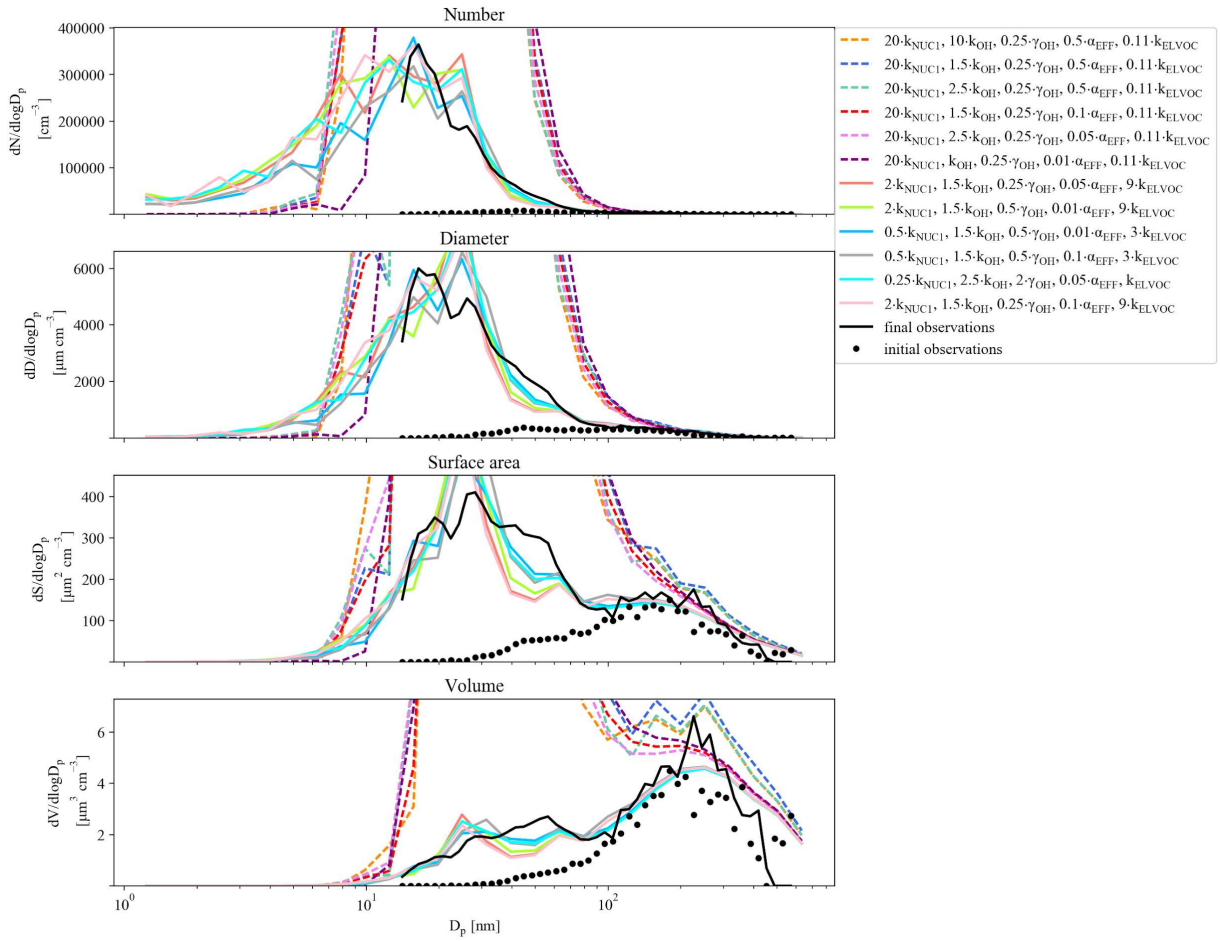

Figure A16. Example of best (solid lines) and worst (dashed lines) fit size distributions compared to the observed (black line) final OFR size distribution for a 0.82 eq days aging case from BEACHON-RoMBAS for the NUC1 nucleation scheme. The fits are determined using the mean error of moments method (see methods); each panel represents a separate moment. The top panel represents the number distribution; the second panel represents the diameter distribution; the third panel represents the surface area distribution; and the final (bottom) distribution represents the volume distribution.

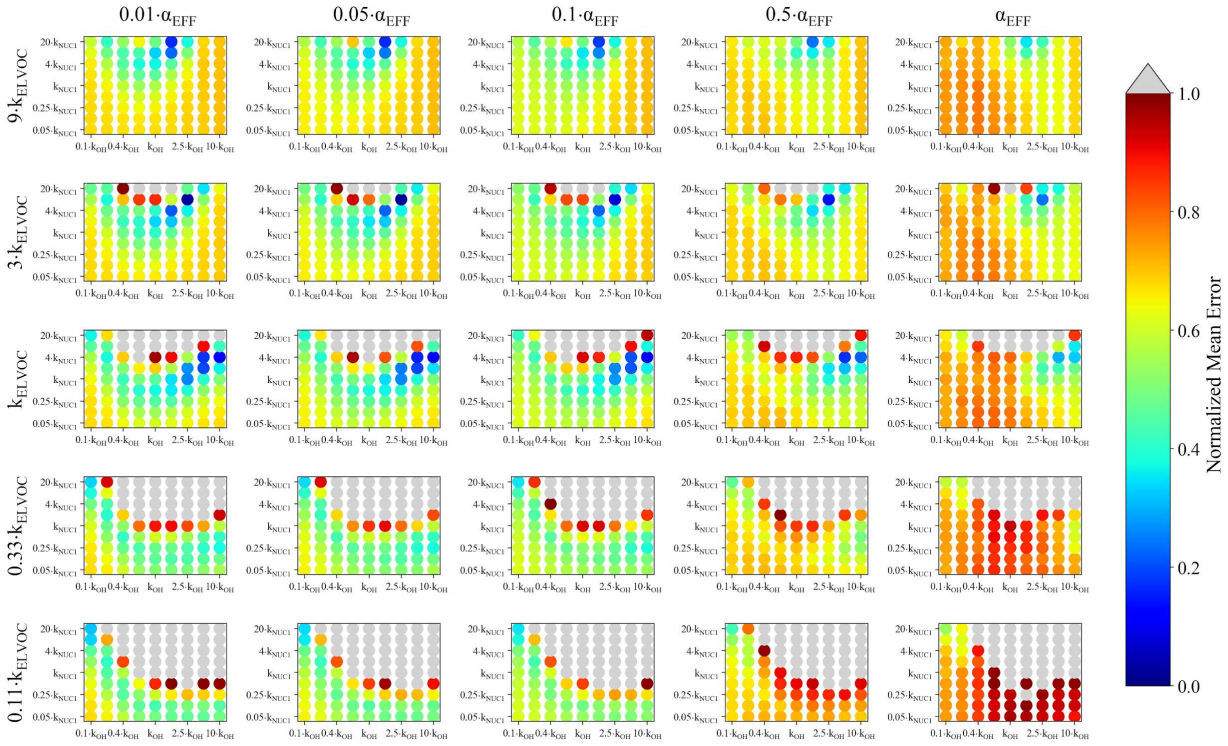

Figure A17. Representation of the parameter space for a 0.91 eq. day aging exposure from BEACHON-RoMBAS for the NUC1 nucleation scheme and base value of the reactive uptake coefficient of 0.6. The effective accommodation coefficient increases across each row of panels; the rate constant of gas-phase fragmentation increases up each column of panels. Within each panel, the rate constant of gas-phase reactions with OH increases along the x-axis and the rate constant for nucleation increases along the y-axis. The color bar indicates the normalized mean error (NME) value for each simulation, with the lowest values indicating the least error between model and measurement. Grey regions indicate regions within the parameter space whose NME value is greater than 1.

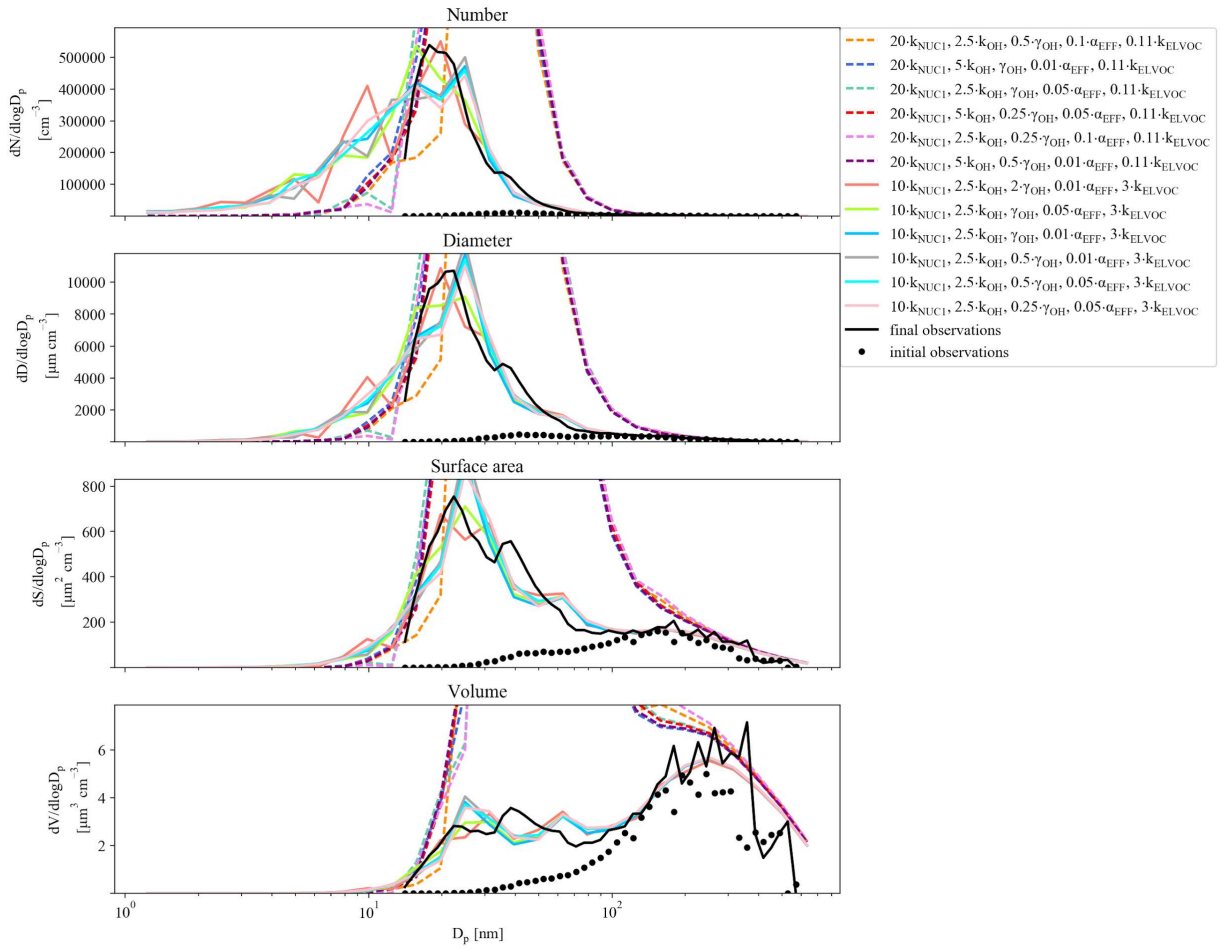

Figure A18. Example of best (solid lines) and worst (dashed lines) fit size distributions compared to the observed (black line) final OFR size distribution for a 0.91 eq days aging case from BEACHON-RoMBAS for the NUC1 nucleation scheme. The fits are determined using the mean error of moments method (see methods); each panel represents a separate moment. The top panel represents the number distribution; the second panel represents the diameter distribution; the third panel represents the surface area distribution; and the final (bottom) distribution represents the volume distribution.

A3. Sensitivity of the model to the NUC2 nucleation scheme for BEACHON-RoMBAS

Figure A19 gives the average NME values across the 0.09-0.9 day eq. aging exposures from BEACHON-RoMBAS examined in this study for the parameter space that lies within (Table 3) the NUC2 nucleation scheme and base value of the reactive uptake coefficient. This figure is qualitatively similar to Fig. 5, which shows the same parameter space except for the NUC1 nucleation scheme.

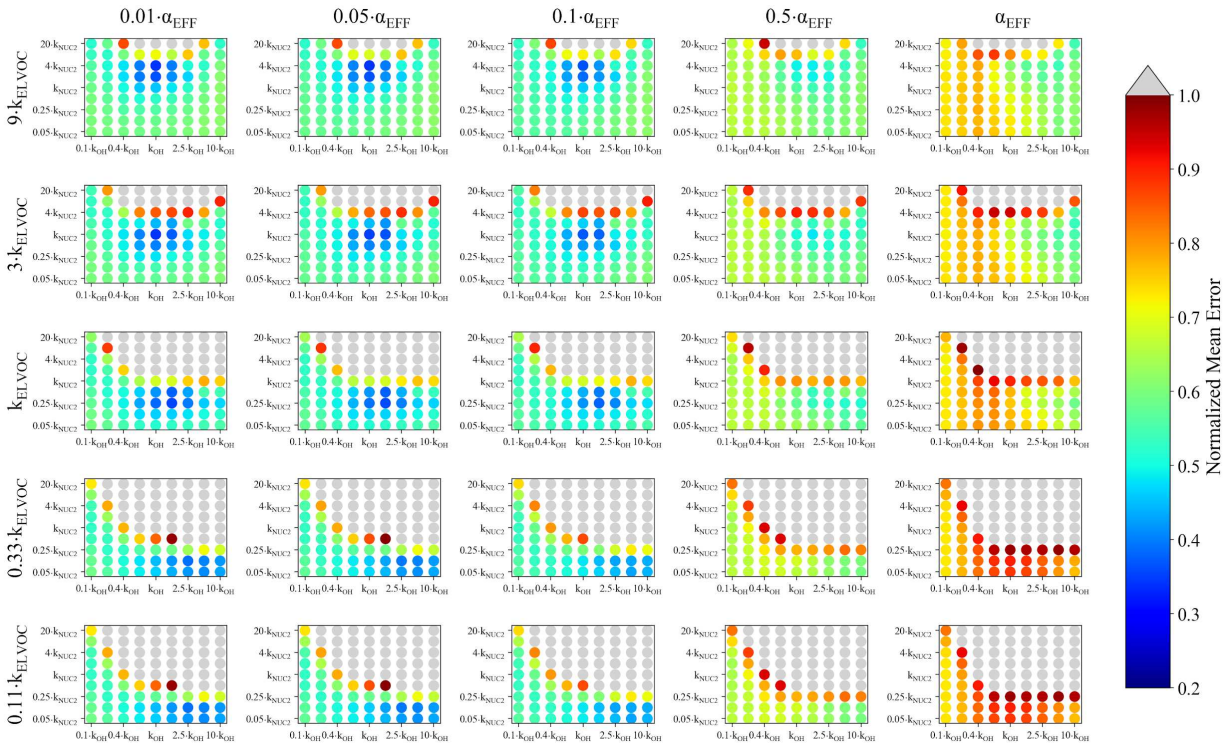

Figure A19. Representation of the parameter space for the average across the 0.09-0.9 day eq. aging exposures from BEACHON-RoMBAS examined in this study for the NUC2 nucleation scheme and base value of the reactive uptake coefficient of 0.6. The effective accommodation coefficient increases across each row of panels; the rate constant of gas-phase fragmentation increases up each column of panels. Within each panel, the rate constant of gas-phase reactions with OH increases along the x-axis and the rate constant for nucleation increases along the y-axis. The color bar indicates the normalized mean error (NME) value for each simulation, with the lowest values indicating the least error between model and measurement. Grey regions indicate regions within the parameter space whose NME value is greater than 1. No averaged case had a NME value less than 0.2 for the cases shown here.

A4. Sensitivity of the model to the heterogeneous chemistry parameter for BEACHON-RoMBAS

In order to determine the model sensitivity to the reactive uptake coefficient, γ_{OH}, we replot the results of Fig. 4 in Fig. A20 to be a function of γ_{OH} (increasing across each column) for the base value of the gas-phase fragmentation rate constant.

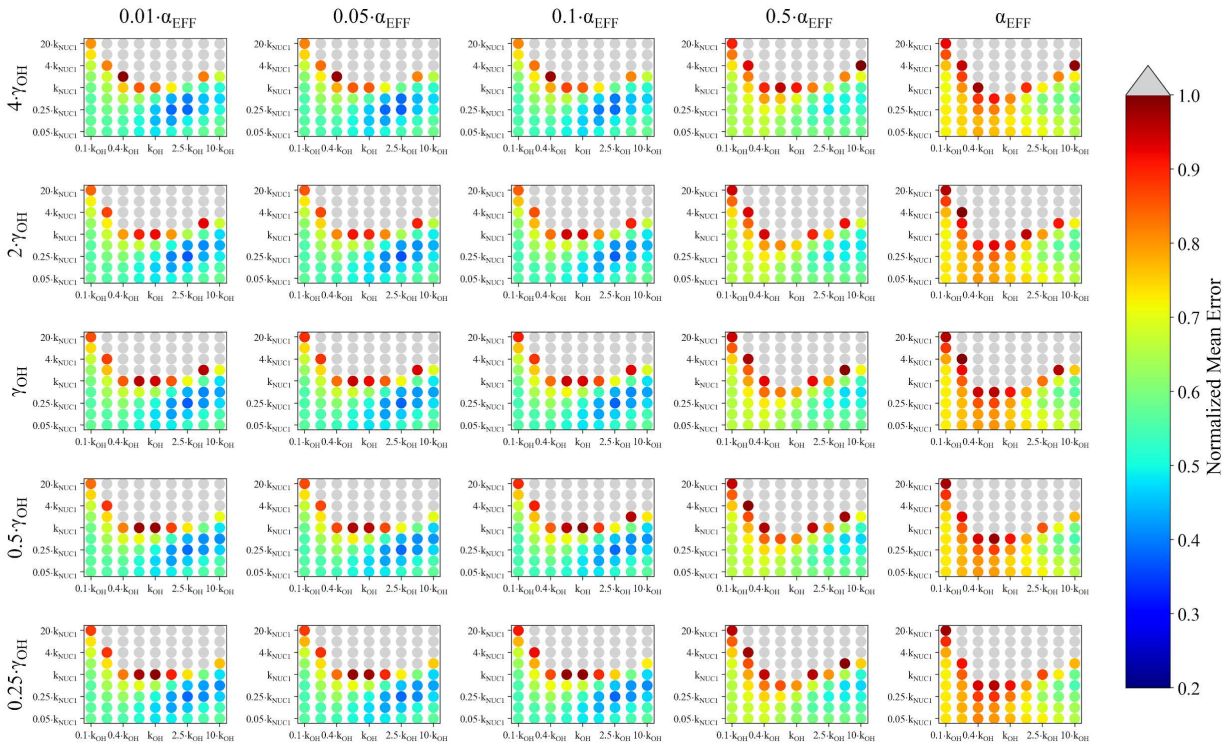

Figure A20. Representation of the parameter space for the average across the 0.09-0.9 day eq. aging exposures from BEACHON-RoMBAS examined in this study for the NUC1 nucleation scheme and base value of the gas-phase fragmentation rate constant (k_{ELVOC}). The effective accommodation increases across each row; the reactive uptake coefficient increases up each column of panels. Within each panel, the rate constant of gas-phase reactions with OH increases along the x-axis and the rate constant for nucleation increases along the y-axis. The color bar indicates the normalized mean error (NME) value for each simulation, with the lowest values indicating the least error between model and measurement. Grey regions indicate regions within the parameter space whose NME value is greater than 1. No averaged case had a NME value less than 0.2 for the cases shown here. This Figure Ehows that for a fixed value of reactive uptake coefficient (each column), the NME values for each set of nucleation rate constants/gas-phase functionalization constants/effective accommodation coefficients do not show significant change.

A5. GoAmazon sensitivity to S/IVOCs

To model the GoAmazon OFR distributions, we initially run TOMAS with the S/IVOC input concentration derived by using the campaign average ratio of MT:S/IVOCs from BEACHON-RoMBAS (Table 2.2), as S/IVOCs were not measured during the GoAmazon campaign. Figures A21 and A22 show that for this initial assumed S/IVOC concentration, we cannot replicate the observed growth (Fig. A22, black solid lines) and instead get poor NME values for all combinations of parameters (Fig. A21).

Figure A21. Representation of the parameter space for a 0.53 eq. day aging exposure from GoAmazon for the NUC1 nucleation scheme and base value of the reactive uptake coefficient of 0.6. The effective accommodation coefficient increases across each row of panels; the rate constant of gas-phase fragmentation increases up each column of panels. Within each panel, the rate constant of gas-phase reactions with OH increases along the x-axis and the rate constant for nucleation increases along the y-axis. The color bar indicates the normalized mean error (NME) value for each simulation, with the lowest values indicating the least error between model and measurement. Grey regions indicate regions within the parameter space whose NME value is greater than 1. In order to see enough growth in the Aitken mode, an increase of between 20-40 times the original S/IVOC input is required. See text and Figs. 6 and A23-A29 for more details.

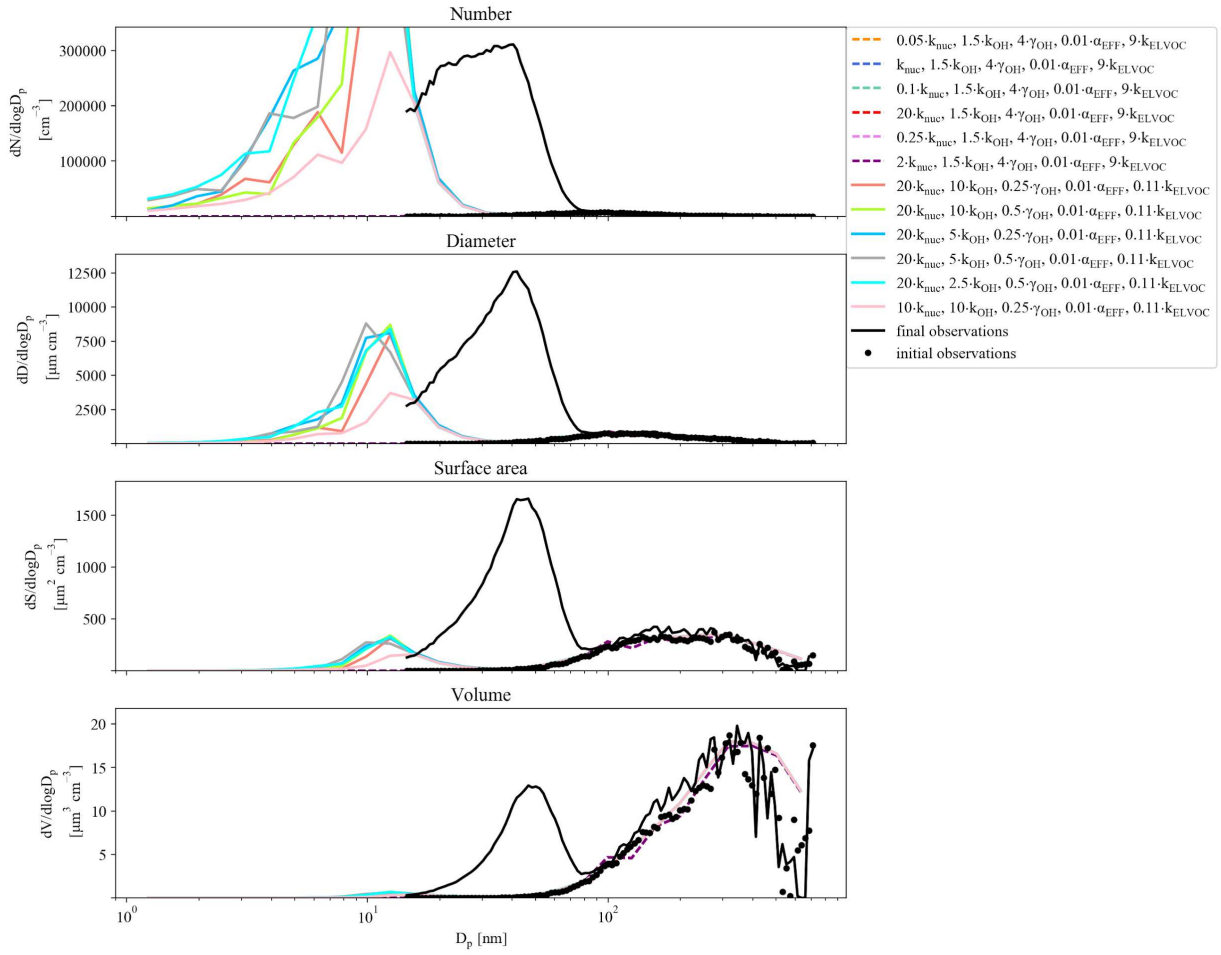

Figure A22. Example of best (solid lines) and worst (dashed lines) fit size distributions compared to the observed (black line) final OFR size distribution for a 0.53 eq days aging case from GoAmazon for the NUC1 nucleation scheme. The fits are determined using the mean error of moments method (see methods); each panel represents a separate moment. The top panel represents the number distribution; the second panel represents the diameter distribution; the third panel represents the surface area distribution; and the final (bottom) distribution represents the volume distribution. In order to see enough growth in the Aitken mode, an increase of between 20-40 times the original S/IVOC input is required. See text and Figs. 6 and A23-A29 for more details.

A6. Sensitivity of the model to the NUC2 and ACT nucleation schemes for GoAmazon

Figures A23 and A24 gives the average NME values across the 0.3-0.6 day eq. aging exposures from GoAmazon examined in this study for the parameter space that lies within the NUC2 nucleation scheme and ACT nucleation scheme, respectively, for base value of the reactive uptake coefficient. These figures use the assumption that the initial S/IVOC concentration is 30 times that of the base S/IVOC concentration (Table 2). Figure A22 is qualitatively similar to Fig. 6, which shows the same parameter space except for the NUC1 nucleation scheme. Figure A23, using the ACT nucleation scheme, shows shifted regions of best-fits as compared to the NUC1 (Fig. 6) and NUC2 (Fig. A22) nucleation schemes.

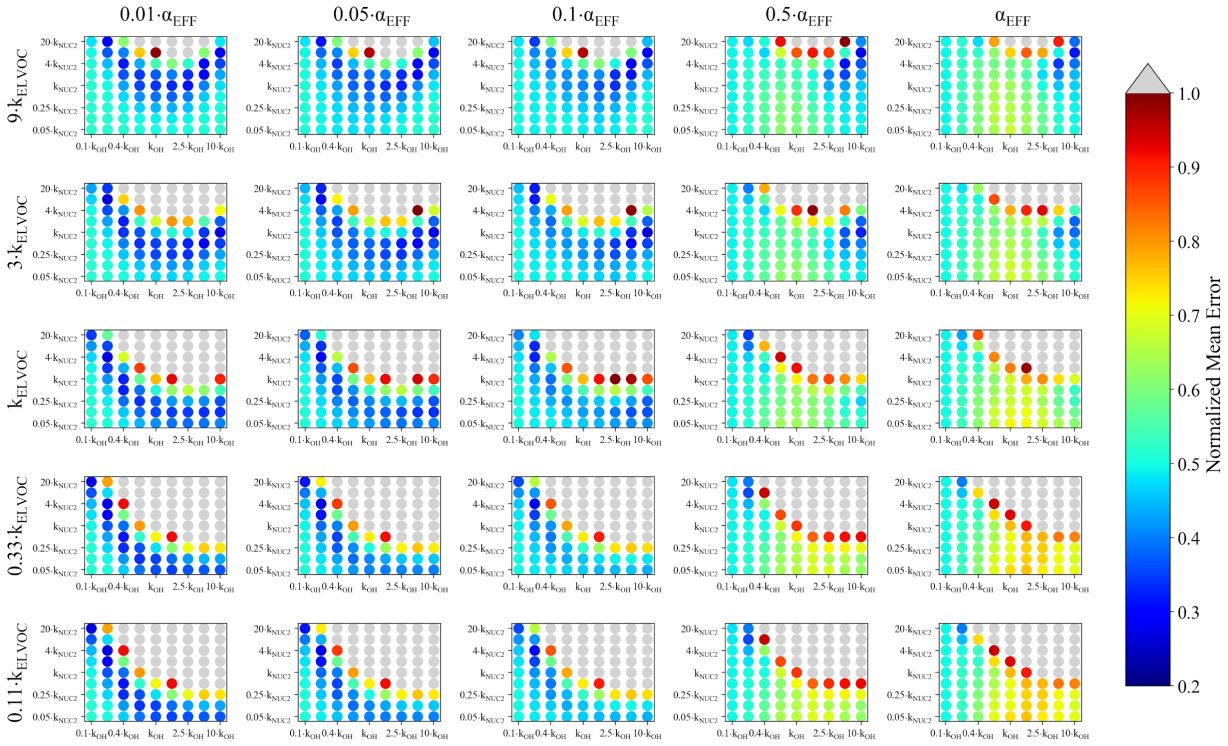

Figure A23. Representation of the parameter space for the average across the 0.3-0.6 day eq. aging exposures from GoAmazon examined in this study for the NUC2 nucleation scheme, base value of the reactive uptake coefficient of 0.6, and assumed S/IVOC concentrations of 30 times that of the baseS/IVOC concentrations. The effective accommodation coefficient increases across each row of panels; the rate constant of gas-phase fragmentation increases up each column of panels. Within each panel, the rate constant of gas-phase reactions with OH increases along the x-axis and the rate constant for nucleation increases along the y-axis. The color bar indicates the normalized mean error (NME) value for each simulation, with the lowest values indicating the least error between model and measurement. Grey regions indicate regions within the parameter space whose NME value is greater than 1. No averaged case had a NME value less than 0.2 for the cases shown here.

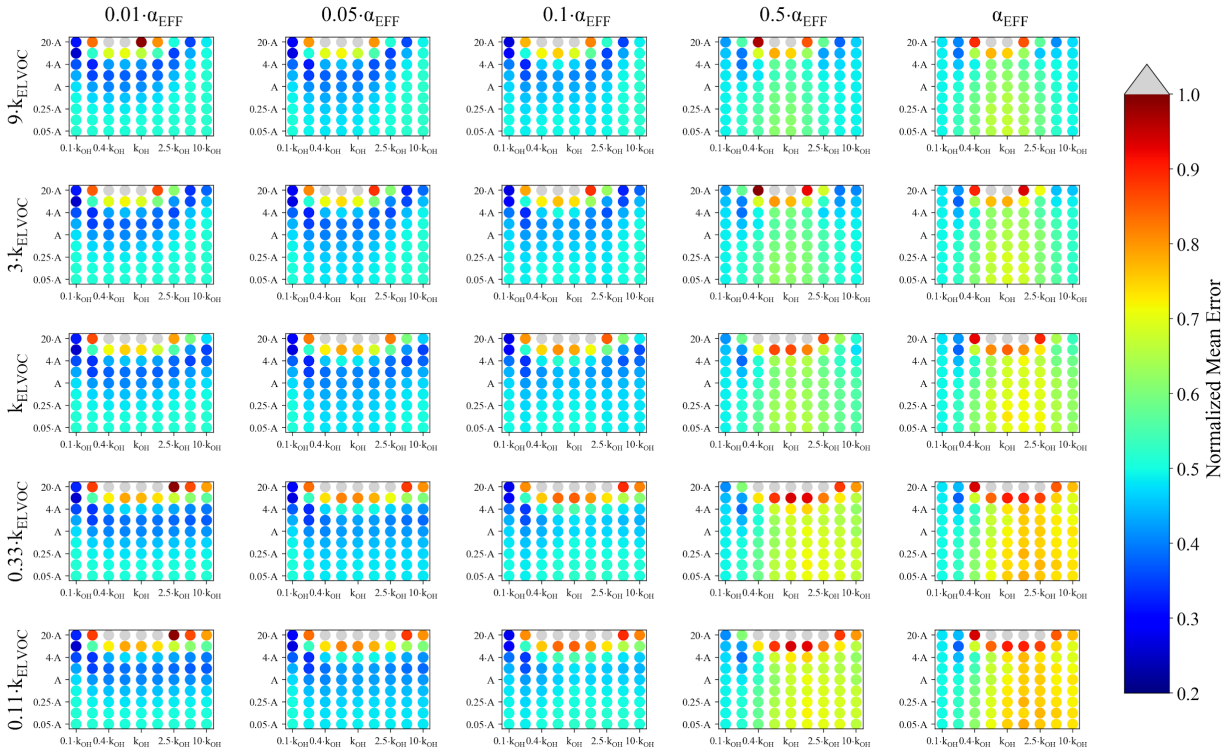

Figure A24. Representation of the parameter space for the average across the 0.3-0.6 day eq. aging exposures from GoAmazon examined in this study for the ACT nucleation scheme, base value of the reactive uptake coefficient of 0.6, and assumed S/IVOC concentration of 30 times that of the base S/IVOC concentration. The effective accommodation coefficient increases across each row of panels; the rate constant of gas-phase fragmentation increases up each column of panels. Within each panel, the rate constant of gas-phase reactions with OH increases along the x-axis and the rate constant for nucleation increases along the y-axis. The color bar indicates the normalized mean error (NME) value for each simulation, with the lowest values indicating the least error between model and measurement. Grey regions indicate regions within the parameter space whose NME value is greater than 1. No averaged case had a NME value less than 0.2 for the cases shown here.

A7. GoAmazon individual exposures and best/worst case distributions

The following are the individual representations of the model simulations for each GoAmazon exposure modelled in this study for the assumption that the initial S/IVOC concentration is 30 times that of the base S/IVOC concentration (Table 2). Figures A25, S27, S29, and S31 give the NME values for the parameter space that lies within (Table 3) the NUC1 nucleation scheme and base value of the reactive uptake coefficient. Figures A26, A28, A30, and A32 plot each observed final moment (solid black lines) used in computing the NME statistic (number, diameter, surface area, and volume) compared to the six TOMAS cases with the lowest (best) NME statistic (solid colored lines) and six TOMAS cases with the highest (worst) NME statistic (solid dotted lines). For comparison, the observed initial moments are also plotted for each moment (dotted black lines).

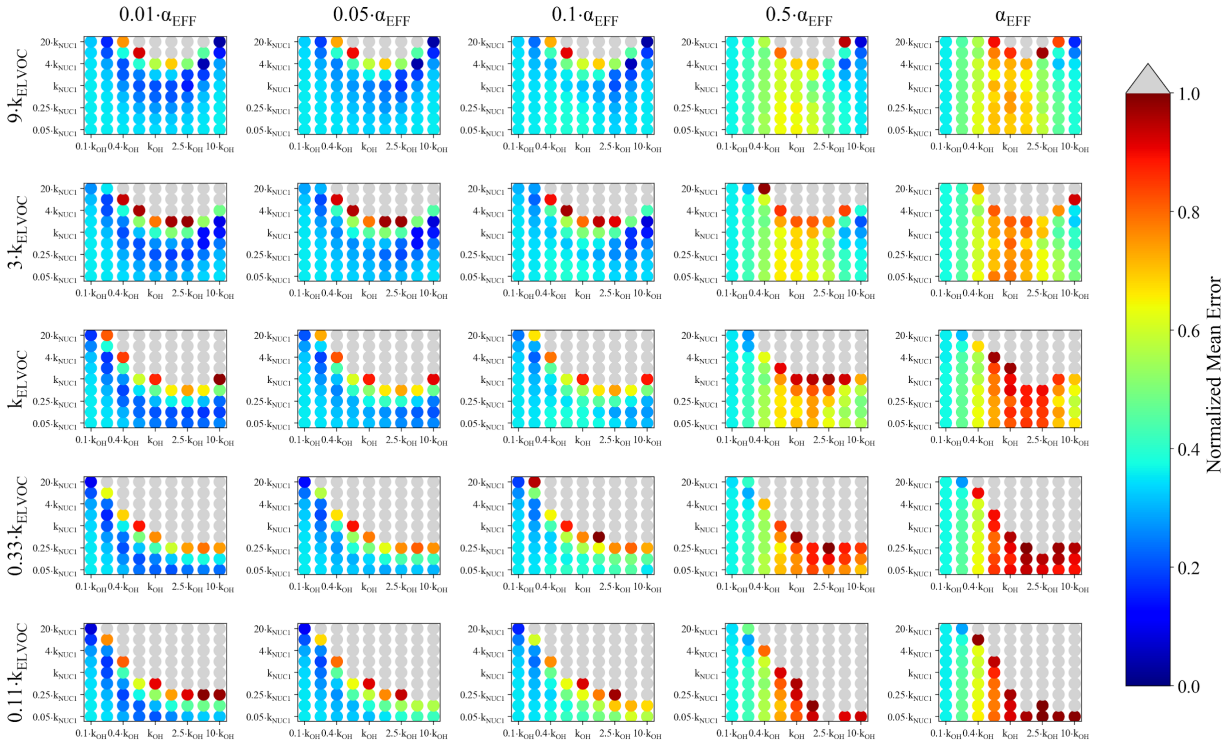

Figure A25. Representation of the parameter space for a 0.39 eq. day aging exposure from GoAmazon for the NUC1 nucleation scheme, base value of the reactive uptake coefficient of 0.6, and 30 times the base S/IVOC input concentration. The effective accommodation coefficient increases across each row of panels; the rate constant of gas-phase fragmentation increases up each column of panels. Within each panel, the rate constant of gas-phase reactions with OH increases along the x-axis and the rate constant for nucleation increases along the y-axis. The color bar indicates the normalized mean error (NME) value for each simulation, with the lowest values indicating the least error between model and measurement. Grey regions indicate regions within the parameter space whose NME value is greater than 1.

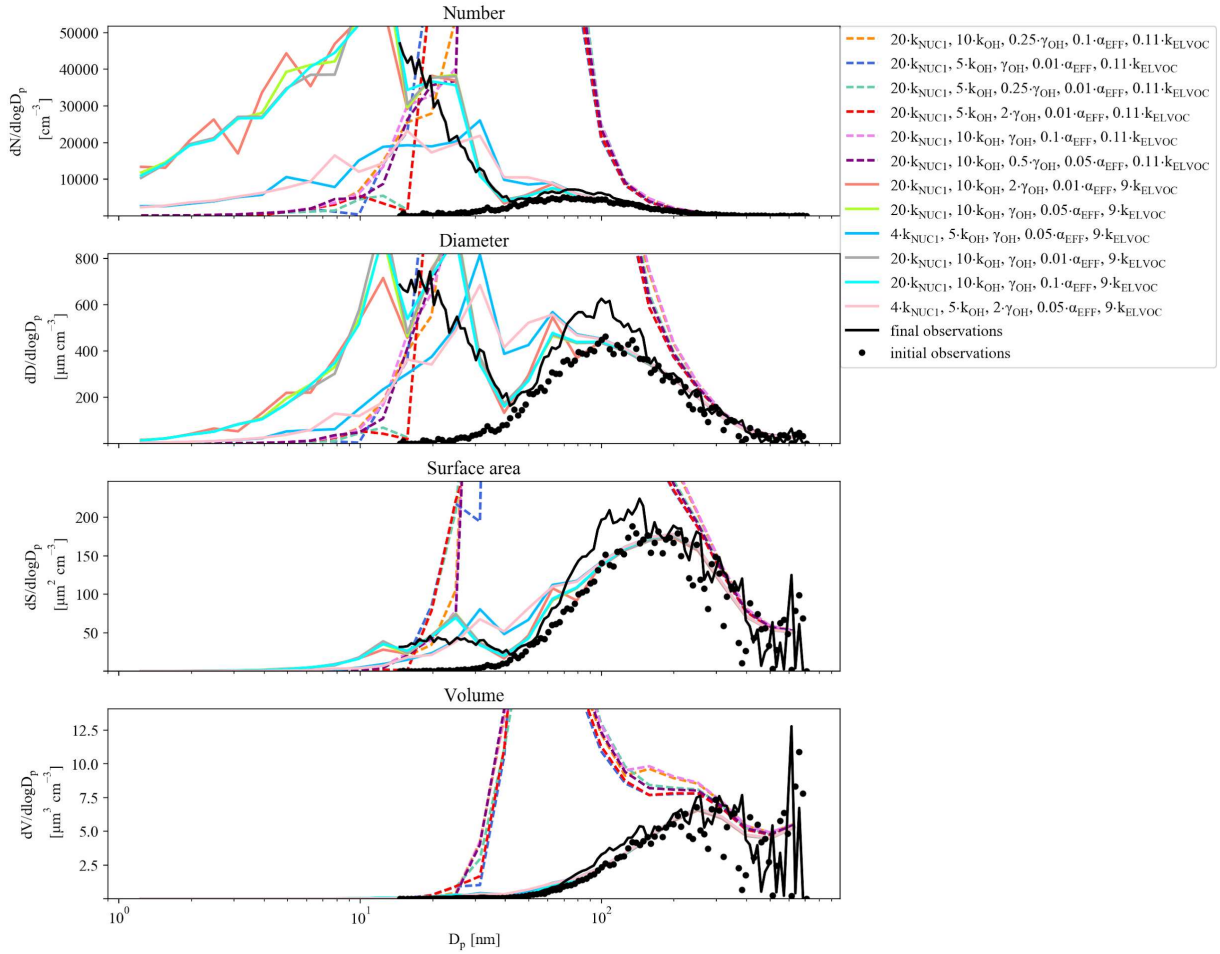

Figure A26. Example of best (solid lines) and worst (dashed lines) fit size distributions compared to the observed (black line) final OFR size distribution for a 0.39 eq. days aging case from GoAmazon for the NUC1 nucleation scheme, using 30 times the base S/IVOC input concentration. The fits are determined using the mean error of moments method (see methods); each panel represents a separate moment. The top panel represents the number distribution; the second panel represents the diameter distribution; the third panel represents the surface area distribution; and the final (bottom) distribution represents the volume distribution.

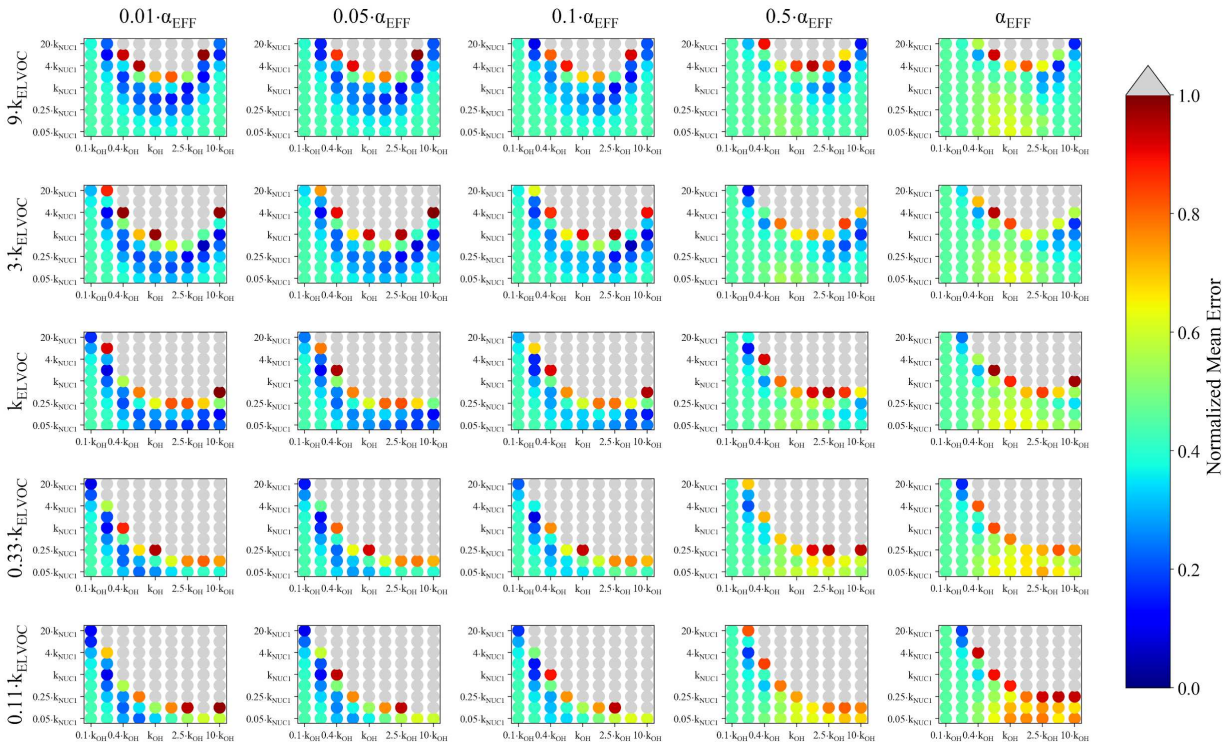

Figure A27. Representation of the parameter space for a 0.40 eq. day aging exposure from GoAmazon for the NUC1 nucleation scheme, base value of the reactive uptake coefficient of 0.6, and 30 times the base S/IVOC input concentration. The effective accommodation coefficient increases across each row of panels; the rate constant of gas-phase fragmentation increases up each column of panels. Within each panel, the rate constant of gas-phase reactions with OH increases along the x-axis and the rate constant for nucleation increases along the y-axis. The color bar indicates the normalized mean error (NME) value for each simulation, with the lowest values indicating the least error between model and measurement. Grey regions indicate regions within the parameter space whose NME value is greater than 1.

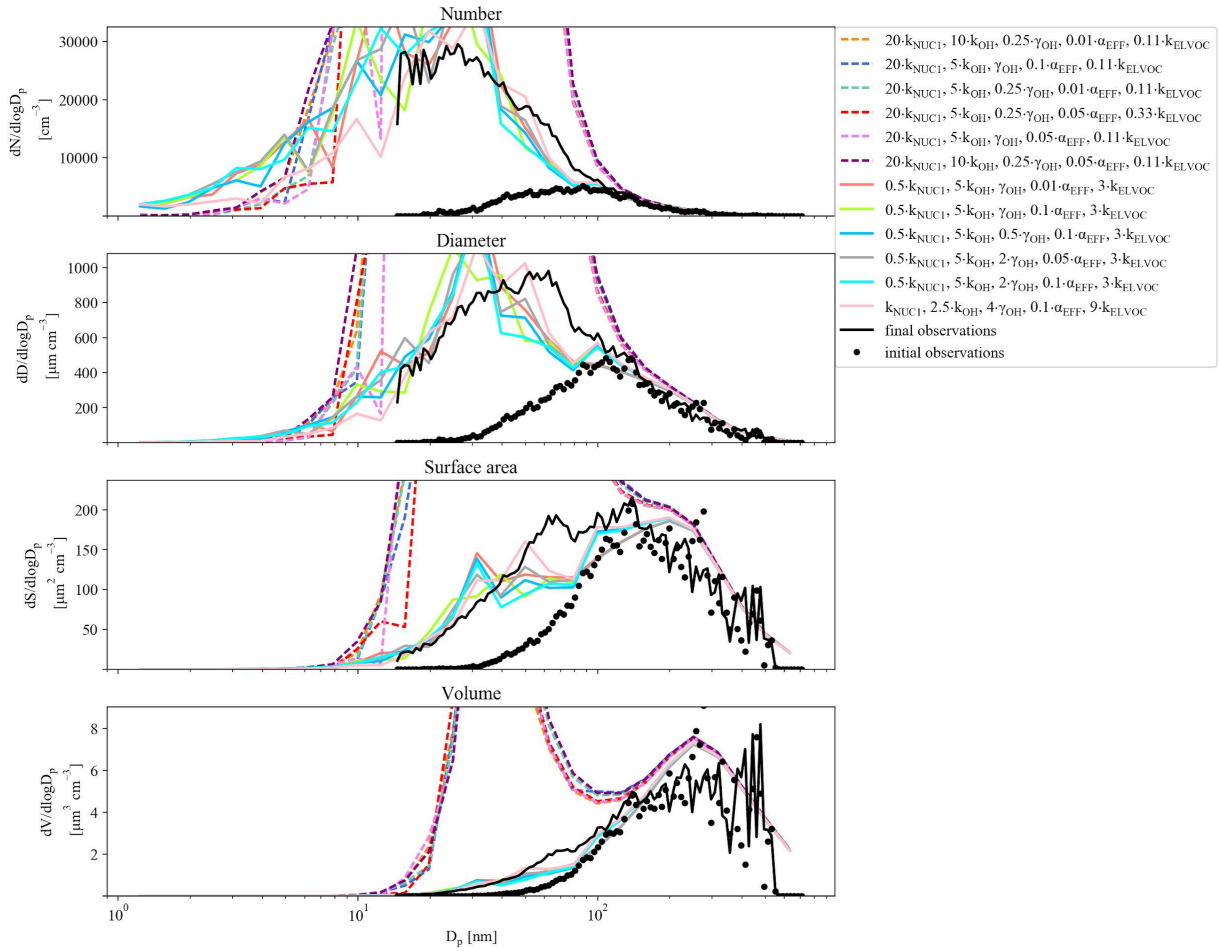

Figure A28. Example of best (solid lines) and worst (dashed lines) fit size distributions compared to the observed (black line) final OFR size distribution for a 0.40 eq days aging case from GoAmazon for the NUC1 nucleation scheme, using 30 times the base S/IVOC input concentration. The fits are determined using the mean error of moments method (see methods); each panel represents a separate moment. The top panel represents the number distribution; the second panel represents the diameter distribution; the third panel represents the surface area distribution; and the final (bottom) distribution represents the volume distribution.

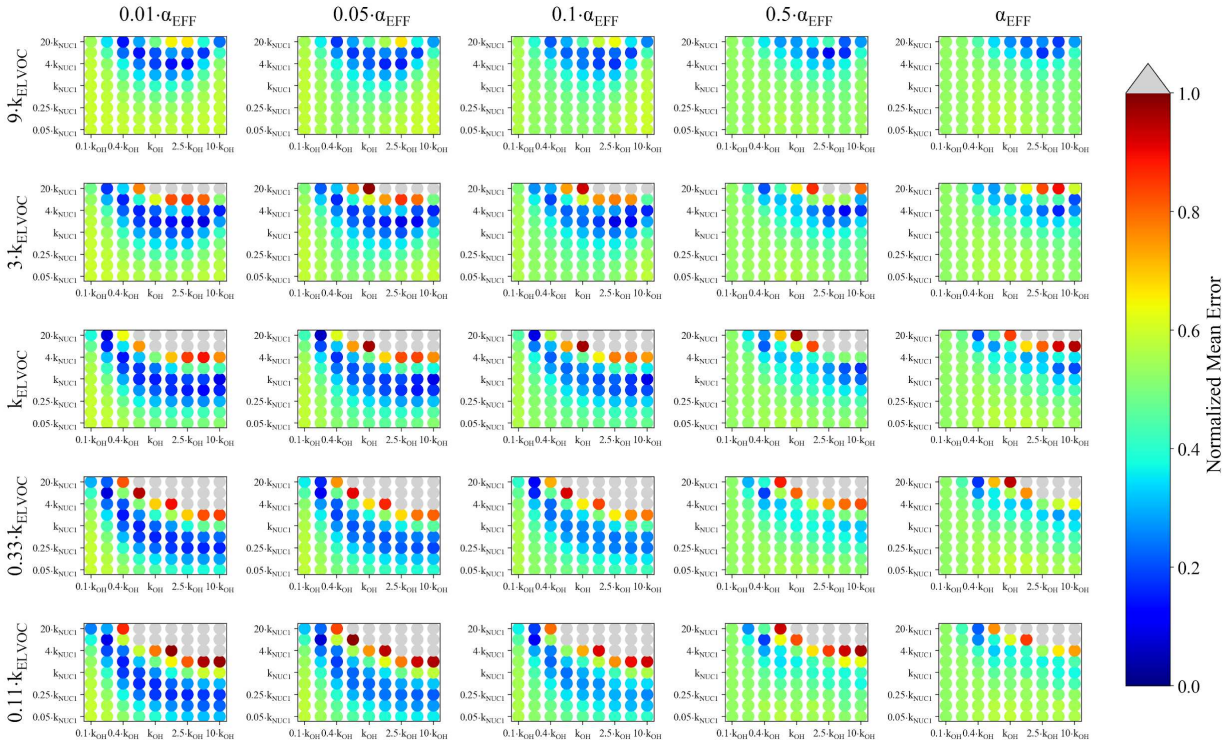

Figure A29. Representation of the parameter space for a 0.51 eq. day aging exposure from GoAmazon for the NUC1 nucleation scheme, base value of the reactive uptake coefficient of 0.6, and 30 times the base S/IVOC input concentration. The effective accommodation coefficient increases across each row of panels; the rate constant of gas-phase fragmentation increases up each column of panels. Within each panel, the rate constant of gas-phase reactions with OH increases along the x-axis and the rate constant for nucleation increases along the y-axis. The color bar indicates the normalized mean error (NME) value for each simulation, with the lowest values indicating the least error between model and measurement. Grey regions indicate regions within the parameter space whose NME value is greater than 1.

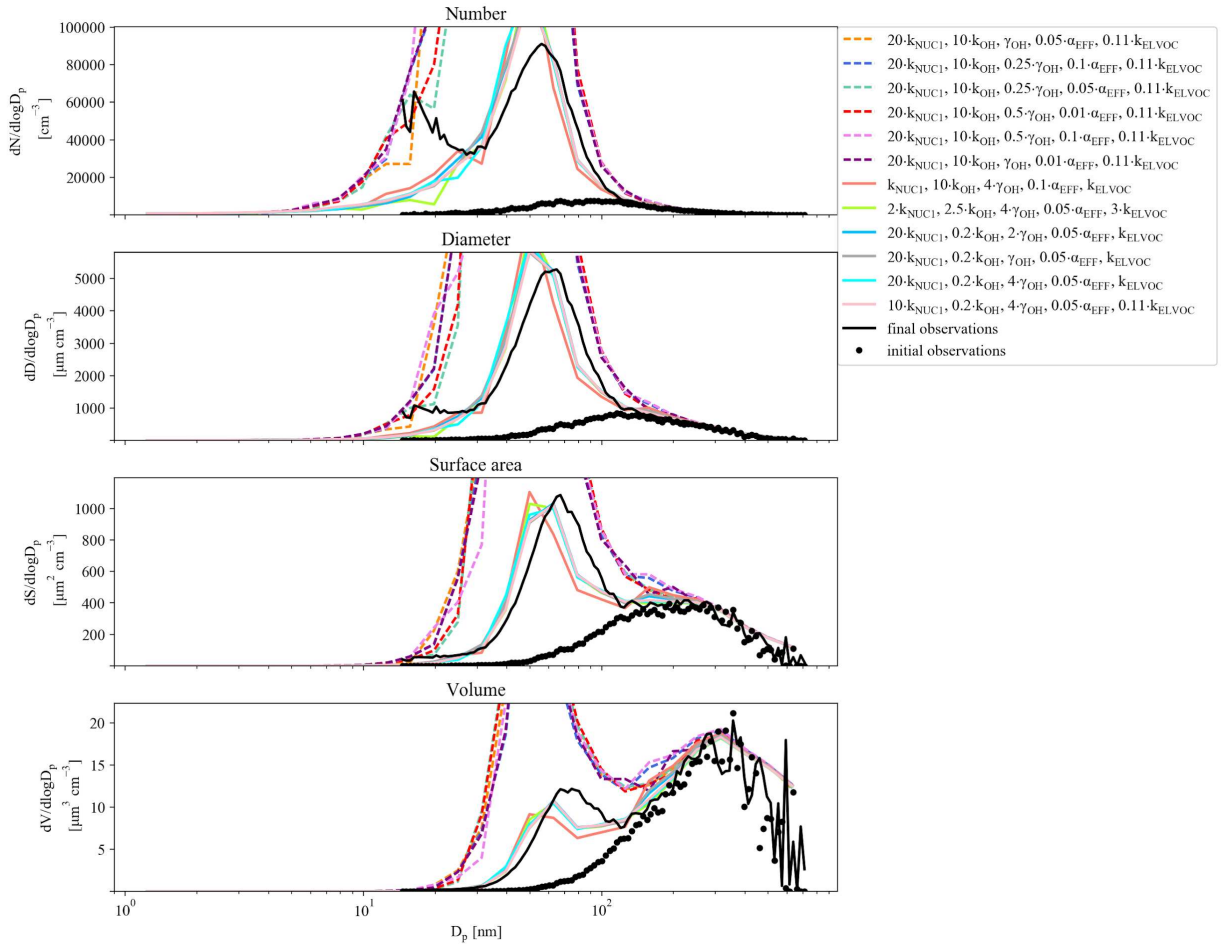

Figure A30. Example of best (solid lines) and worst (dashed lines) fit size distributions compared to the observed (black line) final OFR size distribution for a 0.51 eq days aging case from GoAmazon for the NUC1 nucleation scheme, using 30 times the base S/IVOC input concentration. The fits are determined using the mean error of moments method (see methods); each panel represents a separate moment. The top panel represents the number distribution; the second panel represents the diameter distribution; the third panel represents the surface area distribution; and the final (bottom) distribution represents the volume distribution.

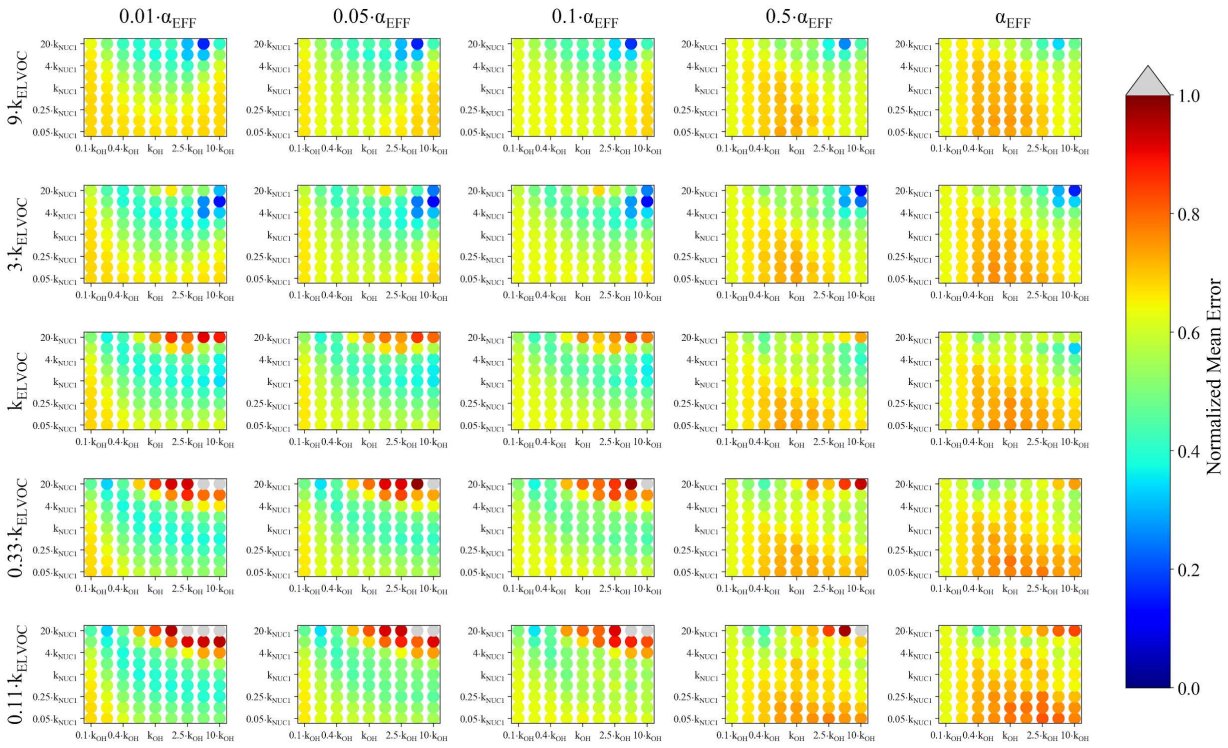

Figure A31. Representation of the parameter space for a 0.53 eq. day aging exposure from GoAmazon for the NUC1 nucleation scheme, base value of the reactive uptake coefficient of 0.6, and 30 times the base S/IVOC input concentration. The effective accommodation coefficient increases across each row of panels; the rate constant of gas-phase fragmentation increases up each column of panels. Within each panel, the rate constant of gas-phase reactions with OH increases along the x-axis and the rate constant for nucleation increases along the y-axis. The color bar indicates the normalized mean error (NME) value for each simulation, with the lowest values indicating the least error between model and measurement. Grey regions indicate regions within the parameter space whose NME value is greater than 1.

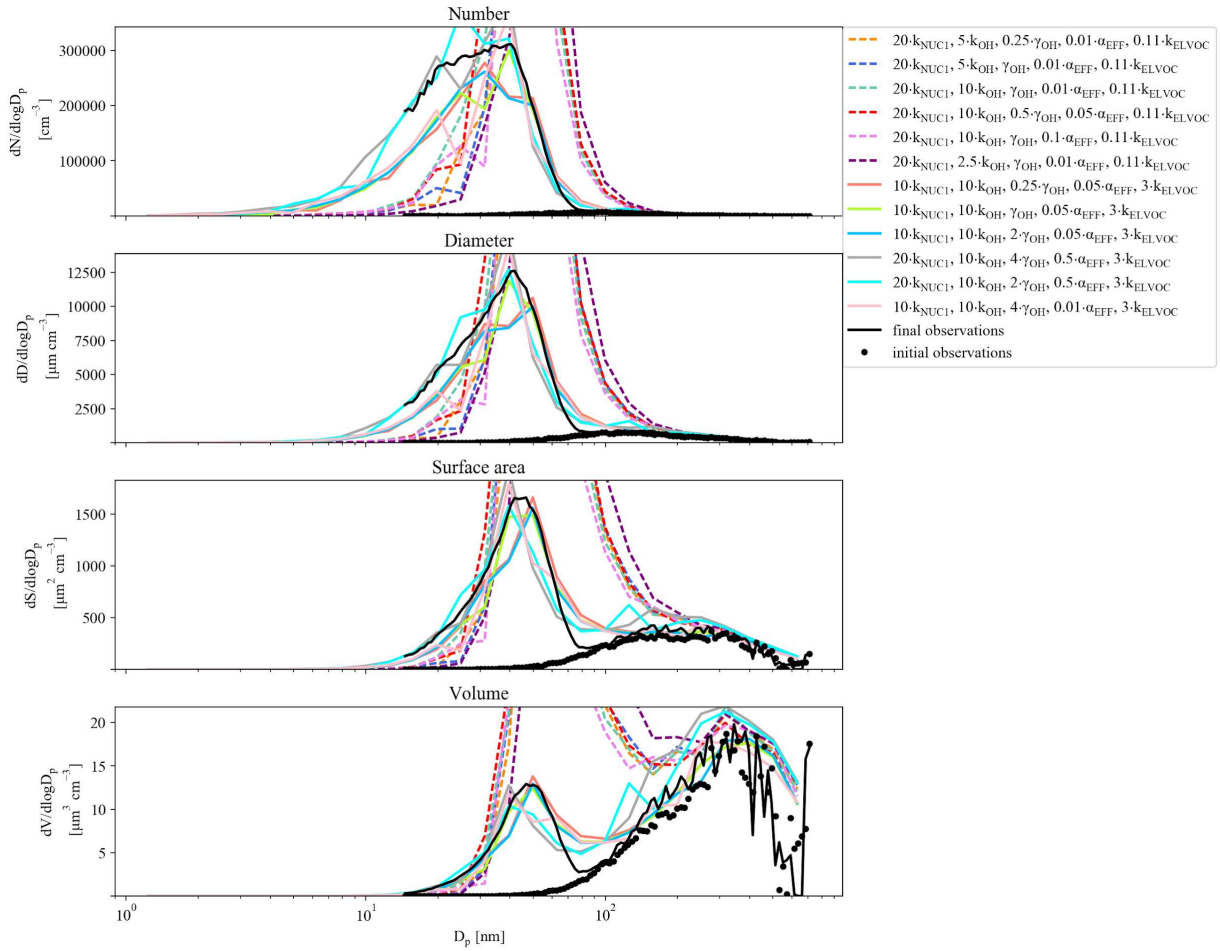

Figure A32. Example of best (solid lines) and worst (dashed lines) fit size distributions compared to the observed (black line) final OFR size distribution for a 0.53 eq days aging case from GoAmazon for the NUC1 nucleation scheme, using 30 times the base S/IVOC input concentration. The fits are determined using the mean error of moments method (see methods); each panel represents a separate moment. The top panel represents the number distribution; the second panel represents the diameter distribution; the third panel represents the surface area distribution; and the final (bottom) distribution represents the volume distribution.

APPENDIX B

SUPPLEMENT TO: THE POTENTIAL ROLE OF METHANESULFONIC ACID (MSA) IN AEROSOL FORMATION AND GROWTH AND THE ASSOCIATED RADIATIVE FORCINGS

B1. Simulated ammonia concentrations

Annually (Fig. B1) and seasonally (Fig. B2) averaged simulated concentrations of ammonia from the GEOS-Chem-TOMAS model. Each map is made from the reported ammonia concentrations for the DEFAULT_NoMSA model.

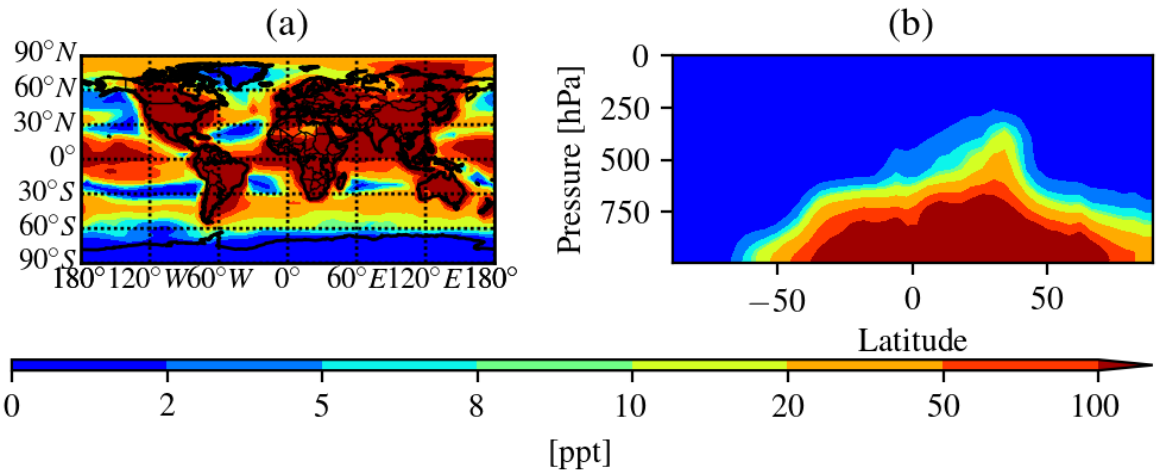

Figure B1. Global annual average predicted NH_3 concentrations at (a) the surface and (b) zonally. For the PARAM_NoNuc and PARAM_Nuc cases, it's assumed that if $[NH_3] < 10$ ppt (blue colors), then the model is under low-base (no free ammonia) conditions (Figure 3.1a).

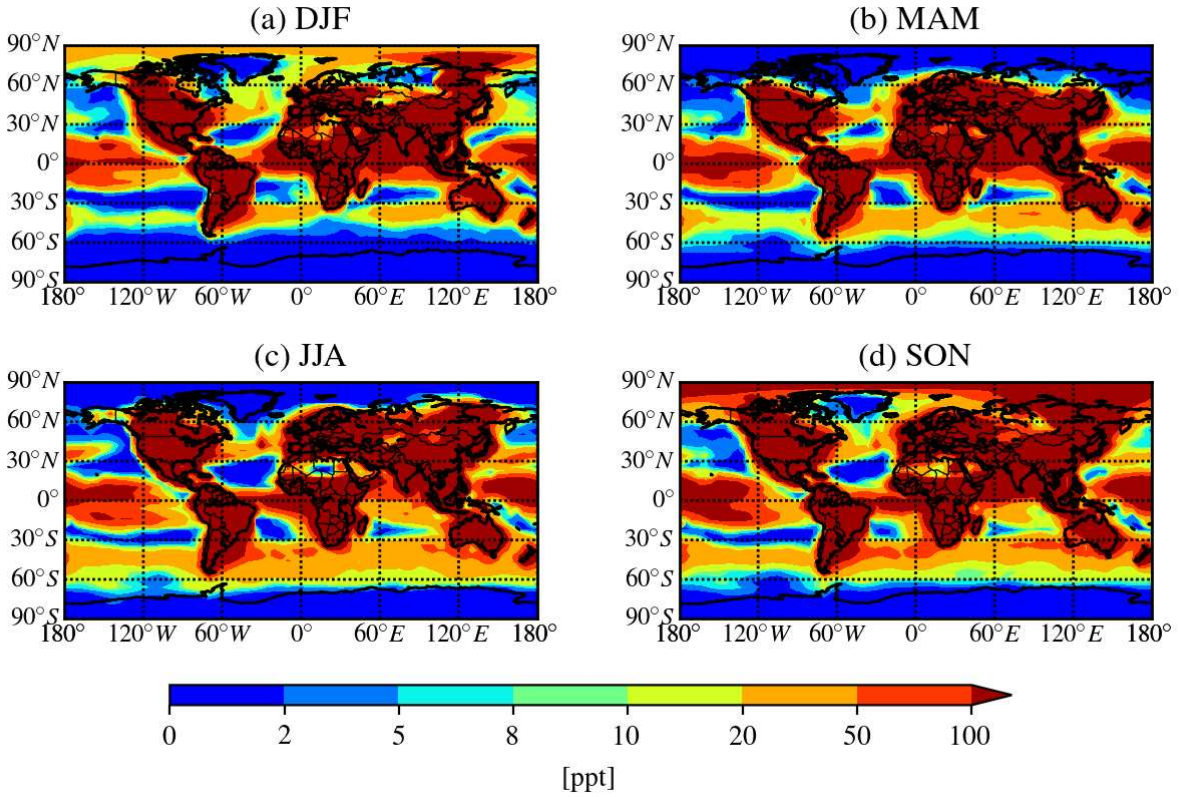

Figure B2. Global seasonal average predicted NH_3 concentrations at the surface for: (a) December, January, February; (b) March, April, May; (c) June, July, August; and (d) September, October, November. For the PARAM_NoNuc and PARAM_Nuc cases, it's assumed that if $[NH_3] < 10$ ppt (blue colors), then the model is under low-base (no free ammonia) conditions (Figure 3.1a).

B2. Comparison of different DMS emission inventories in GEOS-Chem-TOMAS.

We test the sensitivity of the size distribution towards the DMS emissions in two ways: (1) we replace the default DMS emissions inventory for GEOS-Chem v10.01 (Kettle et al., 1999; Kettle and Andreae, 2000) with the updated emissions inventory by Lana et al., (2010) and (2) we increase the default DMS emissions inventory globally by a factor of two. We hereon refer to each inventory as the default DMS inventory, the Lana DMS inventory, and the 2xDMS inventory. The results of these tests are shown in Tables B1-B2 and Figs. B3-B5. Table B1 and Fig. B3 shows the comparisons between each DEFAULT_NoMSA simulation (DEFAULT_NoMSA, DEFAULT_NoMSA_Lana, and DEFAULT_NoMSA_2xDMS) and the NoDMS simulation. This indicates the contribution from sulfate and sulfuric acid produced by DMS/SO_2 oxidation for each DMS emissions inventory. Table B2 and Fig. B4-B5 shows the comparisons between each PARAM_NoNuc case and each DEFAULT_NoMSA case for submicron aerosol mass (only in Table B2), N3 and N80 (Fig. B5) and the AIE and DRE (Fig. B6). It is seen that for the Lana DMS inventory, both the NoDMS (Fig. B3) and PARAM_NoNuc_Lana (Figs. SB4-B5) case comparisons have only small spatial differences and similar magnitude of effects as compared to the default DMS inventory. Thus, if DMS emissions are better simulated by the Lana DMS inventory, our general conclusions would not be changed about the effects of MSA towards the size distribution.

The 2xDMS inventory shows some non-trivial changes in N80 for some regions and levels as compared to the default DMS inventory for the NoDMS comparison (Table B1; Fig. B3), primarily with increases in N80 over the Antarctic between 800-500 hPa and over ~20°S -20° N between 500-100 hPa, and decreases in N80 over 50°-90° N between 1000-750 hPa. The increase in sulfuric acid from DMS/SO_2 oxidation will boost particle formation and growth rates in relatively clean

regions, such as the Antarctic. There will also be a boost from condensed sulfate from aqueous oxidation of DMS, further increasing the sizes but not necessarily number concentration of larger particles. However, the PARAM_NoNuc_2xDMS case is very similar to the PARAM_NoNuc case (Table B2; Figs. B4 and B5) and again, we conclude that even if DMS emissions are globally increased by up to a factor of two, our general conclusions would not be changed about the effects of MSA towards the size distribution.

Table B1. Annual mean % changes at 900 hPa for the contribution of the sulfate and sulfuric acid from DMS/SO_2 oxidation for submicron aerosol mass, N3, N80, and radiative forcing changes in AIE and DRE for each DEFAULT_NoMSA emissions inventory. Positive values of a metric indicate that the sulfate and sulfuric acid increases that metric compared to a simulation with no DMS emissions.

Case	Submicron aerosol mass global (30-90 S) % change	N3 global (30-90 S) % change	N80 global (30-90 S) % change	AIE global (30-90 S) change in mW m^{-2}	DRE global (30-90 S) change in mW m^{-2}
DEFAULT_NoMSA - NoDMS_NoMSA	5.0 % (7.3 %)	7.3 % (19.5 %)	12.2 % (24.3 %)	-46 (-38)	-120 (-170)
DEFAULT_NoMSA_Lana - NoDMS	5.0 % (7.6 %)	7.0 % (19.4 %)	12.6 % (24.8 %)	-51 (-39)	-130 (-200)
DEFAULT_NoMSA_2xDMS - NoDMS	8.0 % (12.6 %)	7.5 % (22.9 %)	16.3% (35.4 %)	-92 (-130)	-220 (-330)

Table B2. Annual mean % changes at 900 hPa for the MSA for submicron aerosol mass, N3, N80, and radiative forcing changes in AIE and DRE for the PARAM_NoNuc simulations using each DEFAULT_NoMSA emissions inventory. Positive values of a metric indicate that MSA increases that metric compared to the DEFAULT_NoMSA case per emissions inventory.

Case	Submicron aerosol mass global (30-90 S) % change	N3 global (30-90 S) % change	N80 global (30-90 S) % change	AIE global (30-90 S) change in mW m^{-2}	DRE global (30-90 S) change in mW m^{-2}
PARAM_NoNuc - DEFAULT_NoMSA	0.7 % (1.3 %)	-3.9 % (-8.5 %)	0.8 % (1.7 %)	-8.6 (-17)	-15 (-26)
PARAM_NoNuc_Lana - DEFAULT_NoMSA_Lana	0.7 % (1.3%)	-3.5 % (-7.1 %)	0.8 % (1.7 %)	-7.8 (-14)	-16 (-28)
PARAM_NoNuc_2xDMS - DEFAULT_NoMSA_2xDMS	1.2 % (2.3 %)	-4.3 % (-7.7 %)	0.3 % (0.6 %)	-6 (-3.1)	-28 (-46)

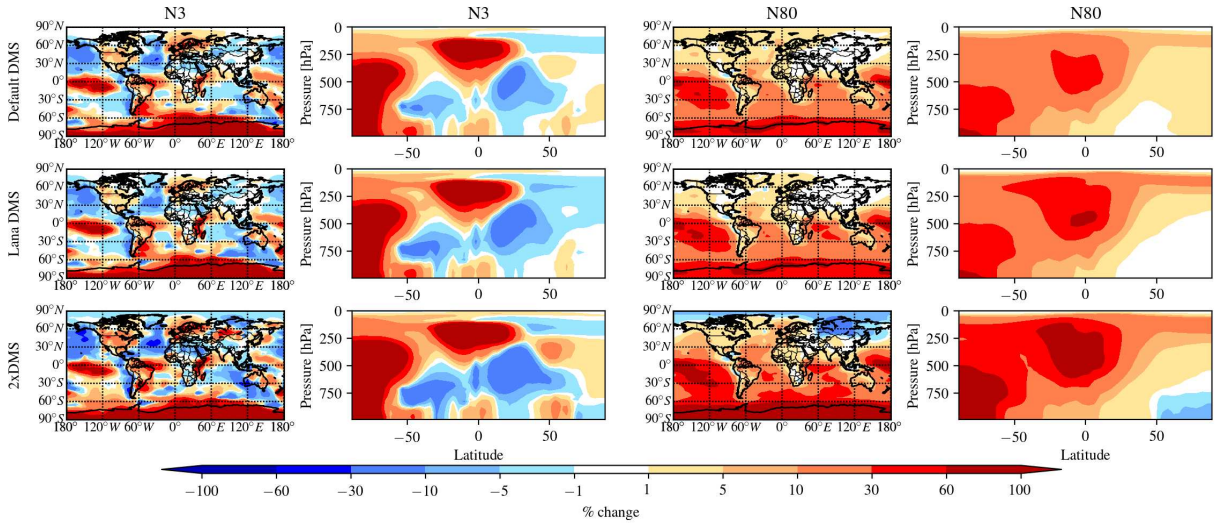

Figure B3. Global annual mean percent change at 900 hPa (first and third column) and global zonal annual mean percent change (second and fourth column) between NoDMS_NoMSA and the DEFAULT_NoMSA case (first row), the DEFAULT_NoMSA_Lana case (second row), and the DEFAULT_NoMSA_2xDMS case (third row). First and second column: N3 (the number concentration of particles with diameters larger than 3 nm). Third and fourth column: N80. Warm colors indicate that the inclusion of DMS/SO_2 oxidation products in the model increases N3/N80.

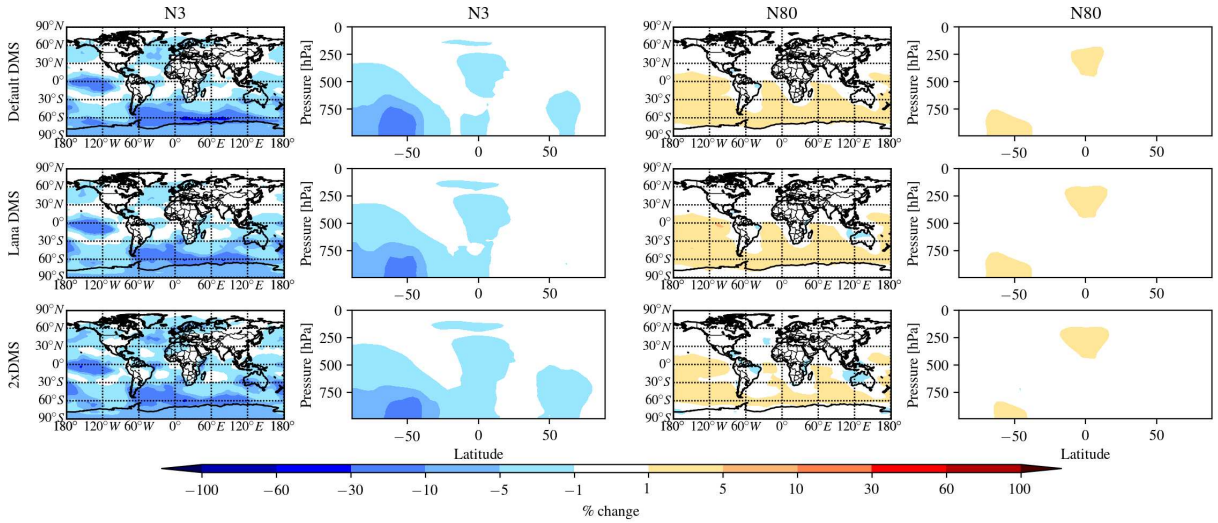

Figure B4. Global annual mean percent change at 900 hPa (first and third column) and global zonal annual mean percent change (second and fourth column) between the DEFAULT_NoMSA case and PARAM_NoNuc case (first row), the DEFAULT_NoMSA_Lana case and PARAM_NoNuc_Lana case (second row), and the DEFAULT_NoMSA_2xDMS case and PARAM_NoNuc_2xDMS case (third row). First and second column: N3 (the number concentration of particles with diameters larger than 3 nm). Third and fourth column: N80.

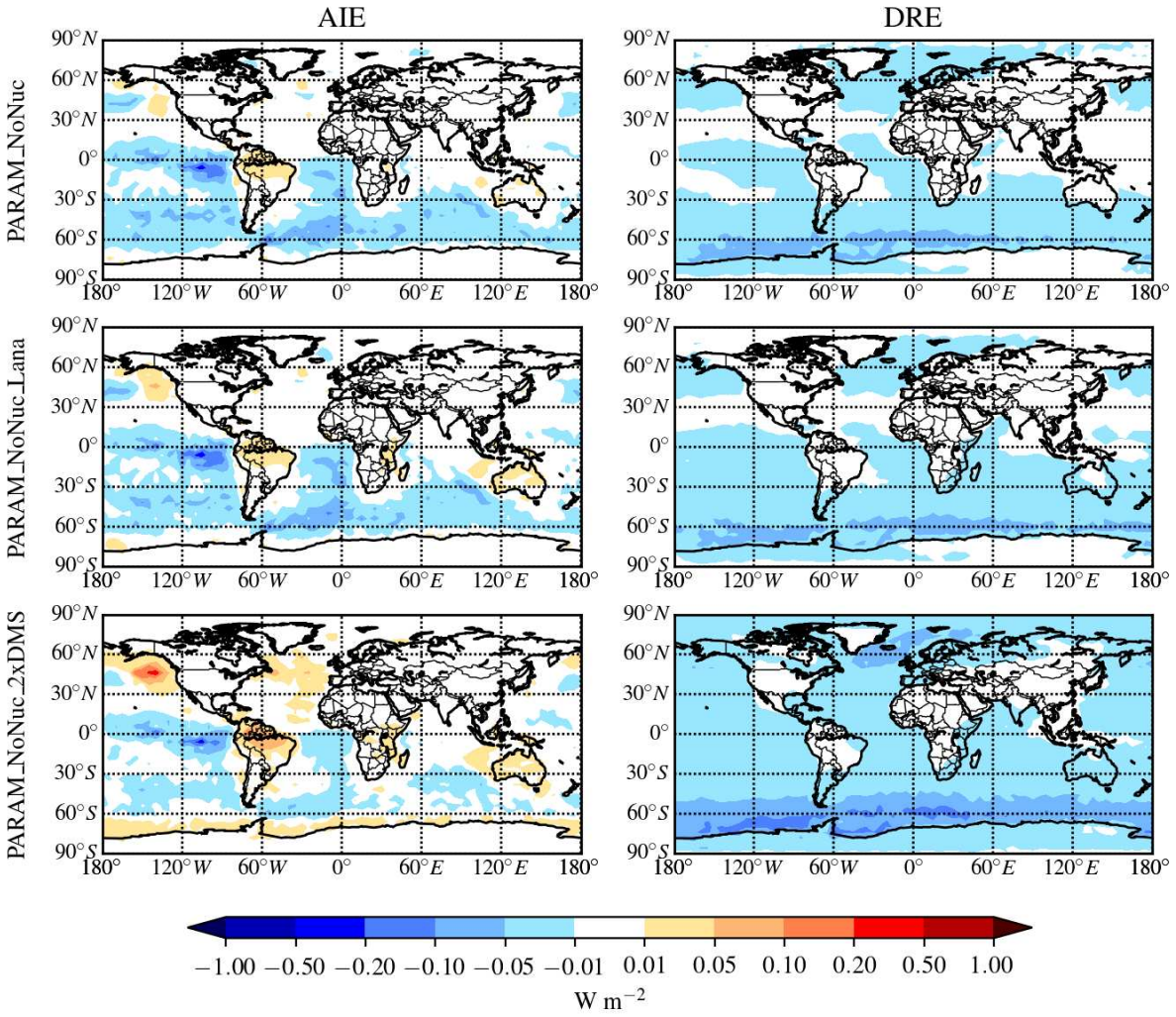

Figure B5. Global annual mean percent change for the AIE (first column) and DRE (second column) between the DEFAULT_NoMSA case and PARAM_NoNuc case (first row), the DEFAULT_NoMSA_Lana case and PARAM_NoNuc_Lana case (second row), and the DEFAULT_NoMSA_2xDMS case and PARAM_NoNuc_2xDMS case (third row).

B3. Global annual mean number concentrations for the DEFAULT_NoMSA case; additional results

Figure B6 provides the number concentrations (N3 and N80) at 900 hPa and zonally for the base case (DEFAULT_NoMSA). Table B3 provides the quantitative values for Fig. 3.6.

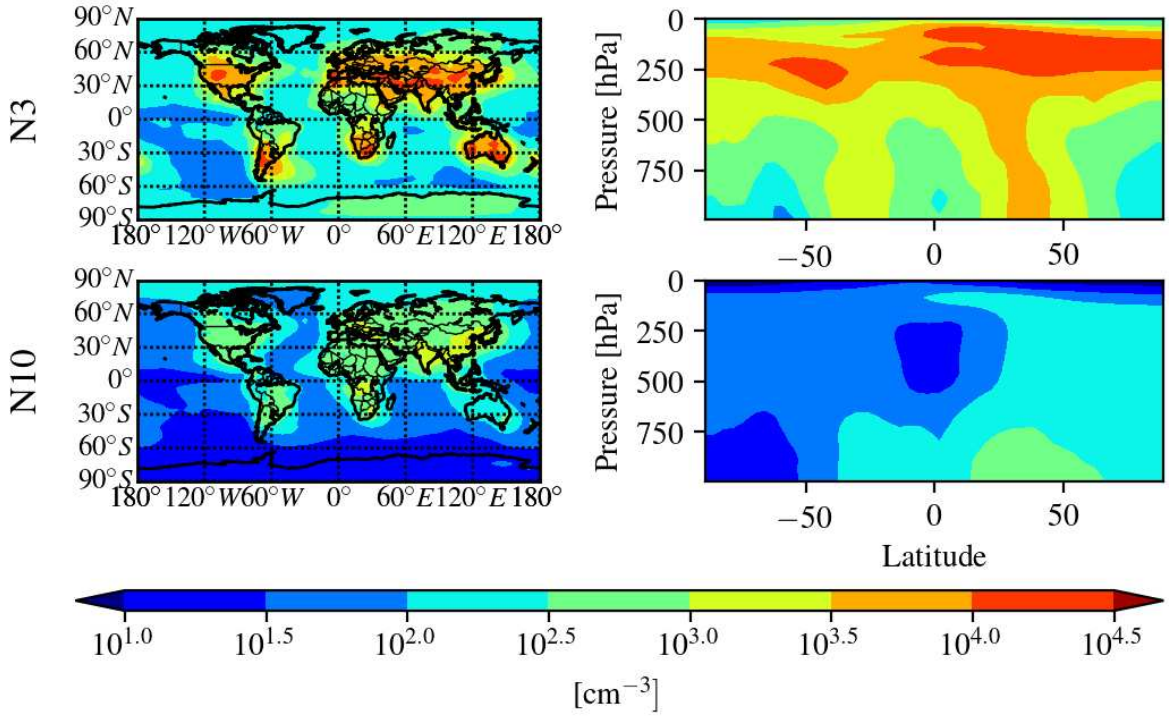

Figure B6. The number concentration (cm^{-3}) normalized to STP for the DEFAULT_NoMSA case. Top row: N3 at cloud level (900 hPa; right) and zonally (left). Bottom row: N80 for cloud level (900 hPa; right) and zonally (left).

Table B3. Annual mean % changes due to MSA at 900 hPa for each MSA simulation relative to the DEFAULT_NoMSA simulation for submicron aerosol mass, N3, N80, and radiative forcing changes in AIE and DRE. Positive values for any metric for PARAM_NoNuc, ELVOC_NoNuc, SVOC_NoNuc, PARAM_Nuc, and ELVOC_Nuc all indicate that the addition of MSA increases that metric relative to the DEFAULT_NoMSA simulation. The DEFAULT_NoMSA-NoDMS_NoMSA row shows the contribution of the sulfate and sulfuric acid from DMS/SO_2 oxidation present in the DEFAULT_NoMSA simulation; positive values of a metric indicate that the sulfate and sulfuric acid increases that metric compared to a simulation with no DMS emissions.

Case	Submicron aerosol mass global (30-90 S) % change	N3 global (30-90 S) % change	N80 global (30-90 S) % change	AIE global (30-90 S) change in mW m^{-2}	DRE global (30-90 S) change in mW m^{-2}
PARAM_NoNuc - DEFAULT_NoMSA	0.7 % (1.3 %)	-3.9 % (-8.5 %)	0.8 % (1.7 %)	-8.6 (-17)	-15 (-26.0)
ELVOC_NoNuc - DEFAULT_NoMSA	1.2 % (2.5%)	-8.9 % (-20.8 %)	9.1 % (22.2 %)	-75 (-150)	-20 (-34)
SVOC_NoNuc - DEFAULT_NoMSA	1.2 % (2.5 %)	-6.0 % (-12.6 %)	-0.2 % (-0.12 %)	7.5 (11)	-25 (-44)
PARAM_Nuc - DEFAULT_NoMSA	0.7 % (1.3 %)	112.5 % (309.9 %)	2.1 % (4.4 %)	-26 (-48)	-14 (-24)
ELVOC_Nuc - DEFAULT_NoMSA	1.2% (2.6%)	153.4 % (397.7 %)	23.8 % (56.3 %)	-180 (-390)	-13 (-20)
DEFAULT_NoMSA - NoDMS_NoMSA (indicates contribution from DMS/SO_2 oxidation)	5.0 % (7.3 %)	7.3 % (19.5 %)	12.2 % (24.3 %)	-46 (-38)	-120 (-170)

B4. ATom-1 and ATom-2 plots

The ATom-1 and ATom-2 campaigns took place during July 28-August 22, 2016, and January 26-February 22, 2017, respectively. Both campaigns took measurements from the Pacific and Atlantic Basin. Figures B7-B10 provide the 1:1 plots for each separate campaign and each separate ocean basin for the main MSA sensitivity cases in this study, PARAM_NoNuc, ELVOC_NoNuc, SVOC_NoNuc, PARAM_Nuc, and ELVOC_Nuc. Also shown are the 5:1 and 1:5 lines. Each subplot indicates the log mean bias (LMB), slope (m), and coefficient of determination (R^2) for each sensitivity case as compared to the measurements. Figures B11-B14 show the zonally averaged simulated MSA concentrations for each model level for each basin and campaign with the corresponding particle-phase MSA measurements overlaid. (The up and down patterns represent the flight tracks of the NASA DC-8 aircraft.)

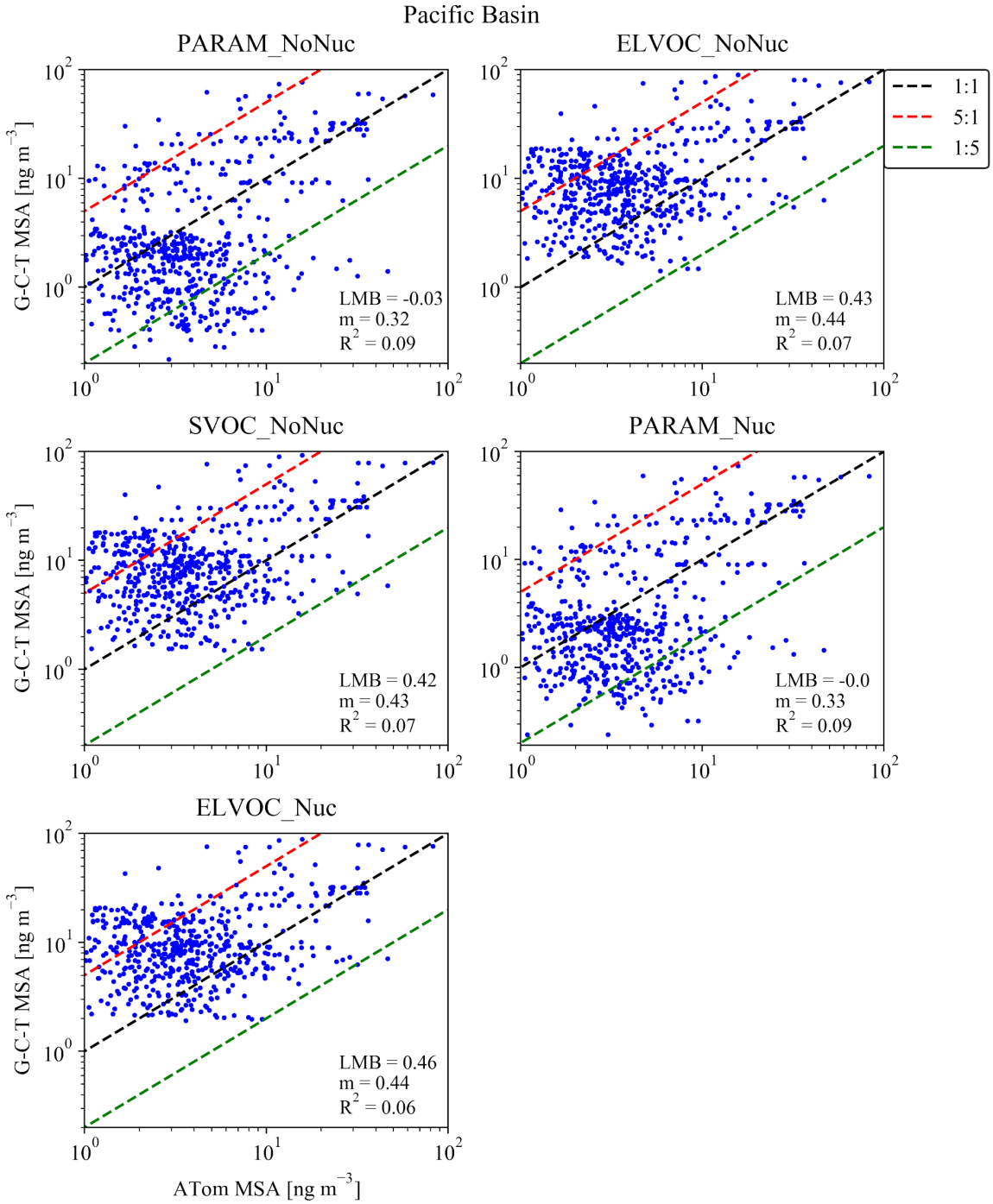

Figure B7. 1:1 (black dashed line) plots for the simulated mean MSA mass for the month of August and measured MSA mass during the ATom-1 campaign (July 28-August 22 2016) for the Pacific basin flight tracks, calculated log-mean bias (LMB), slope (*m*), and coefficient of determination (R^2). The red and green dashed lines indicate 5:1 and 1:5 lines. Simulated MSA mass is calculated by subtracting the total sulfate mass for the base case from each sensitivity case.

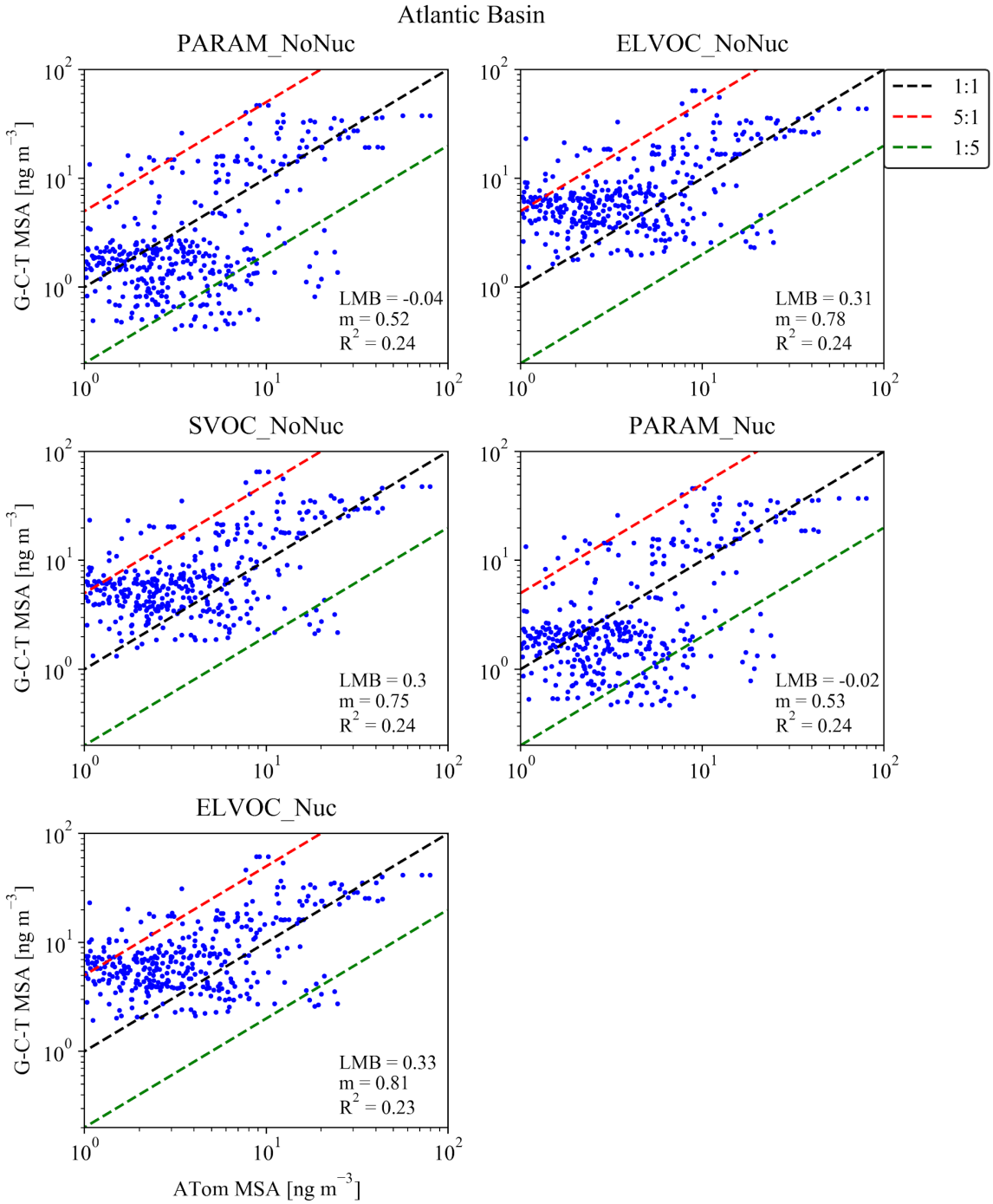

Figure B8. 1:1 (black dashed line) plots for the simulated mean MSA mass for the month of August and measured MSA mass during the ATom-1 campaign (July 28-August 22 2016) for the Atlantic basin flight tracks, calculated log-mean bias (LMB), slope (*m*), and coefficient of determination (R^2). The red and green dashed lines indicate 5:1 and 1:5 lines. Simulated MSA mass is calculated by subtracting the total sulfate mass for the base case from each sensitivity case.

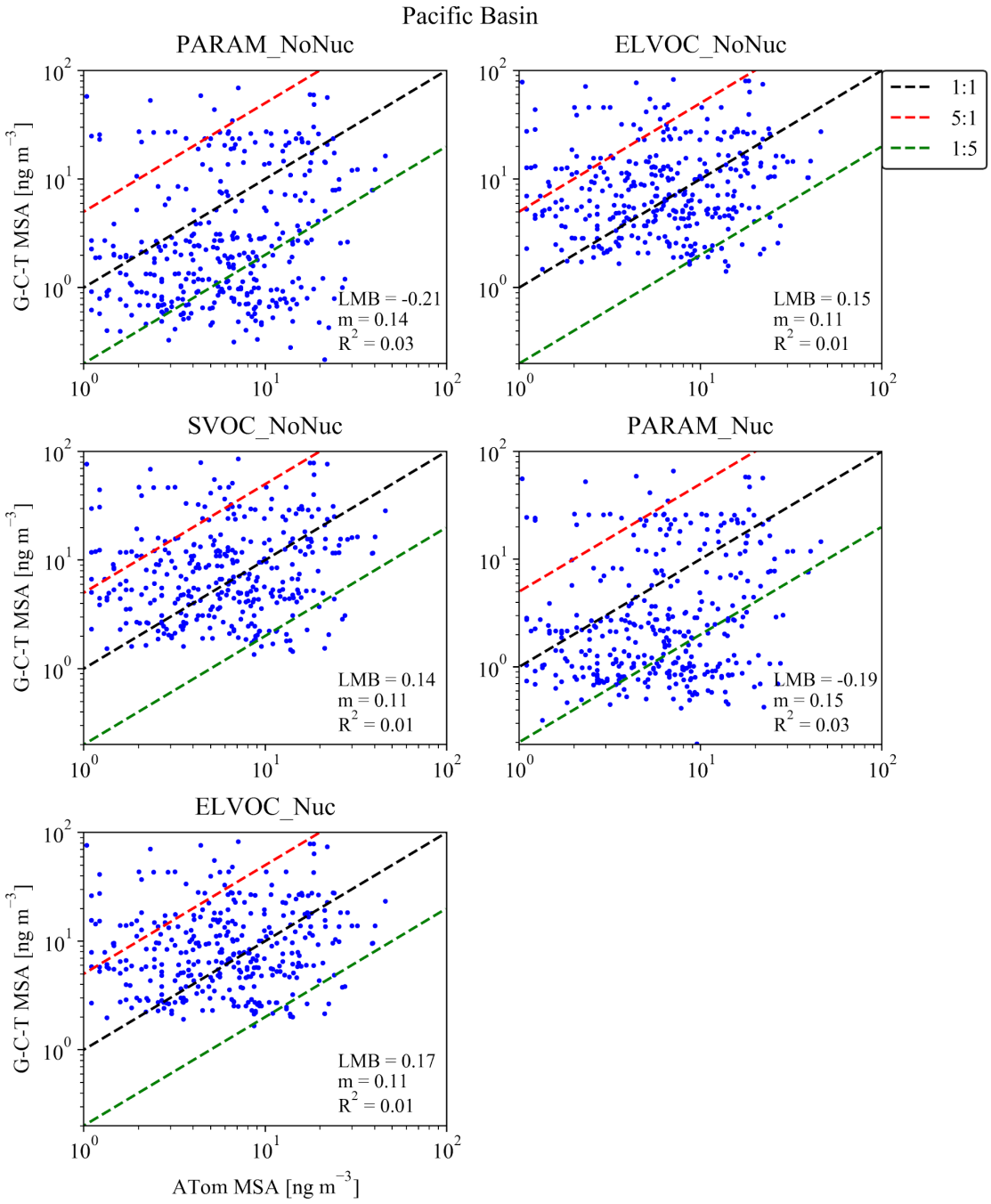

Figure B9. 1:1 (black dashed line) plots for the simulated mean MSA mass for the month of February and measured MSA mass during the ATom-2 campaign (January 26-February 22 2017) for the Pacific basin flight tracks, calculated log-mean bias (LMB), slope (*m*), and coefficient of determination (R^2). The red and green dashed lines indicate 5:1 and 1:5 lines. Simulated MSA mass is calculated by subtracting the total sulfate mass for the base case from each sensitivity case.

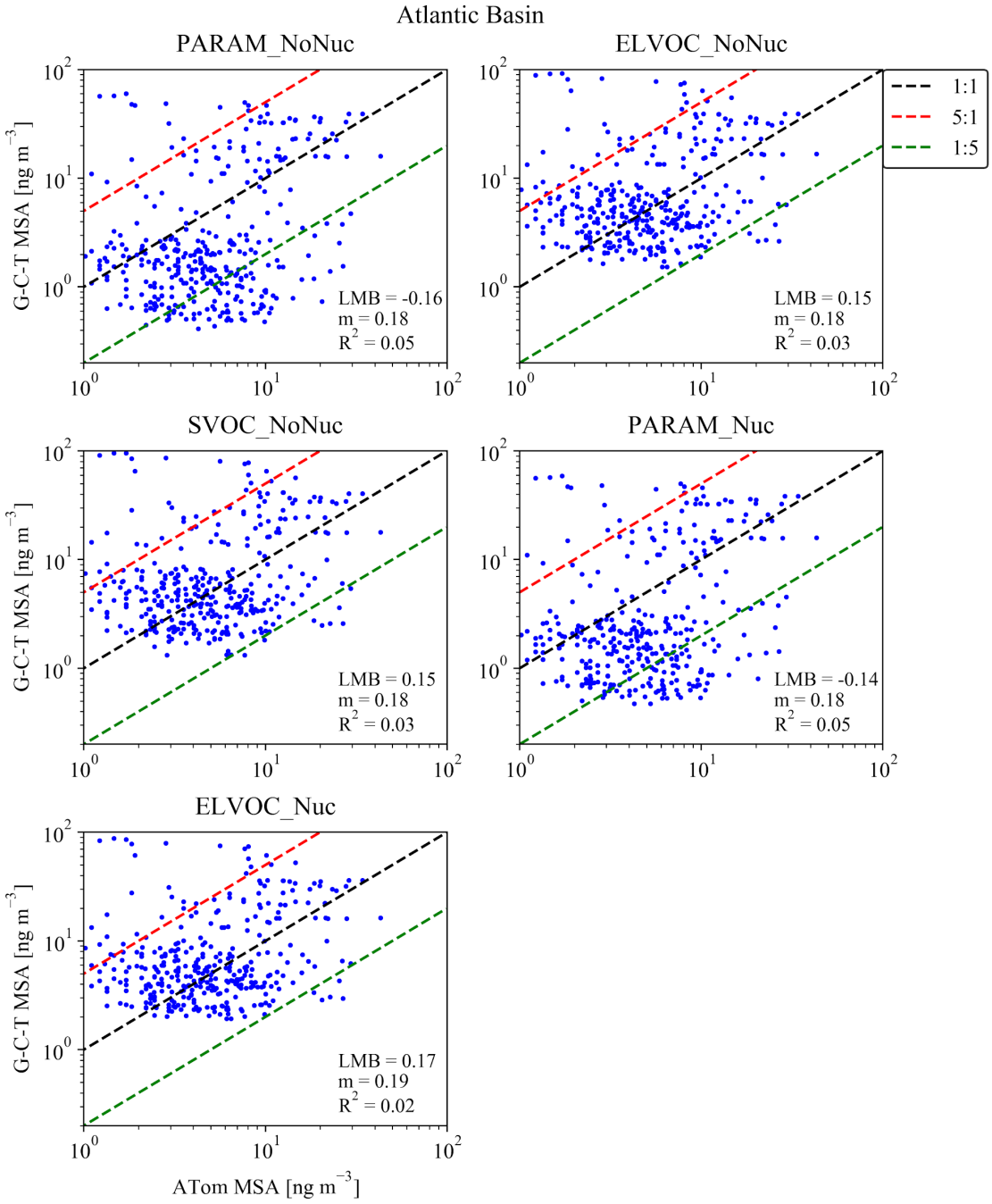

Figure B10. 1:1 (black dashed line) plots for the simulated mean MSA mass for the month of February and measured MSA mass during the ATom-2 campaign (January 26-February 22 2017) for the Atlantic basin flight tracks, calculated log-mean bias (LMB), slope (*m*), and coefficient of determination (R^2). The red and green dashed lines indicate 5:1 and 1:5 lines. Simulated MSA mass is calculated by subtracting the total sulfate mass for the base case from each sensitivity case.

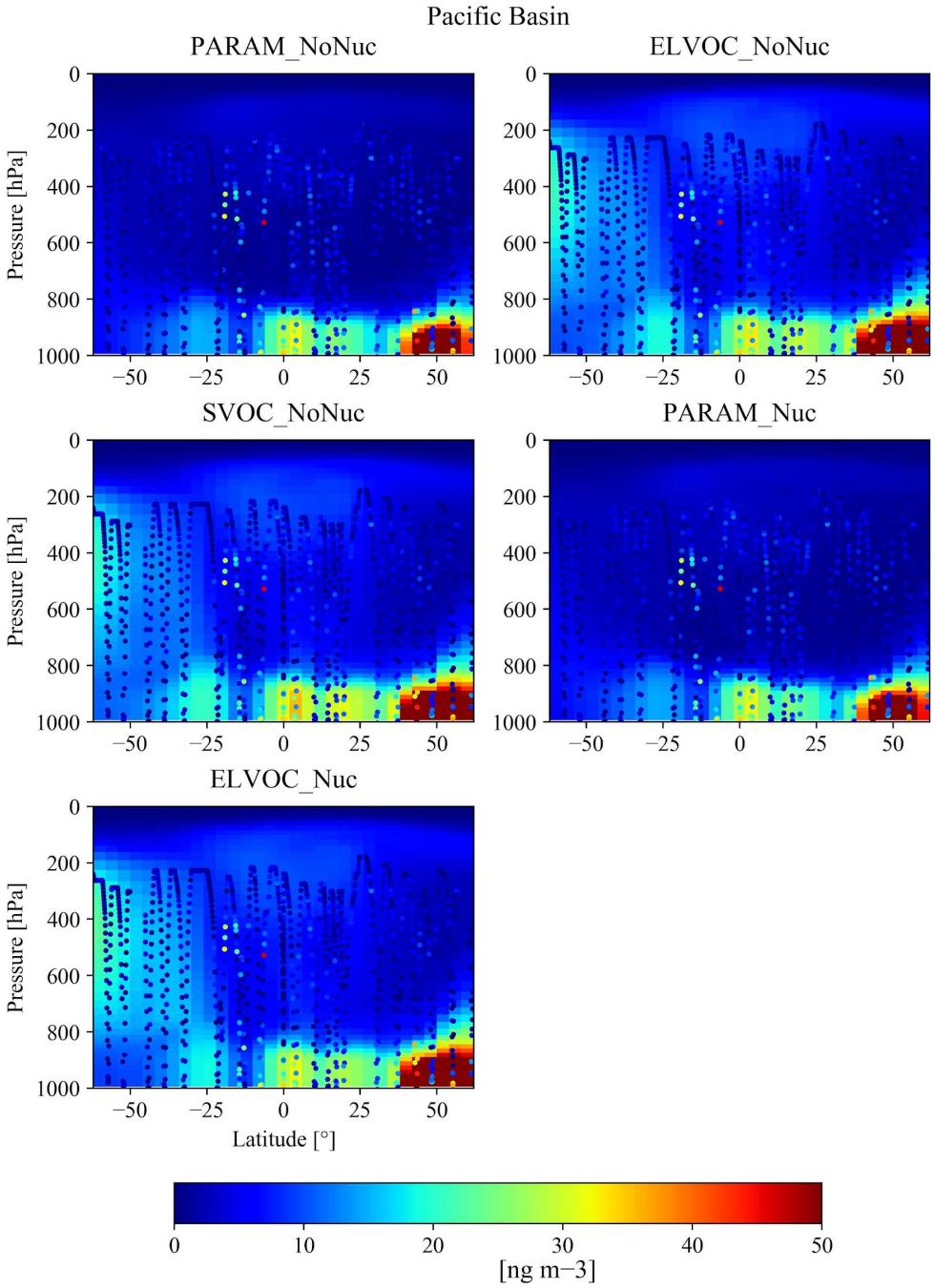

Figure B11. Comparison of simulated mean MSA mass for the month of August to measured MSA mass (circles) during the ATom-1 campaign (July 28-August 22 2016) for the Pacific basin flight tracks. Simulated MSA mass is calculated by subtracting the total sulfate mass for the base case from each sensitivity case.

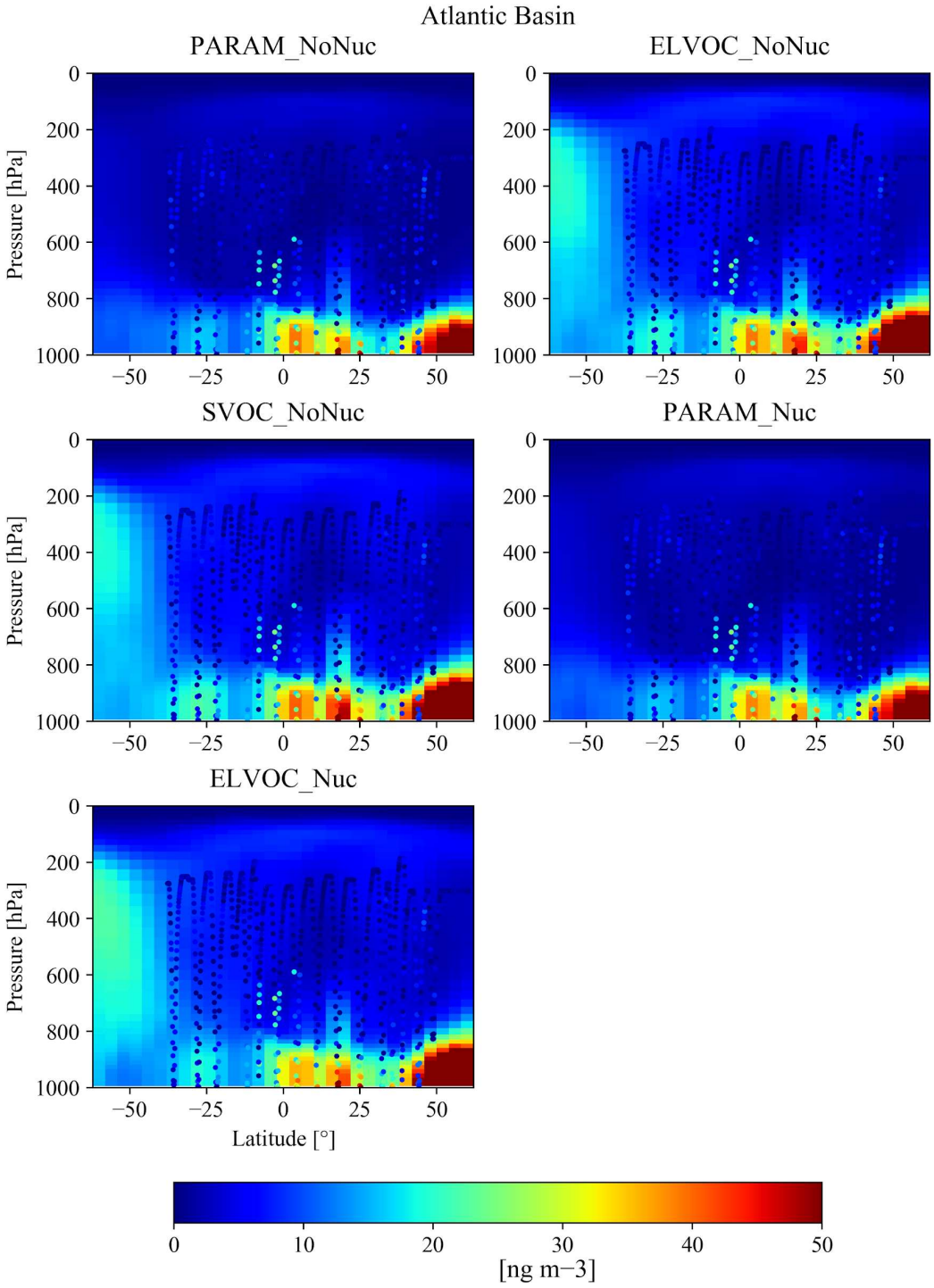

Figure B12. Comparison of simulated mean MSA mass for the month of August to measured MSA mass (circles) during the ATom-1 campaign (July 28-August 22 2016) for the Atlantic basin flight tracks. Simulated MSA mass is calculated by subtracting the total sulfate mass for the base case from each sensitivity case.

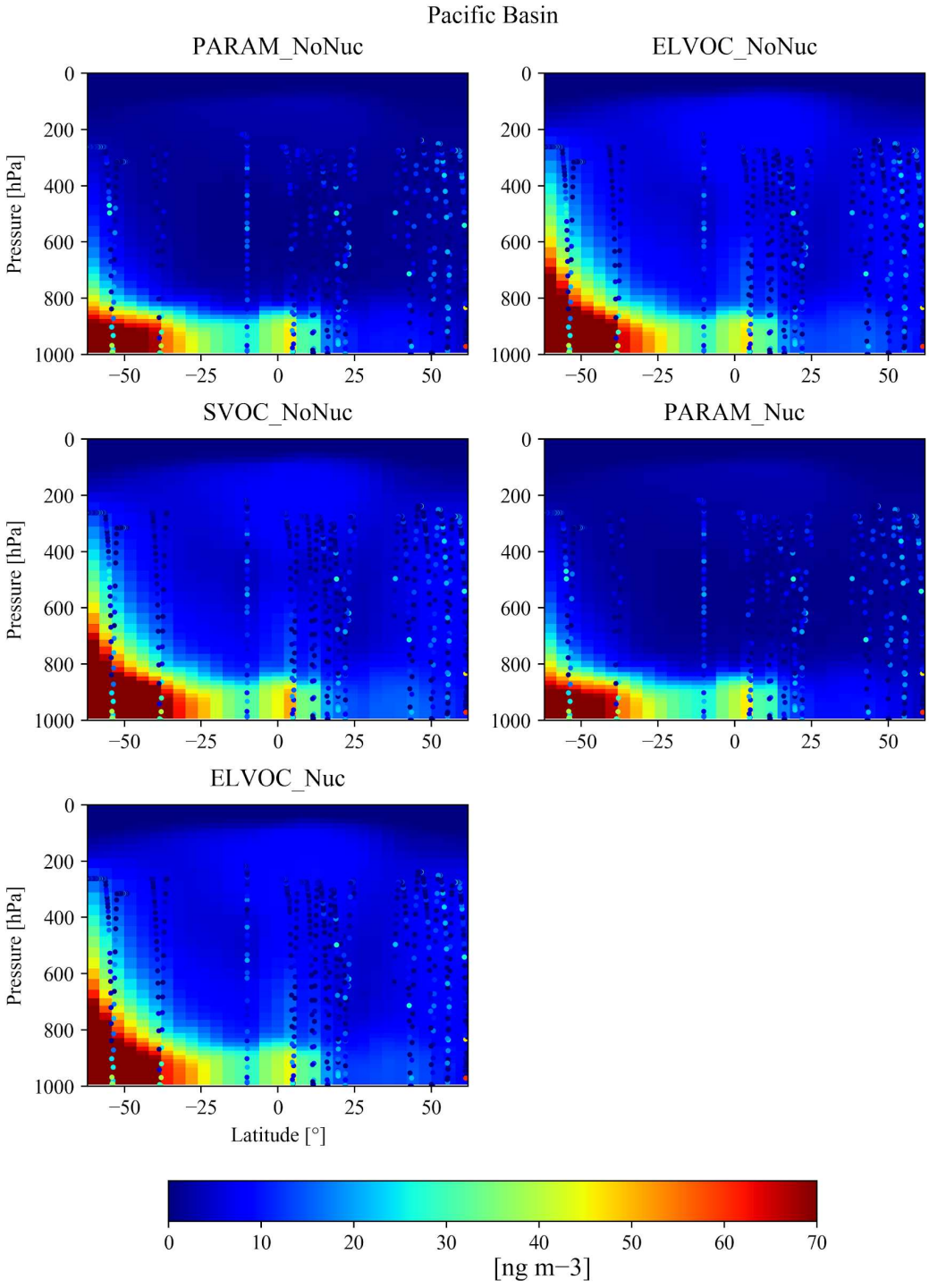

Figure B13. Comparison of simulated mean MSA mass for the month of February to measured MSA mass (circles) during the ATom-2 campaign (January 26-February 22 2017) for the Pacific basin flight tracks. Simulated MSA mass is calculated by subtracting the total sulfate mass for the base case from each sensitivity case.

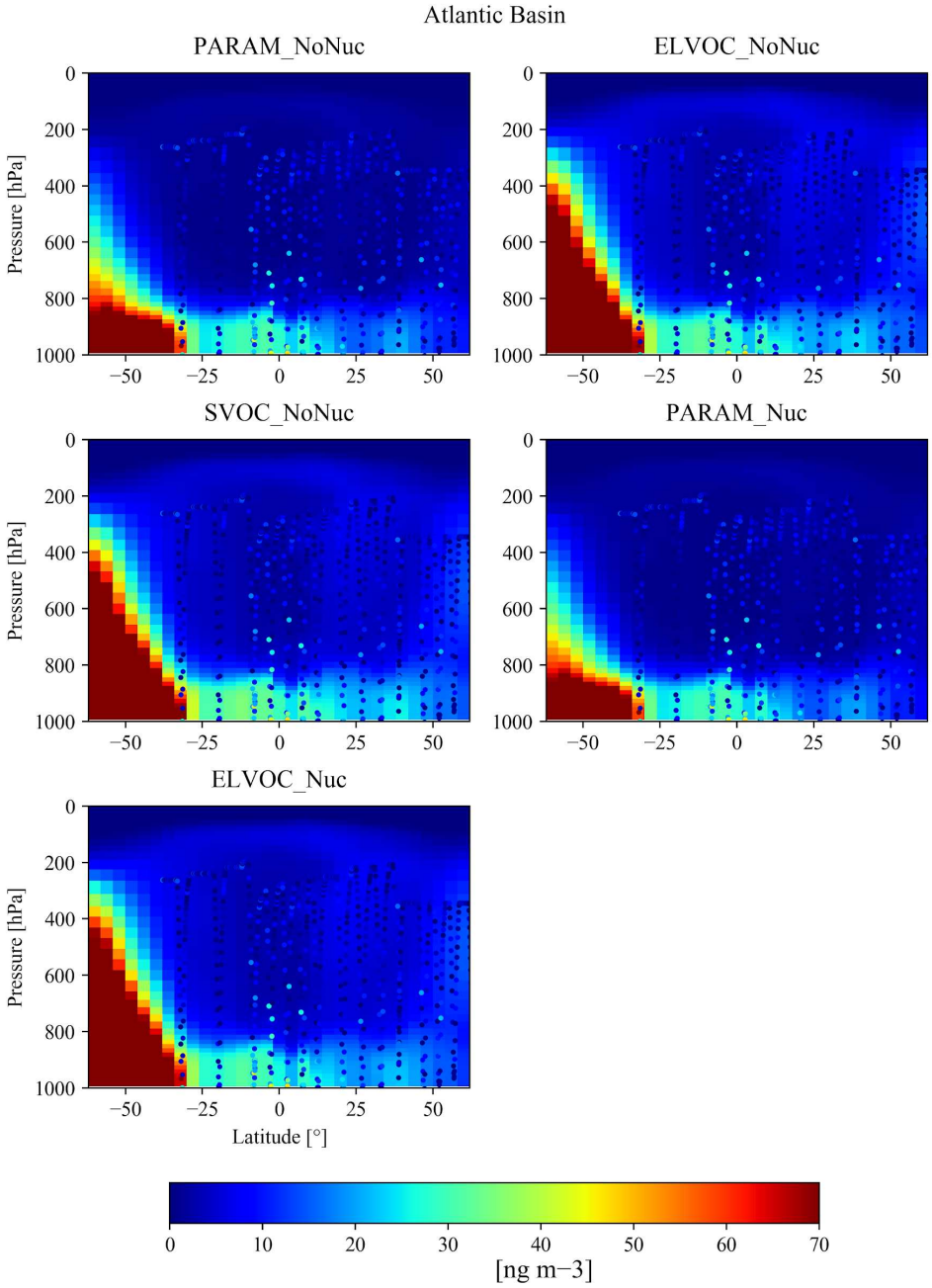

Figure B14. Comparison of simulated mean MSA mass for the month of February to measured MSA mass (circles) during the ATom-2 campaign (January 26-February 22 2017) for the Atlantic basin flight tracks. Simulated MSA mass is calculated by subtracting the total sulfate mass for the base case from each sensitivity case.

B5. MSA Calibration Details for the Aerosol Mass Spectrometer

B5.1. General Approach

As shown first by Phinney et al. (2006), $CH_3SO_2^+$ is a highly specific ion for the identification of MSA in AMS spectra. A number of groups have since used this ion as a calibrated marker for quantification of MSA. Other quantification approaches have also been used but they have often have proven less robust as discussed in Huang et al. (2017).

This quantification procedure requires the determination of two MSA specific quantities (Zorn et al., 2008, Huang et al., 2015, Willis et al., 2016, Huang et al., 2017):

- The ratio of the $CH_3SO_2^+$ ion to the total AMS signal from MSA, $f(CH_3SO_2)$, and
- The relative ionization efficiency of the total AMS response (ion current) from MSA relative to nitrate (the primary AMS calibrant), RIE_{MSA}. Once those quantities are known, the MSA concentration can be determined as follows (based on the general expression for calculating species concentrations in the AMS; Canagaratna et al., 2007):

$$[MSA] = \frac{C}{CE}\frac{MW_{MSA}}{IE_{MSA}}\Sigma I_{MSA} = \frac{C}{CE}\frac{MW_{NO3}}{RIE_{MSA}IE_{NO3}}\frac{I_{CH3SO2}}{f(CH_3SO_2)} \quad \text{(B1)}$$

In this equation I_{CH3SO2} refers to the signal of the marker ion (in ion counts, our measured variable), IE_{NO3} is the ionization efficiency of the instrument for nitrate, CE is the collection efficiency, MW_{MSA} and MW_{NO3} are the molar masses of MSA and nitrate, respectively, and C is a proportionality constant that includes the MS duty cycle, flow calibration, and unit conversions.

Both of these quantities were determined over a series of both laboratory and in-field calibrations (starting at the end of the ATom-1 deployment) by atomizing either pure dilute MSA solutions (Aldrich, >99.9% purity), or dilute solutions that were previously neutralized with excess aqueous ammonia (Aldrich, ACS reagent). The nebulizer output for the neutralized solutions (effectively $NH_4CH_3SO_3$, referred to as AMSA in the following) was size-selected with an SMPS

(TSI 3936) and the aerosol number concentration was recorded with a collocated CPC (TSI 3010). Due to the high amounts of ammonium (from the daily ammonium nitrate calibrations) present in our in-field calibration system, the nebulized pure MSA aerosol was introduced directly into the AMS to avoid neutralization in the SMPS. Hence, for acidic MSA, only the fragmentation pattern was investigated.

B5.2. Estimation of minor ion contributions

In order to account properly for the total ion signal of MSA, the contribution of some ions that had a high background was estimated by indirect means:

- The contribution of both water ions (O^+, HO^+, and H_2O^+, "familyHO" in AMS parlance) and CO_2^+ were obtained from unconstrained linear regressions, so they could be separated from the gas phase contributions. Since the AMS flying on ATom uses a cryopump for background reduction, the water background is low enough for this method to work (typically H_2O:N_2 ~ 0.1 for the background signals).
- The contribution of the sulfur ion (S^+) to the AMS signal was estimated based on the abundance of the (independently fitted) $^{34}S^+$ isotope at low MSA concentrations, and fitted directly at high concentrations (> 1 mg sm^{-3})
- The contribution of CO^+ to the AMS signal was estimated from fitting $C^{18}O^+$, but was found to be negligible at all times (<1%)

Figure B15a shows a typical regression of the different ion species for an AMSA calibration, while Figure B15b shows the contributions of the water, sulfur and CO_2^+ ions to the total signal for all calibrations. On average, the contribution of these ions to the total MSA signal are small (about 5% in total), in contrast to sulfate (discussed in B5.5).

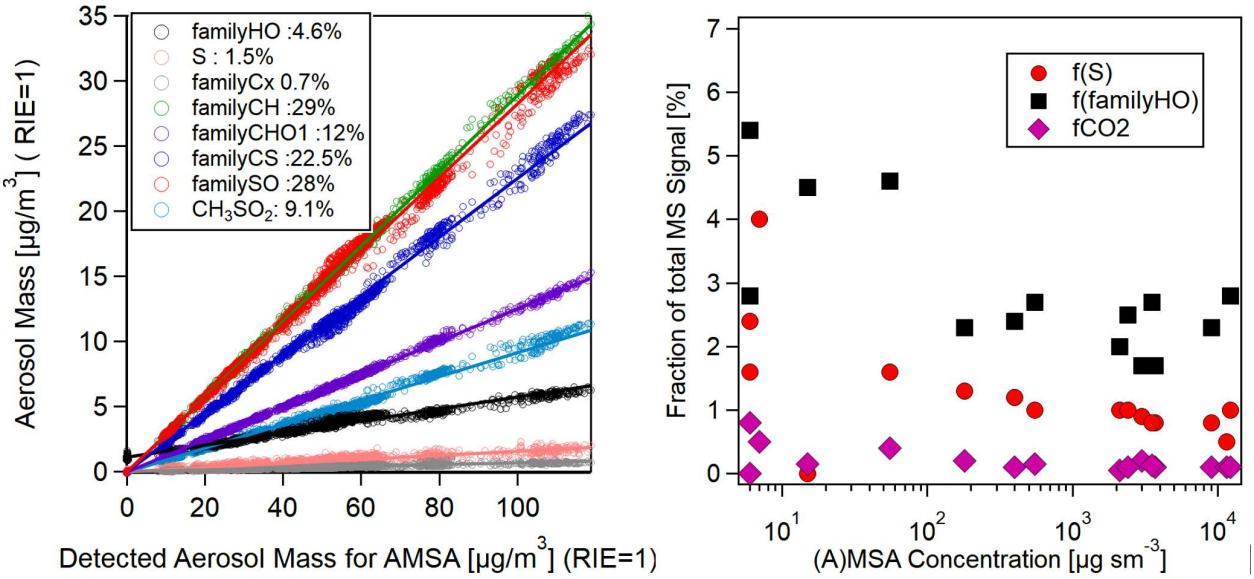

Figure B15. (left) Determination of the fractional ion contributions (summed up into chemical families) in the AMS (including water, sulfur and CO_2) of MSA for an AMSA calibration at intermediate concentrations ([MSA]~10-50 µg sm^{-3}, as determined by SMPS measurements). (right) Contributions of S^+, CO_2^+ and water ions to the total AMS signal of MSA for all the ATom calibrations (calibrations were done with both AMSA and MSA, but only MSA was quantified).

B5.3. Quantification of the Relative Ionization Efficiency of MSA (RIE_{MSA})

RIE_{MSA} was derived from two different approaches:

- Relative to the ammonium *RIE* (*RIE_{NH4}*) after back-to-back calibrations with ammonium nitrate ("ammonium balance method") analogous to the most-commonly used method for the determination of sulfate and chloride *RIE* (Schroder et al., 2018). This assumes that, as in the case of sulfate, the analyzed particles are fully neutralized when introduced into the AMS. In the case of another ammonium salt of an organic acid, ammonium oxalate, some studies have suggested partial evaporation of ammonia prior to analysis (Jimenez et al., 2016). Thermodynamic calculations suggest that this is due to the $H(COOH)_2^+$ being a weak acid (pK_a=4.19, Lide 2008), leading to some formation of molecular oxalic acid and subsequent partitioning of NH_3 to the gas phase, but not of oxalic acid given its much lower vapor pressure. Given that MSA is a strong acid

(pKa=-1.96 (Guthrie, 1978)), this is not expected for AMSA, and in fact no difference in these experiments was observed when the AMSA solution was saturated with NH_4OH (vs just neutralized). This method is independent of AMS transmission, collection efficiency and possible evaporation of the semivolatile AMSA prior to AMS sampling.

Determining the value of RIE_{MSA} that is needed for the AMS to match the aerosol mass calculated from simultaneous measurements by the SMPS/CPC ("mass closure method") (Willis et al., 2016; Huang et al., 2017). This requires generating a monodisperse aerosol with little to no doubly charged particles and knowledge of both the density and collection efficiency of AMSA. In addition, for a semivolatile species such as MSA (p_{vap}=6*10^{-4} Torr at 20^{o} C, Tang and Munkelwitz, 1991) there could be differences due to potential evaporation in the CPC and AMS lines, which would complicate the comparison. Both monodispersity and effective density (which was sometimes lower than the bulk density of 1.48 g cm^{-3}, Lide et al., 2008) were confirmed with particle time-of-flight measurements (PToF). Single particle measurements (described in detail below) confirmed that *CE* was close to 1 and that evaporation was a minor concern. Therefore a *CE* of 1 was used. Assuming negligible evaporation/wall deposition in the lines both methods should yield similar results.

Figure B16 shows data for 2 AMSA calibrations at low concentrations taken one year apart where the RIE_{MSA} for both methods agreed within 5% and the corresponding PToF measurements. We hence report RIE_{MSA} = 1.70 ± 0.08 based on the more accurate ammonium balance method, while using the difference with the mass closure method as a conservative uncertainty estimate. This RIE_{MSA} was used for the all four ATom deployments, given the small change (<5%) in the other RIEs of the instrument over these campaigns.

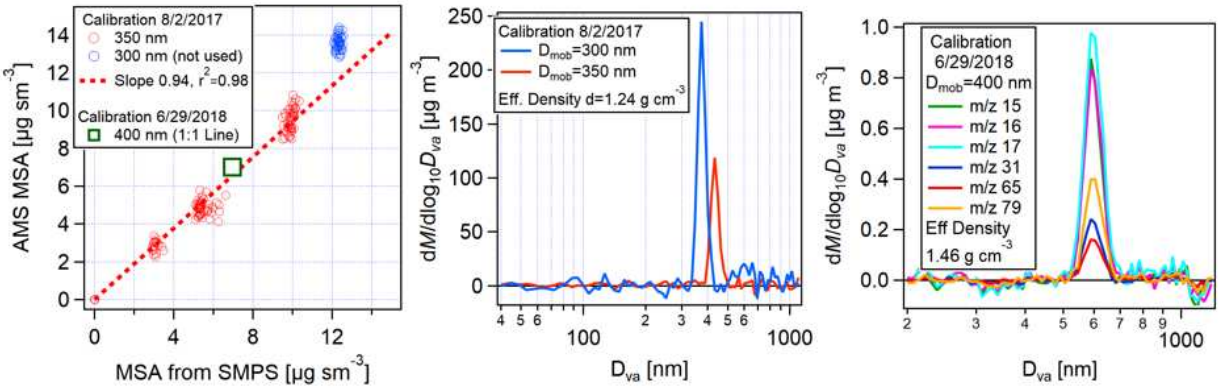

Figure B16. (left) Regression of the AMS response for MSA with the calculated SPMS mass of the test aerosol for two different calibrations of the CU AMS instrument using $NH_4SO_3CH_3$ (AMSA) taken one year apart. AMS response was calculated using f(CH_3SO_2) from the calibration and an RIE_{MSA} derived from the ion balance (1.7 on 8/2/2017, 1.72 on 6/29/2018); the SPMS mass was calculated using the density determined from the D_{va}/D_{geo} ratio for each calibration (DeCarlo et al., 2004). (middle) Particle time-of-flight size distribution of the test aerosol for the 8/2/2017 calibration, used to determine the density and confirm monodispersity. (right) AMS PToF-mode size distribution for the 6/29/2018 calibration, showing the same m/z ions that were used in the analysis of the single particle experiments (Figure B19).

B5.4. Robustness of the MSA Mass Spectral Pattern in the AMS

Zorn et al. (2008) reported that the fragmentation pattern of MSA was highly dependent on vaporizer temperature. Special care was taken during ATom to keep the vaporizer temperature constant at ~600°C by keeping the vaporizer current constant and periodically calibrating the instrument response with $NaNO_3$ (Hu et al, 2017). The MSA fragmentation pattern at low concentrations (comparable and larger than ambient concentrations) was observed to be very stable over the course of the four ATom deployments.

However, significant changes in $f(CH_3SO_2)$ were observed when higher calibration particle concentrations were used (Figure B17a). Figure B17b shows the variability in time of the main ion families that contribute to the MSA signal for a typical AMSA calibration at higher concentrations. While NH_4 shows an very fast and stable response, for MSA a fraction of the signal shows a slower time response after each background cycle (which some ion groups showing this trend stronger

than others; this will be discussed in more detail in Section S5.7). The rate of equilibration is concentration dependent, hence at higher concentrations not only do the relative ion ratios change, but also the overall signal recorded by the AMS, resulting in larger apparent values of RIE_{MSA} at higher concentrations. This effect only appears to be important at very high concentrations of 100s to 1000s of μg m^{-3}, but we document it here since calibrations are often performed at such higher concentrations. Based on these results, we recommend calibrating at concentrations similar to ambient levels.

It is important to note that the magnitude of this effect is very dependent on the acquisition cycle of the AMS: For the CU-AMS, which operates in "fast mode" (6 s closed, 46 s open, Schroder et al., 2018), the time available for MSA reaching some of sort of equilibrium in the ionizer is substantially longer than in the standard AMS acquisition sequence (4 s closed, 6 s open). Hence RIE_{MSA} taken at similar concentrations in the standard AMS acquisition mode may be lower than the values that we reported above. However, it is also possible that the slower response if more important in the CU AMS instrument, as the presence of a cryopump surface cooled to 90 K around the ionizer region will lower the equilibrium temperature of the ionizer, compared to standard AMS instruments. Since at least some of the slow response may be due to particles or gases deposited on the ionizer surfaces, this lower temperature could play a role in the observed slow response.

We are unaware of previous reports on this concentration dependent change in fragmentation pattern, although most of them calibrated over a small range of concentrations (Willis et al., 2016, Huang et al., 2017). It is worth noting that Huang et al. (2015) reports a value of 0.10±0.02 for f(CH_3SO_2), and their error bar does suggest variability on a similar scale as we found for unspecified reasons.

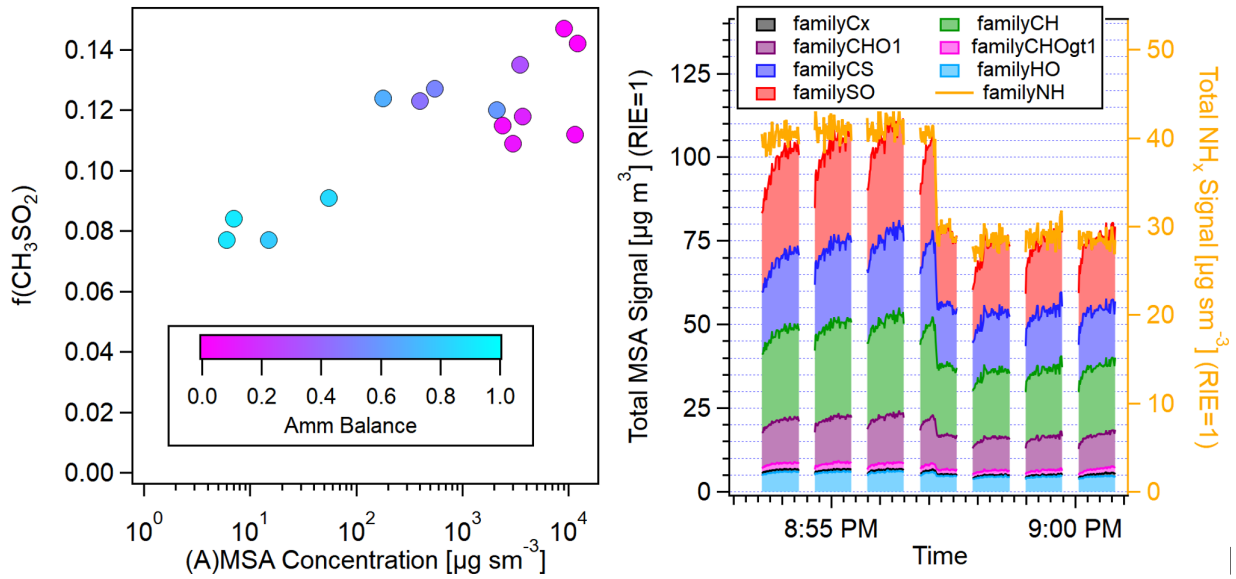

Figure B17. (left) Summary of all the marker ratios found in ATom calibrations as a function of MSA concentration, both using AMSA (excluding ammonium) and MSA. (right) Timeseries of the total ion signal (classified into AMS families) of MSA and NH_4 (both at RIE of 1) for a an AMSA calibration with 50 µg sm-3 of MSA, showing that for each acquisition cycle for some subset of the ions (mostly SOX and CS) there is an equilibration time which depends on concentration and that is not observed for NH_4. This results in a time-dependent response that is especially pronounced at higher concentrations and hence affects both f(CH_3SO_2) and RIE_{MSA} (relative to RIE_{NH4}).

Since all the calibration with acidic MSA in our study were done at high concentrations, this could result in a potential uncertainty in the AMS fragmentation pattern of MSA (vs AMSA) and a potential bias in quantifying MSA in some of the highly acidic environments found in ATom. In order to further address this potential source of uncertainty for the ambient data, the data from the ATom-1 deployment was analyzed by positive matrix factorization (PMF) (Paatero 1994, Ulbrich et al., 2009) to extract a (calibration independent) MSA mass spectral profile. This was done by combining the organic and sulfate ions from the full mission at 1 min resolution (for improved fitting accuracy and detection limits, see Schroder et al., 2018) and performing PMF analysis with the PMF Evaluation Panel (PET) v3.01 (Ulbrich et al., 2009). Best results were achieved after downweighting the SO_x ions by 10x to make their weight in the weighted residual

comparable to those of the larger organic ions. Figure B18a and b compares the spectra of the MSA factor obtained with the MS Spectra from the low concentration AMSA calibrations, showing excellent agreement for all ions except CH_3^+ (which is less specific than most other ions in the spectrum, since it can arise from a myriad of other OA species). Importantly, f(CH_3SO_2) in both cases is nearly identical (7.9% for the PMF factor vs 7.8% for the calibrations), confirming the validity of the low-concentration calibrations and also their applicability for ATom-1 (where no in-field calibrations for MSA were conducted).

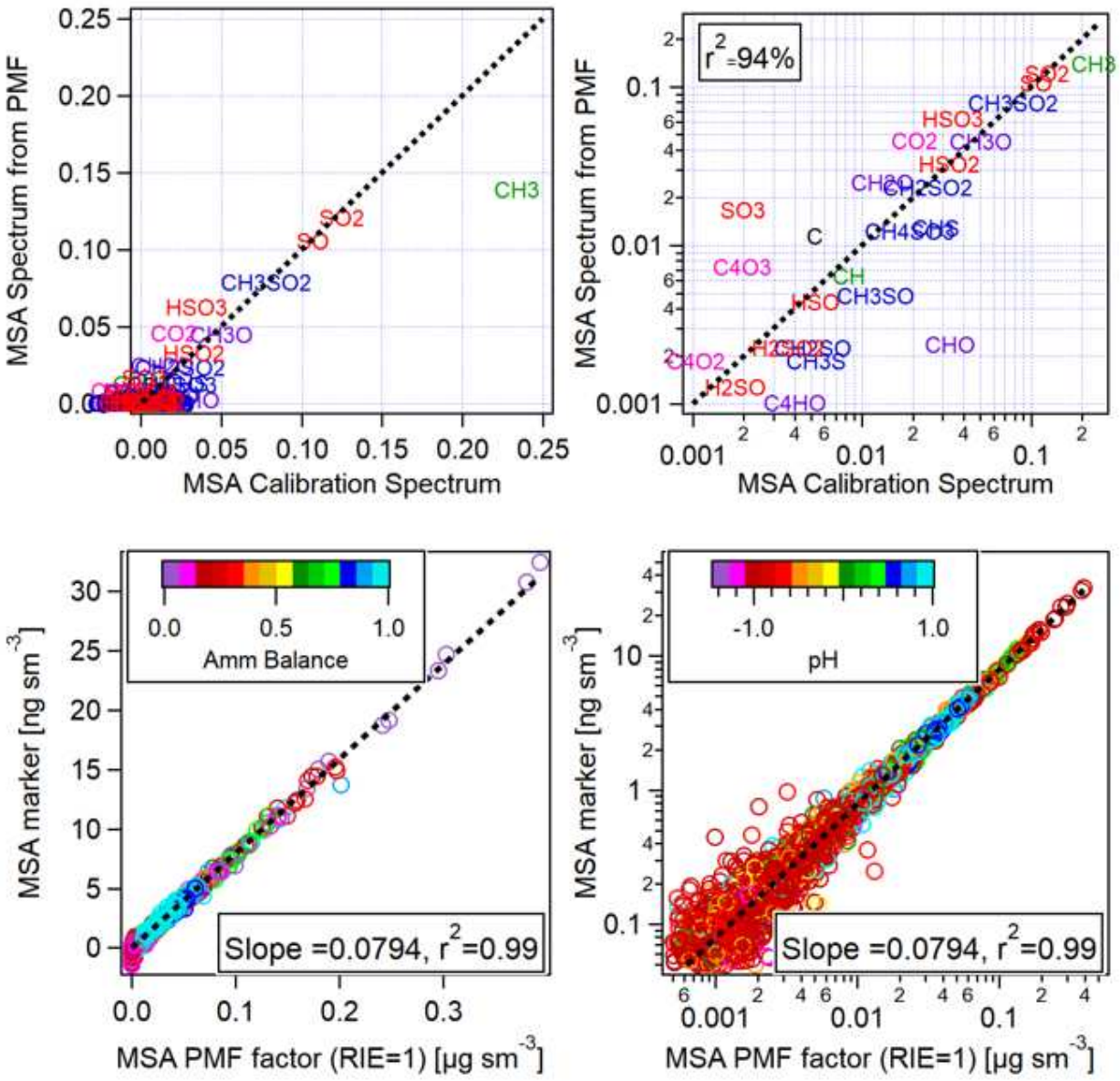

Figure B18. (top) Comparison of the MSA Factor extracted from PMF analysis of the full sulfate+OA dataset during ATom-1 with the calibration spectrum of $NH_4SO_3CH_3$ (AMSA) taken at low concentrations, (a) on a linear scale and (b) on a logarithmic scale . (bottom) Scatter plot of the total signal for the $CH_3SO_2^+$ ion for the ATom-1 campaign vs. the MSA PMF Factor concentration (c) on a linear scale and (d) on a logarithmic scale as a function of acidity. The very highly correlated behavior independent of acidity suggests that for ambient data f(CH_3SO_2) does not significantly change as a function of acidity.

However, the mass spectrum of the PMF Factor is a campaign average that is primarily weighted towards the often not-so-acidic marine boundary layer passes where the factor

concentration was highest. To examine if MSA found under acidic conditions (mostly in the free troposphere) could have a different fragmentation pattern, it is instructive to look at the correlation of the $CH_3SO_2^+$ ion with the PMF factor. If pure MSA had a different $f(CH_3SO_2)$ than AMSA, this would lead to a deviation from the 7.9% slope line prescribed by PMF. However, despite the very high acidities that were sometimes encountered while sampling MSA (pH<0), no significant deviation from linear behavior is observed over several orders of magnitude (Figure B18c and d). We hence conclude that there is no evidence for $f(CH_3SO_2)$ being a function of MSA acidity, and that even if the relative fractions of other ions were to change slightly as a function of acidity, quantification of MSA based on Eq. B1 should not be affected.

Hence, with a value of $f(CH_3SO_2)$ of 0.08±0.003 (average of low concentration calibrations and PMF factor), the combined inverse scaling factor of MSA relative to the CH_3SO_2 ion for ATom is 0.136±0.011, i.e. a combined multiplicative factor of 7.35 to translate $[CH_3SO_2^+]$ (in nitrate-equivalent concentration units; Jimenez et al., 2003) to [MSA] per Eq. B1 (referred in the following as the scaling factor, $S(CH_3SO_2)$).

$$S(CH_3SO_2) = \frac{1}{RIE(MSA)*f(CH_3SO_2)} \quad \text{B2}$$

B5.5 Comparison with previous studies

Table B4 summarizes all the studies where to the best of our knowledge both the marker fraction and the RIE for total MSA signal have been reported. It should be noted that only Willis et al. (2016) and Huang et al. (2017) directly measured RIE_{MSA}. In both cases, the mass closure method was used with reportedly pure, acidic MSA (although some neutralization was observed prior to analysis). While the linearity of their calibrations strongly suggests that doubly charged particles were not sampled, as noted above the shorter acquisition sequence might have resulted in

a smaller RIE_{MSA}, depending on the fraction of slower response in their instruments. In addition, evaporation and neutralization would still be a concern that could possibly lead to a potentially reduced RIE_{MSA}. Phinney et al. (2006) used RIE_{SO4}, while Schmale et al. (2013) used RIE_{OA} (consistent with their determination of MSA by PMF of OA, which also likely explains the low value of $f(CH_3SO_2)$). Both Huang et al. (2015) and Zorn et al .(2008) used an averaged RIE of OA and sulfate (in Zorn's case an arithmetic average, in Huang's case a mass-weighted one).

Table B4: RIE_{MSA}, as well as the relative abundance of the marker ion $f(CH_3SO_2)$ in previously reported calibrations of AMS response to MSA. Also listed is the effective scaling factor that results from these two quantities, $S(CH_3SO_2)$.

$f(CH_3SO_2)$, %	RIE_{MSA}	$S(CH_3SO_2)$	Reference
6.9	1.15	12.6	Phinney et al, 2006 (Q-AMS)
9	1.3	8.6	Zorn et al, 2008
4	1.4	17.9	Schmale et al, 2013 (PMF)
9.7	1.3	8	Huang et al, 2015
12.4	1.33	6.1	Willis et al, 2016
4	1.27	19.7	Huang et al, 2017
7.9	1.70 ± 0.08	7.4	This work

While all reported values for RIE_{MSA} are lower than the one determined in this work, part of this difference may be due to instrument-to-instrument variability. It is worth noting that RIE_{SO4} in the CU AMS (determined by in-situ calibrations) is often significantly higher than the default RIE_{SO4} used by the other groups (1.5-1.7 vs 1.15-1.2) (Canagaratna et al., 2007), which might be

due to a higher general sensitivity in this instrument for larger ions as well as the longer acquisition cycle compared to a regular AMS. However, this may not imply that RIE_{MSA} and RIE_{SO4} should be comparable for a given AMS. Sulfate mass in the AMS (based on the default fragmentation table, Allan et al., 2004) includes a large contribution of water (31%) and sulfur (7%) ions, significantly larger than what was found in this study for MSA (5% total).

Given the high variability in the determinations of $f(CH_3SO_2)$ it would be hence preferable to compare the scaling factor $S(CH_3SO_2)$ used to actually relate CH_3SO_2 to MSA (Table B4), but given that as already discussed, most studies did not directly measure RIE_{MSA}, the variability of this parameter is also quite large. The fact that even in the cases where both RIE_{MSA} and $f(CH_3SO_2)$ were determined (Willis et al., 2016; Huang et al., 2017 and this work) the variability is $S(CH_3SO_2)$ is over a factor of 3 emphasizes the instrumental variability and the need for careful calibrations of both RIE_{MSA} and $f(CH_3SO_2)$ in studies where MSA from AMS data is reported.

B5.6 Details of the Single Particle Calibrations, including CE of pure MSA

Previous AMS studies on MSA have often assumed that due to acidity and phase, MSA should have a collection efficiency (CE, Middlebrook et al, 2012) of 1 (i.e. that pure particles do not bounce off the vaporizer), but this has not been confirmed previously. It is also not clear if the same applies for the semivolatile, yet non-acidic and solid at room temperature AMSA. Hence the CE of AMSA was determined using the single particle method (Canagaratna et al, 2007) using the Event Trigger acquisition mode of the AMS DAQ software.

Both monodisperse 400 nm ammonium nitrate (AN in the following, Aldrich, >99%) and AMSA particles were introduced into the AMS and detected by triggering on *m/z* 30 and 46 (NO^+ and NO_2^+) for AN and *m/z* 15 and 79 for AMSA (CH_3^++NH^+ and $CH_3SO_2^+$) (Figure B19). For the fast evaporating AN, we found that the AMS detected 89% of the particles compared to a

collocated CPC, consistent with the inlet transmission close to 100% efficient observed for this instrument (Schroder et al, 2018). For the AMSA particles that have a similar effective density (1.48 g cm^{-3} for AMSA vs 1.42 g cm^{-3} for AN) and hence should be transmitted at the same rate, we found a ratio of AMS single particle detection to CPC of 93%, hence confirming that for AMSA, CE~1.

Despite the fast vaporization and detection of (nearly) every single particle, the MS spectrum recorded in single particle mode (Figure B19, 200 μs integration time) and ePToF mode (14 ms integration time) show significant differences when compared to the regular (ambient) MS mode (FMS, 1 s integration time, Kimmel et al, 2011). Most of the SO_x^+ ions (and CH_3^+) have lower relative intensities at the shorter integration times, suggesting that these are released on longer timescales from the vaporizer. This different response times and hence, equilibration times for different components of the spectrum are likely also responsible for the spectral changes observed when varying the concentration of MSA over large ranges (Figure B16). For ambient data acquired during the ATom mission, this is clearly not a concern, as shown by the PMF analysis, but this effect could impact laboratory studies involving MSA and AMS detection via the marker method.

B5.7 ATom Data status

As detailed in the headers of the currently posted data (Wofsy et al., 2018), currently some fraction of the MSA mass is attributed to sulfate and some to OA. While these errors are typically small, future revisions will incorporate a correction to those species based on the quantification of MSA detailed above.

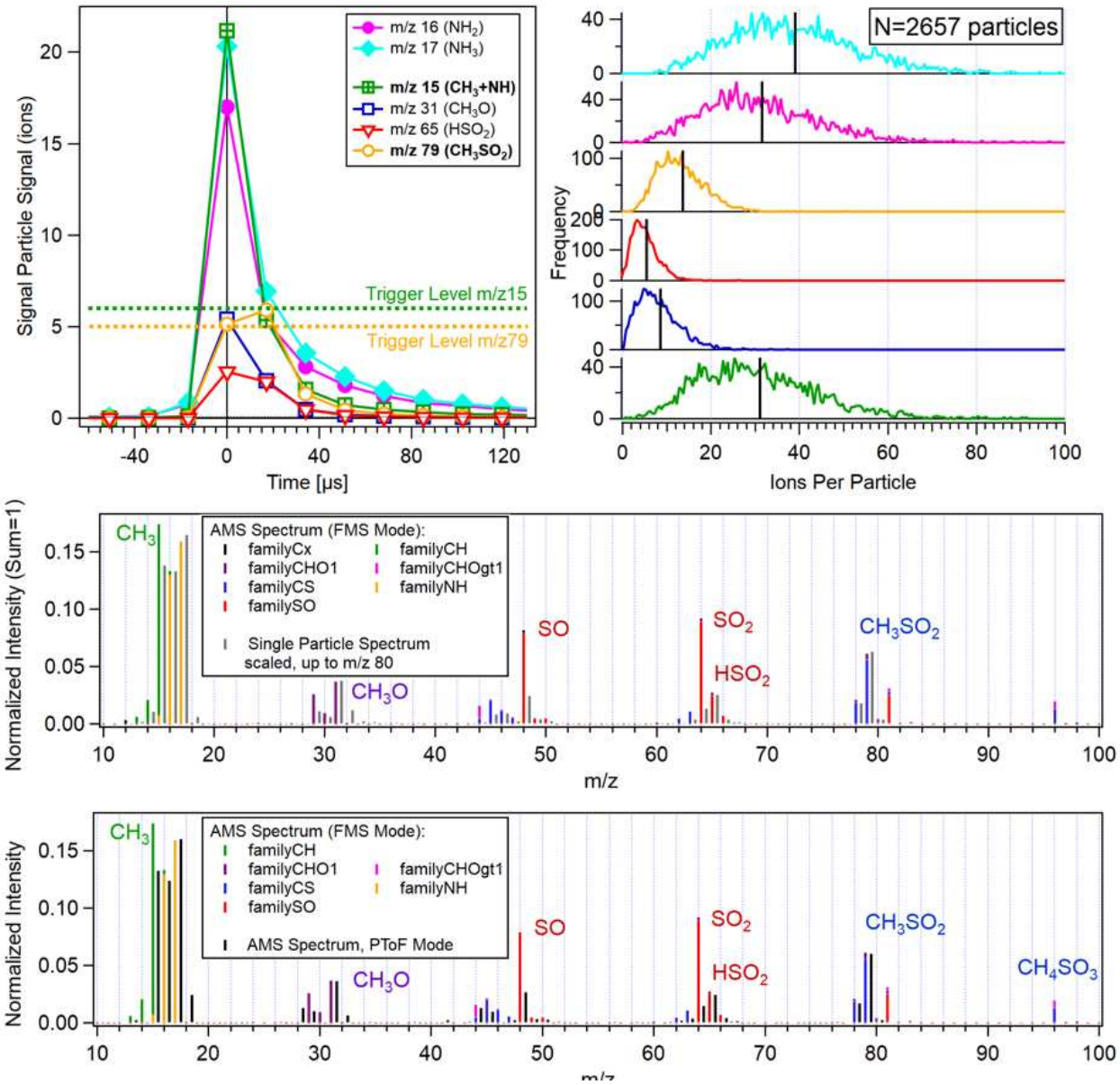

Figure B19. (top left) Average timetraces of the single particle signals at several mass to charge ratios for both the cation (NH_4) and anion (CH_3SO_3) recorded for 400 nm $NH_4CH_3SO_3$ particles being sampled into the AMS in ET mode. To trigger the single particle acquisition, either of the UMR m/z in bold (m/z 15 and 79) had to cross the prescribe threshold (dotted lines). (Right) Histograms of the total ions per particle recorded for each UMR m/z mass (2657 total events). Black lines show the average values used in the IE calculations. (middle) Comparison of the immediate vaporization MS observed in the single particle experiments with the calibration spectrum taken in regular acquisition mode (FMS). (bottom) Comparison of the immediate vaporization MS observed in PToF mode with the calibration spectrum taken in FMS mode.

REFERENCES

Allan, J. D., Delia, A. E., Coe, H., Bower, K. N., Alfarra, M. R. R., Jimenez, J. L., Middlebrook, A. M., Drewnick, F., Onasch, T. B., Canagaratna, M. R., Jayne, J. T. and Worsnop, D. R.: A generalised method for the extraction of chemically resolved mass spectra from Aerodyne aerosol mass spectrometer data, J. Aerosol Sci., 35(7), 909–922, doi:10.1016/j.jaerosci.2004.02.007, 2004.

Canagaratna, M. R., Jayne, J. T. J. T., Jimenez, J. L., Allan, J. D., Alfarra, M. R., Zhang, Q. Q., Onasch, T. B., Drewnick, F., Coe, H., Middlebrook, A. M., Delia, A., Williams, L. R., Trimborn, A. M., Northway, M. J., DeCarlo, P. F., Kolb, C. E., Davidovits, P. and Worsnop, D. R.: Chemical and microphysical characterization of ambient aerosols with the Aerodyne Aerosol Mass Spectrometer, Mass Spectrom. Rev., 26(2), 185–222, doi:10.1002/mas, 2007

Peter F. DeCarlo, Jay G. Slowik, Douglas R. Worsnop, Paul Davidovits & Jose L. Jimenez (2004) Particle Morphology and Density Characterization by Combined Mobility and Aerodynamic Diameter Measurements. Part 1: Theory, Aerosol Science and Technology, 38:12, 1185-1205, DOI: 10.1080/027868290903907

Guthrie, J.P.:Hydrolysis of esters of oxy acids: pKa values for strong acids; Brønsted relationship for attack of water at methyl; free energies of hydrolysis of esters of oxy acids; and a linear relationship between free energy of hydrolysis and pKa holding over a range of 20 pK units, Can. J. Chem., 56:2342-2354, 1978

Hu, W., Campuzano-Jost, P., Day, D. A., Croteau, P., Canagaratna, M. R., Jayne, J. T., Worsnop, D. R. and Jimenez, J. L.: Evaluation of the new capture vapourizer for aerosol mass

spectrometers (AMS) through laboratory studies of inorganic species, Atmos. Meas. Tech., 10(6), 2897–2921, doi:10.5194/amt-10-2897-2017, 2017.

Huang, D. D., Li, Y. J., Lee, B.P and Chan, C. K.: Analysis of Organic Sulfur Compounds in Atmospheric Aerosols at the HKUST Supersite in Hong Kong Using HR-ToF-AMS. Environ. Sci. Tech. 49 (6), 3672-3679 2015

Huang, S., Poulain, L., van Pinxteren, D., van Pinxteren, M., Wu, Z., Herrmann, H. and Wiedensohler, A.: Latitudinal and Seasonal Distribution of Particulate MSA over the Atlantic using a Validated Quantification Method with HR-ToF-AMS, Environ. Sci. Technol., 51(1), 418–426, doi:10.1021/acs.est.6b03186, 2017.

Jimenez, J. L., Canagaratna, M. R., Drewnick, F., Allan, J. D., Alfarra, M. R., Middlebrook, A. M., Slowik, J. G., Zhang, Q., Coe, H., Jayne, J. T., Worsnop, D. R., Rami Alfarra, M., Middlebrook, A. M., Slowik, J. G., Zhang, Q., Coe, H., Jayne, J. T. and Worsnop, D. R.: Comment on "The effects of molecular weight and thermal decomposition on the sensitivity of a thermal desorption aerosol mass spectrometer," Aerosol Sci. Technol., 50(9), i–xv, doi:10.1080/02786826.2016.1205728, 2016.

Kimmel, J. R., Farmer, D. K., Cubison, M. J., Sueper, D., Tanner, C., Nemitz, E., Worsnop, D. R., Gonin, M. and Jimenez, J. L.: Real-time aerosol mass spectrometry with millisecond resolution, Int. J. Mass Spectrom., 303(1), 15–26, doi:10.1016/j.ijms.2010.12.004, 2011.

Lide, D.R. CRC Handbook of Chemistry and Physics 88TH Edition 2007-2008. CRC Press, Taylor & Francis, Boca Raton, FL 2007, p. 3-326

Middlebrook, A. M., Bahreini, R., Jimenez, J. L. and Canagaratna, M. R.: Evaluation of Composition-Dependent Collection Efficiencies for the Aerodyne Aerosol Mass

Spectrometer using Field Data, Aerosol Sci. Technol., 46(3), 258–271, doi:10.1080/02786826.2011.620041, 2012.

Paatero, P. and Tapper, U.: Positive Matrix Factorization - A Nonnegative Factor Model With Optimal Utilization of Error-Estimates of Data Values, Environmetrics, 5(2), 111–126, 1994.

Phinney, L., Richard Leaitch, W., Lohmann, U., Boudries, H., Worsnop, D. R., Jayne, J. T., Toom-Sauntry, D., Wadleigh, M., Sharma, S., Shantz, N., Leaitch, W. R., Lohmann, U., Boudries, H., Worsnop, D. R., Jayne, J. T., Toom-Sauntry, D., Wadleigh, M., Sharma, S., Shantz, N., Richard Leaitch, W., Lohmann, U., Boudries, H., Worsnop, D. R., Jayne, J. T., Toom-Sauntry, D., Wadleigh, M., Sharma, S., Shantz, N., Leaitch, W. R., Lohmann, U., Boudries, H., Worsnop, D. R., Jayne, J. T., Toom-Sauntry, D., Wadleigh, M., Sharma, S. and Shantz, N.: Characterization of the aerosol over the sub-arctic north east Pacific Ocean, Deep. Res. II-Topical Stud. Oceanogr., 53(20–22), 2410–2433, doi:10.1016/j.dsr2.2006.05.044|ISSN 0967-0645, 2006.

Schmale, J., Schneider, J., Nemitz, E., Tang, Y. S., Dragosits, U., Blackall, T. D., Trathan, P. N., Phillips, G. J., Sutton, M. and Braban, C. F.: Sub-Antarctic marine aerosol: dominant contributions from biogenic sources, Atmos. Chem. Phys., 13(17), 8669–8694, doi:10.5194/acp-13-8669-2013, 2013.

Schroder, J. C., Campuzano-Jost, P., Day, D. A., Shah, V., Larson, K., Sommers, J. M., Sullivan, A. P. Campos, T. Reeves, J. M. Hills, A., Hornbrook, R. S., Blake, N. J., Scheuer, E., Guo, H., Fibiger, D. L. McDuffie, E. E., Hayes, P. L., Weber, R. J., Dibb, J. E. Apel, E. C., Jaeglé, L. Brown, S. S. Thornton, J. A. and Jimenez, J. L. Sources and secondary

production of organic aerosols in the northeastern United States during WINTER. Journal of Geophysical Research: Atmospheres, 123, 7771–7796. 2018

Tang, I. N. and Munkelwitz, H. R.: Determination of Vapor Pressure from Droplet Evaporation Kinetics, Journal of Colloid and Interface Science, 141, (1), 1991

Ulbrich, I. M., Canagaratna, M. R., Zhang, Q., Worsnop, D. R. and Jimenez, J. L.: Interpretation of organic components from Positive Matrix Factorization of aerosol mass spectrometric data, Atmos. Chem. Phys., 9(9), 2891–2918, doi:10.5194/acp-9-2891-2009, 2009.

Willis, M. D., Burkart, J., Thomas, J. L., Köllner, F., Schneider, J., Bozem, H., Hoor, P. M., Aliabadi, A. A., Schulz, H., Herber, A. B., Leaitch, W. R. and Abbatt, J. P. D.: Growth of nucleation mode particles in the summertime Arctic: a case study, Atmos. Chem. Phys., 16(12), 7663–7679, doi:10.5194/acp-16-7663-2016, 2016.

Wofsy, S.C., S. Afshar, H.M. Allen, E. Apel, E.C. Asher, B. Barletta, J. Bent, H. Bian, B.C. Biggs, D.R. Blake, N. Blake, I. Bourgeois, C.A. Brock, W.H. Brune, J.W. Budney, T.P. Bui, A. Butler, P. Campuzano-Jost, C.S. Chang, M. Chin, R. Commane, G. Correa, J.D. Crounse, P. D. Cullis, B.C. Daube, D.A. Day, J.M. Dean-Day, J.E. Dibb, J.P. DiGangi, G.S. Diskin, M. Dollner, J.W. Elkins, F. Erdesz, A.M. Fiore, C.M. Flynn, K. Froyd, D.W. Gesler, S.R. Hall, T.F. Hanisco, R.A. Hannun, A.J. Hills, E.J. Hintsa, A. Hoffman, R.S. Hornbrook, L.G. Huey, S. Hughes, J.L. Jimenez, B.J. Johnson, J.M. Katich, R. Keeling, M.J. Kim, A. Kupc, L.R. Lait, J.-F. Lamarque, J. Liu, K. McKain, R.J. Mclaughlin, S. Meinardi, D.O. Miller, S.A. Montzka, F.L. Moore, E.J. Morgan, D.M. Murphy, L.T. Murray, B.A. Nault, J.A. Neuman, P.A. Newman, J.M. Nicely, X. Pan, W. Paplawsky, J. Peischl, M.J. Prather, D.J. Price, E. Ray, J.M. Reeves, M. Richardson, A.W. Rollins, K.H. Rosenlof, T.B. Ryerson, E. Scheuer, G.P. Schill, J.C. Schroder, J.P. Schwarz, J.M. St.Clair, S.D. Steenrod,

B.B. Stephens, S.A. Strode, C. Sweeney, D. Tanner, A.P. Teng, A.B. Thames, C.R. Thompson, K. Ullmann, P.R. Veres, N. Vieznor, N.L. Wagner, A. Watt, R. Weber, B. Weinzierl, P. Wennberg, C.J. Williamson, J.C. Wilson, G.M. Wolfe, C.T. Woods, and L.H. Zeng. 2018. ATom: Merged Atmospheric Chemistry, Trace Gases, and Aerosols. ORNL DAAC, Oak Ridge, Tennessee, USA. https://doi.org/10.3334/ORNLDAAC/1581

Zorn, S. R., Drewnick, F., Schott, M., Hoffmann, T. and Borrmann, S.: Characterization of the South Atlantic marine boundary layer aerosol using an aerodyne aerosol mass spectrometer, Atmos. Chem. Phys., 8(16), 4711–4728, doi:10.5194/acp-8-4711-2008, 2008.

APPENDIX C

SUPPLEMENT TO AGING EFFECTS ON BIOMASS BURNING AEROSOL MASS AND COMPOSITION: A CRITICAL REVIEW OF FIELD AND LABORATORY STUDIES

C1. Additional field campaign information

All studies in Figure 4.1A provide ΔOA/ΔCO from Aerosol Mass Spectrometer (AMS) instruments except the SAFARI observations detailed in Hobbs et al. (2003) and the Vakkari et al. (2014, 2018) studies. Hobbs et al. (2003) provided total excess particulate matter (ΔTPM) divided by ΔCO, as measured by Teflon filters. Although Hobbs et al. (2003) determined a net decrease in PM_{ER} to 0.5 after 0.65 hours of physical (actual) aging for SAFARI, Alvarado and Prinn (2009) provided an alternative analysis to the SAFARI observations that indicated that the initial reported mass was likely biased high. We use the Alvarado and Prinn (2009) corrected ΔTPM to obtain a final PM_{ER} of 1.7 and include both the corrected and uncorrected points in Figure 4.1A. Vakkari et al. (2014, 2018) provided total mass of all particles 1 μm in diameter and smaller, ΔPM_1, normalized by ΔCO, as measured by a differential mobility particle sizer (assuming a density of 1.485 g cm^{-3}).

C2. Additional laboratory campaign information

For all experiments, the selected fuel was allowed to completely burn, fill the FSL chamber, and become well-mixed (~20 minutes). The FLAME III smog chamber and OFR as well as 12 of the FLAME IV smog chamber experiments sampled from the FSL chamber ("chamber burn"). The FIREX experiments and 7 experiments from the FLAME IV smog chamber (Tkacik et al., 2017) instead sampled directly from the FSL exhaust stack ("stack burn"). For each experiment, the fuel was burned to completion.

The FLAME III campaign used two different study designs: Hennigan et al. (2011) used a 7 m^3 environmental ("smog") chamber located directly outside of the FSL facility, with instrumentation for characterizing the chamber experiments in a mobile laboratory parked beside

the chamber. A heated (to 40 C) 12 m stainless steel transfer line with two ejector dilutors pulled smoke at a rate of 15 L min^{-1} from the FSL burn chamber to the smog chamber. For each experiment, the transfer line was conditioned with smoke for 30 minutes before filling the chamber to reduce losses of semivolatile compounds. Ortega et al. (2013) used a 13.1 L oxidation flow reactor (OFR) located within the FSL burn chamber itself with instrumentation for characterizing the OFR experiments located directly outside of the burn chamber. The smog chamber produced OH in four different ways: with natural sunlight only; with UV lights; with both UV lights and sunlight; with UV lights and an injection of HONO, producing further OH with the reaction HONO + νv = OH + NO; and with UV lights, HONO, and natural sunlight. The OFR produced both OH and O_3 from UV lights, but the OH/O_3 ratio was approximately 10 times that of ambient daylight levels. Typically, reaction rates of vapors with OH are more rapid than those with O_3 (Atkinson and Arey, 2003), and thus it was assumed that OH was the dominant reactant in the OFR. The smog chamber sampled 18 burns and 12 distinct fuel types; the OFR sampled 25 different burns and 16 distinct fuel types.

In FLAME IV, Tkacik et al. (2017) used a dual-chamber design: two identical 7 m^3 Teflon smog chambers were located within the FSL burn chamber, with instrumentation for characterization located in a mobile laboratory parked directly outside of the FLS facility. The dual-chamber setup allowed for simultaneous characterizations of a single burn under different perturbations. The dual-chamber used OH and/or O_3 as the primary oxidant. OH was produced using UV lights or UV lights + HONO. In the O_3 experiments, ozone was directly injected into the chamber and was kept otherwise dark in order to test the effects of ozone only ("dark O_3"). Most of the experiments held one chamber as a reference chamber, allowing the smoke to age in the dark without additional oxidants added, although a few experiments directly compared one oxidant

type to another. Nineteen burns and 8 distinct fuel types were studied. For the chamber burns, smoke was transferred at 24 L min^{-1} to each chamber using two ejection dilutors and a 3.048 m stainless steel line, heated to 40 C. Similar to FLAME III, the transfer lines were conditioned with smoke for 30 minutes before filling the chambers for each experiment.

For FIREX, Jathar et al. (in prep) used a 10 m^3 chamber, similar to Hennigan et al. (2011), to perform day- (w/ OH and O_3) and night-time (w/ NO_3) aging experiments. The nighttime experiments were not included in this review. The OH experiments were performed with either HONO or H_2O_2 as the OH precursors, O_3 experiments were performed by injecting O_3 before addition of smoke, and the NO_3 experiments were performed by adding NO and O_3 to allow the gradual build up of NO_3 before smoke was added. Smoke was transferred by an unheated aluminum transfer line, ~25 m long. Six different fuels found in the western US were used to perform a total of 16 experiments, alongside two chamber blanks.

To determine the initial condition of the smoke, each smog chamber burn underwent a primary characterization period of ~2-120 minutes before an oxidant was applied. Due to the short residence time of the OFR, this study instead had a copper bypass line that sampled unprocessed smoke from the FSL chamber and aged smoke from the OFR, switching between the reactor and the bypass line with 1 minute time resolution, and thus the unprocessed smoke in the FSL chamber was assumed to be the initial condition of the smoke within the OFR.

Figure C2 provides the final photochemical age versus the residence (physical) time for each study where reported, colored by OA_{ER}. The residence time within the FLAME III smog chamber experiments was between 3-4.5 hours, with total equivalent photochemical ages ranging between 2.6 and 15.1 equivalent hours. The FLAME III OFR reactor had an average residence time of 180 seconds, with total photochemical ages exceeding 72-120 equivalent hours. However, Figure 4.1C

shows the observed maximum OA enhancement ratio (OA_{ER}) from the FLAME III OFR, which occurred between 40 and 105.6 equivalent hours (Ortega et al., 2013). In Tkacik et al. (2017), the FLAME IV smog chambers experiments had a residence time of 2 hours, with calculated photochemical ages ranging between 1-25 equivalent hours. We note that the photochemical ages during FLAME IV were calculated in only a quarter of the experiments and are deemed to be uncertain. Ahern et al. (2019) instead calculated all enhancements after 1.5 hours of actual aging. The FIREX smog chamber experiments had a residence time of 1-6 hours, with calculated photochemical ages between 0.3 and 8.2 equivalent hours.

All photochemical ages except the dual chamber are calculated using the estimated total OH exposure per experiment and assuming that 1 day of aging is equivalent to 1.5×10^6 molec day cm^{-3} of OH exposure (Palm et al., 2016). The FLAME IV chambers instead assume that 1 day of aging is equivalent to OH and O_3 concentrations of 2×10^6 molec cm^{-3} and 60 ppb, respectively.

There were four methods that PWL was corrected for in these studies:

(1) Hennigan et al., (2011), Tkacik et al., (2017), and FIREX followed Grieshop et al. (2009):

$$OA_{ER} = \frac{OA_t/BC_t}{OA_0/BC_0} \quad \text{(C1)}$$

where OA_t and BC_t are the OA and BC concentrations at time t and OA_0 and BC_0 are the OA and BC concentrations during the initial characterization period. Each study assumed that the aerosol on the chamber walls can still partition with SVOCs and assumed no mass-transfer limitations of the vapors to the particles on the walls (ω=1 case; Weitkamp et al., 2007). This method corrects for both particle losses and losses of vapors that partition to the aerosol on the walls. We note that more recent understanding shows that the chamber walls themselves greatly outcompete the deposited particles for vapor absorption (Krechmer et al., 2016), and thus the analyses with ω are

no longer believed to be accurate; however, the reported laboratory results are still greatly sensitive to this choice of ω and we report both results here. We explore the effect of tubing and wall losses in Section 3.3 and here.

(2) Hennigan et al. (2011) also determined the PWL rate constant for the decay of OA mass during the primary characterization period (75 minutes), and used this to determine particle wall loss. They report upper bound mass enhancements as the mean of this and method 1 above (Figure 4.1C).

(3) Hennigan et al. (2011) and FIREX provides an estimate for a lower bound enhancement, in which condensable vapors are assumed to only partition to suspended particles (ω=0 case; Weitkamp et al., 2007). Hennigan et al. (2011) uses method (2) as a basis to calculate their ω=0 cases; FIREX uses method (1) as a basis to calculate their ω=0 cases.

(4) Ahern et al. (2019) instead corrected both for potential AMS collection efficiency (CE) limitations (Donahue et al., 2013; Docherty et al., 2013; Robinson et al., 2017) and chamber wall losses. To correct for changes in CE, they use a low-volatility POA tracer ion and determine SOA production and POA evaporation through the changing relative contribution from the POA tracer ion signal to the total OA ion signal. They then correct for wall losses, using both the ω=1 and ω=0 cases. We note that this approach may be prone to underestimating CE at longer ages, since the tracer ion may partially be reduced by oxidation or partitioning.

As the residence time is short in the OFR and particle losses are measured to be small, Ortega et al. (2013) instead reports the OA enhancement ratio without correcting for potential wall losses:

$$OA_{ER} = OA_t/OA_0 \quad \text{(C2)}$$

C3. Discussion of Aerosol Mass Spectrometer collection efficiency

AMS collection efficiencies might vary between fresh and aged aerosol: Some studies have suggested that AMS collection efficiency (CE) of OA could vary with aging (Donahue et al., 2013; Robinson et al., 2017), such that fresh OA emissions could have CE near 1 but aged OA may have a CE<=0.5 (Docherty et al., 2013; Robinson et al., 2017). A similar, perhaps correlated, trend in decreasing sensitivity with increasing oxidation is observed in the AMS RIE (relative ionization efficiency) for laboratory generated single compound OA particles (Xu et al., 2018). However, this effect has only been reported for some chamber studies (for non-biomass burning cases), and is typically not observed for ambient data (Middlebrook et al., 2012). The field studies have evaluated possible changes in CE (and also RIE) by comparison to co-located instruments measuring particle volume (e.g. Liu et al., 2017), and to our knowledge none have reported changes in CE*RIE with aging. The same procedure is typically applied in OFR studies (e.g. Palm et al., 2016). In addition, studies using collocated water-soluble organic carbon reached the same conclusions (of lack of mass enhancement) as those with the collocated AMS observations for 500 wildfire plumes sampled from aircraft (Hecobian et al., 2011). Ahern et al. (2019) attempted a correction for the potential change in CE for aged BB aerosol. Their analysis shows a much lower mean and median mass enhancement ratio than the Tkacik et al. (2017) analysis of FLAME IV; however, Tkacik et al. (2017) includes 6 extra experiments and OA enhancements at longer ages than Ahern et al. (2019) does and so the two studies are not directly comparable. We note that other instrumental problems such as limited particle transmission at some sizes, or problems with the instruments being compared to, are often incorrectly interpreted as changes in CE. Overall, this

issue is unlikely to explain the differences between laboratory and field experiments, but deserves further research.

C4. Description of tubing wall loss estimates for laboratory campaigns

In order to provide an estimate of the importance of losses and delays of vapors to the tubing that transports smoke from the burn chamber floor to a smog chamber, we apply the model developed in Pagonis et al. (2017; hereafter 'tubing model') to the smog-chamber set-up used in FLAME III (Hennigan et al., 2011). Pagonis et al. (2017) modelled the transfer of vapors to the tubing between a smog chamber and a proton-transfer-reaction mass spectrometer as an absorptive partitioning process, finding that rapid partitioning of lower-volatility vapors caused significant delays in their transfer through the tubing. Based on the description in Hennigan et al. (2011), we assumed a tubing length of 12 m, a flow rate of 15 L min^{-1}, and a tubing inner diameter of 0.42 inches. We assumed that a continuous flow of smoke entered the chamber for an average time of 15 minutes of smoke per experiment, and ran the model for 15 minutes to determine how much gas-phase material would deposit on the tubing and how much would be transmitted by the end of 15 minutes. The tubing model was developed to estimate vapor losses within a PFA Teflon tube at 23 °C as a function of C* (saturation concentration, in units of μg m^{-3}), noting that other tubing materials, such as the stainless steel tubing that was actually used in FLAME III, lead to longer delays than Teflon and thus larger effects than simulated here (Deming et al., 2019; Liu et al., 2019). Further discussion of tubing materials is in the final paragraph of this section. We neglect potential particle losses to the tubing. We used the VBS distribution from Bian et al. (2017) and assumed an initial mass loading of 50 μg m^{-3} and initial temperature of 23 °C. As the tubing at FLAME III was heated to 40 °C, we estimated the losses that would occur at both tubing

temperatures of 40 °C and 23 °C to estimate the impact of heating (Figure C7). The new volatility distribution at 40 °C was estimated using the Clausius–Clapeyron relation (Cappa and Jimenez, 2010):

$$C*_{new} = C*_{initial} \left(\frac{T_1}{T_2}\right) exp\left(-\frac{L}{R}\left(\frac{1}{T_2} - \frac{1}{T_1}\right)\right) \quad \text{(C3)}$$

where C^*_{new} is the volatility at 40 °C, L is the specific latent heat, R is the specific gas constant (assumed to be 8.314 J mol^{-1} K^{-1}), and T_1 and T_2 and 23 °C and 40 °C, respectively. We assumed L to be 90 kJ mol^{-1}, which conveniently allows for C^*_{new} to shift up by a factor of 10 for 40 °C relative to 23 °C.

We run two bounding cases for the assumption of the tubing at 40 °C (Figure C7). Upon heating from 23 °C to 40 °C, the volatility distribution will shift, with a portion of the aerosol evaporating. However, the residence time for smoke within the tubing was ~4.3 seconds, which may be fast enough to limit evaporation of the particles (Riipinen et al., 2010). Our lower-bound case (Figure C7a) assumes no aerosol evaporates within the temperature shift. Our upper-bound case assumes the volatility distribution immediately repartitions to equilibrium at 40 °C (thus providing more gas-phase material; Figure C7b). In both cases, we assume the aerosol does not evaporate further upon vapor wall losses. In Figure C7, we show the amount of gas-phase material "lost" to the tubing, as well as the amount of evaporated aerosol lost to the tubing for the upper bound case. We also show the results for if the tubing was not heated and kept at 23 °C (Figure C7c).

Finally, we estimate the OA enhancement ratios for each case (Figure C7d):

$$OA_{ER} = \frac{(SOA+POA)}{POA} \quad \text{(C4)}$$

where POA is the assumed POA to enter the chamber (50 μg m^{-3} for the lower bound case at 40 °C and the case at 23 °C, and ~34 μg m^{-3} for the upper bound case at 40 °C, as a portion of the POA is assumed to evaporate upon heating with some evaporated organics being lost to tubing for this case). SOA is calculated assuming that the SOA yield of each bin varies linearly with C*, with a yield of 0.05 for the C*=10^7 μg m^{-3} bin and 1 for the C*=10^2 μg m^{-3} and lower bins. (Bins above C*=10^7 μg m^{-3} are assumed to not have SOA yields for this calculation). We neglect further wall losses in the smog chamber when calculating OA_{ER}. We contrast OA_{ER} for each case to a case in which no tubing was used (that is, the smoke was instantly transferred from the burn chamber to the smog chamber at 23 °C).

An important caveat of this analysis is that although the tubing model was developed based on results for PFA Teflon, the tubing at FLAME III was stainless steel. Deming et al. (2019) shows that dramatically different delay times can occur for absorptive materials (such as Teflon) as compared to adsorptive materials (such as stainless steel), with stainless steel having longer delay times in their study. Thus, parameterizations for adsorptive materials are required to provide a more quantitative estimate of the tubing losses that may have occurred during the smoke experiments. We note that the delay time for adsorptive materials was shown to decrease in Deming et al. (2019) for tubing that had been previously used. In FLAME III, the tubing was pretreated by running smoke through it for 30 minutes prior to each experiment, likely decreasing delay times during the actual experiments.

Table C1. Field campaigns from Figure 4.1A.

Study (refs)	Fire type, environ-ment	Burn area; dilution conditions	Burn conditions	Initial age(s); final age(s) of measurements	Oxidant concentra-tions;	$MASS_{ER}$ (source); $O:C_{ER}$ (source); f_{44}/f_{60_ER} (source)
SAFARI (Hobbs et al., 2003; Alvarado and Prinn, 2009)	One controlled grassland burn in South Africa	10 km^2	Initial MCE= 0.94, aged MCE = 0.93	1 minute; 0.65 hrs (A)	In-plume OH 1.7 x 10^7 molec cm^{-3} (Hobbs)	0.5 (Hobbs), 1.7 (Alvarado); n/a; n/a
SEAC4RS (Liu et al., 2016)	7 agriculture fires in the U.S. midwest	0.16 km^2 to 1.27 km^2	Range of MCE: 0.895 to 0.958	0 minutes; Up to 1.25 hrs (A)	No discussion	1; 1.5-2; n/a
MILAGRO (DeCarlo et al., 2008; Yokelson et al., 2009; Jolleys et al., 2012)	Agricultural and forest fires in the Yucatan peninsula (Mexico).	Each fire assumed to be 1 km^2 (Yokelson); Ave. wind of 2.6 m s^{-1} (Yokelson)	Yokelson: 0.925 (fresh) but this is from a day earlier. DeCarlo: no discussion	DeCarlo: "Fresher", Yokelson: 10-30 minutes, Jolleys: "fresh"; DeCarlo: Up to 18 hrs (P), Yokelson: 1.4 hrs (A)/12 hrs (P), Jolleys: up to 24 hrs (P)	In-plume OH > 10^7 molec cm^{-3} (Yokelson)	0.8 (Jolleys), 1.3 (DeCarlo), 2.3 (Yokelson); 1.8-2.7 (DeCarlo); 5.12 (Jolleys)
Vakkari et al., 2014; 2018	Savanna, grassland, and mixed cropland, grassland, and savanna burns in S. Africa	No discussion	ΔBC/ΔCO: PM_1 enhancement for ΔBC/ΔCO values < 0.02 (unitless)	"Fresh plumes" less than 0.5 hrs old; average ages of 2.4 hours (2014) and 3-5 hours (2018)	No discussion	1.0, 2.0-3.0; n/a; n/a
SCREAM (May et al., 2015)	2 prescribed agricultural	0.36 and 1.47 km^2	0.9-0.93 (1.47 km^2 fire)	"Near source", less than 0.5 hours		0.65 (0.36 km^2 fire),

	burns in U.S. (South Carolina)			(often less than 10 mins); 5 hrs (A; 0.36 km^2 fire) and 2 hrs (A; 1.47 km^2 fire)		1.0 (1.47 km^2 fire); 1.2, 1.4 (range from data); 3.6 (1.47 km^2 fire), 5.4 (0.36 km^2 fire)
Akagi et al., 2012	Prescribed chaparral burn in U.S. (California)	0.81 km^2; Winds between 0.5-2.2 m^{-1}	0.933	"Nascent", collected ~600-1300 m above the plume; up to 12 hrs (P)	In-plume OH $5.27x10^6$ molec cm^{-3}	0.8; n/a; n/a
ARCTAS (Cubison et al., 2011)	Large boreal wildfire in N.W. Saskatchewan	"Large"	"Surface-to-torching" fire	"Near-field"; 5 hrs (P)	No discussion	1.0; 1.44; 3.8
SAMMBA (Brito et al., 2014; Morgan et al., 2019)	Rainforest fires in S.W. Brazilian Amazon	No discussion (Brito); At maximum 5 km^2 but likely smaller	Not explicitly discussed (Brito); MCE of 0.79 (Morgan)	"fresh", "nearby"; > 3 hrs (A) (Brito). "Above the fire" to 3 hrs (A) (Morgan)	No discussion (Brito and Morgan)	1.0 (Brito and Morgan); 2.4 (Brito); n/a
SEAC4RS (Forrister et al., 2015)	Large wildfire in the U.S.	"Large"	Smoldering, with $\Delta rBC/\Delta CO \sim 2.5x10^{-6}$	1 hr (A); 7 hrs (A)	No discussion	0.27; 1.9; n/a
BBOP (Collier et al., 2016)	Wildfires in the western U.S.	No discussion	Fresh: range from 0.86 to 0.96; aged: range from 0.8 to 0.99	1-6 hrs (A); 6-45 hrs (A)	No discussion	1.0; 1.9; n/a
DABEX (Capes et al., 2008; Jolleys et al., 2012)	Agricultural burns (included grasses, shrubs) in W. Africa	0.01-0.1 km^2	Smoldering (visual observations, Capes)	0 hrs (flying above the fresh plumes) (Capes), "fresh" (Jolleys);	No discussion	0.66 (Jolleys), 1.0 (Capes); n/a; 0.55 (Jolleys),

				24-48 hrs (P)		2.2 (Capes)
ACTIVE (Jolleys et al., 2012)	Eucalyptus forests in N. Australia	No discussion	No discussion	"Fresh"; up to 24 hrs (P)	No discussion	0.76; n/a; 2.34
BORTAS (Jolleys et al., 2015)	Boreal forest fires in N. America (Canada)	No discussion	Fresh plumes were from more smoldering; Aged plumes were from more flaming conditions	"Fresh"; 24-120 hrs (A)	No discussion	0.5; n/a; 8.6-9

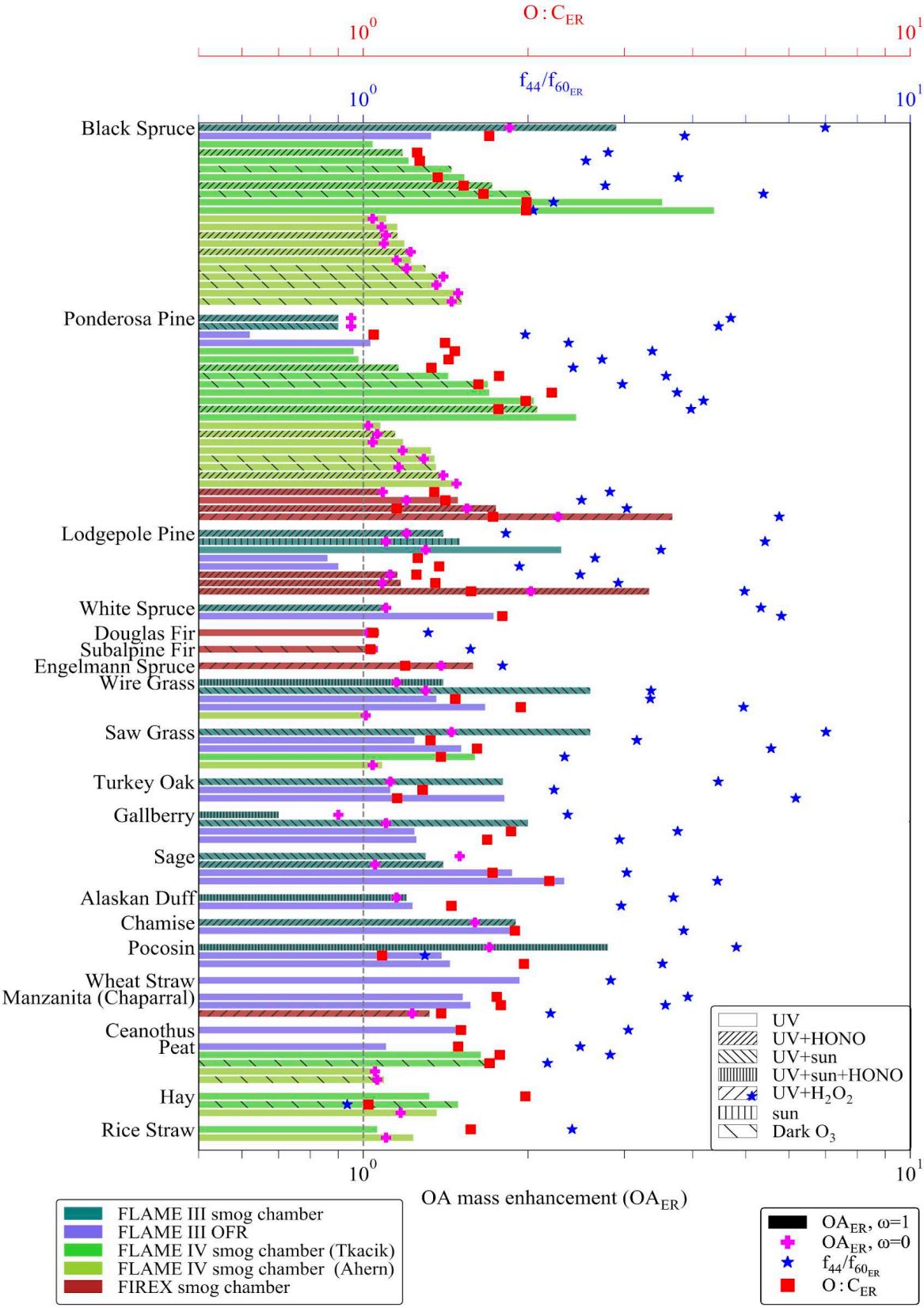
O : C_ER
10^0
10^1
f_44/f_60_ER
Black Spruce
Ponderosa Pine
Lodgepole Pine
White Spruce
Douglas Fir
Subalpine Fir
Engelmann Spruce
Wire Grass
Saw Grass
Turkey Oak
Gallberry
Sage
Alaskan Duff
Chamise
Pocosin
Wheat Straw
Manzanita (Chaparral)
Ceanothus
Peat
Hay
Rice Straw
UV
UV+HONO
UV+sun
UV+sun+HONO
UV+H2O2
sun
Dark O3
OA mass enhancement (OA_ER)
FLAME III smog chamber
FLAME III OFR
FLAME IV smog chamber (Tkacik)
FLAME IV smog chamber (Ahern)
FIREX smog chamber
OA_ER, ω=1
OA_ER, ω=0
f_44/f_60_ER
O : C_ER

Figure C1. Results for each experiment within the laboratory campaigns of Figure 4.1C and D arranged by fuel type. Bars are OA mass enhancement (OA_{ER}) for the ω=1 case for the FLAME III, FLAME IV, and FIREX smog chambers (bottom x axis). For the FLAME III OFR, the bars are the maximum OA_{ER} (not corrected for wall losses). Magenta crosses are for the ω=0 case for the FLAME III, FLAME IV, and FIREX smog chambers, when available. Blue stars are $f_{44}/f_{60_{ER}}$, and red squares are $O{:}C_{ER}$ (top x axis). All metrics are lined up on the same x axis, although each x axis is provided separately for reference. The hatching for each OA_{ER} bar represent the oxidant method used. The vertical grey dashed line at 1 indicates no change from the initial value of a given metric.

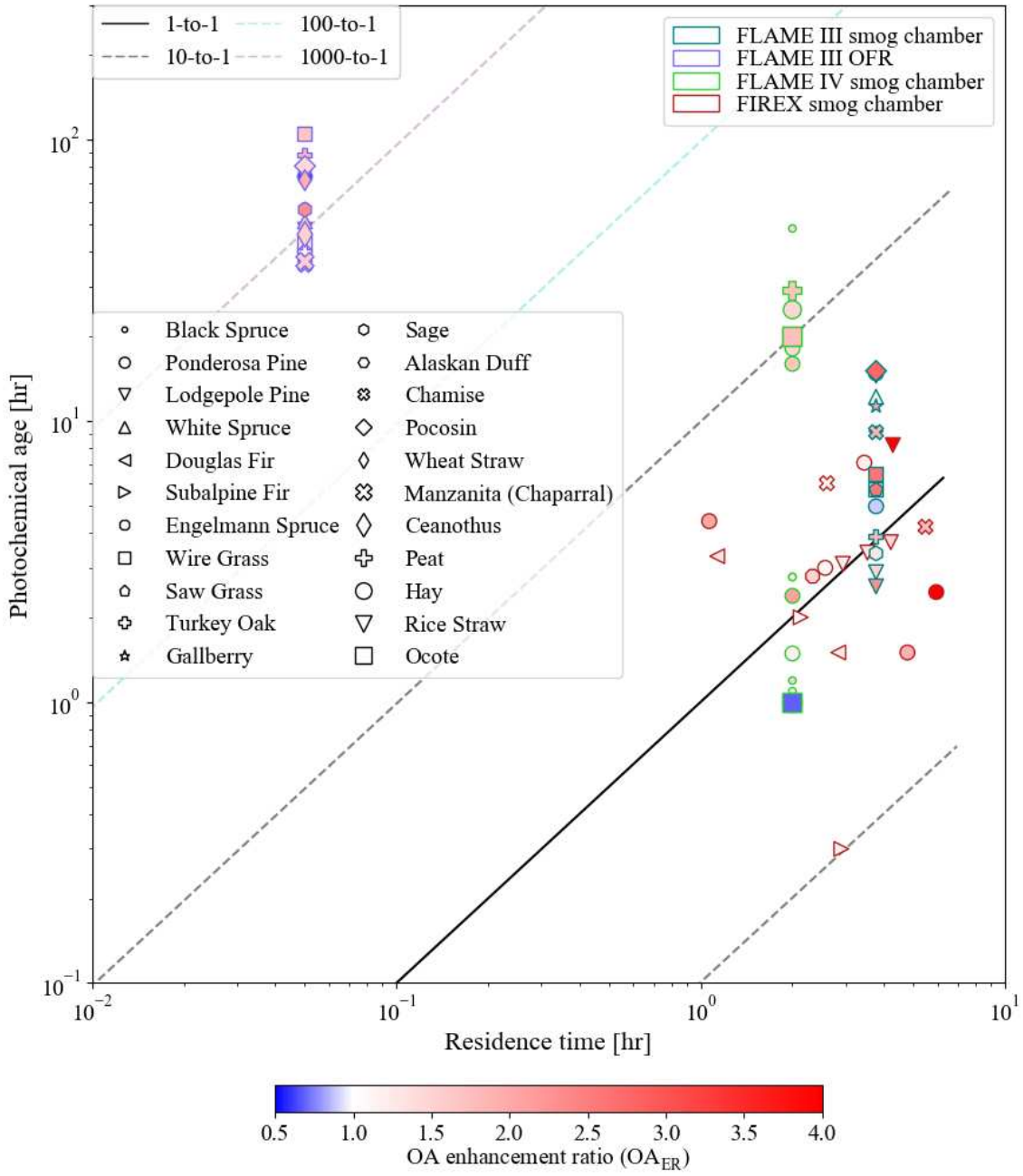

Figure C2. The estimated photochemical age for each residence (actual) time of each aging experiment within the laboratory campaigns of Figure 4.1B, colored by OA enhancement ratio (OA_{ER}). Each symbol represents an individual fuel type. The outline color of each symbol indicates what study a given data point is from. Also shown are the 1-to-1, 10-to-1, 100-to-1, and 1000-to-1 lines. The FLAME III and FLAME IV campaigns did not provide individual residence times, and so the average residence times for each campaign are shown here. For the campaigns that provide both ω=1 and ω=0 data, we show the ω=1 cases.

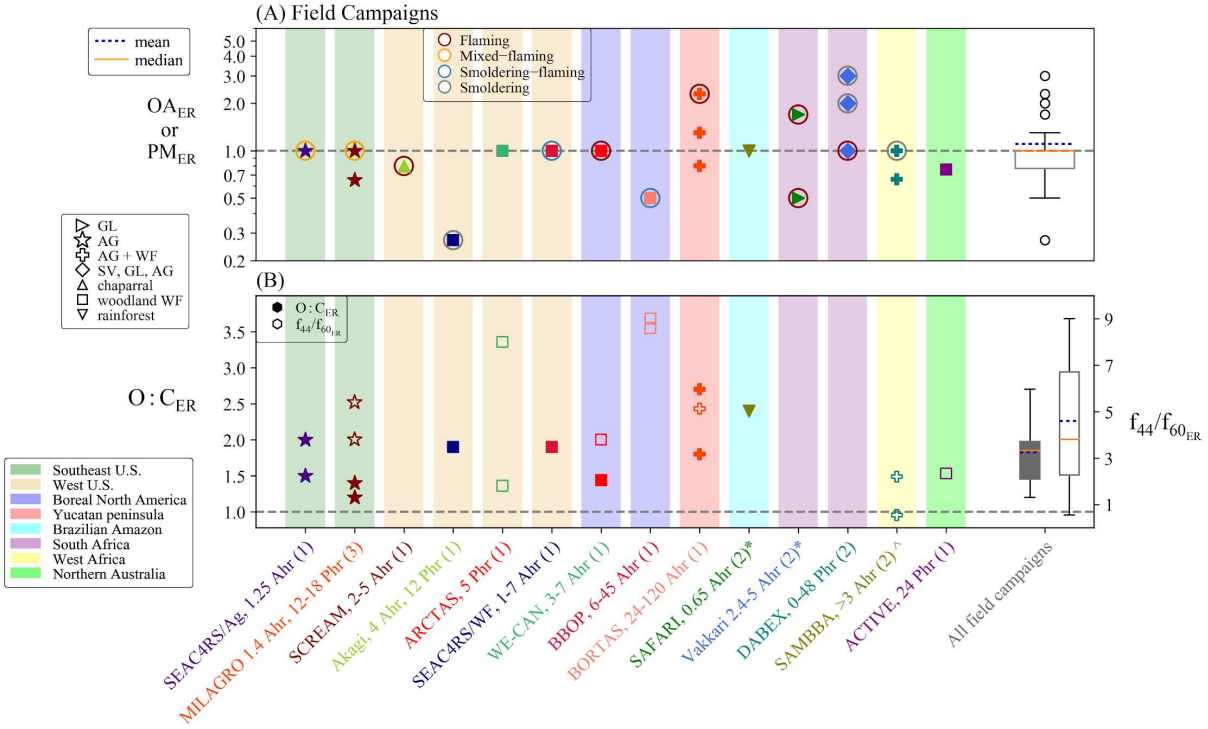

Figure C3. The field studies of Figure 4.1A, B arranged by geographic region. No published studies are available for Asia or Europe.

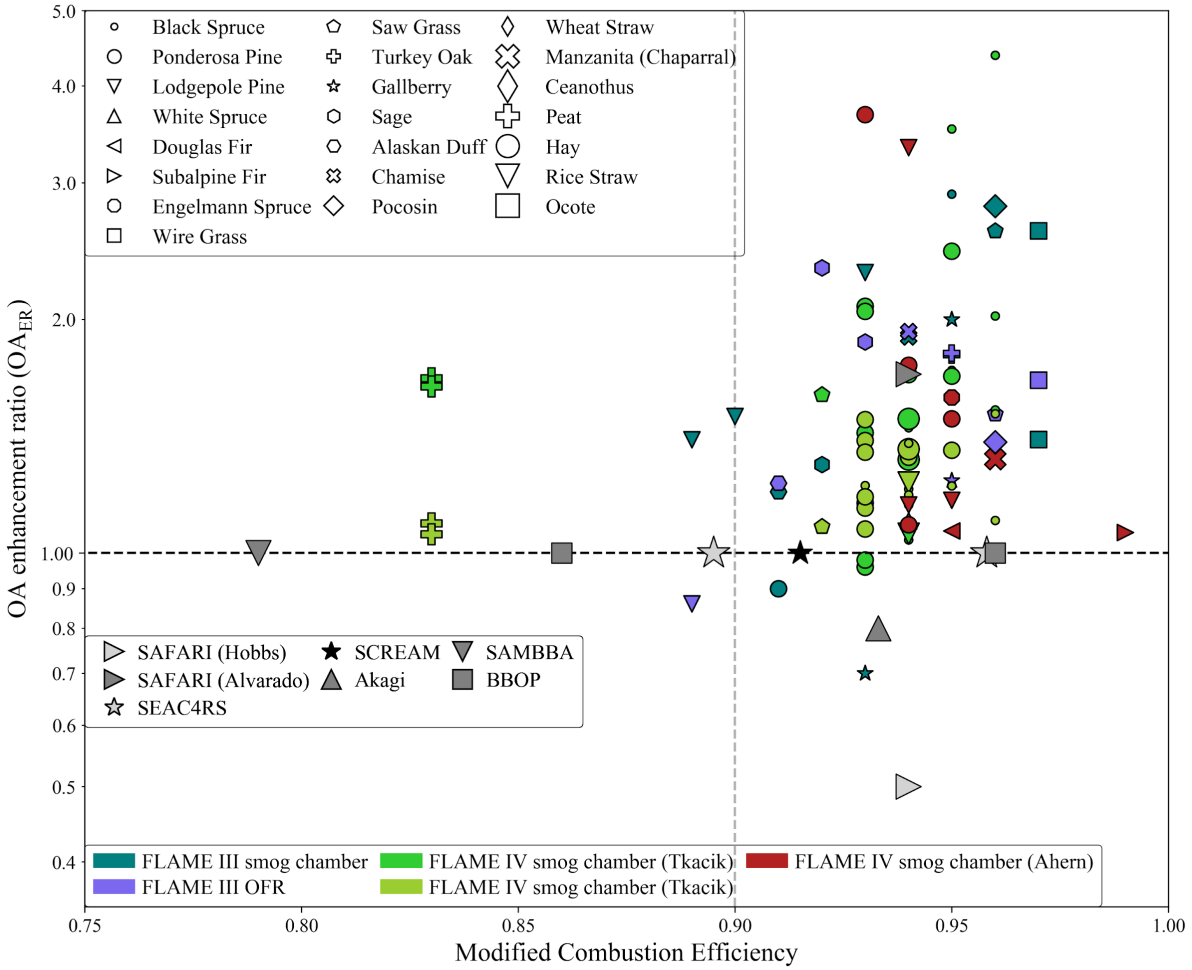

Figure C4. The OA enhancement ratio to the modified combustion efficiency (MCE) for each chamber for all experiments within the laboratory campaigns of Figure 4.1B as well as field campaigns where MCEs were reported in the associated publications. Symbols indicate fuel type and colors indicate study type. The horizontal dashed black line at OA_{ER}=1 indicates no net change in OA mass from the initial mass. The vertical dashed grey line at MCE=0.9 indicates the rough cutoff between flaming and smoldering conditions. MCE values >0.9 indicate more flaming conditions. MCE values <0.9 indicate more smoldering conditions. MCE values around 0.9 indicate mixed flaming and smoldering conditions. Also included on this figure are the studies that report MCE. The SEAC4RS and BBOP campaigns reported a range of MCE, indicated by multiple symbols showing the minimum and maximum MCE values. Similar to Figure 4.1A, we report both estimates of enhancement ratios for SAFARI (Hobbs et al., 2003; Alvarado and Prinn, 2009).

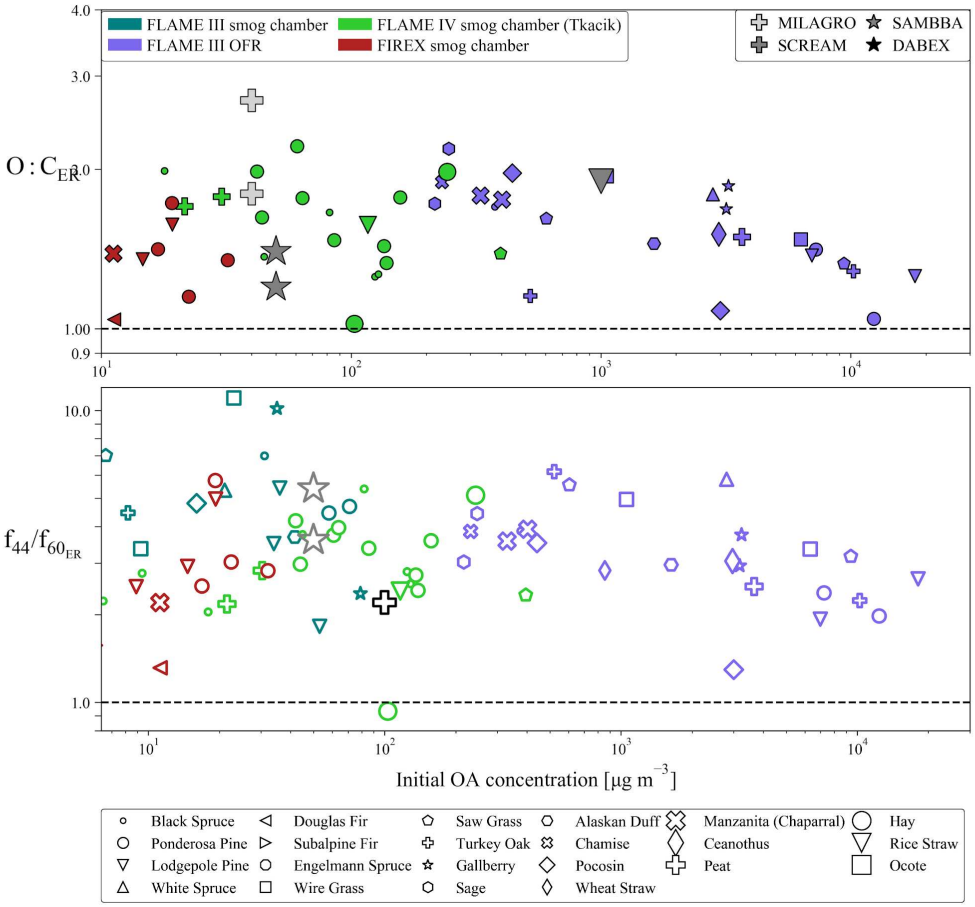

Figure C5. O:C_{ER} (top panel; closed symbols) and $f_{44}/f_{60_{ER}}$ (bottom panel; open symbols) values to the initial OA concentration in µg m^{-3} within each chamber for all experiments within the laboratory campaigns of Figure 4.1B. Symbols indicate fuel type and colors indicate study type. The dashed black line at 1 indicates no net change in either metric from their initial values. Also included are field campaign O:C_{ER} and $f_{44}/f_{60_{ER}}$ values, where initial OA concentrations were available.

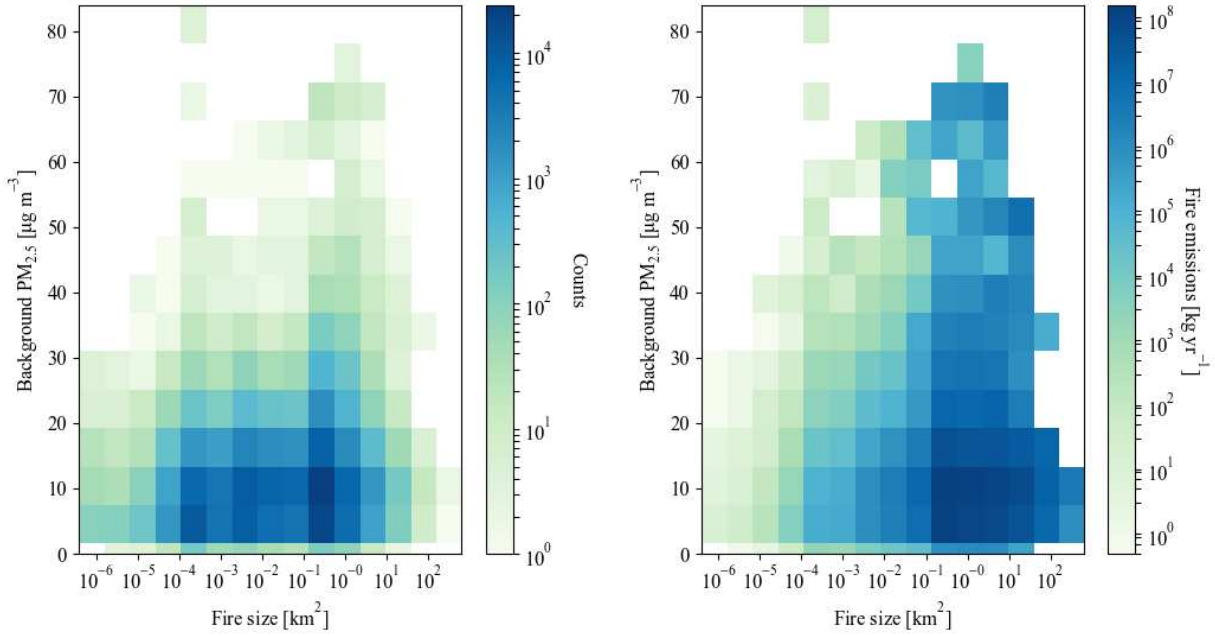

Figure C6. (Left) Two-dimensional histogram of the annual data for the United States in 2014 for the number of recorded fires by fire size in km^2 blackened per day (that is, the total area in km^2 burned per day) from the National Emissions Inventory (U.S. EPA NEI, 2014) against the non-smoke background $PM_{2.5}$ that each fire diluted into. The background $PM_{2.5}$ is a seasonal median estimate of $PM_{2.5}$ without wildland fire smoke influence. It was estimated by kriging daily 24-hr $PM_{2.5}$ concentrations from the EPA Air Quality System (AQS) on days without a smoke plume overhead (according to the Hazard Mapping System fire and smoke product). The dataset is described in more detail in O'Dell et al. 2019. (Right) Total annual $PM_{2.5}$ emissions in kg from each fire size for 2014 from the same dataset against the background $PM_{2.5}$ that each fire diluted into.

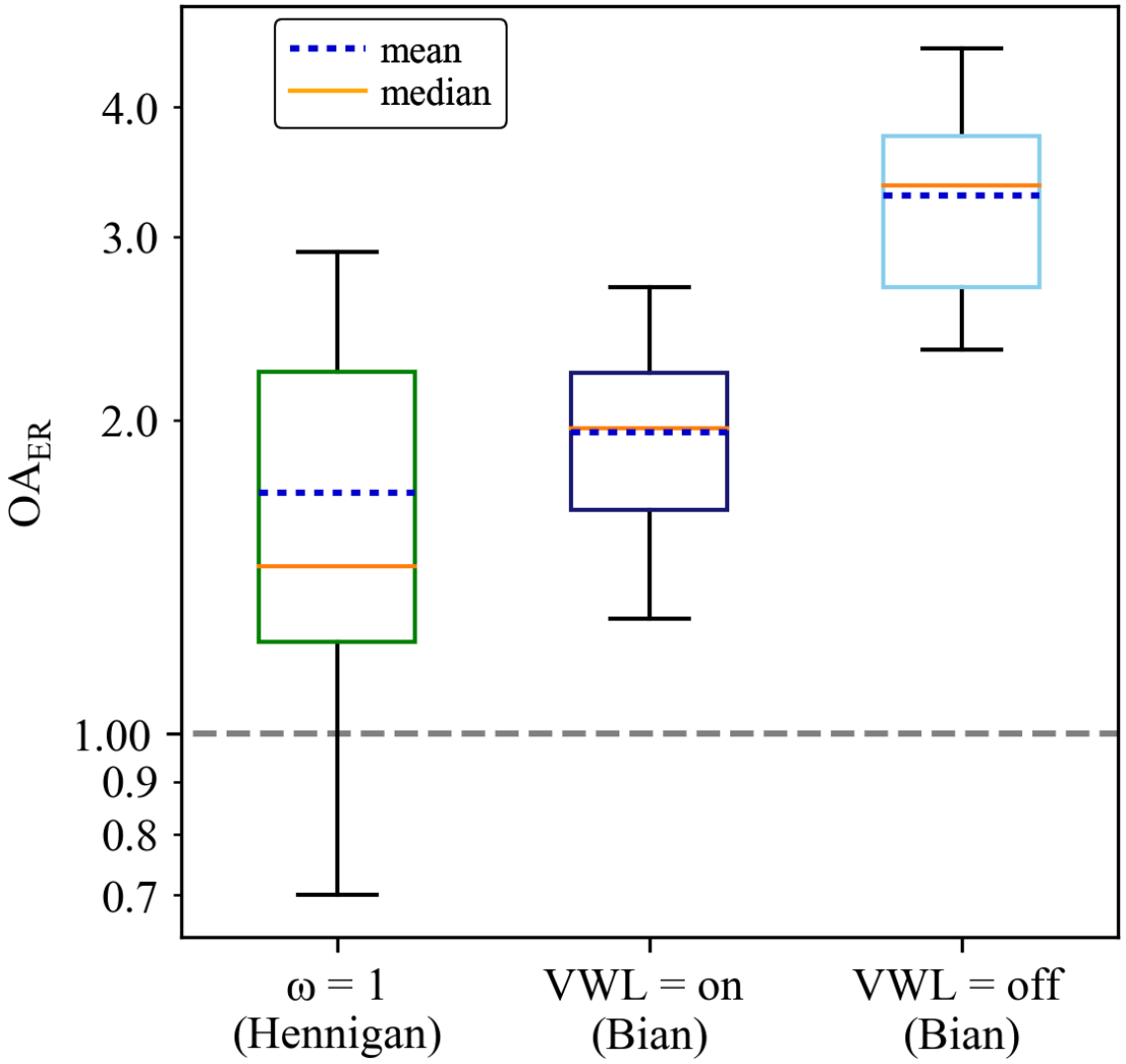

Figure C7. The box-and-whiskers for the OA enhancement ratios (OA_{ER}) smog chamber at FLAME III (Hennigan et al., 2011) and the model results of Bian et al., (2017) for partitioning of vapors to the chamber walls on and off (vapor wall losses; VWL). With partitioning of vapors on, the simulated range of OA_{ER} lies within the observed range. Without partitioning of vapors (i.e., if there were no losses of vapors to chamber walls), OA_{ER} nearly doubles. Bian et al. (2017) used the assumption that ω=1 for their analysis and so the Hennigan et al. (2011) results for this assumption are shown. The dashed grey line at OA_{ER} = 1 indicates no change in OA_{ER} with age.

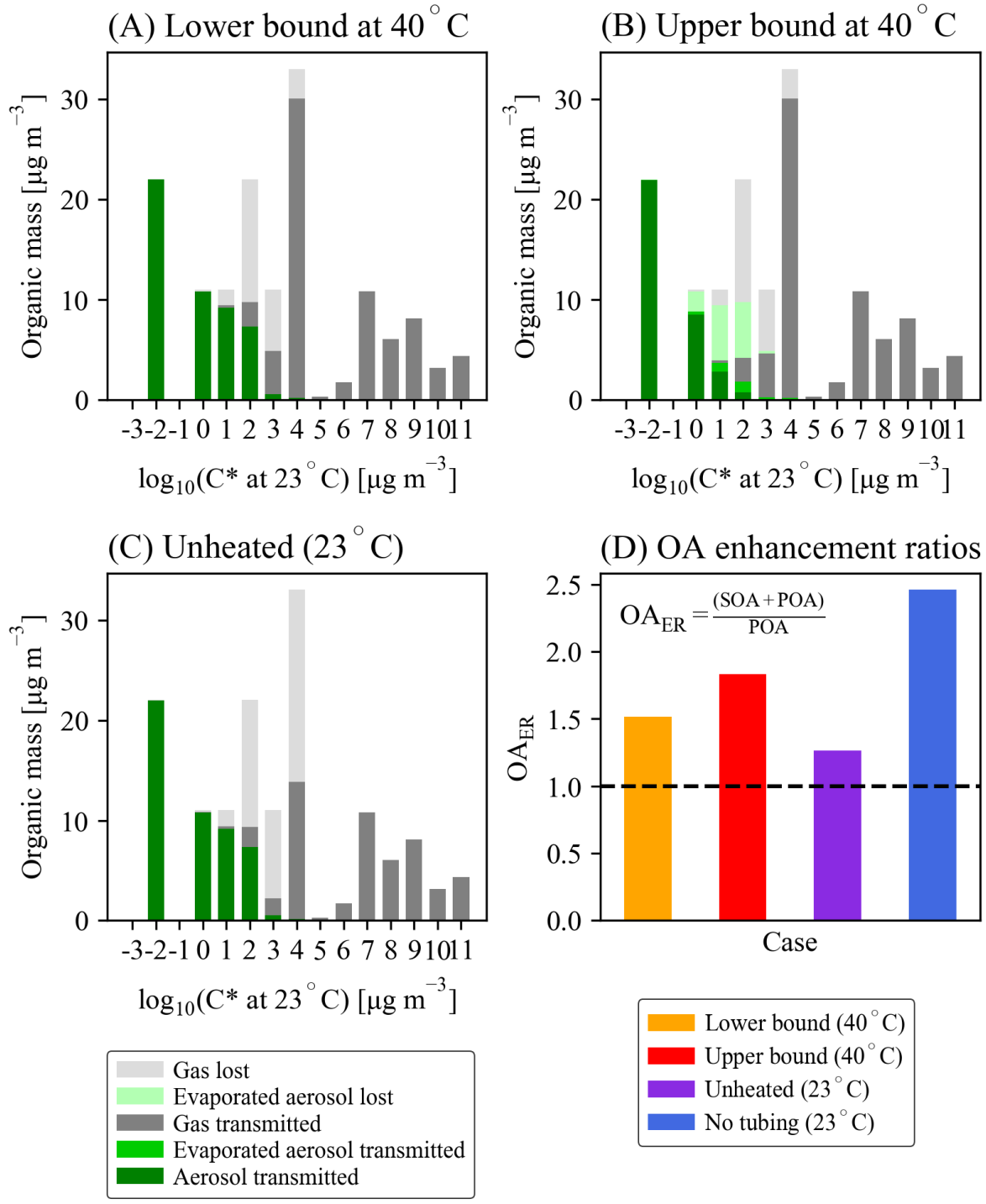

Figure C8. Estimated gas-phase losses of smoke to the transfer lines (tubing) between the burn chamber and the smog chamber, using the setup for FLAME III (Hennigan et al., 2011), assuming the line has been heated from 23 °C to 40 °C and using the Teflon tubing model built in Pagonis et al. (2017). (A) The lower bound case assumes that upon heating from 23 °C, the volatility distribution shifts but the aerosol does not have time to evaporate. (B) The upper bound case

instead assumes that upon heating from 23 °C, the volatility distribution shifts and the aerosol instantly evaporates to reach an instantaneous new equilibrium, which provides a reservoir of evaporated aerosol that may then be transmitted (and recondensed in the smog chamber) or lost to the transfer line. (C) The transmitted and lost volatility distribution if the tubing were not heated. (D) OA enhancement ratios (OA_{ER}) for each case compared to what OA_{ER} is expected if no tubing was used. The dashed black line at $OA_{ER} = 1$ indicates no change in OA_{ER} with age.

APPENDIX D

SUPPLEMENT TO MORE THAN EMISSIONS AND CHEMISTRY: FIRE SIZE, DILUTION, AND BACKGROUND AEROSOL ALSO GREATLY INFLUENCE NEAR-FIELD BIOMASS BURNING AEROSOL AGING

Introduction

The following provides addition model results, including results for all fire sizes and background aerosol concentrations modelled (see text section D1; Figs. D1, D2, D5, D9, and D11) and the results of all sensitivity analyses done in the study (text section D5; Figs. D13-D24). We detail our modeling smoothing techniques in text section S2, provide the calculations for the plume mean diameter and peak lognormal modal width. Text section D3 details a discussion on the formation of SOA and role of condensing vapor volatility on plume mean diameter and peak lognormal modal width and CCN concentrations. Finally, table D1 provides a brief overview of published biomass burning field campaigns, in the context of this study. All citations are provided at the end of this document.

D1. Additional model results

Figure D1 shows the time evolution of smoke organic mass enhancement (ΔOA) and dilution ratios for the base simulations all fire sizes and background concentrations modelled in this study. Figure D2 shows the time evolution of ΔCO for a subset of the fire sizes. ΔCO is not impacted by background aerosol concentration or the aerosol chemistry and coagulation model schemes. Figure D3 shows ΔOA normalized by the enhancement of CO above background (ΔCO) after four hours of aging for all combinations of Chem and Coag simulations for all fire sizes and background concentrations modelled for the base simulations. Figures D4-D5 give the initial and final volatility basis set (VBS) distributions for the base simulations for background aerosol concentrations of 5 and 50 μg m^{-3}, respectively. The k_{OH} from the Jathar et al. (2014) parameterization is sufficiently slow at high C* values that only a small fraction of the highest

volatility bins (~C* ≥ 10^6 μg m^{-3}) undergo oxidative aging within the 4 simulated hours, thus contributing little to final normalized smoke OA. Figure D6 provides ΔOA/ΔCO for the base cases as a function of time for all fire sizes and background concentrations modelled. Shown are the ChemOn_CoagOn and ChemOff_CoagOff cases (as coagulation does not change the total mass significantly). Figure D7 provides the background corrected lognormal diameter, D_g, and lognormal modal width, σ_g, for all background concentrations and fire sizes between 10^{-2} and 100 km^2 for the base cases modelled in this study after 4 hours of aging. Figures D8 and D9 provide the number and volume size distributions for the base cases (Table 5.1) after 4 hours of aging for a subset of the fire sizes (10^{-2}, 1, and 100 km^2) and background aerosol concentrations (0, 5, and 50 μg m^{-3}). We show the total (plume plus background aerosol) size distributions, as well as the background alone size distributions. Figure D10 provides ΔE/ΔCO for the base cases after 4 hours of aging for all background aerosol concentrations and fire sizes between 10^{-2} and 100 km^2. Figure D11 shows the size-dependent mass extinction efficiency for the refractive index used in this study, 1.5 - 0.08i (assuming spherical particles) at a wavelength of 500 nm. Figure D12 provides ΔCCN/ΔCO at 0.2% supersaturation for the base cases after 4 hours of aging for all background aerosol concentrations and fire sizes between 10^{-2} and 100 km^2. It is assumed that both the plume and background aerosol have hygroscopicity parameter (κ) values of 0.2.

D2. Model smoothing

In TOMAS, we use a top hat method for transferring mass between size sections during condensation/evaporation, as described in Stevens et al. (1996). First a top hat representation of the distribution is constructed for each bin, then these are translated according to the analytic solution, and then finally the translated top hats are remapped to the bins. However, in the tophat

method, at times a bin will empty out into an adjacent largest bin, creating oscillations of number/mass within the diameter space. To reduce the noise created by these oscillations during post processing, we transfer mass between adjacent bins in post-processing by moving number to make the mass:number ratio in each bin equal to the geometric mean of the bin mass:number limits. This method conserves total number and mass.

When the fire size distribution is very close to the background size distribution (relevant for fires 10^{-2} km^2 and smaller in this work), the post-processing smoothing of the total size distributions (plume and background) occasionally does not line up with the background-only simulations well enough and poor results are obtained. The following results have been skewed by model noise and are removed from this study:

- The base simulation: The plume peak diameter of the lognormal mode and and lognormal modal width data point for the ChemOff_CoagOn case for the 10^{-2} km^2 fire with a 20 µg m^{-3} background (Fig. D7)
- The sensitivity case of a stability class of B: the smoke extinction data point for the ChemOn_CoagOff case's value for E_{smoke} for the 10^{-2} fire size with a 50 µg m^{-3} background concentration (Fig. D19)

D3. Calculations of the plume geometric mean diameter and peak lognormal modal width

Whitby et al. (1991) determined mathematical relationships between integral moments M_k and the geometric mean diameter (D_g) and peak lognormal modal width ($\sigma_{g,}$) for integer values of k_1 and k_2:

$$D_g = \underline{M}_{k_1}^{\widehat{k_1}} \underline{M}_{k_2}^{\widehat{k_2}} \quad \text{(D1)}$$

$$ln^2(\sigma_g) = \frac{2}{k_1(k_1-k_2)} ln\left(\frac{\underline{M}_{k_1}}{\underline{M}_{k_2}^{r}}\right) \quad \text{(D2)}$$

Where $M_k=M_k/N$, $r = k_1/k_2$, $k_1=1/[r(k_2-k_1)]$, $_{k2}=r/(k_1-k_2)$, and N is the total number concentration. We use each combination of integral moments 1, 2, 3, and 4 for k_1 and k_2 and present the average of each moment combination for D_g and σ_g. (Note that k_1 cannot equal k_2).

D4. Discussion of the impact of volatility-dependent SOA formation on plume σ_g, D_g, and CCN

The size-dependent growth/shrink rates during condensation/evaporation is controlled by two different processes: the volatilities of the condensing vapors and the sizes of the growing particles (in the absence of particle-phase diffusion effects and significant differences in composition with size). For condensation, if the condensing species have a low-enough effective volatility (an effective saturation concentration C^* <~10^{-3} μg m^{-3}), the vapors will condense essentially irreversibly (Pierce et al., 2011; Riipinen et al., 2011; Zhang et al., 2012). Under irreversible condensation, growth rates are independent of D_p in the kinetic regime (particles smaller than ~50 nm) but proportional to $1/D_p$ in the continuum regime (particles greater than ~1 μm; Seinfeld & Pandis, 2006). As a result, irreversible condensation will grow smaller particles more quickly than larger particles in the continuum regime. This effect is seen for the smallest fires in the ChemOff cases (Figs. 5.3 and D6): σ_g increases slightly for these cases, indicating that dilution and evaporation rates are great enough that some of the lower-volatility material is also evaporating off, broadening the distribution. Conversely, if the vapors are instead semivolatile (C*>~10^{-1} μg m^{-3}), vapors will more quickly reach equilibrium at all particle sizes and growth will be in quasi-equilibrium, which is proportional to particle diameter (D_p) for all particle sizes (Pierce et al., 2011; Riipinen et al., 2011; Zhang et al., 2012). Thus, if only semivolatile vapors were condensing (evaporating) in the plume, σ_g would not decrease (increase). This effect can be seen

for most fire sizes in the ChemOff cases in which evaporation of semi-volatile compounds decreases the mean diameter, D_g, but the lognormal modal width, σ_g, remains essentially constant (Figs. 5.3 and D7).

The majority of the simulated plume particles are in the transition and continuum regimes (Fig. D8). In the transition regime, irreversible condensation growth rates will transition in between having no D_p dependence to having a $1/D_p$ dependence (Seinfeld & Pandis, 2006), while quasi-equilibrium condensation always has a D_p dependence. For the ChemOn cases, where SOA is being produced through gas-phase chemistry, σ_g generally decreases in the cases where SOA production dominates (Figs. 5.3 and D7), which indicates that this SOA condensation is occuring closer to the irreversible limit than the quasi-equilibrium limit. It is of note that for the smaller fire sizes (area 0.1 km^2 and smaller), increasing background concentrations leads to less of a total decrease in σ_g in our simulations, as more low volatility vapors are able to condense onto the smoke aerosol (OA evaporation decreases with higher background concentrations as the increased mass from the background aerosol drives partitioning to the aerosol phase; Donahue et al., 2006). Thus, the D_p dependence on growth rates for small fire sizes with higher background concentrations is shifted more towards a proportionality in D_p (quasi-equilibrium) than in $1/D_p$ (irreversible) for the transition and continuum regime-sized particles.

The effects of the irreversible and quasi-equilibrium condensation on D_g discussed above also impact D_g, which in turn impacts CCN concentrations. Figures 5.4 and D7 shows that for the smaller fires, SOA production (moving from chem_off to chem_on simulations) increases D_g while decreasing σ_g as the growth is primarily irreversible. However, for the smallest fires at the lowest background concentrations, evaporation of semi-volatile compounds (initial to chem_off; decreases D_g with ~constant σ_g) competes with approximately irreversible condensation. The net

effect is that D_g remains approximately constant, while σ_g has decreased. As a result, the aged size distribution becomes more narrow but has an approximately constant D_g for the smallest fires at the lowest background concentrations.

D5. Sensitivity tests: accommodation coefficient, rate of OH reactions, stability class

Figures 5.1-5.4 show the results of plume evolution for the base cases, which use an accommodation coefficient of 1.0, the upper-bound chemistry parameterization with a four-bin drop in volatility per reaction with OH, and an atmospheric stability class of D (neutral). Here we briefly discuss the results and main differences from the base cases and sensitivity cases using accommodation coefficients of 0.1 and 0.01, the lower-bound chemistry parameterization with a two-bin drop in volatility per reaction with OH, and atmospheric stability classes of B and F. Figures D12-D22 provide ΔOA/ΔCO, ΔE/ΔCO, ΔCCN/ΔCO, peak diameter (D_g), and lognormal modal width (σ_g) information for a subset of fire sizes (10^{-2}, 1, and 100 km^2) and background aerosol concentrations (0, 5, and 50 μg m^{-3}). We also provide these data for the base cases after 8 hours of aging (Figs D23-D24). The purpose of these cases is to provide an overview of expected shifts in smoke properties under varying chemical and atmospheric conditions as well as age. Note that all colorbars are held fixed to the colorbars used in the main text, expect for the 8 hours of aging figure.

As the accommodation coefficient α decreases (Figs. D9-D12), both the SOA mass uptake and evaporation rates decrease (Seinfeld & Pandis, 2006), leading to decreases in the total aged smoke mass, extinction cross section, and CCN for medium to small fires with low to moderate background aerosol concentrations for ChemOn cases; the largest fire modelled (100 km^2) is not significantly impacted by decreases in α due to the large condensation sink when the particles stay

concentrated in the large plume. Decreasing the rate of chemical reactions by using the lower-bound chemistry simulations with a two-bin drop in volatility per reaction with OH (Figs. D17-D18) decreases the rate at which lower volatility materials are formed, slowing SOA formation for all fire sizes. Fig. D18 (for D_g and σ_g) shows evidence that for the lower-bound chemistry simulations, when chemistry is on, the majority of the vapors that are oxidizing and condensing in the model are semivolatile, as σ_g does not decrease beyond the decrease caused by coagulation in the largest fire and only decreases slightly for the smaller fire sizes (as the growth rate of semivolatile vapors is proportional to particle diameter at all particle sizes; Sect S4).

Decreasing (increasing) the atmospheric stability increases (decreases) the rate of OA evaporation, as dilution rates will increase (decrease) with changing stability (Figs. D19-D22). Finally, extending the base cases from 4 to 8 hours (Figs. D23-D24) allows for more OA evaporation and SOA formation, leading to greater increases (ChemOn) or decreases (ChemOff) in smoke mass and E for all fire sizes and greater increases (ChemOn) in CCNfor fires small enough to not be impacted by coagulation.

While the aged normalized mass and extinction values tend to follow the trends seen for the base cases presented in the main text, the aged normalized CCN values are more variable. In general, the final ΔCCN/ΔCO values are quite sensitive to the relative increases in mass and decreases in σ_g as can be seen in the sensitivity cases (Figs. D13-D22). In cases that lead to smaller mass gains in the largest plumes (e.g. for the lower-bound chemistry assumption) or more stable atmospheric conditions (leading to slower dilution rates; the sensitivity case of a stability class of F), ΔCCN/ΔCO tends to decrease below the initial ΔCCN/ΔCO values in the largest fires, as coagulational losses exceed gains from diameter growth from SOA production (Figs. D15, D17, D21).

D6. Biomass burning field campaigns

Table D1 details many publications on biomass burning field studies that focused on the aging plume. This table is not intended to be a comprehensive overview of biomass burning studies but instead a large sampling of relevant work. Table D1 is organized alphabetically by campaign name and then first author (for studies not associated with named field campaigns).

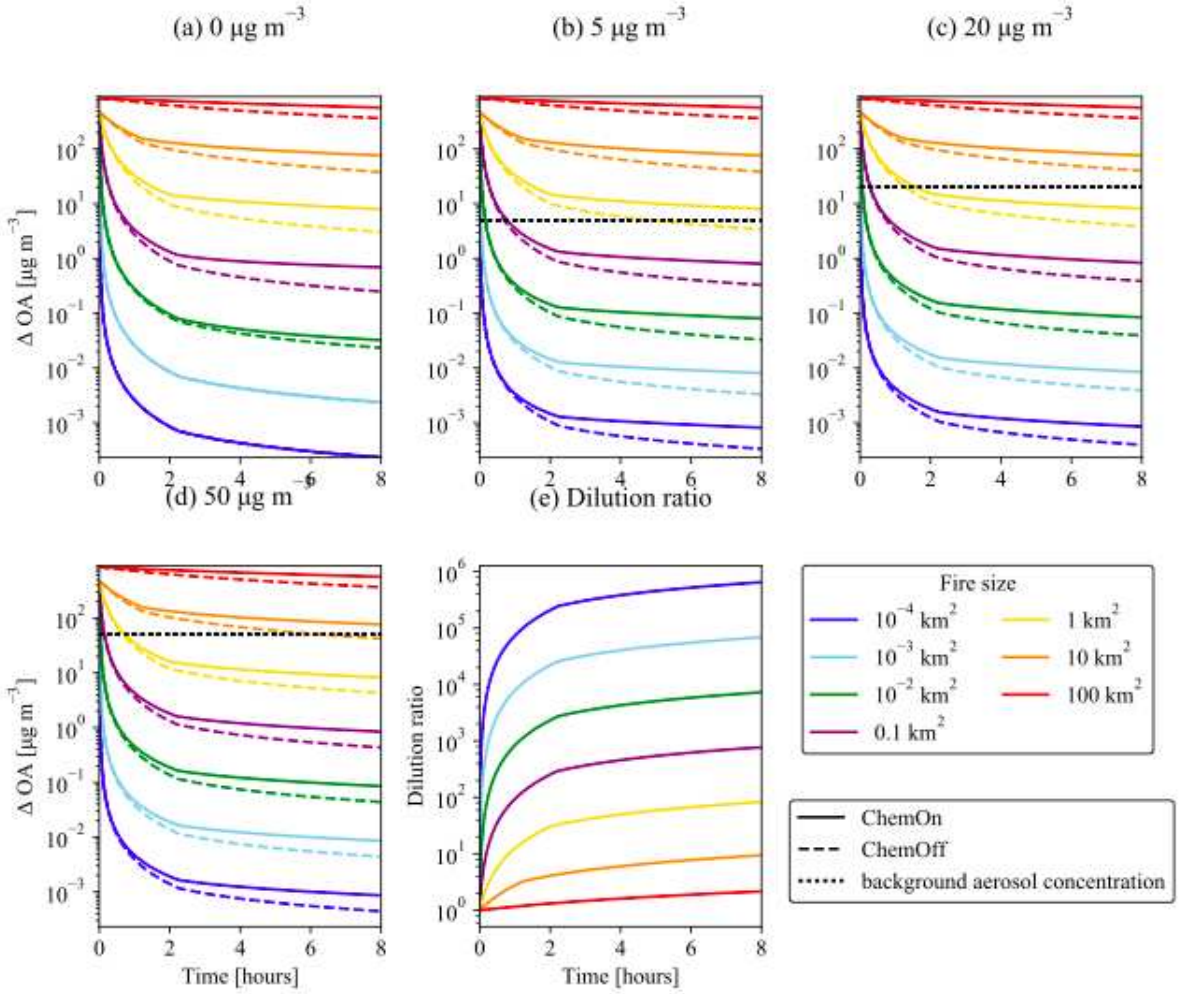

Figure D1. (a)-(d) Time evolution of total smoke organic aerosol mass concentration enhancement (background organic aerosol subtracted off) in the particle phase for chemistry-on (solid lines) and chemistry-off (dashed lines) simulations for the fire areas of 10^{-4}, 10^{-2}, 1, and 100 km^2 (colored lines) and background aerosol concentrations (black dashed lines) of (a) 0, (b) 5 μg m^{-3}, (c) 20 μg m^{-3}, and (d) 50 μg m^{-1}. (e) Time evolution of the dilution ratio for each fire size. Results are for the base simulations (Table 5.1) from the CoagOn version of each ChemOff/ChemOn case.

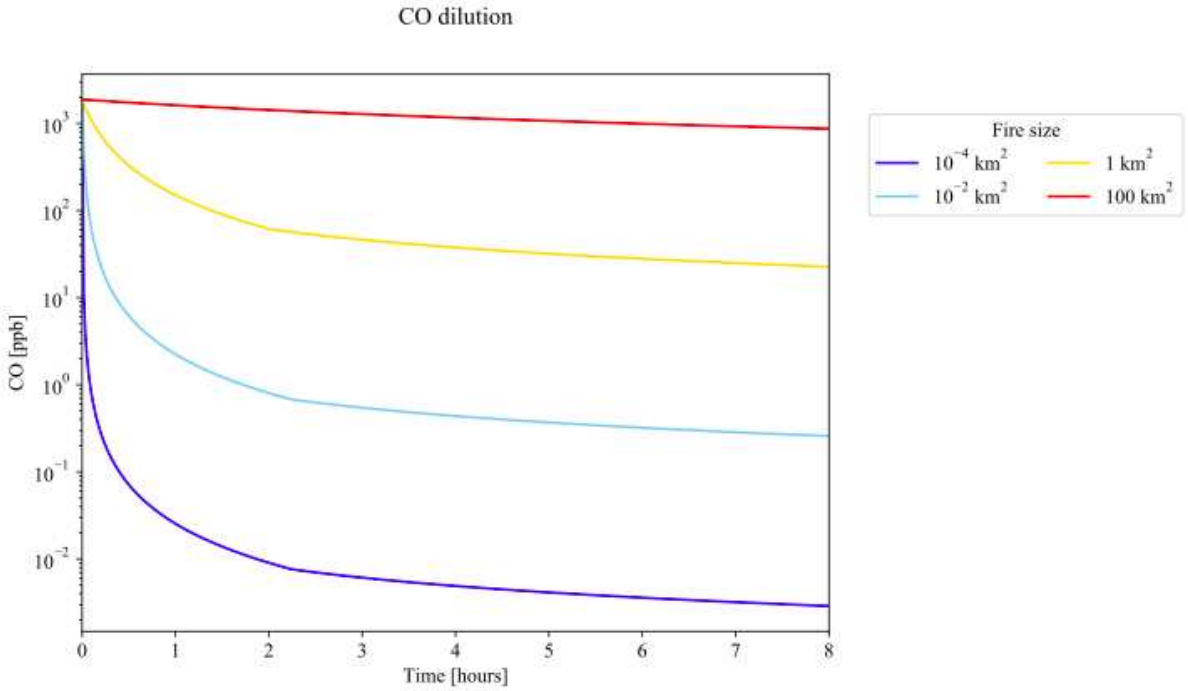

Figure D2. ΔCO dilution for each primary fire size for 8 hours of aging, using the assumptions of the base simulations (Table 5.1). ΔCO is not impacted by background aerosol concentration or the aerosol chemistry and coagulation model schemes.

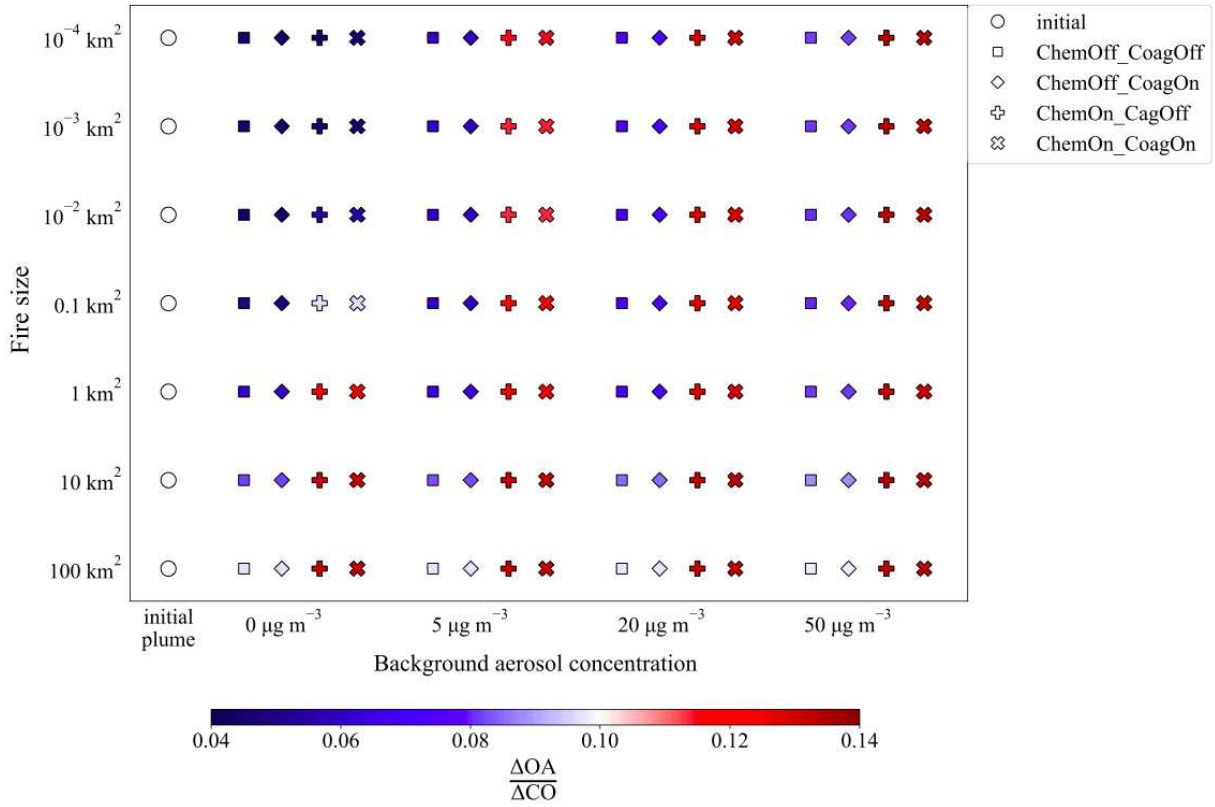

Figure D3. The in-plume normalized organic aerosol mass enhancement (ΔOA/ΔCO) initially and after 4 hours of aging for the ChemOff and ChemOn base cases (Table 1) for all fire sizes and background concentrations modelled. Warm colors indicate an increase in ΔOA/ΔCO after 4 hours of aging, and cool colors represent a decrease. The y axis represents fire size/dilution rate; the x axis represents the background aerosol concentration.

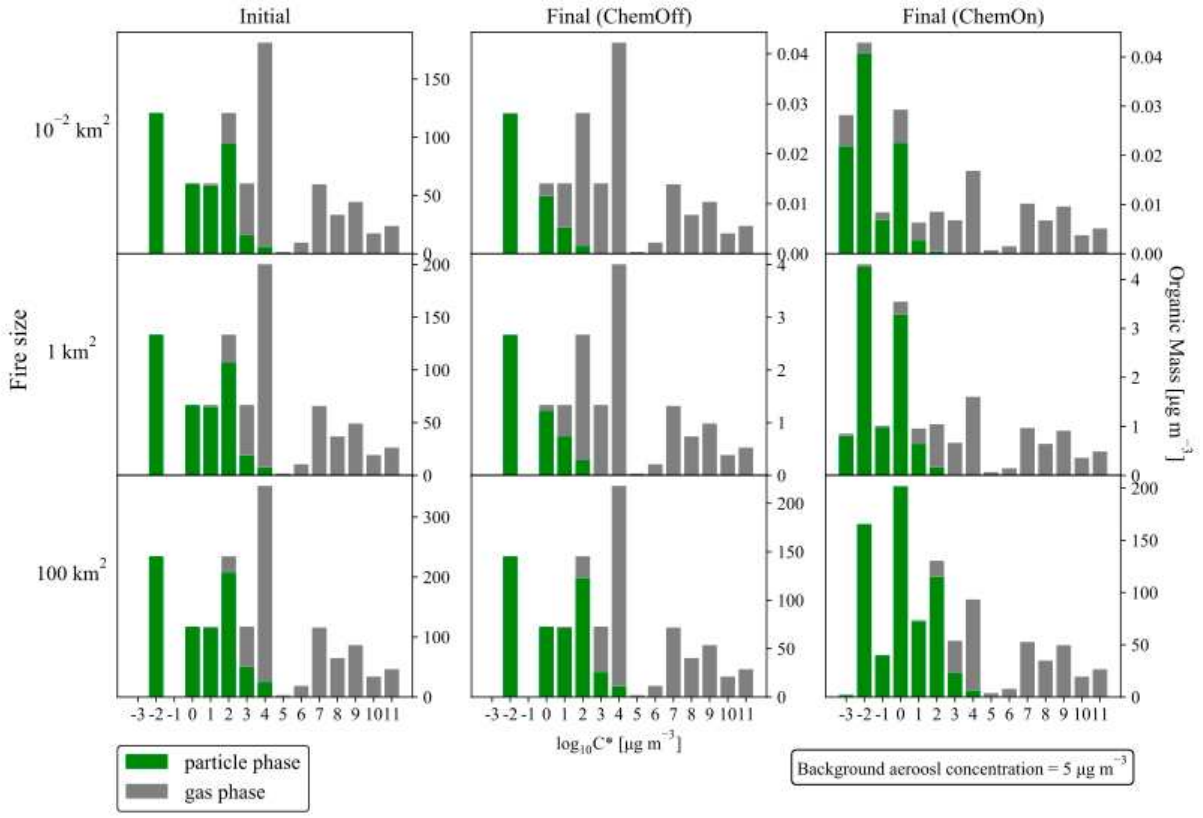

Figure D4. Initial (first column) and final (after 4 hours of aging) VBS distributions for the ChemOff (second column) and ChemOn (third column) base simulations for a background aerosol concentration of 5 µg m^{-3}. Particle phase loadings are in green and gas phase loadings are in grey (all in µg m^{-1}). We use the CoagOn version of each ChemOff/ChemOn case. Shown are fire sizes 10^{-2} km^2 (top row), 1 km^2 (second row), and 100 km^2 (bottom row). The highest volatility bins undergo very little aging as only a small fraction of the material in these bins oxidizes under the k_{OH} parameterization used.

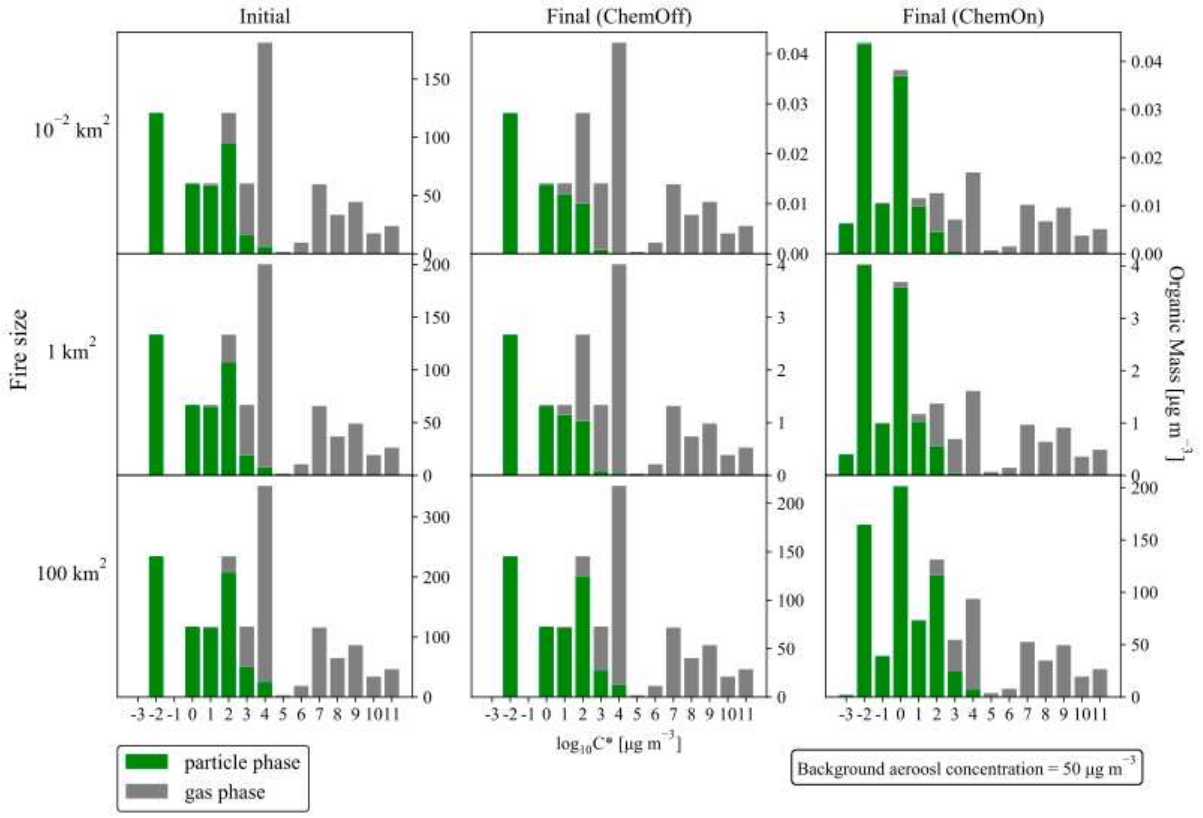

Figure D5. Initial (first column) and final (after 4 hours of aging) VBS distributions for the ChemOff (second column) and ChemOn (third column) base simulations for a background aerosol concentration of 50 µg m^{-3}. Particle phase loadings are in green and gas phase loadings are in grey (all in µg m^{-1}). We use the CoagOn version of each ChemOff/ChemOn case. Shown are fire sizes 10^{-2} km^2 (top row), 1 km^2 (second row), and 100 km^2 (bottom row). The highest volatility bins undergo very little aging as only a small fraction of the material in these bins oxidizes under the k_{OH} parameterization used.

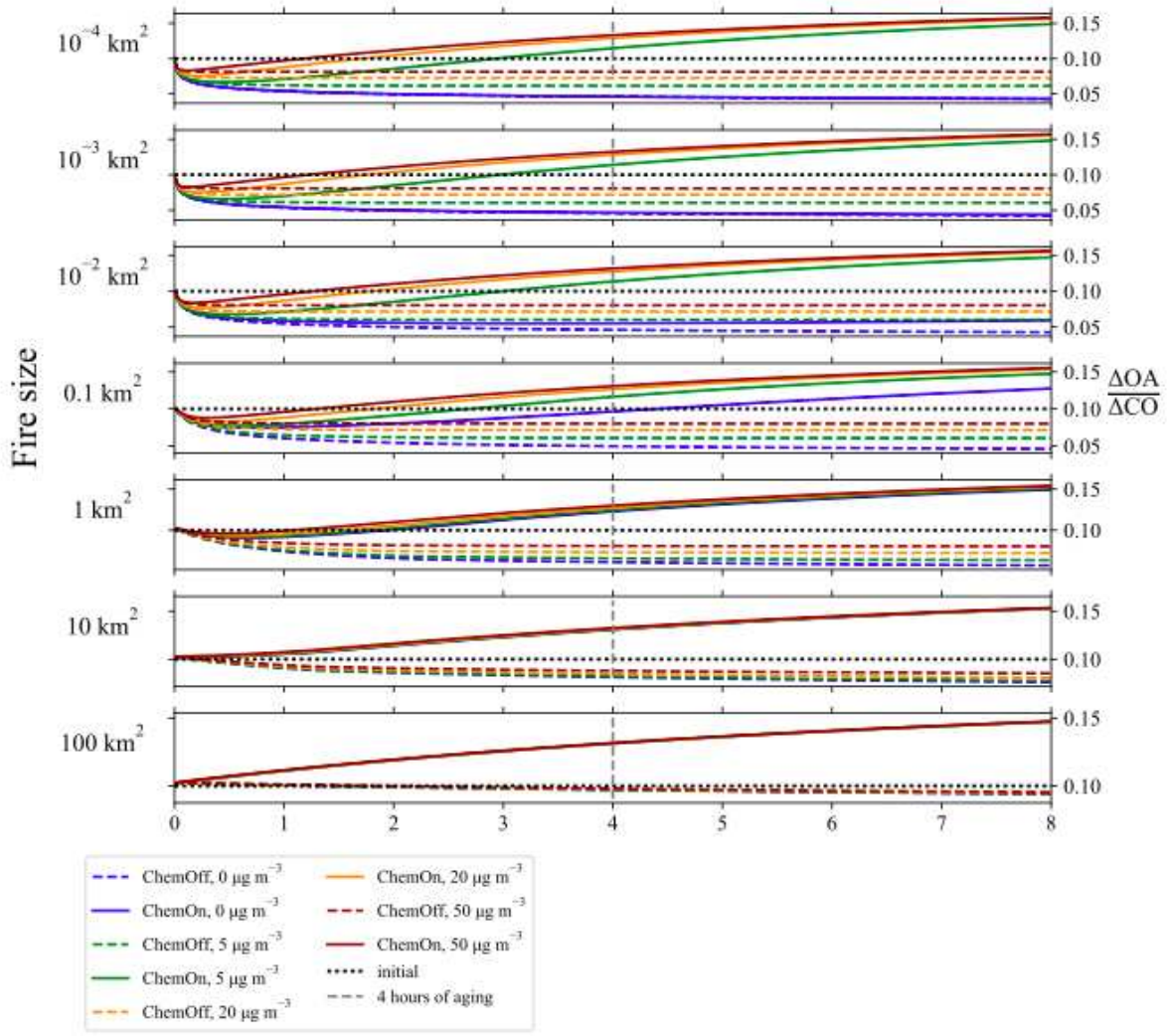

Figure D6. ΔOA/ΔCO for the base cases (Table 5.1). The vertical grey dashed line is set to 4 hours to guide the eye, as the majority of analyses in this study is done for 4 hours of aging in the model. The initial line in each plot is also to guide the eye: cases that go above the initial line indicate a net normalized gain in mass and cases that go below the initial line indicate a net normalized loss in mass.

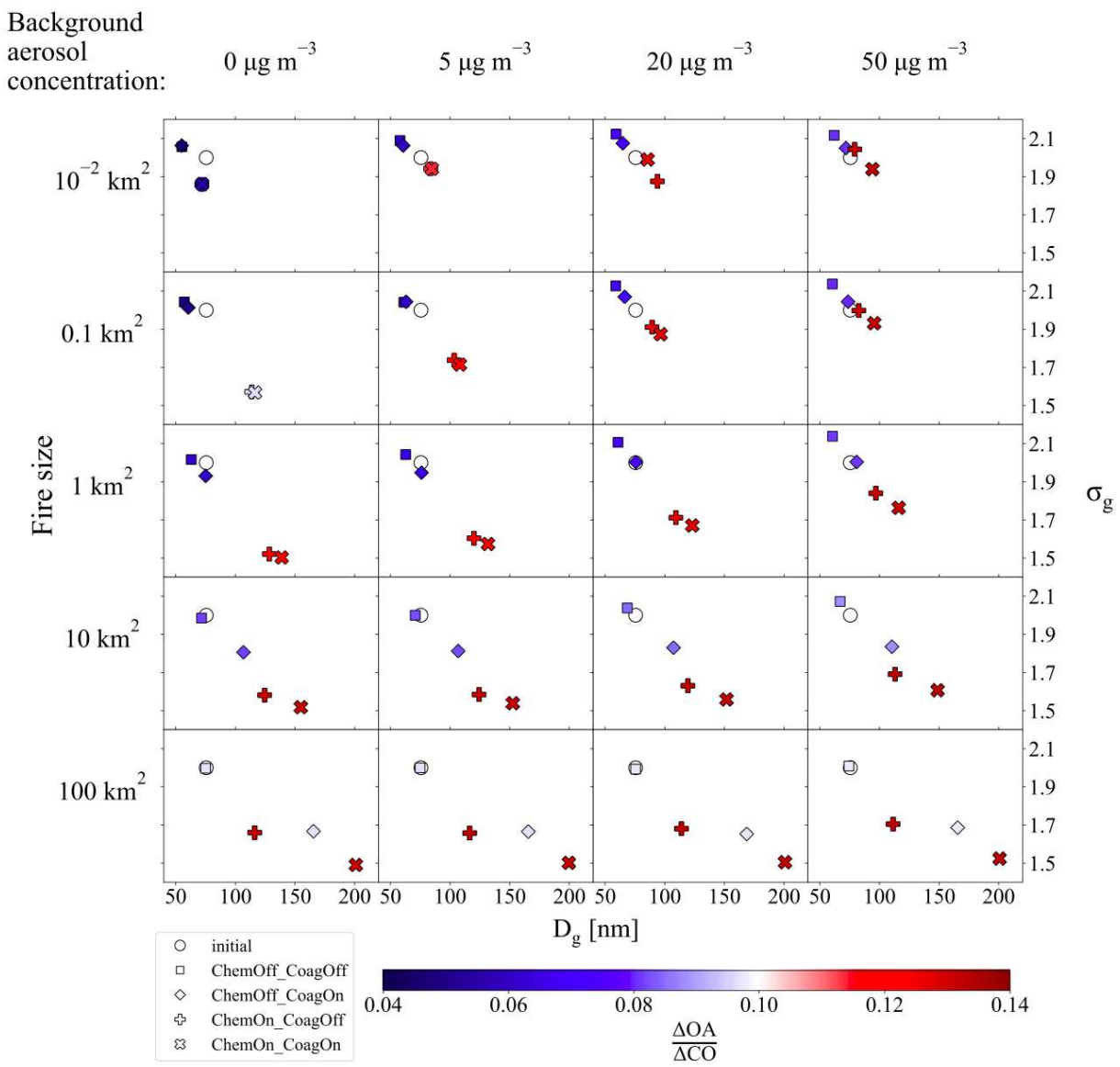

Figure D7. Smoke (background corrected) lognormal median diameter of the lognormal mode (D_g; x axis) and lognormal modal width (σ_g; y axis) after 4 hours of aging for the base cases (Table 1) for all fire sizes between 10^{-2}-100 km^2 and all background aerosol concentrations modelled.. The colorbar is ΔOA/ΔCO initially and after 4 hours of aging for the base cases (same colorbar as Fig D2). The ChemOff_CoagOn case for the 10^{-2} km^2 fire with a 20 μg m^{-3} background was removed due to model noise; for more detail, see Sect. D2.

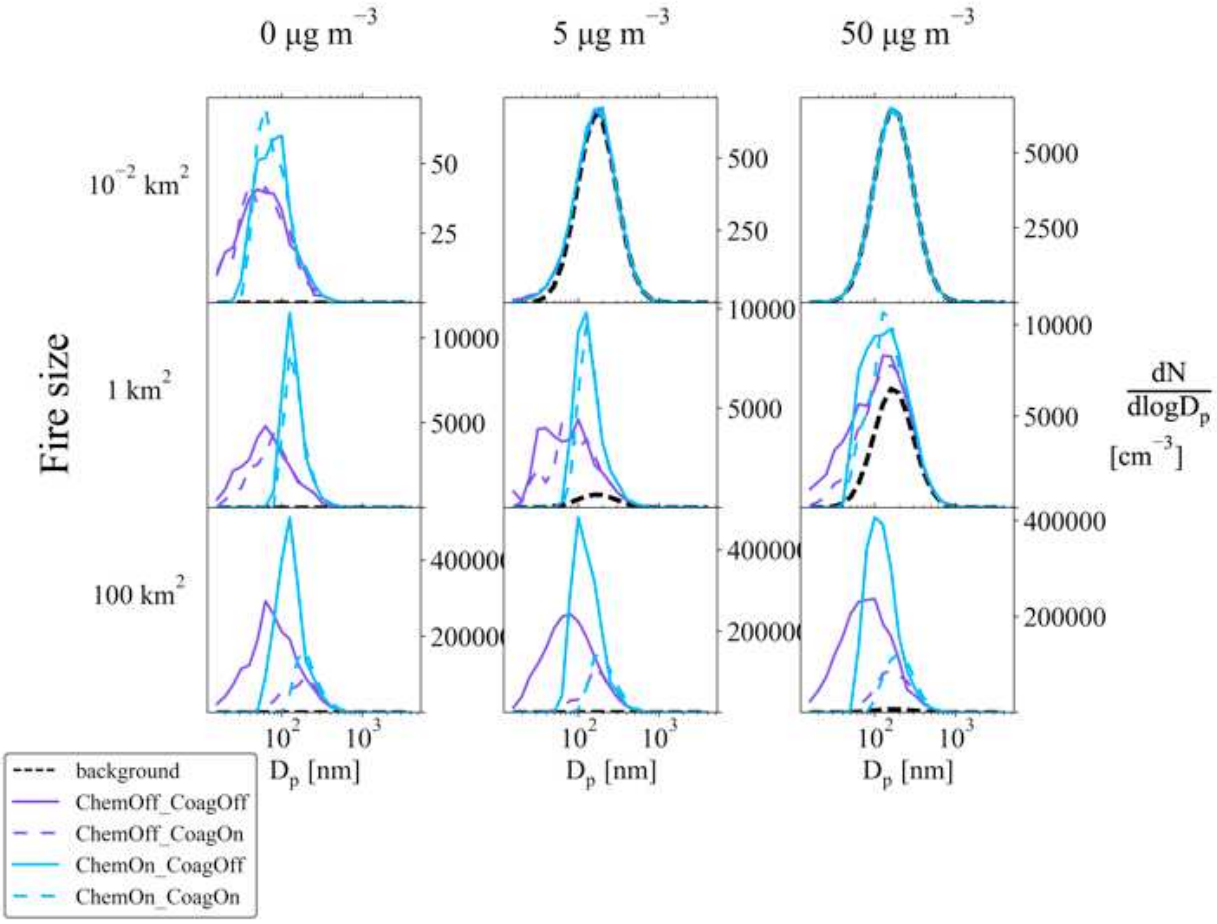

Figure D8. Final number size distributions for the base cases (Table 5.1) after 4 hours of aging. Shown are 10^{-2} km^2 (top row), 1 km^2 (middle row), and 100 km^2 (bottom row)-sized fires with background concentrations of 0 (first column), 5 (second column), and 50 (final column) μg m^{-3}. The colored lines show the combined plume and background size distributions; the black dashed line shows the background alone. The 100 km^2 fires are large enough above background that the background distribution appears close to zero. The 10^{-2} km^2 fire dilutes and evaporates down to essentially the background distribution for the 50 μg m^{-3} case. The distributions were smoothed as described in Sect. D2.

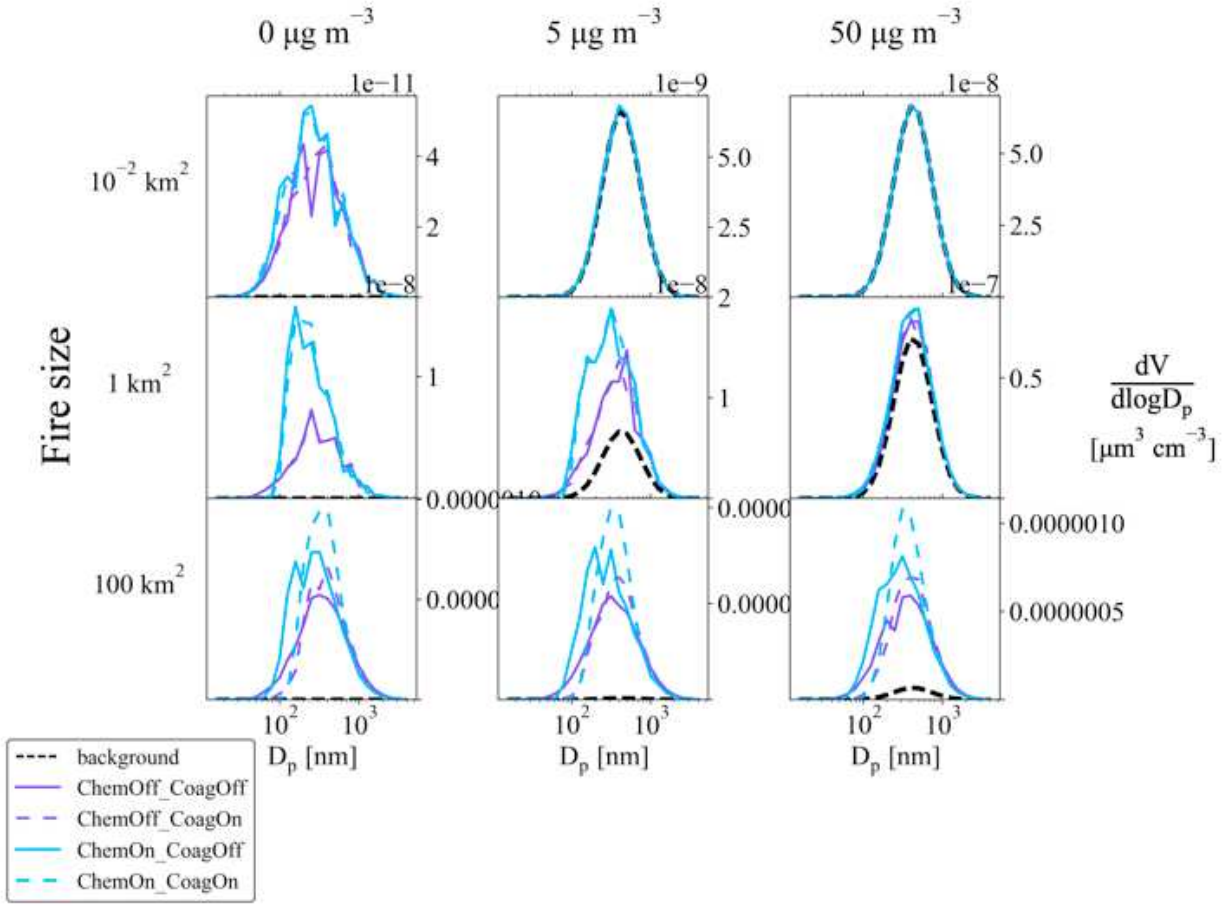

Figure D9. Final volume size distributions for the base cases (Table 1) after 4 hours of aging. Shown are 10^{-2} km^2 (top row), 1 km^2 (middle row), and 100 km^2 (bottom row)-sized fires with background concentrations of 0 (first column), 5 (second column), and 50 (final column) µg m^{-3}. The colored lines show the combined plume and background size distributions; the black dashed line shows the background alone. The 100 km^2 fires are large enough above background that the background distribution appears close to zero. The 10^{-2} km^2 fire dilutes and evaporates down to essentially the background distribution for the 50 µg m^{-3} case. The distributions were smoothed as described in Sect. D2.

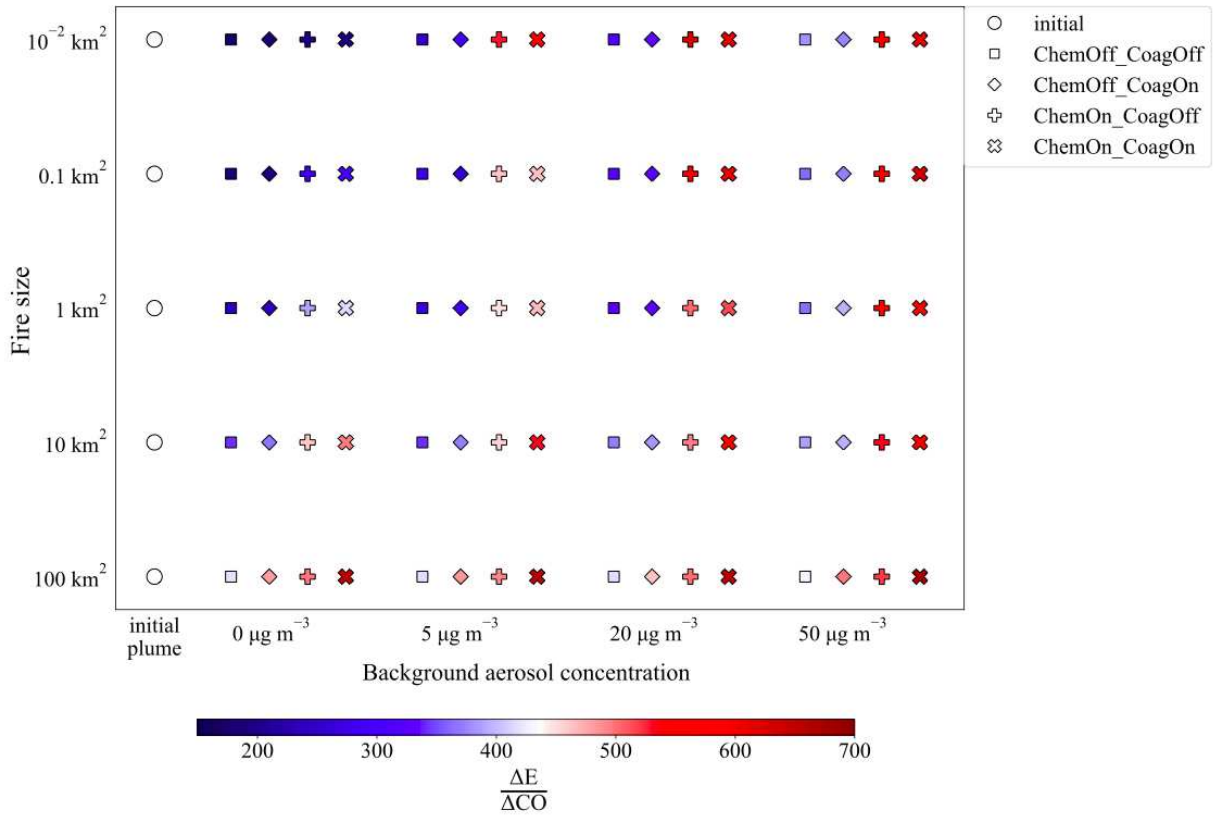

Figure D10. The normalized extinction efficiency ($\Delta E/\Delta CO$) initially and after 4 hours of aging for the primary cases (Table 1) for all fire sizes between 10^{-2}-100 km^2 and all background aerosol concentrations modelled. For this study, we assume spherical particles with a refractive index of 1.5 - 0.08*i* at a wavelength of 500 nm. Warm colors indicate an increase in the normalized values while cool colors represent a decrease.The y axis represents fire size/dilution rate; the x axis represents the background aerosol concentration.

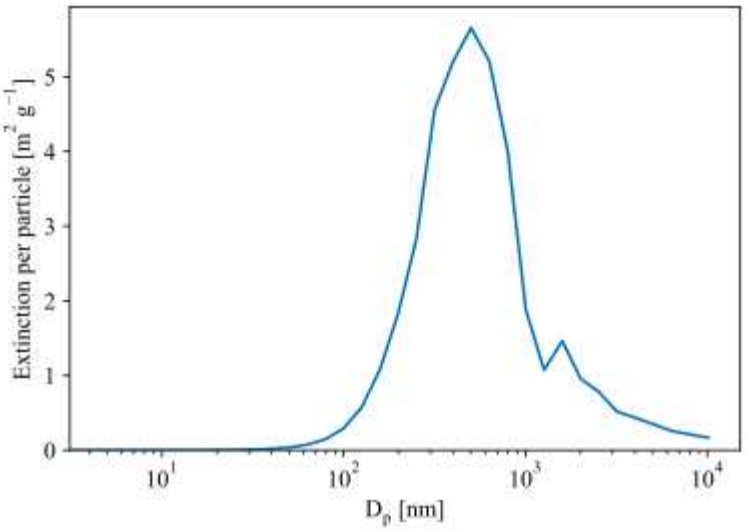

.

Figure D11. Size dependent mass extinction efficiency for a refractive index of 1.5 - 0.08*i* (assuming spherical particles) at a wavelength of 500 nm. The peak scattering efficiency is at ~500 nm.

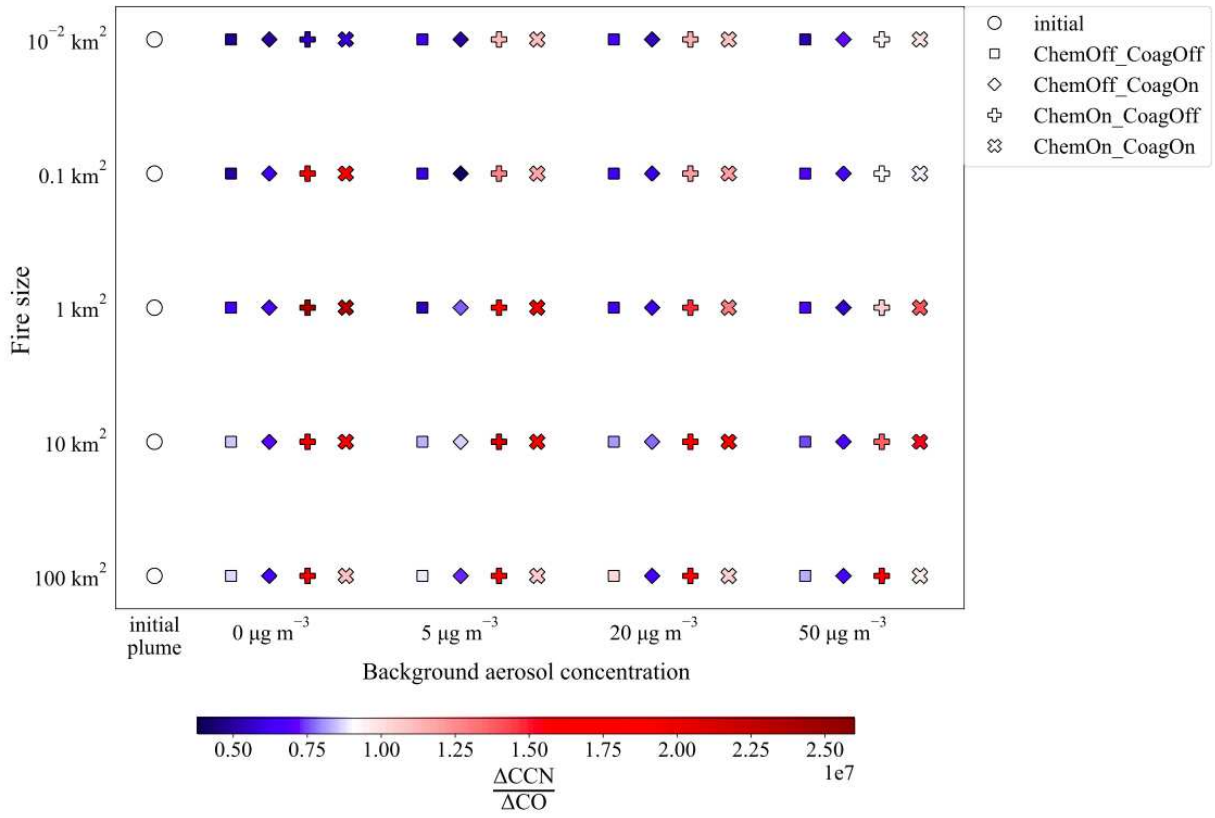

Figure D12. The normalized CCN (ΔCCN/ΔCO) initially and after 4 hours of aging for the primary cases (Table 1) for all fire sizes between 10^{-2}-100 km^2 and all background aerosol concentrations modelled. For this study, we assume spherical particles with a refractive index of 1.5 - 0.08*i* at a wavelength of 500 nm. Warm colors indicate an increase in the normalized values while cool colors represent a decrease. The y axis represents fire size/dilution rate; the x axis represents the background aerosol concentration.

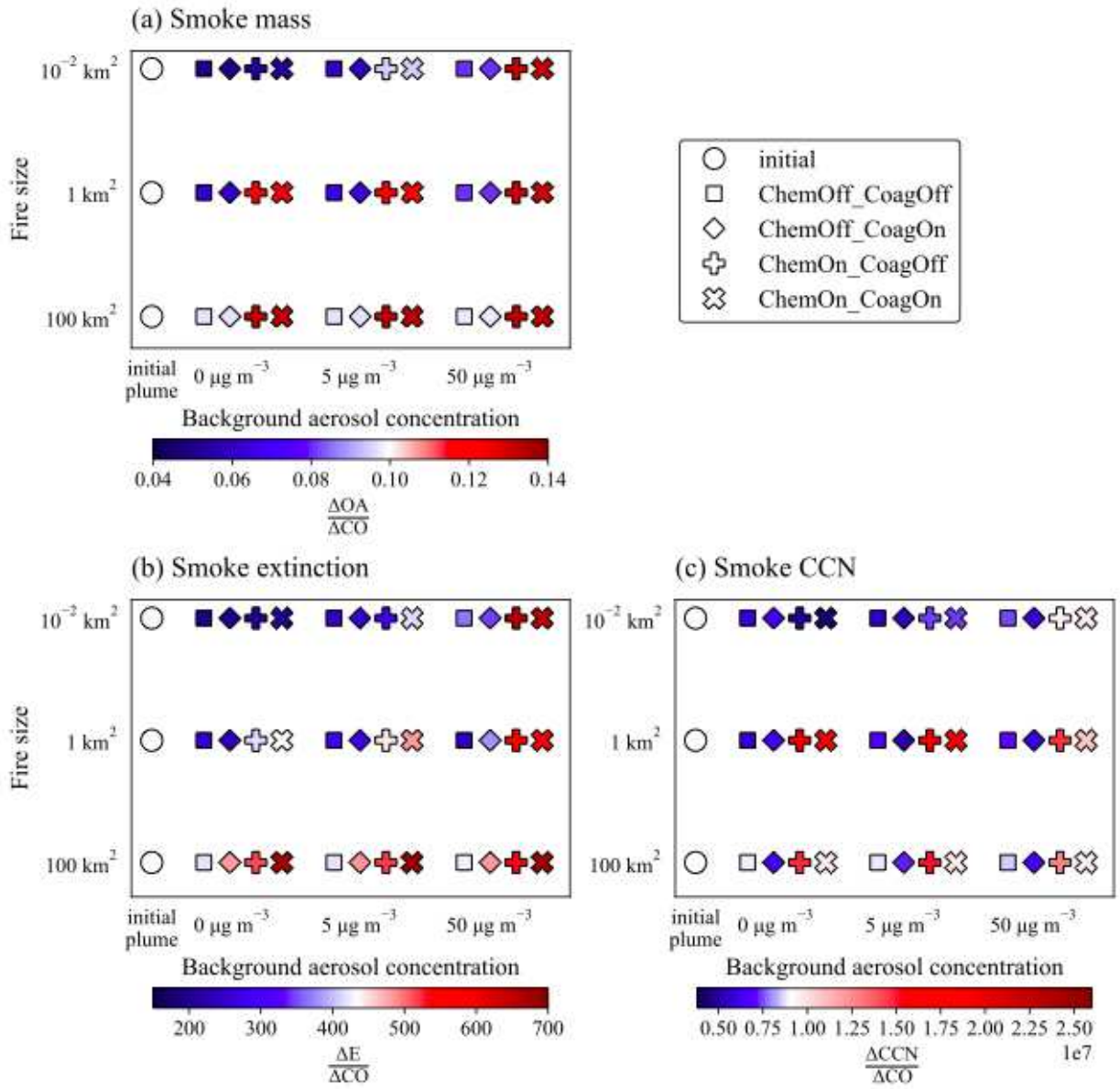

Figure D13. Sensitivity case: accommodation coefficient (α) of 0.1. (a) The in-plume normalized organic aerosol mass enhancement (ΔOA/ΔCO) initially and after 4 hours of aging. (b) The normalized extinction efficiency (Δ*E*/ΔCO) initially and after 4 hours of aging. (c) The normalized CCN (ΔCCN/ΔCO) from smoke aerosol at 0.2% supersaturation initially and after 4 hours of aging. Warm colors indicate an increase in the normalized values while cool colors represent a decrease.

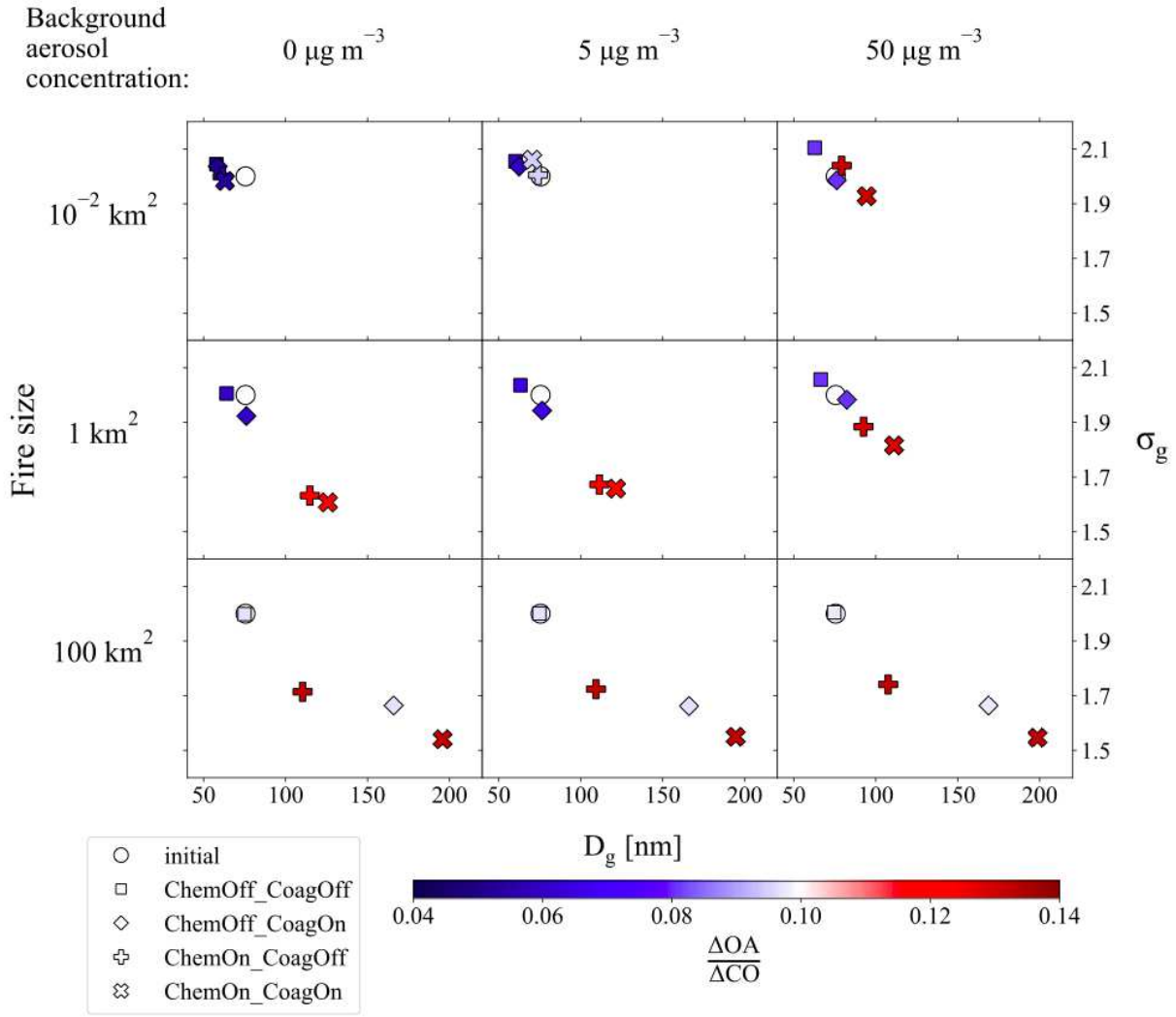

Figure D14. Sensitivity case: accommodation coefficient (α) of 0.1. Smoke (background corrected) lognormal median diameter of the lognormal mode (D_g; x axis) and lognormal modal width (σ_g; y axis) initially and after 4 hours. The colorbar is ΔOA/ΔCO initially and after 4 hours of aging for the base cases (same colorbar as Fig. D12).

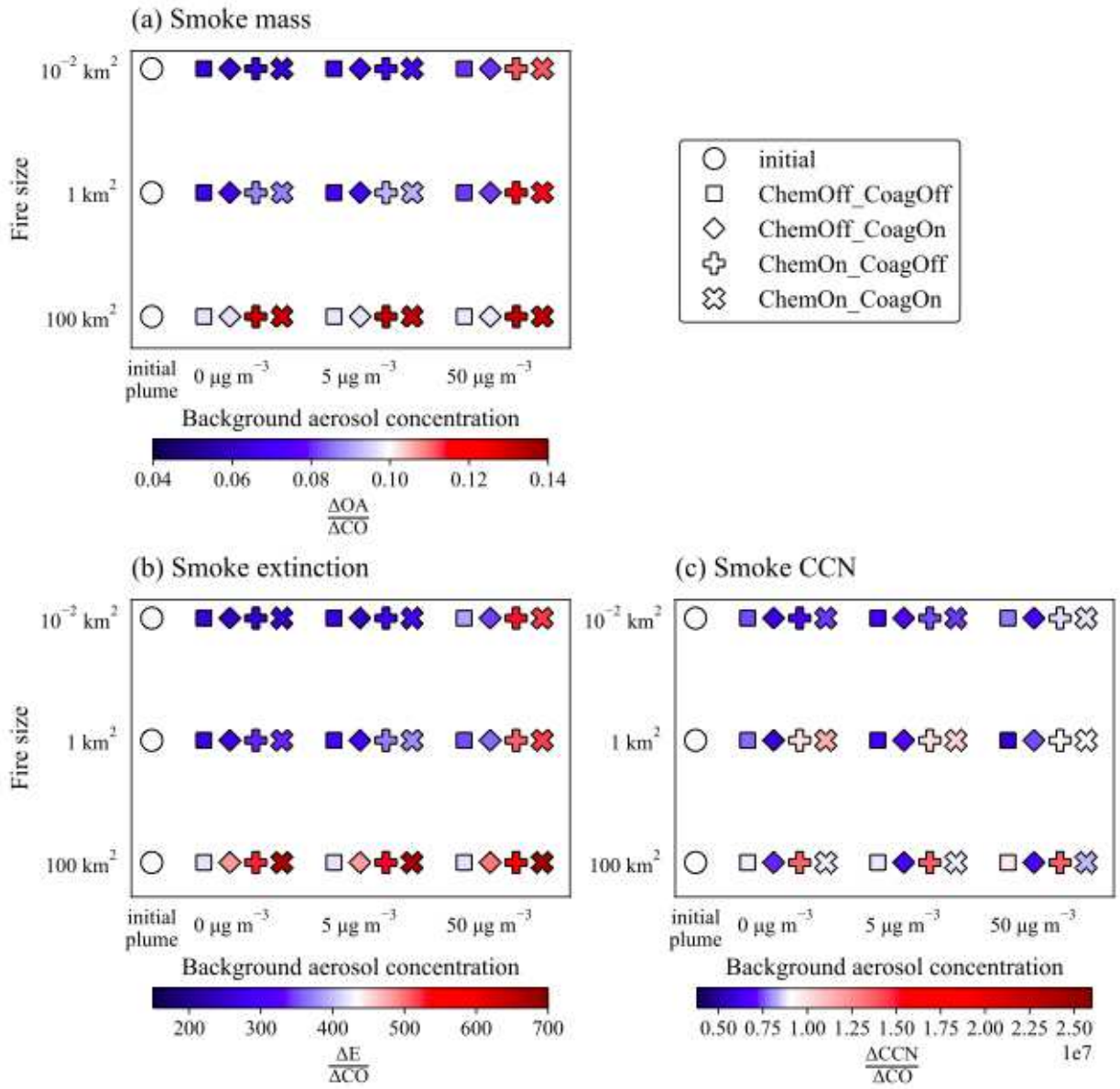

Figure D15. Sensitivity case: accommodation coefficient (α) of 0.01. (a) The in-plume normalized organic aerosol mass enhancement (ΔOA/ΔCO) initially and after 4 hours of aging. (b) The normalized extinction efficiency (ΔE/ΔCO) initially and after 4 hours of aging. (c) The normalized CCN (ΔCCN/ΔCO) from smoke aerosol at 0.2% supersaturation initially and after 4 hours of aging. Warm colors indicate an increase in the normalized values while cool colors represent a decrease.

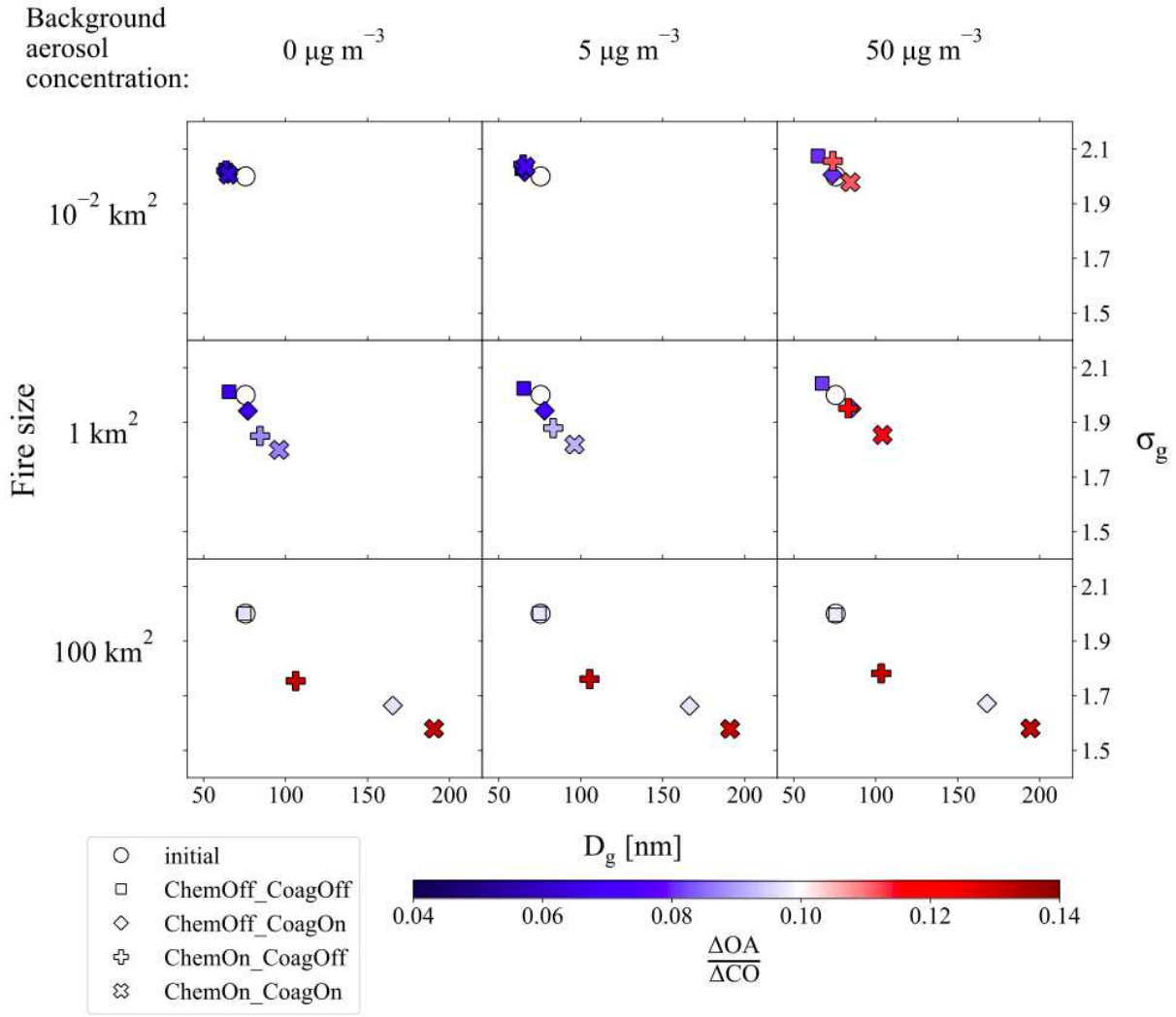

Figure D16. Sensitivity case: accommodation coefficient (α) of 0.01. Smoke (background corrected) lognormal median diameter of the lognormal mode (D_g; x axis) and lognormal modal width (σ_g; y axis) initially and after 4 hours. The colorbar is ΔOA/ΔCO initially and after 4 hours of aging for the base cases (same colorbar as Fig. D14).

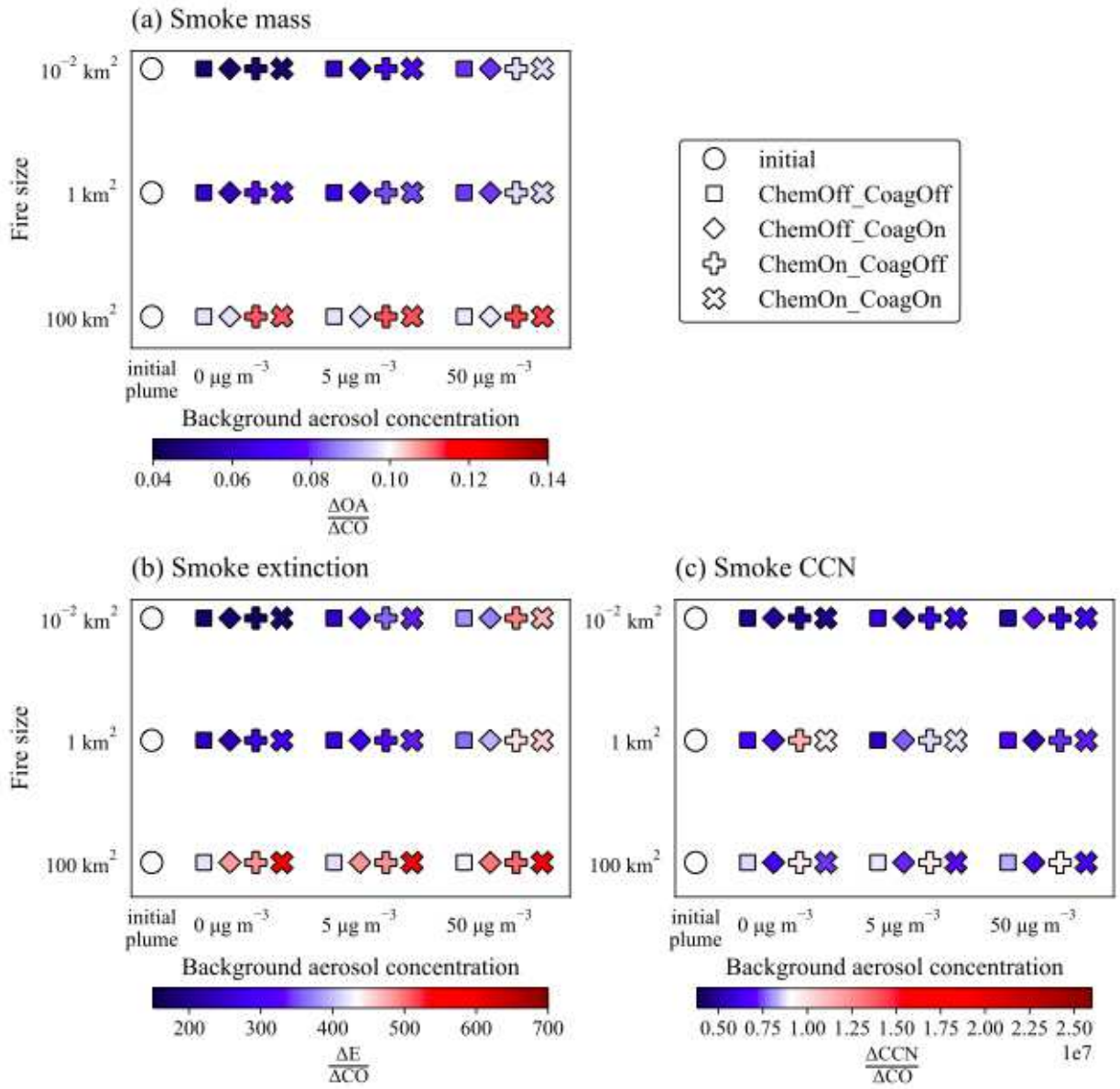

Figure D17. Sensitivity case: chemical production rate, using the rate of reaction with alkanes (Jathar et al., 2014) and a two-bin volatility drop. (a) The in-plume normalized organic aerosol mass enhancement (ΔOA/ΔCO) initially and after 4 hours of aging. (b) The normalized extinction efficiency (Δ*E*/ΔCO) initially and after 4 hours of aging. (c) The normalized CCN (ΔCCN/ΔCO) from smoke aerosol at 0.2% supersaturation initially and after 4 hours of aging. Warm colors indicate an increase in the normalized values while cool colors represent a decrease.

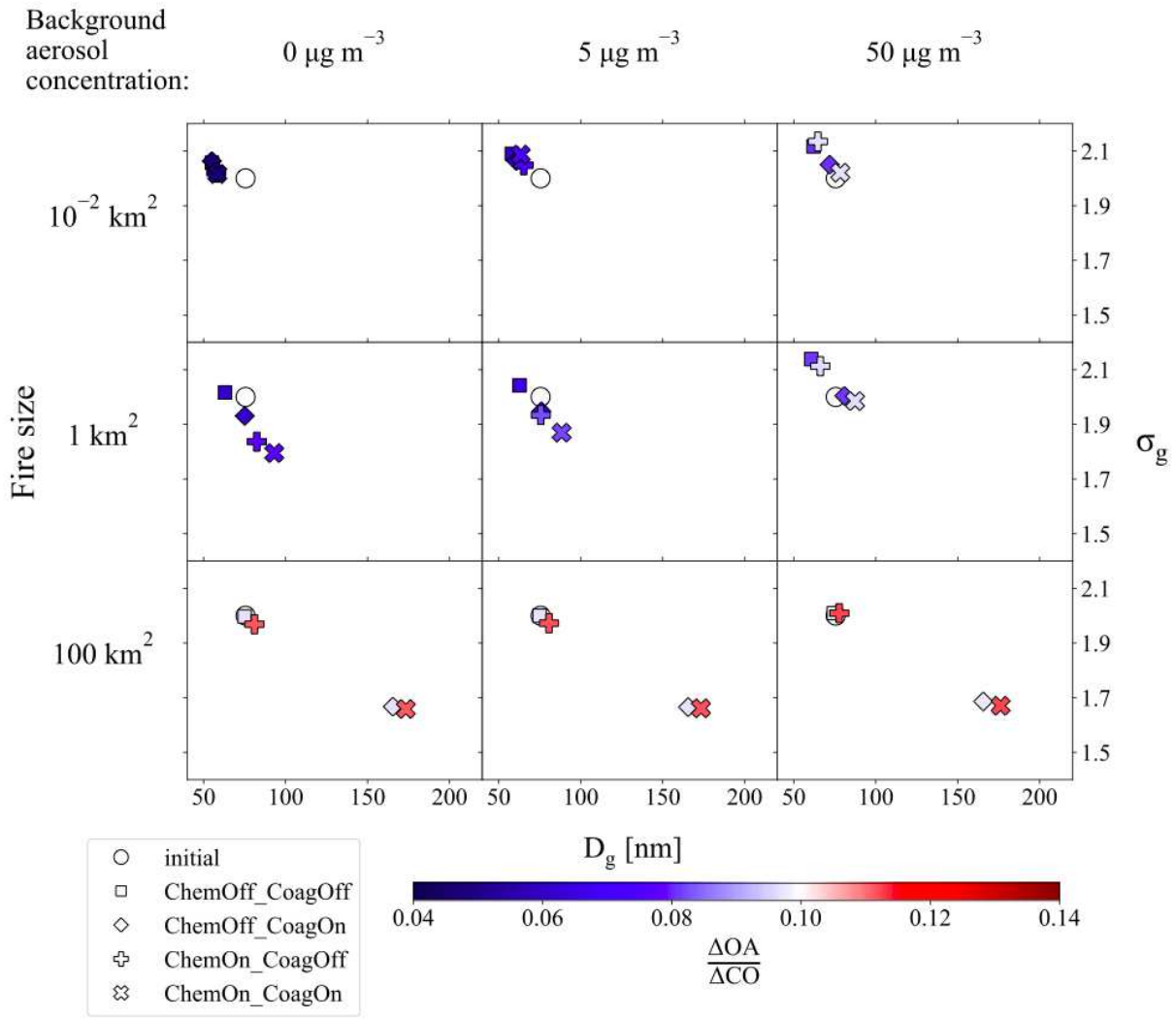

Figure D18. Sensitivity case: chemical production rate, using the rate of reaction with alkanes (Jathar et al., 2014) and a two-bin volatility drop. Smoke (background corrected) lognormal median diameter of the lognormal mode (D_g; x axis) and lognormal modal width (σ_g; y axis) initially and after 4 hours. The colorbar is ΔOA/ΔCO initially and after 4 hours of aging for the base cases (same colorbar as Fig. D16).

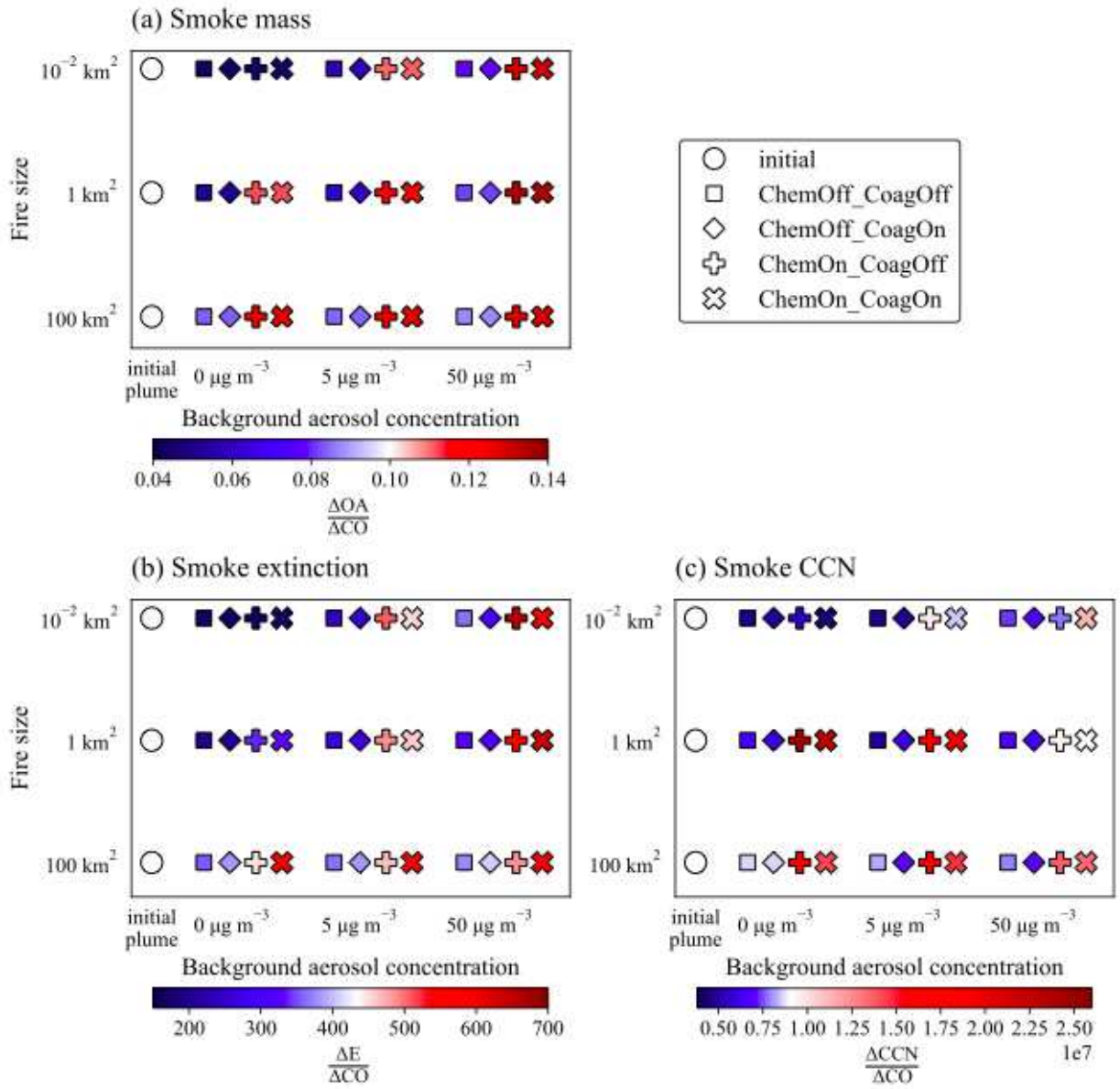

Figure D19. Sensitivity case: stability class of B. (a) The in-plume normalized organic aerosol mass enhancement (ΔOA/ΔCO) initially and after 4 hours of aging. (b) The normalized extinction efficiency (Δ*E*/ΔCO) initially and after 4 hours of aging. (c) The normalized CCN (ΔCCN/ΔCO) from smoke aerosol at 0.2% supersaturation initially and after 4 hours of aging. Warm colors indicate an increase in the normalized values while cool colors represent a decrease.The value for the ChemOn_CoagOFF case for E_{smoke} for the 10^{-2} fire size with a 50 µg m^{-3} background concentration has been removed due to model noise; see Sect. D2 for more details.

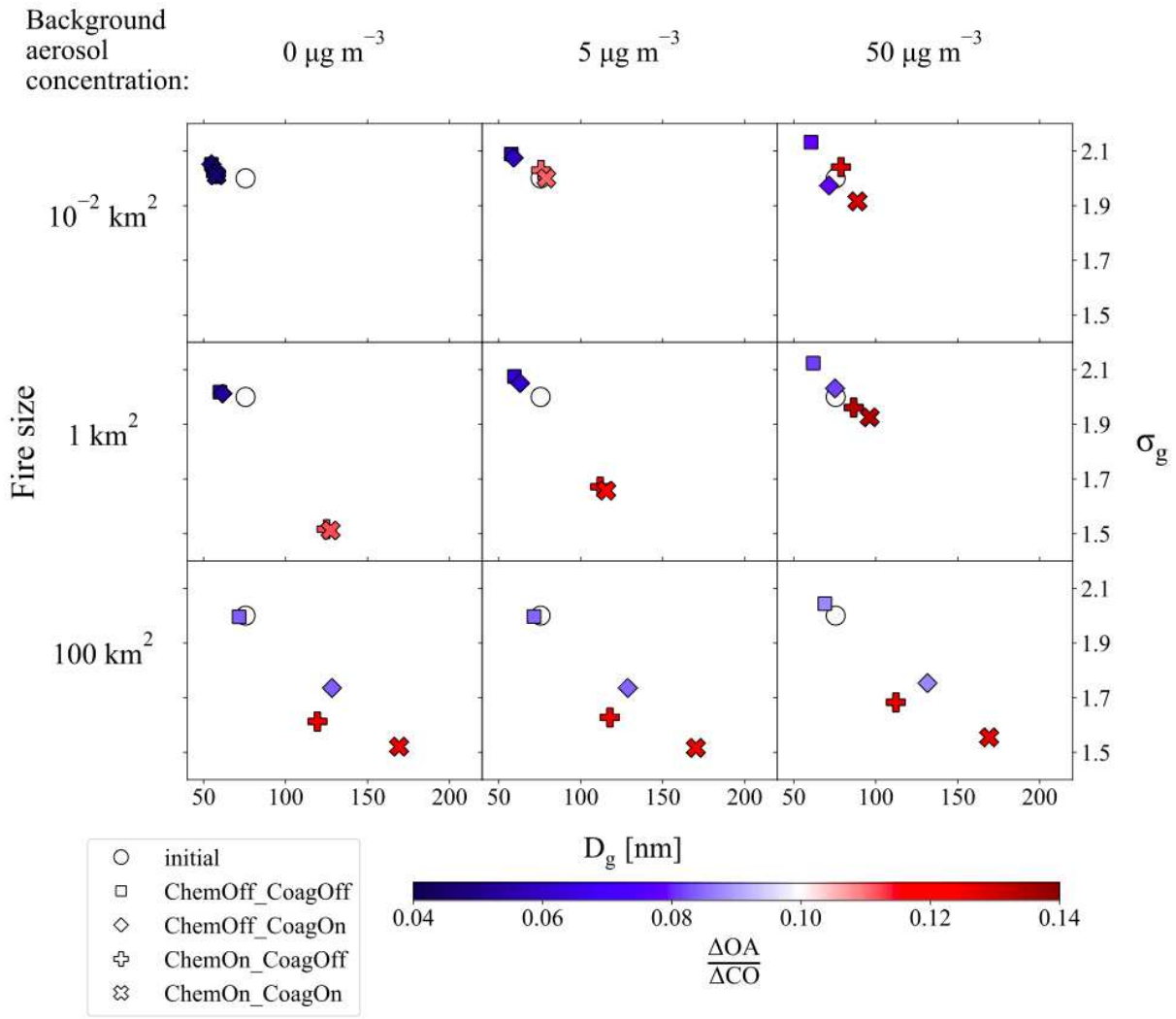

Figure D20. Sensitivity case: stability class of B. Smoke (background corrected) lognormal median diameter of the lognormal mode (D_g; x axis) and lognormal modal width (σ_g; y axis) initially and after 4 hours. The colorbar is ΔOA/ΔCO initially and after 4 hours of aging for the base cases (same colorbar as Fig. D19).

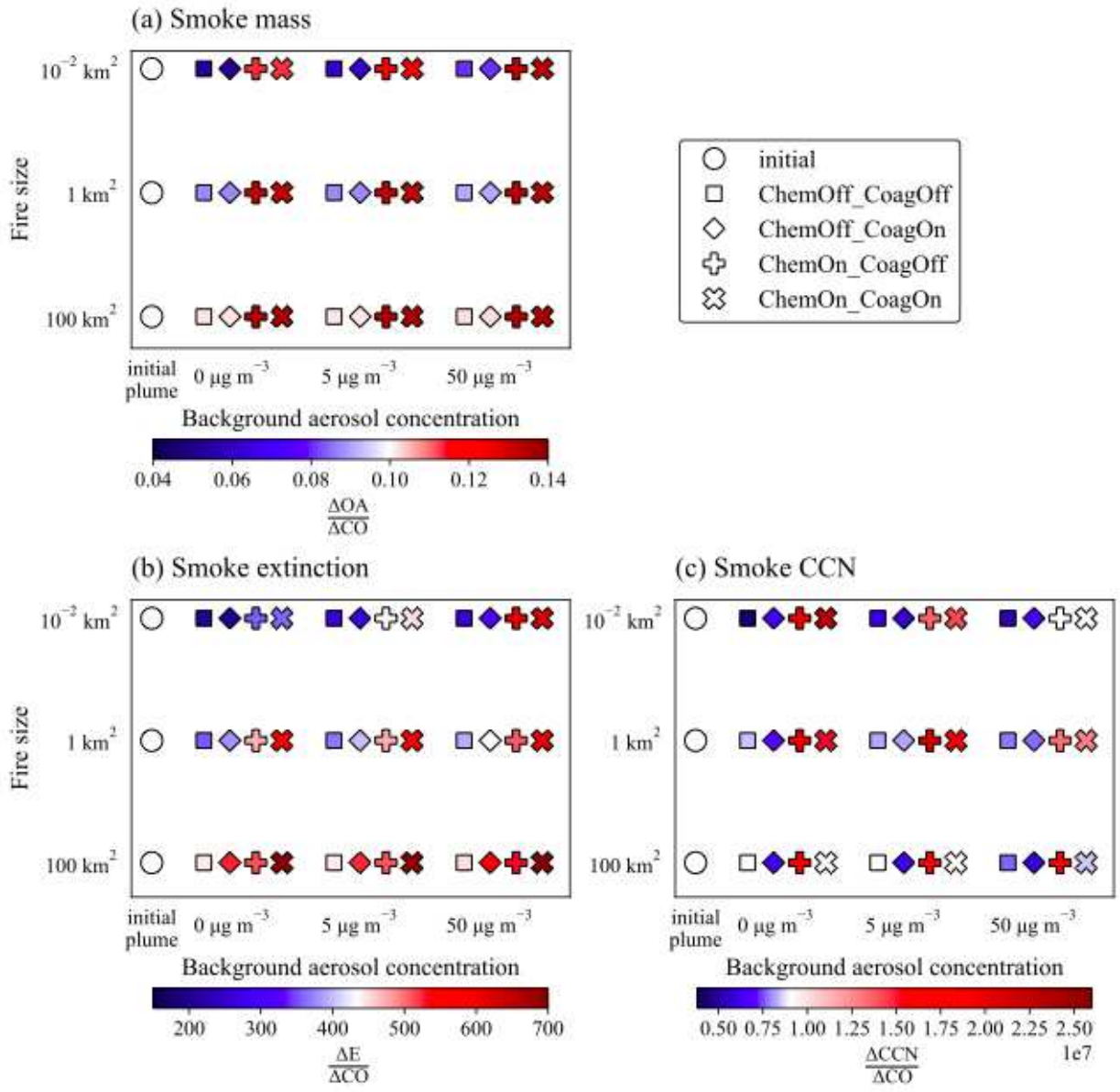

Figure D21. Sensitivity case: stability class of F. (a) The in-plume normalized organic aerosol mass enhancement (ΔOA/ΔCO) initially and after 4 hours of aging. (b) The normalized extinction efficiency (Δ*E*/ΔCO) initially and after 4 hours of aging. (c) The normalized CCN (ΔCCN/ΔCO) from smoke aerosol at 0.2% supersaturation initially and after 4 hours of aging. Warm colors indicate an increase in the normalized values while cool colors represent a decrease.

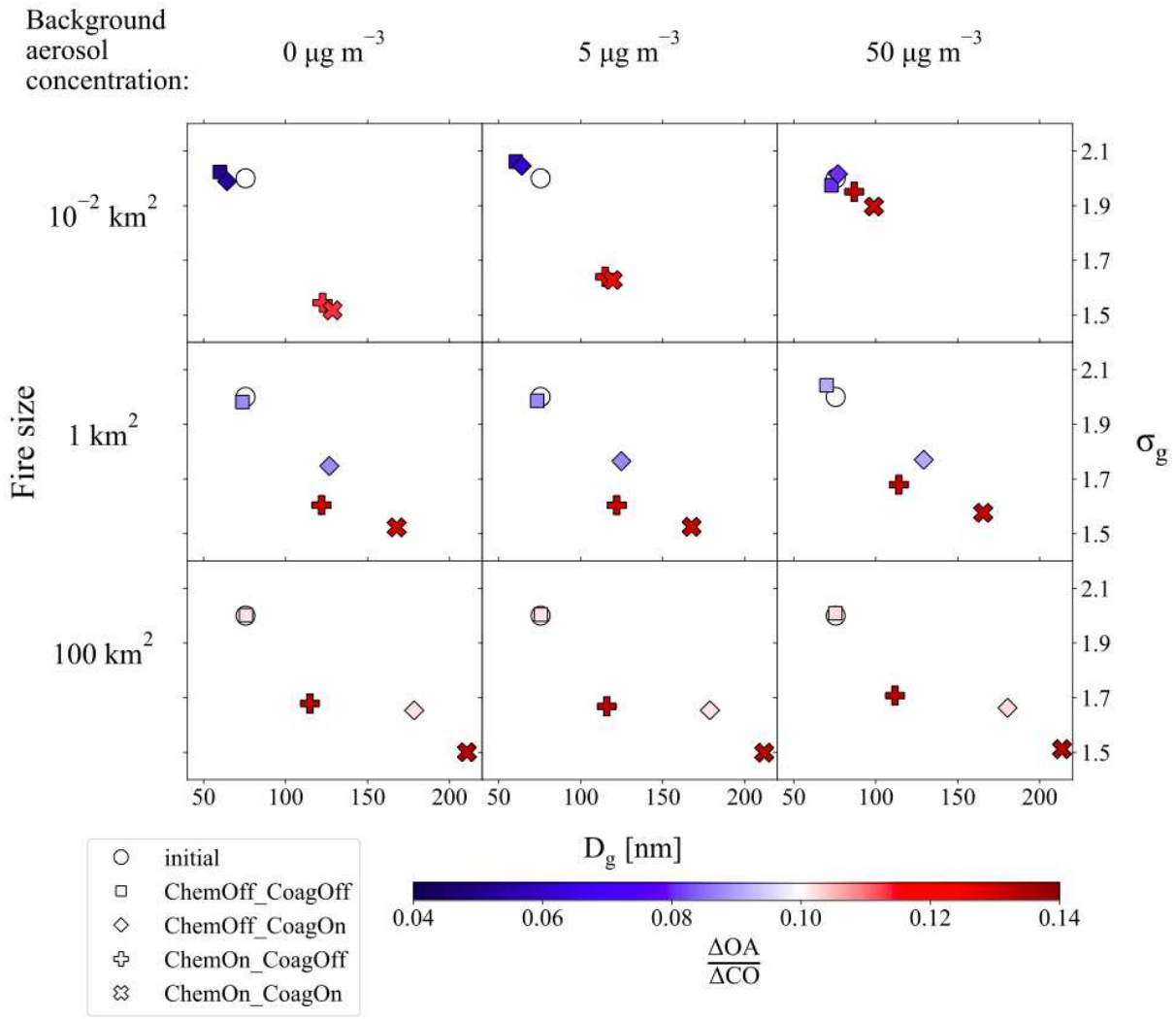

Figure D22. Sensitivity case: stability class of F. Smoke (background corrected) lognormal median diameter of the lognormal mode (D_g; x axis) and lognormal modal width (σ_g; y axis) initially and after 4 hours. The colorbar is ΔOA/ΔCO initially and after 4 hours of aging for the base cases (same colorbar as Fig. D21).

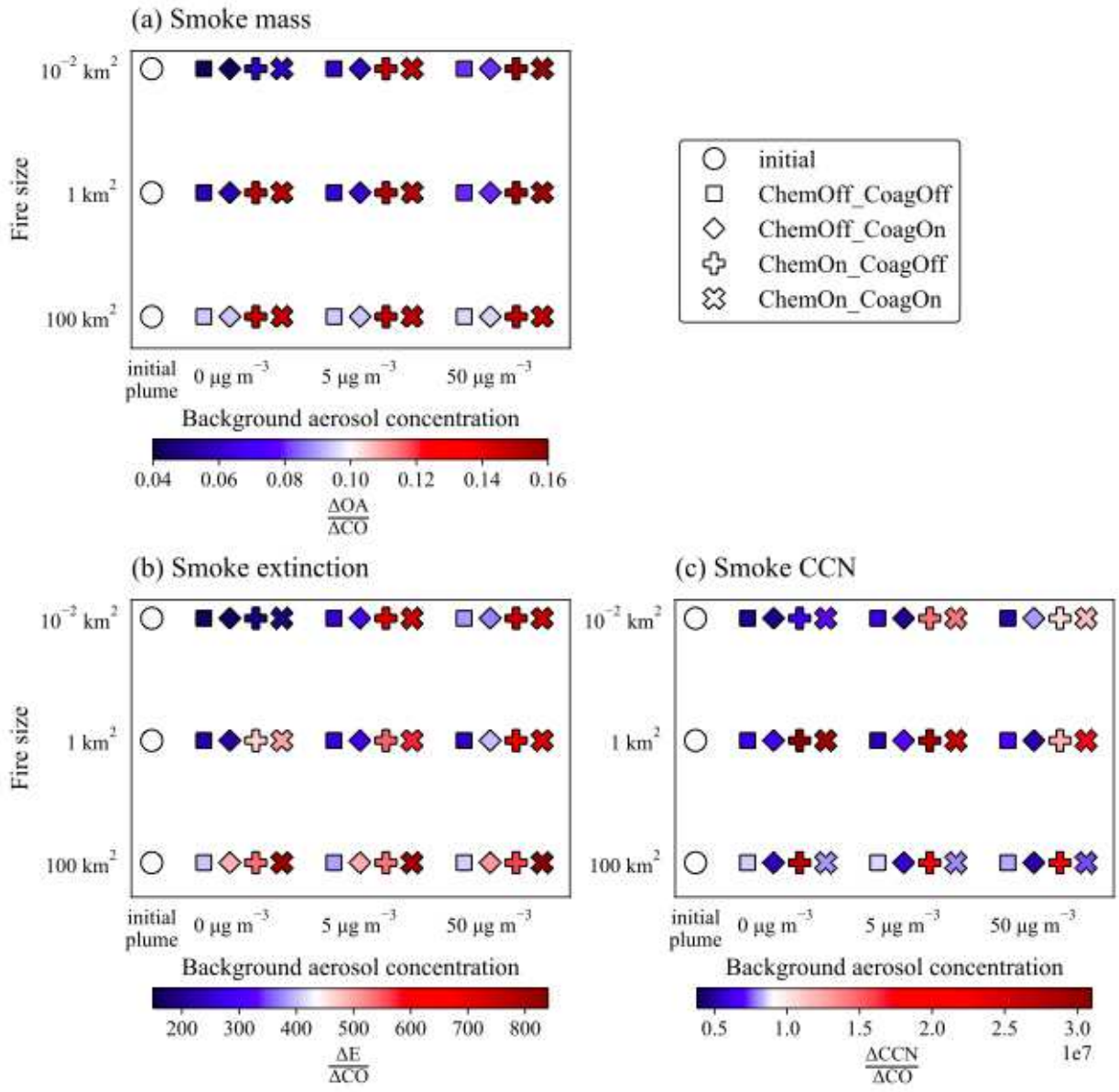

Figure D23. Sensitivity case: aging for 8 hours, using the model settings of the primary cases (Table 1). (a) The in-plume normalized organic aerosol mass enhancement (ΔOA/ΔCO) initially and after 8 hours of aging. (b) The normalized extinction efficiency (Δ*E*/ΔCO) initially and after 8 hours of aging. (c) The normalized CCN (ΔCCN/ΔCO) from smoke aerosol at 0.2% supersaturation initially and after 8 hours of aging. Warm colors indicate an increase in the normalized values while cool colors represent a decrease.Note that the maximum of the colorbar for the smoke mass has been increased from 0.14 to 0.16, the maximum of the colorbar for the smoke extinction has been increased from 700 to 840, and the maximum of the colorbar for smoke CCN has been increased from 2.6×10^7 to 3.1×10^7.

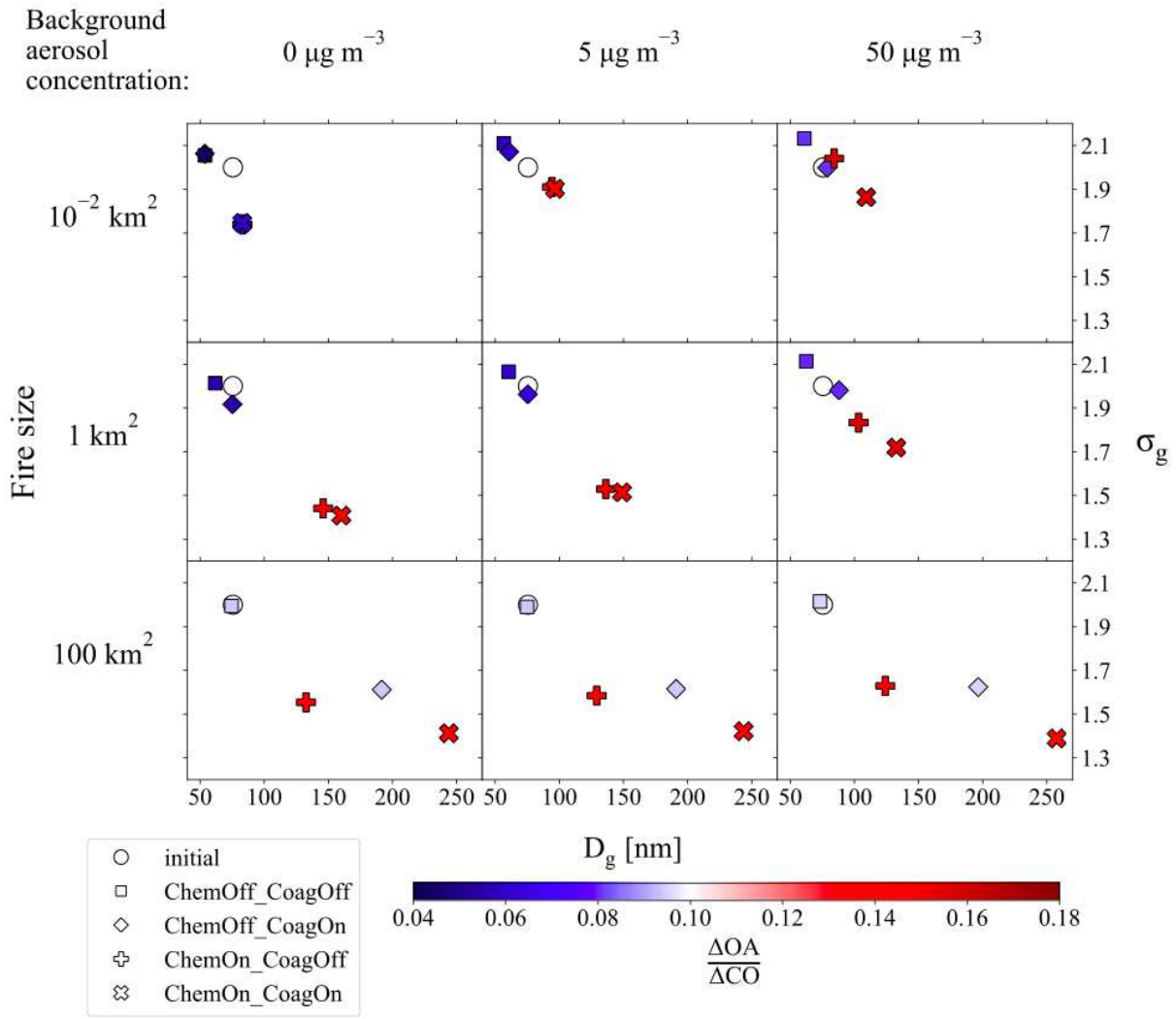

Figure D24. Sensitivity case: aging for 8 hours, using the model settings of the primary cases (Table 1). Smoke (background corrected) lognormal median diameter of the lognormal mode (D_g; x axis) and lognormal modal width (σ_g; y axis) initially and after 8 hours. The colorbar is ΔOA/ΔCO initially and after 4 hours of aging for the base cases (same colorbar as Fig. D23). Note that the maximum of the colorbar for the smoke mass has been increased from 0.14 to 0.16, the x-axis has been increased from 210 to 260 nm, and that the y-axis has been decreased from 1.4 to 1.2.

Table D1. Details of relevant field campaigns of aging biomass burning measurements. (Citations are provided in the main supporting information document.)

Campaign[a]; Citation(s)[b]	Fire size(s); Fire type(s)	Age(s) of measurement; Measurement location	Atmospheric conditions	Background aerosol concentration	Net OA; Net extinction; Net CCN[c]
ARCTAS A, B, C; Cubison et al. (2011), Hecobian et al., (2011)	Not in text; North American wildfires	Up to ~24 hours (Hecobian), up to ~5 hours (Cubison); Aircraft	Not in text	Not in text	Some plumes showed OA loss (Hecobian), many showed no significant change (Hecobian, Cubison); Not included in analysis; Not included in analysis
BBOP; Collier et al. (2016), Zhou et al. (2017)	Not in text; Western U.S. wildfires	8-11 hours (Zhou), 6-45 hours (Collier); Aircraft	Not in text	Not in text	No significant net OA change (both studies); Not included in analysis; Not included in analysis
BORTAS; Jolleys et al. (2015), Sakamoto et al. (2015)	Not in text; North American boreal forest fires	1-5 days (Jolleys), 1-2 days (Sakamoto); Aircraft	Not in text	Not in text	Net OA loss (Jolleys), no significant change (Sakamoto); Not included in analysis; Not included in analysis
DODO and DABEX; Capes 2008	A large number of fires "tens of meters in diameter"	Up to 48 hours; Aircraft	Not in text	Not in text	No significant net OA change; Not included in analysis; Not included in analysis[d]

	; West African agricultural burns				
MILAGRO; Yokelson et al. (2009)	Each fire assumed to be 1 km^2; Yucatan peninsula agricultural burns and forest fires (17 fires)	Up to 1.5 hours; Aircraft	Average wind of 2.6 m s^{-1}, in-plume [OH] > 10^7 molec cm^{-3}	Not in text	Increase in $PM_{2.5}$, attributed to SOA production; Increase in SSA[e]; Not included in analysisd
SAFARI 2000; Abel et al. (2003), Formenti et al. (2003), Hobbs et al. (2003)	10 km^2; Controlled burn in South Africa (grassland)	Not specified (Abel), 1-3 days (Formenti), up to ~40 minutes (Hobbs); Aircraft	"Sunny"[f], in-plume [OH] ~1.7×10^7 molec cm^{-3} (Hobbs)	Not in text	Net OA increase (Formenti), net OA loss (Hobbs); Increase in SSA (Abel)
SAMBBA; Brito et al. (2014)	Not in text; Fires within the southwestern Brazilian Amazon rainforest	Not specified; Ground level	Transition between dry to wet season	Not in text	No significant change in OA; Not included in analysis; Not included in analysis
SCREAM; May et al. (2015)	0.3 km^2 and 1.47 $km^{2,}$ [g]; Prescribed agricultural fires in South Carolina (U.S.)	~2 hours (1.47 km^2 fire), ~5 hours (0.3 km^2 fire); Aircraft	Not in text	Not in text	No significant change in OA for 1.47 km^2 fire (~2 hours old), net OA loss for 0.3 km^2 fire (~5 hours old); Not included in analysis; Not included in

					analysis
SEAC4RS; Forrister et al. (2015), Liu et al. (2016)	Not in text (Forrister), 0.16 km^2-1.27 km^2 (Liu); 2 "large" U.S. wildfires (Forrister), 7 U.S. agricultural fires (Liu)[h]	Up to 3 hours (Forrister), up to 1.2 hours (Liu); Aircraft	Not in text	Not in text	Decrease during first 2 hours and then no net OA change (Forrister), possible net increase in OA for 4 fires and no significant net change for 4 fires (Liu); Not included in analysis Not included in analysis
Interstudy comparison between ACTIVE, DABEX, ITOP, and MILAGRO; Jolleys et al. (2012)	Not in text; northern Australia (ACTIVE), western Africa wildfires (DABEX), boreal forest fires around the Azores (ITOP), Altzomoni (MILAGRO)	Up to days (all campaigns); Aircraft (ACTIVE, DABEX, ITOP), ground level (MILAGRO)	Not in text	Not in text	Small net OA loss; Not included in analysis; Not included in analysis
Akagi et al. (2012)	0.81 km^2; prescribed chaparral burn in California	2.4-4.5 hours; Aircraft	Winds between 0.5-2.2 m s^{-1}, "sunny", 292-297 K, in-plume	Not in text	Net loss of OA (evaporation dominant in first 2 hours, SOA formation observed after

	(U.S.)		[OH] ~5.27×10^6 molec cm^{-3}		that); Increase in scattering efficiency[i]; Not included in analysis
Eagan et al. (1974)	0.04 km^2,[j]; 2 forest fires in Olympic Peninsula (U.S.)	Not given; Aircraft	Not in text	Not in text	Not included in analysis; Not included in analysis; Increase in CCN up to 40 km downwind[k]
Nance et al. (1993)	>~40 km^2; Alaskan wildfire A121 (U.S.)	2 "aged" measurements 15 and 20 km downwind; Aircraft	Not in text	36 μg m^{-3}	No significant change in $PM_{3.5}$; Not included in analysis; Not included in analysis
Radke et al. (1995)	390 km^2 total[l]; Oregon forest fire (U.S.)	Up to 50 hrs; Aircraft	"Low" wind speeds	Not in text	Gain in observed volume concentrations of nucleation, accumulation, and coarse modes in first 10 hours and loss after that; Increase in the optical scattering coefficient in first 10 hours and loss after that; Not included in analysis
Reid et al. (1998)	Not in text; Brazilian	Variable ages, usually ~2-4 days; Aircraft	"Sunny", wind speeds generally < 5	Not given in text but entire	Particle mass concentrations increased, with

	agricultural burns		m s^{-1}	measurement region described as "hazy"	50-75% of this mass increase estimated to be from organics; Increase in mass-scattering efficiency and SSA but decreases in mass absorption efficiency[m]; Not included in analysis
Vakkari et al. (2014; 2018)	Not in text; 60 burns in South Africa (30% savannas, 30% grasslands, 40% mixed cropland, savanna, and grassland) (2014); 5 years of data on savannas, grasslands, and croplands (2018)	Average age of 2.4 hours (2014); 3-5 hours (2018)	Not in text	Not in text	Net increase in OA (2014 and 2018); Increase in extinction and SSA (2014); 2/3^{rds} of plumes showed increases in CCN, 1/3rd of plumes showed no significant change in CCN (2014)

[a]When applicable

[b]Many of these campaigns have further publications associated with them; we only cite the papers that directly contributed information to this table.

[c]We report net OA, net extinction, and net CCN values that have been normalized to an inert tracer (e.g. CO) to account for plume dilution, unless otherwise noted

[d]Total number concentration observed to decrease with age

[e]Single scatter albedo
[f]Terms in quotations indicate the term used in the specific paper (in lieu of a quantitative measurement)
[g]Fire size data from Akagi et al. (2013)
[h]Liu et al. (2105) examined 15 total fires but only 7 aged fires
[i]Although net OA was observed to decrease, net $PM_{2.5}$ was observed to increase
[j]Two fires were examined but only one fire's size was given
[k]The CCN measurements were not corrected for dilution
[l]"Hundreds" of smaller fires were observed within the 390 km^2 fire boundaries
[m]Decreases in mass absorption efficiency with age can indicate a decreasing fraction of black carbon in the aerosol (e.g. Reid et al., 2005)

Table D2. Initial total number concentration for each fire size for the base simulations, as described in Table 5.1.

Fire size (km^2)	Initial total number concentration (cm^{-3})
100	3.02×10^{6}
10	1.70×10^{5}
1	1.61×10^{5}
10^{-1}	1.52×10^{5}
10^{-2}	1.44×10^{5}
10^{-3}	1.36×10^{5}
10^{-4}	1.29×10^{5}

APPENDIX E

SUPPLEMENT TO: DILUTION IMPACTS ON SMOKE AGING: EVIDENCE IN BBOP DATA

E1. BBOP instrumentation and fire detection methods

The FIMS characterizes particle sizes based on electrical mobility as in scanning mobility particle sizer (SMPS). Because FIMS measures particles of different sizes simultaneously instead of sequentially as in traditional SMPS, it provides aerosol size distribution with a much higher time resolution at 1 Hz (Wang et al., 2017). The relative humidity of the aerosol sample was reduced to below ~25% using a Nafion dryer before being introduced into the FIMS. Therefore, the measured size distributions represented that of the dry aerosol particles.

An SPN1 radiometer (Badosa et al. 2014; Long et al. 2010) provided total shortwave irradiance, with a shaded mask applied following (Badosa et al. 2014). The data was corrected for tilt up to 10 degrees of tilt, following (Long et al. 2010). For tilt greater than 10 degrees these values are set to "bad".

E2. Heterogeneous chemistry calculations

We test the impact of heterogeneous chemistry on aerosol mass loss within the smoke plume. We performed a simple calculation of OH molecules collision to the surface of a single particle ranging from 1 nm to 1 μm size in diameter. The following parameters assumed for the calculations:

- OH diffusivity = 3.5e-5 [m2 s-1]
- Constant OH concentration varied from 1e5 to 5e7 [molecules cm-3]
- Molecular weight of organics = 200 [g mol-1]
- Density of organics = 1.4 [g cm-3]
- Total run time = 3 [hours]

As an upper bound calculation, we assume each collision results in removing an organic molecule on the surface of the particle (assumed to be 200 amu), fragmenting and removing the molecule from the particle. The fragmentation products are not assumed to participate in further reaction. Figure E23a shows the resulting final:initial mass ratios after four hours of aging, indicating that for all aerosol sizes captured in this study (>10 nm) and under a range of OH concentrations, >90% of the aerosol mass remains. As a lower bound, we also include a case in which only 10% of all OH collisions result in a mass loss of 200 amu (Figure E23c).

Table E1. Flight description table.

Flight name, date	Number of sets of pseudo-Lagrangian transects	Fire name	Fuel[1]	Missing data[2]
'726a', 07-26-2013	2	Mile Marker 28	grasslands, shrub brush, timber, and timber litter	
'730a', 07-30-2013	1	Colockum Tarps	grass, trees	
'730b', 07-30-2013	2	Colockum Tarps	grass, trees	
'809a', 08-09-2013	1	Colockum Tarps	grass, trees	NO_x
'821b', 08-21-2013	1	Government Flats		O_3

[1]When known

[2]Instruments relevant to this study

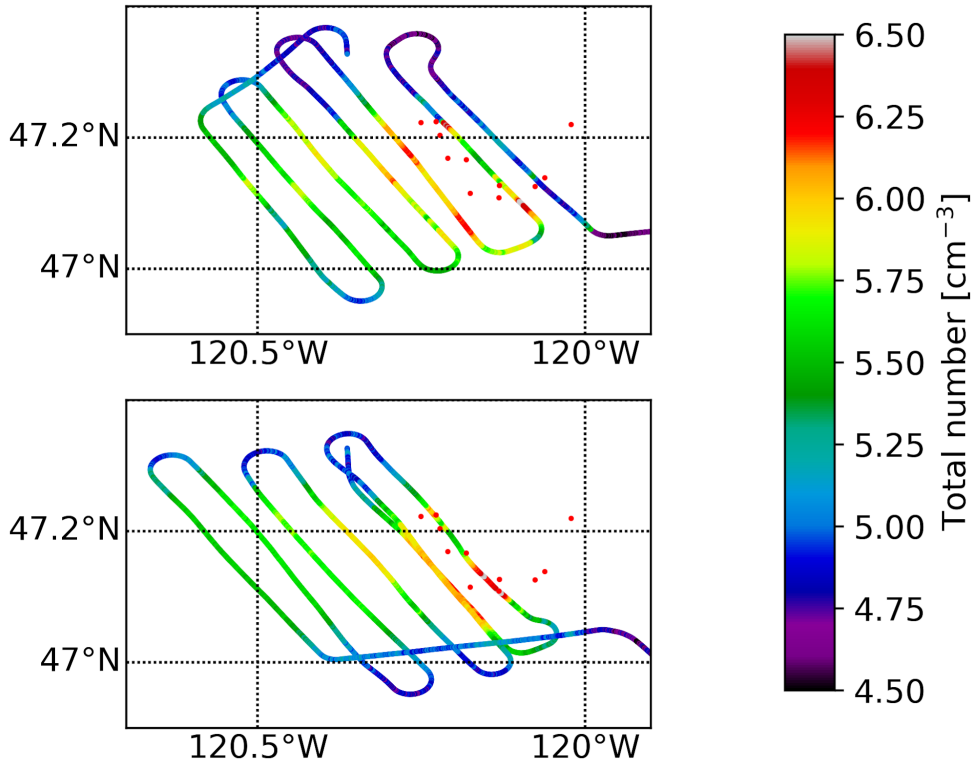

Figure E1. The flight path for flight '730b', colored by the FIMS total number concentration. The red dots are MODIS fire/thermal anomalies. The black star indicates the approximate center of the fire and the black dashed line indicates the approximate centerline of the plume, estimated by the number concentration. The numbers are the leg number.

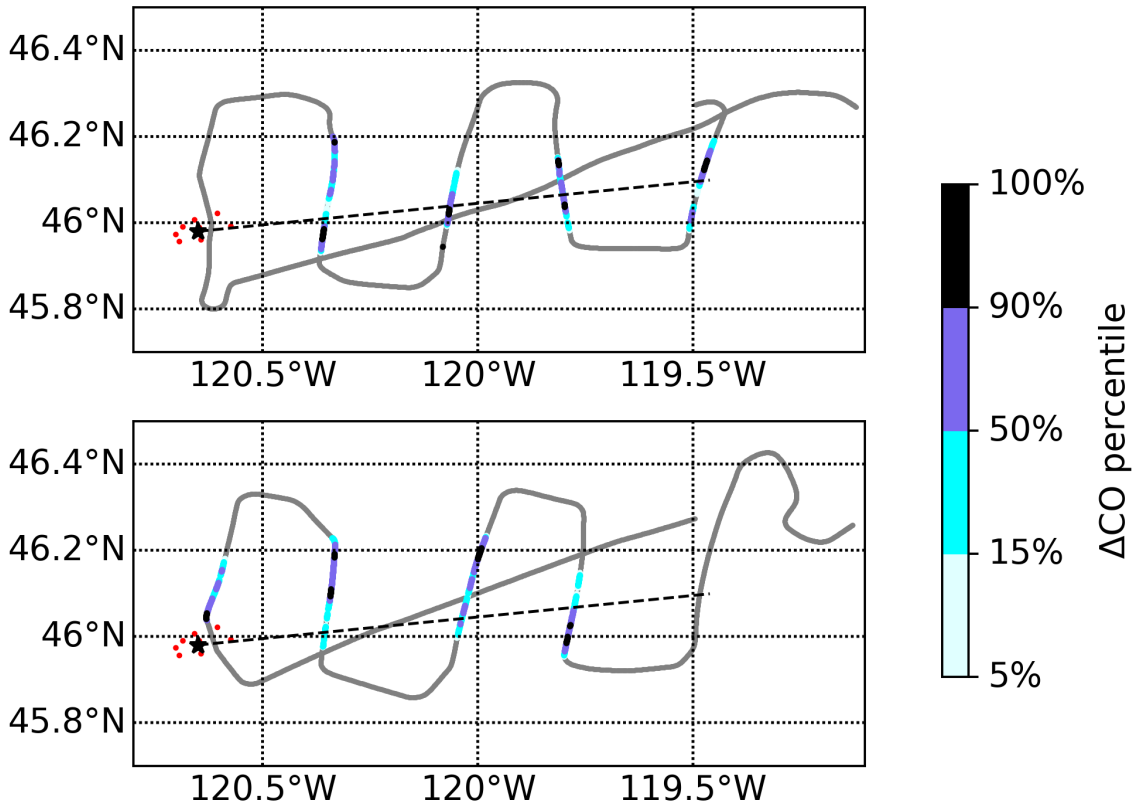

Figure E2. The flight path for '726a'. The legs used in this study are colored by each ΔCO percentile bin used in the main text analyses. There were two complete flight paths for this day. The red dots are MODIS fire/thermal anomalies. The black star indicates the approximate center of the fire and the black dashed line indicates the approximate centerline of the plume, estimated by the number concentration.

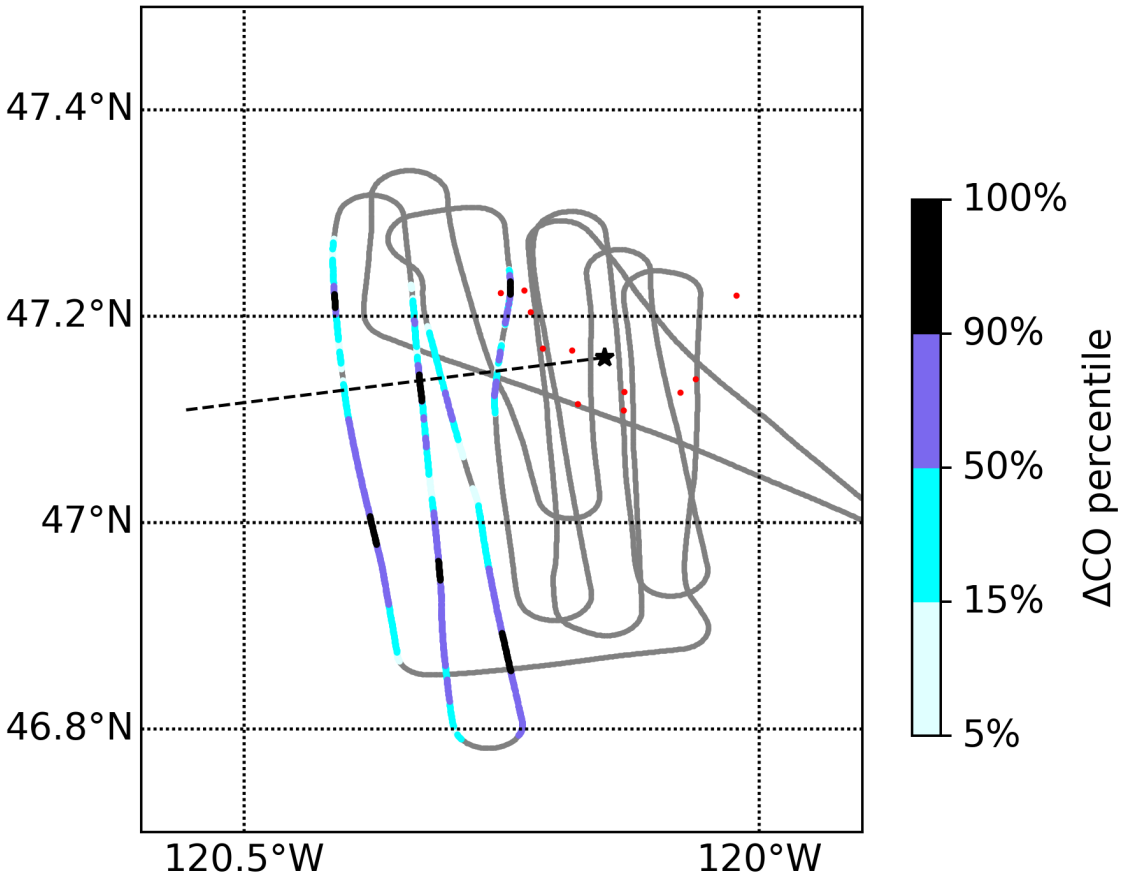

Figure E3. The flight path for '730a'. The legs used in this study are colored by each ΔCO percentile bin used in the main text analyses. The red dots are MODIS fire/thermal anomalies. The black star indicates the approximate center of the fire and the black dashed line indicates the approximate centerline of the plume, estimated by the number concentration.

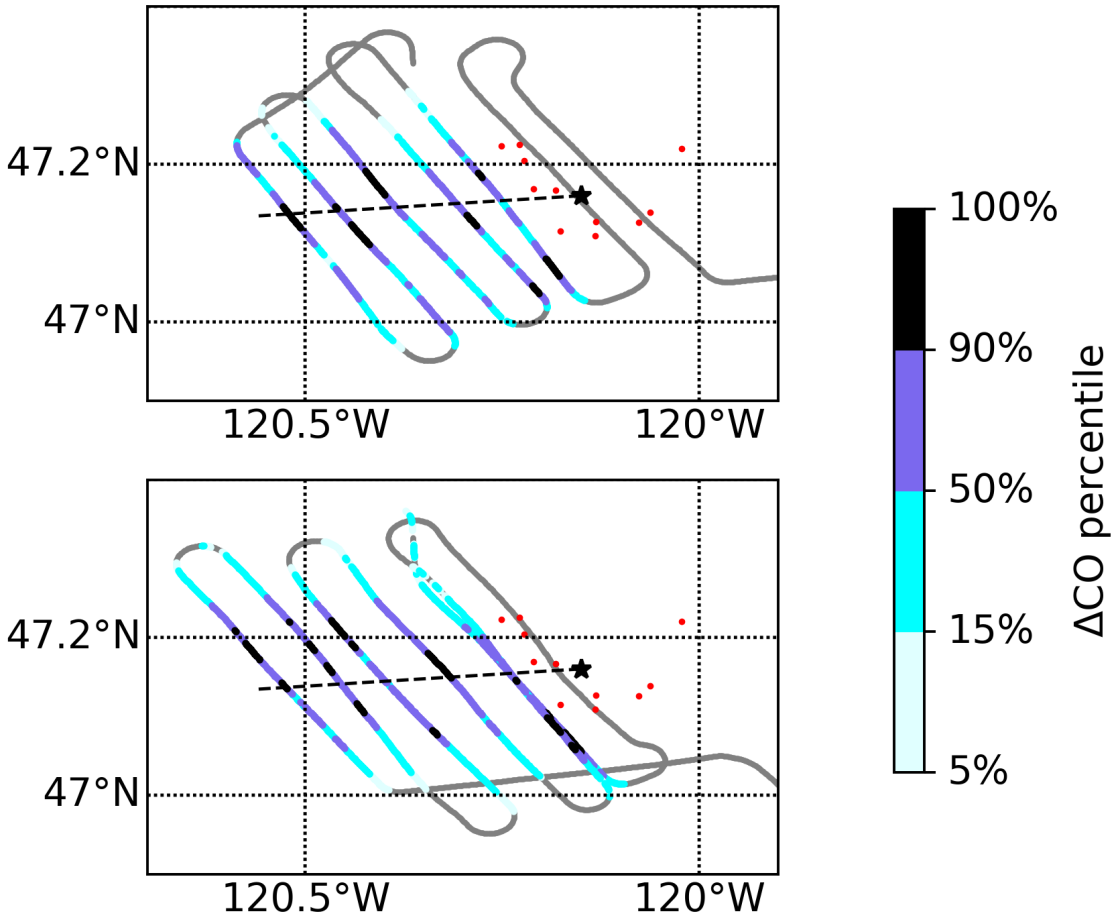

Figure E4. The flight path for '730b'. The legs used in this study are colored by each ΔCO percentile bin used in the main text analyses. There were two complete flight paths for this flight. The red dots are MODIS fire/thermal anomalies. The black star indicates the approximate center of the fire and the black dashed line indicates the approximate centerline of the plume, estimated by the number concentration.

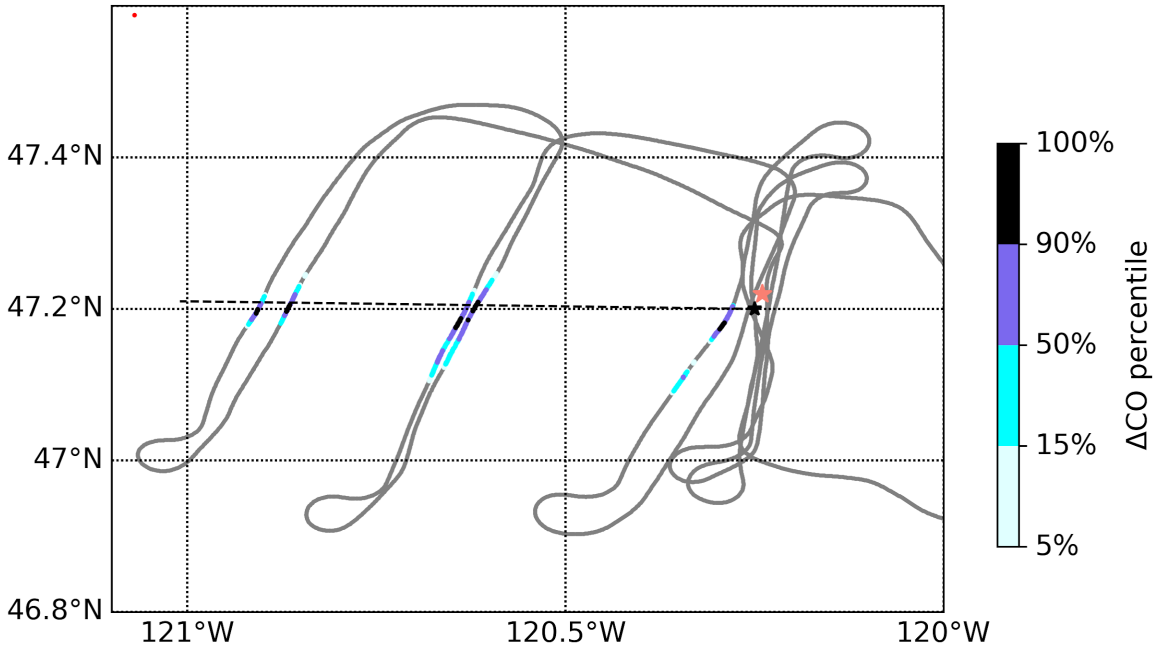

Figure E5. The flight path for '809a'. The legs used in this study are colored by each ΔCO percentile bin used in the main text analyses. The Worldview image for this day had clouds over the fire location at the time of the satellite passover. Thus we estimate a fire center using Worldview and MODIS images for this region on the previous day (8-08-2013) and the following day (8-10-2013) (salmon-colored star). The black star indicates the approximate center of the fire and the black dashed line indicates the approximate centerline of the plume, estimated by the number concentration.

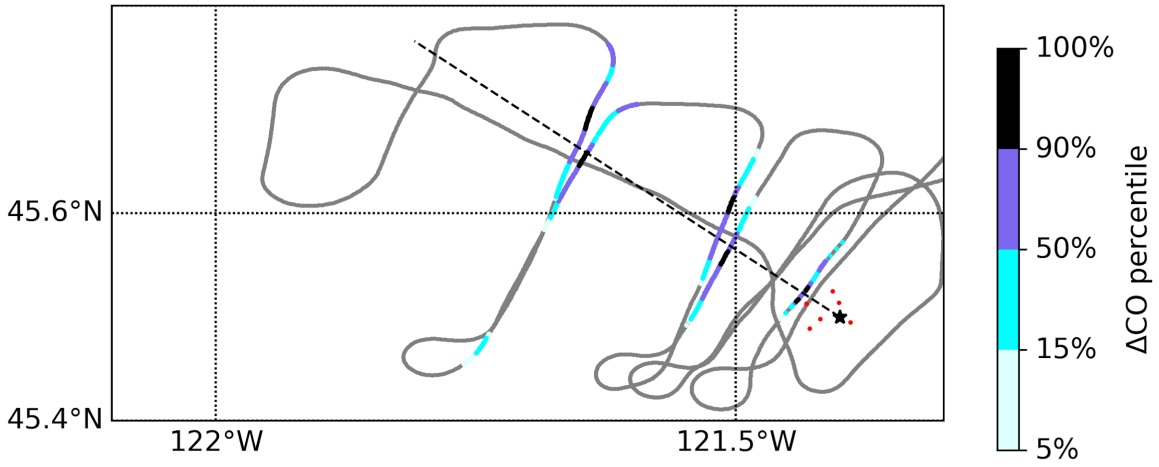

Figure E6. The flight path for '821b'. The legs used in this study are colored by each ΔCO percentile bin used in the main text analyses. The red dots are MODIS fire/thermal anomalies. The black star indicates the approximate center of the fire and the black dashed line indicates the approximate centerline of the plume, estimated by the number concentration.

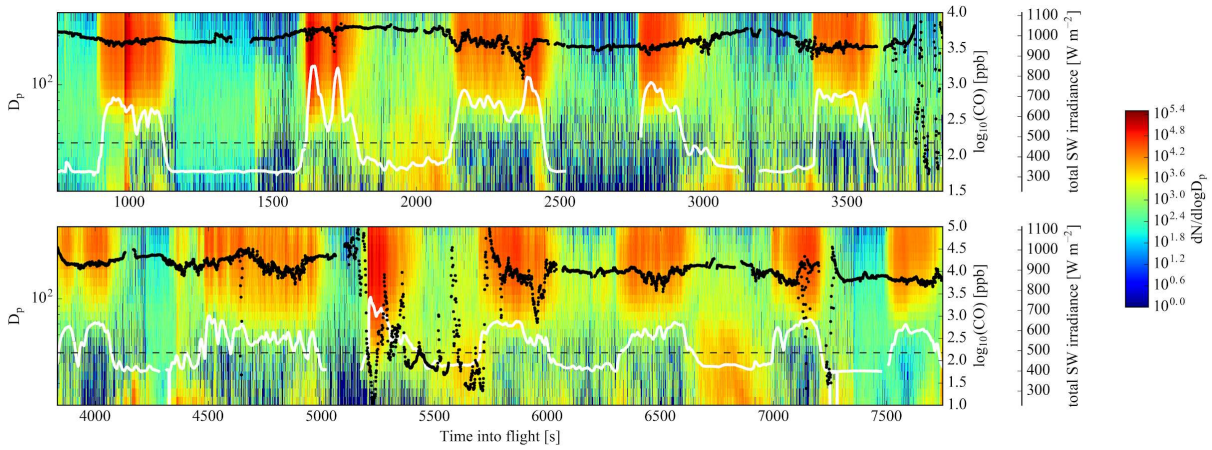

Figure E7. Number size distribution data, $dN/dlogD_p$, from the FIMS; CO (white solid line); and total short wave (SW) irradiance (black dots) data for the '726a' flight. The dotted dashed line indicates CO=150 ppb, our cutoff for in-plume/out-of-plume.

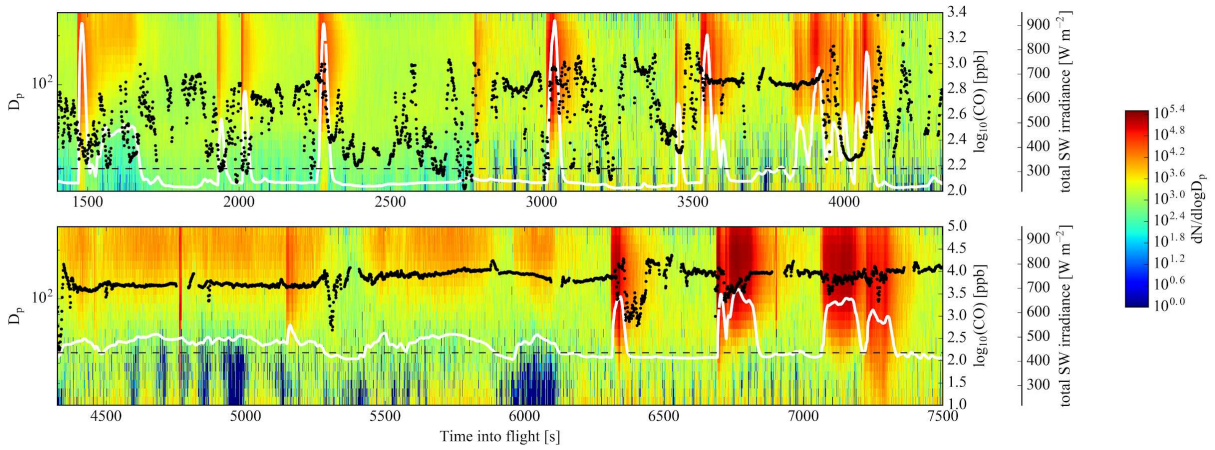

Figure E8. Number size distribution data, $dN/dlogD_p$, from the FIMS; CO (white solid line); and total short wave (SW) irradiance (black dots) data for the '730a' flight. The dotted dashed line indicates CO=150 ppb, our cutoff for in-plume/out-of-plume.

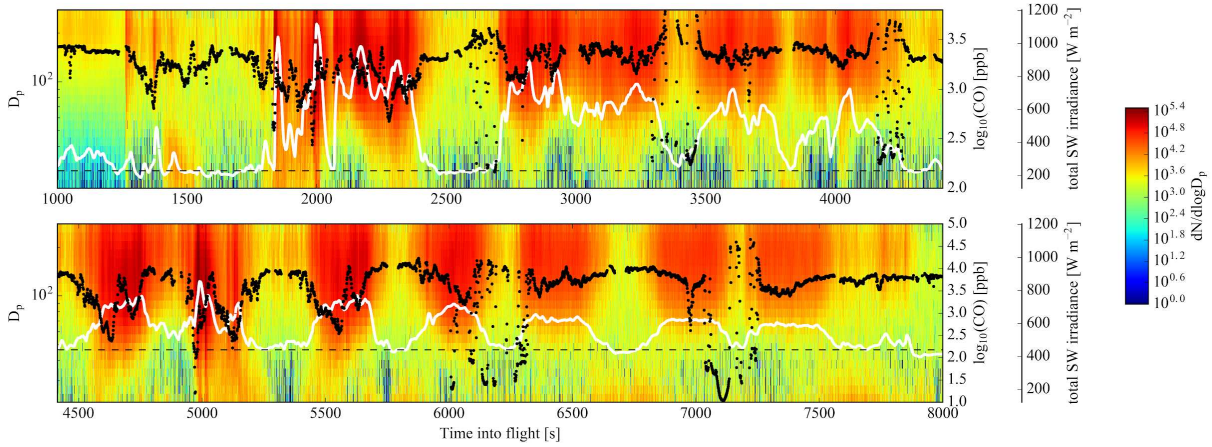

Figure E9. Number size distribution data, $dN/dlogD_p$, from the FIMS; CO (white solid line); and total short wave (SW) irradiance (black dots) data for the '730b' flight. The dotted dashed line indicates CO=150 ppb, our cutoff for in-plume/out-of-plume.

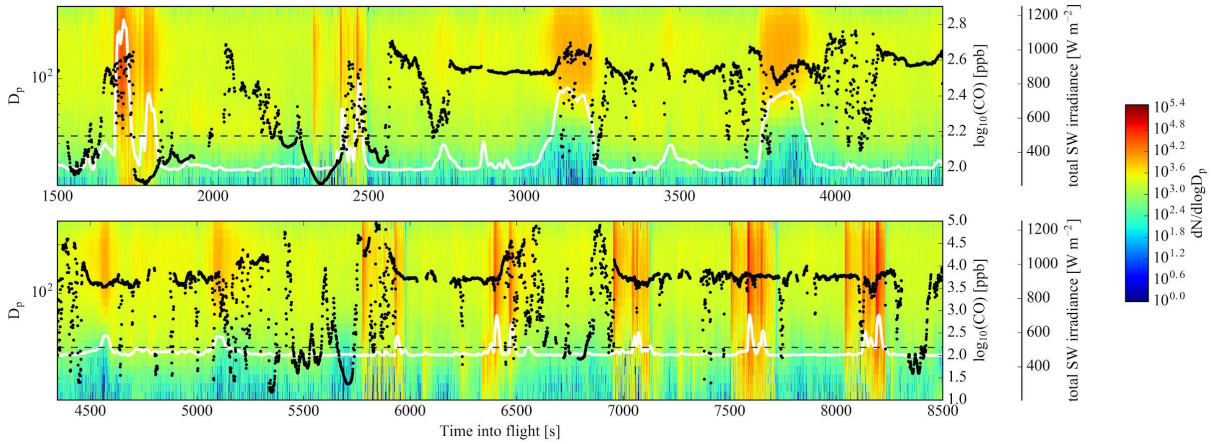

Figure E10. Number size distribution data, $dN/dlogD_p$, from the FIMS; CO (white solid line); and total short wave (SW) irradiance (black dots) data for the '809a' flight. The dotted dashed line indicates CO=150 ppb, our cutoff for in-plume/out-of-plume.

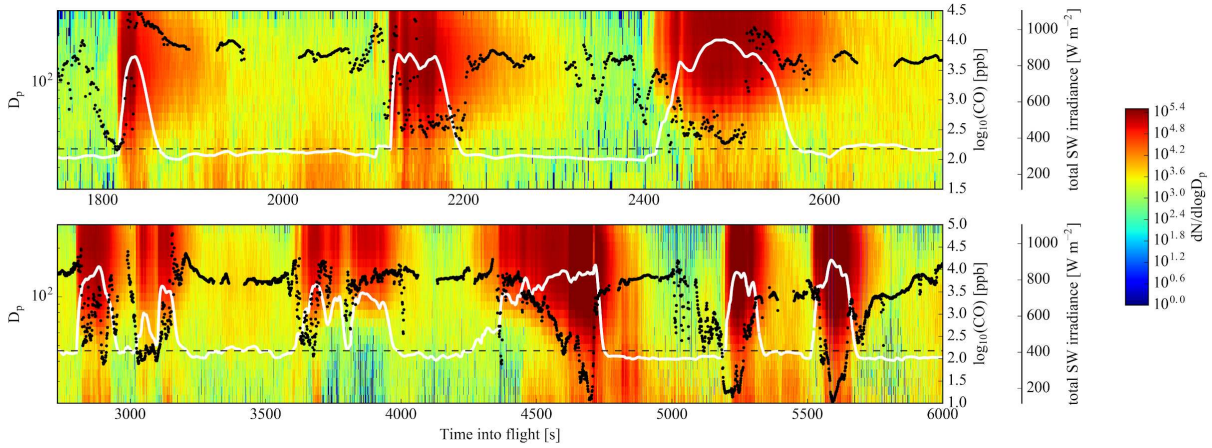

Figure E11. Number size distribution data, $dN/dlogD_p$, from the FIMS; CO (white solid line); and total short wave (SW) irradiance (black dots) data for the '821b' flight. The dotted dashed line indicates CO=150 ppb, our cutoff for in-plume/out-of-plume.

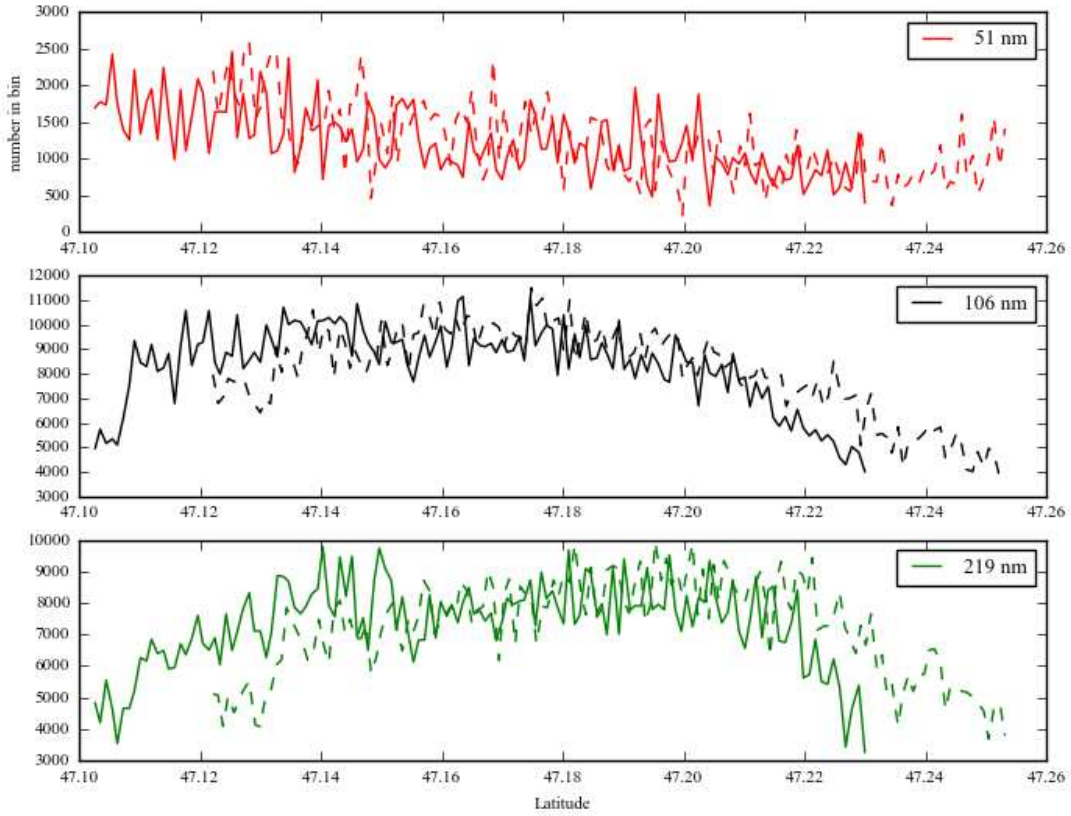

Figure E12. FIMS data for '809a' for the two legs that ~overlap (Figure E5) for the 51, 106, and 219 nm size bins. The solid line is from the plane flying north to south (right to left in this figure) and the dashed line is from the plane flying south to north (left to right in this figure). In the absence of FIMS measurement artifacts, we expect these two lines to roughly match each other.

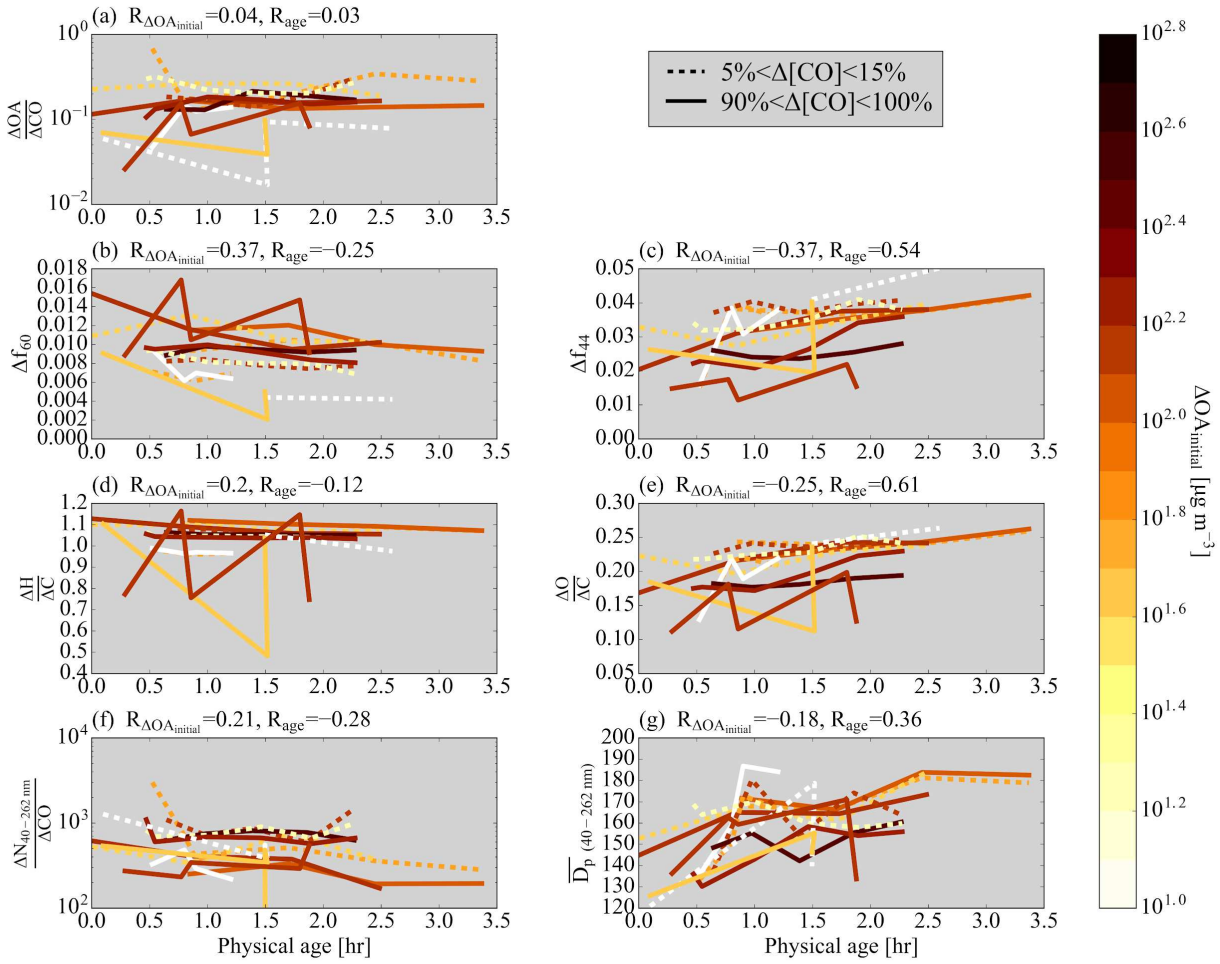

Figure E13. Same as Figure 6.2 but using only the first 50% of data for each leg of the FIMS and CO data for panels f-g.

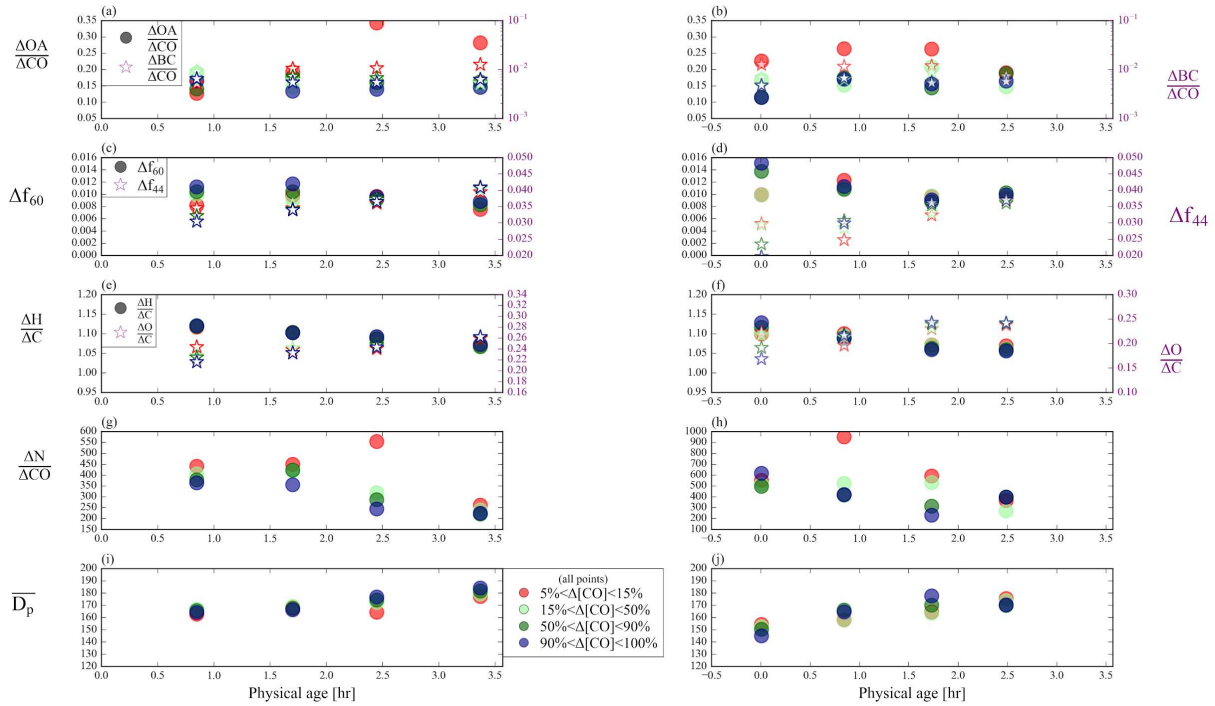

Figure E14. Aerosol properties for the first set (left-hand column) and second set (right-hand column) of pseudo-Lagrangian transects from flight '726a' (a-b) ΔOA/ΔCO (right y-axis) and ΔrBC/ΔCO (left y-axis), (c-d) Δf_{60} (right y-axis) and Δf_{44} (left y-axis), (e-f) ΔH/ΔC (right y-axis) and ΔO/ΔC (left y-axis), (g-h) ΔN/ΔCO, and (i-j) $\underline{D_p}$ against physical age. For each transect, the data is divided into edge (the lowest 5-15% of ΔCO data; red points), core (90-100% of ΔCO data; blue points), and intermediate regions (15-50% and 50-90% of ΔCO data; light green and dark green points). ΔrBC/ΔCO is shown in log scale and the x-axis for the right-hand column has been shifted backwards to improve clarity. Note that the left-hand and right-hand columns do not always have the same y-axis limits.

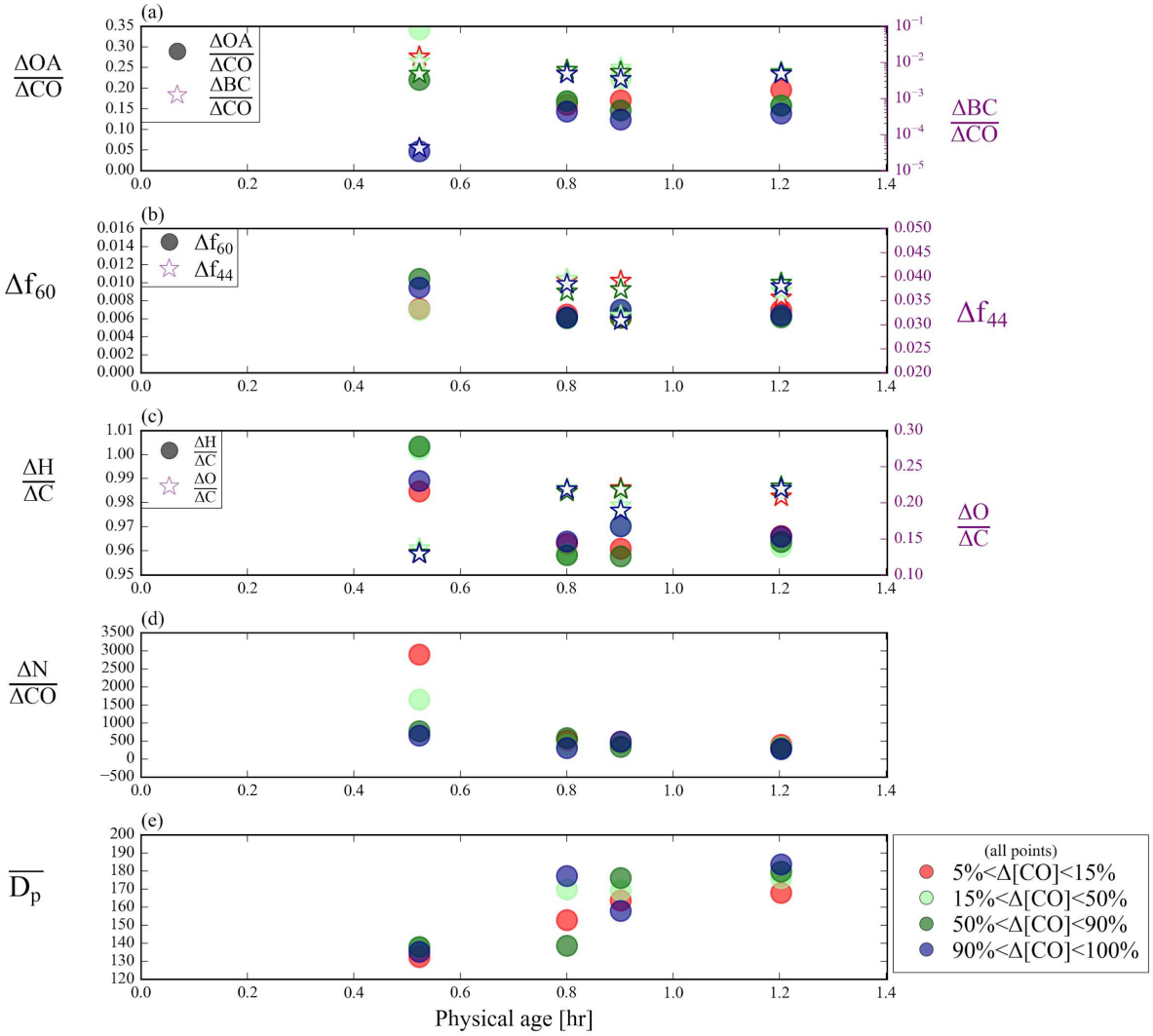

Figure E15. Aerosol properties for the set of pseudo-Lagrangian transects from flight '730a' (a) ΔOA/ΔCO (right y-axis) and ΔrBC/ΔCO (left y-axis), (b) Δf_{60} (right y-axis) and Δf_{44} (left y-axis), (c) ΔH/ΔC (right y-axis) and ΔO/ΔC (left y-axis), (d) ΔN/ΔCO, and (e) $\overline{D_p}$ against physical age. For each transect, the data is divided into edge (the lowest 5-15% of ΔCO data; red points), core (90-100% of ΔCO data; blue points), and intermediate regions (15-50% and 50-90% of ΔCO data; light green and dark green points). ΔrBC/ΔCO is shown in log scale to improve clarity.

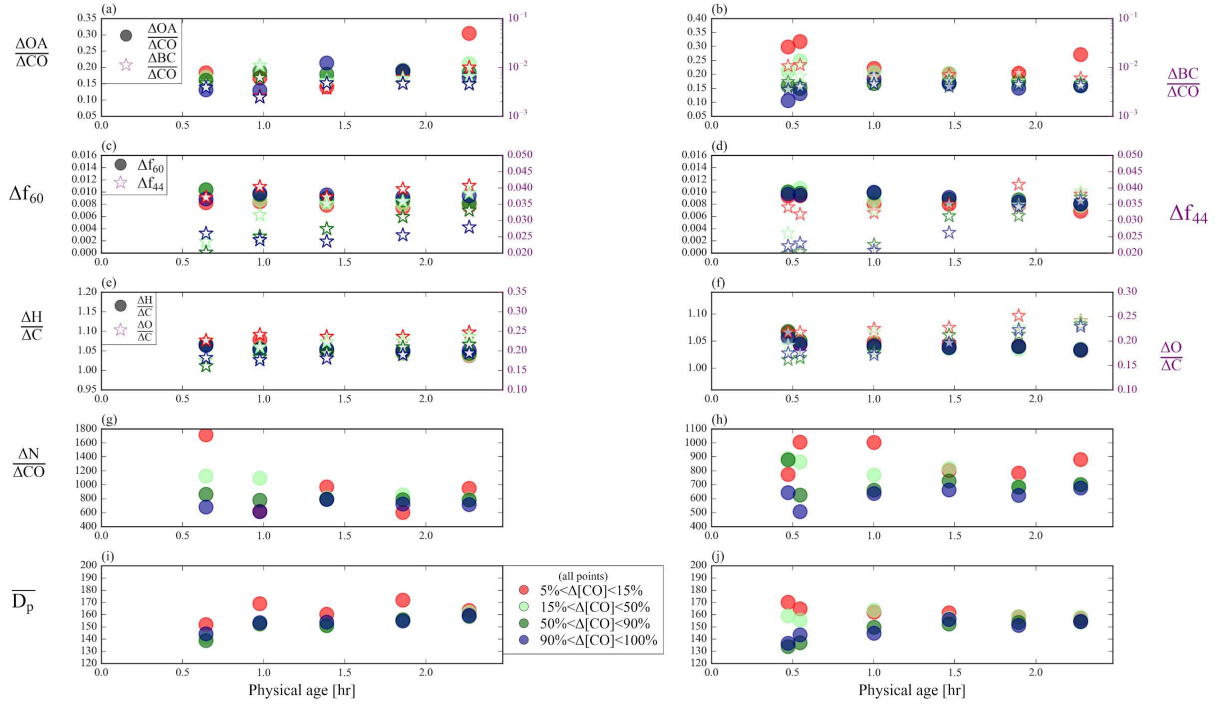

Figure E16. Aerosol properties for the first set (left-hand column) and second set (right-hand column) of pseudo-Lagrangian transects from flight '730b' (a-b) ΔOA/ΔCO (right y-axis) and ΔrBC/ΔCO (left y-axis), (c-d) Δf_{60} (right y-axis) and Δf_{44} (left y-axis), (e-f) ΔH/ΔC (right y-axis) and ΔO/ΔC (left y-axis), (g-h) ΔN/ΔCO, and (i-j) $\underline{D_p}$ against physical age. For each transect, the data is divided into edge (the lowest 5-15% of ΔCO data; red points), core (90-100% of ΔCO data; blue points), and intermediate regions (15-50% and 50-90% of ΔCO data; light green and dark green points). ΔrBC/ΔCO is shown in log scale to improve clarity. Note that the left-hand and right-hand columns do not always have the same y-axis limits.

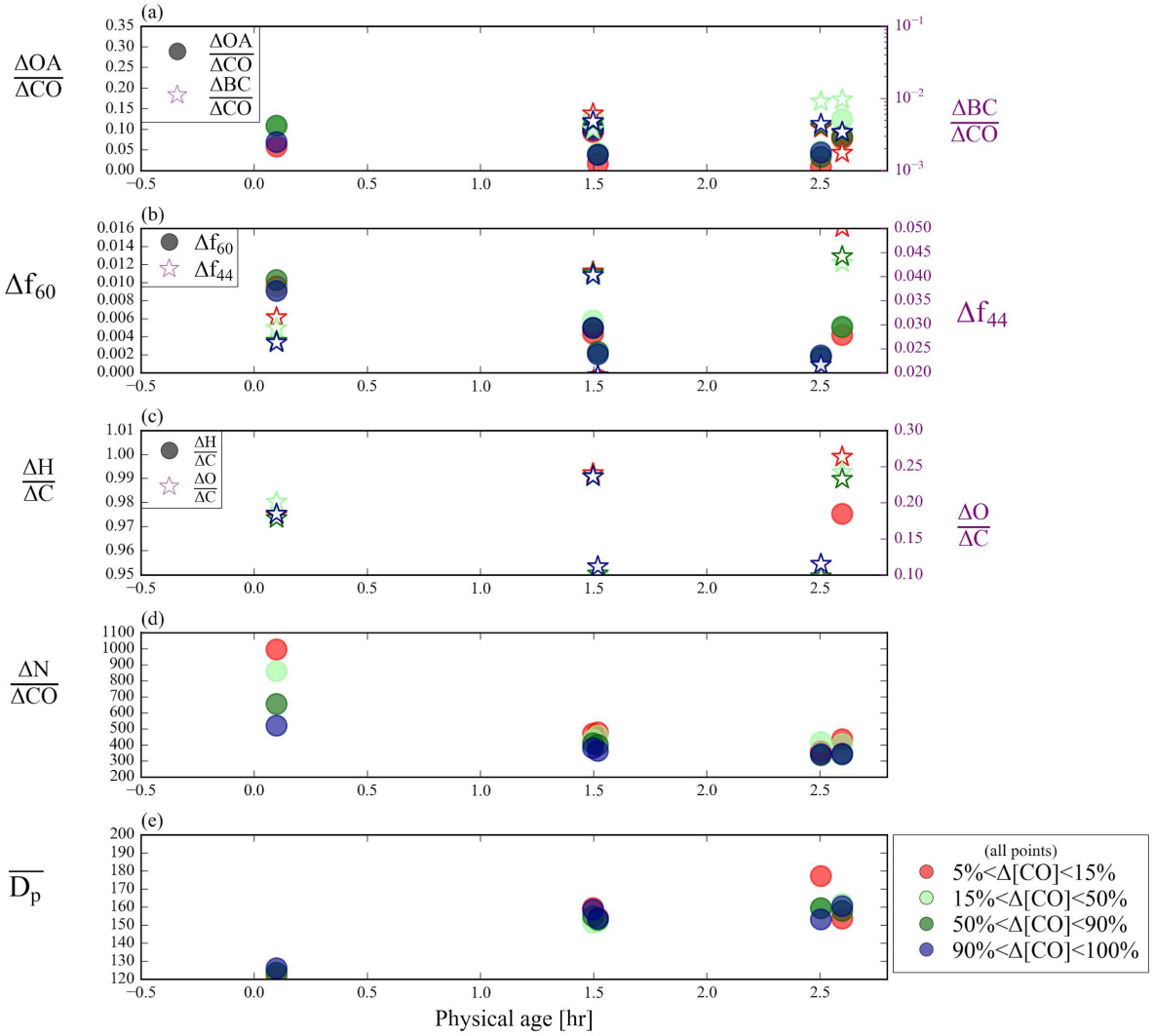

Figure E17. Aerosol properties for the set of pseudo-Lagrangian transects from flight '809a' (a) ΔOA/ΔCO (right y-axis) and ΔrBC/ΔCO (left y-axis), (b) Δf_{60} (right y-axis) and Δf_{44} (left y-axis), (c) ΔH/ΔC (right y-axis) and ΔO/ΔC (left y-axis), (d) ΔN/ΔCO, and (e) $\overline{D_p}$ against physical age. For each transect, the data is divided into edge (the lowest 5-15% of ΔCO data; red points), core (90-100% of ΔCO data; blue points), and intermediate regions (15-50% and 50-90% of ΔCO data; light green and dark green points). ΔrBC/ΔCO is shown in log scale and the x-axis for the right-hand column has been shifted backwards to improve clarity.

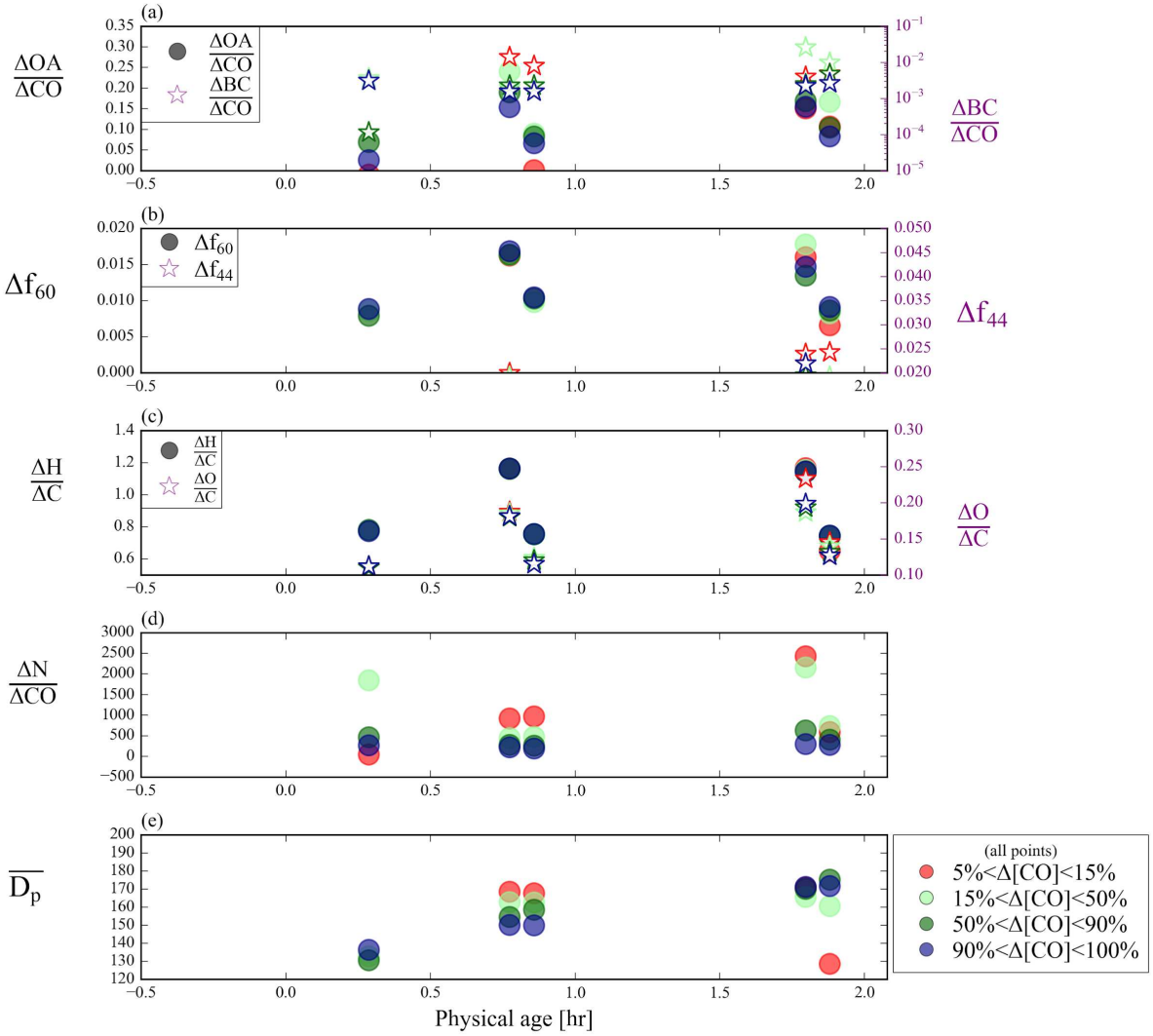

Figure E18. Aerosol properties for the set of pseudo-Lagrangian transects from flight '821b' (a) ΔOA/ΔCO (right y-axis) and ΔrBC/ΔCO (left y-axis), (b) Δf_{60} (right y-axis) and Δf_{44} (left y-axis), (c) ΔH/ΔC (right y-axis) and ΔO/ΔC (left y-axis), (d) ΔN/ΔCO, and (e) $\overline{D_p}$ against physical age.

For each transect, the data is divided into edge (the lowest 5-15% of ΔCO data; red points), core (90-100% of ΔCO data; blue points), and intermediate regions (15-50% and 50-90% of ΔCO data; light green and dark green points). ΔrBC/ΔCO is shown in log scale and the x-axis for the right-hand column has been shifted backwards to improve clarity.

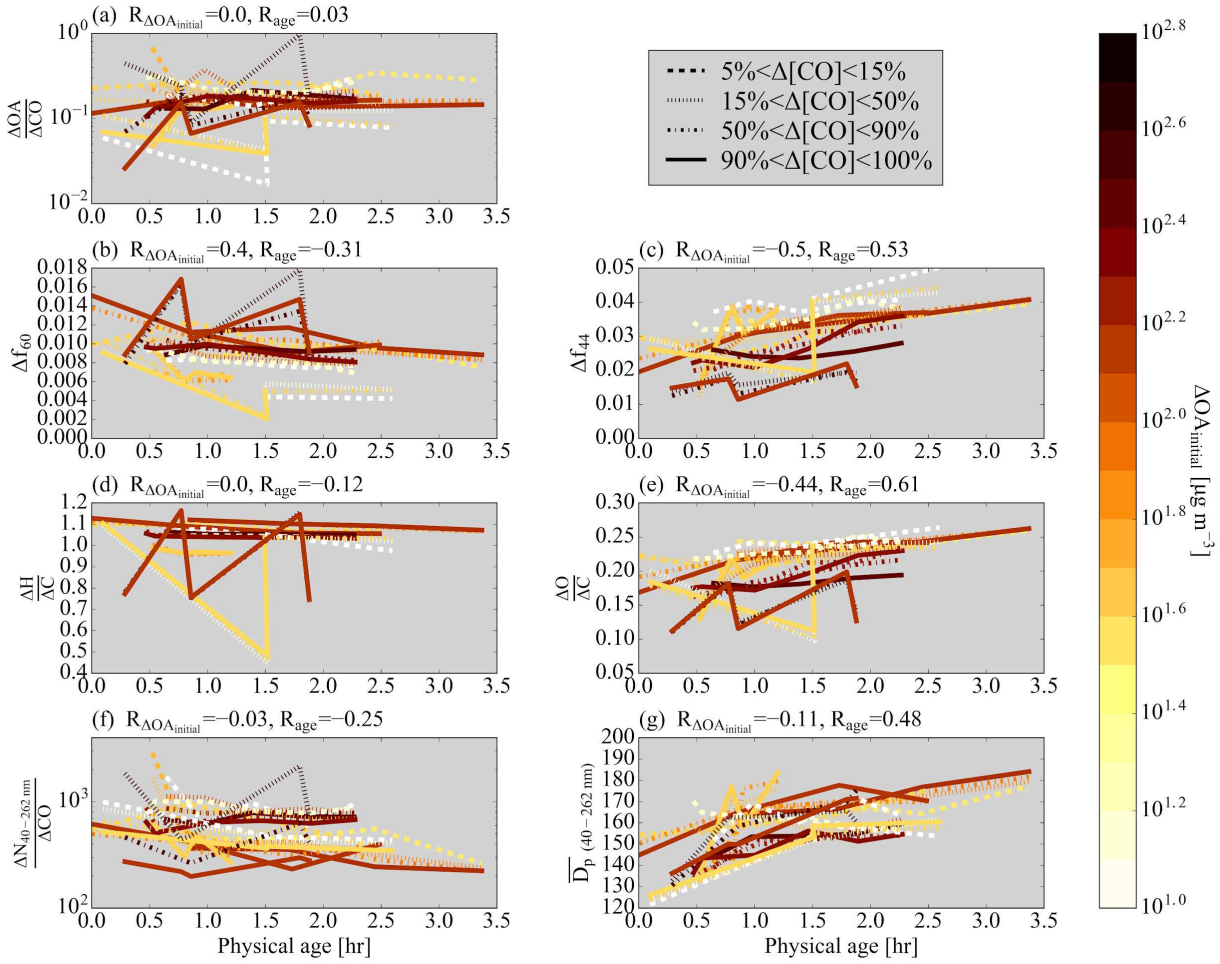

Figure E19. Various normalized parameters as a function of age for the 7 sets of pseudo-Lagrangian transects. Separate lines are shown for the edges (lowest 5-15% of ΔCO; dashed lines) cores (highest 90-100% of ΔCO; solid lines), and intermediate regions (15-50% and 50-90%; dotted and dashed-dot lines). (a) ΔOA/ΔCO, (b) Δf_{60}, (c) Δf_{44}, (d) ΔH/ΔC, (e) ΔO/ΔC, (f) $\Delta N_{40\text{-}262\ nm}/\Delta CO$, and (g) $\underline{D_p}$ between 40-262 nm against physical age for all flights, colored by $\Delta OA_{initial}$. Some flights have missing data. Also provided is the Spearman correlation coefficient, R, between each variable and $\Delta OA_{initial}$ and physical age for each variable. Note that panels (a), (d), and (g) have a log y-axis.

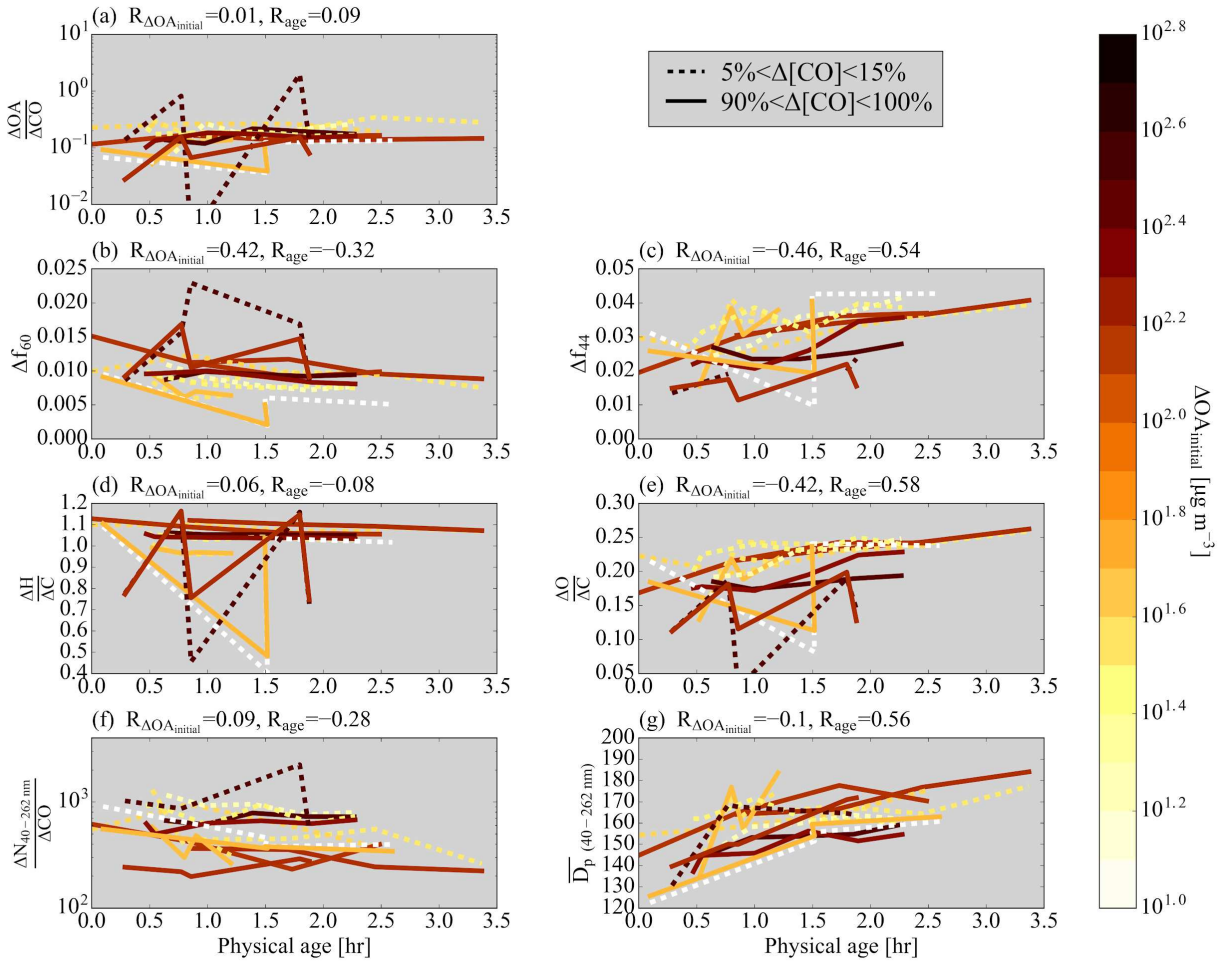

Figure E20. Various normalized parameters as a function of age for the 7 sets of pseudo-Lagrangian transects. Separate lines are shown for the edges (lowest 5-15% of ΔCO; dashed lines) and cores (highest 90-100% of ΔCO; solid lines). (a) ΔOA/ΔCO, (b) Δf_{60}, (c) Δf_{44}, (d) ΔH/ΔC, (e) ΔO/ΔC, (f) $\Delta N_{40\text{-}262\ nm}/\Delta CO$, and (g) $\underline{D_p}$between 40-262 nm against physical age for all flights, colored by $\Delta OA_{initial}$. Some flights have missing data. Also provided is the Spearman correlation coefficient, R, between each variable and $\Delta OA_{initial}$ and physical age for each variable. Note that panels (a), (d), and (g) have a log y-axis. This figure is identical to Figure 6.2 but uses an in-plume CO cutoff of 200 ppb.

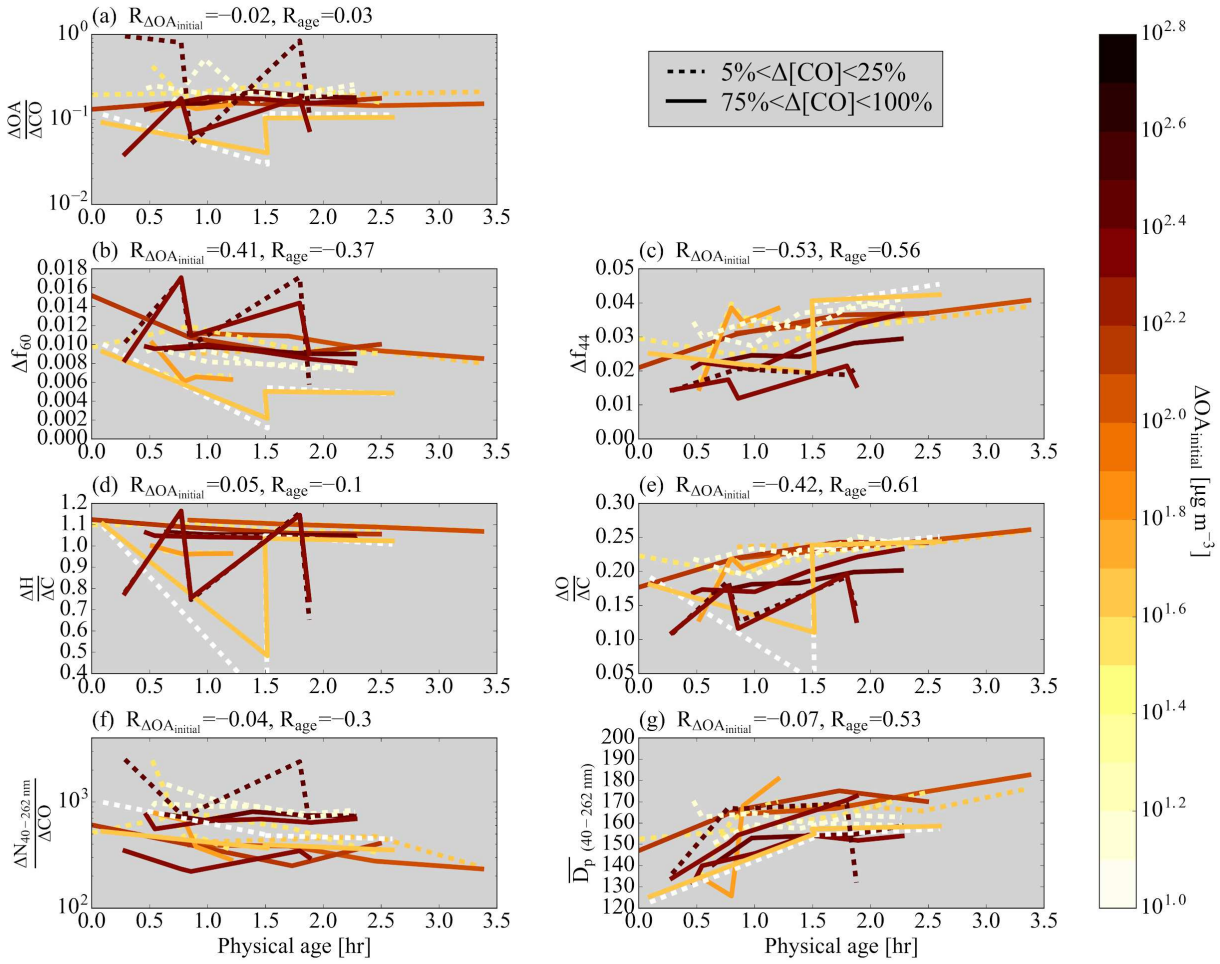

Figure E21. Various normalized parameters as a function of age for the 7 sets of pseudo-Lagrangian transects. Separate lines are shown for the edges (lowest 5-25% of ΔCO; dashed lines) and cores (highest 75-100% of ΔCO; solid lines). (a) ΔOA/ΔCO, (b) Δf_{60}, (c) Δf_{44}, (d) ΔH/ΔC, (e) ΔO/ΔC, (f) $\Delta N_{40\text{-}262\ nm}/\Delta CO$, and (g) $\underline{D_p}$ between 40-262 nm against physical age for all flights, colored by $\Delta OA_{initial}$. Some flights have missing data. Also provided is the Spearman correlation coefficient, R, between each variable and $\Delta OA_{initial}$ and physical age for each variable. Note that panels (a), (d), and (g) have a log y-axis. This figure is identical to Figure 6.2 but uses different ΔCO percentile widths.

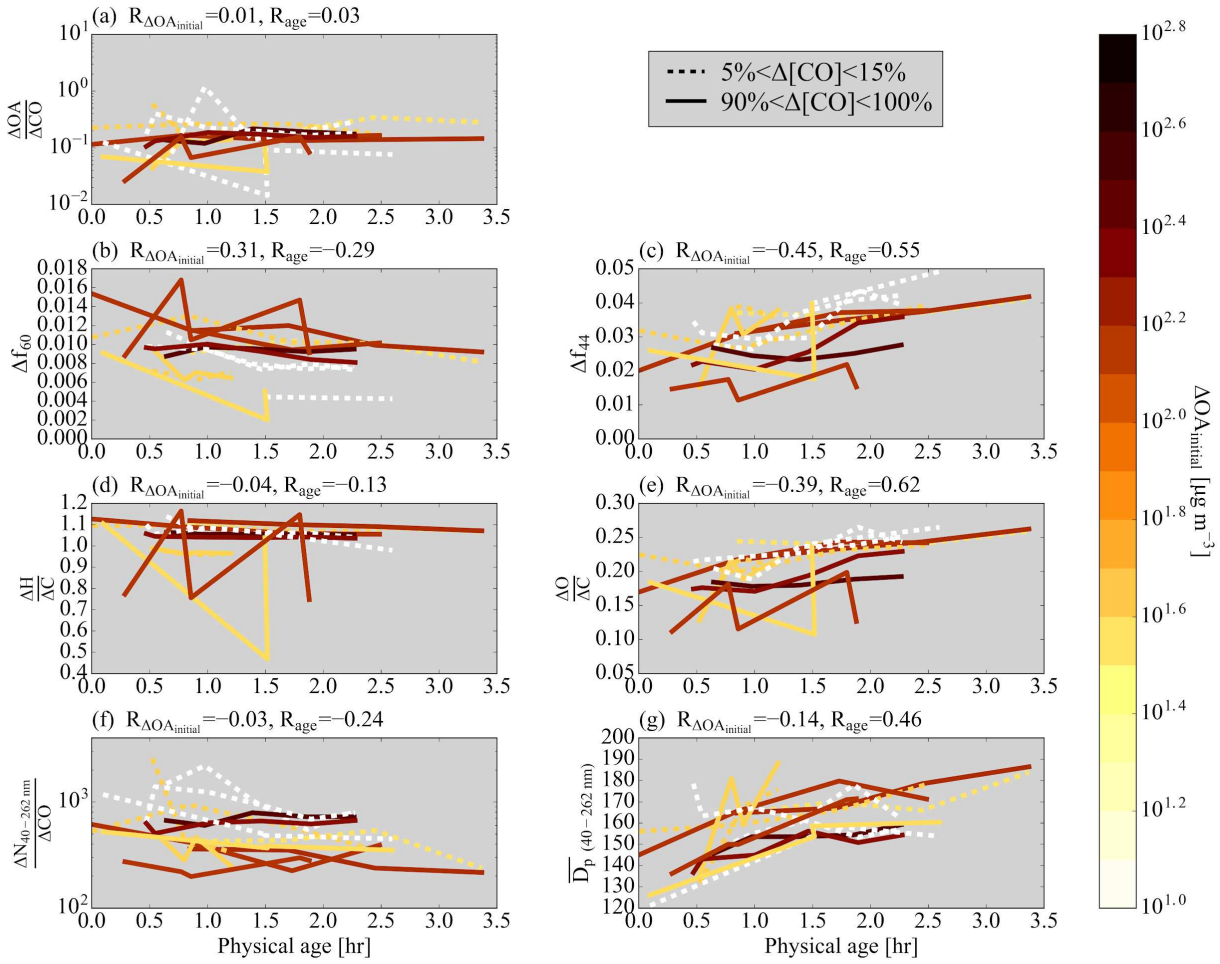

Figure E22. Various normalized parameters as a function of age for the 7 sets of pseudo-Lagrangian transects. Separate lines are shown for the edges (lowest 5-15% of ΔCO; dashed lines) and cores (highest 90-100% of ΔCO; solid lines). (a) ΔOA/ΔCO, (b) Δf_{60}, (c) Δf_{44}, (d) ΔH/ΔC, (e) ΔO/ΔC, (f) $\Delta N_{40\text{-}262\ nm}/\Delta CO$, and (g) $\underline{D_p}$ between 40-262 nm against physical age for all flights, colored by $\Delta OA_{initial}$. Some flights have missing data. Also provided is the Spearman correlation coefficient, R, between each variable and $\Delta OA_{initial}$ and physical age for each variable. Note that panels (a), (d), and (g) have a log y-axis. This figure is identical to Figure 6.2 except that it uses the location of the lowest 25% of CO data to determine the background concentrations of each species.

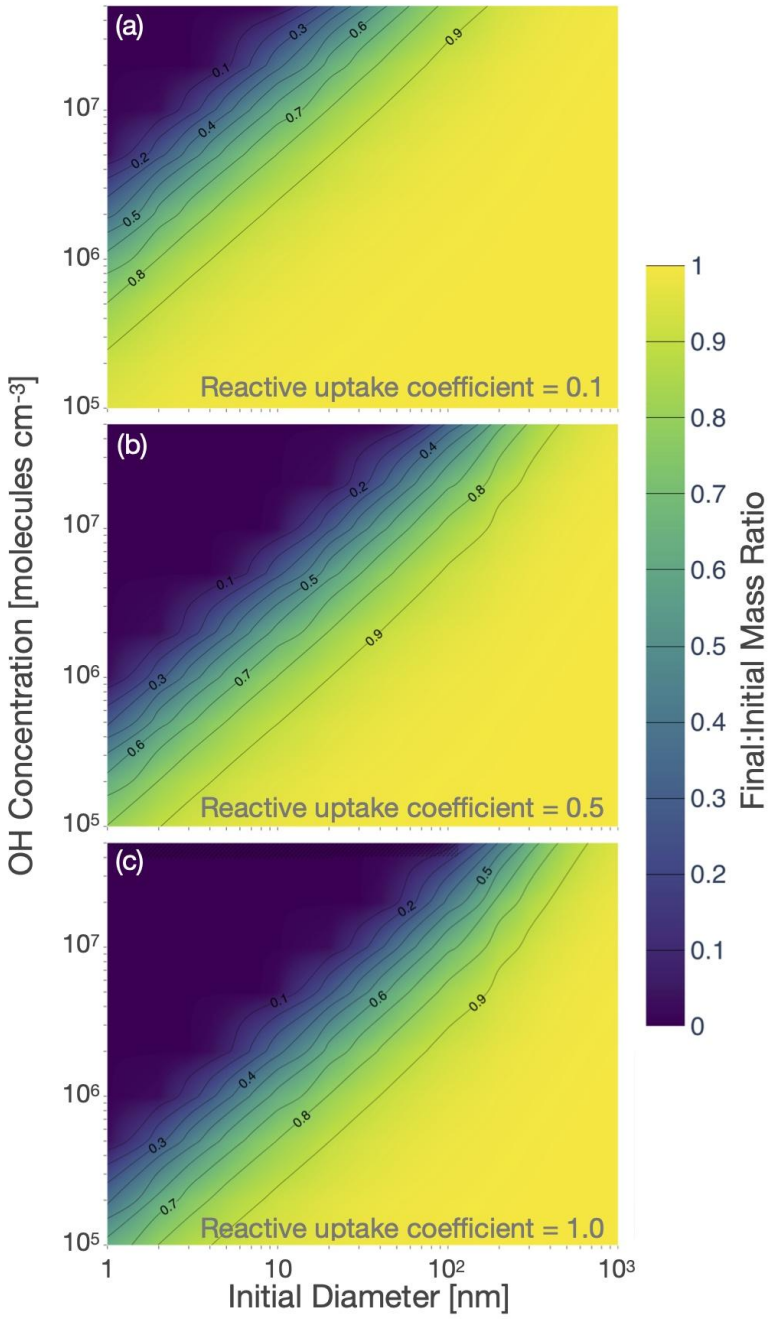

Figure E23. Calculated (final aerosol mass):(initial aerosol mass) ratios for mass loss through heterogeneous chemistry over a range of aerosol diameters and OH concentrations. As an upper-bound case, (a) it is assumed that for each OH collision, 200 amu of mass is lost. As a middle-bound, (b) it is assumed that 50% of OH collisions result in a 200 amu mass loss. As a more-realistic loss rate, (c) assumes that 10% of all OH collisions result in an 200 amu mass loss. See Appendix E for more details.

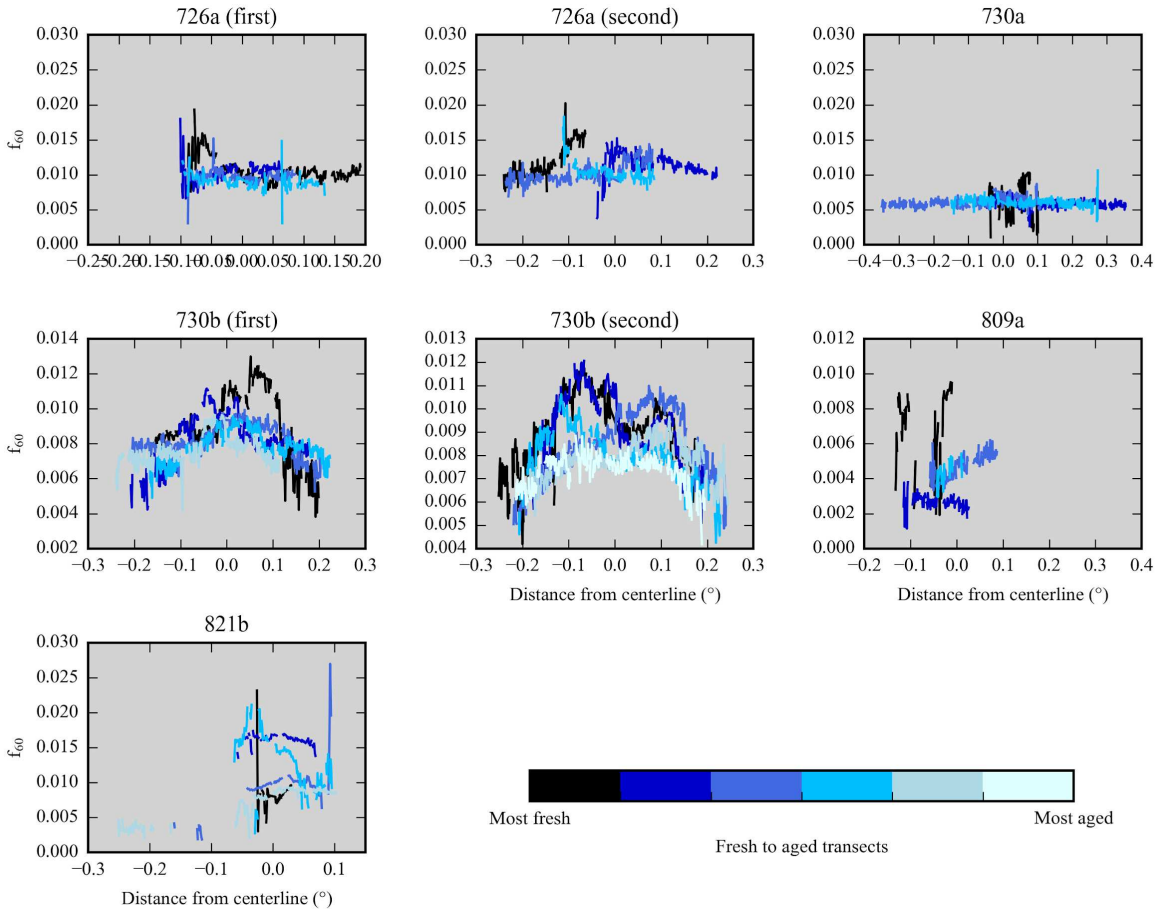

Figure E24. Raw f_{60} data for each flight along each transect included in this study. The titles indicate the flight. The black color indicates the earliest transect, with increasingly lighter colors indicating increasingly downwind transects. The centerline was estimated from the number size distribution and the estimated center of the fire (Figures E1-E6).

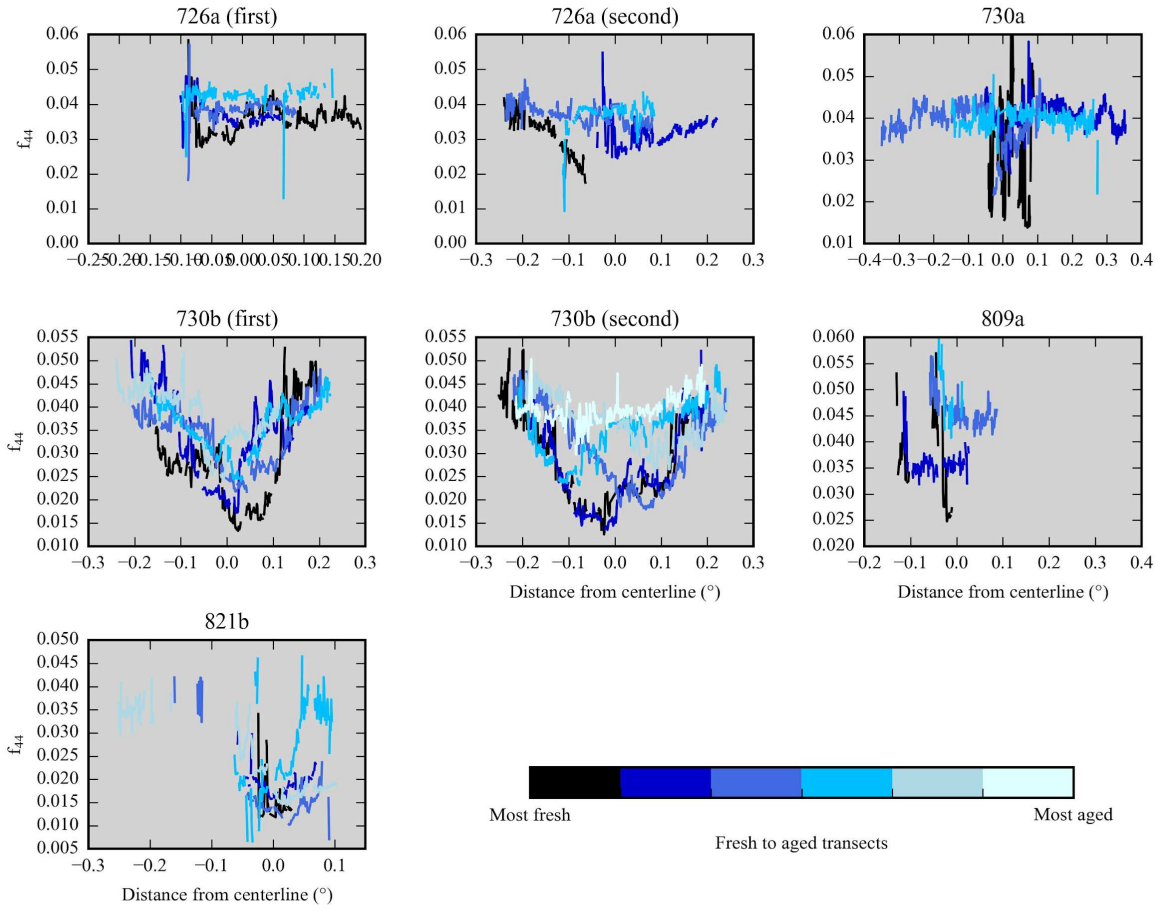

Figure E25. Raw f_{44} data for each flight along each transect included in this study. The titles indicate the flight. The black color indicates the earliest transect, with increasingly lighter colors indicating increasingly downwind transects. The centerline was estimated from the number size distribution and the estimated center of the fire (Figures E1-E6).

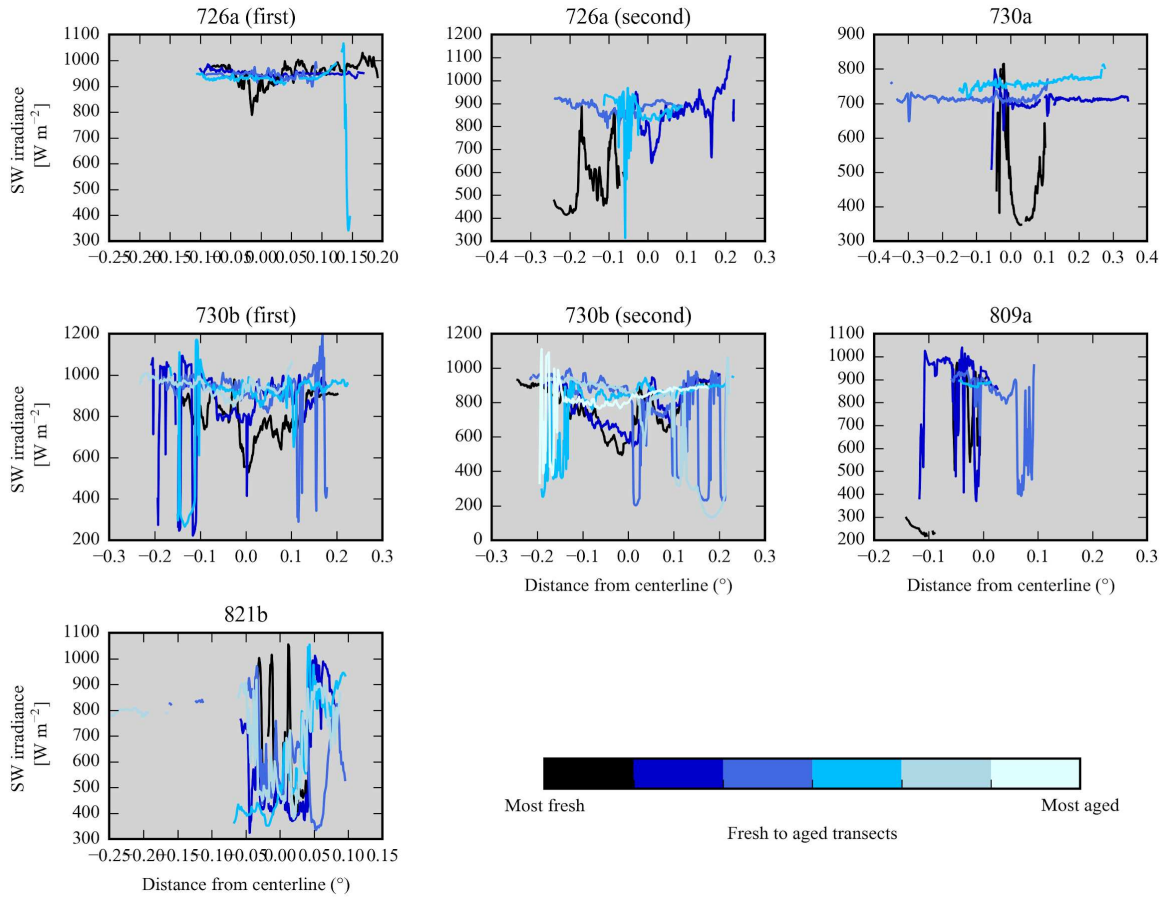

Figure E26. Total in-plume shortwave (SW) irradiance for each flight along each transect included in this study. The titles indicate the flight. The black color indicates the earliest transect, with increasingly lighter colors indicating increasingly downwind transects. The centerline was estimated from the number size distribution and the estimated center of the fire (Figures E1-E6).

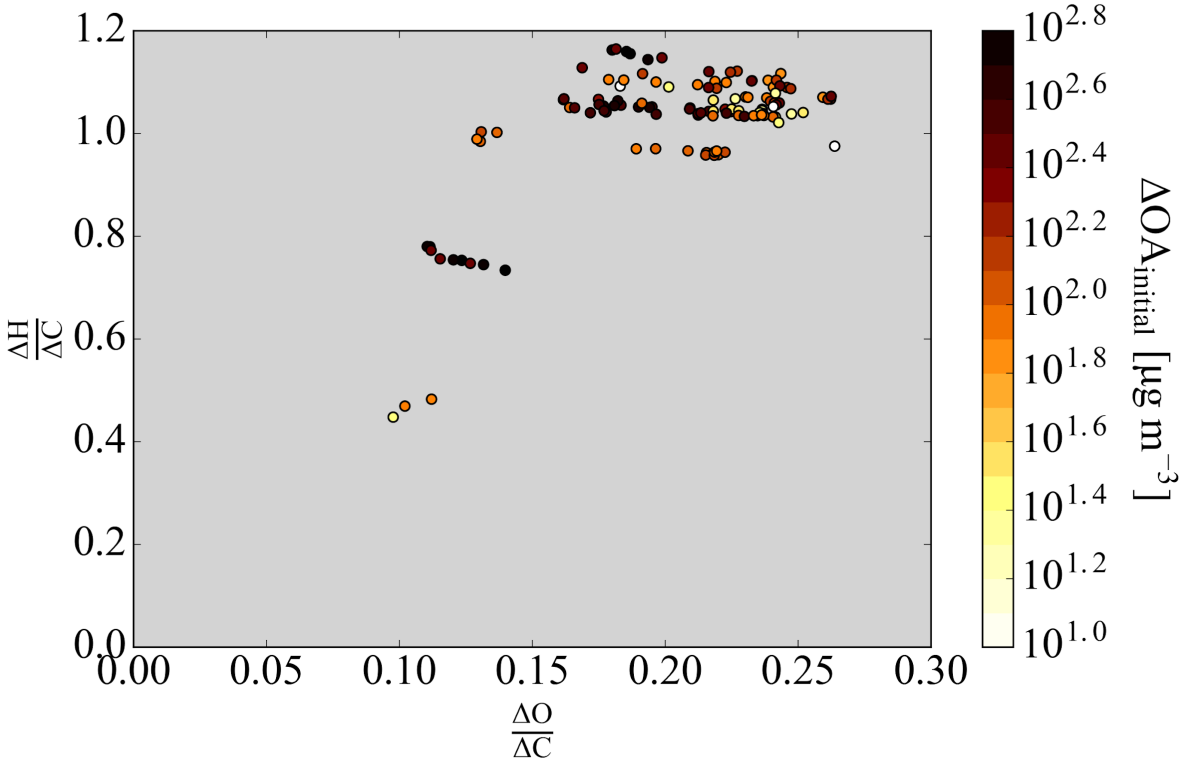

Figure E27. The Van Krevelen diagram of ΔH/ΔC versus ΔO/ΔC for all points in the 7 sets of pseudo-Lagrangian transects, colored by $\Delta OA_{initial}$.

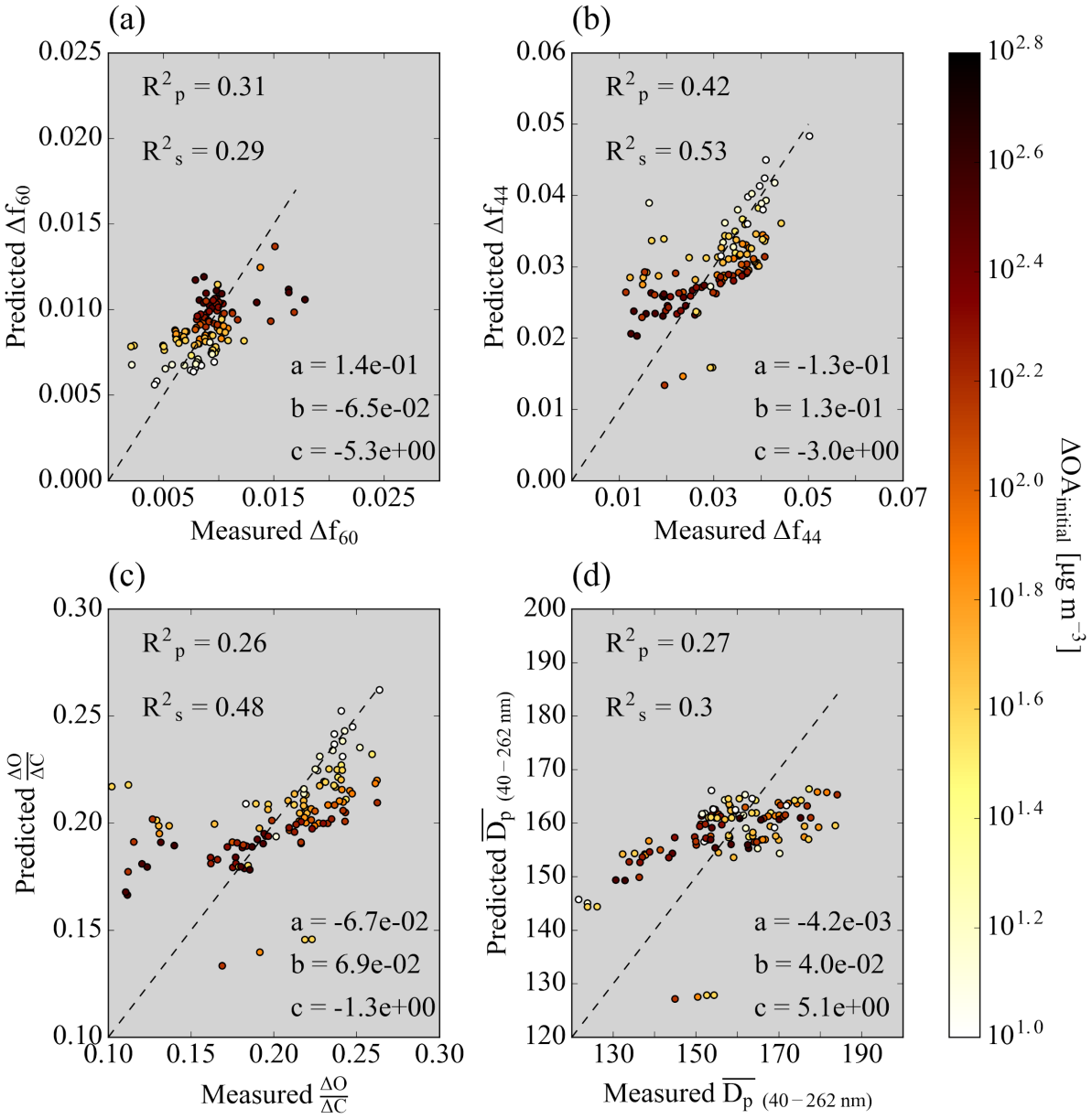

Figure E28. Measured versus predicted (a) Δf_{60}, (b) Δf_{44}, and (c) $\underline{D_p}$ between 40-262 nm, using the equation $ln(X) = a\ ln(\Delta OA_{initial}) + b\ ln(Physical\ age) + c$ where X=Δf_{60}, Δf_{44}, or $\underline{D_p}$. The values of *a, b,* and *c* when the equation is solved for *X* are provided within each subpanel, as are the Pearson and Spearman coefficients of determination (R^2_p and R^2_s, respectively). Included in the fit and figure are all four regions within the plume (the 5-15%, 15-50%, 50-90%, and 90-100% of ΔCO), all colored by the mean $\Delta OA_{initial}$ of each ΔCO percentile range.

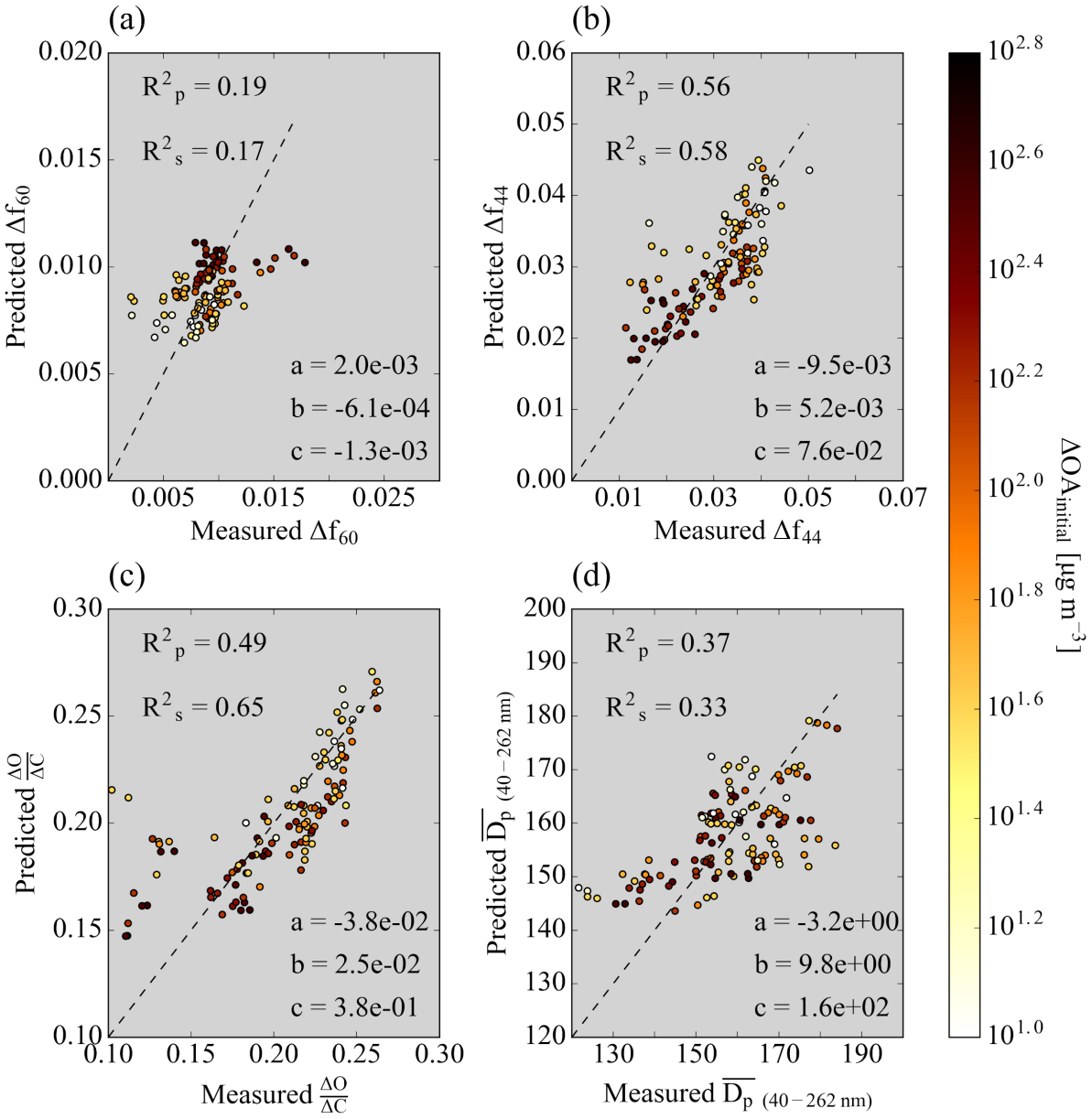

Figure E29. Measured versus predicted (a) Δf_{60}, (b) Δf_{44}, and (c) $\underline{D_p}$ between 40-300 nm, using the equation $X = a\ log_{10}(\Delta N_{\ initial}) + b\ (Physical\ age) + c$ where X=Δf_{60}, Δf_{44}, or $\underline{D_p}$ where X=Δf_{60}, Δf_{44}, or $\underline{D_p}$. Note that the fit here is the same as that in Eq. 2 except that $\Delta N_{initial}$ replaces $\Delta OA_{initial}$. The values of *a, b,* and *c* when the equation is solved for *X* are provided within each subpanel, as are the Pearson and Spearman coefficients of determination (R^2_p and R^2_s, respectively). Included in the fit and figure are all four regions within the plume (the 5-15%, 15-50%, 50-90%, and 90-100% of ΔCO), all colored by the mean $\Delta OA_{initial}$ of each ΔCO percentile range.

REFERENCES

Badosa, Jordi, John Wood, Philippe Blanc, Charles N. Long, Laurent Vuilleumier, Dominique Demengel, and Martial Haeffelin. 2014. “Solar Irradiances Measured Using SPN1 Radiometers: Uncertainties and Clues for Development.” *Atmospheric Measurement Techniques* 7: 4267–83.

Long, C. N., A. Bucholtz, H. Jonsson, B. Schmid, A. Vogelmann, and J. Wood. 2010. “A Method of Correcting for Tilt from Horizontal in Downwelling Shortwave Irradiance Measurements on Moving Platforms.” *The Open Atmospheric Science Journal*. https://doi.org/10.2174/1874282301004010078.

Slade, Jonathan H., and Daniel A. Knopf. 2013. “Heterogeneous OH Oxidation of Biomass Burning Organic Aerosol Surrogate Compounds: Assessment of Volatilisation Products and the Role of OH Concentration on the Reactive Uptake Kinetics.” *Physical Chemistry Chemical Physics: PCCP* 15 (16): 5898–5915.

Wang, J., Pikridas, M., Spielman, S. R., and Pinterich, T.: A fast integrated mobility spectrometer for rapid measurement of sub-micrometer aerosol size distribution, Part I: Design and model evaluation, J. Aerosol Sci., 108, 44-55, 10.1016/j.jaerosci.2017.02.012, 2017.